

Hans Joachim Eichler · Jürgen Eichler
Oliver Lux

Lasers

Basics, Advances and Applications



Springer

Springer Series in Optical Sciences

Volume 220

Founded by

H. K. V. Lotsch

Editor-in-chief

William T. Rhodes, Georgia Institute of Technology, Atlanta, USA

Series editors

Ali Adibi, Georgia Institute of Technology, Atlanta, USA

Toshimitsu Asakura, Hokkai-Gakuen University, Sapporo, Japan

Theodor W. Hänsch, Max-Planck-Institut für Quantenoptik, Garching, Germany

Ferenc Krausz, Ludwig-Maximilians-Universität München, Garching, Germany

Barry R. Masters, Cambridge, USA

Katsumi Midorikawa, Saitama, Japan

Bo A. J. Monemar, Department of Physics and Measurement Technology,
Linköping University, Linköping, Sweden

Herbert Venghaus, Fraunhofer Institut für Nachrichtentechnik, Berlin, Germany

Horst Weber, Technische Universität Berlin, Berlin, Germany

Harald Weinfurter, Ludwig-Maximilians-Universität München, München,
Germany

Springer Series in Optical Sciences is led by Editor-in-Chief William T. Rhodes, Georgia Institute of Technology, USA, and provides an expanding selection of research monographs in all major areas of optics:

- lasers and quantum optics
- ultrafast phenomena
- optical spectroscopy techniques
- optoelectronics
- information optics
- applied laser technology
- industrial applications and
- other topics of contemporary interest

With this broad coverage of topics the series is useful to research scientists and engineers who need up-to-date reference books.

More information about this series at <http://www.springer.com/series/624>

Hans Joachim Eichler · Jürgen Eichler
Oliver Lux

Lasers

Basics, Advances and Applications



Springer

Hans Joachim Eichler
Institut für Optik und Atomare Physik
Technische Universität Berlin
Berlin, Germany

Oliver Lux
Institute of Atmospheric Physics
German Aerospace Center (DLR)
Weßling, Germany

Jürgen Eichler
Beuth Hochschule für Technik
Berlin, Germany

ISSN 0342-4111 ISSN 1556-1534 (electronic)
Springer Series in Optical Sciences
ISBN 978-3-319-99893-0 ISBN 978-3-319-99895-4 (eBook)
<https://doi.org/10.1007/978-3-319-99895-4>

Library of Congress Control Number: 2018952904

© Springer Nature Switzerland AG 2018

This work is subject to copyright. All rights are reserved by the Publisher, whether the whole or part of the material is concerned, specifically the rights of translation, reprinting, reuse of illustrations, recitation, broadcasting, reproduction on microfilms or in any other physical way, and transmission or information storage and retrieval, electronic adaptation, computer software, or by similar or dissimilar methodology now known or hereafter developed.

The use of general descriptive names, registered names, trademarks, service marks, etc. in this publication does not imply, even in the absence of a specific statement, that such names are exempt from the relevant protective laws and regulations and therefore free for general use.

The publisher, the authors and the editors are safe to assume that the advice and information in this book are believed to be true and accurate at the date of publication. Neither the publisher nor the authors or the editors give a warranty, express or implied, with respect to the material contained herein or for any errors or omissions that may have been made. The publisher remains neutral with regard to jurisdictional claims in published maps and institutional affiliations.

This Springer imprint is published by the registered company Springer Nature Switzerland AG
The registered company address is: Gewerbestrasse 11, 6330 Cham, Switzerland

Preface

This book provides a comprehensive overview of various laser sources and their applications in the fields of science, industry, and medicine. After an introduction to the basics of laser physics, different laser types and materials are summarized in the context of a historical survey, outlining the development of laser technology since the first experimental demonstration in 1960. Gas lasers and a wide range of solid-state and semiconductor lasers are described with particular attention to high-power sources. The monograph predominantly focuses on the laser materials while electrical power supplies and mechanical engineering are only sketched.

Laser beam propagation both in free-space and optical fibers, different resonator designs as well as the functionality of various optical and opto-electronic laser components are treated from an engineering point of view. Laser modulation and pulse generation are reviewed leading to the discussion of extreme laser sources with ultra-short pulse widths below femtoseconds and pulse peak powers greater than petawatts. The book also describes techniques for nonlinear frequency conversion extending the range of available laser frequencies into the THz- and X-ray region.

Finally, the great importance of lasers in everyday life and modern technology as well as its potential for future developments is discussed. The focus is on biomedical and material processing applications, but prestigious large-scale projects for gravitational wave detection, laser fusion, and spaceborne lidar missions are also presented.

The book gives a broad and up-to-date coverage of laser photonics and opto-electronics, providing main results and recent advancements rather than in-depth theoretical treatment. Following in the steps of eight German and two Russian editions, this new English edition is targeted not only at university students, physicists, and engineers but also at any scientist and professional applying lasers in biomedicine, material processing, consumer products, and their manufacturing.

We acknowledge the scientific and technical support of recent and present members of the Laser Group at the Technische Universität Berlin, C. Junghans, J. Laufer, S. G. Strohmaier, M. H. Azhdast, and I. Usenov as well as representatives

of the worldwide laser community, V. Artyushenko, ART photonics GmbH, Berlin, Germany, C. Ascheron, Springer Verlag, Heidelberg, Germany, W. Gries, NKT Photonics, Copenhagen, Denmark, W. Bohn, German Aerospace Center, Stuttgart, Germany, D. A. Pintsov, San Diego, USA, and M. Schulze, Coherent Inc., Santa Clara, USA.

Berlin, Germany
October 2018

Hans Joachim Eichler
Jürgen Eichler
Oliver Lux

Contents

Part I Emission of Light and Laser Fundamentals

1	Light, Atoms, Molecules, Solids	3
1.1	Characteristics of Light: Waves and Photons	3
1.2	Atoms: Energy Levels	8
1.3	Many-Electron Atoms	10
1.4	Molecules	13
1.5	Energy Levels in Solids	17
1.6	Energy Bands in Semiconductors	20
	Further Reading	27
2	Absorption and Emission of Light	29
2.1	Absorption	29
2.2	Spontaneous Emission	31
2.3	Light Amplification by Stimulated Emission	32
2.4	Linewidth	35
2.5	Population Inversion, Gain Depletion and Saturation	39
2.6	Light Emission by Accelerated Electrons	41
2.7	Basic Laser Setup	42
2.8	Temporal Emission Behavior	45
	Further Reading	49
3	Laser Types	51
3.1	Wavelengths and Output Powers	53
3.2	Tunable Lasers	57
3.3	Frequency-Stable Lasers	59
3.4	High-Power Lasers	59
3.5	Ultra-short Light Pulses	60
3.6	Beam Parameters and Stability	61
	Further Reading	62

Part II Gas and Liquid Lasers

4	Laser Transitions in Neutral Atoms	65
4.1	Helium–Neon Lasers	65
4.2	Atomic Metal Vapor Lasers	71
4.3	Iodine Lasers	74
	Further Reading	76
5	Ion Lasers	77
5.1	Lasers for Short Wavelengths	77
5.2	Noble Gas Ion Lasers	79
5.3	Metal Vapor Ion Lasers	83
	Further Reading	88
6	Infrared Molecular Gas Lasers	89
6.1	Far-Infrared Lasers	89
6.2	CO ₂ Lasers	92
6.3	CO Lasers	104
6.4	HF Lasers, Chemical Lasers	106
	Further Reading	110
7	Ultraviolet Molecular Gas Lasers	111
7.1	Nitrogen Lasers	111
7.2	Excimer Lasers	114
	Further Reading	120
8	Dye Lasers	121
8.1	Laser Action in Dyes	121
8.2	Laser-Pumped Dye Lasers	124
8.3	Polymer and Liquid Crystal Lasers	129
	Further Reading	130

Part III Solid-State and Semiconductor Lasers

9	Solid-State Lasers	133
9.1	Ruby Lasers	134
9.2	Neodymium Lasers	138
9.3	Erbium, Holmium and Thulium Lasers	147
9.4	Tunable Solid-State Lasers	151
9.5	Diode Pumping and High-Power Operation	158
	Further Reading	164
10	Semiconductor Lasers	165
10.1	Light Amplification in p-n Diodes	168
10.2	GaAlAs and InGaAsP Lasers	170
10.3	Design of Diode Lasers	172

10.4	Characteristics of Diode Laser Emission	184
10.5	Wavelength Selection and Tuning of Diode Lasers	189
10.6	Surface-Emitting Diode Lasers	192
10.7	Semiconductor Lasers for the Mid-IR and THz-Region	195
10.8	Ultraviolet and Visible InGaAs Lasers	199
10.9	Diode Lasers for Optical Communication	201
	Further Reading	203

Part IV Free and Guided Light Wave Propagation

11	Laser Beam Propagation in Free Space	207
11.1	Plane and Spherical Waves, Diffraction	207
11.2	Gaussian Beams	209
11.3	Propagation of Gaussian Beams Through Lenses	216
11.4	Telescopes and Spatial Frequency Filters	219
11.5	Propagation of Multimode, Real Laser Beams	222
	Further Reading	229
12	Optical Resonators	231
12.1	Plane-Mirror Resonators	231
12.2	Spherical-Mirror Resonators	234
12.3	Resonator Configurations and Stability	238
	Further Reading	244
13	Optical Waveguides and Glass Fibers	245
13.1	Optical Materials	245
13.2	Planar, Rectangular and Cylindrical Waveguides	248
13.3	Fiber Types	255
13.4	Fiber Damping, Dispersion and Nonlinearities	260
	Further Reading	266

Part V Optical Elements for Lasers

14	Mirrors	269
14.1	Reflection and Refraction	270
14.2	Dielectric Multilayer Mirrors	275
14.3	Beam Splitters	280
14.4	Phase Conjugate Mirrors	281
	Further Reading	287
15	Polarization	289
15.1	Types of Polarization	289
15.2	Birefringence	291
15.3	Polarizers and Retardation Plates	294
	Further Reading	298

16 Modulation and Deflection	299
16.1 Mechanical Modulators and Scanners	299
16.2 Acousto-optic Modulators	301
16.3 Electro-optic Modulators	305
16.4 Optical Isolators and Saturable Absorbers	308
Further Reading	311
 Part VI Laser Operation Modes	
17 Pulsed Operation	315
17.1 Laser Spiking	316
17.2 Q-Switching	318
17.3 Cavity-Dumping	322
17.4 Mode-Locking	322
17.5 Amplification and Compression	331
Further Reading	334
18 Frequency Selection and Tuning	335
18.1 Frequency Tuning	335
18.2 Longitudinal Mode Selection	336
18.3 Prisms	341
18.4 Gratings	342
18.5 Fabry-Pérot Etalons	344
18.6 Birefringent Filters	346
Further Reading	348
19 Frequency Conversion	349
19.1 Doppler Effect	349
19.2 Nonlinear Optical Effects	350
19.3 Second and Higher Harmonic Generation	351
19.4 Parametric Amplifiers and Oscillators	357
19.5 Stimulated Raman Scattering and Raman Lasers	359
19.6 Supercontinuum Generation	363
Further Reading	365
20 Stability and Coherence	367
20.1 Power Stability	367
20.2 Frequency Stability	369
20.3 Shot Noise and Squeezed States	373
20.4 Coherence	375
Further Reading	378

Part VII Laser Metrology and Spectroscopy

21 Photodetectors	381
21.1 Radiometric and Photometric Quantities	381
21.2 Thermal Detectors	382
21.3 Vacuum Photodetectors	385
21.4 Semiconductor Detectors	389
21.5 Autocorrelation and FROG	394
Further Reading	395
22 Spectrometers and Interferometers	397
22.1 Prism Spectrometers	397
22.2 Grating Spectrometers	399
22.3 Double Beam Interferometers	399
22.4 Fabry-Pérot and Fizeau Interferometers	401
22.5 Optical Heterodyne Detection	403
22.6 Optical Frequency Combs	404
Further Reading	406

Part VIII Material Processing, Medicine and Further Applications

23 Material Processing	409
23.1 Laser Interaction with Materials	409
23.2 Lasers for Material Processing	411
23.3 Processing Applications	414
Further Reading	421
24 Medical Applications and Biophotonics	423
24.1 Operating Regimes of Medical Lasers	423
24.2 Laser Surgery	428
24.3 Biophotonics and Spectroscopic Diagnostics	435
24.4 Biological Aspects of Laser Safety	445
Further Reading	458
25 Further Applications and Future Potential	459
25.1 Lasers in Everyday Life and Consumer Goods	460
25.2 Optical Communication	467
25.3 Light Detection and Ranging	470
25.4 Holography and Interferometry	475
25.5 Free-Electron Lasers, X-Ray and XUV Lasers, Atom Lasers	479
25.6 Gravitational Wave Detection and Extreme High-Power Lasers	494
25.7 Perspectives of Laser Development	499
25.8 Economic Aspects	502
Further Reading	504
Index	505

Part I

Emission of Light and Laser Fundamentals

Since the experimental realization of the first lasers, the ruby laser in 1960 and the helium–neon laser in 1961, many further systems have been developed. At the beginning of this book, the basics of laser physics are introduced, followed by the description of the most important and prevalent laser types: gas and liquid lasers as well as solid-state and semiconductor lasers. Afterward, the focus is put on optical elements and electronic components used for modification and characterization of laser beams. The large variety of laser systems, their different operating modes, and their manifold properties allow for numerous applications in science and technology as well as in everyday life. The enormous application potential of lasers is presented in the final chapters.

Chapter 1

Light, Atoms, Molecules, Solids



In contrast to light emitted by light bulbs, gas discharge lamps or LEDs, lasers are characterized by low divergence, narrow linewidth, high intensity and the possibility for generating short pulses. The following chapter provides an overview of the fundamentals required for the understanding of lasers. In particular, the properties of light and the energy states of atoms, molecules and solids which emit light by laser transitions are discussed.

1.1 Characteristics of Light: Waves and Photons

Simplified models are often used for the description of light. A first approach are light rays emerging from light sources, e.g. the sun or a laser. According to quantum theory, these rays can be considered as straight stream of light particles or photons that are emitted from the source. However, the bending of light around the corners of an obstacle which occurs for example when light is guided through a narrow aperture cannot be explained by the particle model. Here, light is better described in terms of waves. A unified theory taking account of the wave-particle duality of light requires advanced mathematics and will thus not be used in the following. For most phenomena either the particle model or the wave model is sufficient for understanding the behavior of light. For instance, light absorption and emission is best described in terms of the particle model, whereas the wave model is most appropriate for explaining light propagation and interference.

Light Waves, Electromagnetic Radiation

In wave optics light is regarded as electromagnetic wave which is a transverse wave of a coupled electric field \mathbf{E} and magnetic field \mathbf{H} which oscillate periodically at the

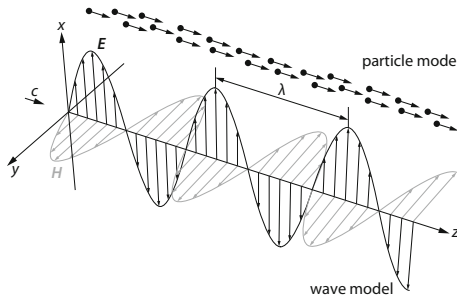


Fig. 1.1 Electric \mathbf{E} and magnetic field \mathbf{H} of a plane wave at a fixed time. The wave propagates along the z direction, while the distance to the light source is assumed to be large compared to the wavelength λ (far field regime). The figure also illustrates the particle model which considers light as a stream of photons

same frequency f . The vectors \mathbf{E} and \mathbf{H} are perpendicular to each other and perpendicular to the direction of energy and wave propagation, as shown in Fig. 1.1, which depicts the two fields at a fixed time along the propagation direction.

For visualizing the spatial structure of light waves, the wave fronts (or phase fronts) are considered, e.g. planes of maximum field amplitude at a fixed time. The distance between adjacent phase fronts is the wavelength λ . While the phase fronts of a plane wave are parallel planes, they are concentric spheres in case of a spherical wave, as illustrated in Fig. 1.2. A spatially narrow portion of a wave can be regarded as a beam whose the propagation direction is perpendicular to the respective wave fronts. The frequency f , wavelength λ and propagation velocity c are related to each other:

$$\boxed{c = \lambda \cdot f}. \quad (1.1)$$

In vacuum, the light velocity is $c = 2.998 \times 10^8$ m/s. The reciprocal of the wavelength $1/\lambda$ is referred to as wavenumber (unit: cm^{-1}). A more comprehensive treatment of light propagation is given in Chap. 11.

Most optical phenomena can be accounted for by only considering the electric field. However, the field (strength) is difficult to measure because of the high

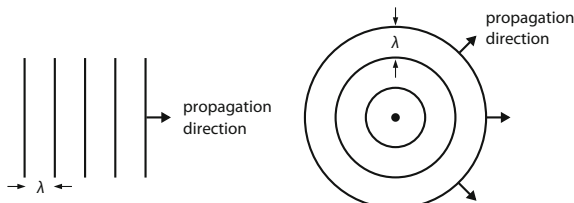


Fig. 1.2 Simplified illustration of light waves. Left: plane wave propagating in one direction, right: spherical wave propagating in radial directions. The propagation direction is perpendicular to the phase fronts (or wave fronts) which are indicated as black lines and describe planes or spheres of equal phase, e.g. maximum amplitude

frequency of light. Instead the power density or intensity I can be determined which is defined as the time-averaged square of the field amplitude E :

$$I = \sqrt{\epsilon\epsilon_0/\mu\mu_0} \cdot \overline{E^2}. \quad (1.2)$$

In this equation, $\epsilon_0 = 8.854 \times 10^{-12}$ As/Vm is the vacuum permittivity, ϵ is the relative permittivity, $\mu_0 = 4\pi \times 10^{-7}$ Vs/Am is the vacuum permeability and μ is the relative permeability. The horizontal bar on top of E^2 indicates the temporal average. The units of the electric field E and the intensity I are V/m and W/m², respectively. The proportionality constant $Z = \sqrt{\epsilon\epsilon_0/\mu\mu_0}$ has the dimension of an impedance and is thus referred to as wave impedance. For vacuum and air ($\epsilon = 1$, $\mu = 1$), the impedance is $Z = \sqrt{\epsilon_0/\mu_0} \approx 377 \Omega$.

In a transparent medium, light propagation is slower than in vacuum and the light velocity c' is given as

$$c' = c/n. \quad (1.3a)$$

The material constant n is the refractive index which is related to the relative permittivity and permeability:

$$n = \sqrt{\epsilon\mu}. \quad (1.3b)$$

When light is incident on the interface between two media of different refractive indices n_1 and n_2 , the relationship between the angle of incidence α_1 and the angle of refraction α_2 is described by Snell's law:

$$n_1 \sin \alpha_1 = n_2 \sin \alpha_2, \quad (1.4)$$

where the angles are defined with respect to the normal to the interface.

The intensity I , which describes the power density per area carried by the wave, is related to the energy density ρ (per volume), thus defining the energy transmitted per unit area and time:

$$I = \rho c, \quad (1.5)$$

Photons

According to quantum theory, light can be discussed in terms of both particles and waves. In the particle model, light is considered as quanta of the electromagnetic field or photons which carry the energy W and move at the speed of light c

$$\boxed{W = hf = hc/\lambda}. \quad (1.6)$$

Here, $h = 6.626 \times 10^{-34}$ Js is Planck's constant, while f and λ are the frequency and wavelength, respectively. In atomic or laser physics, the photon energy is

conveniently given in the unit electron volt which is written as eV. 1 eV is the amount of energy ($W = eU$, $e = 1.602 \times 10^{-19}$ As) gained by the charge of a single electron moving across an electric potential difference U of one volt:

$$1 \text{ eV} = 1.602 \times 10^{-19} \text{ J}. \quad (1.7)$$

When the wavelength of the light λ is known in μm , the corresponding photon energy is $W = 1.24 \mu\text{m} \text{ eV}/\lambda$.

The energy density ρ and intensity I of light are related to the photon density Φ (photons per area) and photon flux φ (photons per area and time) as

$$\rho = hf \cdot \Phi, \quad (1.8a)$$

$$I = hf \cdot \varphi. \quad (1.8b)$$

Polarization

In case the direction of the electric field vector \mathbf{E} is confined to a fixed plane along the direction of propagation, the wave is said to be linearly polarized. A more detailed discussion of polarization properties of light is provided in Chap. 15. The light of most light sources (sun, light bulb, gas discharge lamp) is unpolarized and can be regarded as a random mixture of waves with all possible polarization states.

Fig. 1.3 Spectral sensitivity of the human eye:
 $V(\lambda)$ = light-adapted (photopic) case,
 $V'(\lambda)$ = dark-adapted (scotopic) case

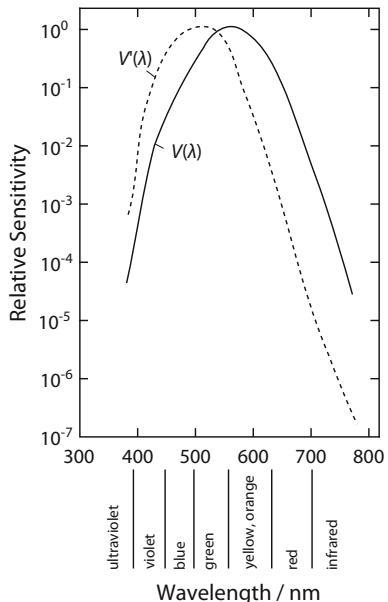
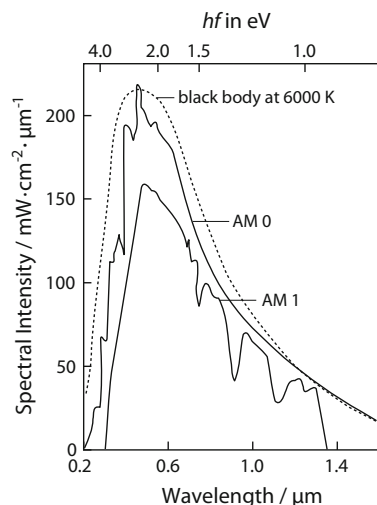


Table 1.1 Designations, wavelengths λ , frequencies f and photon energies hf of electromagnetic radiation

Designation	λ	f	hf
Gamma radiation	<50 pm	$>6 \times 10^{18}$ Hz	>24.8 keV
X-ray	<10 nm	$>3 \times 10^{16}$ Hz	>124 eV
Vacuum-ultraviolet (VUV)	<100 nm	$>3 \times 10^{15}$ Hz	>12.4 eV
Far-ultraviolet (UV-C)	<280 nm	$>1.07 \times 10^{15}$ Hz	>4.4 eV
Mid-ultraviolet (UV-B)	<315 nm	>950 THz	>3.9 eV
Near-ultraviolet (UV-A)	<380 nm	>790 THz	>3.3 eV
Visible	<780 nm	>390 THz	>1.6 eV
Near-infrared (IR-A)	<1.4 μm	>210 THz	>0.9 eV
Near-infrared (IR-B)	<3 μm	>100 THz	>0.4 eV
Mid-infrared (IR-C)	<50 μm	>6 THz	>25 meV
Far-infrared, THz radiation (IR-C)	<1 mm	>300 GHz	>1.24 meV
Microwaves	<1 cm	>30 GHz	>124 μeV
Radio waves	<1 km	>300 kHz	>1.24 neV

The given spectral regions are not sharply defined, note that the values are only approximates ($1 \text{ eV} = 1.602 \times 10^{-19} \text{ J}$)

Fig. 1.4 Solar spectrum in comparison with the emission spectrum of a black body at 6000 K (AM = air mass, AM0 = spectrum above Earth's atmosphere, AM1 = spectrum on Earth below atmosphere)



The Color of Light

Visible light is the narrow band of wavelengths which can be perceived by the human eye and represents only a very small portion within the enormous range of wavelengths of the electromagnetic spectrum. The color of the light is determined by its frequency or wavelength, respectively. The sensitivity of the eye varies

strongly with the wavelength, as shown in Fig. 1.3. The visible spectral region is followed by the ultraviolet range towards shorter wavelengths and by the infrared spectral range towards longer wavelengths (Table 1.1). The solar spectrum has its maximum in the visible spectral range and can be approximated by the emission spectrum of a black body at 6000 K (Fig. 1.4).

1.2 Atoms: Energy Levels

The hydrogen atom is the simplest atom, consisting of a positively charged proton and a negatively charged electron which is bound to the nucleus by the attractive Coulomb force. According to the Bohr model, the electron orbits the nucleus along a circular path, where only certain orbit radii are permitted (Fig. 1.5), corresponding to discrete energies E_n . The electron energies are determined by the principal quantum number n as follows:

$$E_n = -E_i/n^2 \quad n = 1, 2, 3, \dots \quad (1.9)$$

with E_i being the ionization energy. For the hydrogen atom, the energy is $E_i = 13.6$ eV.

The energy values (or energy levels) E_n can be illustrated by energy level diagrams as shown in Fig. 1.6. The negative sign indicates that the inner orbits are related to lower electron energies than the outer orbits. Hence, energy has to be supplied for lifting the electron from a lower to a higher orbit, or to ionize it. The principal quantum number $n = 1$ belongs to the orbit with the smallest radius $r_1 = 0.53 \times 10^{-10}$ m and the lowest energy $E_1 = -E_i = -13.6$ eV.

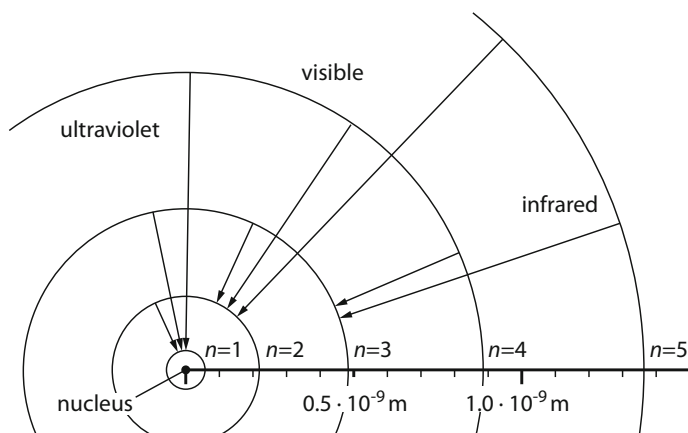
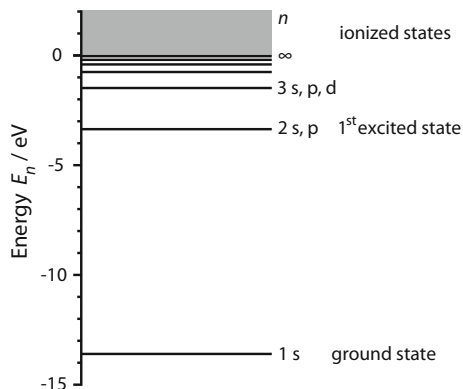


Fig. 1.5 Electron orbitals in a hydrogen atom. The orbit radii are $r_n = 0.53 \times 10^{-10} n^2$ meter

Fig. 1.6 Energy level diagram of the hydrogen atom with the main quantum numbers $n = 1, 2, 3$ and the orbital quantum number $l = s, p, d, f, \dots$, i.e. $l = 0, 1, 2, 3, \dots$



The Bohr model was superseded by modern *quantum mechanics* where the state of an electron in an atom is represented by a wave function Ψ_{nlm_l} which is defined by three quantum numbers n, l , and m_l (Table 1.2). The square of the wave function $|\Psi|^2$ is the probability distribution describing the chance of finding an electron at a certain position (Fig. 1.7). The additional spin quantum number m_s is related to the intrinsic angular momentum of the electron, i.e. the rotation of the electron about its own axis.

In the field of laser physics, the generation of light in atoms, molecules and solids is of foremost importance and related to the transition of electrons from higher to lower energy levels, as indicated by arrows in Fig. 1.5. The atomic transitions result in spectral lines which are characteristic for the respective atom.

Table 1.2 Quantum numbers n, l, m_l, m_s describing electronic states in the hydrogen atom and states of single electrons in many-electron atoms

Quantum number	Possible values	Physical meaning
Principal quantum number n	1, 2, 3, ... \triangleq K-, L-, M-shell	Significant for energy of the state (for many-electron atoms the energy is also determined by the other quantum numbers), measure for the orbit radius
Azimuthal quantum number l	0, 1, 2, 3, ... ($n - 1$) \triangleq s, p, d, f, ... (n values)	Significant for the orbital momentum of the state, determines the shape of the electron density distribution which is only radial symmetric for $l = 0$
Magnetic quantum number m_l	$-l \leq m_l \leq l$ ($2l + 1$) values	Significant for the orbital momentum of the state along a certain spatial direction (e.g. magnetic field), determines the orientation of the atom in space
Spin quantum number m_s	$m_s = -\frac{1}{2}, +\frac{1}{2}$ 2 values	Significant for the intrinsic angular momentum of the state, determines the spin of the electron with respect to a certain direction in space

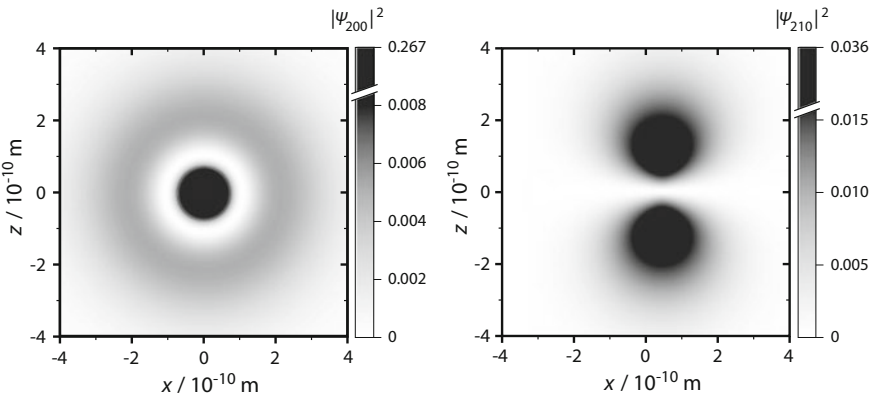


Fig. 1.7 Spatial distribution of the probability density $|\Psi_{nlm_i}|^2$ of electrons in a hydrogen atom in the first excited state $n = 2$. The quantum number m_s was omitted, because the probability density is the same for $m_s = \pm 1$. The distributions are rotational symmetric around the z -axis. The values of the probability density are given in 10^{30} m^{-3}

1.3 Many-Electron Atoms

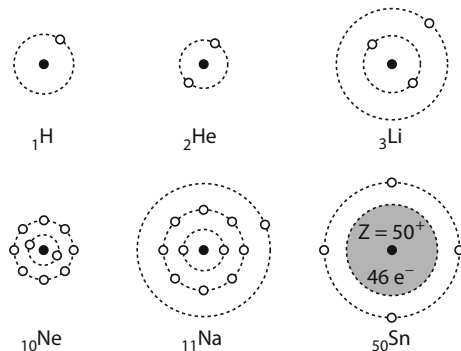
Atoms consist of a positively charged nucleus surrounded by a negatively charged electron shell which usually contains multiple electrons orbiting around the nucleus in the presence of its Coulomb field. The latter is partly screened by the inner-shell electrons so that the combined electric fields of the nucleus and all the inner-shell electrons acting on any of the outer-shell electrons can be approximated as being radial and the same for all the outer-shell electrons in the atom, meaning that every outer-shell electron sees an identical potential that is only a function of its distance from the nucleus (central field approximation).

As a consequence, like for the hydrogen atom, any electronic state $\Psi_{nlm_lm_s}$ is defined by a set of four quantum numbers (n, l, m_l, m_s) according to Table 1.2. The Pauli exclusion principle states that each electron in the atom has a unique set of quantum numbers.

The order in which the atomic orbitals are filled follows several rules, according to which the orbitals with a lower $(n + l)$ value are filled before those with higher $(n + l)$ values. In the case of equal $(n + l)$ values, the orbital with a lower principal quantum number is filled first. Due to the Pauli exclusion principle, every shell (electrons with equal n) can hold $2n^2$ electrons. The successive filling of the electron shells can be comprehended by regarding the electron shell diagrams of atoms with increasing atomic number (Fig. 1.8). At atomic numbers greater than 18, irregularities occur in shell configurations in the periodic table of elements. This is especially striking for rare-earth elements which have unfilled inner shells.

The electron energy in many-electron atoms is not only determined by the principal quantum number n , but also by the azimuthal quantum number l . As

Fig. 1.8 Electron shell diagrams of selected atoms illustrating the distribution of electrons in different shells in an atom. The sizes are not true to scale



shown in Table 1.2, l can take values from 0 to $(n - 1)$, corresponding to a subdivision of the main electron shells into n sub-shells. Each sub-shell holds up to $2(2l + 1)$ electrons which are defined by different combinations of magnetic and spin quantum numbers m_l , m_s . The allocation of the electrons to the different sub-shells is called electron configuration, where the following nomenclature is consistently used in the literature: $n_1 l^a$. Here, the upper index a denotes the number of electrons in the respective sub-shell, which is determined by the principal and azimuthal quantum numbers $l = 0, 1, 2, 3$ are replaced by the letters s, p, d, f. The ground state of neon in this nomenclature is then designated as $1s^2 2s^2 2p^6$.

Electron Coupling

Aside from the attractive interaction between the nucleus and the electrons, repulsive Coulomb forces additionally exist between the individual electrons. Furthermore, an interaction occurs between the magnetic moments induced by the electron's orbit around the nucleus and its spin (spin-orbit coupling). As a result, the energy levels vary with the magnetic and spin quantum numbers (splitting of energy levels). Depending on the strength of the Coulomb and spin-orbit interaction the coupling of the angular momenta is treated in different ways. Here, three limiting cases are considered:

1. *LS coupling* (Russell-Saunders coupling) occurs when the Coulomb interaction is large compared to the spin-orbit interaction (usually for light atoms with less than 30 electrons). In this case, the single spins from each electron interact among themselves and are combined to a total spin angular momentum S , while the single orbital angular momenta couple to a total orbital angular momentum L . Due to the spin-orbit coupling, S and L are combined to form a total angular momentum J . The magnitudes of the resulting momenta are expressed in terms of the quantum numbers S , L and J ($L = 0, 1, 2, 3, \dots = S, P, D, F, \dots$).

2. *jj coupling* occurs in heavier atoms where the spin-orbit interaction is large compared to the Coulomb interaction. Here, the orbital angular momentum of each electron couples to the corresponding individual spin angular momentum, originating an individual total angular momentum with quantum number j . The latter, in turn, combine to the total angular momentum of the atom.
3. *jl coupling* (Racah coupling) occurs when the Coulomb interaction is large compared to the spin-orbit coupling for the inner electrons, but small for the outer electrons. This case is important for describing the emission spectra of heavy noble gases such as xenon.

A further quantum number that is of significance for all coupling schemes is the parity quantum number P . P can take the values $P = \pm 1$ and describes the symmetry of the wave function under reflection in space ($\Psi(x) \rightarrow \Psi(-x)$). The parity of a given wave function can be inferred from the orbital angular momenta of the electrons in each shell. For $\sum l_i = \text{odd}$, $P = -1$, whereas $P = +1$ for an even sum. States with odd parity are denoted by the upper index “o” at the right of the LS designation.

Selection Rules

The state of an atom can be changed by absorption or emission of a photon. However, the occurring transitions from one quantum state to another are constrained by selection rules. Examples of selection rules are summarized in Table 1.3. Transitions which do not obey the rules are called forbidden transitions and often related to meta-stable energy states. Absorption and emission of light is elaborated in Sect. 2.1.

Table 1.3 Selection rules for the absorption and emission of light by atoms and ions by electric dipole transitions

Selection rule	Remarks
$\Delta J = 0, \pm 1$ But: $J_{\text{initial}} = 0 \rightarrow J_{\text{final}} = 0$ forbidden	A photon has the momentum $h/2\pi$ (for dipole radiation), hence the total angular momentum J or its orientation has to change
$\sum l_i$ odd \leftrightarrow $\sum l_i$ even, i.e. no transitions between states of equal parity	The photon has even parity and the parity is a multiplicative quantum number
Only in case of LS coupling: $\Delta L = 0, \pm 1$, but: $L_{\text{initial}} = 0 \rightarrow L_{\text{final}} = 0$ forbidden	Follows from $\Delta J = 0, \pm 1$ and “intercombination prohibition”
$\Delta S = 0$ “Intercombination prohibition”, i.e. no transitions between states with different multiplicity	The photon has no magnetic moment

1.4 Molecules

Molecule is an electrically neutral configuration of two or more nuclei and an electron cloud where single electrons can either be associated to a certain nucleus or be uniformly located in the structure of the molecule. The energy states of molecules are much more complex than those of isolated atoms, since molecules not only possess energies related to electronic states, but also vibrational and rotational energies.

Electronic States

Molecules are formed by the balance between the attractive and repulsive Coulomb forces acting on the nuclei and electrons. The chemical bonds of molecules can be understood by considering a system consisting of two atoms, e.g. H and Cl. The atoms attract each other and form a diatomic molecule, whereby a mutual distance of the involved nuclei r_0 (internuclear distance) is established (Fig. 1.9a). If the

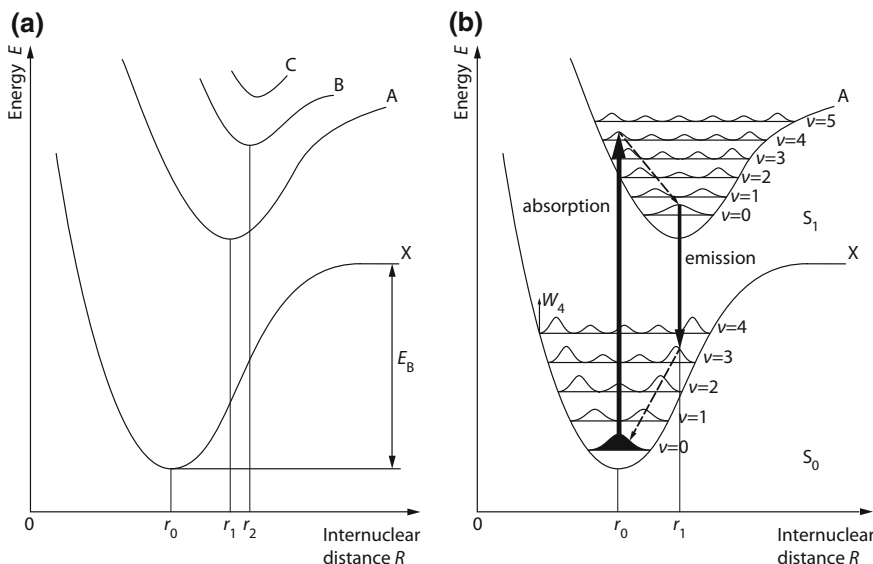


Fig. 1.9 **a** The potential curve X schematically depicts the potential energy of a diatomic molecule in dependence on the internuclear separation. The binding energy is denoted as E_B . Potential curves of excited states are designated with A, B, C, etc. **b** The vibration levels are denoted $v = 1, 2, 3, \dots$. The figure also illustrates the spatial distributions of the probability density W_v . Vibronic transitions most likely occur between states having overlapping maxima of the probability density distribution and without changes in the positions of the nuclei (Franck–Condon principle). S_0 is often referred to a ground state with antiparallel electron spins (see also Fig. 8.2)

separation between the atoms is reduced, the repulsive forces between the nuclei increase immensely, whereas the attractive forces predominate as the internuclear distance grows.

The potential curve X shown in Fig. 1.9a represents the interaction energy (potential energy) of a diatomic molecule in dependence on the internuclear distance r . The curve has a minimum at $r = r_0$ (equilibrium internuclear distance). In order to break the molecular bond and to separate the atoms, the binding energy E_B which corresponds to the depth of the potential well is required. The curve designated with the letter X is associated to the electronic ground state. Like in atoms, electrons can be excited to higher electronic states, resulting in potential curves at higher energies. Transitions of the molecule from the ground state to an excited state (denoted as A, B, C, etc.) involves a change in the internuclear separation (r_1, r_2, r_3 , etc.) as well as the binding energy.

The quantum numbers characterizing the electronic state of diatomic molecules are summarized in Table 1.4. Electronic transitions from higher to lower states results in the emission of electromagnetic radiation, often in the ultraviolet spectral range. The selection rules which apply to electric dipole transitions in molecules are given in Table 1.5.

Vibrations and Rotations

Aside from the electronic energy of molecules, two additional energy contributions are present due to the relative motion of the constituent atoms. Firstly, vibration of the atoms about the equilibrium position can occur. Secondly, the molecule as a whole

Table 1.4 Quantum numbers for diatomic molecules

Quantum number	Possible values	Physical meaning
Λ	$0, 1, 2, \dots \triangleq \Sigma, \Pi, \Delta$	Projection of the total orbital angular momentum onto the internuclear axis
S	Half-integer values	Projection of the total spin angular momentum onto the internuclear axis
$2S + 1$	$0, 1, 2, \dots$	Multiplicity, written as superscript on the left of the orbital angular momentum
Ω	$\Lambda + S, \Lambda + S - 1, \dots, \Lambda - S $	Projection of the total angular momentum onto the internuclear axis, written as subscript on the right of the orbital angular momentum
P	g, u $+, -$	Parity, space reflection symmetry Reflection symmetry along an arbitrary plane containing the internuclear axis
v	$0, 1, 2, \dots$	Vibrational quantum number
J	$0, 1, 2, \dots$	Rotational quantum number

Table 1.5 Selection rules for the absorption and emission of light by molecules (electric dipole transitions)

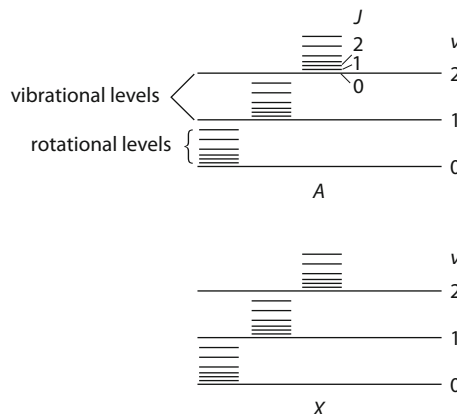
Selection rule	Remarks
$\Delta \Lambda = 0, \pm 1$	This holds for diatomic molecules
$\Delta v = \pm 1$	This holds for transitions between vibrational states within the same electronic state
$\Delta v = 0, \pm 1, \dots$	This holds for transitions between different electronic states. According to the Franck–Condon principle the distance from the nucleus does not change (Fig. 1.9b). In case of similar potential curves (no change in distance from the nucleus), $\Delta v_e = 0$ is preferred. In case of shifted potential curves X and A, v changes
$\Delta J = 0, \pm 1$	$\Delta J = 0$ holds only for electronic transitions. For rotational transitions within the same electronic state: $\Delta J = +1$ (R-branch) or $\Delta J = -1$ (P-branch)

can rotate about its principal axes of inertia. Hence, the total energy E of a molecule is composed of the electronic, vibrational and rotational energy E_e , E_v and E_J :

$$E = E_e + E_v + E_J. \quad (1.10)$$

In this case the energy is defined positive and not negative, as is the case of the H-atom. The energy of the ground states set to zero.

The electron energy is typically in the range from $E_e = 1\text{--}20$ eV. The vibration energy ranges from $E_v = 0.01\text{--}0.5$ eV, while the rotation energy is smaller than ≈ 0.01 eV. The energy level diagram of a molecule is hence more complex than that of atoms. According to Fig. 1.10 (and Fig. 1.9b), each electronic state (X, A, B, C, ...) is further subdivided into a number of equidistant vibrational levels. Each of these vibrational energy states can in turn involve multiple rotational levels. The vibration and rotation energies are quantized so that the corresponding energy levels are described by the quantum numbers $v = 0, 1, 2, 3, \dots$ and $J = 0, 1, 2, 3, \dots$,

Fig. 1.10 Energy levels in a molecule indicating electronic (X and A), vibrational and rotational states

respectively. The latter should not be confused with the total angular momentum quantum number. The vibrational and rotational energies E_v and E_J are given by

$$E_v = \left(v + \frac{1}{2}\right)hf, \quad (1.11)$$

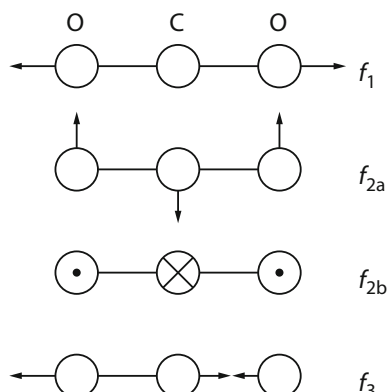
$$E_J = hcB_r J(J+1), \quad (1.12)$$

with $h = 6.626 \times 10^{-34}$ Js and $c = 3 \times 10^8$ m/s being Planck's constant and the vacuum speed of light, while f and B_r are the molecular vibration frequency and the rotational constant, respectively.

Molecules can be excited to various rotational-vibrational states (Fig. 1.9b). Relaxation to lower levels results in the emission of radiation, whereby transitions between electronic, vibrational and rotational levels that satisfy the selection rules (Table 1.5) are possible. Depending on the energy difference of the involved states, the emission wavelength is in the ultraviolet (between electronic states), infrared (between vibrational states) or far-infrared (between rotational states) spectral range.

Polyatomic molecules can vibrate in many different ways where the number of fundamental vibrations (or modes) is given by the number of atoms within the molecule. For non-linear molecules containing N atoms, the number of fundamental vibrations is $(3N - 6)$, whereas it is $(3N - 5)$ for linear molecules. This is illustrated at the example of the CO₂ molecule which is a linear, symmetric, triatomic molecule, as shown in Fig. 1.11. Here, $3 \cdot 3 - 5 = 4$ fundamental vibrations are possible: the symmetric stretching vibration with frequency f_1 , two degenerate bending vibrations with frequency $f_{2a} = f_{2b}$ and the asymmetric stretching vibration with frequency f_3 . In quantum mechanics, degenerate means that different levels have the same energy. The degree of degeneracy gives the number of different levels with the same energy. Each vibration can be excited independently from the others, while the energy in each mode is quantized. For the designation of

Fig. 1.11 Fundamental vibrations of the CO₂ molecule consisting of a central carbon atom which is bound to two oxygen atoms. The vibration frequencies are $f_1, f_{2a} = f_{2b}, f_3$



the CO_2 vibrational states, different nomenclatures are used. In the Herzberg notation, the quantum numbers for each vibration v_1 , v_2 , and v_3 are written as $(v_1\ v_2\ v_3)$, where the superscript l denotes the degree of degeneracy of the bending vibration. Alternatively, the vibrational state of the CO_2 molecule can be labelled with a five-digit (so-called HITRAN) designation $(v_1\ v_2\ l\ v_3\ r)$. The ranking index r takes account of the occurrence of resonances between levels of similar energy known as Fermi resonances (see Sect. 6.2).

The simple molecules containing only a few atoms discussed in this section are employed in infrared and ultraviolet gas lasers (Chaps. 6, 7). Dye molecules with much higher complexity are also important for laser physics as will be elaborated in Chap. 8.

1.5 Energy Levels in Solids

Solids consist of a large number of atoms or molecules which are arranged in an orderly, (usually) repeating pattern—the crystal structure. Some atoms give electrons to the solid and remain as ions in the crystal. Due to the mutual interaction of the atoms, the discrete energy levels of the isolated atoms split into energy bands consisting of a large number of closely spaced levels which can be regarded as a continuum of levels. The electrical and optical properties of the solids are primarily defined by the structure of the two uppermost, filled or partially filled bands. In partially filled bands electrons can move under the influence of electric fields and produce a current. In contrast, electrical conduction is prevented in fully filled bands due to the Pauli exclusion principle which prohibits the electrons from occupying identical states and thus the movement within the band.

A coarse classification of solids can hence be performed on the basis of the electrical conductivity. In metals, the uppermost energy band is partially filled, leading to a high conductivity which is related to a strong optical absorption so that metals are not appropriate as laser gain media. In insulators, the conduction band is unoccupied which inhibits electrical conduction. The energy difference to the subjacent band, the valence band, which is referred to as band gap energy, is too large to be overcome by absorption of visible light. Consequently, insulators such as glasses, ceramics or crystals are transparent in their pure form.

Semiconductors are intermediate between metals and insulators in terms of their electrical conductance. At low temperatures or in pure materials there is no conductivity since the conduction band is empty, while the valence band is fully occupied. The band gap energy is 1.2 eV for silicon and 1.5 eV for GaAs. This energy can be supplied by an increase in temperature or by irradiation of light, thus making the semiconductor electrically conducting. Moreover, doping of the medium provides the generation of additional electrons in the conduction band. The characteristics of the energy bands of semiconductors as well as electron transitions leading to absorption and emission of light are covered in Sect. 1.6 and Chap. 10.

Transparent Crystals Doped with Foreign Atoms

Configuration disorder or the incorporation of foreign atoms introduces defects in the lattice structure of solids. Electrons that are bound to those impurities show characteristic energy states which are determined by the crystallographic defect and the surrounding crystal lattice.

In solid-state lasers, crystals or glasses are doped with foreign atoms or ions, mostly from metals like Ti, Ni, Cr, Co, Ni, or rare-earth elements like Nd, Ho and Er. Ruby represents a typical example for such a combination of (host) crystal and dopant. Here, chromium ions (Cr^{3+}) are doped into a corundum (Al_2O_3) crystal where they replace some of the Al^{3+} -ions with a typical dopant concentration of 0.05% (see Sect. 9.1). The electrostatic crystal field influences the Cr^{3+} -ions, but is usually weaker than the Coulomb interaction between the electrons in the atom. Nevertheless, it has an effect on the energy levels of the Cr^{3+} , as shown in Fig. 1.12. On the left-hand side the energies of the free ions are given. Owing to the cubic component of the crystal field, the energy levels are shifted and split, resulting in new isolated energy states as well as several energy bands which are indicated on the right-hand side of the diagram. The trigonal component of the field and the spin-orbit coupling give rise to further splitting (not shown in the figure). It should

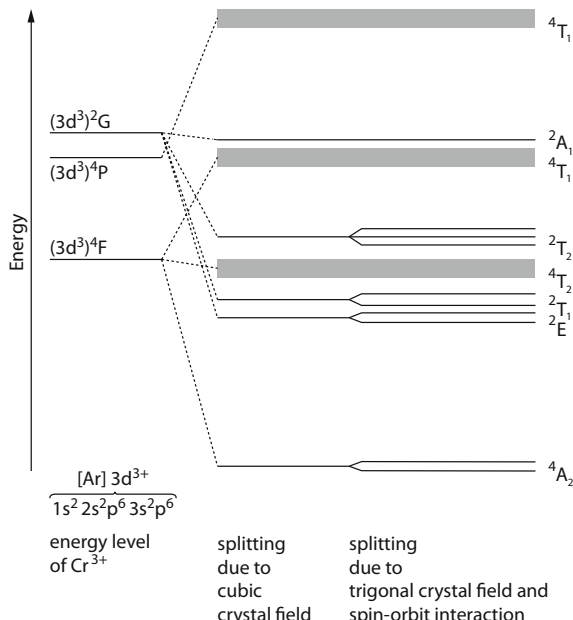


Fig. 1.12 Energy level diagram of a ruby crystal ($\text{Cr}^{3+}:\text{Al}_2\text{O}_3$)

be noted, that the denotation of the energy states using the letters A, E, T, ... is not related to the orbital angular momentum, but to the symmetry properties of the electron distributions.

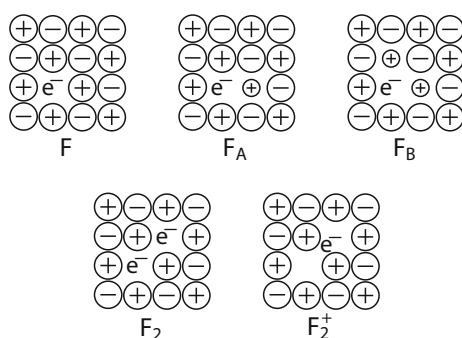
The energy levels of rare-earth ions are of particular importance in the context of doped crystals. Here, optical transitions occur between levels of the partially filled 4f-shell. Since the 4f-shell is strongly screened by the outer (filled) shells, the impact of the crystal field is minor compared to the interatomic interaction. Hence, the energy levels of the rare-earth ions that are doped into crystals are very similar to those of the free ions. This is especially relevant for neodymium lasers that are based on YAG crystals (see Sect. 9.2).

Color Centers

Alkali halide crystals consist of an alkali and a halogen atom. The alkali gives one electron to the halogen atom. Thus, the alkali has a positive charge and the halogen a negative (e.g. cation K^+ and anion Cl^-). Alkali halide crystals can be produced with a surplus of alkali metal atoms. The corresponding lack of halogen atoms leads to anionic vacancies in the crystal, as depicted in Fig. 1.13. The valence electrons of the excess alkali atoms are not bound and thus trapped in the vacancies. Such an electron is called color center (or F-center from German “Farbzentrums”), as it tends to absorb light in the visible spectrum such that the usually transparent material becomes colored. The interaction between the color center electron and the surrounding alkali atoms results in discrete energy states, although there is no central atom associated to the electron. The energy spacing between the excited states is on the order of a few eV, giving rise to the characteristic color of the crystal.

Aside from the described simple F-center, there is wide range of other color centers that are of particular importance for laser applications. For instance, the F_A -center represents a halide vacancy in the immediate neighborhood of an impurity alkali atom of smaller size replacing the host lattice cation, while the F_B -center is an F-center in the neighborhood of two foreign atoms. Further examples are illustrated in Fig. 1.13.

Fig. 1.13 Color centers in alkali halide crystals (\oplus : alkali, e.g. K^+ , \ominus : halogen, e.g. Cl^- , \oplus : alkali of smaller size)



1.6 Energy Bands in Semiconductors

Semiconductors can be described by bands of electronic energy levels lying close to each other. Without thermal excitation ($T = 0$ K), these bands are either completely filled with electrons or they are empty. The highest filled band is denoted valence band and the lowest unfilled is called conduction band (Fig. 1.14a). Both bands are separated by the band gap which, for semiconductors, has a value between 0.1 and 3 eV. Thermal or light excitation can change the energy of an electron so that it passes from the valence band into the conduction band, thus producing a positive charge in the valence band, called a *hole*. The reverse process of the recombination of an electron from the conduction band with a hole is also possible and releases energy, for example by emission of a photon. External electrical fields can be used to move electrons in the conduction band to participate in the conduction of electricity (n-type conduction). The resulting holes are said to be positively charged and lead to electrical conductivity in the valence band as well (p-type conduction). The conductivity is small at low temperatures in semiconductors since there are only a few mobile electrons and holes available in the conduction and valence band, respectively.

Energies of Electrons and Holes

The electrons in a band have not only different energies but also different momenta and wave vectors. For free electrons, the momentum p is given by the product of the

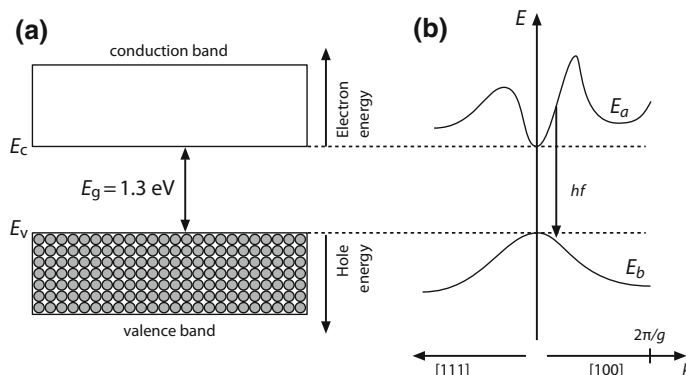


Fig. 1.14 **a** Conduction and valence band of a semiconductor shown for indium phosphide (InP). At $T = 0$ K, the valence band is fully filled with electrons (circles), while the conduction band is empty (non-conducting state). **b** Energy momentum relation of an electron in the conduction (E_a) and a hole in the valence band (E_b) of InP. The maximum value of k is given by the lattice constant g ($k = 2\pi/g$). The symbols [111] and [100] denote a certain spatial direction within the crystal (Miller's indices). The recombination of an electron-hole-pair leads to the generation of a photon hf , by the. The selection rule for this optical transition is $\Delta k = 0$

electron mass m_0 and the velocity v : $p = m_0v$. Since electrons can be described in terms of both particles and waves (wave-particle duality), a wavelength λ can be assigned to it which is related to the momentum:

$$p = h/\lambda = \hbar k, \quad (1.13)$$

where $k = 2\pi/\lambda$ is the amount of the wave vector and $\hbar = h/2\pi$ is the (reduced) Planck constant.

The momentum is sometimes simply expressed as k , leading to a relationship between the kinetic energy E_{free} and momentum p of a free electron as follows:

$$E_{\text{free}} = \frac{m_0 v^2}{2} = \frac{p^2}{2m_0} = \frac{\hbar^2 k^2}{2m_0}. \quad (1.14)$$

This quadratic equation is a good approximation for electrons close to the lower edge of the conduction band (see Fig. 1.14b).

The influence of neighboring electrons in the conduction band is accounted for by introducing an effective electron mass m_c and by adding the lower band edge energy of the conduction band E_c , so that the energy of an electron in the conduction band reads:

$$E_a = E_c + \frac{\hbar^2 k^2}{2m_c}. \quad (1.15a)$$

Likewise, the energy of a hole in the valence band is given by

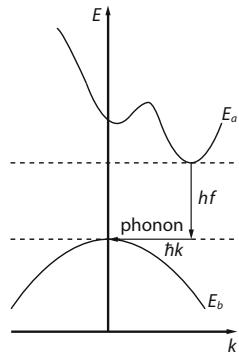
$$E_b = E_v - \frac{\hbar^2 k^2}{2m_v} \quad (1.15b)$$

with E_v being the upper band edge energy of the valence band and m_v is the effective mass of the holes. The band gap energy is then $E_g = E_c - E_v$. Equations (1.15a) and (1.15b) are only valid for energies close to the band gap and for small momenta, whereas significant deviations are apparent for larger values of k (see Fig. 1.14b).

Direct and Indirect Semiconductors

If the maximum of the valence band and the minimum of the conduction band occur at the same k value, the semiconductor is called *direct*, which means that the momenta of the minimum energy electrons and the maximum energy holes are the same. In *indirect* semiconductors, such as silicon, the conduction band minimum is shifted against the valence band maximum in the k -space (Fig. 1.14b). Light absorption and emission are mainly realized by transitions between the bands without a significant change of the electron momentum $0 \leq \hbar k \leq h/g$ (with a lattice

Fig. 1.15 Simplified band structure of the indirect semiconductor silicon. A transition from the minimum of the conduction band to the maximum of the valence band involves a change in electron momentum



constant of $g \approx 10^{-10}$ m) since the photon momentum $\hbar k_p = h/\lambda_p$ (with a wavelength $\lambda_p \approx 10^{-6}$ m) is small in comparison to the electron momentum. In particular, electronic transitions from the energetic minimum of the conduction band, where most electrons are located, to the maximum of the valence band in direct semiconductors, take place with $\Delta k \approx 0$. In contrast, for indirect electronic transitions with $\Delta k \neq 0$, momentum has to be transferred to the solid in the form of lattice vibration, called phonons (see Fig. 1.15). These processes are less probable due to the participation of three partners: photon, electron and phonon. Hence, direct semiconductors are the more effective photon emitters and thus commonly used in lasers and light-emitting diodes.

Density of States and Fermi Distribution

Calculation of the emission properties of semiconductors requires knowledge of the distribution of the electrons and holes in the conduction and valence band, respectively. The density of the electrons with a certain energy E is the mathematical product of the density of states (DOS) per unit energy and the occupation probability. The density of states ρ describes the possible number of electrons or holes dN per energy interval dE ($\rho = dN/dE$). Near the respective band edge $\rho_c(E)$ and $\rho_v(E)$ and can be expressed for the conduction and valence band as follows:

$$\boxed{\rho_c(E) = \frac{(2m_c)^{3/2}}{2\pi^2\hbar^3} (E - E_c)^{1/2}, \quad E \geq E_c}, \quad (1.16)$$

$$\boxed{\rho_v(E) = \frac{(2m_v)^{3/2}}{2\pi^2\hbar^3} (E_v - E)^{1/2}, \quad E \leq E_v}. \quad (1.17)$$

Since electrons (as well as holes) with a certain energy can move in different directions, an energy state can be multiply occupied. The deduction of (1.16) and (1.17) is given in the section on electron waves in semiconductors at the end of this section.

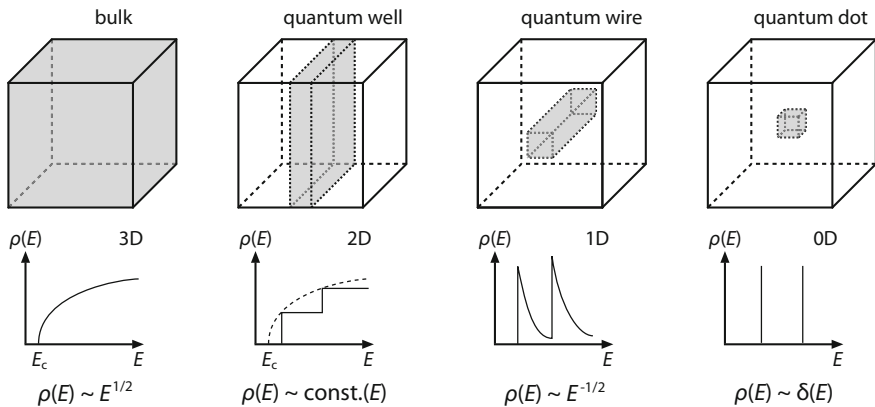


Fig. 1.16 Density of states in different confinement configurations: bulk material (3D), quantum well (2D), quantum wire (1D) and quantum dot (0D)

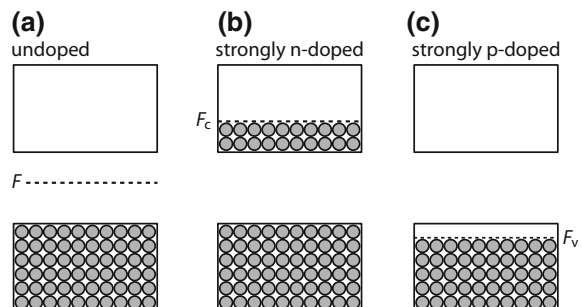
When the charge carriers are confined in space, e.g. in small structures with dimensions of only a few nanometers, the electronic states become quantized at discrete energy levels (quantum confinement). Hence, the density of states of the electrons and holes can no longer be described by the continuous functions in (1.16) and (1.17). Instead, $\rho(E)$ is a step function for a two-dimensional (quantum well), and scales with $E^{-1/2}$ for a one-dimensional structure (quantum wire), as shown in Fig. 1.16. The ultimate limit is the quantum dot, where the carriers are confined in all three directions leading to a series of delta functions at the allowed energy levels.

The probability $f(E)$ that an energy state E is occupied with an electron at a given temperature T , is given by the Fermi distribution:

$$f(E) = \frac{1}{\exp[(E - F)/kT] + 1}, \quad (1.18)$$

with the Boltzmann constant k and the energy of the Fermi level F , while thermodynamic equilibrium between the charge carriers in the conduction and valence

Fig. 1.17 **a** Fermi level F in an undoped (intrinsic) semiconductor, **b** quasi-Fermi level F_c in the conduction band for high n-doping, **c** quasi-Fermi level F_v in the valence band for high p-doping. The occupation of electrons (circles) is indicated at $T = 0$ K



band is assumed. The Fermi level can be considered as a hypothetical energy level of an electron which has a 50% probability of being occupied at any given time. For undoped or intrinsic semiconductors, F lies approximately in the middle of the band gap (Fig. 1.17a). According to the Pauli exclusion principle which states that no more than one electron can occupy a given energy state, $f(E) \leq 1$. The probability that an energy state is free or occupied by a hole is therefore given by $1 - f(E)$.

Doping

The electrical characteristics of a semiconductor material can be considerably changed by doping. Introducing *donors* (atoms with more valence electrons than the base material) produces a surplus of freely mobile electrons (n-type semiconductors), whereas doping with *acceptors* (atoms with less valence electrons than the base material) causes a surplus of holes (p-type semiconductors), leading to an increased electrical conductivity. While the Fermi level is lifted towards the conduction band by n-doping, it is lowered towards the valence band by p-doping. In case of strong doping, the Fermi level is shifted into the conduction band (n-doping) or valence band (p-doping) which results in a partially occupied band, as depicted in Fig. 1.17b, c. Hence, the semiconductor behaves like a metal, it is degenerate. Such semiconductors are employed for diode lasers.

Charge Carrier Injection

Electrons and holes can be produced optically, i.e. by the irradiation of light or by injection of a current into the p-n junction zone of a diode laser. The change of the electron density dN in the time interval dt in case of a current I is given by the following rate equation:

$$\frac{dN}{dt} = \frac{I}{eV} - \frac{N}{\tau}, \quad (1.19)$$

where I is the injection current, V the volume of the active zone, N the electron density, τ the lifetime of the charge carriers and e the electronic charge. In the stationary case ($dn/dt = 0$) is $N = I\tau/eV$, which means that the electron density N is directly proportional to the injection current.

Since there is no thermal equilibrium within the bands during charge carrier injection, definition of a Fermi distribution according to (1.18) is not valid. Nevertheless, the charge carriers can be in equilibrium within each band, which is particularly the case when the energy relaxation times within one band are considerably shorter than the transition times between the bands. This condition is met for most of the widely used semiconductor materials. The device is considered to be

in “quasi-equilibrium” which allows to define separate quasi-Fermi levels F_c and F_v that are located within the conduction or the valence band, respectively. F_c defines up to which energy the conduction band is occupied $T = 0$ K. Without charge carrier injection, the quasi-Fermi levels F_c and F_v coincide and the common Fermi level F lies in the middle of the band gap for undoped semiconductors.

Figure 1.18 shows the charge carrier distribution of a semiconductor in quasi-equilibrium. The probability that an energy level E within the conduction band is occupied by an electron is given by the Fermi distribution $f_c(E) = (\exp[(E - F_c)/kT] + 1)^{-1}$. Likewise, the occupation probability of an energy level E in the valence band being occupied by a hole is $1 - f_v(E) = 1 - (\exp[(E - F_v)/kT] + 1)^{-1}$. The corresponding charge carrier density of the electrons in the conduction band is then $n(E) = \rho_c(E) \cdot f_c(E)$, while that of the holes in the valence band is $p(E) = \rho_v(E) \cdot (1 - f_v(E))$. The total electron density N in the conduction band is connected with the Fermi level F_c :

$$N = \int_{E_c}^{\infty} n(E) dE = \frac{(2m_e)^{3/2}}{2\pi^2\hbar^3} \int_{E_c}^{\infty} \frac{(E - E_c)^{1/2}}{\exp[(E - F_c)/kT] + 1} dE. \quad (1.20)$$

For $T = 0$ K, the relationship between electron density and Fermi level simplifies to

$$N(T = 0) = \frac{(2m_e)^{3/2}}{2\pi^2\hbar^3} \int_{E_c}^{F_c} (E - E_c)^{1/2} dE = \frac{(2m_e)^{3/2}}{3\pi^2\hbar^3} (F_c - E_c)^{3/2}. \quad (1.21)$$

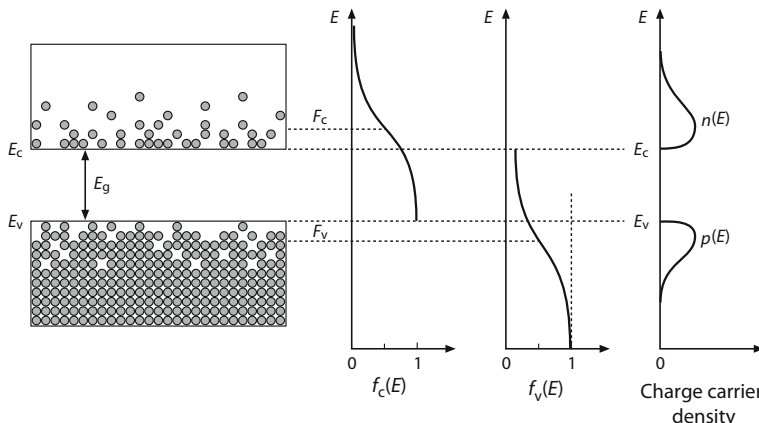


Fig. 1.18 Semiconductor in thermal quasi-equilibrium: Fermi distributions $f_c(E)$ and $f_v(E)$ as well as charge carrier densities of the electrons $n(E)$ and positive holes $p(E)$ in the conduction and valence band

Electron Waves in Semiconductors

For many problems in semiconductor physics, such as the calculation of density of states or the understanding of quantum well lasers, it is convenient, if not necessary, to regard electrons as waves. The determination of the DOS $\rho_{c,v}$ according to (1.16) and (1.17) is carried out by considering a semiconductor cube of edge length L (volume $V = L^3$) and assuming an electron wave function ψ which satisfies periodic boundary conditions, e.g. $\psi(x, y, z) = \psi(x + L, y, z)$, y and z correspondingly. These boundary conditions are fulfilled by the following k -values

$$k = \pm n \frac{2\pi}{L}, \quad (1.22)$$

with n being an integer or zero. Condition (1.22) suggests that electrons can be described as standing-waves oscillating in the cube, with their k -values differing by $2\pi/L$. Since this holds for all three dimensions, an electron state is said to occupy the volume $(2\pi/L)^3 = (2\pi)^3/V$ in the k -space. The number of allowed states can now be derived by picturing a volume element in k -space as a spherical shell of radius k and thickness dk : $4\pi k^2 dk$. Here, the number of electron states within this volume element can be calculated by dividing the volume element by the volume of an electron state, yielding:

$$N = \frac{4\pi k^2}{(2\pi)^3} V dk. \quad (1.23)$$

In the next step, the density of states can be calculated as the number of states per volume and per dk , while a factor of 2 has to be taken into account due to the two possible spin directions of electrons (Pauli exclusion principle).

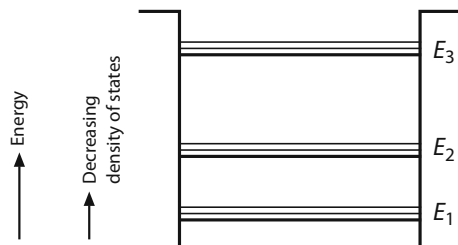
$$\boxed{\rho(k) = N/(V dk) = \frac{k^2}{\pi^2}}. \quad (1.24)$$

Finally, the energies according to (1.15a) and (1.15b) are inserted in order to obtain the density of states in the conduction and the valence band $\rho_c(E)$ and $\rho_v(E)$ given in (1.16) and (1.17). For this purpose, dk has to be converted to dE in $\rho(k) = N/(V dk)$.

Quantum Wells

A quantum well is a semiconductor structure where a thin layer of one material (e.g. GaAs) is sandwiched between two layers of a material with a wider band gap (e.g. AlAs). The thickness of the inner layer is typically in the range of 1 to 50 nm,

Fig. 1.19 Electron states with energies E_1 , E_2 and E_3 in a quantum well



which is comparable to the de Broglie wavelength of the electrons and holes. Consequently, the quantization of the k -values becomes significant leading to discrete energy levels (or energy sub-bands) of the carriers, as shown for the conduction band in Fig. 1.19 as well as in Fig. 1.16.

Further Reading

1. W. Demtröder, *Atoms, Molecules and Photons* (Springer, 2010)
2. G.A. Agoston, *Color Theory and Its Application in Art and Design* (Springer, 1987)
3. K. Shimoda, *Introduction to Laser Physics* (Springer, 1986)

Chapter 2

Absorption and Emission of Light



After introduction of the basic properties of atoms, molecules, solids and semiconductors in the first sections, the interaction of light with matter will be presented in the following. This comprises, in particular, the description of light absorption, emission and amplification as these processes are fundamental for laser operation.

2.1 Absorption

Light is absorbed whilst passing through a medium. Assuming a plane wave with intensity I_0 (unit W/m^2) which is incident on an absorbing layer of thickness d (Fig. 2.1), the intensity of the transmitted wave $I = I(d)$ is proportional to the incident intensity while decreasing exponentially with the thickness according to the Beer-Lambert Law:

$$I(d) = I_0 \exp(-\alpha d). \quad (2.1)$$

The material specific quantity α (dimension: m^{-1}) is referred to as absorption coefficient. Typical values are $\alpha \approx 1 \dots 10 \text{ km}^{-1}$ for glass fibers or $\alpha \approx 1 \text{ nm}^{-1}$ for metals.

The process of absorption can be treated on an atomic scale. Atoms or molecules have discrete or quantized energy states E_1, E_2, E_3, \dots , which are illustrated in an energy level diagram as shown in Fig. 2.2. In liquids (e.g. dye solutions) and solids, a large number of sharp energy levels are closely spaced, forming broad energy bands. In the unperturbed case, all atoms or molecules are in the ground state, i.e. the state with the lowest energy E_1 . When light with frequency f_{12} is incident on the atom, the transition to a higher energy level E_2 is initiated, provided the following condition is met:

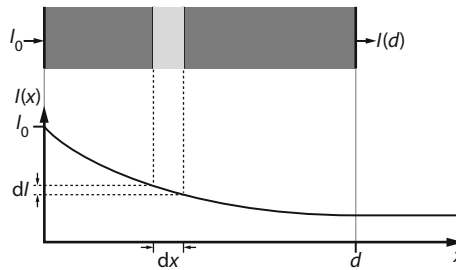


Fig. 2.1 Propagation of light through an absorbing medium of thickness d

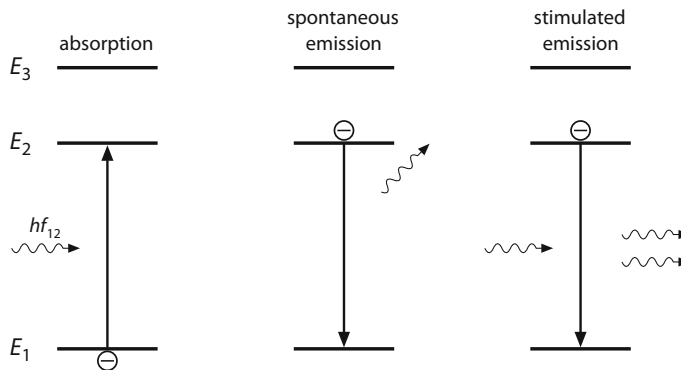


Fig. 2.2 Absorption: An incident photon hf_{12} excites an electron from a lower energy state E_1 to a higher state E_2 . The photon is annihilated in this process. Spontaneous emission: An electron in an excited state falls into a lower energy state, thereby emitting a photon. Stimulated emission: An incoming photon interacts with an excited electron and initiates the transition to a lower energy state. This produces a second photon with the same properties (frequency, phase, polarization, direction). The incident electromagnetic field is amplified

$$E_2 - E_1 = hf_{12}. \quad (2.2)$$

with $h = 6.626 \times 10^{-34}$ Js being Planck's constant.

The excitation of the atom involves the annihilation of the photon so that the intensity I of the incident light is reduced—and absorption has occurred. The absorption coefficient is related to the number of absorbed photons or number of transitions respectively per unit time and unit volume $dN_1/dt|_a$. The subscript “a” denotes that the transition originated from absorption. $dN_1/dt|_a$ is proportional to the density of atoms N_1 in the ground state (population density) and to the photon flux φ (photons per area and time):

$$\left. \frac{dN_1}{dt} \right|_a = -\sigma_{12} N_1 \varphi. \quad (2.3)$$

The proportionality factor σ_{12} is the absorption cross-section and describes the effective area of the atom for absorbing the photons. The negative sign is due to the decreasing ground state population density N_1 upon absorption.

The rate of atomic transitions can also be associated to the photon density Φ (photons per volume) using $d\Phi/dt$. Replacing $\Phi = \varphi/c$ [see (1.5) and (1.8)], and using $c = dx/dt$ yields

$$\frac{dN_1}{dt} \Big|_a = \frac{d\Phi}{dt} = \frac{1}{c} \frac{d\varphi}{dt} = \frac{dx}{dt} \frac{d\varphi}{dt} = \frac{d\varphi}{dx}. \quad (2.4)$$

Since the photon flux ϕ is proportional to the intensity I (1.8b), (2.3) and (2.4) can be combined, leading to a relationship which describes the decrease in intensity due to absorption:

$$\boxed{\frac{dI}{dx} \Big|_a = -\sigma_{12} N_1 I}. \quad (2.5)$$

Here, the term $\alpha = -\sigma_{12} N_1$ represents the absorption coefficient introduced in (2.1) which results from integration with boundary conditions $I(0) = I_0$ and $I(d) = I$.

The absorption coefficient α scales with the density of atoms N_1 , in the ground state, e.g. with the concentration of a dye solution. The absorption cross-section σ_{12} can be expressed in terms of the Einstein coefficient for absorption B_{12} , if the natural linewidth (see Sect. 2.4) is obtained:

$$\sigma_{12} = B_{12} h f_{12} / c. \quad (2.6)$$

2.2 Spontaneous Emission

The question arises as to what happens to the atoms in the excited states. They spontaneously return to the ground state after a certain time interval (Fig. 2.2). The released energy can be emitted as a photon. This process is called spontaneous emission. Since the direction in which the photon propagates is random and thus not necessarily the same as that of the absorbed photon, the incident radiation is indeed attenuated, as assumed in the above equations. The decrease in population density of the upper state N_2 due to spontaneous emission is described by the spontaneous emission lifetime τ :

$$\boxed{\frac{dN_2}{dt} \Big|_{sp} = -\frac{N_2}{\tau}}. \quad (2.7)$$

The reciprocal of the lifetime $A = 1/\tau$ represents the Einstein coefficient for spontaneous emission, in case the decay to the ground state is entirely radiative.

Table 2.1 Lifetimes of selected laser levels and stimulated emission cross-sections

Laser gain medium	λ (nm)	τ_2 (upper level)	τ_1 (lower level)	σ (cm^2)
He–Ne	633	10 ... 20 ns	12 ns	3×10^{-13}
Ar ⁺	488	9 ns	0.4 ns	
Excimer (KrF)	248	1 ... 10 ns	< 1 ps	10^{-16}
CO ₂	10,600	1 ... 10 ms		10^{-16}
Low pressure			100 ns	
High pressure			1 ns	
Rh6G (dye)	600	5 ns	≤ 10 ps	2×10^{-18}
Ruby	694	3 ms	∞	2×10^{-20}
Nd:YAG	1064	230 μs	30 ns	8×10^{-19}
Nd:glass	1064	300 μs	50 ... 100 ns	4×10^{-20}
GaAs	800	4 ns		10^{-16}

Typical lifetimes are $\tau \approx 10^{-9}$ s for permitted (electric dipole) transitions and $\tau \approx 10^{-3}$ s for forbidden transitions from metastable states. Only ground states are stable with $\tau = \infty$.

The relaxation of the electron may also occur non-radiatively ($A = 0$), for instance, through interaction with lattice vibrations which leads to heating of the material or through collision processes. Although the transition from the upper state to the lower state does not involve the emission of a photon, the upper state lifetime τ' is limited: $\tau' < 1/A$. The spontaneous emission lifetimes of several upper laser states are presented in Table 2.1.

2.3 Light Amplification by Stimulated Emission

Besides spontaneous emission which was well-known for a long time through the observation of fluorescence, Albert Einstein postulated the process of stimulated emission in 1917. According to his theory, the transition of an excited atom to a lower energy state does not only occur spontaneously, but can also be initiated by an incoming photon of appropriate frequency, i.e. fulfilling Bohr's condition. Stimulated emission is the reverse process of absorption. In analogy to relations (2.3) and (2.5), the number of processes per unit time and unit volume $dN_2/dt|_{\text{st}}$ is given as follows:

$$\frac{dN_2}{dt} \Big|_{\text{st}} = -\sigma_{21} N_2 \varphi, \quad (2.8a)$$

$$\boxed{\frac{dI}{dx} \Big|_{\text{st}} = \sigma_{21} N_2 I.} \quad (2.8b)$$

In these equations, N_2 denotes the density of atoms in the excited state with energy E_2 ; σ_{21} is the cross-section for stimulated emission, while t and x represent

the time and coordinate along the propagation direction, respectively. The subscript “st” indicates that the relations refer to the process of stimulated emission. Since the power density I of the incident radiation increases, the sign is positive as opposed to (2.5).

While spontaneous emission occurs at random directions, the photons that are generated through stimulated emission propagate in the same direction as the incident photon. In the wave picture of light, the emitted wave is coherent to the incident wave, meaning that it has the same frequency and phase.

Thermodynamic or quantum-mechanical considerations lead to the conclusion that the cross-sections for absorption and stimulated emission are identical if the involved energy states have the same number of sublevels:

$$\boxed{\sigma_{12} = \sigma_{21} = \sigma} \text{ and } B_{12} = B_{21} = B. \quad (2.9)$$

The Einstein coefficients A and B are related to each other as

$$\frac{A}{B} = \frac{8\pi h f_{12}^3}{c^3}. \quad (2.10)$$

In case the states with energies E_1 and E_2 contain sub-levels, the numbers of sub-levels (or degrees of degeneracy) g_1 and g_2 have to be taken into account:

$$\boxed{g_1 \sigma_{12} = g_2 \sigma_{21}}. \quad (2.11)$$

In contrast to spontaneous emission, stimulated emission leads to amplification of the incident light. The emitted photons have the same frequency, phase and direction as the stimulating photons.

Gain Factor

The operation principle of a laser is based on stimulated emission. Hence, spontaneous emission is neglected in the following.

The amplification, or gain $dI|_{\text{st}}$, provided by stimulated emission counteracts the absorption $dI|_a$, so that the overall change in intensity I reads

$$dI = dI|_a + dI|_{\text{st}}. \quad (2.12)$$

For energy levels with degrees of degeneracy $g_1 = g_2$, substitution of (2.5) and (2.8b) and integration over the thickness of the medium d results in

$$\frac{I}{I_0} = \exp(\sigma(N_2 - N_1)d) \quad (2.13a)$$

or

$$G = \frac{I}{I_0} = \exp(g d). \quad (2.13b)$$

The incident intensity is I_0 and I is the intensity behind a layer of thickness d . For $N_2 > N_1$, the intensity increases and the light is amplified in the medium, as the argument of the exponential function becomes positive. Light amplification by stimulated emission of radiation is the fundamental mechanism of the laser, thus giving it its name. Amplification only occurs if there are more atoms in the upper energy level 2 than in the lower level 1. An additional condition is imposed regarding the photon energy of the incident light which has to be equal to the energy difference between the two levels. The ratio of light intensity before and after propagation through the medium is referred to as gain factor or simply gain G . The quantity

$$g = \sigma(N_2 - N_1). \quad (2.14)$$

is called gain coefficient in analogy to the absorption coefficient defined in (2.1). For small values of $g d$, the gain can be approximated as follows:

$$G = \exp(g d) \approx 1 + g d. \quad (2.15)$$

The gain obtained in a one meter long gas discharge tube of a helium–neon laser is on the order of $G = 1.1$. The gain is said to be $g d = 10\%$. Higher gain factors of $G = 10$ are realized in optically-pumped Nd:YAG lasers. For a crystal length of $d = 5$ cm, the gain coefficient is calculated to $g = \ln G/d = 0.46 \text{ cm}^{-1}$. Further examples for gain factors are provided in the description of the different laser types.

Boltzmann Distribution

The major challenge in realizing a laser is fulfilling the condition $N_2 > N_1$, i.e. achieving a higher population in an excited level 2 than in a lower energy level 1. This condition is known as population inversion and deviates from thermal equilibrium, where most atoms are in the ground state. Collisions between the atoms lead to a few excited atoms, populating the states with energies E_1, E_2, E_3, \dots . The corresponding population densities N_1, N_2, N_3, \dots are given by the Boltzmann distribution, if the system is in thermal equilibrium., the following relation can be derived from thermodynamic considerations:

$$\boxed{\frac{N_2}{N_1} = \frac{g_2}{g_1} \exp\left(-\frac{E_2 - E_1}{kT}\right)}, \quad (2.16)$$

with T being the absolute temperature in Kelvin and $k = 1.38 \times 10^{23} \text{ J/K} = 8.6 \times 10^{-5} \text{ eV/K}$ denoting Boltzmann's constant. g_1 and g_2 are the numbers of sub-levels of the states 1 and 2. At room temperature is $T = 300 \text{ K}$ and

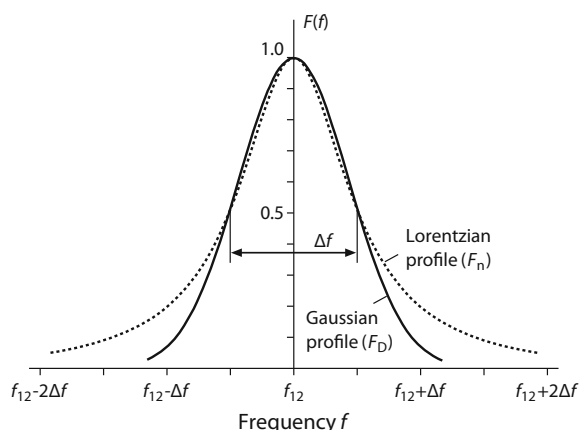
$kT = 24.9$ meV. Excited states with energies of a few eV which would be suitable for light emission are only weakly populated in thermal equilibrium. For $T \rightarrow \infty$, the population of the two states become equal according to (2.18): $N_1 = N_2$. Population inversion, and hence laser operation cannot be achieved in thermal light sources. Formally, this is only accomplished for “negative temperatures”.

2.4 Linewidth

Until now, the energy levels $E_1 = E_2$ were assumed to be sharp and light absorption and emission only occurred at frequency f_{12} . However, de facto, the levels and spectral lines have a finite width which needs to be included in the equations. For this purpose, the line shape function $F(f)$ is introduced in the following that describes the frequency-dependence of the cross-section $\sigma(f) = \sigma \cdot F(f)$ and thus of the absorption and gain coefficients. The latter is given as $g(f) = g \cdot F(f)$, where g is the maximum value. Examples of line shape functions are depicted in Fig. 2.3.

The spectral linewidth broadening is classified into homogeneous and inhomogeneous contributions. Spontaneous emission and, for instance, the influence of collisions in gases or lattice vibrations in solids result in a homogeneous broadening represented by a Lorentzian line shape function. Here, the broadening mechanism is equally affecting all the radiating or absorbing atoms (or ions or molecules). Besides, there are inhomogeneous processes which cause different atoms to interact with different frequency components so that the absorption and emission cross sections have different spectral shapes for different atoms. Inhomogeneous broadening gives rises to a Gaussian line shape function as illustrated in Fig. 2.3. Typical examples are the Doppler broadening, where the transition frequency depends on the velocity of the atoms or the Stark effect in solids where the local electric field is different for each absorbing or emitting atom, thus changing the energy levels in an inhomogeneous way.

Fig. 2.3 Line shape functions: Gaussian and Lorentzian profile



Natural Linewidth

The natural linewidth is determined by the lifetimes τ of the states involved in a transition and gives rise to homogeneous broadening. According to Heisenberg's uncertainty principle, the energy levels have a finite width:

$$\boxed{\Delta E = \frac{\hbar}{2\pi\tau}}. \quad (2.17)$$

Using Bohr's condition $hf_{12} = E_2 - E_1$, this translates to a finite linewidth of the spectral line

$$\boxed{\Delta f_n = \frac{1}{2\pi} \left(\frac{1}{\tau_1} + \frac{1}{\tau_2} \right)}, \quad (2.18)$$

with τ_1 and τ_2 being the lifetimes of the lower and upper energy level, respectively. A more detailed treatment yields the line shape function

$$F_n(f) = \frac{(\Delta f_n/2)^2}{(f - f_{12})^2 + (\Delta f_n/2)^2}. \quad (2.19)$$

This function represents a Lorentzian profile, as depicted in Fig. 2.3. The lifetime values summarized in Table 2.1 can be used to calculate the natural linewidth of several important laser types. However, the observed linewidths of the optical transitions (Table 2.2) are significantly broader, since further broadening mechanisms are present, resulting in additional contributions to the linewidth.

Table 2.2 Linewidths and broadening mechanism of selected laser transitions

Laser gain medium	λ (nm)	Linewidth	Broadening mechanism
He-Ne (gas temperature: 300 K)	633	1.5 GHz	Doppler, inhomogeneous
Ar ⁺ (gas temperature: 2000 K)	488	4 GHz	Doppler, inhomogeneous
Excimer (KrF)	248	10 THz	Overlapping vibrational levels
CO ₂	10,600		
10 mbar, 300 K		60 MHz	Doppler, inhomogeneous
1 bar		4 GHz	Collisions, homogeneous
10 bar		150 GHz	Overlapping rotational levels
Rh6G (dye)	600	80 THz	Overlapping vibrational levels
Ruby	694	330 GHz	Lattice vibrations, homogeneous
Nd:YAG	1064	120 GHz	Lattice vibrations, homogeneous
Nd:glass	1064	7.5 THz	Stark effect, inhomogeneous
GaAs	800	10 THz	Energy bands in periodic crystal field

Collisional Broadening

Elastic collisions between gas particles cause homogeneous broadening. As the number of collisions increases with the gas pressure, it is also referred to as pressure broadening. When elastic collisions occur during the emission of radiation, the phase of the emitted light wave is changed. As a result, the emitted radiation consists of finite wave trains of a mean duration τ_c of unperturbed phase, but with random phase shifts due to collisions. A Fourier analysis leads to a Lorentzian line shape function, where the full width at half maximum (FWHM) Δf_c is given by the mean time between two collisions. For $\tau_1 = \tau_2 = \tau_c$, the linewidth reads in analogy to (2.18):

$$\boxed{\Delta f_c = \frac{1}{2\pi\tau_c}}. \quad (2.20)$$

The collision rate and hence the linewidth can be derived from the laws of thermodynamics:

$$\Delta f_c = \sqrt{\frac{3}{4m kT}} \cdot d^2 p, \quad (2.21)$$

where m and d are the mass and the diameter of the atoms or molecules, respectively. k is Boltzmann's constant, while T and p are the temperature and pressure of the gas. The linewidth due to collisional broadening Δf_c scales with the gas pressure and is usually much larger than the natural linewidth Δf_n . For a helium–neon laser, the values are $\Delta f_n \approx 10$ MHz and $\Delta f_c \approx 100$ MHz.

A similar homogeneous broadening mechanism is present in solids where interactions of the radiating atoms or ions with lattice vibrations (phonons) are responsible for a Lorentzian profile of the spectral lines. This thermal broadening is observed, e.g. in ruby or Nd:YAG lasers (Table 2.2).

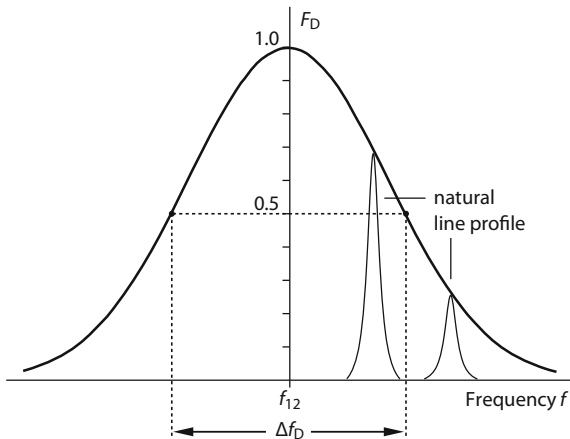
Doppler Broadening

The inhomogeneous Doppler broadening is caused by the motion of the emitting particles which shortens or lengthens the frequency of the emitted photon (Doppler effect). The shifted frequency f'_{12} measured on a detector is related to the velocity v ($v \ll c$) of the atoms or molecules as follows:

$$f'_{12} = f_{12}(1 \pm v/c), \quad (2.22)$$

where f_{12} is the frequency of the photon emitted from a non-moving particle. The sign indicates whether the particle moves towards or away from the detector. For gases in thermal equilibrium, the velocity distribution follows Maxwell-Boltzmann

Fig. 2.4 Doppler broadening results in a Gaussian line shape which is typically broader than the natural line profile



statistics, so that the line shape function has a Gaussian profile (Fig. 2.4) according to

$$F_D(f) = \exp\left(-\left(\frac{2(f-f_{12})}{\Delta f_D}\right)^2 \ln 2\right), \quad (2.23)$$

with a full width at half maximum

$$\boxed{\Delta f_D = \frac{2f_{12}}{c} \sqrt{2 k T \ln 2 / m}.} \quad (2.24)$$

Note that, for equal FWHM, the Gaussian profile converges more rapidly to zero with increasing distance from the center as compared to the Lorentzian profile (Fig. 2.3). The Doppler broadening Δf_D is about 1.5 GHz for a helium–neon laser and hence much broader than both the natural linewidth Δf_n and collisional broadening Δf_c .

Further Broadening Mechanisms

Broadening owing to spatially inhomogeneous crystal fields are relevant in *glass lasers* (Table 2.2), where the laser-active (rare-earth) ions doped into the glass are affected differently depending on their location. This results in a frequency shift and the statistical Stark effect. In *semiconductor lasers*, broadening originates from the band structure, whereby the width is determined by the energy distribution of the electrons and holes.

In most cases, multiple broadening mechanisms individually contribute to the linewidth of a transition. The natural linewidth is usually neglectable. Collisional

and Doppler broadening are the major processes in gas lasers with the latter being dominant at low pressures. Homogeneous broadening due to lattice vibrations or inhomogeneous broadening through the statistical Stark effect are present in *solid-state lasers*. Particularly broad homogeneous linewidths are observed in *dyes*, as densely spaced rotational-vibrational levels are broadened due to the interaction between the molecules.

2.5 Population Inversion, Gain Depletion and Saturation

Population inversion ($N_2 > N_1$) is a prerequisite for light amplification and laser operation. This section provides a brief overview of the different pumping mechanisms used for the realization of an inversion. A more detailed explanation is given in the description of different laser types.

Gas lasers are mostly pumped by electric discharge in the gas which leads to population of the upper laser level via electron or atom collisions. In gas lasers containing only one species, e.g. in noble gas ion lasers, the excitation occurs by electron collisions. If multiple gas species are present, as it is the case for the helium–neon and the CO₂ laser, the resonant energy transfer between different atoms or molecules can be exploited through collisions of the second kind. Here, it is favorable if one particle possesses a long-lived state from which the upper laser level of the other atom or molecule can be populated. Other approaches used in gas lasers are: pumping by chemical reaction (HF laser) or by gas dynamic processes (e.g. in special CO₂ lasers) or more rarely by optical pumping.

Solid-state lasers and *dye lasers* are pumped optically using a pump light source with high brightness in the spectral region that is addressed for the excitation of the upper laser level. Flash lamps, various continuous light sources and, most importantly, lasers are employed for this purpose.

Semiconductor lasers are mostly pumped by current injection, i.e. by the injection of electrons into the valence band which represents the upper laser level. In the last years, also optically-pumped semiconductor lasers were developed.

Gain Saturation

In case of population inversion, light which passes through the medium at a frequency within the linewidth of the corresponding transition, is amplified. The relationship for the gain coefficient g introduced in (2.14) is only valid at low light intensities. At higher intensities, the population of the upper level is more and more depleted as the intensity increases, resulting in gain reduction, as shown in Fig. 2.5. For homogeneous saturation (Fig. 2.6), the intensity-dependence of the gain reads

Fig. 2.5 Gain factor in dependence on intensity

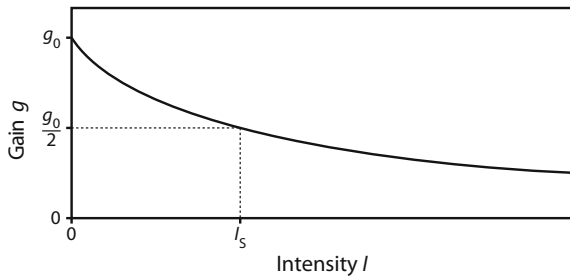
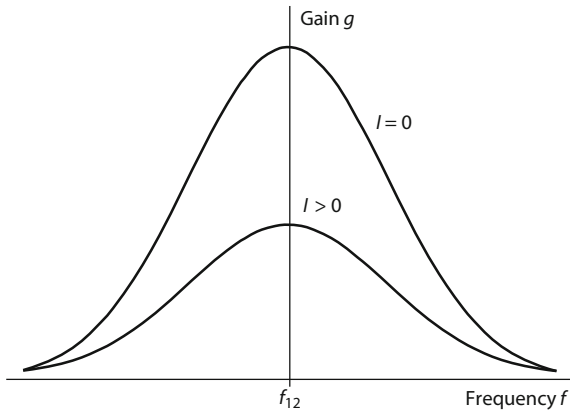


Fig. 2.6 Homogeneous broadening of the line profile: if light with intensity I is amplified in a medium, the gain is homogeneously saturated



$$\boxed{g = \frac{g_0}{1 + I/I_s}}, \quad (2.25)$$

where g_0 is the gain coefficient at very low intensity ($I \rightarrow 0$) and I_s denotes the saturation intensity which can be calculated from rate equations, yielding

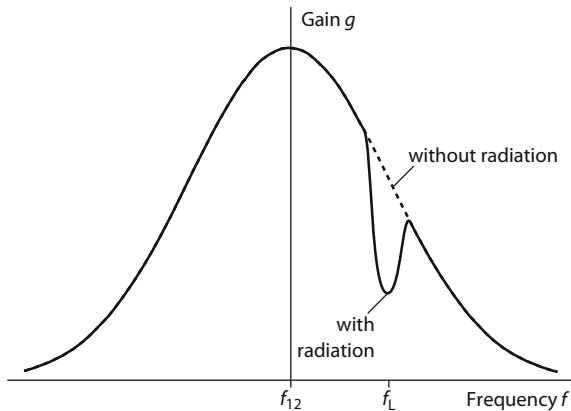
$$I_s = \frac{hf_{12}}{\sigma_{21}\tau}, \quad (2.26)$$

with σ_{21} being the cross-section for stimulated emission, while τ is the upper level lifetime.

One example for *homogeneous* saturation are transitions with natural linewidth. Here, an increase in intensity gives rise to a uniform, homogeneous saturation of the line profile, as illustrated in Fig. 2.6. The same characteristic is present for spectral lines that are broadened by lattice vibrations, for example in Nd:YAG lasers.

A different saturation behavior, however, is observed for inhomogeneously broadened lines such as Doppler broadened lines. Each atom or molecule is characterized by its velocity v which can change over time. Due to the Doppler effect, the velocity is associated to a certain transition frequency f . When light with a frequency f_L passes through the medium, it interacts only with those atoms having a suitable velocity or frequency, respectively. Hence, selective gain depletion in the

Fig. 2.7 Saturation of an inhomogeneously broadened line (spectral hole burning): If light with frequency f_L is amplified in a medium, the gain at this frequency is depleted, leading to a “hole” in the spectral gain distribution



spectral range around the incident frequency f_L occurs which is referred to as spectral hole burning and depicted in Fig. 2.7. The width of the hole is on the order of the natural linewidth Δf_n or the collisional broadening Δf_c , if the latter is larger. The hole vanishes once the incident intensity is switched off. The described behavior appears in gas lasers, e.g. in helium–neon or CO₂ lasers.

2.6 Light Emission by Accelerated Electrons

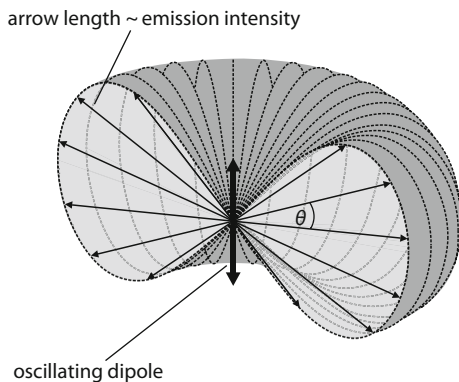
Light is generated by electron transitions in atoms, molecules and solids from excited states with energy E_2 to states with lower energy E_1 . As outlined in the previous sections, the difference energy is released as photons. In a quantum-mechanical picture, the emission process involves a superposition of the electron wave functions in the two “stationary” states. The resulting spatial oscillation of the charge density at the frequency $f_{12} = (E_2 - E_1)/\hbar$ can be interpreted as an oscillating dipole. The radiation characteristic of such a dipole is illustrated in Fig. 2.8. The radiated intensity is zero along the oscillation axis and has its maximum perpendicular to the axis.

For a single atom, the shown angular distribution represents the probability of the photon to be emitted into a certain direction after a large number of subsequent excitation and emission processes.

The angular distribution in Fig. 2.8 requires a fixed orientation of the radiating particle. If there is an ensemble of particles, e.g. atoms, with random orientations or the particles changes its orientation between subsequent emission events, a spherically symmetric distribution of the emitted photons.

The described oscillation of the charge density is an example for a non-constant acceleration. A similar scenario exists in a synchrotron light source where electrons move in circular orbits. Here, radial acceleration occurs as only the direction of the velocity vector is changing, while the magnitude of the vector remains constant. The synchrotron radiation emitted by the accelerated electrons is characterized by a

Fig. 2.8 Polar diagram of the radiation emitted by an oscillating dipole represented by the bold arrow. The emission intensity is proportional to $\cos^2\theta$, where θ is the angle between the emission direction and the direction perpendicular to the dipole. No radiation is emitted in the direction of the dipole, i.e. $\theta = 90^\circ$



broad continuous spectrum due to the statistical oscillations of the many electrons around the orbit and the statistical nature of the emission itself.

Electron oscillations can also be realized by a spatially periodic magnetic field (undulator) which is oriented perpendicular to the main axis of electron propagation, resulting in light emission at a corresponding frequency. This principle is applied in free-electron lasers (FEL) and will be discussed in Sect. 25.5.

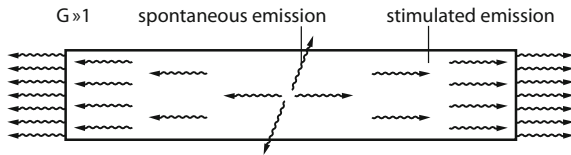
2.7 Basic Laser Setup

In lasers, light initially generated by spontaneous emission is amplified by stimulated emission. A precondition for laser action is that the stimulated emission process predominates over the spontaneous process. In order to fulfill this condition, the gain of the laser medium must be enormously large to allow for sufficient amplification in a single pass (“superradiant laser”), or multiple passes of the photons through the medium have to be realized. The latter leads to the classic configuration of lasers consisting of an active medium and mirrors.

Superradiant Lasers

A superradiant laser can be understood as a primary stage of a laser. It consists of a rod-shaped material in which population inversion is achieved, as shown in Fig. 2.9. Initially, spontaneous emission occurs in all directions. Photons that are emitted along the rod axis experience the largest gain as they travel the longest way through the medium. If the gain factor is large enough, intense radiation is produced. In the high-gain regime, the divergence of the output beam becomes large, as opposed to lasers utilizing a low-gain medium. Nitrogen lasers often operate as superradiant lasers as the gain coefficient can be as high as 1 cm^{-1} .

Fig. 2.9 Schematic of a superradiant laser operating without cavity



Threshold Condition

In most materials, the gain is too low for obtaining superradiant laser emission. The simplest approach for increasing the gain is to use a longer laser medium, but this has technical limitations. Instead the material is placed between two parallel mirrors in order to realize multiple passes of the light through the medium (Fig. 2.10). In this way, the light intensity grows until a stationary equilibrium value is reached (stationary case). However, light amplification is only accomplished if the gain factor G is large enough to exceed the losses. The latter are determined by the reflectance R of the mirrors and the transmission factor T which describes the additional losses per round-trip inside the cavity, e.g. introduced by diffraction, scattering. This leads to the so-called threshold condition:

$$[G R T \geq 1]. \quad (2.27)$$

For different reflectances R_1 and R_2 of the two mirrors, the geometric mean

$$[R = \sqrt{R_1 R_2}]. \quad (2.28)$$

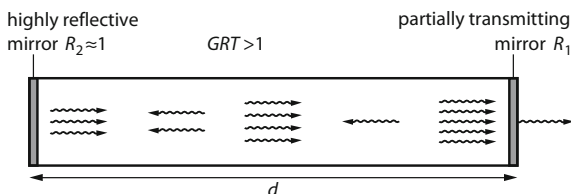
has to be inserted.

The threshold condition (2.27) can be expressed in terms of the difference in population density $N_2 - N_1$ by substituting the gain factor defined in (2.13):

$$G R T = R T \exp(\sigma(N_2 - N_1) d), \quad (2.29)$$

with the cross-section for stimulated emission σ and the thickness of the medium d . Using the approximation $1/x \approx 1 - x$ for $x \approx 1$, the threshold condition in case of low losses ($R T \approx 1$) reads

Fig. 2.10 Principle setup of a linear laser resonator



$$\boxed{N_2 - N_1 \geq \frac{\ln(1/RT)}{\sigma d} \approx \frac{1-RT}{\sigma d}}. \quad (2.30)$$

For solid-state lasers (e.g. Nd:YAG), the threshold for the population of the upper level is on the order of $N_2 \approx 10^{17} \text{ cm}^{-3}$. Lower values are possible for gas lasers, whereas semiconductor and dye lasers require larger population of the upper level. Note that degeneracy of the levels was not considered in the above equations and can be implemented by substituting $N_2 - N_1$ with $N_2 - (g_2/g_1) N_1$.

Stationary Laser Operation

The laser beam is coupled out of the cavity through a partially transmitting mirror ($R_1 < 100\%$), while the other mirror should be highly-reflective ($R_2 \approx 100\%$). In the stationary case, the initial gain G has fallen to the stationary gain G_L , which, for homogeneous broadening, is given according to (2.25):

$$G_L = \exp(g d) = \exp\left(\frac{g_0 d}{1 + I/I_s}\right). \quad (2.31)$$

Hence, under stationary conditions, $G_L R T = 1$, the intensity inside the resonator (intra-cavity intensity) is

$$I = I_s \left(\frac{g_0 d}{\ln(1/RT)} - 1 \right). \quad (2.32)$$

In the regime of low gain ($1 + g d \approx 1$) and low losses ($R T \approx 1$), this can be approximated to

$$\boxed{I \approx I_s \left(\frac{g_0 d}{1-RT} - 1 \right)}. \quad (2.33)$$

Here, I_s denotes the saturation intensity, g_0 is the gain coefficient at very low intensity ($I \rightarrow 0$), d is the length of the active medium, T is the transmission factor and R is the reflectance of the mirrors as defined in (2.28).

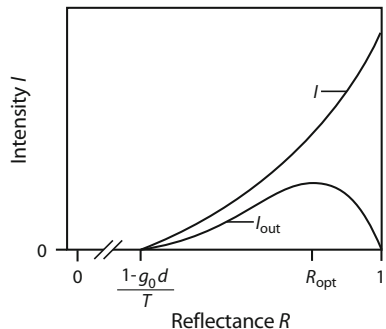
The output intensity is then given as follows:

$$\boxed{I_{\text{out}} = \frac{I}{2} (1 - R_1) \approx I(1 - R)}. \quad (2.34)$$

The factor $\frac{1}{2}$ indicates that the total intensity is composed of the intensities of two waves traveling in opposite directions inside the resonator. The approximation in the last part of the equation assumes that $R_2 = 1$ and $R_1 \approx 1$, so that $R = \sqrt{R_1} \approx (1 + R_1)/2$.

Equations (2.33) and (2.34) can be used to estimate the output intensity of a laser, if the gain coefficient g_0 and the saturation intensity I_s are known. These

Fig. 2.11 Dependence of the intra-cavity intensity I and the output intensity I_{out} on the reflectance $R = \sqrt{R_1}$. The reflectance of the rear mirror is assumed to be $R_2 = 1$



quantities can also be derived from the cross-sections or Einstein coefficients, respectively.

The dependence of the intra-cavity intensity I and output intensity I_{out} upon the reflectance $R = \sqrt{R_1}$ is depicted in Fig. 2.11. The diagram shows that an optimum reflectance R_{opt} exists for which maximum output intensity is obtained. For a helium–neon laser, R_{opt} is in the range between 95 and 99%, while it is between 20 and 90% for solid-state lasers and only 5% for high-gain excimer lasers.

2.8 Temporal Emission Behavior

The dynamics of continuous and pulsed laser emission can be modelled by rate equations describing the temporal evolution of the photon density in the resonator and of the energy level populations in the gain medium participating in the laser process. A distinction is made between three-level and four-level lasers, as shown in Fig. 2.12. One of the few important three-level laser systems is the ruby laser. In solid-state lasers, level 3 is in both cases a broad absorption band from which energy is quickly transferred to the upper laser level 2 ($\tau_{32} \ll \tau_{21}$). The major disadvantage of a three-level laser is the fact, that the lower laser level is the ground state, so that strong pumping is required for attaining population inversion. Hence, a four-level laser is favorable, as the lower laser level can be depleted by transitions to a lower level, as it is the case for the Nd:YAG laser.

The rate equation for the population density N_1 of the lower laser level reads

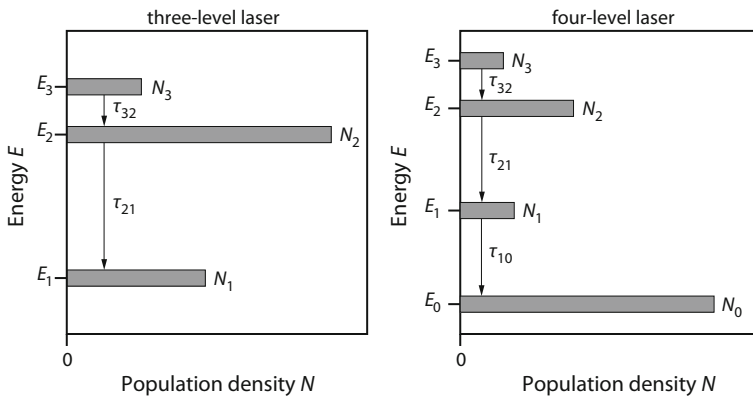


Fig. 2.12 Energy levels E_i and population densities N_i of a three-level laser (a) and a four-level laser (b)

Using the photon density $\Phi = \varphi/c$ (1.5) and (1.8) introduced above and considering (2.3) and (2.8), one obtains

$$\frac{dN_1}{dt} = \sigma \cdot c(N_2 - N_1)\Phi + \frac{N_2}{\tau_{21}} - \frac{N_1}{\tau_{10}}. \quad (2.36)$$

Assuming that the pump level decays very rapidly ($N_3 \approx 0$), the rate equation for the upper laser level population density N_2 is given as follows:

$$\begin{aligned} \frac{dN_2}{dt} &= + \left| \frac{dN_1}{dt} \right|_a - \frac{N_2}{\tau_2} - \left| \frac{dN_2}{dt} \right|_{st} + W_p N_0 \\ &+ \text{absorption} - \text{spont. emission} - \text{st. emission} + \text{pump rate}. \end{aligned} \quad (2.37a)$$

$$= -\sigma \cdot c(N_2 - N_1)\Phi - \frac{N_2}{\tau_{21}} + W_p N_0. \quad (2.37b)$$

W_p represents the normalized pump rate (number of photons per unit time) and the product $W_p \cdot N_0$ describes how many particles are excited to the upper laser level per unit volume per unit time. The quantity $\tau_2 = (1/\tau_{21} + 1/\tau_{20})^{-1}$ is the lifetime of the upper laser level E_2 .

The sum of all population densities N is identical with the density of laser atoms, e.g. $1.4 \times 10^{20} \text{ cm}^{-3}$ for the Nd:YAG laser

$$N = N_0 + N_1 + N_2. \quad (2.38)$$

The rate equation for the photon density Φ can be written as

$$\frac{d\Phi}{dt} = - \left| \frac{dN_1}{dt} \right|_a + \frac{\eta N_2}{\tau_{21}} + \left| \frac{dN_2}{dt} \right|_{st} - \frac{\Phi}{\tau_r},$$

— absorption + spont. emission + st. emission — emission

(2.39)

where η is the portion of the spontaneous emission which is emitted along the resonator axis. Since the laser light is predominantly generated by stimulated emission, the term for spontaneous emission can be neglected. Using the relations (2.3) and (2.8), the differential equation thus reads

$$\frac{d\Phi}{dt} = \sigma c(N_2 - N_1)\Phi - \frac{\Phi}{\tau_r}. \quad (2.40)$$

Here, the (outcoupled laser) emission and additional intra-cavity losses determine the photon lifetime inside the resonator

$$\tau_r = \frac{d}{c(1 - RT)}, \quad (2.41)$$

with d being the length of the gain medium. For an ideal four-level laser, the lower level lifetime is very short, so that $N_1 \approx 0$ and $N \approx N_0 + N_2$. The change in population density of the upper laser level is hence simply given by the pump rate reduced by the spontaneous and stimulated emission:

$$\frac{dN_2}{dt} \approx W_p N_0 - \frac{N_2}{\tau_2} - N_2 \sigma c \Phi. \quad (2.42)$$

The photon density is decreased by the outcoupling of the laser beam (plus additional losses), while it is increased by the stimulated emission:

$$\frac{d\Phi}{dt} \approx - \frac{\Phi}{\tau_r} + N_2 \sigma c \Phi. \quad (2.43)$$

These equations represent a coupled nonlinear system that has no simple general solution. Therefore, only the stationary solution is introduced in the following. Time-dependent solutions which are necessary to explain relaxation oscillations in cw lasers or laser spiking occurring in pulsed sources are discussed in more detail in Sect. 17.1.

Stationary Solutions of the Rate Equations

For the stationary case $d\Phi/dt = 0$, (2.43) can be written in form

$$N_{2,s} = \frac{1}{\tau_r c \sigma} = \frac{1 - RT}{\sigma d}, \quad (2.44)$$

while the index “s” refers to stationary. This relation corresponds to the threshold condition (2.30) introduced above under the assumption $N_1 \approx 0$. The stationary photon density follows from $dN_2/dt = 0$ and (2.42):

$$\Phi_s = \frac{W_p N_{0,s} - N_{2,s}/\tau_2}{N_{2,s} \sigma c}. \quad (2.45)$$

Inserting (2.44) yields

$$\Phi_s = \tau_r N_{0,s} (W_p - W_{\text{thr}}) \approx \tau_r N (W_p - W_{\text{thr}}). \quad (2.46)$$

In a four-level laser, the stationary population density in the ground state $N_{0,s}$ can be approximated by the total population density N , as only a few atoms are excited. The threshold pump rate W_{thr} , introduced in (2.46), is given as

$$W_{\text{thr}} = \frac{N_{2,s}}{N_{0,s}} \frac{1}{\tau_2}. \quad (2.47)$$

Hence the number of atoms (per unit volume per unit time) that have to be excited to the upper laser level to reach the threshold is

$$W_{\text{thr}} N_{0,s} = N_{2,s} / \tau_2. \quad (2.48)$$

According to (2.47), the stationary photon density increases linearly with pump rate W_p above threshold pump rate W_{thr} . Consequently, the output intensity P that is emitted through a beam cross-section A reads

$$P = A(1 - R)hfc \Phi_s \sim W_p - W_{\text{thr}}, \quad (2.49)$$

corresponding to an intensity

$$I = P/A = (1 - R)hfc \Phi_s \sim W_p - W_{\text{thr}}. \quad (2.50)$$

Such a linear dependence is for instance observed for solid-state lasers where W_p is proportional to the power or energy of the pump light source. The relation (2.50) is also applicable for semiconductor lasers, where W_p is proportional to the injection current. The equation can be identified with the previously found relationship (2.33). In both cases the intensity I scales with the pump rate above threshold, assuming that the gain coefficient g_0 increases with W_p .

The rate equations and stationary solutions presented in this section have been discussed with a particular view to four-level (solid-state) lasers. Similar relations can be deduced for three-level lasers, such as the ruby laser.

Further Reading

1. G.A. Reider, *Photonics: An Introduction* (Springer, 2016)
2. A. Yariv, P. Yeh, *Photonics: Optical Electronics in Modern Communications* (Oxford University Press, 2006)

Chapter 3

Laser Types



The acronym *laser* stands for light amplification by stimulated emission of radiation and describes the fundamental mechanism for the generation of laser radiation. Stimulated emission was already postulated in 1917 by Albert Einstein who described it as one of three processes for how light interacts with matter in order to explain Planck's (radiation) law and quantum hypothesis. However, it wasn't until 1960 that Theodore H. Maiman exploited this process for the first realization of coherent light. The light sources used by then, the sun, light bulbs or gas discharge lamps, emit light in all directions and at various frequencies, whereas the laser produces a highly-collimated beam with narrow spectral linewidth. The undirected radiation of conventional light sources results from the random spontaneous emission of the excited atoms. In contrast, the process of stimulated emission produces identical photons that are of equal energy and phase and travel in the same direction. The propagation direction of a laser beam is determined by the axis of the optical resonator which is, in the simplest case, formed by two mirrors that are arranged on each side of the laser medium. Up to today, more than 10,000 different laser transitions are known generating radiation in the wavelength range from below 10 nm to over 1 mm, thus covering the X-ray, ultraviolet, visible and infrared spectral region. Unlike conventional light sources, lasers are characterized by the following properties:

- narrow spectral linewidth
- low divergence
- high power density
- possibility for generating ultra-short light pulses.

The narrow spectral linewidth is associated to a high frequency stability, monochromatism as well as a high temporal coherence of the light. The low divergence is related to a high beam quality and linked to a high spatial coherence.

Overview of Types

Lasers can be classified by different criteria. The following classification is frequently used:

- semiconductor lasers,
- solid-state lasers,
- liquid lasers,
- gas lasers,
- free-electron lasers.

Optically-pumped solid-state lasers and semiconductor (or diode) lasers are the most prevalent types, while the family of liquid lasers primarily includes dye lasers.

The major challenge in developing a laser is the realization of population inversion in the laser medium which is a prerequisite for light amplification. The energy required for the excitation of the medium can be provided by various means. The first ruby laser was pumped by using an external light source—an approach that was subsequently taken for the development of further so-called optically-pumped lasers. Similarly, laser materials can be excited by electron or other particles beams. These types should not be confused with free-electron lasers, in which electrons themselves represent the gain medium. Gases are usually excited by electrical energy through gas discharge, whereas current injection is done in semiconductor lasers. In conclusion, lasers can also be categorized in terms of the mechanism used for exciting the gain medium:

- optically-pumped lasers (e.g. excitation with flash lamps, continuous lamps, other lasers),
- electron beam-pumped lasers (e.g. realized in special gas and semiconductor lasers),
- gas discharge lasers (e.g. glow, arc or hollow cathode discharge),
- chemical lasers (excitation by chemical reaction),
- gas dynamic lasers (population inversion by expansion of a hot gas),
- injection laser (excitation by current injection in a semiconductor).

The different laser types have very distinct properties. The current state-of-the-art in laser development is represented by the best performance values given in Table 3.1. For comparison, the values from the year 2000 are provided as well.

Further improvement of these values is expected in the next years. However, it should be noted that the parameters presented in Table 3.1 were individually reached by special lasers that were developed for specific fundamental research purposes. A broader range of applications is addressed with less sophisticated,

Table 3.1 Best performance values of lasers today (left column) and in 2000 (right column)

Wavelength range	0.1 nm to 1 mm	10 nm to 1 mm
Frequency stability	10^{17}	10^{15}
Power in continuous wave operation	10^8 W	10^6 W
Peak power in pulsed operation	10^{17} W	10^{13} W
Peak intensity in pulsed operation	10^{25} W/cm ⁻²	10^{20} W/cm ⁻²
Pulse duration	10^{-17} s	10^{-15} s

commercial systems. For the selection of an appropriate laser source, this chapter provides an overview of their most important properties like wavelength and output power. The detailed characteristics of the different laser types are then discussed in the following chapters.

3.1 Wavelengths and Output Powers

The emission wavelengths and typical output powers of several commercial laser sources are summarized in Table 3.2. Frequency conversion techniques such as second and third harmonic generation or Raman conversion (see Sects. 19.2–19.5) as well as frequency tuning allow to reach any wavelength between 10 nm and 1 mm. Nevertheless, certain spectral regions are easier to access than others. In particular, a large multitude of laser materials is available for generating high-power output in the near infrared region.

Laser can be operated in pulsed or continuous (wave) mode. For continuous wave (cw) lasers, the output power (given in Watt) is an important parameter. For pulsed lasers, several quantities are relevant: the pulse energy E_p (in Joule), the pulse duration τ and the time between successive pulses T . The pulse peak power P_p , i.e. the maximum occurring optical power, can be calculated from these parameters as follows:

$$\boxed{P_p = \frac{E_p}{\tau}}. \quad (3.1)$$

This equation holds true for rectangular pulses, while a constant factor has to be inserted in case of other pulse shapes. For instance, the peak power of a Gaussian-shaped pulse having a FWHM pulse width τ_{FWHM} is approximately given by $P_p \approx 0.94E_p/\tau_{\text{FWHM}}$.

The average output power P_{av} of a pulsed laser sources is defined as

$$\boxed{P_{\text{av}} = \frac{E_p}{T} = E_p \cdot f_p}, \quad (3.2)$$

where $f_p = 1/T$ is the pulse repetition frequency.

Table 3.3 provides an overview of the output parameters of different laser sources, grouped into gas, solid-state, liquid (dye) and semiconductor lasers. Gas lasers are electrically-pumped by gas discharge except for the long-wave molecular lasers which are optically-pumped using CO₂ lasers. Solid-state and dye lasers are optically-pumped by gas discharge lamps or other lasers. For example, the widely-used Nd:YAG laser can be pumped using xenon flash lamps (for pulsed operation) or krypton arc lamps (for continuous operation). However, diode lasers are mostly used for both operation modes due to the higher pump efficiency. Dye

Table 3.2 Selected commercial laser sources, sorted by emission wavelength

Wavelength (range) (μm)	Laser type	Operation mode, typical average output power
0.152	F ₂ excimer laser	Pulsed, a few W
0.192	ArF excimer laser	Pulsed, a few W
0.222	KrCl excimer laser	Pulsed, a few W
0.248	KrF excimer laser	Pulsed, a few 10 W
0.266	Nd laser, fourth harmonic	Pulsed, a few 0.1 W
0.308	XeCl excimer laser	Pulsed, a few 10 W
0.325	He-Cd laser	CW, a few mW
0.337	N ₂ laser	Pulsed, a few 0.1 W
0.350	ArC, KrC laser	CW, 2 W
0.351	XeF excimer laser	Pulsed, a few 10 W
0.355	Nd laser, third harmonic	Pulsed, a few 10 W
0.38–0.55	GaN diode laser	CW, 10 mW
0.3–1.0	Dye laser	Pulsed, a few 10 W
0.4–0.9	Dye laser	CW, a few W
0.442	He-Cd laser	CW, a few 10 mW
0.45–0.52	ArC laser	CW, mW up to 30 W
0.51–0.58	Cu laser	Pulsed, a few 10 W
0.532	Nd laser, second harmonic	CW and pulsed, 100 W cw
0.543	He-Ne laser, green	CW, a few 0.1 mW
0.632	He-Ne laser, red	CW, up to 100 mW
0.63–0.67	InGaAsP diode laser	CW, 10 mW
0.694	Ruby laser	Pulsed, a few W
0.7–0.8	Alexandrite laser	Pulsed, a few W
0.7–1	Titanium-sapphire laser	CW and pulsed, a few W
0.75–0.98	GaAlAs diode laser	CW and pulsed, up to 1 W
0.8–2.4	Cr:LiSAF and other vibronic lasers	CW, about 1 W
1.03	Yb (fiber or disk) laser	CW and pulsed, more than 10 kW cw
1.06	Nd (fiber or disk) laser	CW and pulsed, more than 1 kW cw
1.15	He-Ne laser, NIR	CW, mW
1.1–1.6	InGaAsP diode laser	CW and pulsed, mW cw
1.32	Iodine laser	Pulsed, up to MW cw
1.32	Nd laser	CW and pulsed, a few W cw
1.52	He-Ne laser	CW, mW
1.54	Er (fiber) laser	CW, a few W
1.65	Er laser, resonantly-pumped	CW and pulsed, a few W cw
1.9	Tm fiber laser	CW, a few 10 W

(continued)

Table 3.2 (continued)

Wavelength (range) (μm)	Laser type	Operation mode, typical average output power
2–4	Xe–He laser	CW, mW
2.06	Ho (fiber) laser	CW and pulsed, up to 100 W cw
2.6–3.0	HF laser	CW and pulsed, up to 100 W cw
2.7–30	lead-salt diode laser	CW, mW
3–300	Quantum cascade laser	CW, a few W
2.9	Er laser	Pulsed, up to 100 W
3.39	He–Ne laser, MIR	CW, mW
3.6–4	DF laser	CW and pulsed, up to 100 W cw
5–6	CO laser	CW, 10 W
9–11	CO ₂ laser	CW and pulsed, a few kW cw
40–1000	Far-infrared laser	CW, up to 1 W

Table 3.3 Wavelengths, typical average output powers, pulse energies and pulse duration of widely-used laser sources

Laser type	Material	λ (μm)		P (W)	E_p (J)	τ
<i>Gas lasers</i>						
Excimer laser	ArF	0.19		1	20 ns	
	KrF	0.25 (gas discharge)		1	10 ns	
	XeCl	0.308	–	1	20 ns	
Nitrogen laser	N ₂	0.34	–	0.1	1 ns	
He–Cd laser	Cd	0.32–0.44	0.05	–	–	
Noble gas ion laser	Kr ⁺	0.33–1.09	10	–	–	
	Ar ⁺	0.35–0.53	20	–	–	
Copper metal vapor laser	Cu	0.51; 0.58	–	0.002	20 ns	
He–Ne laser	Ne	0.63; 1.15; 3.39	0.05	–	–	
HF laser	HF	2.5–4	10.000	1	1 μs	
CO laser	CO	5–7	20	0.04	1 μs	
CO ₂ laser	CO ₂	9–11	15.000	10.000	10 ns	
Optically-pumped molecular laser	H ₂ O	28; 78; 118	0.01	10 ^{−5}	30 μs	
	CH ₃ OH	40–1200	0.1	0.001	100 μs	
	HCN	331; 337	1	0.001	30 μs	
<i>Solid-state lasers</i>						
Ruby laser	Cr: Al ₂ O ₃	0.69		400	10 ps	

(continued)

Table 3.3 (continued)

Laser type	Material	λ (μm)	P (W)	E_p (J)	τ
Alexandrite laser	Cr: BeAl ₂ O ₄	0.7–0.8		1	10 μs
Titanium-sapphire laser	Ti:Al ₂ O ₃	0.7–1.0	50	–	6 fs
Vibronic solid-state laser		0.8–2.5			
Glass laser	Nd:glass	1.06	1000		1 ps
		0.21; 0.27; 0.36; 0.53 (incl. harmonic generation)			
YAG laser	Nd: YAG	1.06	1000	400	10 ps
		1.05–1.32 (7 lines with frequency selection elements)			
Ho laser	Ho:YLF	2.06	5	0.1	100 μs
Er laser	Er:YAG	2.94	1	1	100 μs
Color center laser	e.g. KCl	1–3.3	0.1	–	–
Dye lasers		0.4–0.8	1	25	6 fs
		0.05–12 (incl. harmonic generation)			
<i>Semiconductor lasers</i>					
Gallium nitride laser	GaN	0.38–0.53	10		
Zinc selenide laser	ZnSe	0.42–0.50			
	GaAlAs	0.65–0.88	10		5 ps
Gallium arsenide laser	GaAs	0.904			
	InGaAsP	0.63–2			
Lead-salt diode laser	PbCdS	2.8–4.2	0.001		
	PbSSe	4–8			
	PbSnTe	6.5–32			
Quantum cascade laser		3–300	1		

lasers are primarily pumped by noble gas ion lasers or excimer lasers, while in semiconductor lasers the pumping mechanism involves the injection of electrons, i.e. electrical current. This enables high efficiency and compact designs. As for gas and solid-state lasers, low divergence and narrow linewidth emission is achieved with diode lasers which are nowadays available at emission wavelengths from the ultraviolet to infrared spectral range. Hence, diode lasers are the preferred laser type, unless specific requirements such as high output powers or very low divergence have to be met.

3.2 Tunable Lasers

All lasers can be tuned in frequency within a certain frequency range Δf . Differentiation of the relation $f = c/\lambda$ yields

$$\frac{\Delta f}{f} = -\frac{\Delta \lambda}{\lambda}, \quad (3.3)$$

with $\Delta\lambda$ being the wavelength range, while f and λ denote the center frequency and wavelength, respectively. The frequency tuning range of a helium-neon laser is about $\Delta f = 10^9$ Hz with a center frequency at $f = 5 \times 10^{14}$ Hz. This corresponds to a relative tuning range of $\Delta f/f = 2 \times 10^{-6}$. The term *tunable laser* in a narrower sense, however, only refers to lasers that provide a much broader relative tuning range of $\Delta f/f = |\Delta\lambda/\lambda| = 10^{-2}-10^{-1}$. The properties of such lasers are shown in Fig. 3.1. The different systems are described in the next chapters.

Dye lasers were mostly used as tunable systems in the last decades of the 20th century. The various dye solutions allow for the generation of ultraviolet, visible and infrared light from 0.3 to 1.5 μm wavelength, while the tuning ranges are on the order of $\Delta f/f = 5-15\%$. Although dye laser can be pumped by flash lamps, better beam quality is achieved when using solid-state or gas lasers as pump sources. *Color center* (or *F-center*) lasers are configured similarly and produce radiation from the near-infrared up to 3 μm wavelength. Here, NaCl or other Alkali halide crystals with different impurities are employed. Since the gain media of dye and color center lasers are unstable, these sources have been more and more superseded by *vibronic solid-state lasers* that are based on oxide and fluoride crystals doped with metal ions. The most famous one is the titanium-sapphire ($\text{Ti}: \text{Al}_2\text{O}_3$) laser which has a broad tuning range from 700 to 1050 nm and higher efficiency than dye lasers. Additionally, emission in the visible spectral range can be obtained by second harmonic generation.

Tunable output in the ultraviolet region is provided by *excimer lasers*, albeit the relative tuning range is only up to 1%. Broader tunability is accomplished by frequency-doubling or tripling of tunable lasers emitting at longer wavelengths. Furthermore, difference-frequency generation in optical parametric oscillators (OPOs) and other frequency conversion techniques can be applied.

Molecular lasers are adequate sources for the mid- and far-infrared spectral range, as they offer a multitude of emission lines, which can be addressed individually and allow for discontinuous tuning from one line to the adjacent one. At high pressures, line broadening results in spectral overlap of the lines, thus enabling continuous tuning.

Semiconductor lasers can be tuned by changing the pump current and/or the diode temperature, resulting in tuning ranges of 0.1–1%. The spectral range from 0.38 to 30 μm is covered with various laser diode materials and material compositions, while quantum cascade lasers have established for the region from 3 to 300 μm , as depicted in Fig. 3.1.

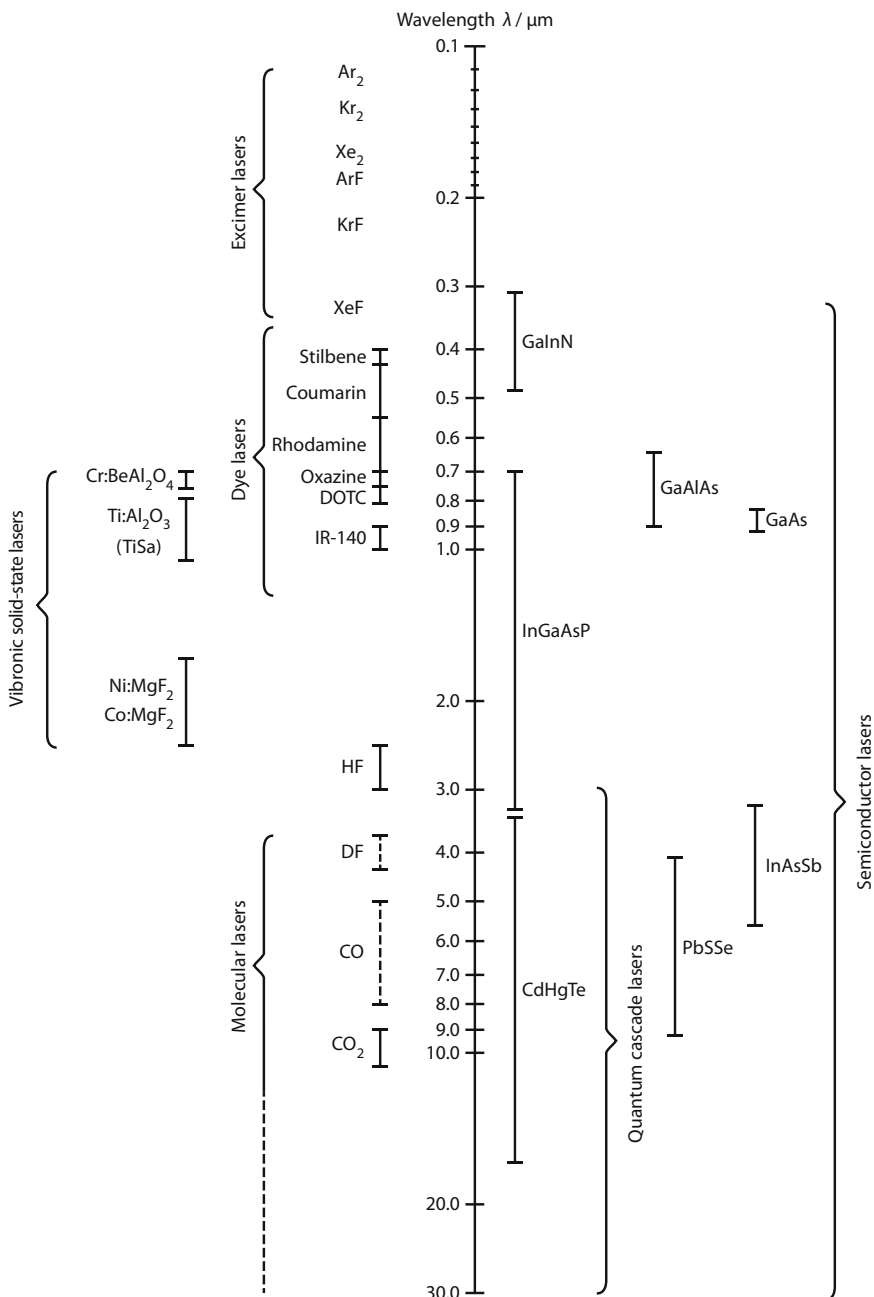


Fig. 3.1 Continuously tunable laser sources. Ruby, Nd:YAG and other classical solid-state lasers are tunable over only about 1 nm = 0.001 μm

3.3 Frequency-Stable Lasers

Lasers emitting at a fixed frequency can be frequency-converted by means of nonlinear optical processes. For instance, the generation of the second, third or even higher harmonics can be accomplished in specific nonlinear crystals. Optical parametric oscillators (OPOs) are employed for continuous tunability as outlined in the previous section, while stimulated Raman scattering is a very efficient tool for generating new laser wavelengths in spectral regions which are difficult to access with conventional laser media. These frequency conversion techniques are elaborated in Sects. 19.2–19.5.

Applications in the fields of interferometric metrology and holography require lasers with high frequency stability. The theoretical limit in terms of frequency stability of a laser is discussed in Sect. 20.2. In principle, any laser can be stabilized to a certain emission frequency within its gain bandwidth, however this involves more or less complex methods. In the low-power regime, semiconductor and fiber lasers incorporate grating structures allow for high frequency stability and very narrow linewidth in the MHz-regime. Frequency-stable emission is also possible in helium-neon and argon lasers by controlling the length of the laser cavity.

The stabilization techniques are highly evolved, so that the stability of lasers can be measured by ^{133}Cs atomic clocks which offer an accuracy of about $\Delta f/f \approx 10^{-15}$. Since the light velocity is an exact defined quantity of 29,979,458 m/s since 1983, the absolute wavelength of a laser can hence only be determined with a maximum accuracy of 10^{-15} , although higher frequency stabilities on the order of a few tens of mHz at 1.5 μm (200 THz), i.e. $\Delta f/f \approx 10^{-16}$ have been accomplished in recent years. Here, the stability is only limited by thermal noise of the used laser resonators.

The advancement of ultra-stable lasers has boosted the development of optical atomic clocks which are based on narrowband optical transitions in an ensemble of atoms or single ions, instead of using microwave oscillators as in ^{133}Cs atomic clocks. Due to the much higher frequencies of the probed transitions, optical atomic clocks now outperform the best microwave Cs atomic clocks in terms of precision, approaching frequency uncertainties on 10^{-18} . Such high frequency stabilities demanding immense technical efforts are not required for most applications.

3.4 High-Power Lasers

When discussing the output power of lasers, one has to distinguish between continuous wave and pulsed operation, as the latter can provide high peak powers even at low average output powers. The CO₂ and solid-state lasers, especially the Nd: YAG laser, represent the most prevalent high-power sources and are mostly employed for material processing or, at lower powers, for medical surgery. Commercial, continuous CO₂ lasers emitting at 10.6 μm wavelength are available

in the power regime up to 100 kW, while Nd:YAG lasers operating at 1.06 μm and fiber lasers provide cw output powers from 10 to 20 kW. The major advantage of solid-state lasers compared to CO₂ lasers is the fact, that the near-infrared radiation can be guided in glass fibers.

Pulsed Nd:glass lasers offer pulse peak powers of about 10 terawatts (10^{13} W) at pulse durations of about 1 ns (10^{-9} s). Such high powers are necessary for investigating laser-induced fusion processes and are reached in only a few laboratories in the world, as large facilities are required for this purpose.

Even higher pulse peak powers can be obtained with ultra-short pulse lasers, e.g. the titanium-sapphire laser, however the pulse durations are much shorter in the fs- to ps-regime. Pulsed output at powers on the order of a few gigawatts (10^9 W) can be achieved with simple tabletop solid-state lasers.

Excimer lasers have been intensively developed in the recent years, so that output powers comparable to solid-state lasers can be reached, yet only pulsed operation is possible. Nevertheless, excimer lasers are of interest due their shorter emission wavelength which strongly influences the interaction of the laser light with different media, e.g. in material processing or medical applications. While thermal processes are dominant in case of solid-state and CO₂ lasers, excimer lasers allow for the direct breaking of chemical bonds, thus enabling sharp cutting edges in ceramics or the human eye without causing thermal damage of the adjacent material.

The highest cw output powers of a few megawatts (10^6 W) were obtained in chemical HF- or DF lasers which were intended for military purposes (antimissile defense), but have not found practical use. Extreme output powers are also targeted with other laser systems such as free-electron lasers which are not very prevalent due to the large facilities required for their realization.

High-power diode laser systems are becoming more and more important for various applications in both science and technology, as they offer high compactness and high efficiency. Moreover, they are available at wavelengths from 800 to 1000 nm and hence can be guided in fibers. Powers exceeding 10 kW have been demonstrated, while the achieved beam quality is usually quite poor. Nevertheless, further improvements can be expected in the next years.

3.5 Ultra-short Light Pulses

Laser allow for the generation of ultra-short pulses with durations below 1 femtosecond (10^{-15} s). Spectral analysis of a short pulse yields a frequency bandwidth Δf which is related to the pulse duration τ as follows:

$$\boxed{\Delta f \cdot \tau \geq \frac{1}{2\pi}}. \quad (3.4)$$

The constant $1/2\pi$ holds for Gaussian-shaped pulses, while other constants ranging from 0.1 to 1 apply for other pulse shapes. The quantities Δf and τ describe the $1/e^2$ -widths of the pulse in the frequency and time domain, respectively. If the

full width at half maximum (FWHM) values $\Delta f'$ and τ' are regarded, the time-bandwidth product reads:

$$\boxed{\Delta f' \cdot \tau' \geq \frac{2 \ln 2}{\pi} \approx 0.44}. \quad (3.5)$$

Higher harmonic generation in gases (see Sect. 19.3) enables the formation of even shorter pulses in the attoseconds regime (10^{-18} s). Here, the photon energies are nearly 100 eV corresponding to 15 nm wavelength.

From the relationship between pulse duration and bandwidth follows that broadband lasers are most appropriate for short pulse generation. For this reason, the shortest pulses are currently realized with titanium-sapphire lasers that are pumped by frequency-doubled Nd-based solid-state lasers. The TiSa laser operates at multiple longitudinal modes forming a broad emission spectrum. Passive mode-locking (Sect. 17.4) induces a fixed-phase relationship between the modes, resulting in a short pulse with duration of only a few fs. Further shortening of the pulse is accomplished by nonlinear pulse compression (Sect. 17.5). Mode-locking of other laser types is also possible, however the narrower bandwidth of most laser sources leads to longer pulses. For instance, picosecond (10^{-12} s) pulses can be produced with Nd:glass lasers, while 100 ps are reached with gas lasers. Short laser pulses are relevant for the investigation of rapid biological, chemical and technical processes. This approach is referred to as temporal high resolution microscopy and is unrivalled in the fs-regime, as electrical measurement techniques are limited to picoseconds and longer time scales.

3.6 Beam Parameters and Stability

Aside from the major laser properties

- wavelength, frequency,
- power, energy and
- pulse duration,

there are further important parameters which will be discussed in the following chapters:

- efficiency, technical effort,
- beam quality, transverse mode structure, spatial coherence,
- beam divergence, focusability, beam quality,
- polarization.

Moreover, several stability characteristics are relevant:

- amplitude stability (short-time fluctuations, long-term drifts of cw lasers),
- stability of the pulse amplitude, pulse duration, pulse shape, pulse repetition frequency (jitter),

- frequency stability, linewidth, temporal coherence,
- pointing stability, polarization stability.

For the practical application of lasers, the proper knowledge and determination of these parameters is necessary for achieving acceptable application results. Furthermore, economic factors such as costs of acquisition and maintenance as well as service life, etc. have to be considered. Laser with various properties are produced and sold by numerous companies. An overview of companies can be found in journals on lasers and photonics.

The construction of laser requires fine mechanical, optical and electronic know-how. For gas lasers additional knowledge in vacuum technology is demanded. A more complex technology is mandatory for growing laser crystals as well as for the fabrication of semiconductor layers which form the basis of diode lasers. The realization of large-scale and reliable laser sources and facilities is only possible with industrial development and fabrication methods.

In the following chapters, the different laser types are discussed individually starting with the gas lasers. Gas lasers cover a very broad range of emission wavelengths from the far-infrared to the X-ray spectral region. Depending on the lasing particles (atoms, ions, molecules) and type of laser transitions, the following spectral regions can be reached:

- Infrared: molecules, vibrational and rotational transitions (Chap. 6)
- Visible: atoms and ions, electronic transitions (Chaps. 4 and 5)
- Ultraviolet: molecules, electronic transitions (Chap. 7)
- X-ray: ions, electronic transitions (Sect. 25.5)

In contrast, dye, solid-state and semiconductor lasers (Chaps. 8, 9 and 10) primarily emit in the visible and near-infrared spectral range, while free-electron lasers (Sect. 25.5) show a similarly broad range as gas lasers.

Further Reading

1. L.W. Anderson, J.B. Boffard, *Lasers for Scientists and Engineers* (World Scientific Publishing Company, 2017)
2. F. Träger, *Handbook of Lasers and Optics* (Springer, Berlin, 2007)
3. A.E. Siegman, *Lasers* (University Science Books, 1990)

Part II

Gas and Liquid Lasers

Only about half a year after T. H. Maiman's demonstration of the ruby laser, A. Javan, W. R. Bennett, and D. R. Herriott observed laser operation from an electric discharge in a mixture of helium and neon gases in December 1960. The helium–neon laser not only was the first gas laser but also the first laser that operated continuously. Since then, laser oscillation has been demonstrated for more than 10,000 different transitions in atoms, ions, and molecules in the gas phase, generating radiation at wavelengths ranging from the far-infrared ($\lambda > 100 \mu\text{m}$) to the soft X-ray region (0.1–10 nm). The spectral range from the near-infrared to the ultraviolet (UV) region can also be addressed with dye lasers which are based on a liquid dye solution as the gain medium. The broad gain bandwidth of dye lasers enables wide wavelength tunability and the generation of ultra-short pulses by mode locking.

Although diode and (frequency-converted) solid-state lasers have replaced liquid dye and gas lasers in a number of applications, the latter still represent workhorses in research as well as in scientific, industrial, and medical applications. Their applications range from material processing to ophthalmic surgery. The relevance of gas lasers is reflected by the prominent position that they occupy in the laser industry. Sales of gas lasers in 2017 are estimated to more than \$1 billion compared to about \$12 billion for the total laser market.

Chapter 4

Laser Transitions in Neutral Atoms



Atoms can produce a multitude of emission lines in the visible spectral region, as shown for the hydrogen atom in Fig. 1.5, where electron transitions to the quantum state $n = 2$ (Balmer series) involve the emission of radiation at wavelengths 410, 434, 486 and 656 nm, amongst others. However, laser operation in hydrogen atoms is prevented by the formation of stable H_2 molecules under normal conditions. Hence, dissociation of the molecules would be required during the gas discharge to produce a hydrogen gas. The generation of visible light is possible by using the noble gas neon which exists in monatomic form under standard conditions. Excitation of neon by collisions with helium atoms forms the basis for the realization of the helium–neon laser. Aside from laser emission in the visible spectral range, the He–Ne laser can also produce ultraviolet light, yet laser operation in this region is hindered by the fact that the lower laser level is the ground state in this case, thus impeding population inversion. UV lasers hence mainly rely on transitions in ions and molecules. The same holds true for the infrared spectral range, as the photon energies related to infrared transitions are much smaller than the pump energies required for populating the upper laser level in atoms. Higher quantum efficiency for generating infrared radiation is obtained in molecules which possess light-emitting states close to the ground state.

4.1 Helium–Neon Lasers

The helium–neon laser emits in the visible spectral range and provides output powers from below 1 mW up to several 10 mW. Most commercially available He–Ne lasers operate in the low-power regime at about 1 mW and are employed as alignment lasers as well as in optical metrology and holographic applications due to their high spatial coherence and power stability and long lifetime. In many applications, e.g. in barcode scanners or laser printers, the He–Ne laser has been replaced by more compact and efficient diode lasers, especially in the red and infrared

spectral range. Nevertheless, it is still superior in terms of spectral stability and narrow bandwidth. Apart from the most prominent emission line at 633 nm, He–Ne lasers can also produce orange (612 nm), yellow (594 nm) and green (543 nm) laser emission, while the selection of the laser wavelength is achieved by the use of selective mirrors or prisms.

Energy Level Diagram

The energy levels of helium and neon relevant for the operation of the He–Ne laser are depicted in Fig. 4.1. The laser transitions occur in the neon atom, with the strongest lines being at 633, 1153 and 3391 nm (see Table 4.1).

The electron configuration of the neon ground state is $1s^2 2s^2 2p^6$, so that the first electron shell ($n = 1$) and second shell ($n = 2$) are fully occupied with 2 and 8

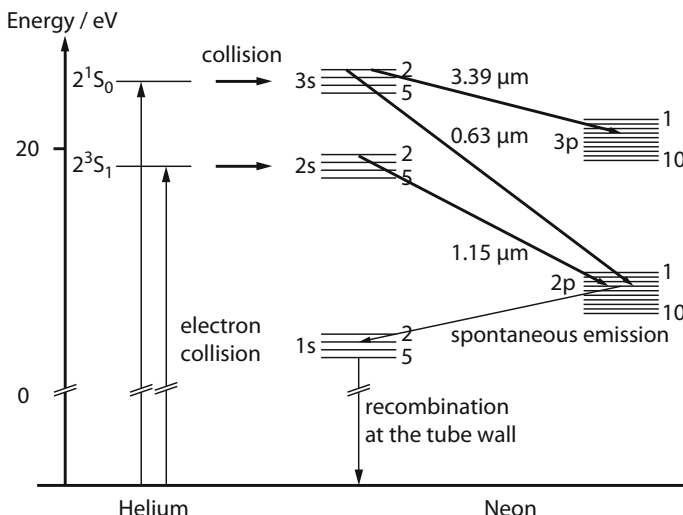


Fig. 4.1 Energy level diagram of a helium-neon laser. The level designation is given in terms of the Paschen notation, e.g. $3s_2$ to $3s_5$ and $2p_1$ to $2p_{10}$. In an electric gas discharge tube, electrons collide with He atoms and excite them to metastable states. Some of the excited lighter He atoms transfer their energy to the heavier Ne atoms by collisions. The relaxation of the excited Ne atoms results in the emission of visible or near-infrared radiation

Table 4.1 Transitions of the most intense emission lines of the helium-neon laser

LS coupling scheme	Paschen notation	Emission wavelength (nm)
$5s\ ^1P_1 \rightarrow 4p\ ^3P_2$	$3s_2 \rightarrow 3p_4$	3391
$4s\ ^1P_1 \rightarrow 3p\ ^3P_2$	$2s_2 \rightarrow 2p_4$	1153
$5s\ ^1P_1 \rightarrow 3p\ ^3P_2$	$3s_2 \rightarrow 2p_4$	633

electrons, respectively (see Fig. 1.8). The higher electronic states shown in Fig. 4.1 result from the excitation of a valence electron to the 3s, 4s, 5s, ..., 3p, 4p, ... levels, leaving a $1s^2 2s^2 2p^5$ configuration of the atomic core which couples to the excited electron. According to the LS coupling scheme (Sect. 1.3), the energy levels of the neon atom are described by the one-electron state of the valence electron (e.g. 5s) and the total orbital angular momentum L (= S, P, D, ...) of the coupled system. The full designation further includes the multiplicity $2S + 1$ (upper index) as well as the total angular momentum J (lower index). Alternatively, the phenomenological notation according to Paschen is often used. Here, the s-and p-states are denoted as 1s, 2s, 3s, ... and 2p, 3p, ..., while the sub-levels are numbered consecutively from 2 to 5 (for s-states) and from 1 to 10 (for p-states).

Pumping Mechanism

The active medium of the He–Ne laser is a mixture of helium and neon gases, in which energy is supplied by means of electric discharge. The upper laser levels of the neon atoms (2s- and 3s-states according to Paschen) are selectively populated through collisions with metastable helium atoms ($2^3S_1, 2^1S_0$) that are in turn excited by electron collisions. The collisions between the different atomic species not only involve a transfer of kinetic energy, but also the excitation of the neon atoms, while the helium atoms revert to a lower state. A collision of this type is referred to as collision of the second kind:



where the asterisk denotes an excited state. The energy difference between excited state of the helium atom and the 2s-level of neon is on the order of $\Delta E = 50$ meV. This is roughly twice the thermal energy at 300 K. The excess energy is transformed into kinetic energy and finally dissipated as heat. Similar conditions are present for the population of the 3s-level of the neon atom. The resonant energy transfer from the helium to the neon atoms is the crucial pump mechanism for realizing inversion, while selective population of the upper laser levels is facilitated by the long lifetime and hence high density of the metastable helium states. Owing to the selection rules for electric dipole transitions, the upper laser levels 2s and 3s can only decay into lower p-levels, leading to lifetimes of about 100 ns which is ten times longer than the lifetimes of the lower laser levels, thus promoting laser operation.

Wavelengths

In the following, the most important laser transitions shown in Fig. 4.1 and Table 4.1 should be discussed. The most common emission line at 633 nm

wavelength is produced by the transition $3s_2 \rightarrow 3p_4$. The lower laser level is depleted by spontaneous emission into the 1s-level within 10 ns. This state is stable with respect to electric dipole transitions and therefore decays into the ground state primarily through collisions with the tube wall. The resulting long lifetime of the 1s-state leads to a high population and re-excitation to the 2p- and 3p-levels by electron collisions during the gas discharge. Consequently, since a fraction of the energy delivered to the Ne excited states will reside in the lower laser levels, the steady state population inversion is reduced, which limits the efficiency and output power available from the laser. As the gain and efficiency decrease with the tube diameter, the diameter is usually not larger than 1 mm in practice. In turn, the output power of the He–Ne laser is typically limited to several mW.

The configurations 2s, 3s, 2p and 3p involved in the laser process are split into a number of sub-levels. This leads to additional transitions in the visible spectral range that are listed in Table 4.2. For the emission lines in the visible spectral range, the quantum efficiency is not very high (10%). The energy level diagram in Fig. 4.1 illustrates that the upper laser level is about 20 eV above the ground state, while the photon energy of the red laser light is only about 2 eV.

Infrared emission at 1153 and 1523 nm is obtained from $2s \rightarrow 2p$ transitions. Lasers operating at these wavelengths are commercially available. The emission line at 3391 nm is characterized by a very high gain. In the low-signal regime, i.e. for single-pass propagation of low signals, the gain coefficient is on the order of 20 dB/m. This corresponds to a factor of 100 for a 1 m-long laser resonator. The upper laser level is the same as for the prominent transition at 633 nm and the other visible laser emission lines.

The high gain of the 3391 nm radiation is due to the very short lifetime of the lower laser level $3p_4$ as well as to the long wavelength or low frequency, respectively. In general, the ratio between stimulated and spontaneous emission

Table 4.2 Wavelengths, output powers and spectral linewidths for different laser transitions of the helium-neon laser

Color	Wavelength (nm)	Transition (Paschen notation)	Output power (mW)	Spectral width (MHz)	Gain (%/m)
Infrared	3391	$3s_2 \rightarrow 3p_4$	>10	280	10,000
Infrared	1523	$2s_2 \rightarrow 2p_1$	1	625	
Infrared	1153	$2s_2 \rightarrow 2p_4$	1	825	
Red	640	$3s_2 \rightarrow 2p_2$			
Red	635	$3s_2 \rightarrow 2p_3$			
Red	633	$3s_2 \rightarrow 2p_4$	>10	1500	10
Red	629	$3s_2 \rightarrow 2p_5$			
Orange	612	$3s_2 \rightarrow 2p_6$	1	1550	1.7
Orange	604	$3s_2 \rightarrow 2p_7$			
Yellow	594	$3s_2 \rightarrow 2p_8$	1	1600	0.5
Green	543	$3s_2 \rightarrow 2p_{10}$	1	1750	0.5

The most intense lines are printed in bold type

increases with decreasing frequency. Hence, the low-signal gain generally scales as $g \sim f^{-2}$.

Without the use of frequency-selective elements, the He–Ne laser emits at 3391 nm wavelength. Oscillation of the infrared emission line can be suppressed by employing selective resonator mirrors or by exploiting the absorption in the Brewster windows of the discharge tube. In this way, the laser threshold for the 3391 nm radiation can be significantly increased, thus favoring the weaker red line at 633 nm.

Laser Configuration

The electrons required for the pumping process are produced in a discharge tube (Fig. 4.2) which represents the key component of the He–Ne laser and which is operated at voltages of about 2 kV and currents between 5 and 10 mA. The tube has a length of typically 10–100 cm with commercial devices tending to the short end of this range. The diameter of the discharge capillary is about 1 mm and determines the diameter of the emitted laser beam. Extension of the tube diameter results in a reduction of the optical efficiency, as depletion of the 1s-level predominantly occurs through collisions with the tube wall as explained above.

Optimum output power at 633 nm is achieved at total gas pressures p fulfilling the condition $p \cdot D \approx 500 \text{ Pa mm}$, with D being the bore diameter of the tube. Thus, for a discharge tube diameter of 2 mm, the He–Ne total pressure should be approximately $250 \text{ Pa} \approx 1.9 \text{ Torr}$. The He:Ne mixing ratio also depends on the desired laser wavelength. For red emission at 633 nm, a He:Ne ratio of 5:1 is suggested, whereas a ratio of 10:1 is preferable for operation at the infrared line at 1153 nm.

Due to inefficient pumping mechanism, the overall efficiency of the He–Ne laser emitting at the 633 nm line is only 0.1%. However, the lifetime of 20,000 operating hours is very long compared to other laser sources. The gain is on the order of $g \cdot d \approx G - 1 \approx 5\%$ for the red line and even lower for the other visible

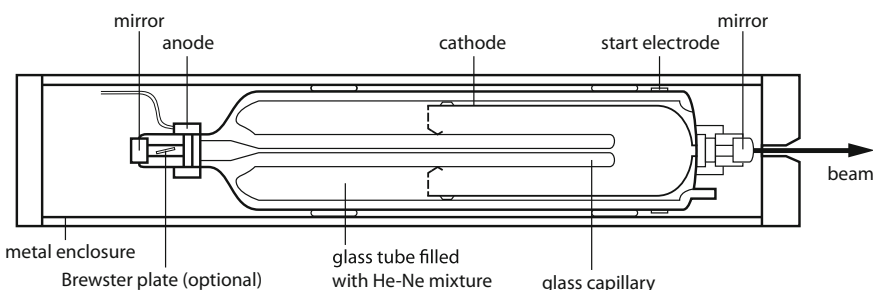


Fig. 4.2 Schematic setup of a helium-neon laser generating polarized output in the mW-regime

transitions, so that resonator mirrors with high reflectivity are required. In most commercial devices designed for mass production the mirrors are directly applied to the windows of the assembly.

Laser Properties

The polarization direction of the output radiation is adjusted by inserting a Brewster plate into the resonator, as shown in Fig. 4.2. The reflectivity of an optical surface becomes zero if the light is incident at the so-called Brewster angle and its polarization direction is parallel to the plane of incidence. Light polarized along this direction is hence transmitted through the Brewster window without loss (see Sect. 15.3). In contrast, the reflectivity of the window is high for the light component that is polarized perpendicularly to the plane of incidence thus suppressing laser oscillation of this component. The degree of polarization, i.e. the power ratio of the polarization components that are oriented parallel and perpendicular to the desired polarization direction, is typically 1000:1 in commercial systems. Without the use of Brewster plates, the emitted radiation of a He–Ne laser is unpolarized or randomly polarized.

The laser normally operates in the fundamental transverse mode (TEM_{00}), while multiple longitudinal modes oscillate simultaneously. For a typical resonator length (distance between the highly reflective rear mirror and the partially reflective outcoupling mirror) of $L = 30$ cm, the frequency spacing between the modes is $\Delta f' = c/2L = 500$ MHz. The center frequency of the red emission line is at 4.7×10^{14} Hz. Since light amplification occurs within a spectral range of $\Delta f = 1500$ MHz (Doppler width), the laser operates at three different longitudinal modes: $\Delta f/\Delta f' = 3$. The coherence length is on the order of 20–30 cm. By shortening the resonator length ($L \leq 10$ cm) oscillation of a single longitudinal mode is achieved. However, due to mechanically- or thermally-induced changes in the optical path length between the resonator mirrors, the absolute frequencies of the resonator eigenmodes vary over time. Consequently, even in single-mode operation, the laser emission frequency is not stable but fluctuates within the gain bandwidth Δf . Stabilization of the laser frequency to the center of emission line can be accomplished by active control of the resonator length, e.g. by using a piezoelectric actuator attached to one of the mirrors and an electronic feedback loop. The frequency stability of commercially available He–Ne lasers is on the order of a few MHz, while the stabilization to the sub-Hz-regime has been accomplished with research laboratory setups.

Laser operation at the different emission lines given in Table 4.1 is realized by employing appropriate resonator mirrors or intra-cavity prisms in order to selectively amplify the radiation at the desired wavelength while suppressing stronger lines. However, the output power at the weaker lines is only 10% or less compared to that achievable for the 633 nm line. As for the infrared emission wavelengths, He–Ne lasers operating at the various visible wavelengths are commercially available.

4.2 Atomic Metal Vapor Lasers

Copper and gold vapor lasers represent the most important atomic metal vapor lasers emitting in the visible and adjacent spectral ranges. The wavelengths are in the yellow and green (Cu) as well as in the red and ultraviolet (Au) region (Figs. 4.3 and 4.4). Metal vapor lasers are characterized by high output power (1–10 W, even up to 100 W for Cu) and high efficiency compared to other gas lasers (>1% for Cu). Continuous wave operation is prevented by the long lifetime of the lower laser level. In pulsed operation, repetition rates in the kHz-range are obtained (Table 4.3). Due to the combination of high power and fast pulse repetition rate, metal vapor lasers were of particular interest for material processing, as they enable high machining rates. In addition, they were applied for efficient optical pumping of

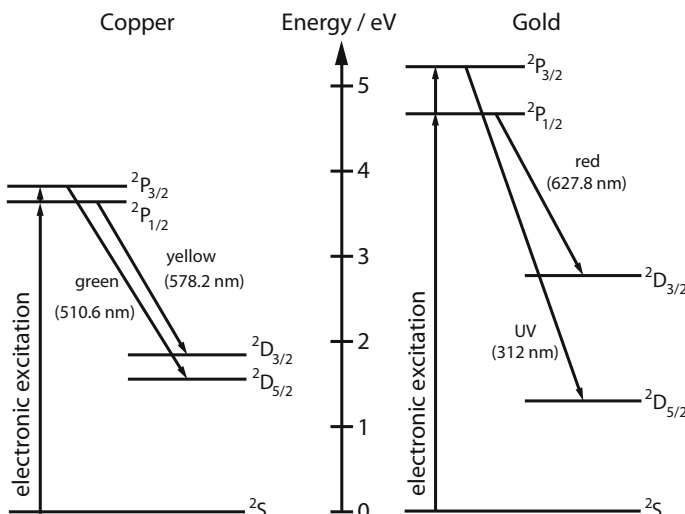


Fig. 4.3 Energy level diagram of a Cu (left) and an Au (right) metal vapor laser

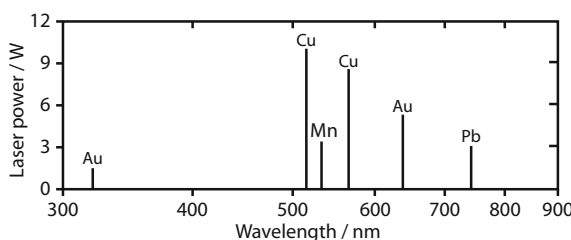


Fig. 4.4 Emission wavelengths and typical output powers of various metal vapor lasers

Table 4.3 Typical properties of commercial copper and gold vapor lasers

Parameter	Unit	Cu laser	Au laser
Wavelength	nm	510.6/578.2	627.8
Average power	W	100	10
Pulse energy	mJ	10	2
Pulse duration	ns	15–60	15–60
Pulse peak power	kW	<300	50
Pulse repetition rate	kHz	5–15	6–10
Beam diameter	cm	2–8	2–8
Beam divergence	mrad		
Stable resonator		3–5	3–5
Unstable resonator		0.5	0.5

dye lasers. In the last two decades, they have increasingly been superseded by less technically demanding solid-state and fiber laser systems.

Energy Level Diagram

The relatively high overall efficiency of 0.2% (Au) and >1% (Cu) can be explained with the respective energy level diagrams which are very similar for the two metal vapor lasers. Figure 4.3 reveals that the quantum efficiency, i.e. the ratio between the laser photon energy and the pump energy, is about 0.6 for the copper laser, resulting in overall efficiencies that are higher compared to the He-Ne or the Ar laser. The upper laser level is populated by electron collisions in a gas discharge. Due to the opposite parity with respect to the ground state, the excitation occurs strongly selective, while a permitted transition from the upper laser level (2P -states) to the ground state leads to a short lifetime of 10 ns. However, at a sufficiently high atomic density ($>10^{13} \text{ cm}^{-3}$), the spontaneous emission is re-absorbed (radiation trapping), leading to an effective upper level lifetime of about 10 ms. Hence, laser operation is only enabled by radiation trapping at high gas densities. At lower densities, the lifetime is too short and the losses introduced by spontaneous emission are too large.

Since the lower laser levels (2D -states) have the same parity as the ground state, an optical transition is forbidden according to quantum-mechanical selection rules. The lower laser levels are therefore metastable, as the population can only be depleted by slow processes including diffusion of the atoms to the walls of the laser cell. The relaxation time ranges from 10 μs to several 100 μs depending on the operating conditions. Hence, population inversion is only achieved for a brief period of about 100 ns until a significant population of the 2D -state has built, the inversion is lost and lasing stops (self-termination). For this reason, copper and gold vapor lasers can only operate in pulsed mode with pulse durations shorter than 100 ns. The period that is required for the depletion of the lower laser level between

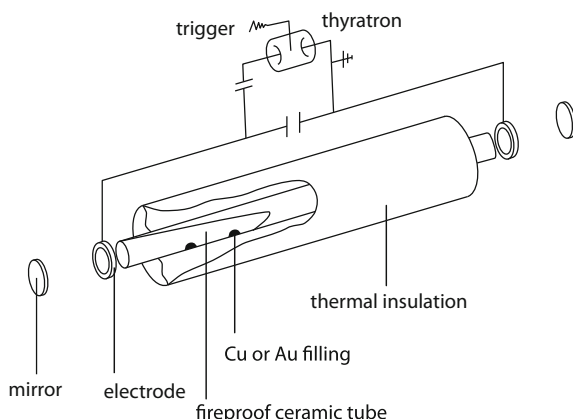
two pulses additionally limits the pulse repetition rate to a few kHz, while high pulse energies (up to 10 mJ) can be readily generated, corresponding to average output powers of several watts. Commercial copper vapor lasers (CVLs) can provide up to 100 W in a 60 mm-diameter beam and operating at a pulse repetition frequency of 10 kHz. At higher frequencies (20 kHz), the pulse energy decreases by a factor of 20 and the pulse duration is halved.

The copper laser emits at two wavelengths in the green (510.6 nm) and yellow (578.2 nm) spectral range, which are produced simultaneously. The relative intensities primarily depend on the operating temperature. At optimum conditions, the output power of the green line accounts for 2/3 of the overall power. Separation of the two components is usually carried out in the output beam. Commercial gold vapor lasers (GVLs) mainly operate at the red line at 627.8 nm. The emission wavelengths and typical output powers of further atomic metal vapor lasers (Mn and Pb) are illustrated in Fig. 4.4. The atomic vapor laser discussed in this section should not be confused with the copper (or silver and gold) ion lasers which produce cw emission in the UV spectral region down to 220 nm (see end of Sect. 5.3).

Laser Configuration

The pulsed gas discharge is ignited between a pair of electrodes placed at each end of a thermally insulated ceramic tube that has a length of typically 1 m and a diameter of 1–8 cm, as displayed in Fig. 4.5. The heat introduced in the discharge tube vaporizes the metal as the temperature reaches up to 1500 °C for the Cu laser and even 1600 °C for the Au laser. The quality of the gas discharge and hence the laser performance can be improved by adding pressurized neon gas at about

Fig. 4.5 Schematic of a metal vapor laser. The setup is enclosed in an evacuated tube which acts as a gas buffer



3000 Pa as a buffer. The metal vapor condenses on cool spots of the tube and needs to be refilled after about 300 h of operation. The operational lifetime of the laser tubes is 1000–3000 h.

The metastable final state of the laser transition necessitates pulsed excitation (10 kV, 1 kA) at repetition rates of several kHz. Moreover, water or air cooling of the laser is required due to the high operating temperatures. The latter can be significantly reduced by substituting the pure metals by metal halides such as copper chloride, copper bromide, copper iodide or copper acetate which form vapors at much lower temperatures in the range from 200 to 600 °C, thus reducing the technical effort. However, the utilization of metal compound vapors increases the complexity of the pump mechanism, as an additional discharge pulse is required to dissociate the vapor molecules prior to the excitation pulse. Here, a delay between the two pulses of 180–300 µs has to be ensured for optimal laser operation.

The high differential gain of 0.1–0.3 cm⁻¹ (for Cu) places low demands on the laser mirrors and laser operation occurs even without mirrors. In commercial systems, the discharge tube is sealed with glass windows while external mirrors with reflectivities of typically 100 and 10% form the laser cavity. Stable resonators result in a multi-mode output beam of 2–8 cm diameter, homogeneous intensity distribution and beam divergence of 3–5 mrad. Smaller divergence of about 0.5 mrad at the expense of lower output power is obtained with unstable resonators. The bandwidth of a single copper emission line is 6–8 GHz.

4.3 Iodine Lasers

Atomic iodine lasers emitting at 1.3 µm wavelength can be classified into two types: the chemical and the optically-pumped iodine laser. For applications requiring very high power the chemical oxygen iodine laser (COIL) is preferred. The laser belongs to the group of chemical lasers as population inversion is realized by a chemical reaction. In a COIL, chemically excited oxygen O₂^{*} in a metastable state, e.g. produced from H₂O₂, is mixed in a supersonic flow with atomic iodine that is generated from CH₃I or C₃H₇I in a gas discharge. Turbulent mixing is effective, as fast-moving iodine atoms merge with slow-moving oxygen molecules. The energy of the latter is transferred to the iodine atoms by collisions according to



Chemical lasers can reach very high pulse energies and output powers in the MW-regime, since the energy is effectively stored in the chemical compounds. In this way, the metastable oxygen molecule serves as an energy reservoir in a flowing system and iodine can be mixed to the flow far downstream. This provides a very efficient pumping technique which separates the energy generation, and hence the heat release from the optical cavity. Although only low electrical power supply is required for operation, the necessary recycling of the reactants is rather challenging.

Therefore, these lasers are not widely used also because their wavelength can be readily produced by semiconductor and solid-state lasers.

Prior to the realization of the chemical iodine laser, the optically-pumped iodine laser was demonstrated. It relies on the dissociation of iodine-containing molecules by means of ultraviolet light, resulting in atomic iodine in an excited state, e.g.

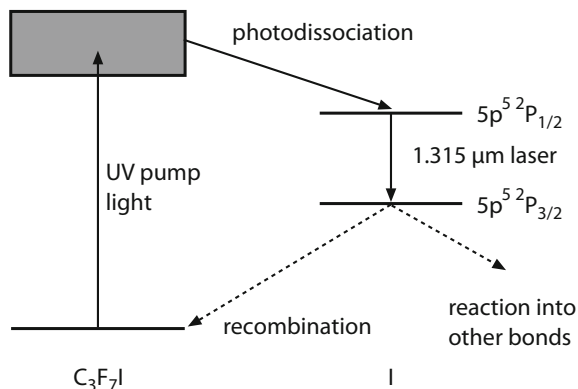


whereby the number of atoms in the ${}^2\text{P}_{1/2}$ -state is larger than the number of atoms in the ${}^2\text{P}_{1/2}$ -ground state, thus providing population inversion.

The energy level diagram shown in Fig. 4.6 illustrates the generation of atomic iodine through photodissociation of $\text{C}_3\text{F}_7\text{I}$ (or alternatively CH_3I) by intense ultraviolet light (around 300 nm) from flash lamps. The laser transition occurs between the $5\text{p}^5 {}^2\text{P}_{1/2}$ - and $5\text{p}^5 {}^2\text{P}_{3/2}$ -state, leading to emission at $1.315 \mu\text{m}$. The involved states result from the fine structure splitting of the ground state configuration $[\text{Kr}]4\text{d}^{10}5\text{s}^25\text{p}^5$. Both states have the same orbital angular momentum $L = 1$, and hence the same parity, so that electric dipole transitions are forbidden. Laser emission thus arises from magnetic dipole transitions. The gas cycle can be either open where the used gas is removed by a vacuum pump, or closed involving recycling of the circulating gas. Apart from the use of flash lamps, optical pumping of iodine lasers using sunlight was investigated already in the late 1980s and beginning 1990s (solar-pumped lasers).

The iodine laser mostly operates in pulsed mode which allows for recombination of the molecular fragments after each pulse. Continuous mode is possible in configurations with longitudinal gas flow and under pumping with Hg high-pressure lamps, reaching about 40 mW output power. The following operating modes can be distinguished: long-pulse mode (around $3 \mu\text{s}$, 3 J), Q-switched mode (around 20 ns , 1 J) and mode-locked mode (2 ns down to 0.1 ns). In the latter case, the bandwidth can be increased by employing a buffer gas, leading to shorter pulse durations (see Sect. 3.5). The pulse repetition rates reach up to 10 Hz . Short pulses with high pulse peak power generated by Q-switching or mode-locking can be

Fig. 4.6 Energy level diagram of a chemical oxygen iodine laser (COIL)



frequency-converted by means of higher harmonic generation, resulting in output wavelengths at 658, 438 and 329 nm.

Power scaling is obtained with oscillator-amplifier arrangements providing high pulse energies in the kJ-range and pulse peak powers in the TW-range. For this reason, iodine lasers are of interest for military, in particular aerial applications, also because its 1.3 μm wavelength falls into the atmospheric transmission window. Furthermore, they were initially considered as a driver for laser fusion, which, however, is nowadays pursued by employing solid-state (Nd:glass) lasers, as outlined in Sect. 25.6.

Further Reading

1. H.J. Eichler, I. Usenov, *Lasers, Gas. The Optic Encyclopedia* (Wiley-VCH, 2018)
2. G. Brederlow, E. Fill, K.J. Witte, *The High-Power Iodine Laser* (Springer, 1983)
3. B.E. Cherrington, *Gaseous Electronics and Gas Lasers* (Pergamon Press, 1979)
4. R. Beck, W. Englisch, K. Gürs, *Table of Laser Lines in Gases and Vapors* (Springer, 1976)
5. C.S. Willett, *Introduction to Gas Lasers: Population Inversion Mechanisms* (Pergamon Press, 1974)

Chapter 5

Ion Lasers



Ion lasers are similar to atomic gas lasers with the difference that the laser transition occurs in ions, i.e. atoms in which the number of electrons is less than the number of protons in the nucleus, resulting in a positive net charge. Like in atoms, the residual electrons in ions can be excited, while relaxation to lower states involves the emission of light. As every atom can be converted into different ions by the ionization of one or more electrons, a multitude of additional emission lines can be produced.

Ions are generated in a gas discharge by the collision of atoms with electrons, excited atoms or other ions. Hence, gas discharge not only initiates atomic electron transitions and the associated generation of radiation, but also light emission resulting from electron transitions in ions. The outer electrons in ions are strongly bound to the nucleus by the Coulomb field, leading to a large spacing of the energy levels as well as shorter emission wavelengths compared to atoms.

Aside from electrical discharge, ions can be excited in laser-induced plasmas. Here, the beam of a pulsed high-power laser is focused onto a solid target which is in turn vaporized. The extreme energy densities present in the gas lead to the generation of electrons and ions, while very high degrees of ionization are obtained. Highly-ionized gases and plasmas emit short-wavelength light and are suitable for realizing X-ray lasers, as discussed in Sect. 25.5.

Ions can also be incorporated in solids as structural components or defects in crystal lattices where they exist in stable form. In contrast, ions in a gas discharge or other plasmas tend to recombine with electrons to form stable atoms. Defect ions are the basis of the most relevant solid-state lasers which will be treated in Chap. 9.

5.1 Lasers for Short Wavelengths

The energy levels E_n of the outermost electron (valence electron) of an ion can be derived by approximating hydrogen-like orbitals. Here, the charge of the nucleus is reduced by the charge of the screening inner-shell electrons, resulting in an effective

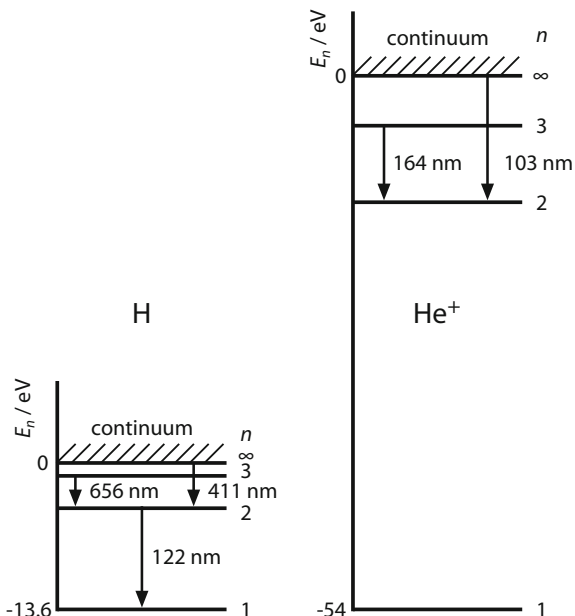
atomic charge or effective atomic number Z , respectively. In this simplified hydrogenic model, the valence electron only experiences the field of a point-like charge, so that the energy levels are given according to Bohr's theory of the hydrogen atom as follows:

$$E_n = -13.6 \text{ eV } Z^2/n^2, \quad (5.1)$$

where n is the principal quantum number. For $Z = 1$, the relation describes the energy levels of the hydrogen atom, as discussed in Sect. 1.2. Ionized helium (He^+) has one outer electron and so that $Z = 2$, while Li^{2+} is described by $Z = 3$, etc. In ions ($Z \geq 2$) the electron energies are larger than in atoms, which is due to the larger effective atomic charge leading to a stronger bonding of the valence electron. This is illustrated in Fig. 5.1 depicting the energy level diagrams of hydrogen and singly ionized helium (He^+). Equation (5.1) only holds true for one-electron atoms like H, He^+ or Li^{2+} . Nevertheless, the trend of increasing electron energies with increasing degree of ionization is also observed in other ions.

Laser transitions usually occur between two excited states in atoms or ions (four-level laser), as it is difficult to establish population inversion with respect to the ground state (three-level laser). Transitions between excited states in the hydrogen atom and other neutral atoms lead to the emission of visible and infrared light, whereas shorter wavelengths in the ultraviolet spectral range are produced by transitions in ionized atoms, as shown for the He^+ -ion in Fig. 5.1. Even

Fig. 5.1 Electron energy levels in the hydrogen atom (left) and singly-ionized helium (right)



shorter-wavelength radiation can be generated with higher ionized atoms (see Sect. 25.5). It should be noted that neither hydrogen nor singly ionized helium have been demonstrated as adequate media for laser operation so far. The two systems were chosen as simple examples for describing the fundamental differences between atoms and ions in terms of their spectral emission properties.

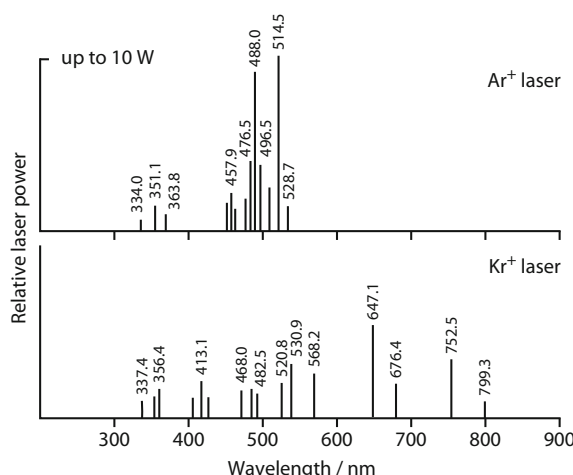
Another approach for realizing light emission at wavelengths that are shorter than those of visible light is the utilization of molecules. Here, the electron energies are similar to atoms; however, the ground state can split into various vibrational and rotational sub-levels or even be unstable like for excimers. This allows transitions from excited electronic states to the ground state with large transition energies, resulting in ultraviolet radiation. Such UV molecular lasers are specified in Chap. 7.

5.2 Noble Gas Ion Lasers

Electric discharge in the noble gases neon, argon, krypton and xenon enables laser action at more than 250 emission lines ranging from 175 nm to about 1100 nm.

Generally, the higher the degree of ionization, the higher the photon energies and thus the shorter the wavelength, as the binding energy of the valence electron increases. The continuous wave argon ion laser represents the most important member of the ion lasers. It delivers output powers above 100 W in the blue-green range and up to 60 W in the near-UV spectral region. Extension to the near-infrared range is provided by the krypton ion laser which offers cw output of several watts. The strongest emission lines of the two ion lasers are shown in Fig. 5.2.

Fig. 5.2 The strongest emission lines of cw argon (top) and krypton (bottom) ion lasers



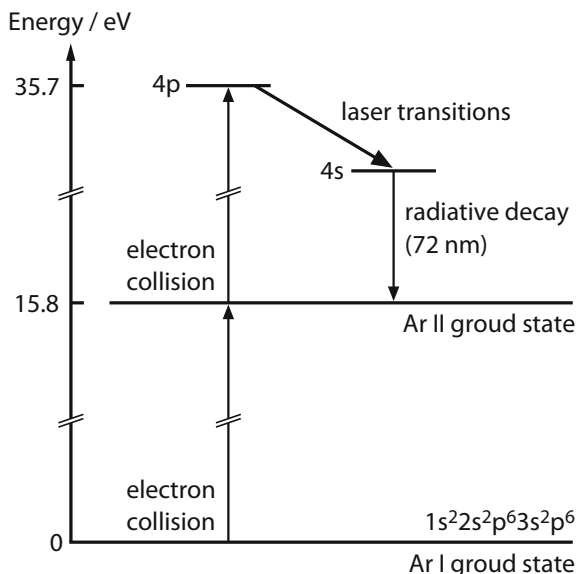
Argon Ion Lasers

The main excitation scheme of the argon ion laser is depicted in the energy level diagram in Fig. 5.3. The argon atom is ionized by electron collision, while a second collision excites the ion to the upper laser level. Alternatively, the population of the upper level is accomplished by radiative transitions from higher levels or by electron collision excitation from lower metastable states of the argon ion. Usually, all the three processes contribute to the upper level population, where cascading transitions from higher levels account for about 25–50%.

The 4p upper laser level is 35.7 eV above the ground state of the argon atom and about 20 eV above that of the argon ion. Hence, only highly energetic electrons participate in the excitation process and the quantum efficiency is low (<8%). The latter refers to the ground state of the argon ion, which can be re-excited in the discharge. The lower laser level is depleted rapidly (1 ns) by radiative decay yielding emission at 72 nm wavelength, whereas the lifetime of the 4p-state is considerably longer (10 ns). Consequently, population inversion is achieved despite the relatively inefficient excitation mechanism.

Splitting of the 4p- and 4s-states allows for multiple laser transitions with different intensities. The 10 most prevalent transitions are shown in Fig. 5.4 together with the corresponding emission lines from which the lines at 488.0 nm (blue) and 514.5 nm (green) are the most intense ones. Commercial argon lasers operating at these wavelengths offer 0.1 W output power with air cooling and several watts if water cooling is implemented (Table 5.1). Due to the two-stage excitation process, the power of the argon laser scales nearly quadratically with the applied pump

Fig. 5.3 Energy levels and excitation process of the argon laser. Ar I is the spectroscopic designation of the argon atom, while Ar II denotes the argon ion Ar^+



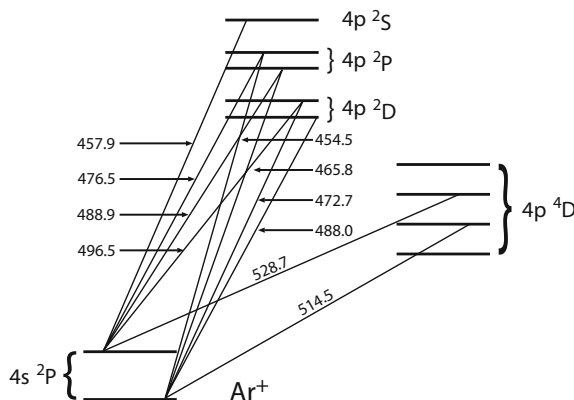


Fig. 5.4 $4s \rightarrow 4p$ transitions of the argon laser. The most intense emission occurs at 488.0 nm (blue) and at 514.5 nm (green)

Table 5.1 Output power of a 20 W-argon ion laser at different emission lines

Conventional optics		UV optics	
Wavelength (nm)	Power (W)	Wavelength (nm)	Power (W)
528.7	2	385.1–351.1	3
514.5	10	363.8–333.6	5
501.7	2	335.8–300.3	2
496.5	3	305.5–275.4	0.6
488.0	10		
476.5	3		
472.7	1		
465.8	1		
457.9	1		
454.5	1		
All lines	20		

Most argon ion lasers have less power

current. High-power argon lasers require high current densities, i.e. high currents on small cross-sections, in order to provide the required ionization and excitation. This imposes larger technical efforts compared to helium-neon lasers.

Further increase in the current density results in two-fold ionization of the argon atom which requires an ionization energy of 43 eV. Additional laser levels exist about 25–30 eV above the Ar^{2+} ground state, producing ultraviolet emission at 334, 351 and 364 nm. Specialized lasers provide a few watts of output power at these wavelengths. However, such UV argon lasers are hardly used anymore, as high current densities and strong magnetic fields are necessary.

Laser Configuration

Efficient excitation of the Ar⁺-ion laser requires electron densities of at least 10^{14} cm^{-3} in the gas discharge and is achieved at current densities of about 800–1000 A cm⁻². Pure argon gas at pressures between 1 and 100 Pa is used, while the electric field along the discharge is on the order of 4 V cm⁻¹, resulting in neutral gas temperatures of up to 5000 K. The high power densities entail considerable technical efforts in the construction of the laser tubes which usually consist of water-cooled ceramics, mostly beryllium oxide (BeO) having a high heat conductivity comparable to aluminum. Since BeO powders are highly toxic, the disposal of the tubes should be carried out by the supplier companies. Aluminum is not suitable as tube material, as it is a good conductor of electricity, thus preventing the discharge inside the tube. For argon lasers operating in pulsed mode, quartz tubes are employed.

Due to the high electron density, the electrons are radially pushed outwards which decreases the current density. This effect is compensated by an external magnetic field that is generated by a long coil surrounding the tube. The resulting Lorentz force experienced by the electrons leads to a circular or spiral trajectory and confines the discharge in the center of the tube along. This reduces the impact of the plasma on the materials of the tube and hence significantly prolongs its lifetime. Additionally, the pumping rate and the efficiency of the laser is increased. The high currents are directly obtained from dispenser cathode, while cooled copper is typically utilized as an anode.

The high currents present in the discharge induce a transfer of momentum from the electrons to the gas, resulting in a gas drift towards the cathode. The gas in the laser is consumed, as the discharge drives the ions towards the wall of the bore tube. In commercial systems, the loss of gas is automatically compensated by a connected gas reservoir.

In contrast to the He–Ne laser, wall effects do not play a role in establishing population inversion, so that large tube diameters can be realized. The gain factor for the 488 nm-line is about $G = 1.35$ for a 50 cm-long tube. For the purpose of good beam quality, the beam diameter is limited to 1.5–2 mm. The overall efficiency is typically below 0.1%.

Simultaneous emission of multiple laser wavelengths is achieved by using broadband laser mirrors, while insertion of a Brewster prism into the laser resonator enables wavelength selection. Here, the beam is incident on the prism surface at the Brewster angle to avoid reflection losses. The other side of the prism is oriented perpendicular to the laser beam which was refracted on the first surface. The perpendicular rear surface is highly reflective. Since the refraction angle inside the prism is wavelength-dependent, rotation of the prism allows for selection of the desired emission line. Typical output power of a 20 W argon ion laser with and without wavelength selection are provided in Table 5.1.

Owing to the elevated temperatures in the discharge zone, the linewidth is Doppler-broadened to 6 GHz. Without frequency-selective elements, the coherence

length is in the cm-range. For argon lasers employed in holographic applications, this value is increased by the use of an etalon which reduces the linewidth to 5 MHz. Almost every commercial noble gas ion laser provides fundamental transverse mode (TEM_{00}) output. In spite of the stress on the tubes, particularly the erosion of the walls, introduced by the high currents and temperature, several 1000 h of operation can be attained.

Krypton Ion Lasers

The discharge tubes in krypton ions lasers are nearly identical in construction. However, since the gas consumption is higher than in argon lasers, a larger gas reservoir is required. The strongest emission line of the Kr^+ laser is at 647 nm (red) yielding several watts of output power. The relative intensities of the other lines ranging between 337.4 and 799.3 nm wavelength (Fig. 5.2) are strongly pressure-dependent. Therefore, lasers designed for wavelength selection usually offer active pressure control. The low efficiency of the krypton laser necessitates higher current densities compared to argon lasers of comparable power. In addition, the larger mass of the krypton ions causes an increased sputtering, so that most lasers are water-cooled, whereas air-cooling is sufficient for low-power argon lasers. More compact, air-cooled krypton lasers are also commercially available, but typically only produce 50–100 mW of output power.

Argon and krypton ion lasers used to be standard devices for generating red and blue-green emission which was applied in laser printing, compact disc manufacturing and laser shows, but also in medicine for retina treatment, i.e. the attachment of the retina to the wall of the eyeball. For many applications, noble gas ion lasers have been replaced by more compact and efficient blue and green diode lasers providing watt-level output powers and by solid-state lasers like the frequency doubled Nd:YAG laser delivering cw output powers up to 100 W at 532 nm wavelength. The development of plasma tubes that are capable of operating at current densities exceeding 1500 A cm^{-1} has enabled the generation of deep ultraviolet (200–300 nm) laser emission from argon, krypton and xenon. For instance, 2.5 W of total power can be obtained with a krypton laser operating at multiple emission lines from 242 to 266 nm wavelength, while 6 W were demonstrated for an argon laser emitting at a group of lines between 275 and 306 nm.

5.3 Metal Vapor Ion Lasers

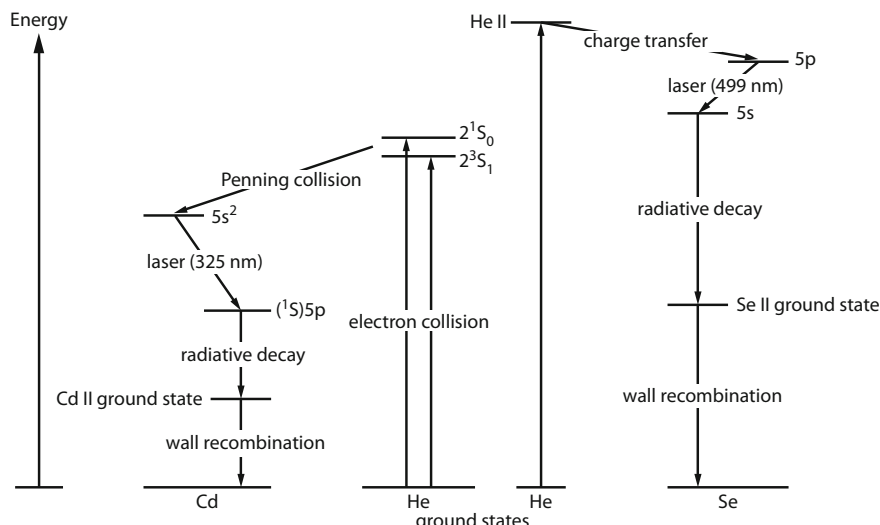
Besides the noble gas ion lasers, another group of gas lasers is the metal vapor ion lasers from which the helium-cadmium and helium-selenium laser are the most relevant members, producing continuous emission from the infrared to the

Table 5.2 Emission wavelengths of the He–Cd and He–Se laser

Ion	Transition	Wavelength (nm)	Output power of commercial systems (mW)
Cd II	$6\ g\ ^2G_{9/2} \rightarrow 4f\ ^2F_{7/2}$	636.8 (red)	
Cd II	$4f\ ^2F_{7/2} \rightarrow 5d\ ^2D_{5/2}$	537.8 (green)	
Se II	$5p\ ^2D_{3/2} \rightarrow 5s\ ^2P_{1/2}$	530.5 (green)	
Se II	$5p\ ^2D_{5/2} \rightarrow 5s\ ^2P_{3/2}$	525.3 (green)	
Se II	$5p\ ^4D_{5/2} \rightarrow 5s\ ^4P_{3/2}$	517.6 (green)	
Se II	$5p\ ^4D_{5/2} \rightarrow 5s\ ^4P_{5/2}$	506.9 (blue-green)	
Se II	$5p\ ^4D_{3/2} \rightarrow 5s\ ^4P_{3/2}$	499.3 (blue)	
Se II	$5p\ ^4D_{5/2} \rightarrow 4p\ ^4P_{3/2}$	497.6 (blue)	
Cd II	$5s\ ^2D_{5/2} \rightarrow 5p\ ^2P_{3/2}$	441.6 (blue)	100
Cd II	$5s\ ^2D_{3/2} \rightarrow 5p\ ^2P_{1/2}$	325.0 (UV)	10

ultraviolet spectral region. Excitation of the metal ions is realized by energy transfer from helium. The subsequent laser transitions in the Cd⁺- (=Cd II) and Se⁺- (= Se II) ions lead to 11 emission lines from 887.7 to 325.0 nm and 46 lines from 1258.6 to 446.8 nm wavelength, respectively. The strongest lines are summarized in Table 5.2, while Fig. 5.5 depicts the energy level diagrams of the He–Cd and He–Se laser.

The underlying process for exciting the Cd⁺-ions to the upper laser level is the Penning collision, where excited helium atoms in the metastable $2\ ^1S_0$ and $2\ ^3S_1$ states transfer their energy to the cadmium atoms, thereby ionizing them. As a result

**Fig. 5.5** Energy level diagram of the He–Cd (left) and the He–Se laser. Cd II and Se II denote the Cd⁺- and Se⁺-ions

of the Penning ionization, the helium atoms return to the ground state, while the Cd⁺-ions are in the 5s²-state. The excess energy is transformed into kinetic energy of the released electron. In the He–Se laser, excitation of the Se⁺-ions occurs by collisions with helium ions produced in the gas discharge. The upper laser levels are populated through charge transfer in collisions between a selenium and a helium ion. The helium ion is transformed into an atom, while the selenium atom is ionized and excited to the 5p-state, as illustrated in Fig. 5.5. Charge transfer also takes place in He–Cd lasers.

The excitation processes are initiated either in glow discharges in quartz tubes or in hollow-cathode discharges. In the former case, the metal vapor pressure is increased by heating a metal reservoir (Cd: 350 °C, Se: 270 °C) in the vicinity to the anode. Owing to the cataphoresis, i.e. the discharge-induced drift of the positively charged metal ions towards the cathode, a homogeneous metal vapor pressure of about 8 Pa is established in the discharge tube. Maximum population of the upper laser levels by electron-impact collisions requires currents in the plasma on the order of 100 mA.

A special type of the He–Cd laser uses the hollow-cathode configuration. Here, the electrode separation is much smaller compared to the glow discharge version, leading to a transverse geometry of the discharge. Accordingly, the plasma generates electron energies and densities higher than those obtainable with the longitudinal discharge where the discharge axis coincides with the optical axis of the laser. Consequently, additional emission lines in the red and green spectral range are generated in addition to the familiar blue and UV lines (see Table 5.2).

Commercial He–Cd lasers are usually operated continuously and provide fundamental transverse mode output at low powers up to 70 mW in the blue (441.6 nm) and 25 mW in the ultraviolet range. Simultaneous oscillation at the red, green and blue emission lines in hollow-cathode He–Cd lasers enables the generation of white light which is applied in optical image processing systems. Furthermore, the short-wavelength emission, combined with its low beam divergence (<2.0 mrad) and near-diffraction-limited spot size, make the He–Cd laser suitable for applications such as flow cytometry (cell detection and counting) or circuit inspection that require high photon energies and excellent beam quality. He–Se lasers typically offer up to 5 mW of output power in the visible region between 460 and 650 nm wavelength, while the desired emission lines can be selected by appropriate resonator mirrors.

The lifetime of He–Cd lasers is about 6000 h, but only half as long when operated in the UV. It is primarily limited by contamination of the discharge, deposition of cadmium metal on the optics as well as exhaustion of the helium. The overall efficiency of about 0.01% is comparable to that of helium–neon and argon lasers.

Laser operation can also be realized in other metal vapor ions such as copper, gold or silver. Since high energies are required for vaporization of these metals, hollow-cathode discharge configurations are employed in this case. The metal vapor is thus produced by collisions of noble gas ions with the metal cathode (sputtering). The noble gas ions are formed in the gas discharge, so that an external heating for

vaporization is not required. The metal vapor ion lasers should not be confused with the pulsed copper or gold atomic vapor lasers discussed in Sect. 4.2.

Neon–copper and helium–silver lasers are of particular interest, as they are the only lasers that directly provide continuous output in the UV region down to 220 nm at output powers up to 1 W (copper ion laser). Commercial devices operate in long-pulse mode (100 μ s pulse duration, 10 Hz repetition rate) in order to prolong the lifetime. Alternative cw laser sources emitting at such short wavelengths are the frequency-doubled argon ion laser (244 nm) and the fifth-harmonic Nd:YAG laser (213 nm).

Diode-Pumped Alkali Vapor Lasers

In the last decade, diode-pumped alkali vapor lasers have attracted increasing attention. Optical pumping of alkali metal (lithium, sodium, potassium, cesium, rubidium) vapors was one of the first laser concepts at the end of 1950s. These vapor atoms have only one valence electron in their outer shell which makes their physics relatively simple. However, the strong reactivity of alkali metals and the lack of pump sources hampered the realization of alkali metal vapor lasers. Consequently, although the first optically-pumped cesium laser was demonstrated already in 1962, it found no application and more than 40 years passed until commercial NIR diodes laser sources became available which allowed for efficient pumping of alkali vapors. From that time, various alkali lasers have been successfully pumped using different solid-state and diode lasers and powers have been increased since then. The pump and laser wavelengths of relevant alkali metal vapor lasers are given in Table 5.3.

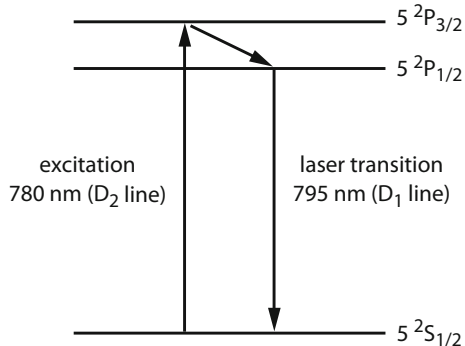
In alkali lasers, energy is not stored in the gain medium owing to the high rates for spontaneous emission from the upper levels. In order to stimulate transitions from the $5\ ^2P_{3/2}$ level to the $5\ ^2P_{1/2}$ level before spontaneous emission can occur, buffer gases like ethane are used.

Atomic gas lasers like the He–Ne laser rely on transitions far above the ground state which results in low laser efficiency. In contrast, the single valence electron of alkali metal vapors has a pair of low-lying energy levels, as shown for rubidium in Fig. 5.6. In this relatively simple laser system, electrons are optically-pumped from the ground state to the higher-energy $5\ ^2P_{3/2}$ state by excitation at 780 nm

Table 5.3 Characteristics of alkali metal vapor lasers

Alkali metal	Pump wavelength (nm)	Laser wavelength (nm)	Quantum efficiency (%)
Cs	852	895	95.3
Rb	780	795	98.1
K	766	770	99.6
Na	589.0	589.5	99.9
Li	670.96	670.98	99.997

Fig. 5.6 Energy level diagram of the rubidium laser



wavelength, the so-called D₂ line. After relaxation to the lower 5²P_{1/2} state, the electrons return to the ground state and emission occurs at the D₁ line at 795 nm. Pumping of rubidium lasers can be realized by using aluminum gallium arsenide (AlGaAs) laser diodes emitting at the D₂ line.

Due to the close spacing of the involved energy levels, the difference between the pump and laser photon energy—the quantum defect—is very small in alkali lasers. The quantum defect for rubidium is only $q = 1 - E_{D2}/E_{D1} = 0.019$, corresponding to a quantum efficiency of $E_{D2}/E_{D1} = 1 - q = 98.1\%$, see Table 5.3). This quantum defect is significantly smaller compared to ytterbium (0.09) and neodymium (0.24) used in solid-state lasers.

Rubidium lasers have been pumped by titanium-sapphire (TiSa) lasers emitting at the D₂ line. For instance, employing a mixture of rubidium, helium and ethane, 30 mW of output power at 795 nm are produced at 180 mW of pump power, which corresponds to an overall optical conversion efficiency of 17%. Even higher efficiencies near 30% can be obtained for TiSa-pumped cesium lasers, yielding output powers of several hundreds of milliwatts at 895 nm wavelength.

Pumping of rubidium with diode stacks providing 1 kW of pump power allows for generating more than 200 W of peak power in pulsed mode, and up to 145 W in cw mode. However, power scaling of diode-pumped alkali metal vapor lasers to the kilowatt level is challenging, as the absorption lines of the alkali vapors are very narrow, thus requiring precise matching of the absorption lines with the broad emission bands (typically 2–3 nm width) of laser diodes. Moreover, the degradation of optical components caused by reactions with hydrocarbons, has to be avoided.

The development of alkali lasers was particularly motivated by the fact that the resulting laser output can have much higher beam quality compared to the diode lasers used as pump sources. Hence, in combination with their high efficiency, alkali laser can provide a significant brightness enhancement of high-power diode lasers which is of interest for kilowatt-class industrial applications. However, powerful fiber and disk solid-state lasers have emerged that can dissipate heat well enough to generate high-quality beams reaching output powers of more than 100 kW, while offering additional advantages of solid-state lasers that are small, rugged and reliable.

Further Reading

1. C.E Little, *Metal Vapour Lasers* (Wiley, 1999)
2. B.E. Cherrington, *Gaseous Electronics and Gas Lasers* (Pergamon Press, 1979)
3. C.S. Willett, *Introduction to Gas Lasers: Population Inversion Mechanisms* (Pergamon Press, 1974)

Chapter 6

Infrared Molecular Gas Lasers



Laser emission in the infrared spectral region can be generated with molecular gas lasers by exploiting transitions between vibrational and rotational energy levels. Purely rotational transitions without changing the vibrational state of the molecule involves the emission of photons with low energy, corresponding to long-wavelength radiation in the spectral range from 25 μm to 1 mm. This leads to the far-infrared lasers (Sect. 6.1). The energy differences between vibrational-rotational levels of the same electronic state are larger, hence shorter wavelengths ranging from 5 to 30 μm are emitted from lasers based on such transitions. The CO₂ laser operating at wavelengths around 10 μm represents the most important member of this group of lasers and will be comprehensively discussed in Sect. 6.2. Electronic transitions in molecules result in visible and ultraviolet emission. Here, the nitrogen (Sect. 7.1) and excimer lasers (Sect. 7.2) are of particular relevance.

6.1 Far-Infrared Lasers

The spectral range between 50 μm and 1 mm (sub-millimeter waves) is referred to as far-infrared (FIR) region. The corresponding frequencies are in the interval from 0.3 and 6 THz, so that these waves are also often called Terahertz radiation. Far-infrared laser typically provide output powers from 100 mW up to 1 W at frequencies between 0.1 and 10 THz and are therefore mainly employed for molecular spectroscopy and other scientific applications. Apart from FIR lasers, THz radiation can be also produced with gyrotrons, backward wave oscillators (BWOs), GaAs-Schottky diode multipliers, quantum cascade lasers, free-electron lasers, synchrotron light sources, as well as by nonlinear difference frequency mixing.

Optically-Pumped FIR Lasers

Far-infrared lasers are mostly optically-pumped and can produce hundreds of different emission lines. The configuration and operation principle will be outlined using the example of the CH₃F (methane fluoride) laser which is pumped by the 9.55 μm emission of the CO₂ laser, as shown in Fig. 6.1. The pump radiation is coupled into the laser cavity at an angle to the resonator axis, while a partially transmitting metal mesh mirror is used as output coupler. Typical laser parameters are given in Table 6.1. The simplified energy level diagram of the CH₃F laser is depicted in Fig. 6.2 showing the strongest laser transitions. In the figure *J* denotes the rotational quantum number and *K* is the quantum number describing the component of the angular momentum along the symmetry axis of the CH₃F molecule. The output characteristics of other FIR molecular gas lasers are provided in Table 6.1.

The methanol (CH₃OH) laser emits in a very broad wavelength range between 40 and 1200 μm. Commercial systems are offered together with the corresponding pump lasers (see Table 6.2). The quantum efficiency of FIR lasers is between less than 1 and 30%. The optical-to-optical efficiency is lower, as the energy of the laser photons is smaller than that of the pump photons.

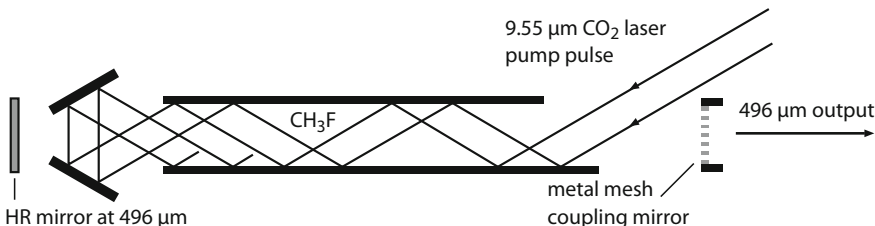


Fig. 6.1 Schematic of a CH₃F far-infrared laser which is pumped by a CO₂ laser (from Kneubühl and Sigrist (2008))

Table 6.1 Characteristics of far-infrared lasers (courtesy of J. Hecht)

Type	Wavelength (μm)	CW output power (mW)	Pulse parameters	Pump mechanism
H ₂ O	28	10	Pulsed operation possible	Electrically
	78			
	119			
D ₂ O	66		2.5 μs, 40 mJ	Optically
CH ₃ OH	112	100		Optically
HCN	337	100		Electrically
	311	3		
CH ₃ F	496		50 ns, 50 mJ	Optically

Fig. 6.2 Simplified energy level diagram of a CH₃F far-infrared laser. A CO₂ laser operating at the P(20) line (see Fig. 6.4) at 9.55 μm wavelength is used as pump source (J = rotational quantum number, K = quantum number describing the component of the angular momentum along the symmetry axis of the CH₃F molecule)

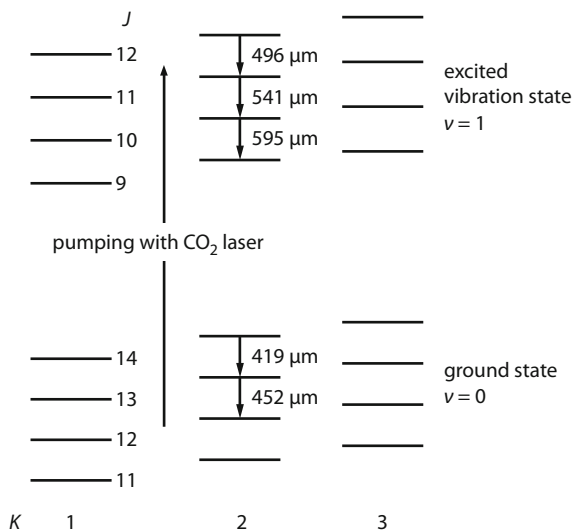


Table 6.2 Commercial far-infrared lasers, sorted by emission wavelength

Wavelength (μm)	Type	Wavelength (μm)	Type
41.0	CD ₃ OD	255	CD ₃ OD
46.7	CH ₃ OD	375	C ₂ H ₂ F ₂
57.0	CH ₃ OD	433	HCOOH
70.6	CH ₃ OH	460	CD ₃ I
96.5	CH ₃ OH	496	CH ₃ F
118.8	CH ₃ OH	570	CH ₃ OH
148.5	CH ₃ NH ₂	599	CH ₃ OH
163.0	CH ₃ OH	764	C ₂ H ₂ F ₂
184.0	CD ₃ OD	890	C ₂ H ₂ F ₂
198.0	CH ₃ NH ₂	1020	C ₂ H ₂ F ₂
229.1	CD ₃ OD	1022	C ₁₃ H ₃ F ₂

Electrically-Pumped FIR Lasers

Excitation of FIR lasers through gas discharge is only possible for stable and simple molecules, since larger molecules would dissociate in the discharge. The first molecular FIR lasers were operated using longitudinal discharge configurations. The gain media were H₂O, HCN and ICN, where the latter produced the longest wavelength emission at 774 μm. Later on, transverse discharge configurations, comparable to the transverse excited atmosphere (TEA) CO₂ laser (Sect. 6.2), were used, e.g. for the CH₃F laser. The most relevant electrically-pumped FIR laser is the HCN laser having strong emission lines at 311 and 337 μm which result from transitions between vibrational-rotational levels of the molecule. Typical output

powers are listed in Table 6.1. FIR lasers are primarily employed for high-resolution spectroscopy of molecules and Rydberg atoms as well as for the spectroscopy of solids, the analysis of magneto-optic effects and the investigation of plasmas. Due to the long emission wavelengths, the operation of FIR lasers and the accompanied measurement techniques and diagnostics require particular methods and materials. The laser mirrors have to be fabricated from ZnSe, silicon or a special crystalline quartz. The laser beam can be coupled out through a central hole or a metal mesh is utilized as output coupler (Fig. 6.1).

6.2 CO₂ Lasers

One of the most important lasers for industrial applications, especially for material processing, is the CO₂ laser. It is characterized by high output powers up to nearly 100 kW in cw mode and very high wall-plug-efficiencies of 10–20%. For scientific applications, low-power versions are available delivering about 1 W, while CO₂ lasers applied in medicine typically provide 10 W of output power. Pulsed systems produce laser pulses with durations ranging from the ns- to the ms-range. Pulse energies up to 100 kJ have been demonstrated for the purpose of laser fusion. The CO₂ laser generates emission in the infrared region between 9 and 11 μm. There is a large variety of different CO₂ laser configurations which all have their technical and commercial relevance.

Excitation Processes

The CO₂ molecule is a linear, symmetric molecule with the carbon atom balanced against the two oxygen atoms. As explained in Sect. 1.4, the molecule can perform four different fundamental vibrations which can be excited independently: the symmetric stretching vibration with frequency f_1 , two degenerate bending vibrations with frequency $f_2 = f_{2a} = f_{2b}$ and the asymmetric stretching vibration with frequency f_3 . The resulting three sets of energy levels are illustrated in Fig. 6.3. The respective ground states are denoted as (01¹0), (10⁰0) and (00⁰1), where the superscript indicates the degree of degeneracy of the bending vibration. Laser emission is originated from transitions between the (00⁰1)-state and the (02⁰0)- or (10⁰0)-state, leading to wavelengths around 9.6 and 10.6 μm, respectively. The laser medium consists of a CO₂–N₂–He gas mixture which is excited in a gas discharge. Population of the upper laser level (00⁰1) is partially achieved by inelastic electron collisions. The efficiency of this process is larger compared to the excitation of the (02⁰0) or (10⁰0) levels, since the transition (00⁰0) → (00⁰1) is optically allowed. More important than the electron excitation is the excitation through collisions of the second kind with metastable N₂ molecules produced in the discharge, as indicated in Fig. 6.3. Molecular nitrogen has no permanent magnetic

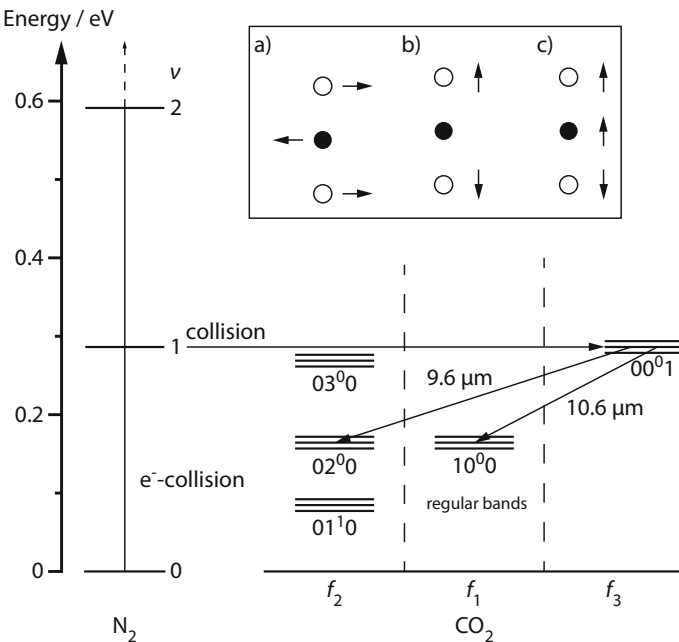
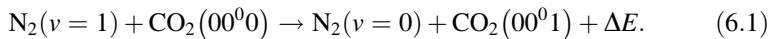


Fig. 6.3 Energy level diagram of the CO₂ laser. Population of the upper laser level is achieved by collisions of the CO₂ molecules with metastable N₂ molecules, resulting in a multitude of laser emission wavelengths ranging from 9.6 to 10.6 μm (see also Fig. 6.5). The fundamental vibrations (frequencies f₁, f₂, f₃) of the CO₂ molecule associated with the respective energy levels are depicted in the box on top

dipole moment, so that optical transitions between vibrational levels of the same electronic state are forbidden, according to the parity selection rule (see Sect. 1.4). Hence, the nitrogen vibrational levels of the electronic ground state with $v = 0, 1, 2$, etc. are metastable, acting as an energy reservoir which can excite the CO₂ molecules as follows:



The somewhat serendipitous fact that the first excited asymmetric stretch state (00⁰1) is almost exactly in resonance ($\Delta E \approx -18 \text{ cm}^{-1} = -2.2 \text{ meV}$) with the lowest vibrational level of nitrogen N₂ is the key to the remarkable efficiency and enormous available output powers of the CO₂ laser, as it leads to a very efficient population of the upper laser level without transferring pump energy to the low-lying states of the CO₂. The population of the (00⁰1) level is further increased by energy transfer from nitrogen molecules at higher vibrational levels, e.g. $v = 2$. Another reason for the high efficiency of the CO₂ laser is the small energy ($\sim 0.3 \text{ eV}$) required to reach the upper laser level. This energy is possessed by a large fraction of the discharge electrons which is in contrast to the He-Ne laser

where 40 times higher electron energies are required (see Fig. 4.1). Hence, only the high-energy tail of the electron energy distribution contributes to the population of the upper laser level, resulting in a much lower efficiency.

Depending on the lower vibrational level of the laser transition, emission occurs in two different wavelength ranges around 9.6 and 10.6 μm . Figure 6.4 depicts the so-called regular bands participating in the laser transitions of the CO₂ laser. The bands contain hundreds of lines, as the vibrational levels are further divided into rotational levels. Continuous-wave CO₂ usually only operate in the 10.6 μm region, which is due to the fast energy transfer between the involved energy levels, as will be elaborated later in the text. The diagram visualizes the extraordinarily high quantum efficiency of about 45% which additionally explains the high overall efficiency of the laser.

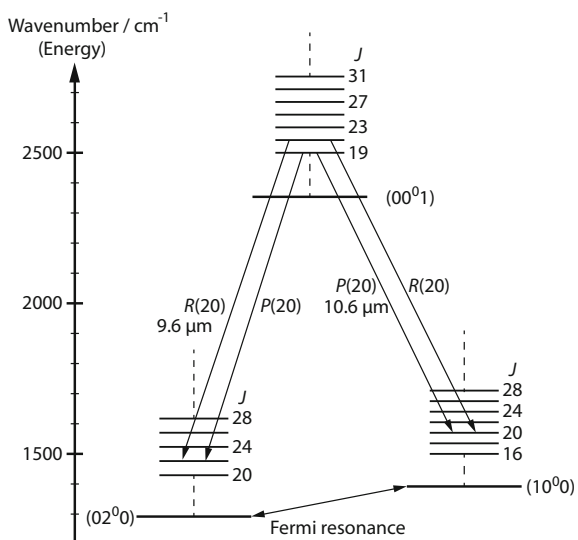
The helium gas within the gas mixture, typically 60–80%, is not involved in the laser process, but serves for increasing the gas pressure in the discharge tube as well as for improving the heat removal, thus enhancing the stability of the discharge. Furthermore, the lower laser level is depleted by collisions with He-atoms.

Energy Level Diagram

In the harmonic approximation, the total vibrational energy of the CO₂ molecule in a state (v_1, v_2, v_3) is given according to (1.11) by

$$E_v = \left(v_1 + \frac{1}{2}\right)hf_1 + \left(v_2 + \frac{1}{2}\right)hf_2 + \left(v_3 + \frac{1}{2}\right)hf_3, \quad (6.2)$$

Fig. 6.4 Splitting of the vibrational-rotational energy levels of the CO₂ molecule. The states (02⁰0) and (10⁰0) are strongly coupled (Fermi resonance), leading to mixed states which were earlier denoted (10⁰I) and (10⁰II). The more recent designations are (10001) and (10002), respectively



where the vibrational energies of the symmetric stretching, bending and the asymmetric stretching vibrations are $hf_1 = 1351.2 \text{ cm}^{-1}$, $hf_2 = 672.2 \text{ cm}^{-1}$ and $hf_3 = 2396.4 \text{ cm}^{-1}$, respectively.

The depletion of the lower laser levels which represent a mixing of (02⁰0) and (10⁰0) is problematic, as the lifetimes for radiative transitions of several milliseconds are relatively long. Like for the He–Ne laser, wall collisions play a significant role in shortening the lifetime. In addition, collisions with other molecules, especially helium, are of particular importance, since the intermediate level (01¹0) is depleted without depopulating the upper laser levels. Furthermore, the high thermal conductivity of the helium leads to reduced discharge temperatures, thus decreasing the thermal population of the lower laser levels of the CO₂. Apart from the (00⁰1) level representing the upper laser level for the regular bands, the (00⁰2) level is populated in the gas discharge, giving rise to the sequence bands. The population of the (00⁰*n*) vibrational levels follows the Boltzmann distribution, where temperatures up to about 3000 K are reached. The lifetime of the excited (00⁰*n*) levels is about 2 ms, while a very fast relaxation process (100 ns) involving collisions between CO₂ molecules maintains the Boltzmann distribution. Since the energy levels (00⁰1), (00⁰2), etc. are not exactly equidistant (anharmonic oscillator), the emission lines of the sequence bands are slightly shifted with respect to those of the regular bands.

The designation of the two lower laser levels shown in Fig. 6.4 is incomplete and often denoted more precisely as (10⁰0)_I and (10⁰0)_{II}, taking into account the near coincidence of the levels (10⁰0) and (02⁰0). In general, the resonance between the (10⁰*n*) and (02⁰*n*) levels of the regular (*n* = 1) and sequence bands (*n* > 1) (Fermi resonance) results in superposition of the eigenfunctions of the respective states. The mixed states are then designated as (10⁰*n*)_{I/II}.

Fermi resonances also occur for higher excited states involving more than only two levels. For a better differentiation between the resulting mixed states, a modified nomenclature of the CO₂ energy levels is used. Here, the quantum numbers v_1 , v_2 , l and v_3 are simple written one after another, while the lower Roman index is replaced with the so-called ranking index *r*, denoting the relative location of the energy level within a Fermi polyad: (v_1 v_2 l v_3 n r). In this notation, the aforementioned lower laser levels of the CO₂ laser are referred to as (10001) and (10002). A further example for a Fermi resonance is the superposition of the states (30⁰1), (22⁰1), (14⁰1) and (06⁰1), resulting in a Fermi tetrade which consists of four mixed states. The corresponding energy levels are then ranked by their energy and denoted as (30001), (30002), (30003) and (30004).

Laser Emission Lines

The splitting of the vibrational levels into rotational bands, as indicated for the regular bands in Fig. 6.4, results in a multitude of emission lines in the output spectrum of the CO₂ laser. The rotational energy E_J is characterized by the rotational quantum number *J* as introduced in (1.12):

$$E_J = hcB_r J(J+1), \quad (6.3)$$

The rotational constant B_r is related to the mass moment of inertia of the molecule. h is Planck's constant and c the speed of light. Due to the symmetry of the CO₂ molecule and the zero nuclear spin of the ¹⁶O atoms, only even rotational quantum numbers J are present for the symmetric vibrations, e.g. (10⁰0). In contrast, J is always odd for asymmetric vibrations, e.g. (00⁰1). If ¹⁶O is replaced by an isotope with non-zero nuclear spin, J can have both odd and even numbers. According to the selection rules that hold for electric dipole transitions in molecules (Table 1.5), the rotational quantum number has to change by unity, i.e. $\Delta J = \pm 1$. Transitions with $\Delta J = -1$ form a set of lines called the P-branch, whereas those with $\Delta J = +1$ are called R-branch. The notation of the CO₂ laser transition follows from the sign of the change in the rotational quantum number of the lower level (P or R) while referring to the lower laser level, e.g. P(20) for the transition $J = 20 \rightarrow J' = 19$. The transitions shown in Fig. 6.4 result in various emission lines forming the P- and R-branches between 9.4 and 10.6 μm, as depicted in Fig. 6.5. The two pairs of branches are related to the two different final vibrational states (10⁰0)_I and (10⁰0)_{II} [corresponding to (10001) and (10002)] of the Fermi doublet.

The gain of the single laser lines indicated in Fig. 6.5 follows from the different population of the involved rotational levels which is given by the Boltzmann distribution under consideration of the statistical weight of the respective levels. The population of the rotational levels within one vibrational state depends on temperature T and are given as

$$N_J \propto (2J+1) \exp[-hcB_r J(J+1)/k_B T], \quad (6.4)$$

with k_B being the Boltzmann constant.

The degree of degeneracy $2J+1$ increases with the quantum number J , while the exponential factor decreases. The rotational level with the largest population can be derived from (6.4), yielding

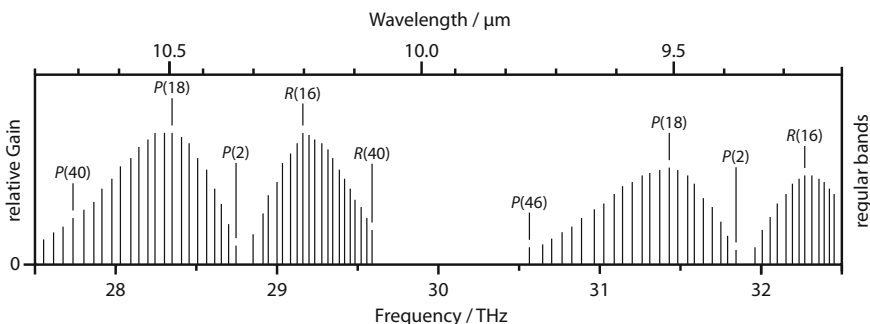


Fig. 6.5 Emission lines of the CO₂ laser

$$J_{\max} \approx \left(k_B T / 2 h c B_r - \frac{1}{2} \right)^{1/2}. \quad (6.5)$$

For a temperature of $T \approx 350 \dots 400$ K, maximum population is calculated for $J_{\max} \approx 17$. Consequently, the strongest laser emission lines in the P- and R-branch will be observed for the transitions involving this rotational level and are denoted as P(18) and R(16), respectively. The approximation in (6.5) is in accordance with the measured laser lines shown in . The relaxation process which maintains the thermal distribution also during laser operation leads to a thermalization time of less than 1 μs.

Wavelength tuning of the CO₂ laser can be accomplished by highly reflective gratings incorporated in the resonator which separate the different emission lines. The distance between adjacent lines is in the range of 30–50 GHz. The tuning range within a single emission line is limited by the Doppler broadening and is about 50 MHz in the low-pressure regime. Laser operation can be achieved at up to 80 lines simultaneously ranging from 9.2 to 10.8 μm. Application of ¹⁸O- and ¹³C-isotopes allows for an extension of this range, while continuous tuning is obtained at high pressures.

The diameter of the laser tube and the mode aperture determine whether the laser operates in fundamental transverse mode (TEM₀₀) or if multiple transverse modes oscillate. Since the longitudinal mode spacing is typically on the order of a few hundreds of MHz, e.g. 200 MHz for a resonator length of 75 cm, and thus larger than the Doppler broadening (50 MHz), CO₂ lasers usually operate in single longitudinal mode.

Continuous Wave and Pulsed Operation

The fast energy equalization (or thermalization) between the rotational levels has significant implications for the emission spectrum of the CO₂ laser. In continuous wave (cw) operation without frequency selection the strongest lines around P(20) will dominate. The latter will first oscillate leading to a reduced population of the respective rotational level. As the thermalization time (<1 μs) is shorter than the lifetime (related to spontaneous and stimulated emission), the fast energy equalization results in a reduction of the population for all rotational levels, leaving the Boltzmann distribution unaffected. This process is comparable to homogeneous gain saturation. As a result, the gain of the first oscillating line is always maximal, since the population is rapidly reestablished by the neighboring rotational states. Continuous wave CO₂ lasers hence emit only the one emission line that has the highest gain over the resonator losses, even without inserting frequency-selective elements into the resonator.

The upper laser lifetime of about 2 ms allows for the storage of energy during the pumping process and thus enables Q-switching of the CO₂ laser (see Sect. 17.2).

Energy transfer between different rotational levels is not possible during the emission of the short (nanosecond) Q-switched pulse. Therefore, the population of the strongest line will be quickly depleted, giving rise to laser operation at the adjacent emission lines, provided the respective gain reaches the laser threshold. Consequently, multi-wavelength emission at multiple lines of the P- and R-branches is present for Q-switched CO₂ lasers in the low-pressure regime. At high pressure, the energy transfer between the rotational levels is significantly enhanced, as the collision rate between the CO₂ molecules is drastically increased. If the thermalization time is shorter than the pulse duration, the Boltzmann distribution is maintained within the pulse, resulting in single line emission of the Q-switched output. In the following, different types of operation of the CO₂ laser will be discussed in detail.

Lasers with Slow Axial Gas Flow

The typical configuration of a longitudinally-pumped CO₂ laser consists of a water-cooled glass tube of 1 to 3 cm diameter, as shown in Fig. 6.6. An axial direct-current (DC) discharge is produced in axial direction in the CO₂-He-Ne gas mixture. The optimal gas composition depends on the tube diameter, flow speed and the output coupler reflectivity and is for instance 9% CO₂, 11% N₂ and 80% He at a total pressure of 20 mbar = 20 hPa. The gas flow enables the removal of dissociation products such as CO and O₂ from the active volume. The laser power can be controlled by the discharge current, reaching up to 100 W per meter of discharge tube and an overall efficiency of more than 10%.

At high currents the gain is reduced, as the thermal population of the lower laser level increases with temperature. The current at maximum output power is about 80 mA at 14 mbar total gas pressure and 2.5 cm tube diameter. The laser power

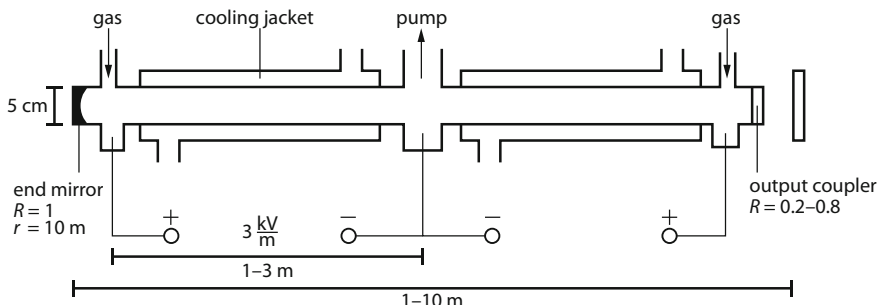


Fig. 6.6 Schematic of a longitudinal CO₂ laser, consisting of two segments. The sequencing of additional segments allows for active lengths of up to 10 m. The output coupler can be realized by an uncoated germanium plate with $R \approx 70\%$

and hence the efficiency depend only weakly on the tube diameter so that substantial power scaling is not possible. Cooling of the discharge is mainly performed through heat transfer towards the tube wall, which is embedded in water cooling jackets. Commercial CO₂ lasers are equipped with a gas cylinder containing about 10 L of the specified gas mixture at a pressure of 140 bar lasting for 50 h of operation. The in- and outflow of fresh and consumed gas is automatically carried out in these systems which are successfully applied for the material processing of small components. However, for medical applications requiring several tens of watts, the sealed-off CO₂ laser has prevailed on the market.

Sealed-Off Lasers

The drawback of external gas supply in CO₂ lasers with slow axial flow is avoided in sealed-off CO₂ lasers where the dissociation products CO and O₂ are chemically transformed by adding small amounts of H₂O, H₂ and O₂. Moreover, the electrode material plays a key role, since platinum or nickel (500 K) act as catalysts for the transformation of CO into CO₂. The most important chemical reactions are



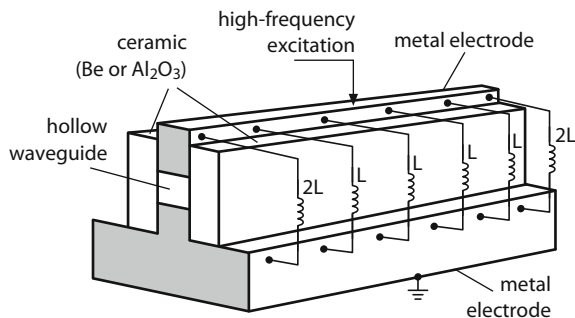
where the asterisk indicates excited vibration states of the molecules.

Continuous discharge is typically operated in gas mixtures typically containing 20% CO₂, 20% N₂ and 60% He at a total pressure of 1000 to 2500 Pa. The output power is limited by the heating of the gas mixtures which increases the thermal population of the lower laser level as well as by the dissociation of CO₂. Powers up to 60 W per meter and several thousands of operation hours are achieved. Aside from applications in medicine and material processing CO₂ lasers in sealed-off configuration are employed in spectroscopy.

Waveguide Lasers

Low-power applications are addressed with waveguide CO₂ lasers which consist of BeO- or Al₂O₃-capillaries of 1 mm diameter constituting dielectric waveguides. Rectangular cross-sections are common as well. In waveguide lasers, the radiation is reflected from the walls, forming standing-waves like it is the case with microwaves in hollow conductors. The construction of waveguides reduces the diffraction losses which would be very large for regular configurations with small

Fig. 6.7 Schematic of a waveguide CO₂ laser with high-frequency excitation (L : inductivity)



cross-section, considering that a diameter of 1 mm corresponds to about 100 times the laser wavelength ($\approx 10 \mu\text{m}$). An analogous design of a He–Ne laser would incorporate a tube with a diameter of only 0.06 mm.

Excitation can be performed by longitudinal direct-current discharge following a similar scheme as depicted in Fig. 6.6. A different design involving a high-frequency excitation at about 30 MHz is shown in Fig. 6.7. Here, the high-frequency current flows perpendicular to the laser beam which has the advantage of about hundred times reduced electrode voltages, while the induced electric field is almost identical for longitudinal and transverse discharge. As a result, gas-chemical processes at the cathode are prevented. Moreover, high-frequency discharges are characterized by a high stability.

Waveguide lasers offer compact and sealed-off configurations, whereby the small diameter promotes the heat dissipation at the wall so that water-cooling is not necessary in most cases. Due to the small tube diameter, the waveguide laser is usually operated at relatively high pressures of 20,000 Pa, leading to high powers per volume and high gain on the order of 0.04 cm^{-1} . Hence, output powers of 1–2 W are readily obtained for resonator lengths around 10 cm, while tens of watts are produced for longer tubes. The high gas pressure results in broadening of the spectral lines to about 1 GHz, thus providing frequency tuning over this range. Lasers of this type are preferentially applied in the fields of IR spectroscopy, metrology and trace gas detection for the purpose of environmental protection.

Lasers with Fast Gas Flow

Laser powers in the kW-regime are obtained by realizing a fast flow of the gas mixture through the discharge volume in order to minimize the residence time of the gas in the discharge. In this way, the gas temperature, and hence the thermal population of the lower laser level, is kept low. Additionally, the dissociation products are quickly removed. The combination of both effects allows for very high powers of more than 400 W per meter of the discharge tube length, while axial gas flow speeds up to 300 m/s enable relatively good beam quality of the laser output.

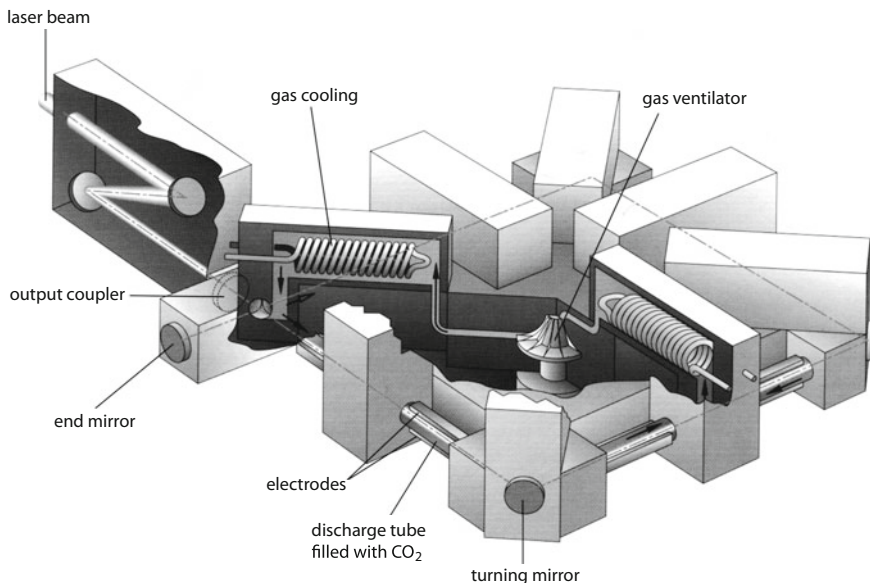


Fig. 6.8 CO₂ laser (about 10 kW output power) used for material processing. The gas flows through the transversely oriented discharge tubes (20 cm length) almost at the speed of sound. The hot gas is cooled in a heat exchanger (courtesy of Trumpf)

Figure 6.8 depicts the schematic diagram of a commercial CO₂ laser producing about 10 kW of output power which is used for material processing.

High-Frequency Excitation of CO₂ Lasers

Two different developments are currently ongoing in terms of CO₂ lasers in material processing applications. On the one hand, compact, sealed lasers are employed for precise machining (and for medical purposes). On the other hand, large-scale high-power lasers with axial or transverse gas flow are widely used. Both types can be operated with high-frequency excitation providing a homogenous energy distribution in the discharge, and in turn, higher beam quality and efficiency compared to direct-current excitation. The high-frequency power is mostly capacitively applied to two parallel electrode plates which are oriented perpendicularly to the laser beam (see Fig. 6.7). Insertion of a dielectric material, e.g. glass, between the metal electrodes and the plasma prevents contact of the plasma with the metal surfaces. This diminishes the contamination of the gas so that even kW systems can be operated without gas exchange. Furthermore, high-frequency discharge does not involve a cathode or ballast resistors resulting in higher stability of the laser. However, the high-frequency technology required for coupling of the radiation into the low-impedance plasma is quite challenging.

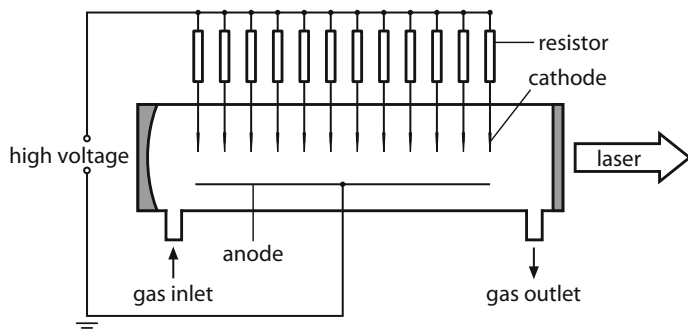


Fig. 6.9 Schematic of a gas laser with transverse discharge, e.g. CO₂ laser

Transverse Excited Atmospheric Pressure (TEA) Lasers

The output power of longitudinal CO₂ lasers can be scaled by increasing the applied voltage and/or the gas pressure up to about 100 mbar. At higher pressures, however, the discharge becomes unstable. In pulsed discharges ($\approx 1 \mu\text{s}$) laser operation is achieved before instabilities arise, thus allowing gas pressures above 1 bar. Since the electric field reaches 100 kV/m, transverse electrodes are used, as depicted in Fig. 6.9. This configuration is called transversely excited atmospheric pressure laser, or simply TEA laser.

For homogeneous expansion of the discharge over a large volume, the gas is pre-ionized by electron beams or UV radiation. Commercial TEA lasers are offered with pulse energies up to several kJ at pulse repetition rates of 3 min^{-1} . 50 J of

Table 6.3 Typical parameters of CO₂ lasers in different configurations

Type/application	Maximum output power	Pulse energy; pulse peak power	Pulse duration; pulse repetition frequency
Sealed-off laser (Ma, Me)	100 W		
Waveguide laser (SM, S, Me)	50 W		
Laser with slow axial flow (Ma)	<kW		
– Pulsed (Ma)		1 J/L; kW/m	> μs ; 100 Hz
– Continuous-wave (Ma)			100 ns; 1 kHz
Laser with fast gas flow (Ma)	100 kW		
TEA laser (Ma)		10 J/L; GW	0.1 ... 10 μs ; kHz
Gasdynamic laser (Ma)	100 kW	10 J	
High-pressure laser (S, U)	See TEA and waveguide laser		

Ma-material processing, Me-medicine, SM-single-mode laser, S-spectroscopy, U-ultra-short pulses

pulse energy are produced per liter of the gas mixture, resulting in pulse peak powers in the GW-range at pulse durations of 0.1–10 µs. The output pulse of TEA lasers typically consists of one main pulse of 0.1–0.5 µs duration, followed by an about 1 µs long trailing edge. While the main pulse comes from the direct excitation of the laser levels in the discharge, the slow component originates from the energy transfer from the N₂ to the CO₂ molecules. Due to the high pressure, the spectral line is broadened to a few GHz, thus enabling mode-locking and pulse durations down to 100 ps. Typical parameters of the TEA laser and other CO₂ laser configurations are summarized in Table 6.3. Relevant applications range from plasma research and spectroscopy to photochemistry and the marking of workpieces.

Gas Dynamic CO₂ Lasers

In gas dynamic lasers the population inversion is realized by fast expansion of a hot gas. Here, a gas mixture (8% CO₂, 92% N₂) is heated to about 1400 K and compressed to 17 bar, resulting in a population of the upper and lower laser levels (in thermal equilibrium) of about 10 and 25%, respectively. The gas mixture is then expanded to 0.1 bar through an array of parallel nozzles, cooling it to 350 K. Since the lifetime of the upper laser level is much longer than that of the lower level, the lower level is depleted significantly faster, a population inversion is built up. The optimum expansion speed is on the order of Mach 4. The $v = 1$ vibrational level of the N₂ molecules remains occupied upon expansion and hence acts as energy reservoir which additionally populates the upper laser level. The laser axis is perpendicular to the gas flow direction. Continuous gas dynamic CO₂ laser provides output powers up to 80 kW. In pulsed operation, high-energy pulses in the ms-range can be generated. Nevertheless, this laser type has not found practical application.

Tunable CO₂ High-Pressure Lasers

For pressures exceeding 10 bar, pressure broadening in a natural CO₂ mixture is comparable to the spacing of the rotational levels (30–50 GHz). For other isotopes (¹²C¹⁶O¹⁸O), these values are halved, since the number of allowed rotational transitions is doubled. Hence, continuous wavelength tuning is possible within single P- and R-branches (see Fig. 6.5). Electron beam pre-ionization of the gas mixture is beneficial at high pressures of about 50 bar. The broad bandwidth of high-pressure CO₂ lasers enables the generation of ultra-short pulses, yielding pulse durations below 30 ps. The spatial characteristics of the distinct types of commercial CO₂ lasers are given in Table 6.4.

Table 6.4 Spatial properties of commercial CO₂ lasers

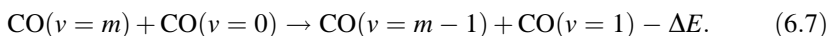
Type	Beam diameter (mm)	Divergence (mrad)
Laser with axial flow	5–70	1–3
Sealed-off laser	3–4	1–2
Waveguide laser	1–2	8–10
TEA laser	5–100	0.5–10

Perspectives

After many decades of research and development, CO₂ lasers nowadays represent a mature technology. However, they have partially been superseded by solid-state lasers, fiber lasers and quantum-cascade lasers. Nevertheless, they are highly relevant for many applications in material processing where they also enter new fields of application such as the processing of polymers and composite materials that have no absorption bands in the NIR spectral range. Moreover, CO₂ lasers are still widely employed in laser surgery, as outlined in Sect. 24.2. Finally, the price reduction in recent years, especially promoted by Chinese companies, has boosted the interest in CO₂ lasers.

6.3 CO Lasers

The CO laser is very similar to the CO₂ laser in terms of the laser design. Like in the CO₂ laser, nitrogen and helium are admixed to the laser-active carbon monoxide gas. The main differences are the emission wavelength around 5 μm and the excitation mechanism. The latter is illustrated in the energy level diagram of the CO laser shown in Fig. 6.10. The figure also depicts the diagram of the CO₂ laser for comparison. Being a diatomic molecule, CO has only one fundamental vibration and thus a single series of vibrational levels. In pulsed and continuous discharges, population of these levels occurs by collisions of CO molecules with electrons and with metastable N₂ molecules, where nearly 90% of the electron energy can be transferred to vibrational energy of the CO molecules. Furthermore, the quantum efficiency can be very high, as the lower level of a certain laser transition can become the upper laser level of another transition (cascading). In the discharge, both lower and higher vibrational levels are excited. The most relevant relaxation process of upper levels involves the transfer of vibrational energy of a higher state to the ground state ($v-v$ energy transfer):



The spacing between the vibrational levels of the CO molecule is not equidistant (anharmonic oscillator), but becomes closer with increasing quantum number v . The

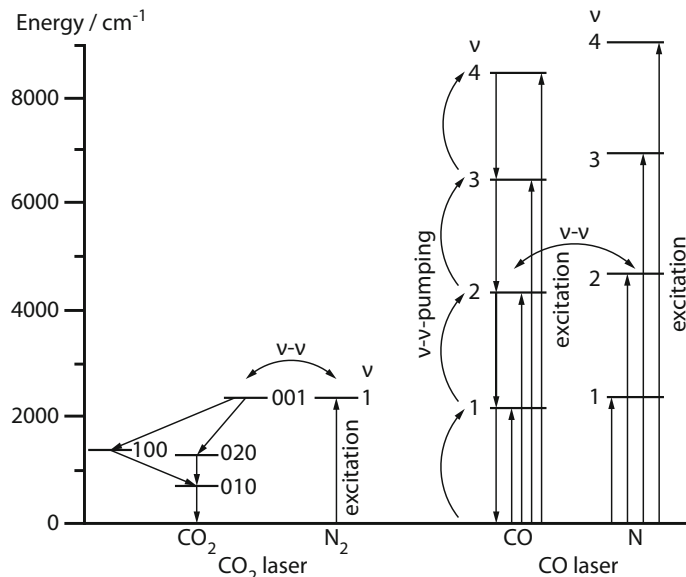


Fig. 6.10 Comparison of the energy level diagrams of the CO_2 laser (left) and CO laser (right). Population of the CO vibration levels occurs through electron collisions, collisions with excited N_2 molecules and transitions from higher vibration levels. Laser transitions of the CO laser are e.g. $v_{\text{CO}} = 4 \rightarrow 3, 3 \rightarrow 2, 2 \rightarrow 1, 1 \rightarrow 0$

resulting energy defect ΔE can be overcome by the translation energy of the molecule. However, if the gas temperature T is low, so that $\Delta E > k_{\text{B}}T$, $v-v$ -relaxation of the upper vibrational states to the ground state only occurs up to a certain level. In this way, population inversion is established since higher vibrational levels are not depleted by relaxation according to (6.7).

The lower the temperature, the lower is the quantum number up to which the relaxation process takes place. For air-cooled discharge tubes (wall temperature \approx room temperature), inversion is predominantly created between the vibrational levels with quantum number $v = 9$ and $v = 8$. Laser operation of the CO laser does not necessarily require a complete inversion of the involved vibrational states. Instead, the inversion of the rotational levels involved in the laser process is sufficient (partial inversion).

Key element of the CO laser is an efficient gas cooling. Hence, the discharge tubes were usually cooled to 77 K using liquid nitrogen. In arrangements based on convection cooling, supersonic gas flows are used. Improvement of the gas cooling and enhancement of the stability is accomplished by adding helium to the gas mixture. Furthermore, the supplementary input of nitrogen positively influences the electron speed. The discharge configurations employed in CO lasers are identical to those used in CO_2 lasers. Typical parameters for a 1 m-long, air-cooled discharge tube with diameter of 2 cm are: filling pressure 1600 Pa He, 58 Pa CO, 400 Pa N_2 ;

burning voltage 9 kV; discharge current 20 mA; cw output power 25 mW, efficiency 12%. Commercial CO lasers are offered with output powers from 2 to 20 W in the spectral range from 5 to 6 μm . Pulsed sources can reach 40 mJ of pulse energy at pulse durations on the order of a few μs .

While the theoretical quantum efficiency of the CO_2 laser is 41%, the corresponding value of the CO laser is nearly 100% which is due to the cascade mechanism of the lasing process (Fig. 6.10), thus providing very high electrical-to-laser power efficiencies. However, the overall efficiency of the CO laser used to be diminished by the substantial cooling power required for stable operation. Moreover, the cryogenic cooling made these systems complex and not very cost-effective for commercial use. Nowadays, sealed devices working at room temperature are available. Here, precise control of the gas chemistry in the laser tube enable high purity of the gas mixture, while RF sources produce optimal discharge conditions for the excitation of CO molecules directly via electron collisions.

The interest in CO lasers derives from its broadband mid-IR output which contains a multitude of emission lines resulting from the anharmonicity of the vibrational potential. The wavelength spectrum typically ranges from 4.744 μm , corresponding to the P(9)-transition from the first to the zeroth vibrational level ($v = 1 \rightarrow v = 0$), to 8.225 μm , corresponding to the P(8)-transition from the 37th to the 36th level ($v = 37 \rightarrow v = 36$). With regards to material processing applications, the shorter wavelength of the CO laser offers two advantages over the CO_2 laser. Firstly, the usually higher absorption of many materials such as metals, polymers, dielectrics, ceramics and composites at shorter wavelengths leads to more efficient processing with a smaller heat affected zone. Secondly, since the minimum spot size scales linearly with the wavelength, CO laser beams can be focused twice as tightly under similar focusing conditions, resulting in four times higher power densities compared to CO_2 lasers. In combination with the stronger absorption in some materials at 5 μm , processing with the CO laser can be performed at significantly lower powers.

6.4 HF Lasers, Chemical Lasers

Laser action can be realized in a number of molecules by chemical reactions. Hydrogen fluoride (HF) is the most prominent and best investigated example of this class of laser materials. Due to the enormous energy storage capabilities of chemical compounds, chemical lasers can achieve very high output powers. The energy density per volume stored in chemical compounds is several orders of magnitude higher compared to electrical capacitors. Most chemical lasers are based on vibrational transitions in diatomic molecules generating emission in the infrared spectral region between 1 and 10 μm (see Table 6.5). Large-scale configurations were studied for military applications, especially for the development of spaceborne systems.

Table 6.5 Several chemical lasers

Active medium	Chemical reaction	Wavelength (μm)
I	$\text{O}_2^* + \text{I} \rightarrow \text{O}_2 + \text{I}^*$	1.3
HF	$\text{H}_2 + \text{F} \rightarrow \text{HF}^* + \text{H}$	2.6–3.5
HF	$\text{H} + \text{F}_2 \rightarrow \text{HF}^* + \text{F}$	2.6–3.5
HCl	$\text{H} + \text{Cl}_2 \rightarrow \text{HCl}^* + \text{Cl}$	3.5–4.2
DF	$\text{D}_2 + \text{F} \rightarrow \text{DF}^* + \text{D}$	3.5–4.1
DF	$\text{D} + \text{F}_2 \rightarrow \text{DF}^* + \text{F}$	3.5–4.1
HBr	$\text{H} + \text{Br}_2 \rightarrow \text{HBr}^* + \text{Br}$	4.0–4.7
CO	$\text{CS} + \text{O} \rightarrow \text{CO}^* + \text{S}$	4.9–5.8
CO_2	$\text{DF}^* + \text{CO}_2 \rightarrow \text{CO}_2^* + \text{DF}$	10–11

Energy Level Diagram and Excitation Processes

The underlying process for initiating lasing in chemical compounds is a chemical reaction where one product of the reaction is a molecule in an excited vibrational state. For instance, excited hydrogen fluoride is produced by the exothermic reaction



where nearly 70% of the excess energy of $\Delta E = 132 \text{ kJ/mol} = 1.3 \text{ eV/molecule}$ is expended on the excitation of the HF molecule up to the $v = 3$ vibrational level. Transitions between this and lower vibrational levels $v \leq 3$ results in laser emission, as population inversion is established due to the selective excitation by the chemical reaction.

The energy level diagram of the HF laser is illustrated in Fig. 6.11. Reaction of the starting materials F and H_2 according to (6.8) releases the energy ΔE which is distributed over different vibrational levels $v = 0, 1, 2, 3$ of the end product HF, however additional thermal energy is required for the population of the $v = 3$ level. The relative population of the levels is determined by the respective transition rates k_0 , k_1 , k_2 , and k_3 . The ratio between the rates is approximately $k_0:k_1:k_2:k_3 = 0.15:0.3:1.0:0.5$. Hence, the vibrational level with quantum number $v = 2$ has the highest population and inversion with respect to the $v = 1$ level is built.

Every vibrational state is subdivided into rotational levels. For diatomic molecules, only a single series of rotational levels exists with quantum numbers $J = 0, 1, 2, 3, \dots$, as depicted in Fig. 6.12 for the two vibrational states $v = 1$ and $v = 2$. Transitions between these rotational levels give rise to the strongest emission lines of the HF laser in the wavelength range between 2.7 and 3.3 μm (Fig. 6.12). The intense 2 P(3)-line belonging to the P-branch is exemplarily shown in Fig. 6.11. Here, the Fig. 2 in the notation indicates the vibrational quantum number of the initial state and the Fig. 3 denotes the rotational quantum number of the end state.

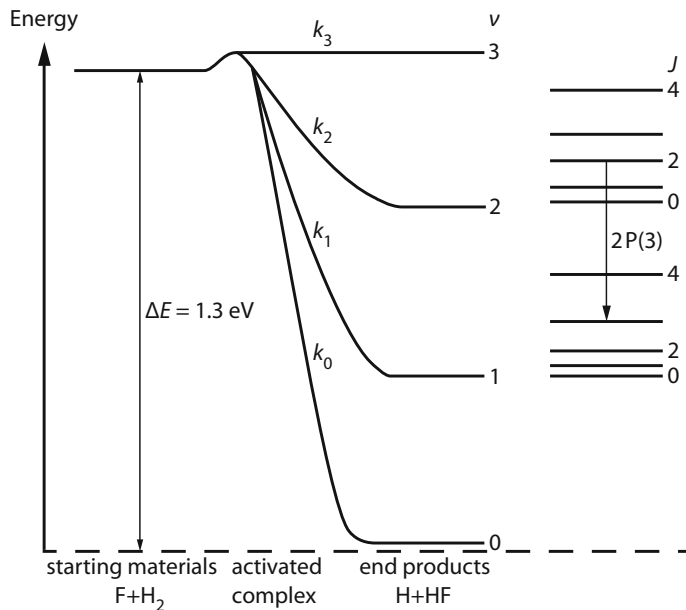


Fig. 6.11 Energy level diagram of a HF laser

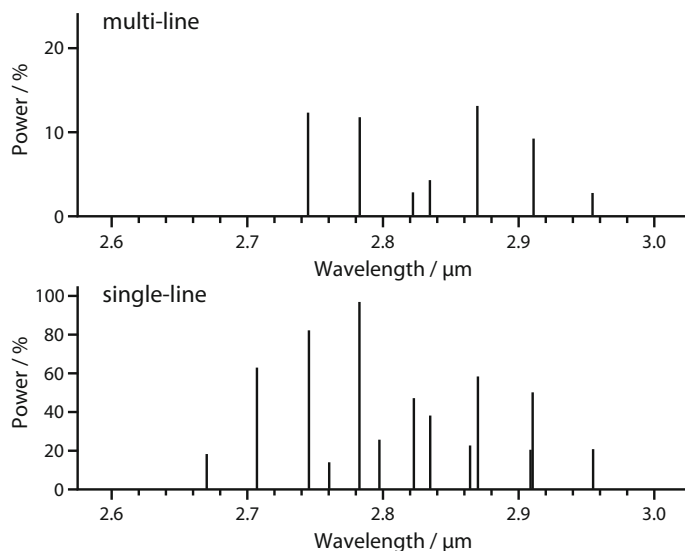
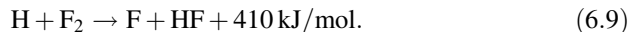


Fig. 6.12 Emission lines of a HF laser. *Multi-line*: in case of broadband resonator mirrors multiple lines oscillate simultaneously. *Single-line*: in case of intra-cavity frequency-selective elements (e.g. gratings) only one line is present

The reaction according to (6.8) requires atomic fluorine F, which can be produced through an exothermic reaction of molecular F₂ with atomic hydrogen:



The combination of the two chemical reactions (6.8) and (6.9) leads to a chain reaction, so that the number of excited HF molecules exceeds the number of originally produced F atoms. Furthermore, the released reaction heat in (6.9) allows the excitation of the HF molecule to higher vibrational states and, thus enabling laser action involving levels up to $v = 6$.

Laser Configuration

The HF molecules are formed in a gas discharge from molecular F₂ and H₂ which, in turn, are provided by fluorine and hydrogen donators such as SF₆ and C₂H₆ or H₂. Atomic fluorine is created through dissociation in the discharge. The discharge technology employed in HF lasers is similar to that of the CO₂ and CO laser, while transverse discharge arrangement comparable to the TEA configuration are mostly preferred. The gas mixture is pre-ionized through ultraviolet radiation. The addition of helium and oxygen improves the discharge stability and oxidizes dissociated sulfur (from SF₆) to SO₂. The fill pressure is in the range from 2000 to 60,000 Pa with the mixing ratio depending on the use of the F- and H-donators. A typical pressure ratio between the F- and H-compounds is 10:1. The applied voltages are on the order of 20–40 kV. In multi-line operation, commercial HF laser can generate pulse energies of several joules, while energies of 1 kJ have been demonstrated in experimental setups. The pulse duration is between 50 and 200 ns. The consumed gas is pumped away from the discharge volume. However, it can be re-used after separation of HF. In this way, the laser can be operated over several hours with a single filling if a small amount of SF₆ and H₂ is supplied.

Thermal or microwave dissociation of F₂ generates a flow of atomic fluorine which is mixed with H₂ in a reaction volume, hence realizing continuous laser operation. An exemplary design of a HF laser is sketched in Fig. 6.13. Here, atomic

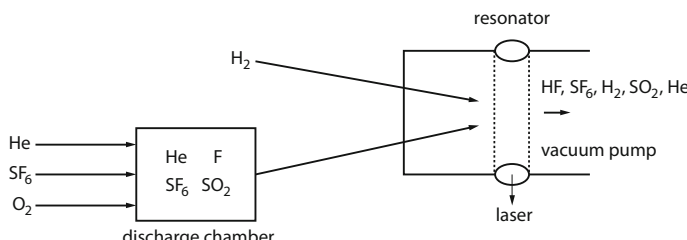


Fig. 6.13 Schematic of a HF laser with discharge outside of the resonator

fluorine is produced in a discharge chamber outside of the laser resonator, whereas mixing and chemical reaction with hydrogen are performed inside the resonator. HF lasers of this type are offered with cw output powers ranging from 1 to 150 W. In special designs, up to 10 kW of output power can be achieved. Since the excitation energy is supplied by a chemical reaction, the electrical efficiency can reach 70%.

Continuous and pulsed lasers are either operated in multi-line mode or a single emission line can be selected (see Fig. 6.12). Wavelength selection is usually realized by means of a rotatable grating inside the resonator. In single-line mode, the laser power is reduced to about 10% of the multi-line power. Fundamental transverse mode operation is possible, yet unstable resonators are mostly used if high beam quality is desired. The gases employed in HF and DF lasers are highly corrosive. Thus, even commercial systems are primarily suitable for laboratory use.

Further Reading

1. H.J. Eichler, I. Usenov, *Lasers, Gas. The Optic Encyclopedia* (Wiley-VCH, 2018)
2. V.V. Apollonov, *High-Energy Molecular Lasers* (Springer, 2016)
3. W.J. Wittemann, *The CO₂ Laser* (Springer, 1987)

Chapter 7

Ultraviolet Molecular Gas Lasers



Pulsed laser output in the ultraviolet spectral range is generated by transitions between electronic levels in molecules. Stable diatomic molecules like H₂, N₂ and excimers, especially the noble gas halides ArF, KrF and XeCl, are used as laser-active media. Excimers are molecules which only shortly exist in an excited state and quickly dissociate when returning to the ground state. An overview of the strongest UV laser emission lines produced by molecules is given in Table 7.1. Nitrogen and excimer lasers are available as commercial systems. Due to their high efficiency, the importance of noble gas halide lasers for generating UV laser radiation is comparable to that of CO₂ for the infrared spectral region.

7.1 Nitrogen Lasers

The nitrogen laser represents a technically simple system and has thus been built in many laboratories and also by students for educational purposes. The laser produces short pulses at repetition rates of about 100 Hz, while the pulse duration is in the ns-or sub-ns-regime under atmospheric pressure conditions. The strongest emission line at 337 nm is suitable for optical pumping of dye lasers. Other applications of the N₂ laser are found where UV lamps had been employed before, e.g. in the analysis of fluorescence. The main drawback of this laser type is the low energy storage capability of the nitrogen gas, which limits the pulse energy to a few tens of millijoules at a poor efficiency of less than 1%. Hence, excimer and frequency-tripled Nd:YAG lasers are rather used for generating UV laser output.

Energy Level Diagram

The output radiation of the N₂ laser originates from C $^3\Pi_u \rightarrow$ B $^3\Pi_g$ transition (Fig. 7.1; Sect. 1.4), where the main emission line at 337.1 nm involves the lowest

Table 7.1 Wavelengths of the most important molecular gas lasers emitting in the UV spectral region

Active medium	Wavelength (nm)
XeF	351–353
N ₂	337
XeCl	308
Br ₂	291
XeBr	282
KrF	248
KrCl	222
ArF	193
CO	181–197
ArCl	175
Xe ₂	172
H ₂ , D ₂ , HD (Lyman band)	150–162
F ₂	157
Kr ₂	146
Ar ₂	126
H ₂ (Werner band)	123
H ₂ (Werner band)	116

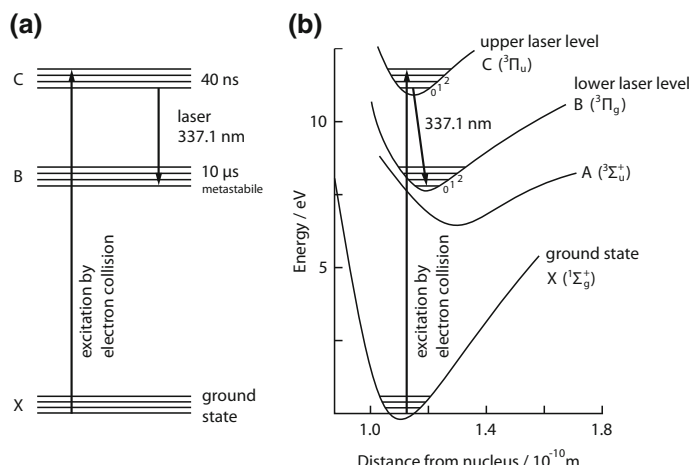


Fig. 7.1 **a** Simplified energy level diagram of the nitrogen laser. The main laser transition occurs between the lowest vibrational levels of the C and B electron states. **b** Schematic of a detailed energy level diagram including the potential curves of the involved energy states in the nitrogen molecule

vibrational levels ($v = 0$) of the two electronic states. Transitions between different vibrational levels of the same electronic states result in additional ultraviolet emission wavelengths with lower intensity. If other electronic states are involved, infrared laser output can be produced as well.

The gain coefficient of nitrogen lasers can be as high as 1 cm^{-1} so that powerful radiation is generated already without optical feedback provided by mirrors. Such superradiant lasers can reach beam divergence and spectral bandwidth comparable to regular lasers based on resonators. Nevertheless, the application of laser mirrors (100% and about 8% reflectivity) improves the beam quality and increases the pulse energy.

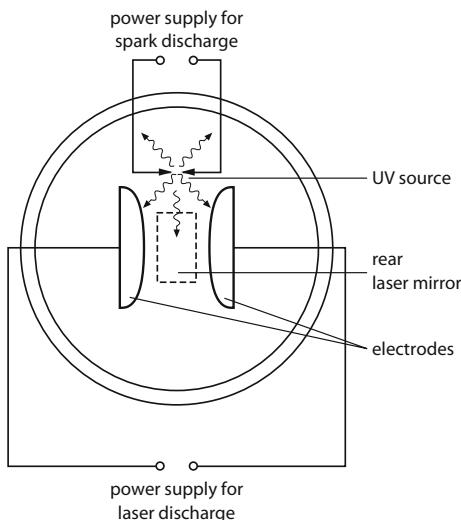
The excitation process of the nitrogen laser is rather unfavorable for efficient lasing, since the lifetime of the upper laser level (40 ns) is significantly shorter than that of the lower level (10 μs). Therefore, the upper level ($\text{C } ^3\Pi_u$) is efficiently populated from the ground state through electron collisions initiated in pulse gas discharges. The effective lifetime of the upper level can be extended up to 10 ms by energy transfer from higher N_2 levels through collisions with other molecules in the gas. Population inversion is thus only achieved in pulsed operation which requires pulsed discharges at high voltages and high currents with rise times that are shorter than the lifetime of the upper laser level. The short-time inversion and its subsequent depletion results in the emission of a laser pulse in the ns-regime. At longer excitation, the population of the lower laser level accumulates and the lasing stops (self-termination). The B-Level decays spontaneously into a metastable A-state which has a long lifetime of a few seconds. Consequently, the depletion of the lower laser level is hindered, thus limiting the repetition rate to about 100 Hz. Higher frequencies require a fast gas exchange.

Laser Configuration

The discharge in N_2 lasers is mostly realized in a transverse arrangement (Fig. 7.2) using pure nitrogen as a filling gas. The configuration resembles that of excimer lasers that are sometimes also filled with nitrogen and can be alternatively operated as N_2 lasers. The optimal gas pressure depends on the actual discharge geometry and ranges between 3×10^3 and 10^5 Pa . The pulse duration is pressure-dependent being on the order of 0.3 ns at atmospheric pressure and up to 20 ns at several tens of pascals. Shorter pulse durations of 100 ps can be obtained with very short cavities. Commercial nitrogen lasers can provide 10 mJ of output pulse energy at repetition rates of up to 100 Hz, corresponding to pulse peak powers in the kW- to MW-range. As the laser emission originates from multiple transitions involving different rotational levels, the spectral bandwidth of the laser is about 0.1 nm and a coherence length around 1 mm.

Like for many laser sources with high gain coefficient, the output beam quality of the N_2 laser is rather poor and the beam divergence is usually in the range of several mrad. The radiation is unpolarized and consists of multiple longitudinal and transverse modes. Laser operating in the high-power regime show a rectangular beam profile which follows the discharge geometry, e.g. with a cross-section of 6 mm \times 30 mm, as indicated in Fig. 7.2. Large-scale nitrogen lasers require a permanent gas flow of typically 0.1–40 l/min. Most commercial systems are

Fig. 7.2 Cross-section of a transversely-pumped nitrogen or excimer laser with spark discharge for UV pre-ionization



air-cooled, while water-cooling is applied in devices operating at higher repetition rates. Although the design and technology of the laser heads can be simple, substantial experience is necessary regarding the complex electronic circuits for fast switching of the high voltage, e.g. 30 kV in 2 ns, in thyratrons.

7.2 Excimer Lasers

Excimers are molecules that are characterized by the absence of a stable ground state. The acronym excimer stands for excited dimer and describes the fact that the (mostly) diatomic molecule (dimer) only exists in an excited state where it is “stable” for a short time. Once the molecule relaxes to the ground state, e.g. by emitting radiation, it quickly breaks down into its constituent atoms. Hence, the ground state has an extremely short lifetime compared to the excited state. In excimer lasers, the unstable ground state acts as the lower laser level, which is beneficial for realizing population inversion due to its short lifetime. Most lasers are based on noble gas halides such as ArF^* , KrF^* , XeCl^* , XeFl^* or noble gas dimers like Ar_2^* and Kr_2^* . The asterisk indicates the excited nature of the molecule. Most noble gases do not form chemical compounds in their ground state. Therefore, the interaction of noble gases with chemically aggressive halogens in electrical discharges where excited ions were produced was investigated. Here, the emission of intense ultraviolet light was observed, thus initiating the development of excimer

lasers. Nowadays, excimer laser can generate high-energy UV output with pulse energies in the joule-range and average output powers of more than 300 W. Commercial systems almost exclusively rely on noble gas halides emitting from 193 to 351 nm wavelength. Their configurations are similar to nitrogen and TEA CO₂ lasers. Despite the corrosivity of the used halogens, the excimer laser has emerged as an important laser source for the UV spectral region, as it is widely used in numerous industrial, medical and scientific applications.

Energy Level Diagram

The energy states of a noble gas halogen used in excimer lasers are shown in Fig. 7.3. The diagram depicts the potential energy of the molecules as a function of the distance between the nuclei. The letter R represents the noble gas (rare gas) atom, while X is the halogen atom. The potential curve of the ² Σ is very flat or exhibits a weak minimum. For XeCl*, the depth of the potential is on the order of the thermal energy kT , so that the molecules are thermally unstable and spontaneously dissociate. According to Fig. 7.3, the ground state is split into a ² Σ - and a ² Π -level with the potential of the latter being strongly repulsive.

The excited states ² Σ - and ² Π of KrF* are characterized by deep minima, corresponding to the respective equilibrium internuclear distances of the atoms where the molecule is strongly ionically bound. As the excited noble gas atom is similar to an alkali atom, the chemical bond of the noble gas halides is comparable to alkali halides like NaCl. A positive noble gas ion R⁺ is bound to a negative

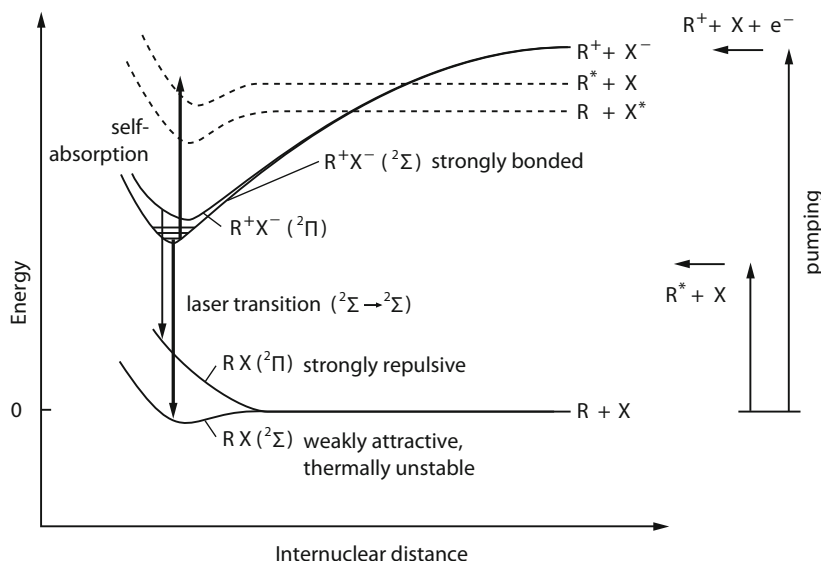


Fig. 7.3 Energy level diagram of an excimer laser (R = noble gas, e.g. Kr, X = halogen, e.g. F)

halogen ion X^- . Weak covalent bonding of the molecules is also possible, e.g. between an excited noble gas atom R^* and a halogen atom in the ground state or vice versa. This is indicated by the dashed lines in Fig. 7.3.

In the case of KrF^* , the excimers are mainly formed by collisions of excited Kr atoms (Kr^*) with F_2 :



When Kr^* and F_2 approach, the Kr^* atom transfers one of its valence electrons to the F_2 molecule, thus forming F_2^- and Kr^+ . The attraction between the two ions results in the splitting of the F_2^- molecule and the two F^- anion bonds to the Kr^+ cation to build KrF^* . This reaction is called harpoon reaction, as the electron from one of the particle “jumps” to the other, creating a cation and an anion which subsequently attract each other.

Simultaneously, recombination of the ions produced in the gas discharge occurs. This process requires the presence of a third partner M, usually helium (referred to as the buffer gas) to satisfy both energy and momentum conservation:

Fig. 7.4 Simplified energy level diagram of the KrF^* laser

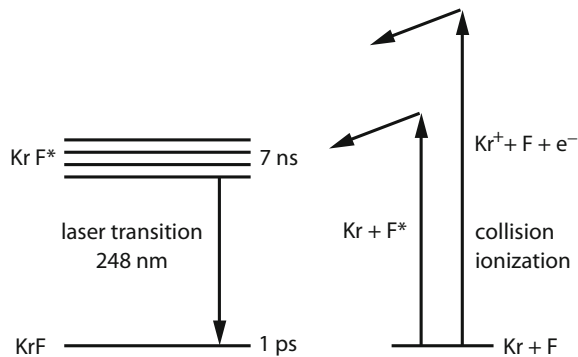
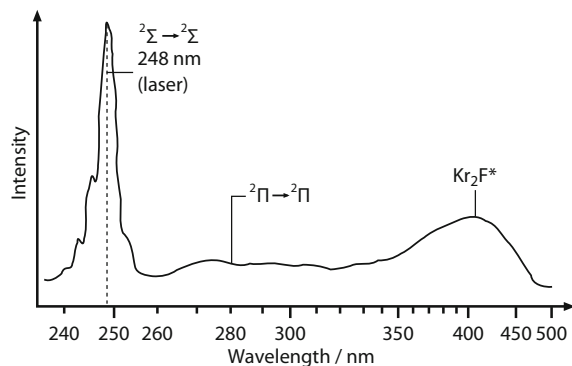


Fig. 7.5 Emission spectrum of the KrF^* excimer





The chemical reactions for the production and recombination described here using the example of KrF* are analogous for other excimers (Fig. 7.3).

Figure 7.4 shows a simplified energy level diagram of the KrF* laser. The emission is generated by transitions from the bound excited $^2\Sigma$ -state to the unstable ground state of KrF which dissociates within about 1 ps into its two atoms, resulting in (almost) no population of the lower laser level. This constitutes ideal conditions for laser operation. In contrast, the upper level lifetime is e.g. 7 ns for KrF* and 16 ns for XeF*.

The spontaneous emission spectrum of KrF* created in a discharge is depicted in Fig. 7.5, representing a typical spectrum of noble gas halides. The two bands in the ultraviolet range are attributed to $^2\Sigma \rightarrow ^2\Sigma$ - and $^2\Pi \rightarrow ^2\Pi$ -transitions, while a further band around 400 nm can be assigned to the triatomic excimer Kr₂F*.

In general, laser operation in the UV region is more challenging to obtain compared to longer emission wavelengths. This is primarily due to the fact that the spontaneous emission rate which is related to the Einstein coefficient $A = 1/\tau$ increases with the third power of the radiation frequency f [see (2.10)], i.e. the shorter the wavelength, the shorter is the excited state lifetime τ . In other words, for a given lifetime $\tau = 1/A$, the Einstein coefficient for stimulated emission is inversely proportional to the third power of the radiation frequency, $B \sim 1/f^3$. In excimer lasers, this circumstance is aggravated by the highly dissociative final state of the laser transition which results in a broad spectral bandwidth, and thus a relatively small frequency-dependent stimulated emission cross-section σ . Atomic and molecular transitions typically have cross-sections in the range from $\sigma = 10^{-15}$ to 10^{-12} cm^2 , whereas the transitions in excimer lasers show cross-sections of about 10^{-16} cm^2 . The small cross-section for stimulated emission necessitates strong pumping in order to achieve laser action. For this reason, continuous operation of excimer lasers has not been accomplished so far. The required high discharge currents rapidly cause instability of the discharge as well as material problems.

Laser Configuration

In commercial excimer lasers, the excitation occurs in a high-voltage discharge. Due to the high gas pressures, the discharge axis is usually oriented perpendicularly to the laser beam, leading to laser designs that are comparable to nitrogen or TEA CO₂ lasers (Fig. 7.2). The electrical power densities of 100 MW per liter gas volume required for achieving sufficient gain can only be reached in pulsed operation.

The forming reaction of KrF* according to (7.1) is more relevant than the recombination reaction (7.2). The back-reaction of the fluorine radical is enabled by a fast gas exchange between two subsequent pulses. Here, flow speeds of several tens of ms⁻¹ are required to allow for repetition rates of about 1 kHz, considering

the laser beam width of typically 5 mm. The gas pressure is around 3 bar, while the mixture contains 5–10% of the laser-active noble gas, 0.1–0.5% of the halogen and a buffer gas (helium or neon). For instance, the gas composition used for a XeCl laser is as follows: 4–5 mbar HCl, 80 mbar Xe, 2.4 bar Ne. Homogeneous discharge is achieved by pre-ionization at an electron density of $\approx 10^9 \text{ cm}^{-3}$. For this purpose, UV radiation (100–200 nm) from an additional spark or corona discharge or X-radiation is employed. At high gas pressure, the homogeneous discharge collapses and splits into multiple discharge channels after a few 10 ns. Therefore, the high-voltage pulses ($\approx 50 \text{ kV}$) are limited to durations of 10–30 ns. High pumping rates result in high gain coefficients on the order of $0.1\text{--}0.2 \text{ cm}^{-1}$, thus providing pulse energies of up to 4 J per liter gas volume, which is similar to CO₂ lasers. The population density of the upper laser level is about $10^{14}\text{--}10^{15} \text{ cm}^{-3}$ and the overall efficiency of such excimer lasers is 1–2%.

Owing to the transition from a bound to a free state, the spectral bandwidth of the output emission is relatively large (1–2 nm). Moreover, the short pulse duration involves a small number of round-trips in the resonator, resulting in only very weak competition between the different longitudinal modes which individually arise within the gain bandwidth. Consequently, simultaneous oscillation of $10^5\text{--}10^7$ modes is observed, corresponding to coherence lengths as short as 0.1 mm. The beam profile is often rectangular (Fig. 7.2) with cross-sectional areas of typically 1 cm × 2 cm. Improvement of the usually poor beam quality can be accomplished in unstable resonators.

Due to the high gain, only low requirements are imposed on the resonator mirrors. The output coupler can be realized by an uncoated glass plate with a Fresnel reflectivity of 4% per surface at 0° incidence angle. Fused silica is one of the standard materials utilized in the ultraviolet spectral range. Its transmission decreases towards shorter wavelengths. Furthermore, it is sensitive to hydrofluoric acid which can be created in the discharge. Hence, MgF₂ or CaF₂ is used as window material in commercial excimer lasers, while sapphire (Al₂O₃) with its good thermal conductivity is preferred in high-power systems. Because of the strong corrosive properties of the laser gas, dielectric coatings, e.g. anti-reflection coatings, are usually only applied on the outer surfaces of the tube windows. Most commercial excimer lasers are equipped with a vacuum pump for the gas exchange. The

Table 7.2 Typical parameters of commercial excimer lasers

Laser parameter	Unit	F ₂ *	ArF*	KrF*	XeCl*	XeF*
Wavelength	nm	157	193	248	308	351
Pulse energy	mJ	10–40	10–500	10–600	300–1000	400
Pulse duration	ns	10–30				
Repetition rate	Hz	2000	400	400	400	400
Average power	W	80	80	180	500	100
Operation lifetime	10^6 pulses	50	100	250	100	70

removed gas is toxic and must be properly contained and disposed of. The number of pulses per gas filling is given in Table 7.2. Normally, a laser head can be used for different gas mixtures which allows for the consecutive generation of different laser output wavelengths within the UV spectral region. The laser gas needs to be continuously cleaned during operation, as the chemically aggressive halogens form molecules with the tube materials which contaminate the gas. For example, fluorine creates CF_4 and other impurities like freons that can be removed by means of a cold-trap.

The shortest wavelength (157 nm) is produced by the F_2 laser which resembles the described excimer lasers in terms of the underlying chemical processes, laser configuration and electronics. This laser is based on a gas mixture consisting of 99.85% He and 0.15% F_2 . The required power density in the gas volume is a factor of 10 higher compared to the excimer lasers due to the high ionization energy of He and F_2 .

The parameters of the most important commercial excimer lasers are summarized in Table 7.2. Regarding scientific applications, excimer lasers are used both as primary sources and, particularly the XeCl laser, as pump sources for tunable dye lasers employed in laser spectroscopy in the UV region. Furthermore, they have found a broad range of applications in photochemistry, micro-material processing, photolithography as well as in medicine for the precise ablation of tissue.

Excimer Laser Lithography

Excimer lasers are widely-used in photolithography machines for the manufacturing of semiconductor integrated circuits, microprocessors and chips. Currently, KrF and ArF lasers emitting at 248 and 193 nm wavelength are employed as tools for high-resolution lithography which also often referred to as excimer laser lithography. A challenge of this technology is the relatively large linewidth of 1 nm which leads to chromatic aberration, and hence to diffuse structures if lenses are used in the beam path. Therefore, spectral narrowing of the excimer laser emission is mandatory for achieving high accuracy in the production process. For the KrF laser, this is accomplished by using reflection gratings (see Sect. 18.4) and additional etalons (Sect. 18.5) which reduce the linewidth to 0.3 pm. In ArF lasers, a special resonator design in combination with a concave grating result in spectral narrowing down to 0.4 pm.

An alternative approach for avoiding chromatic aberrations is the utilization of mirror optics, as mirrors rely on reflection, not refraction, to form images. However, the reflectance varies strongly with the angle of incidence and depends on the polarization of the light (Sect. 15.1). In order to prevent large variations in the reflectance, the degree of polarization of the laser has to be increased in case mirror optics are employed. Moreover, spectral narrowing of the linewidth to a few tens of pm is performed.

Crystallization of Silicon Layers, Drilling and Microstructuring of Fiber Bragg Gratings

A further field of application for excimer lasers is the production of liquid crystal displays (LCDs) and organic light-emitting diodes (OLEDs), where the UV laser output is used for annealing of amorphous silicon layers. The layers are first deposited on the display glass substrate on which the amorphous structure of the glass is adopted. In order to increase the charge carrier mobility, the layers are subsequently transformed into polycrystalline silicon through laser exposure. In this way, the resulting thin-film structures, e.g. transistors, can be produced in smaller size, which is especially important with regards to the resolution of the display, as the area occupied by the transistors is lost for the actual display operation. Moreover, smaller transistors allow for faster frame rates which is of interest for video applications. Regarding OLEDs, polycrystalline transistors are required for proper operation, as they can carry higher currents.

Excimer lasers are also applied in the fabrication of fine nozzles. For inkjet printers, the nozzles are drilled into a plastic material (mostly polyimide) by mask projection. In contrast, tiny holes are drilled individually into glass by a focused UV laser beam for manufacturing injection needles.

UV laser radiation permanently alters the refractive index of transparent materials within the exposed volume. This effect is exploited for writing fiber Bragg gratings (FBGs) into glass fibers. Here, a periodic modulation of the refractive index is induced in a short segment of the fiber core along the fiber axis. The inscribed structure acts as a dielectric mirror (Sect. 14.2), e.g. in fiber lasers, since only light at wavelengths that satisfy Bragg's condition are reflected. In transmission, the FBG can be used as an optical filter, where the filter wavelength is determined by the grating period. Fabrication of FBGs can be carried out by means of excimer lasers. For instance, UV pulses from a KrF laser operating at 248 nm wavelength are focused into the fiber core from the side, while the beam profile is modulated by a periodic mask in order to realize the desired periodicity of the grating.

Further Reading

1. D. Basting, G. Marowski, *Excimer Laser Technology* (Wiley-VCH, 2004)
2. K.L. Kompa, H. Walther (eds.), *High-Power Lasers and Applications* (Springer, 1977)

Chapter 8

Dye Lasers



Tunable laser action in the spectral range from 300 nm to 1 μm and beyond can be achieved with dye lasers. Since the first realization of a dye laser in 1966, far more than 100 laser-active dyes in aqueous or organic solutions (with concentrations on the order of 10^{-3} mol/l) have been studied. Dye lasers are pumped optically, usually by other laser sources, and can operate both in continuous and pulsed mode, offering high pulse energies and very high average output powers. Moreover, the broad bandwidth enables the generation of ultra-short pulses down to the fs-regime. Due to the versatility of dye lasers, they are suited for many applications in the UV, visible spectral range and near-infrared range including spectroscopy, medicine, particularly dermatology as well as astronomy, biology and metrology. Nevertheless, dye lasers have been largely superseded by solid-state lasers over the last years.

8.1 Laser Action in Dyes

Stimulated emission in dye lasers is based on fluorescence transitions in dye molecules. Laser dyes are large (many-atom) molecules with conjugated bonds, i.e. alternating single and double bonds, and an extended π -electron system, which results in a strong absorption band in the visible spectral range and a high fluorescence efficiency. Dyes are grouped into families such as coumarin, rhodamine, pyrromethene, pyridine, fluorescein or pyridine and can be further distinguished by numbers which indicate slightly different chemical structures within one family, leading to somewhat different ranges of emission wavelengths. For instance, coumarin 47, 102 or 153 is used for lasers emitting in the blue to green spectral region. The chemical structure of a typical dye molecule is shown in Fig. 8.1. The electronic states are classified into singlet and triplet states corresponding to a total spin of $S = 0$ or $S = 1$. In the singlet state, the electron spins are anti-parallel, while they are parallel in the triplet state. The lowest energy states within the two term

Fig. 8.1 Structure of Rhodamine 6G

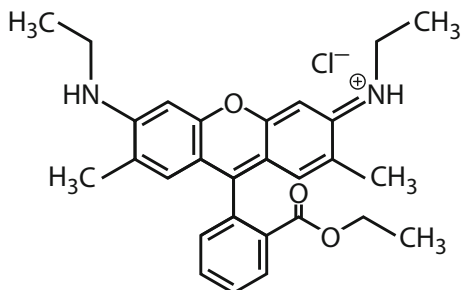
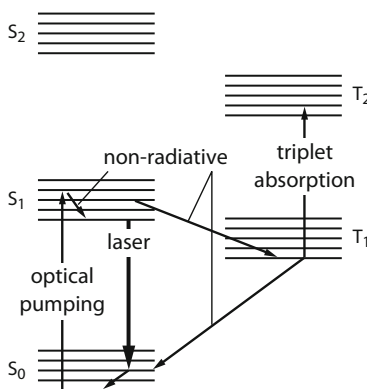


Fig. 8.2 Energy level diagram of a dye laser



systems are denoted S_0 and T_1 , and the higher states are designated as S_1 , T_2 , S_2 , etc. (Fig. 8.2). Transitions between singlet and triplet states are forbidden by quantum mechanical selection rules and thus only occur with very low probability (see selection rule $\Delta S = 0$ in Table 1.3).

The electronic levels are subdivided into a number of vibrational and rotational levels. These levels are substantially broadened to bands by the interaction with the solvent, so that single vibrational or rotational levels cannot be resolved in absorption or fluorescence spectra. For the sake of simplicity, the excited states within the electronic bands S_0 , S_1 , T_1 , etc. are referred to as vibrational levels.

Dye solutions are characterized by a strong absorption over a broad spectral range which results from $S_0 \rightarrow S_1$ transitions (singlet absorption), as depicted in Fig. 8.3. Upon absorption, the excited electrons are transferred to the lowest S_1 vibrational level through fast (picoseconds) non-radiative transitions. After a few nanoseconds, radiative relaxation to vibrational levels of the S_0 ground state occurs with high quantum efficiency. The emitted light is shifted to longer wavelengths compared to the absorbed light (Fig. 8.3). The excited vibrational states of the S_0 ground state rapidly decay into the lowest state by collisions with the solvent molecules within picoseconds. As these transitions are non-radiative, they involve heating of the dye liquid.

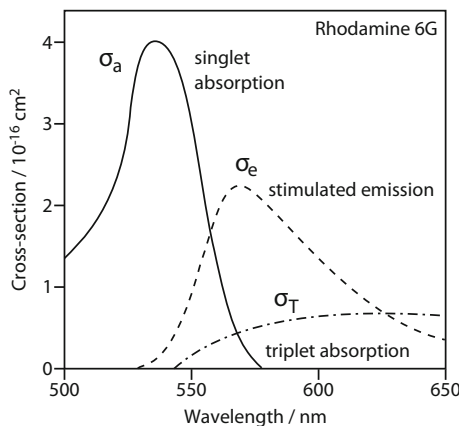


Fig. 8.3 Wavelength-dependence of the cross-section for singlet absorption, triplet absorption and stimulated emission in Rhodamine 6G

Optical Pumping

Lasing in dyes is achieved by optical pumping, where the lowest S_1 vibrational level serves as the upper laser level. Its lifetime of about 1 ns is longer than that of the lower laser level which is an excited vibrational level of the S_0 ground state. The efficiency of the excitation process suffers losses due to absorption into higher singlet states ($S_1 \rightarrow S_2$) as well as through non-radiative transitions to the triplet state ($S_1 \rightarrow T_1$). Intense pumping results in strong population of the S_1 state. Since the energy spacing between the different singlet states is approximately equidistant, $S_1 \rightarrow S_2$ transitions are likely to occur which hinders laser operation. Moreover, the long lifetime of the metastable T_1 state (10^{-7} – 10^{-3} s) leads to accumulation of many dye molecules in this state during the pumping process. These “trapped” molecules cannot participate in the lasing process. Instead, they can be excited into higher triplet states by absorption of the radiation to be amplified, thus impeding or suppressing laser operation.

The $S_0 \rightarrow S_1$ transition takes place within about 10 ns. Hence, if pumped by short pulses with durations on the order of a few to tens of ns, triplet effects are negligible. However, for pump pulse durations longer than 100 ns or in case of continuous excitation, triplet-triplet-absorption can introduce significant losses in the laser excitation cycle. For diminishing these effects, a so-called “triplet quenching” agent, e.g. oxygen or cyclooctatetraene (COT, C_8H_8), can be added to the dye solution which reduces the triplet population via collisions. An alternative approach that is commonly applied in cw dye lasers is a fast flow of the dye solution. At flow speeds of 10 to 100 m/s, the dye molecules pass through the laser-active zone within 1 μ s which prevents accumulation of molecules in the triplet state.

Table 8.1 Typical parameters of some dye lasers pumped by different sources (from Kneubühl and Sigrist (2008)). The cited tuning ranges are reached by using multiple dyes

Pump source	Average power (W)	Pulse peak power (W)	Pulse duration	Linewidth
Flash lamp	100	10^5	0.1–3 μ s	Multimode: 10–100 pm Single-mode: 0.1 pm
Nd:YAG laser (532 nm, 355 nm)	1	10^6	10 ns	100 MHz
N ₂ laser	1	10^5	1–10 ns	Fourier-limited
Excimer laser	100	10^7	1–10 ns	

Flash Lamp Pumping

The utilization of flash lamps for optical pumping of dye lasers allows for economical configurations. In most devices, the lamps are coaxially aligned around a cylindrical laser cuvette, forming a double cylinder. The inner cylinder contains the dye solution and is surrounded by the discharge channel in the outer cylinder (jacket). The lamps are specially designed to show short rise times (100 ns), thus realizing laser pulses with durations from 0.1 to 3 μ s. Short pump pulse durations are required for avoiding triplet effects, as mentioned above. The pump energies are usually between 50 and 500 J. Alternatively, linear xenon flash lamps (10–60 J) are employed that are similar to those used for pumping solid-state lasers. Flash lamp-pumped dye lasers can reach average output powers up to 10 W, corresponding to pulse energies in the joule-range at 1–100 Hz repetition rate. However, this requires mechanical circulation of the dye solution in order to prevent heating effects which also diminish the beam quality of the output beam and complicate single transverse mode operation. The overall efficiency for the conversion from electrical energy (for the flash lamps) to laser output energy is about 0.5%. Characteristic parameters of dye lasers pumped by flash lamps and lasers are given in Table 8.1. Flash lamp-pumped systems are particularly suited for obtaining high laser energy and high average output power.

8.2 Laser-Pumped Dye Lasers

Dye lasers for spectroscopic applications are primarily pumped by other pulsed or continuous wave lasers, as this offers selection of the optimal pump wavelength for efficient excitation of the used dye. In this way, detrimental heating is avoided, and a good beam quality is achieved.

Pulsed Lasers

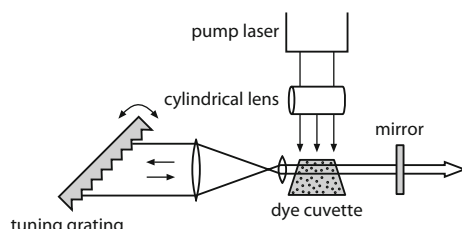
The most important pump sources for dye lasers are pulsed lasers emitting in the ultraviolet or visible spectral range: N₂ laser (337 nm), excimer laser (UV) as well as frequency-doubled or -tripled Nd:YAG laser (532, 355 nm). The pump lasers are designed to provide nanosecond pulses with peak powers between 1 and 100 MW, while the pulse duration is shorter than the inverse of the transition rate S₁ → T₁, thus preventing accumulation of molecules in the triplet state. This enables the usage of dyes that are inapplicable for flash lamp pumping due to their high S₁ → T₁ transition rate. Since a pulse duration of 1 ns corresponds to a length (of the wave packet) of 30 cm, the resonator length of the dye laser has to be much shorter, so that the wave propagates through the medium as often as possible. The pump laser can be coupled into the dye solution either longitudinally or transversely. The latter configuration is favored in pulsed systems, as illustrated in Fig. 8.4.

Here, the pump radiation is focused into the dye cuvette by means of a cylindrical lens. Strong absorption occurs, and maximum inversion is established in a focal line of 0.2 mm width. For selection of the output wavelength, the narrow laser beam is expanded by a telescope or multiple prisms and reflected from a diffraction grating. Expansion of the beam results in a larger beam area incident on the grating and, in turn, a narrower spectral linewidth of the laser emission, as the resolution of the grating increases with the number of grating facets interacting with the light wave. Linewidths down to 0.1 nm can be accomplished. Another reason for expanding the beam is the reduction of the power density and divergence of the radiation. In case Nd:YAG or excimer lasers are used as pump sources, the pulse repetition rate can reach several 100 Hz.

Pulsed excitation can be applied for a multitude of laser-active dyes with various properties. The spectral emission ranges of different dye compounds that are pumped by excimer lasers are plotted in Fig. 8.5, showing that the wavelength range from 300 to 1000 nm is completely covered.

The major advantage of laser-pumped dye lasers is the possibility to generate short ns-pulses with high pulse peak powers in the MW-range and with pulse repetition rates above 100 Hz. Moreover, it enables broad tuning ranges, especially if UV lasers are employed as pump sources.

Fig. 8.4 Schematic of a pulsed, transversely-pumped dye laser



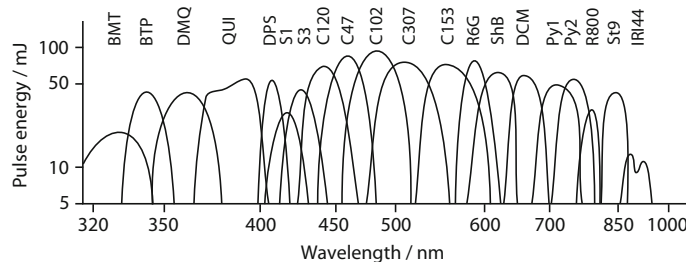


Fig. 8.5 Tuning ranges and typical output pulse energies of various dye lasers pumped by excimer lasers (spectra taken from Coherent datasheet)

Continuous Lasers

Dye lasers applied in high-resolution spectroscopy are often pumped by continuous wave argon or krypton ion lasers. Here, a stream of dye solution passes through the focal area of the pump beam. Because of the fast flow, triplet population and associated absorption are reduced. Two typical laser designs are shown in Figs. 8.6 and 8.7. In the first configuration, the pump and dye laser output beam propagate coaxially which requires special coatings on the resonator mirrors so that the pump radiation is transmitted. The more common setup according to Fig. 8.7 involves an additional curved mirror outside the laser cavity that focuses the pump beam into the dye. This design has the advantage that the dye which flows in a high-velocity jet, can be tilted at the Brewster's angle to the incoming pump light, hence avoiding reflection losses at the surface of the stream. In addition, the laser beam is polarized. However, tilting of the dye stream results in an elliptical distortion of the intensity distribution of the output beam (astigmatism). This effect is compensated by the folded resonator configuration, since reflection from a tilted concave mirror also introduces an astigmatic deformation of the beam. The laser threshold depends on the focusing conditions of the pump radiation and the number of optical elements in the resonator, ranging from several mW to a few W. Depending on the used dye, up to 30% of the injected pump power is converted. The frequency-selective intra-cavity elements depicted in Figs. 8.6 and 8.7 will be discussed in detail in Chap. 18 and briefly described in the following.

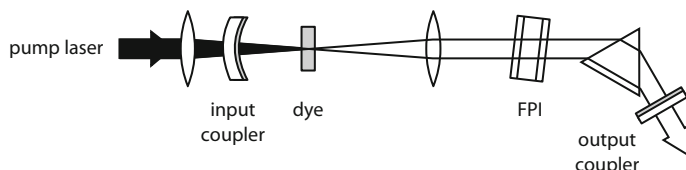


Fig. 8.6 Schematic of a longitudinally-pumped dye laser. Frequency selection is realized by means of a prism and a Fabry-Pérot interferometer (FPI)

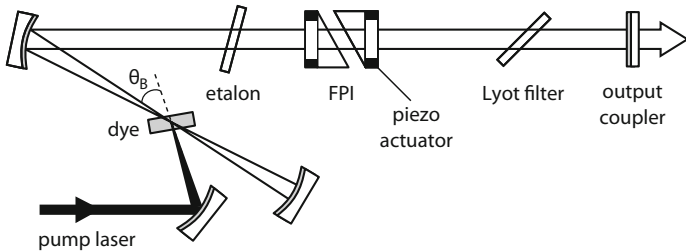


Fig. 8.7 Schematic of a folded dye laser for continuous wave operation. Frequency selection is realized by means of an etalon, a Fabry-Pérot interferometer (FPI) and a Lyot filter

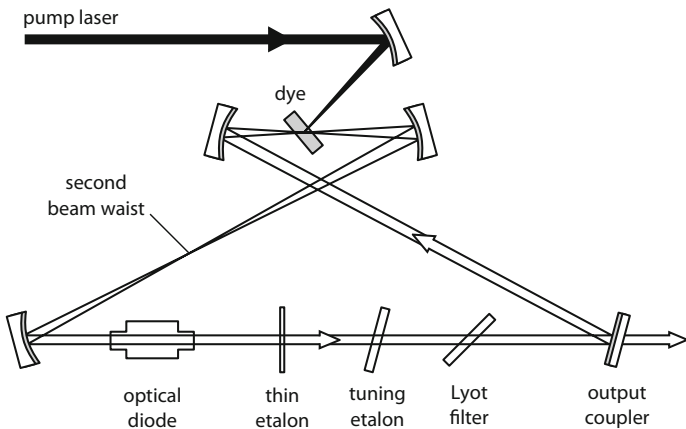
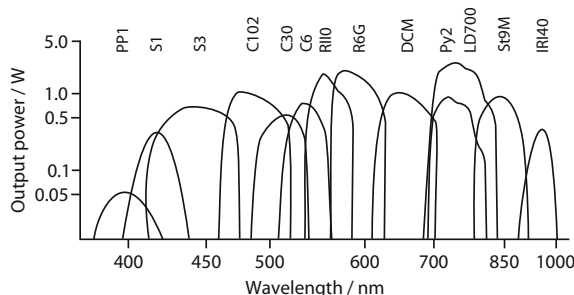


Fig. 8.8 Ring dye laser operating in single longitudinal mode

In continuous wave dye lasers, single longitudinal mode operation with high frequency stability (MHz to kHz) can be achieved by active stabilization of the temperature and resonator length. In linear resonators, as in Figs. 8.6 and 8.7, standing-waves are formed which leads to a spatial modulation of the gain along the laser-active medium by saturation of the inversion in the antinodes of the standing wave. This effect is known as spatial hole burning (Sect. 18.2) and causes instability of the mode due to competition from nearby longitudinal modes that occupy a volume that is less saturated. Consequently, the single-mode output power is limited in standing wave cavities, so that ring lasers (Fig. 8.8) are preferred for generating powerful and narrowband output. Here, unidirectional traveling waves can be generated by insertion of an optical diode into the cavity.

The latter is usually realized by a combination of a Faraday rotator and a polarizer which ensures that polarized light can only pass in one direction, while counterpropagating light suffers high losses. Thus, the formation of standing-waves and, in turn, spatial hole burning is avoided in ring laser configurations. As a result,

Fig. 8.9 Tuning ranges and typical output powers of various dye lasers pumped by cw Ar⁺ or Kr⁺ lasers (spectra taken from Coherent datasheet)



all molecules can contribute to the laser process, which enables single longitudinal mode output powers that are higher than in linear resonators by a factor of 15.

The tuning ranges for continuously-pumped dye lasers are shown in Fig. 8.9, covering the entire visible and the near-infrared region up to 1 μm. In case of UV pumping, the spectral range of cw dye lasers extends to the near-UV.

The large tuning range of dye lasers represents one of their main benefits. Different optical elements like gratings, prisms, filters and etalons are used for wavelength selection. While gratings are mainly employed in pulsed dye lasers, wavelength tuning in cw systems is performed using birefringent (or Lyot) filters. Birefringent filters consist of a polarizer and a birefringent plate (usually quartz) which is placed at the Brewster's angle with respect to the beam orientation in the cavity (Sect. 18.6). Tuning over broad ranges of about 100 nm is realized by rotating the filter about the axis perpendicular to the plate, resulting in a wavelength-dependent transmission through the polarizer. Laser linewidths down to 0.1 nm, comparable to gratings, can be obtained. Further spectral narrowing is achieved by insertion of additional Lyot filters with larger thickness or Fabry-Pérot etalons, as shown in Figs. 8.6 and 8.7. For ensuring single longitudinal mode operation, three filters and two etalons are typically used, while the transmission of all the wavelength-selective elements as well as the resonator length have to be changed when tuning the single-mode output. Mode-hop-free tuning ranges of about 100 GHz have been achieved in this manner. Despite the favorable properties of dye lasers, it should be noted that many laser dyes and some of the used solvents are poisonous and partly even carcinogenic. Therefore, (frequency-doubled) titanium-sapphire lasers and fiber lasers (Chap. 9) are advantageous in terms of handling and thus preferred for generating tunable output in the visible and near-infrared range.

Ultra-short Pulse Generation

Lasers with broad spectral bandwidth are characterized by a multitude of longitudinal modes that oscillate independently with a random phase relationship between each other. By means of mode-locking the modes can be superimposed such that short pulses are produced at regular intervals ($t = 2L/c$). In cw-pumped dye lasers, synchronous pumping and passive mode-locking are applied (see Sect. 17.4).

Table 8.2 Ultra-short pulse generation in dye lasers

Method	Pulse duration	Length of the wave packet
Pulsed excitation	100 ps	50,000 wavelengths (cycles)
Synchronous pumping	100 fs	50 wavelengths
Passive mode-locking	25 fs	12 wavelengths
+ Pulse compression	6 fs	3 wavelengths

Synchronous pumping is realized by using a mode-locked ion laser providing pulses with durations of 200 ps at an average power of about 1 W. The pump beam is focused into the dye as depicted in Fig. 8.7. A prerequisite for the generation of ultra-short pulses is that the resonator length of the pump and dye laser are identical within a few μm . In this case, the gain in the laser medium is modulated at the round-trip frequency $f = c/2L$ of the light wave circulating in the resonator. Additionally, the relaxation time of the upper laser level of the dye ($\approx 5 \text{ ns}$) has to be shorter than the round-trip time $2L/c$ in the resonator. As opposed to passive mode-locking, it is not the round-trip loss that is modulated, but the round-trip gain. The produced dye laser pulses are two to three orders of magnitude shorter than the pump pulses, yielding pulse durations of $0.1 \text{ ps} = 100 \text{ fs}$.

Even shorter pulses down to 25 fs are obtained in continuously-pumped, passively-mode-locked dye lasers. Here, mutual stabilization of the resonator lengths of the pump and dye laser is not necessary. Mode-locking (Sect. 17.4) is achieved by a saturable absorber. Originally, ring laser configurations (without an optical diode), were used. In contrast to the setup shown in Fig. 8.8, the resonator is designed such that a second focus is formed in the cavity. This is where the saturable absorber with a thickness of about $10 \mu\text{m}$ is placed. As a result, two counterpropagating pulses are produced and interact inside the absorber. While the intensity of a single pulse is not sufficient for saturating the absorber, the interference of both pulses leads to an enhanced intensity and saturates the absorber, resulting in steeper edges of the colliding pulses. Hence, pulse shortening occurs in every round-trip until an equilibrium with concurrent pulse broadening effects, e.g. group velocity dispersion, is established. This technique is called colliding pulse mode-locking (CPM) and was a first crucial step in generating sub-100 fs pulses.

However, nowadays, comparable pulse durations can be reached with passive absorbers also in linear resonators similar to the configuration shown in Fig. 8.7. Further shortening of dye laser pulses is accomplished by pulse compression in glass fibers (Table 8.2), leading to wave trains of only a few wavelengths or cycles, respectively.

8.3 Polymer and Liquid Crystal Lasers

Like in semiconductor lasers (Chap. 10), distributed feedback (DFB) lasers (Sect. 10.5) can be built from organic materials. Polymers mixed with laser-active dyes or fluorescent polymers that serve as gain medium itself are used for this

purpose. Currently, these structures can only be pumped optically and operated in pulsed mode, as the operating times are limited by the photochemical stability of the organic emitter. Nevertheless, the main advantage over conventional dye lasers is the more compact and practicable design.

The DFB structure is produced either by etching or mechanical scribing of a periodic groove pattern into the organic film layer, or by applying the organic film onto a periodically structured substrate. In general, organic DFB lasers are not tunable, as the emission wavelength is determined by the grating constant. If an elastomer (rubber) is utilized, however, stretching of the film alters the grating constant, thus enabling broadband tuning of the laser emission.

In terms of applications, organic semiconductors have the highest development potential. Although organic light-emitting diodes (OLEDs) reach lifetimes of many thousands of hours and electrical-to-optical conversion efficiencies of greater than 20%, the realization of an organic laser diode has not been demonstrated until now.

Aside from the described artificially produced organic DFB structures, self-organized periodic structures are suitable for generating laser emission. One example are cholesteric liquid crystals which consist of rod-shaped molecules that organize along a predominant direction in certain layers, thus creating optical anisotropy. The predominant direction rotates periodically, whereby a helical long-range ordering is developed. This results in a one-dimensional modulation of the dielectric properties. When the liquid crystal is mixed with a laser dye, laser emission can be achieved. The periodicity of the helical structure can be influenced by temperature changes or electric fields which allows for wavelength tuning, where the tuning range is only limited by the emission range of the used dye molecule.

Further Reading

1. S. Forget, S. Chénais, *Organic Solid-State Lasers* (Springer, 2013)
2. F.K. Kneubühl, M.W. Sigrist, *Laser* (Vieweg + Teubner, 2008)
3. F.J. Duarte (ed.), *High-Power Dye Lasers* (Springer, 1991)
4. F.J. Duarte (ed.), *Dye Laser Principles* (Academic Press, 1990)

Part III

Solid-State and Semiconductor Lasers

Over the last decades, solid-state and semiconductor diode lasers have become the most important laser sources. Their high efficiency and wavelength diversity alongside with enhanced reliability and robustness make them essential for many applications. While solid-state lasers are particularly relevant for material processing, spectroscopy, atmospheric monitoring, and precision metrology, diode lasers are also indispensable in optical communication and storage accounting for about half of the total laser revenue. This part of the book is divided into two chapters covering various configurations and structures of the two laser types. In Chap. 9, lasers based on ruby and different rare-earth doped host materials are discussed, together with tunable solid-state laser sources where the focus is on the titanium–sapphire laser. Moreover, different pumping schemes and geometries are outlined comprising diode-pumped disk and fiber lasers. Chapter 10 provides a comprehensive overview of semiconductor lasers. After introducing the physical background of light amplification in diodes, the most prevalent structures and material compositions are presented with regard to emission characteristics, wavelength tunability, and applications. Both edge-emitting and the emerging group of surface-emitting are reviewed, while also considering semiconductor diode lasers for the Mid-IR and THz as well as violet and blue spectral regions. Finally, the importance of semiconductor lasers for the field of optical communication is highlighted.

So-called solid lasers, e.g., based on oxide and fluoride crystals or glass, were mostly optically pumped by different types of lamps, whereas diode lasers are directly excited by electrical currents. However, as the semiconductor laser material is also a solid, these laser sources may be also considered as solid-state lasers. Lamp pumping of solid-state lasers has been largely replaced by diode laser pumping so that the technology of solid-state lasers including fiber lasers is merging with the diode laser technology.

Chapter 9

Solid-State Lasers



Single crystals or glasses that are doped with light emitting atoms are used as the gain medium in solid-state lasers. In crystals, the atoms exist in the form of ions. Aside from conventional rods and slabs with lengths of several cm, technologies based on disks or fibers with thicknesses, respectively diameters of 10–100 μm become more and more prevalent. Most solid-state lasers are based on transition metal ions such as Ti, Cr and Co or rare-earths such as Nd, Ho, Er, Tm or Yb. For the latter group, laser operation often relies on transitions within partially filled inner electron shells that are effectively screened by the outer shells and thus only weakly influenced by the crystal field. As a result, narrowband transitions in the visible to near-infrared spectral region occur. Besides, broadband levels exist which are addressed for realizing tunable lasers.

Doping of solids involves replacing a small amount (10^{-4} – 10^{-1}) of atoms of the host material with laser-active atoms from another element. The density of laser-active particles is on the order of 10^{19} cm^{-3} , which is much higher than in gas lasers (10^{15} – 10^{17} cm^{-3}). Excitation of the gain medium is realized by optical pumping using lamps, laser diodes or other laser sources. Since the upper level lifetime is usually quite long, solids can store considerable amounts of energy which enables high output pulse energies and peak powers at short pulse durations. The host material—crystal or glass—has to provide good optical, mechanical and thermal properties, e.g. high transparency, hardness and thermal conductivity. While oxides and fluorides are preferred as crystalline host materials, silicates and phosphates are the most used laser glasses.

Among the group of oxides, especially sapphire and garnets—also known as gemstones—are of relevance for lasers. The first laser material was chromium-doped sapphire (Al_2O_3), called ruby. From the large group of garnet crystals, yttrium aluminum garnet (YAG) is widely used as host for various rare-earth dopants, most prominently neodymium. Besides, vanadates like YVO_4 and tungstates like $\text{KGd}(\text{WO}_4)_2$ are often employed. CaF_2 and YLiF_4 (YLF) represent well-studied fluorides that can also be doped with a broad range of ions, including Nd^{3+} , Ho^{3+} and Er^{3+} .

The class of vibronic solid-state lasers is formed by materials for which the energy levels are spectrally broadened due to the interaction of the valence electrons with lattice vibrations in the crystal. This allows for broadband tunability of the laser output wavelength. Important members of this group are the alexandrite laser ($\text{Cr}^{3+}:\text{BeAl}_2\text{O}_4$) and the titanium-sapphire laser ($\text{Ti}^{3+}:\text{Al}_2\text{O}_3$). Another class of tunable lasers is based on alkali halide crystals with crystallographic defects, resulting in the formation of color centers (see Sect. 1.5). In the following, the most relevant commercial solid-state lasers emitting in the spectral range from 0.7 to 3 μm are discussed.

9.1 Ruby Lasers

The first realization of a laser is generally attributed to T. H. Maiman from the Hughes Research Laboratories in California, dating back to 1960. Following this breakthrough, intense research on lasers has been conducted worldwide. While the first lasers in the Federal Republic of Germany were built in the Siemens laboratories in Munich, the development of a ruby laser was accomplished only shortly afterwards in Jena, in the former German Democratic Republic.

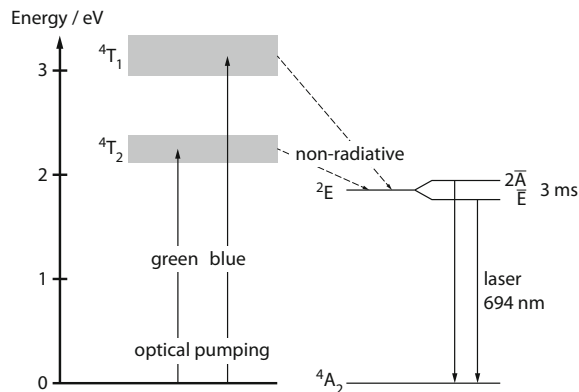
The ruby laser is based on a synthetic ruby crystal as gain medium, consisting of a sapphire (Al_2O_3) host crystal which is doped with chromium: $\text{Cr}^{3+}:\text{Al}_2\text{O}_3$. Before the pulling process, 0.05 percent by weight (wt%) of chromium oxide (Cr_2O_3) are added to the Al_2O_3 melt. In this way, about 10^{19} Al^{3+} -ions per cm^3 are substituted in the crystal lattice for Cr^{3+} -ions, giving the crystal its reddish color. The laser transitions occur in the electron shells of the Cr^{3+} -ions.

Energy Level Diagram

The simplified energy level diagram of the ruby laser is depicted in Fig. 9.1. Here, the term symbols do not correspond to the designations introduced for free atoms or ions, but follow from crystal field theory describing the interaction between the Cr^{3+} dopants and the electric field of the surrounding host crystal atoms. Upon optical pumping, typically by using xenon flash lamps, electrons are excited from the ${}^4\text{A}_2$ -ground state to the ${}^4\text{T}_{2-}$ and ${}^4\text{T}_1$ -bands, from where they non-radiatively relax to the upper laser level ${}^2\text{E}$ within 1 ns. This level is split into the $2 \bar{\text{A}}$ - and the $\bar{\text{E}}$ -level with an energy spacing of 29 cm^{-1} . Due to a rapid (>1 ns) energy transfer between the two sub-levels, their respective population can be described by a Boltzmann distribution. At room temperature, the population of both levels is nearly equal as a result of the small energy difference.

For the same reason, the $2 \bar{\text{A}}$ - and the $\bar{\text{E}}$ -level are strongly coupled having a long (common) lifetime of 3 ms. Consequently, many electrons can accumulate in the upper laser level during a short intense pump pulse, thus realizing population

Fig. 9.1 Energy level diagram and pump and laser transitions of the ruby ($\text{Cr}^{3+}:\text{Al}_2\text{O}_3$) laser

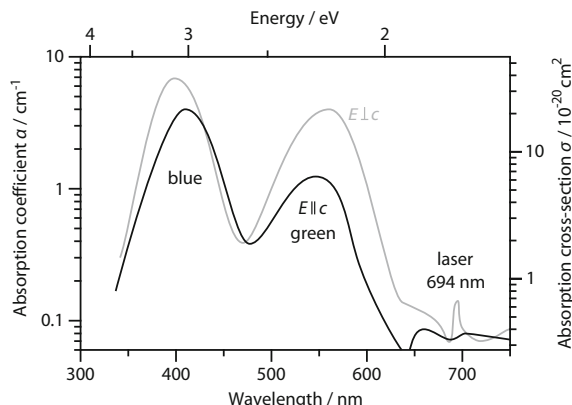


inversion with respect to the ground state. The resulting fluorescence emission consists of the R_1 - and the R_2 -line corresponding to the transitions from the \bar{E} - and the $2\bar{A}$ -level, respectively. The laser threshold for the latter one is higher, so that the laser normally only operates on the R_1 emission line at 694 nm wavelength.

The absorption spectrum of ruby is plotted in Fig. 9.2, showing that the absorption cross-section is anisotropic, i.e. it depends on the direction of the pump light field E with respect to the crystal axis c . The same holds for the emission cross-section; hence, the laser emission is polarized along the direction for which the stimulated emission cross-section is highest.

The ruby laser is a three-level system, which is unfavorable, as about 50% of the atoms have to be excited in order to achieve population inversion, and in turn, light amplification. This requires high pump energies for reaching the laser threshold. On the other hand, the long lifetime of the metastable upper laser level (3 ms) is favorable, as the pump peak powers can be kept moderately low. Because of the high pump rates, however, the ruby laser is mostly operated in pulsed mode. A further disadvantage arising from the three-level system is the self-absorption which particularly occurs in weakly pumped regions of the crystal.

Fig. 9.2 Absorption spectrum of ruby (doping concentration: $1.9 \times 10^{19} \text{ cm}^{-3}$ in Al_2O_3) at room temperature. The upper and lower curve show the spectrum for the electric field of the radiation being parallel and perpendicular to the c -axis of the crystal, respectively (from Koechner (2006))



An alternative to the ruby laser is provided by the Pr:YLF laser which has several emission lines in the red spectral range. As it is a four-level laser system, considerably lower pump energies are required compared to the ruby laser. Although YLF crystals show less mechanical stability than ruby crystals, they are easy to handle as host crystals in laser systems.

Ruby Laser Emission

The emission wavelength of the ruby laser (R_1 -line) is 694.3 nm at room temperature. The line is homogeneously broadened to 300 GHz. The broadening is caused by lattice vibrations which modulate the resonance frequency of each lasing ion at very high frequency. The laser wavelength can be shifted to 693.4 nm by cooling of the ruby crystal to 77 K (liquid nitrogen temperature). Apart from that, the laser can operate at the R_2 emission line at 692.9 nm if the dominant R_1 -line which has a higher gain coefficient is suppressed.

The maximum extractable pulse energy of a ruby laser can be estimated from the chromium concentration of about $n \approx 1.6 \times 10^{19} \text{ cm}^{-3}$ and the photon energy $hf = 1.8 \text{ eV} = 2.86 \times 10^{-19} \text{ Ws}$. In the strong pumping regime, the ground state is fully depleted and the energy density stored in the $2\bar{A}$ - and the \bar{E} -levels is $E = n \cdot hf = 4.6 \text{ J/cm}^3$. Hence, the maximum energy density per laser pulse is $E_{\text{pulse}} \approx n/2 \cdot hf = 2.3 \text{ J/cm}^3$, provided that the upper laser level is no longer pumped during the emission.

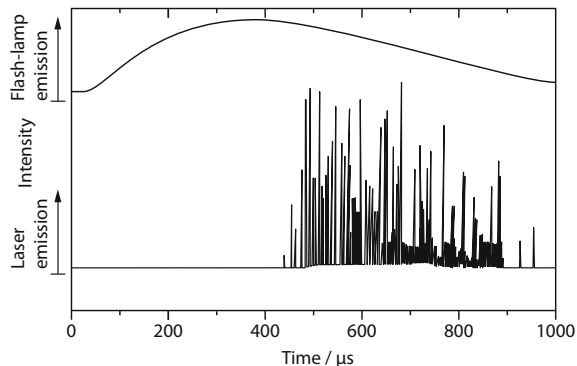
Like other solid-state lasers, the ruby laser can be deployed in different operation modes: normal pulsed mode, Q-switched mode and mode-locked mode (Table 9.1). Continuous wave operation with output powers of about 1 mW has no practical relevance. In normal pulsed mode, the emission is not continuous, but characterized by strong intensity fluctuations known as spiking (see Fig. 9.3 and Sect. 17.1).

Spiking occurs during the onset of laser oscillation, e.g. after switching on the pump source. While the laser intensity grows, the gain does not instantly adjust to the level according to the optical input power. This gives rise to several overshoots in the laser output until the laser reaches the steady-state level, at which the laser gain is saturated down enough to just equal the total cavity losses. Spiking is especially pronounced in lasers where the upper-state lifetime is much larger than the cavity damping time, i.e. in solid-state lasers with short resonator lengths. The cavity damping time is the mean period in which a photon remains in the resonator. Here, the switch-on dynamics are in most cases characterized by quasi-periodic

Table 9.1 Operation modes of the ruby laser ($\lambda = 694.3 \text{ nm}$) and typical emission parameters

Operation mode	Pulse duration	Pulse peak power	Pulse energy (J)
Normal pulse	0.5 ms	100 kW	50
Q-switched	10 ns	100 MW	1
Mode-locked	20 ps	5 GW	0.1

Fig. 9.3 Normal emission pulses (spikes, lower curve) of a ruby laser upon flash lamp excitation (upper curve)



spikes with rather chaotic intensity variations. Only under certain conditions regular relaxation oscillations are observed. Since the upper-state lifetime is substantially smaller than the cavity damping time in most gas lasers, spiking is not observed in these systems. Although spiking is considered to be a detrimental effect, the behavior can be useful for special applications in material processing. Interaction of the first high-power spikes with the matter leads to an enhancement of the absorption, thus improving the quality of the processing result.

In order to achieve defined laser output parameters at high power levels, master oscillator power amplifier (MOPA) systems are employed. Here, the spectral, spatial and temporal properties such as linewidth, beam divergence and pulse duration of the laser are controlled in the low-power master oscillator, while output power is scaled in the power amplifier. This decoupling of the performance aspects from the generation of high powers provides flexibility in the design of the laser at the expense of higher complexity. The maximum gain coefficient of a ruby amplifier is $g = 0.2 \text{ cm}^{-1}$ corresponding to an amplification factor $G = e^4 \approx 50$ for a 20 cm-long rod. It should be noted, that this value only holds for low incident intensities.

Output Parameters and Applications

Commercial ruby laser rods are fabricated in lengths up to 30 cm and diameters up to 2.5 cm. The optimum dopant concentration is 0.05 wt% of Cr_2O_3 which corresponds to a concentration of Cr^{3+} -ions of about $n \approx 1.6 \times 10^{19} \text{ cm}^{-3}$, as mentioned above. The energy required for reaching the laser threshold is then $E_{\text{thr}} \approx n/2 \cdot hf_{\text{pump}} = 3.2 \text{ J/cm}^3$, with $hf_{\text{pump}} = 2.5 \text{ eV} = 4 \times 10^{-19} \text{ J}$ the pump pulse photon energy. However, due to the losses experienced during the conversion from electrical to optical energy as well as during the coupling of the pump light into the laser rod, the electrical threshold pump energy densities of about 100 J/cm^3 are considerably higher. At pump energy densities of $200\text{--}800 \text{ J/cm}^3$, output energies E_{out} in the range of $2\text{--}4 \text{ J/cm}^3$ are obtained depending on the pump pulse duration. The pump source has to be adapted to the absorption spectrum of the ruby

(Fig. 9.2). Optical pumping involves heating of the crystal which can introduce thermal lensing effects, so that the repetition rate is usually limited to a few Hz. The laser configuration is similar to the Nd:YAG laser which will be described in the next section.

Ruby lasers are rarely used in industry, mainly because of their low repetition rates and low efficiency of only about 1%. One application, however, was holography. For this purpose, the number of longitudinal modes has to be significantly reduced in order to achieve coherence lengths of several meters. This is accomplished by using frequency-selective elements like Fabry-Pérot etalons (Sect. 18.5) which results in spectral narrowing from 300 GHz to e.g. 30 MHz. MOPA systems providing output energies from 1 to 10 J are employed to produce large holographic images with ruby lasers.

By now, diode-pumped ruby lasers have been demonstrated, producing cw output powers of more than 100 mW. The linewidth can be smaller than 1 MHz, corresponding to coherence lengths over 100 m, which makes these devices suitable for holography, but also biomedical applications, e.g. in hematology or DNA sequencing.

9.2 Neodymium Lasers

The most important solid-state lasers are the neodymium lasers where the radiation is produced by optical transitions in Nd^{3+} -ions that can be doped into different host materials. For laser purposes, yttrium aluminum garnet ($\text{Y}_3\text{Al}_5\text{O}_{12}$, or simply YAG) single crystals or different glasses are mostly used as hosts. YAG has favorable mechanical and thermal properties and is therefore employed for numerous continuous wave and pulsed lasers. The high gain of neodymium-doped YAG (Nd:YAG) makes the Nd:YAG laser extremely attractive for various applications in science and technology, particularly in material processing, medicine, spectroscopy, as well as for pumping other lasers.

Apart from Nd:YAG, most commonly used neodymium-doped gain media are Nd:YVO₄, Nd:YLF and Nd:glass. The Nd:YVO₄ (yttrium vanadate) laser features very high pump and laser cross sections and larger gain bandwidth compared to Nd:YAG. Moreover, thermally-induced depolarization loss in high-power lasers is effectively eliminated by the birefringent nature of the vanadate crystal. However, due to the lower upper-state lifetime, its capability for energy storage is lower compared to Nd:YAG, resulting to lower output pulse energies.

Yttrium lithium fluoride (YLiF_4 or simply YLF) is also birefringent and shows high UV transparency which is favorable for pumping with xenon flash lamps. The fact that heating of the crystal results in a defocusing thermal lens can be exploited for achieving better beam quality. Since the emission wavelength of Nd:YLF lasers (1053 nm) fits well with the gain peak of Nd:glass, they are employed as mode-locked oscillators or preamplifiers for Nd:glass amplifier chains, e.g. in high-energy laser systems dedicated for laser fusion experiments (Sect. 25.6).

Silicates and phosphates are mostly used as glassy host materials. Nd:glass lasers exhibit a broad emission bandwidth which enables the generation of ultra-short pulses. The doped glasses can be produced in large dimensions with very good optical quality. Hence, they are of interest for high-energy amplifiers. Cw operation is possible in glass fibers. The microscopic disorder in the glass materials leads to a reduced thermal conductivity which is detrimental for high-power lasers, as it can lead to strong thermal lensing and thermal fracture. In glass fibers, thermal effects are less important.

Energy Level Diagram

Pure YAG is a colorless, optically isotropic garnet with cubic crystal structure. By doping the melt with Nd_2O_3 , about 1% of the Y^{3+} -ions are replaced by Nd^{3+} , resulting in a Nd^{3+} density of $n = 1.4 \times 10^{20} \text{ cm}^{-3}$. As the ionic radii of both rare-earths differ by 3%, strong doping introduces causes local distortion, and in turn, stress in the host crystal. The electronic configuration $\{\text{Kr}\} 4\text{d}^{10}4\text{f}^35\text{s}^25\text{p}^6$ of the Nd^{3+} -ion is characterized by a partially filled 4f sub-shell. For free ions, this configuration leads to different energy states that are denoted according to the LS coupling scheme, e.g. ${}^4\text{F}_{3/2}$ or ${}^4\text{I}_{11/2}$. The impact of the crystal field is weak

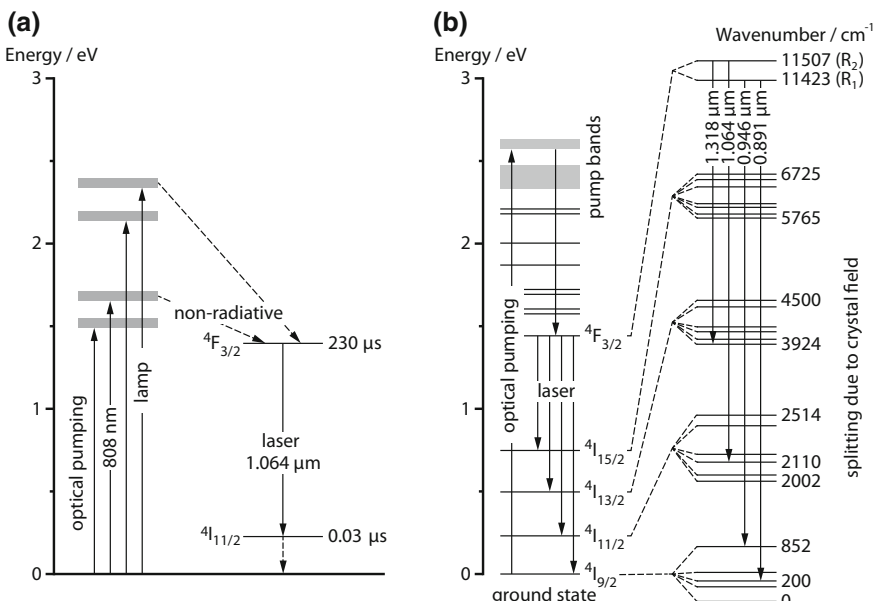


Fig. 9.4 **a** Energy level diagram of the Nd:YAG laser operating at 1.064 μm. **b** Further laser transitions of the Nd:YAG laser (from Kaminskii (1996))

Table 9.2 The most important cw laser emission lines of flash lamp-pumped Nd:YAG lasers at room temperature

Wavelength (μm)	Transition	Relative intensity
1.0520	$R_2 \rightarrow Y_1$	46
1.0615	$R_1 \rightarrow Y_1$	92
1.0641	$R_2 \rightarrow Y_3$	100
1.0646	$R_1 \rightarrow Y_2$	≈ 50
1.0738	$R_1 \rightarrow Y_3$	65
1.0780	$R_1 \rightarrow Y_4$	34
1.1054	$R_2 \rightarrow Y_5$	9
1.1121	$R_2 \rightarrow Y_6$	49
1.1159	$R_1 \rightarrow Y_5$	46
1.1227	$R_1 \rightarrow Y_6$	40
1.3188	$R_2 \rightarrow X_1$	34
1.3200	$R_2 \rightarrow X_2$	9
1.3338	$R_1 \rightarrow X_1$	13
1.3350	$R_1 \rightarrow X_2$	15
1.3382	$R_2 \rightarrow X_3$	24
1.3410	$R_2 \rightarrow X_4$	9
1.3564	$R_1 \rightarrow X_4$	14
1.4140	$R_2 \rightarrow X_6$	1

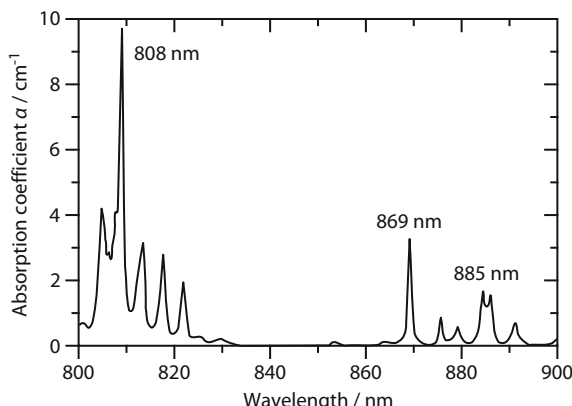
X and Y correspond to the $^4F_{3/2}$ and $^4I_{11/2}$ manifolds shown in Fig. 9.4, respectively. The indices enumerate the sub-levels starting from the lowest (from Koechner (2006))

compared to the $\text{Cr}^{3+}:\text{Al}_2\text{O}_3$ system, as the 4f shell is screened by the 5s and 5p electrons. Hence, the energy states of the Nd^{3+} -ions embedded in the crystal largely correspond to those of free ions, while the electric crystal field causes a splitting of the levels. Figure 9.4a depicts the simplified energy level diagram of Nd:YAG. Most commercial lasers of this type emit at the most intense line at $1.064 \mu\text{m}$ which is produced by transitions between the $^4F_{3/2}$ and $^4I_{11/2}$ levels. Additional laser emission lines of Nd:YAG are shown in the more detailed diagram in Fig. 9.4b and summarized in Table 9.2.

Excitation is achieved by optical pumping into broad energy bands and subsequent non-radiative transitions into the upper laser level. The released energy is deposited as heat in the crystal. The absorption coefficient as a function of the excitation wavelength is plotted in Fig. 9.5, indicating the different pump bands, from which the energy is transferred to the upper laser level.

The $^4F_{3/2}$ level has a long lifetime of about $230 \mu\text{s}$ which results from the fact that electric dipole transitions between 4f manifold levels are forbidden by the parity selection rule for free ions. This selection rule is abrogated by the impact of the crystal field on the embedded ions, giving rise to “forbidden lines”. The lower laser level $^4I_{11/2}$ is rapidly depleted in 30 ns by non-radiative transitions to the ground state. Being 0.24 eV above the ground level, the $^4I_{11/2}$ level is practically not populated at room temperature.

Fig. 9.5 Absorption spectrum of Nd:YAG (doping concentration: 1 at%). Optical pumping of a Nd:YAG laser can be realized by using laser diodes emitting at 808, 869 or 885 nm wavelength



Laser Emission

The Nd laser is a four-level system which has the benefit that the laser threshold is comparably low. When YAG is used as host crystal, the emission lines are homogeneously broadened by thermal lattice vibrations. At room temperature, the linewidth is about 100 GHz which is relatively narrow for solids and allows for high gain already at low pump power. Hence, Nd:YAG is well suited as an active medium for cw high-power lasers.

Under normal operating temperatures, Nd:YAG only emits the strongest $^4F_{3/2} \rightarrow ^4I_{11/2}$ -line at 1064.15 nm wavelength. Utilization of frequency-selective elements inside the resonator like etalons, prisms or selective mirrors, enables the generation of numerous other lines, as listed in Table 9.2. The table gives the relative intensity of various laser transitions between the different $^4F_{3/2}$ - and $^4I_{11/2}$ -sub-levels generated by a special cw Nd:YAG laser. The intensities are normalized to the most prominent line at 1064.15 nm. While most commercial systems operate at this line, emission at 1319 nm or 1338 nm ($^4F_{3/2} \rightarrow ^4I_{13/2}$ transitions) as well as at 946 nm wavelength ($^4F_{3/2} \rightarrow ^4I_{9/2}$ transition) is also possible in Nd:YAG (Fig. 9.4b). Since the lower laser level is a sub-level of the ground state in the latter case, the 946 nm laser is a quasi-three-level system, thus requiring significantly higher pump intensities and operation at lower temperatures.

Customary YAG laser rods have a length of up to 150 mm and a diameter of up to 10 mm. The crystal is usually doped with about 0.7 wt% of neodymium, corresponding to a Nd^{3+} -ion concentration of $1.4 \times 10^{20} \text{ cm}^{-3}$. Using a 75 mm-long Nd:YAG laser rod with a diameter of 6 mm, an output power of more than 300 W can be obtained at an overall efficiency of up to 4.5%. The laser threshold is at about 2 kW of electrical power applied for krypton arc lamps that are used as continuous pump source. For many applications, optical pumping with laser diodes is more favorable in terms of efficiency, manageability and lifetime.

Continuously-pumped YAG lasers can also be operated in pulsed mode by periodic Q-switching, producing pulses with pulse durations of several 100 ns, peak

Table 9.3 Operation modes of the Nd:YAG laser ($\lambda = 1064.15$ nm) and typical emission parameters

Excitation	Operation mode	Pulse repetition rate	Pulse duration	(Pulse peak) Power
Continuous	Continuous	–	–	W-kW
Continuous	Q-switched	0–100 kHz	0.1–0.7 μ s	100 kW
Continuous	Cavity-dumped	0–5 MHz	10–50 ns	
Continuous	Mode-locked	100 MHz	10–100 ps	
Pulsed	Normal pulse	Up to 200 Hz	0.1–10 ms	10 kW
Pulsed	Q-switched	Up to 200 Hz	3–30 ns	10 MW
Pulsed	Cavity-dumped	Up to 200 Hz	1–3 ps	10 MW
Pulsed	Mode-locked	up to 200 Hz	30 ps	A few GW

powers of a few 100 kW and repetition rates in the kHz-range. Shorter pulses from 10 to 100 ps are generated by means of active mode-locking (see Table 9.3). Due to the four-level nature of the Nd:YAG laser, continuous operation is readily possible, as opposed to the ruby laser. In case of pulsed excitation, lower pump energies and thus higher efficiencies are achieved compared to cw pumping. The output energy of a flash lamp-pumped Nd:YAG laser as a function of the electrical pump energy is depicted in Fig. 9.6. The data were obtained for a small crystal (50 mm length, 6 mm diameter) and for different resonator configurations. The output energy also strongly depends on the operation mode of the laser. Comparison of typical emission parameters of cw- and pulsed-pumped Nd:YAG lasers in different modes (normal pulse, Q-switched, cavity-dumped, mode-locked) is provided in Table 9.3. In normal pulsed mode, spiking occurs as described for the ruby laser (Fig. 9.3). The beam quality declines with increasing pump power, so that master oscillator power amplifier configurations are usually employed for generating high-power output with

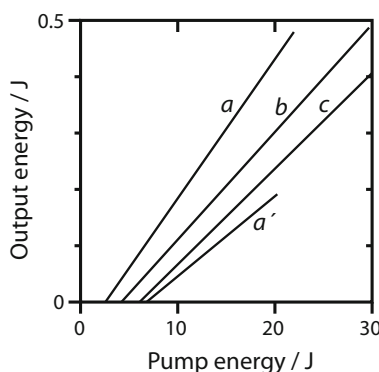


Fig. 9.6 Typical output energy of a Nd:YAG laser operating in fundamental transverse mode with 6 mm crystal diameter, 50 mm crystal length and a pump pulse duration of 100 μ s. The three slopes *a*, *b* and *c* are obtained for different resonator configurations. *a'* depicts the laser performance in case of active Q-switching using a Pockels cell (10 ns laser pulse duration)

low divergence. However, as a pump energy density of 1 J/cm^3 stored in the upper laser level results in a low-signal gain coefficient as high as $g = 4.7 \text{ cm}^{-1}$, parasitic lasing can occur in amplifiers, especially at low pulse repetition rates, where the stored energy is higher.

Nd:Cr:GSGG Laser

Aside from the YAG laser, there is a multitude of other crystalline materials that can be used as hosts for neodymium. In the case of Nd:Cr:Gd₃Sc₂Ga₃O₁₂ (GSGG) the broad absorption bands of chromium ions (Cr³⁺) in the visible spectral range are exploited for the pumping process (see Fig. 9.2). The actual laser process occurs in the Nd³⁺-ions after the pump energy is very efficiently ($\approx 100\%$) transferred from the Cr³⁺-ions to the upper laser level ${}^4F_{3/2}$, increasing the overall efficiency to 5%.

One drawback of GSGG is the occurrence of strong thermal effects which result from its lower thermal conductivity and heat capacity compared to YAG, while the other material parameters are similar. Since the gain is slightly lower and the saturation is a bit higher, and due to the high efficiency, Nd:Cr:GSGG is of interest for producing low average output powers.

While flash lamps were originally used for optical pumping, single-mode and multimode laser diodes around 665 nm are nowadays employed as pump sources. In this way, lasing thresholds as low as 14 mW, slope efficiencies above 20% and output powers exceeding 700 mW have been demonstrated in cw operation. The free running emission wavelength is 1061 nm, but lasing can also be obtained at multiple lines between 1051 and 1111 nm. Mode-locking by means of a saturable Bragg reflector allows for the generation of 6 ps-long pulses with an average power of 160 mW.

Nd:YLF Laser

In contrast to Nd:YAG, ${}^4F_{3/2} \rightarrow {}^4I_{11/2}$ transitions in Nd:LiYF₄ (Nd:YLF) lead to laser emission at 1053 and 1047 nm. Since the YLF crystal is birefringent, the gain is polarization-dependent and the light produced at the two emission lines is perpendicularly polarized. Hence, generation of the stronger line at 1047 nm or the weaker one at 1053 nm can be controlled by rotating a polarizer inside the resonator. The 1053 nm radiation of Nd:YLF lasers can be amplified in neodymium-doped phosphate glasses, so that such combinations are applied as master oscillator power amplifier systems. The Nd:YLF laser can also operate at 1313 nm or 1321 nm wavelength (${}^4F_{3/2} \rightarrow {}^4I_{13/2}$ transitions), where both lines have again perpendicular polarization.

The cross-section for stimulated emission and the gain of Nd:YLF is about a factor of two smaller compared to Nd:YAG. However, YLF shows a weaker thermal lensing. This results from the fact that heating of the crystal gives rise to a

defocusing thermal lens that can be approximately compensated by the focusing lens formed from the bulging of the end-faces. Also, the birefringence of the crystal effectively eliminates thermally-induced depolarization. The pulses generated in cw-pumped mode-locked Nd:YLF lasers are about half as long (10 ps) as usually obtained in Nd:YAG.

Polarization-Maintaining Host Crystals

A major disadvantage of Nd:YAG crystals is the strong, cross-sectional varying birefringence that is introduced by heating during optical pumping. Thermally-induced birefringence gives rise to depolarization loss and diminishes the beam quality, especially of high-power systems. This effect is avoided in polarization-maintaining crystals such as Nd:YLF, or Nd:YALO. The latter is also known as Nd: YAP (yttrium aluminium perovskite, YAlO_3) and was largely produced in Russia. As the fabrication of crystals with high optical quality is more complicated than for YAG, Nd:YAP is not very common as laser medium. Moreover, thermal lensing is twice as strong compared to YAG. In this context, Nd:YLF shows the best performance for the reasons discussed in the section above. However, YLF crystals are quite expensive and can only be produced in small dimensions.

Diode-Pumped Laser Crystals

The most important diode-pumped solid-state lasers (see Sect. 9.5) based on Nd-doped crystals are Nd:YAG, Nd:YLF and Nd:YVO₄. The Nd:YVO₄ (yttrium vanadate, YVO₄) laser has a much higher absorption cross section than Nd:YAG, e.g. five times higher at 808 nm, which enables shorter crystal lengths. Furthermore, like Nd:YLF, Nd:YVO₄ is birefringent so that thermally-induced depolarization effects are strongly reduced.

Ytterbium-doped crystals are also used as diode-pumped laser media. Yb:YAG lasers emit at 1047 and 1030 nm and can be pumped with laser diodes operating at 968, 941 and 936 nm wavelength. The small quantum defect between pump and laser photons results in high pump efficiencies above 90% as well as in low heat deposition in the crystal which facilitates the configuration of high-power lasers. Yb:YAG is not suited for lamp pumping, since the absorption lines are too narrow for efficient excitation.

Lamp-Pumped Nd Lasers

In lamp-pumped Nd lasers, the gas discharge lamp is arranged parallel to the laser rod in a pump chamber whose inner surface is highly reflective, this providing

Fig. 9.7 Configuration for optical pumping of a solid-state laser using a gas discharge lamp

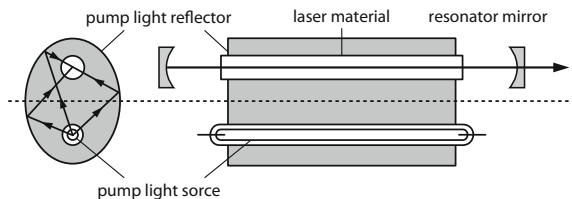
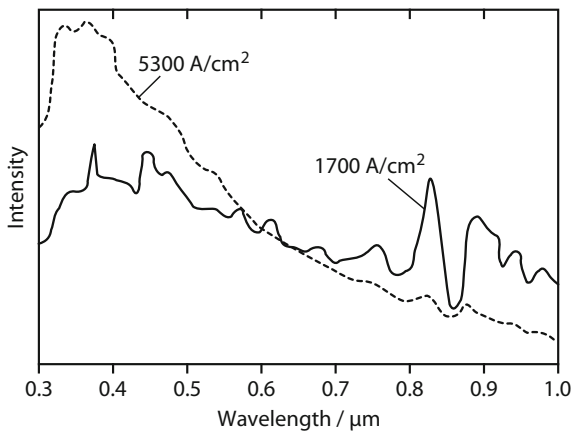


Fig. 9.8 Emission spectrum of a Xe flash lamp (0.4 bar) at different current densities



efficient coupling of the pump light into the laser material (Fig. 9.7). Homogeneous illumination of the laser rod is usually achieved by using pump chambers made of diffusely reflecting materials. In double elliptical pump configurations two lamps are integrated in the pump chamber. The heat produced during the pumping process is mostly dissipated by water cooling. For pulsed systems, Xe flash lamps (0.6–2 bar) are employed, whereas high-pressure Kr lamps (4–6 bar) are used for cw lasers. As the output spectrum of Xe flash lamps (Fig. 9.8) has only poor overlap with the absorption spectrum of Nd:YAG (Fig. 9.5), the absorption efficiency is rather low. Better adaptation and, in turn, a higher efficiency is obtained with GaAlAs diode lasers emitting between 805 and 809 nm.

Glass Lasers

Instead of crystals, glasses, e.g. silicate or phosphate glasses based on SiO_2 or P_2O_5 , can be doped with neodymium or other laser-active ions. Laser glasses are usually fabricated in larger dimensions and with higher doping concentrations than crystals, which allows for higher output energies and powers. The pulse repetition rates, however, are smaller than in crystalline lasers and continuous operation is more challenging due to the lower thermal conductivity. Owing to the amorphous structure of the glasses, the linewidth is about 50 times broader compared to

crystals, hence enabling the synthesis of shorter pulses, as the minimum pulse duration that can be reached by mode-locking is inversely proportional to the laser bandwidth (Sect. 17.4).

Doped glasses can be pulled and stretched to produce thin glass fibers and to build diode-pumped fiber lasers. In this way, Nd fiber lasers providing up to 1 kW of diffraction-limited output power are realized. By exploiting up-conversion processes in fibers, visible light can be generated when pumping with infrared laser diodes. For instance, thulium-doped fluoride glass fibers emit blue laser light, while Nd-doped fibers of the same type even produce UV radiation.

Nd:glass Laser

The Nd:glass laser is a four-level system. In contrast to the crystalline counterpart, the environment of the Nd^{3+} -ions is inhomogeneous and mostly disordered, causing a considerable broadening of the levels, and in turn, the emission lines to several THz. As opposed to Nd:YAG, the dominant laser transition starts from the lowermost $^4\text{F}_{3/2}$ -sub-level (Fig. 9.4). The lower laser level in the $^4\text{F}_{11/2}$ -manifold is slightly shifted, so that the emission wavelength is also around 1060 nm if silicate glasses are used as host materials. The exact wavelength depends on the glass type and can very be about 10 nm. Hence, Nd-doped silicate glasses can be used to amplify the output of Nd:YAG oscillators. Phosphate glasses exhibit a larger stimulated emission cross-section at 1054 nm wavelength.

Due to the broad linewidth, the gain in Nd:glass is considerably lower (about 30 times) than in Nd:YAG. For a pump energy density of 1 J/cm^3 stored in the upper laser level, the low-signal gain coefficient is only 0.16 cm^{-1} . Consequently, a large amount of energy can be stored in the medium, before the laser threshold is reached. For instance, a pulse peak power of 27 TW in a 90 ps-long pulse has been generated using a Nd:glass laser and subsequent amplifier.

Although the gain in Nd:glass is lower than in YAG, it is well suited as amplifier medium due to the simpler fabrication of large-scale rods reaching meters in length and diameters of up to 10 cm. Nd:glass disk with diameters of more than 50 cm are employed in laser amplifiers applied in laser fusion research (Sect. 25.6). The Nd doping concentration mostly on the order of 3 wt%, but can even be higher. Glasses are characterized by low thermal conductivity ($\approx 1 \text{ W m}^{-1} \text{ K}^{-1}$). The resulting problems in terms of heat deposition prevent operation of Nd:glass lasers in cw mode or at high repetition rates.

Commercial glass lasers usually operate at pulse repetition frequencies below 1 Hz. As an example, the operation parameters of a commercially available device are given as follows. The laser is based on a 15 cm-long glass rod with a diameter of 1.2 cm. The resonator is formed by a concave highly-reflective mirror (radius of curvature: 10 m) and a flat output coupler with a reflectivity of about 45%. The two laser mirrors are spaced by 70 cm. If a spiral flash lamp is used as pump source, the threshold pump energy is about 1 kJ. At 5 kJ of pump energy, nearly 70 J of output power are emitted. The beam divergence is 10 mrad.

Table 9.4 Material parameters of ruby, Nd:YAG and Nd:glass (from Koechner (2006))

Parameter	Unit	Ruby	Nd:YAG	Nd:glass
Wavelength	nm	694.3	1064.15	1062.3
Photon energy	10^{-19} J	2.86	1.86	1.86
Refractive index		1.763 o 1.755 eo	1.82	1.51–1.55
Stimulated emission cross-section	cm^2	2.5×10^{-20}	50×10^{-20}	3×10^{-20}
Spontaneous lifetime	μs	3000	230	300
Doping concentration	cm^{-3} wt%	0.16×10^{20} 0.05	1.4×10^{20} 0.75	2.8×10^{20} 3.1
Fluorescence linewidth	cm^{-1}	11	6.5	300
Thermal conductivity at 300 K	$\text{W m}^{-1} \text{K}^{-1}$	42	14	1.2
Thermal expansion coefficient	10^{-6} K^{-1}	5.8	8	7–11
Inversion at $g = 0.01 \text{ cm}^{-1}$	cm^{-3}	840×10^{16}	1.1×10^{16}	33×10^{16}
Stored energy at $g = 0.01 \text{ cm}^{-1}$	J cm^{-3}	2.3	0.002	0.06
Gain coefficient g at 1 J	cm^{-1}	0.087	4.73	0.16

Comparison of Laser Materials

Relevant physical properties of ruby, Nd:YAG and Nd:glass are summarized in Table 9.4. Nd:YAG crystals are particularly suited for cw operation, while more energy can be stored in ruby and Nd:glass, thus enabling the generation of intense pulses. Due to the large linewidth of Nd:glass, ultra-short pulses below 100 fs can be produced, whereas on 10 ps are achieved with Nd:YAG lasers.

9.3 Erbium, Holmium and Thulium Lasers

More than 100 emission lines have been experimentally demonstrated for erbium and holmium ions in various crystals and glasses. Erbium lasers emitting around 1.6 and 3 μm wavelength and holmium lasers operating around 2 μm are commercially produced.

Erbium Laser

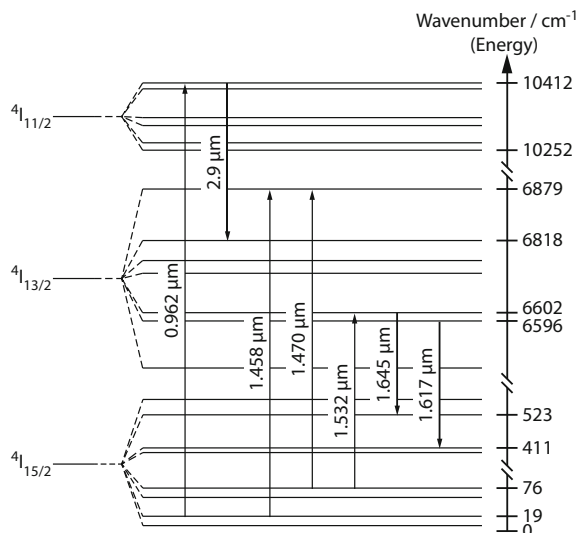
The erbium laser has emerged as an important laser source for various applications in the near-infrared spectral range. Depending on the addressed laser transitions, it provides emission wavelengths in the range from 2.7 to 2.9 μm or around 1.6 μm . Radiation at 2.9 μm is relevant for medical applications due to the strong absorption of water in this spectral region (absorption coefficient: $\approx 10^4 \text{ cm}^{-1}$)

which allows for precise ablation of tissue. Erbium lasers operating in the “eye-safe” spectral range at $1.6\text{ }\mu\text{m}$ have gained increasing attention in the last decade, as they are of particular interest in the fields of free-space communication, telemetry as well as light detection and ranging (lidar).

Crystalline Er lasers are based on YAG, YAP, YSGG or YLF hosts with high doping concentrations if emission around $2.9\text{ }\mu\text{m}$ is desired. For instance, 50% of the yttrium (Y^{3+}) ions are substituted for erbium (Er^{3+}) ions in Er:YAG crystals. On the contrary, fairly low concentrations from 0.5 to 2% are used for generating laser output at $1.6\text{ }\mu\text{m}$ wavelength. The term diagrams of the Er^{3+} -ions (Fig. 9.9) are similar for different host crystals and only slightly differ in the relative position of the energy levels.

Like in other solid-state lasers, erbium lasers are optically-pumped by lamps or diode lasers, e.g. at $0.96\text{ }\mu\text{m}$. The involved levels are split into several sub-levels due to the Stark effect, leading to bands of about 5 nm width that contribute to the excitation process. The diagram in Fig. 9.9 depicts the Stark splitting of the lowest three energy states. Since the $^4\text{I}_{13/2}$ -level has a longer lifetime (about 5.6 ms) than the $^4\text{I}_{11/2}$ -level (0.1 ms), the pump pulses have to feature fast rise times for laser operation at $2.9\text{ }\mu\text{m}$. The lower laser level has to be depleted between subsequent pulses which limits the repetition rate of the laser. The transfer and distribution of the pump energy to the various Er^{3+} -levels is a complex process. Apart from the simple spontaneous decay of the upper states, transfer processes among neighboring erbium ions occur. For instance, the energy released upon the depletion of the lower laser level of the $2.9\text{ }\mu\text{m}$ -transition ($^4\text{I}_{11/2}$) is used for the excitation of electrons from the $^4\text{I}_{13/2}$ - to the $^4\text{I}_{9/2}$ -level (up-conversion). Moreover, population of the upper laser level through $^4\text{I}_{9/2} \rightarrow ^4\text{I}_{11/2}$ transitions involves the participation of many phonons.

Fig. 9.9 Energy level diagram and pump and laser transitions of the Er:YAG laser

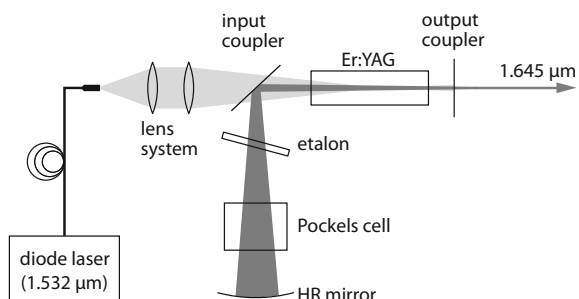


Pulsed erbium lasers emitting around $3\text{ }\mu\text{m}$ wavelength provide output energies from 10 to 100 mJ. Higher energies can be obtained with additional amplifier stages. As Er:YAG has only low gain, Er-doped YAP or YSGG is employed as amplifier medium ($g_0 \approx 0.15\text{ cm}^{-1}$), thus offering gain factors above 3 if 8 cm-long crystals are employed. Q-switching is realized by using electro-optic modulators or piezo-electric components that are based on frustrated total internal reflection (FTIR) (see Sect. 16.1).

The energy level diagram in Fig. 9.9 reveals that emission at 1.617 and $1.645\text{ }\mu\text{m}$ wavelength can be generated in Er^{3+} -ions under participation of different Stark sub-levels of the lowest energy states $^4\text{I}_{13/2}$ and $^4\text{I}_{15/2}$. Population of the upper laser levels is achieved by optical pumping around $1.5\text{ }\mu\text{m}$, more precisely 1.458 , 1470 and $1.532\text{ }\mu\text{m}$ wavelength. As the pump levels belong to the same manifold ($^4\text{I}_{13/2}$) as the upper laser level, the excitation process is referred to as resonant pumping. The small quantum defect of this (quasi-two-level) laser process results in high quantum efficiency and small heat dissipation into the gain medium. The realization of resonantly-pumped erbium lasers has been boosted by the development of high power InP-based laser diodes emitting in the range from 1.45 to $1.53\text{ }\mu\text{m}$. The experimental setup of a compact Q-switched diode-pumped Er:YAG laser emitting at $1.645\text{ }\mu\text{m}$ is shown in Fig. 9.10. The laser is pumped by a diode laser whose output spectrum is adapted to the narrow erbium absorption line at $1.532\text{ }\mu\text{m}$, so that about 96% of the pump radiation is absorbed. This leads to an overall efficiency of 25% and output pulse energy of 6 mJ. Much higher energies exceeding 100 mJ can be reached by means of additional diode-pumped amplifiers.

Pulsed laser output at 1.617 and $1.645\text{ }\mu\text{m}$ wavelength can be applied for carbon dioxide and methane detection over long distances, respectively. Hence, Er:YAG lasers represent a promising alternative to rather complex optical parametric oscillators and amplifiers that are currently used for airborne and satellite-borne lidar systems for measuring the concentration of atmospheric trace gases. Furthermore, lasers around $1.6\text{ }\mu\text{m}$ are applied for “eye-safe” laser ranging. Radiation at wavelengths longer than $1.4\text{ }\mu\text{m}$ is strongly absorbed in the eye’s cornea (penetration depth 0.1 mm) and therefore less hazardous compared to radiation that is focused onto the retina (factor 5×10^5) (see Sect. 24.4). Nevertheless, it should be noted that the quality “eye-safe” depends not only on the emission wavelength, but also on the laser power and beam divergence.

Fig. 9.10 Schematic of a resonantly diode-pumped and Q-switched Er:YAG laser emitting at $1.645\text{ }\mu\text{m}$



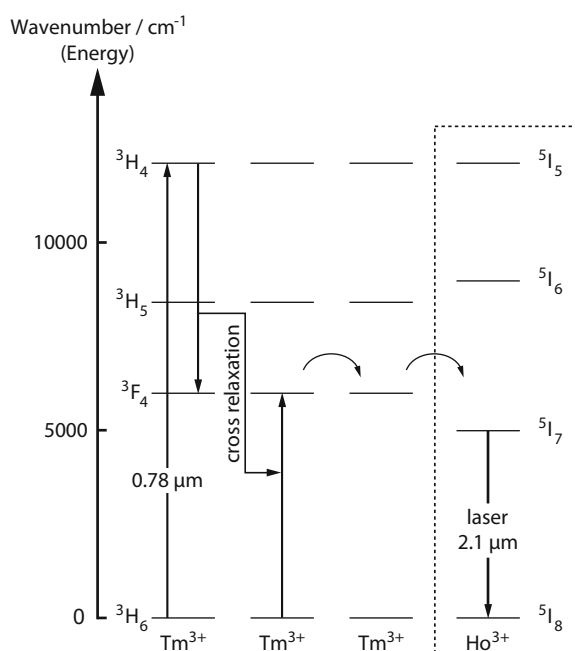
Erbium is also prominent as a dopant for glass fibers. Er-doped fibers are essential components in telecommunication where they serve as laser amplifiers at $1.55\text{ }\mu\text{m}$ wavelength. Here, optical pumping is performed using laser diodes at 0.98 or $1.470\text{ }\mu\text{m}$.

Holmium and Thulium Laser

Holmium lasers are important laser “eye-safe” sources emitting around $2\text{ }\mu\text{m}$. Main fields of applications include laser ranging, medicine, particularly urology, and to an increasing extent material processing. Holmium can be doped into the same host crystals as erbium. The most relevant emission line is at $2.1\text{ }\mu\text{m}$ corresponding to the $^5\text{I}_7 \rightarrow ^5\text{I}_8$ transition which ends at the ground state (Fig. 9.11). Consequently, the lamp-pumped holmium laser only operates in pulsed mode at room temperature, while cw mode operation requires diode pumping. Pulse energies up to 500 mJ can be obtained, e.g. in Q-switched mode.

Ho:YAG is a common laser material that can be pumped by flash lamps. Excitation of electrons to the higher ^5I -levels and subsequent relaxation leads to population of the upper laser level $^5\text{I}_7$ which has a lifetime of 8.5 ms . A more recent technology is the diode-pumped Tm,Ho:YAG laser. The addition of thulium ions enhances the overall efficiency, as the $^3\text{H}_4$ -level in Tm^{3+} is populated by absorption of the pump radiation at $0.78\text{ }\mu\text{m}$. The following Tm–Tm cross relaxation involves

Fig. 9.11 Energy level diagram of a diode-pumped Tm,Ho:YAG laser. The Tm^{3+} -ions are excited by optical pumping at $0.78\text{ }\mu\text{m}$ wavelength. One pump photon generates two excited Tm^{3+} -ions due to a cross relaxation process. The energy is then transferred to a Ho^{3+} -ion leading to population of the upper laser level



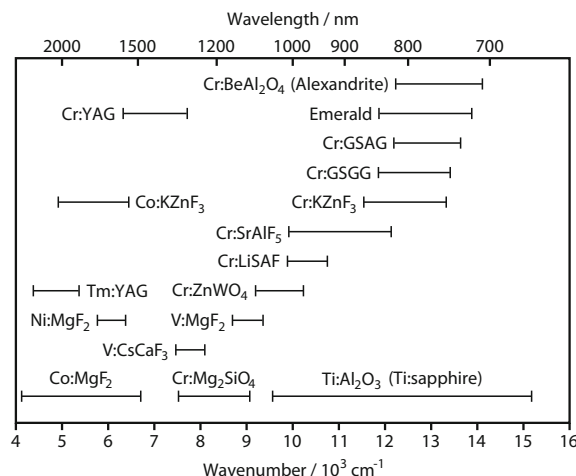
an energy transfer via further Tm^{3+} -ions to the Ho^{3+} -ions, so that the upper laser levels are additionally populated. Apart from that, laser operation in the thulium ions can occur through $^3H_4 \rightarrow ^3H_6$ transitions, yielding laser emission from 1.9 to 2.0 μm . These wavelengths are of interest for ablative surgery.

9.4 Tunable Solid-State Lasers

Broad wavelength tunability is accomplished in solid-state lasers based on titanium, vanadium, chromium, cobalt, nickel and thulium ions that are doped into various host crystals. The impact of the crystal field on these ions is stronger compared to neodymium, so that closely spaced electronic levels are split into many sub-levels. This situation is comparable to dye lasers where the electronic states are subdivided into vibrational levels. The emission spectra of such solids are therefore characterized by strongly (vibronically) broadened lines. Hence, like dye lasers, vibronic solid-state lasers offer the opportunity to continuously tune the output wavelength over a broad range of up to 30% of the central wavelength.

The tuning ranges of several vibronic solid-state lasers are depicted in Fig. 9.12, showing that these laser types cover the red and near-infrared spectral range. However, only a few of the listed materials can be pumped with flash lamps, while most of them require Nd:YAG, Kr^+ -ion or Ar^+ -ion lasers as pump sources. Furthermore, laser operation based on nickel, chromium and vanadium ions necessitates nitrogen temperatures, so that the commercial use of these systems is limited. In the following, the alexandrite laser and the titanium-sapphire laser will be discussed in more detail, as they represent the most important examples of vibronic solid-state lasers.

Fig. 9.12 Tuning ranges of various vibronic solid-state lasers (from Koechner (2006))



The alexandrite laser can be pumped with flash lamps which allows for simple configurations. Titanium-sapphire crystals are mostly pumped using other lasers, preferentially frequency-doubled Nd:YAG lasers at 532 nm, or recently by green diode lasers. This results in somewhat more complex laser setups, but very broad tuning ranges. For this reason, the titanium-sapphire laser has become more prevalent than the alexandrite laser.

Alexandrite Laser

Alexandrite is a variety of a chrysoberyl (BeAl_2O_4) crystal, that is doped with 0.14 wt% ($5 \times 10^{19} \text{ cm}^{-3}$) of chromium (Cr^{3+}) ions. The energy level diagram is similar to that of ruby (see Fig. 9.13) containing the same energy levels of the Cr^{3+} -ions. However, as the influence of the crystal lattice field is stronger in alexandrite, the energy levels, particularly the ground level, are considerably broadened and contain a number of vibrational levels. Like in the ruby laser, the vibronically broadened $^4\text{T}_2$ - and $^4\text{T}_1$ -states act as pump bands. Wavelength tunable operation of the alexandrite laser is based on transitions between the lowest level within the $^4\text{T}_2$ -band (lifetime $\approx 260 \mu\text{s}$) and different vibrational levels of the ground state band $^4\text{A}_2$, representing a four-level laser system. The width of the band determines the continuous tuning range of the vibronic alexandrite laser which spans the spectral region from 701 to 818 nm.

Apart from the vibronic transitions, the alexandrite laser can also lase on the $^2\text{E} \rightarrow ^4\text{A}_2$ transition yielding emission at 680 nm wavelength. Here, the energy

Fig. 9.13 Energy level diagrams and laser transitions of a ruby (left) and alexandrite (right) laser

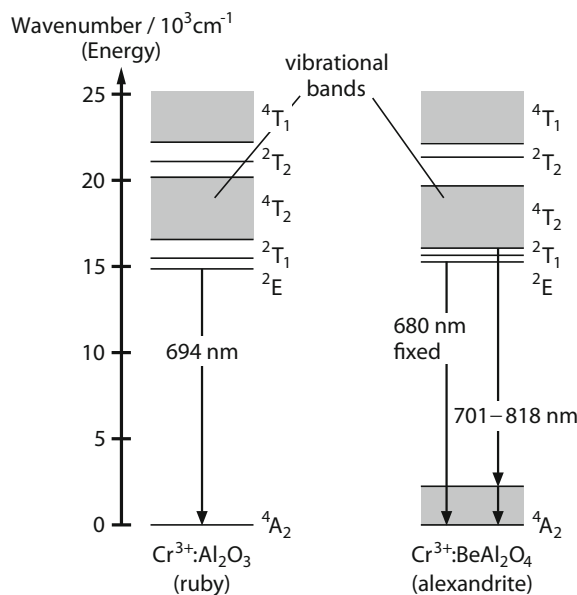


Table 9.5 Operation modes of the alexandrite laser ($\lambda = 755$ nm) and typical emission parameters

Operation mode	Pulse duration	Pulse energy	Pulse repetition rate	Average power
Continuous	—	—	—	≤ 60 W
Normal pulse	200–300 μ s	≤ 5 J	5–30 Hz	≤ 100 W
Q-switched	10–100 ns	≤ 1 J	10–100 Hz	≤ 20 W
Mode-locked	5–500 ps	≤ 1 mJ	10–100 Hz	—

transfer to the upper laser level (lifetime ≈ 1.54 ms) and the laser process are similar as in ruby. The combination of a three-level and a four-level laser in one material is an interesting feature of alexandrite that is also present in emerald Cr^{3+} $\text{Be}_3\text{Al}_2(\text{SiO}_3)_6$.

Alexandrite crystals can be pumped with flash lamps or continuous arc lamps. Their practical designs are comparable to other solid-state lasers. The gain and thus the pulse energy increases with temperature, while the gain peak shifts to longer wavelengths. This effect can be explained by the fact that the long-lived ${}^2\text{E}$ -level acts as energy storage which thermally populates the upper laser level within the ${}^4\text{T}_2$ band ($\Delta E \approx 800 \text{ cm}^{-1}$). Hence, as the temperature increases, the vibronic continua in ${}^4\text{T}_2$ are successively populated from ${}^2\text{E}$ in accordance with the Boltzmann distribution and the stimulated emission cross-section grows. However, raising the temperature also tends to populate the lower laser levels, so that most alexandrite lasers are operated around 100 °C.

Wavelength selection is realized by means of birefringent filters that are characterized by high damage threshold and allow for simple configurations and low losses. Typical output parameter of alexandrite lasers in different operation modes are summarized in Table 9.5.

The most important field of application for alexandrite lasers is dermatology, where such lasers are employed for tattoo and hair removal as well as for treating visible leg veins and pigmented lesions (Sect. 24.2). In the case of tattoo removal, the utilization of Q-switched alexandrite lasers was considered the standard of care. The laser treatment involves the selective destruction (photothermolysis) of black, blue and green ink particles ($\approx 0.1 \text{ } \mu\text{m}$) that are then absorbed by macrophages and eliminated. The shorter emission wavelength of alexandrite lasers, e.g. compared to Nd:YAG lasers, is also beneficial for removing fine hairs.

Titanium-Sapphire Laser

Since its first realization in 1982, the titanium-sapphire (TiSa) laser has been extensively studied and today represents the most widely used tunable solid-state laser. The great interest in this material is driven by its broad tuning range from

about 700–1050 nm which can be traced back to the lack of self-absorption from the upper laser level.

The gain medium is based on a sapphire (Al_2O_3) crystal in which Ti^{3+} -ions are substituted for Al^{3+} -ions at a typical doping concentration of 0.1 wt%. The Ti^{3+} -ion has one electron in the outer shell. Interaction of this electron in $3d^1$ -configuration with the cubic component of the crystal field leads to splitting into the 2E - and $^2T_{2g}$ -levels, as shown in the energy level diagram in Fig. 9.14. Further splitting is caused by the trigonal component of the crystal field as well as spin-orbit coupling, while the resulting sub-levels are not resolved due to broadening by lattice vibrations.

The absorption and fluorescence spectra are plotted in Fig. 9.15. The emission wavelengths range from 670 to 1100 nm with a maximum around 800 nm. Titanium-sapphire has a broad absorption band around 500 nm, which enables pumping with frequency-doubled Nd:YAG lasers at 532 nm wavelength at high efficiencies of 50%. The upper level lifetime is only 3 μs at 20 °C, so that flash lamp pumping is challenging. Nevertheless, the utilization of special lamps featuring short excitation flashes has been demonstrated to provide laser output powers exceeding 100 W at efficiencies of several percent.

Like pure sapphire, TiSa crystals feature very good mechanical stability and high thermal conductivity. When selecting a crystal, the so-called figure of merit (FOM) describing the crystal quality has to be considered. It is defined as the ratio between the absorption coefficients at 490 and 820 nm wavelength. Good crystals are characterized by FOM values ranging from 300 to 1000.

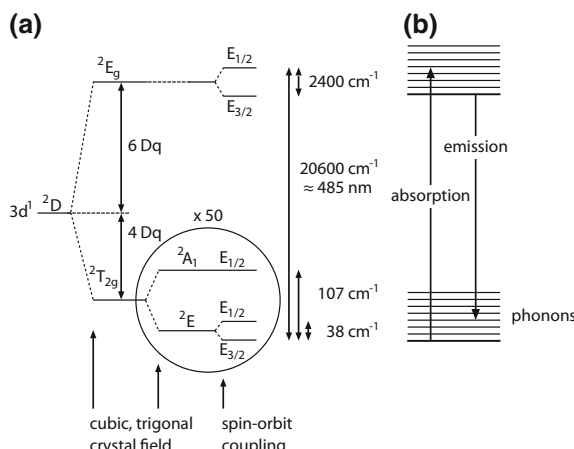


Fig. 9.14 **a** Energy level diagram of the Ti^{3+} -ion in sapphire (Al_2O_3). The levels arise from splitting of the $3d^1$ configuration due to the crystal field which is characterized by a strong cubic and a weak trigonal component. Further splitting results from spin-orbit coupling, while broadening of the involved laser levels is originated from lattice vibrations (phonons). (The parameter Dq is a measure of the strength of the crystal field). **b** Simplified energy level diagram of the titanium-sapphire laser

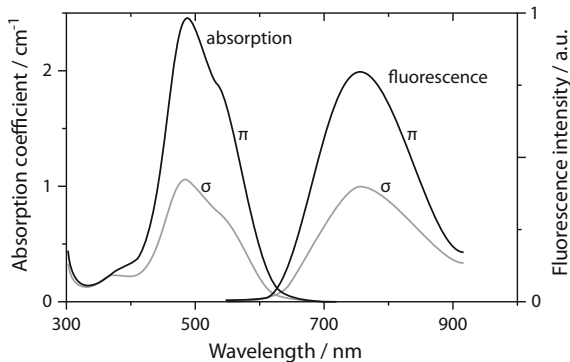


Fig. 9.15 Absorption and fluorescence spectrum of sapphire doped with Ti_2O_3 (0.1 wt%) for light polarized parallel (π) and perpendicular (σ) to the c -axis of the sapphire crystal (courtesy of A. Hoffstt, Institute of Optics and Atomic Physics of the TU Berlin and company Elight)

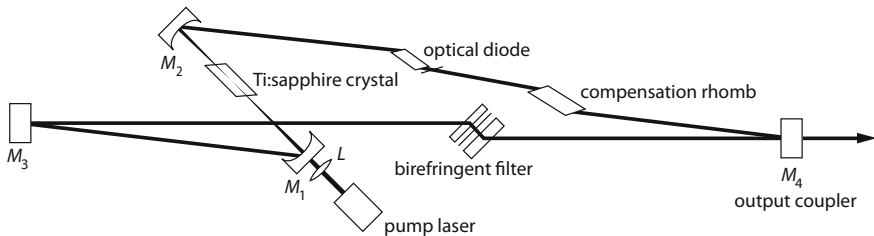


Fig. 9.16 Schematic of a commercial titanium-sapphire laser (Coherent, model 899-01). The beam of a frequency-doubled Nd:YAG pump laser at 532 nm wavelength is coupled into the folded resonator formed by mirrors M_1 , M_2 , M_3 , M_4 and focused into the TiSa crystal using lens L . Unidirectional propagation of the laser is realized by means of an optical diode inside the resonator, thus preventing a standing-wave pattern and, in turn, spatial hole burning. The laser wavelength can be continuously tuned from 700 to 1000 nm by a birefringent filter

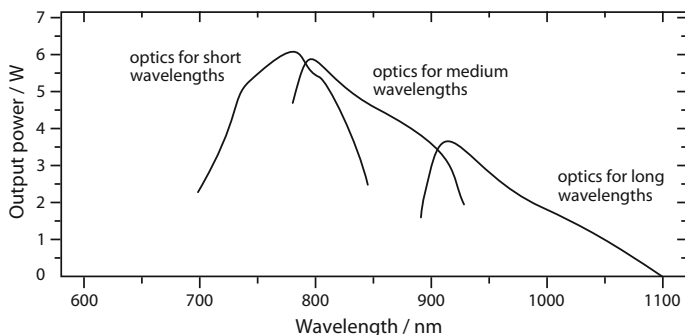


Fig. 9.17 Tuning ranges of a commercial titanium-sapphire laser (courtesy of Coherent)

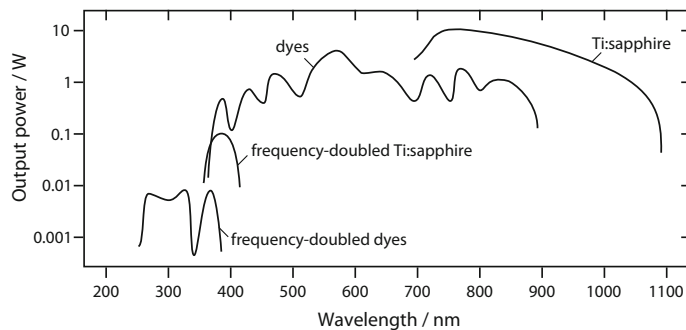


Fig. 9.18 Tuning ranges of continuous wave titanium-sapphire lasers compared to continuous wave dye lasers (courtesy of Coherent)

Since the TiSa laser offers a broader tuning range and higher output power than dye lasers (Chap. 8), it has replaced the formerly used dye lasers, especially those operating in the spectral region around 800 nm. Figure 9.16 depicts the design of a commercial TiSa laser, while typical tuning curves are shown in Figs. 9.17 and 9.18.

Ytterbium Lasers

Diode-pumped Yb-doped lasers have various advantages and differences compared to Nd-based lasers. The electronic level structure is simpler and the quantum efficiency and upper level lifetime are larger. Among the group of ytterbium lasers, the Yb:YAG laser is the most important one. Its energy level diagram is displayed in Fig. 9.19, depicting the four Stark levels of the $^2F_{7/2}$ -ground state and the three levels of the excited $^2F_{5/2}$ -level. Each level is further split into 11–23 sub-levels whose energy degeneracy is removed by the electric field in the crystal lattice.

The absorption bands at 940 and 968 nm are about five times broader than the 808 nm-line in Nd:YAG (Fig. 9.20). Lasing in Yb:YAG occurs over a broad range from 1025 to 1053 nm, while in a non-selective resonator, the line at 1030 nm is dominant. Another emission peak is observed around 1050 nm.

A drawback that is related to the small quantum defect of Yb-based lasers is the quasi-three-level nature of such systems. Hence, relatively high pump intensities are required which make it more difficult to fully exploit the potential of Yb:YAG laser for achieving high power efficiency. This behavior is especially pronounced if the laser operates at short emission wavelengths, as the terminal laser level is closer to the ground level (Fig. 9.19). Furthermore, in case of end-pumped configurations, the small difference between pump and laser wavelength necessitates the use of (dichroic) laser mirrors with steep transmission curves.

Fig. 9.19 Energy level diagram and laser transitions of the Yb:YAG laser. Diode pumping at 940 nm results in tunable laser operation from 1025 to 1053 nm

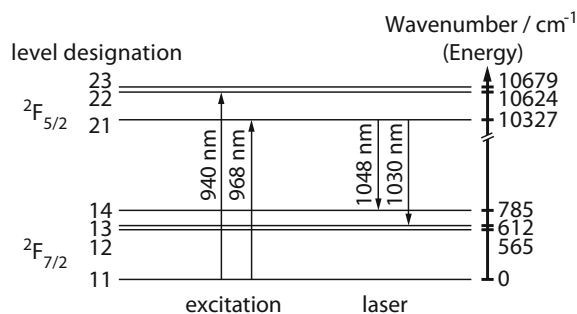
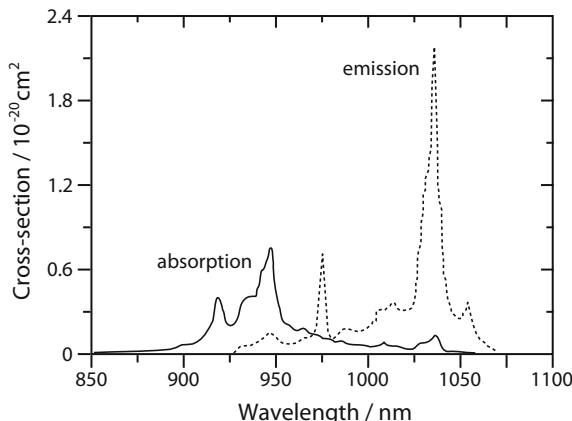


Fig. 9.20 Absorption and emission spectrum (cross-section) of Yb:YAG (15 at% doping) at room temperature



The Yb:YAG laser can be realized as disk lasers and operated both in continuous and pulsed mode. These systems can generate more than 1 kW of cw output power with high beam quality or even higher powers with non-diffraction-limited beam quality. Furthermore, Yb-doped glass is well-suited for building high-power (double-clad) fiber lasers and amplifiers, also delivering output powers in the kW-regime with very high efficiencies and diffraction-limited beam quality.

Yb is sometimes used as co-doping material in Er fiber lasers due to its higher absorption cross-section and the higher possible doping density in typical laser glasses, thus allowing much shorter pump absorption lengths and higher gain.

The existence of broadband optical transitions is a prerequisite for the generation of ultra-short pulses which is fulfilled by the TiSa laser. Hence, pulses shorter than 100 fs can be produced in commercial TiSa systems. While these lasers are pumped by frequency-doubled Nd:YAG lasers in the green spectral range, the strong absorption lines of Yb:YAG can be addressed by InGaAs pump laser diode systems that are available with powers of several tens of watts. This facilitates the development of ultra-short pulsed lasers. The highest output powers of femtosecond Yb:YAG lasers are obtained in passively-mode-locked (see Sect. 17.4) disk laser configurations. However, passive mode-locking involves instabilities that are

caused by the relatively small emission cross-section of Yb-based gain media. Comparably large cross-sections are found for tungstate crystals such as potassium gadolinium tungstate ($\text{KGd}(\text{WO}_4)_2$, or simply KGW). The energy level diagram and spectra of Yb:KGW are similar to Yb:YAG.

In commercial systems, the Yb:KGW crystal is usually pumped from multiple sides using laser diodes providing pump powers of tens of watts, while the pump light is delivered by glass fibers. The laser emits from about 1020 to 1060 nm with a maximum at 1048 nm. Passive mode-locking realized by a Bragg reflector results in the generation of 500 fs-pulses, while the repetition rate is around 80 MHz depending on the resonator lengths. A subset of the produced pulses can be amplified in a regenerative amplifier (also diode-pumped), yielding Watt-level average output powers at kHz repetition rates.

9.5 Diode Pumping and High-Power Operation

Diode laser pumping of solid gain media allows for compact and efficient laser sources with high beam quality. As this approach does not involve gas discharges for excitation, diode-pumped all-solid-state lasers are also characterized by high mechanical stability and long lifetime. Moreover, the pump radiation from diodes can be coupled into glass fibers which offers new possibilities in the design of laser systems. High output powers in the multi-kW-regime are obtained in disk and fiber lasers which provide a very effective heat management.

Diode Laser Pumping of Solid-State Lasers

The development of powerful pump diode lasers in the 1980s led to drastic advancement in the solid-state laser technology, as it brought major improvements in terms of efficiency, lifetime, size and other crucial laser properties.

In diode-pumped solid-state lasers (DPSSLs), the pump radiation from the laser diode (or array) is injected into the gain medium by means of lenses, where it is almost completely absorbed. In commercial devices, both longitudinal (Fig. 9.21) and transverse (Fig. 9.22) pumping schemes are used. In the longitudinal (or end-pumped) arrangement, the pump beam is focused into the laser material through one of the end-faces of the laser rod. Dual-side pumping with two diodes lasers can be realized in folded laser resonators. The spot diameter (typically 50–300 μm) is determined by the diameter of the fundamental transverse (TEM_{00}) mode of the laser resonator, as proper mode-matching is required for efficient longitudinal pumping. The laser mirror through which the pump radiation is coupled into the resonator is highly-reflective ($R \approx 100\%$) for the laser wavelength (e.g. 1064 nm), but transparent for the pump wavelength (e.g. 808 nm).

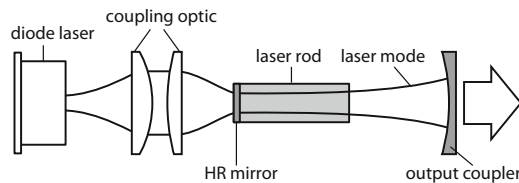
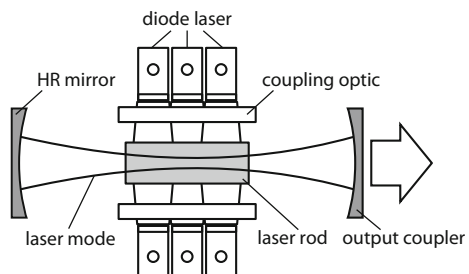


Fig. 9.21 Diode-pumped solid-state laser. In a longitudinally-pumped or end-pumped solid-state laser the pump radiation from a diode laser is coupled into the laser rod through one of the resonator mirrors. The excited volume is adapted to the volume of the fundamental transverse mode (TEM_{00}), which ensures good beam quality

Fig. 9.22 In a transversely-pumped or side-pumped solid-state laser the pump radiation from multiple diode lasers (bars or stacks) is coupled into the laser rod through its lateral surface



Typical diode-pumped Nd:YAG systems operating in the low-power regime employ diode arrays with powers of a few watts, providing pump efficiencies of 50%. The laser rod is about 1 cm long with a diameter of 0.5 mm. In very efficient devices, nearly every pump photon generates a laser photon. The overall efficiency of diode-pumped Nd:YAG systems is on the order of 10%. Since the heat deposition in the laser crystal is significantly reduced, such lasers provide very good beam quality. Continuous wave TEM_{00} mode operation with several watts of output power is possible. Moreover, the emission shows very high temporal stability, while lifetimes of 10,000 h and more are reached.

Higher laser powers are reached in transverse pumping configurations, as shown in Fig. 9.22. Further longitudinal and transverse arrangements are illustrated in Fig. 9.23. Nd:YVO₄ crystals are especially suited for diode pumping, as they feature very high absorption cross-section. In addition, much higher gain can be achieved compared to Nd:YAG. Diode-pumped neodymium lasers can also be operated in Q-switched and mode-locked mode. Apart from Nd-doped gain media, other laser crystals can be pumped with laser diodes as well. The energy level diagrams of several rare-earth ions and the respective pump and laser transitions are depicted in Fig. 9.24.

Tunable laser emission from 780 to 920 nm as well as the generation of mode-locked pulses down to 10 fs is achieved in Cr³⁺:LiSrAlF₆ (often denoted as Cr:LiSAF) crystals. Since diode pumping in the red spectral region is feasible for such lasers as opposed to green diode pumping of TiSa lasers, they can be much cheaper. However, the output powers are lower and the wavelength tuning range is smaller compared to TiSa systems.

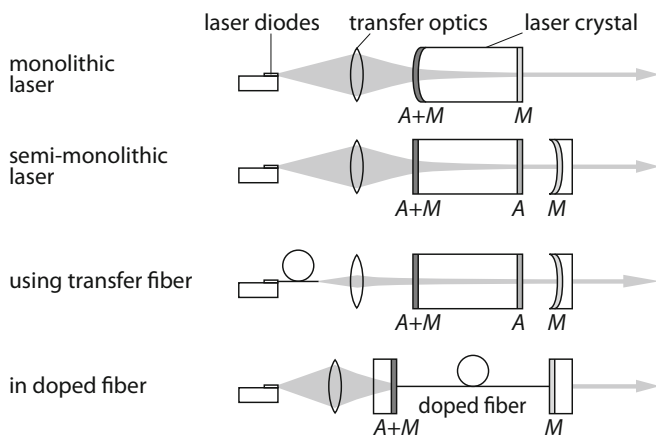
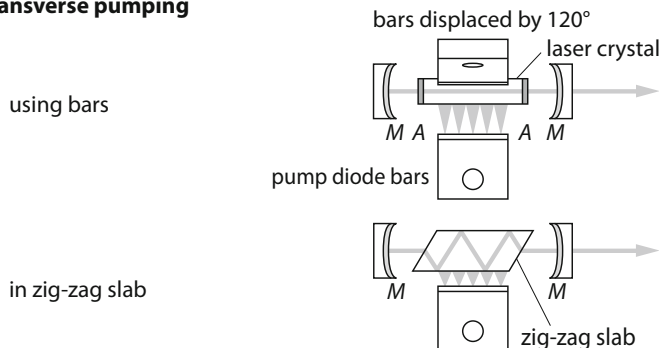
longitudinal pumping**transverse pumping**

Fig. 9.23 Longitudinal and transverse pumping schemes of diode-pumped solid-state lasers (A—anti-reflective coating at the pump wavelength, M—laser mirror)

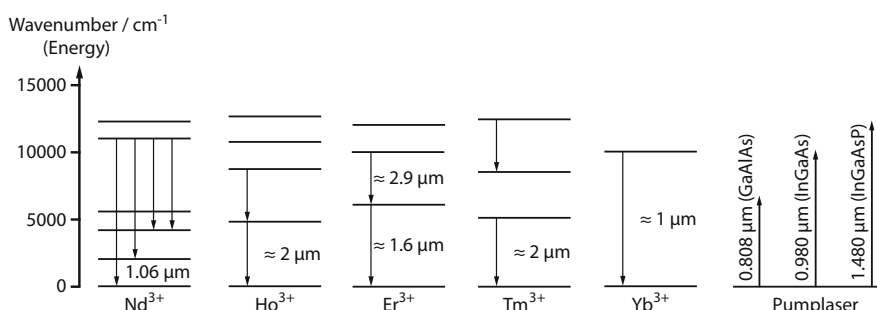


Fig. 9.24 Simplified energy level diagrams and laser transitions of the most important lasing rare-earth ions and pump wavelengths of suitable diode lasers (see also Figs. 9.4, 9.9, 9.11 and 9.19) (from Kaminskii (1996))

For realizing commercial systems emitting in the visible spectral range, frequency-doubling crystals are integrated into the laser resonator. In this way, continuous emission at green (532 nm for Nd:YAG) or blue wavelengths and in TEM₀₀ mode can be obtained at conversion efficiencies more than 50%.

Yb-doped YAG and YLF-crystals are of particular interest for high-power lasers. These gain media allow for much higher quantum efficiencies than Nd-doped materials, as outlined in the previous section. The development of diode-pumped solid-state lasers has marked a significant progress in laser technology which enabled the generation of visible and infrared radiation with high efficiency and good beam quality.

Disk Lasers

Disk lasers are based on a thin layer of a laser gain medium that is coated with a highly reflective mirror and attached to a heat sink, as shown in Fig. 9.25. The cross-sectional shape of the disk is often cylindrical with diameters of about 10 mm, while the thickness is considerably smaller than the laser beam diameter, e.g. 0.2 mm. The gain medium is pumped by diode lasers with the pump beam being incident on its free surface, resulting in a one-dimensional temperature gradient along the laser beam axis. In combination with the heat sink, this diminishes the thermal load in the material, which leads to a good beam quality even at very high output powers of several tens of kW.

Due to the short length of the active medium, the gain per round-trip and the pump light absorption are rather low. These problems are solved by using high doping concentrations and by realizing multiple passes of the pump radiation through the disk, respectively. Short-pulse generation with high pulse energies is complicated, since only little energy can be stored in the small gain volume. Nevertheless, picosecond disk lasers with 50–100 MHz repetition rate and average output powers of 200 W have been demonstrated.

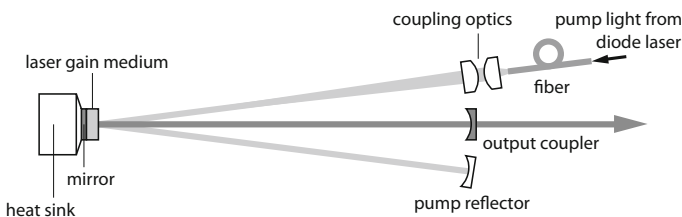


Fig. 9.25 Schematic of a disk laser. The laser crystal is a thin disk which is mounted on a heat sink while the pump radiation is incident on the free surface. Due to the low absorption of the gain material, the reflected pump light can be guided to the disk a second time via a retroreflector. Multiple reflectors can be employed to further enhance the absorption efficiency (multi-pass pumping)

Fiber Lasers

Laser glasses can be pulled into thin glass fibers that can be optically-pumped through one end-face, preferentially by laser diodes (Fig. 9.26). Such fiber lasers deliver diffraction-limited fundamental mode output if a single-mode fiber is used. The large ratio between surface area and active volume facilitates heat dissipation, so that additional cooling is not necessary.

Higher output powers are achieved with double-clad fibers, as shown in Fig. 9.27. The active core that determines the beam quality of the system is surrounded by an inner cladding (sometimes also referred to as pump core) in which the pump light propagates. The pump light is restricted to this region by an outer cladding with lower refractive index, and also partly leaks into the core, where it is absorbed by the laser-active ions. The cross-section of the inner cladding is usually not circular, but hexagonal or D-shaped (Fig. 9.28) in order to increase the overlap of the propagation modes of the inner cladding with the active core area. The cw output power of double-clad fiber lasers can reach several kilowatts in single-mode operation, i.e. $M^2 \approx 1$, and is primarily limited by nonlinear effects such as stimulated Raman scattering as well as by optical damage. High-power single-mode operation requires larger core diameters. This, in turn, demands smaller differences in refractive index between core and cladding. The resulting small numerical aperture causes increased bending losses. For more details see Sect. 13.4.

Further increase in the core diameter up to $100\text{ }\mu\text{m}$ while maintaining single-mode output is accomplished in photonic crystal fibers (PCFs) (Sect. 13.3). Here, the doped core is surrounded by air-filled capillaries that are periodically arranged over the cross-section, thus forming a cladding that confines the light in the core. Likewise, double-clad PCFs can be constructed with very high numerical aperture which additionally reduces the requirements concerning the brightness of the pump source. Yb-doped SiO_2 PCFs in MOPA arrangements produce pulsed output with energies of several mJ, multi-MW peak powers, average power of 50 W and nearly diffraction-limited beam quality.

Using multimode fibers with core diameters of several $100\text{ }\mu\text{m}$ or fibers bundles consisting of many combined single-mode fiber lasers (Fig. 9.29) enable laser powers up to 100 kW at the expense of reduced beam quality ($M^2 \gg 1$).

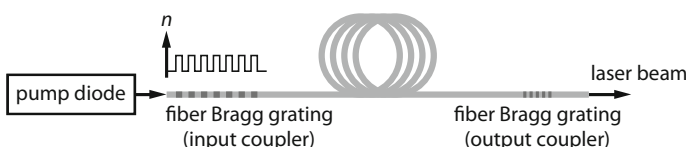


Fig. 9.26 Schematic of a linear fiber laser. The fiber ends contain fiber Bragg gratings that act as (multilayer) laser mirrors due to their periodic refractive index modulation. Typical fiber lengths are in the range of $1\text{--}10\text{ m}$

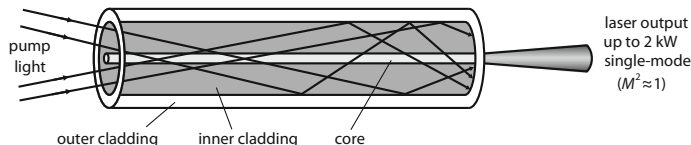


Fig. 9.27 Double-clad fiber laser: The laser radiation is guided in the (laser-active) single-mode core, while the pump radiation propagates in the surrounding multimode (inner) cladding. This allows high-power single-mode output at core diameters from about 10 to 40 μm . The pump light is absorbed over the entire fiber length

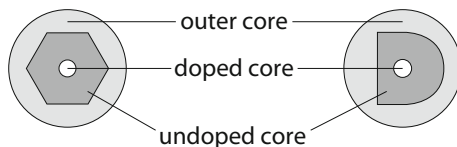
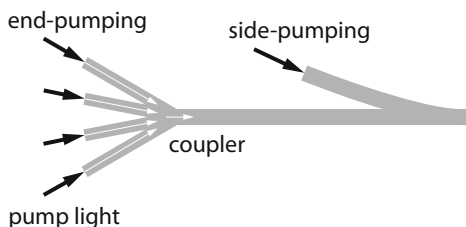


Fig. 9.28 Hexagonal or D-shaped pump cores prevent the pump radiation from remaining in the outer core, thus ensuring optimal absorption of the pump light in the doped core

Fig. 9.29 Pumping of a high-power fiber laser system can be accomplished by end- or side-pumping. The output of multiple pump laser diodes is combined by splicing fibers together in a coupler



Silica glass (SiO_2) is primarily used as fiber material which is transparent up to 2.3 μm and can be doped with various rare-earth ions:

- Neodymium: emission at 1064 nm
- Ytterbium: emission from 1030 to 1080 nm, higher doping compared to Nd is possible
- Erbium: emission from 1530 to 1620 nm (“eye-safe” spectral range), frequency-doubling to around 800 nm provides alternative to TiSa lasers co-doping with ytterbium leads to higher absorption efficiency
- Thulium: emission from 1750 to 2100 nm (“eye-safe” spectral range)
- Holmium: emission from 2050 to 2150 nm, often pumped with thulium lasers at 1950 nm or powerful diode lasers.

Another interesting fiber material is the heavy fluoride ZBLAN which is a family of glasses with the composition $\text{ZrF}_4\text{-BaF}_2\text{-LaF}_3\text{-AlF}_3\text{-NaF}$. ZBLAN glass is superior to silica in terms of infrared transmittance, as it features an optical transmission window extending from 0.3 μm up to 7 μm . However, it is more fragile and sensitive to acids. Moreover, the optical quality of the fibers is degraded by the

formation of crystallites during the fabrication process. The concentration of crystallites was shown to be reduced by growing ZBLAN in zero gravity which reduces convection processes. Hence, the aerospace company *Made In Space* started manufacturing ZBLAN in space for commercial purposes in 2017. Doping of ZBLAN with Tm, Ho, Ho/Pr, Dy and Er enables laser emission up to 4 μm .

Visible laser emission can be produced in fibers that are pumped by infrared lasers diodes via up-conversion processes. This involves the excitation of higher-energy levels through multi-stage absorption processes, so that laser emission at shorter wavelengths is generated. In this way, blue and ultraviolet light is produced in Tm- or Nd-doped ZBLAN fibers, respectively. Pumping of Tm at 1120 nm wavelength leads to blue laser emission at 482 nm wavelength with output powers of up to 100 mW. Such powers are, however, readily available with blue or green diode lasers (Sect. 10.8). Praseodymium-doped lasers (possibly with ytterbium co-doping) can directly produce red, orange, green or blue output.

Erbium-doped fibers are nowadays of great commercial importance, as they are employed as optical amplifiers (erbium-doped fiber amplifiers, EDFA), for 1.55 μm wavelength in the very large field of telecommunication. Thulium-doped fibers, pumped at 1.047 μm or 1.4 μm , serve as fiber amplifiers in the so-called S-band between 1.46 and 1.53 μm . Raman fiber amplifiers which are based on stimulated Raman scattering (see Sect. 19.5) represent a low-noise alternative. Mode-locked fiber lasers for generating ultra-short pulses are further discussed in Sect. 17.4. Such systems are available at average powers of 1 kW and are employed in micro material processing and nanotechnology as well as in eye surgery and dermatology.

Fiber lasers can be tailored to operate at any desired pulse duration from femtoseconds and picoseconds to continuous mode while providing high output powers. A further advantage over conventional laser designs is the fact that the laser beam is built and guided in the fiber where it is protected against environmental influences, resulting in stable laser emission. Consequently, fiber lasers are increasingly replacing other types of solid-state lasers. Nevertheless, conventional laser configurations are still important for achieving high pulse energies. Systems consisting of diode-seeded oscillators, preamplified by fiber amplifiers and further amplified by solid-state rod amplifiers, are evolving as the state-of-the-art in high-power pico- and femtosecond laser sources.

Further Reading

1. V. Ter-Mikirtychev, *Fundamentals of Fiber Lasers and Fiber Amplifiers* (Springer, 2014)
2. B. Denker, E. Shklovsky (eds.), *Handbook of Solid-State Lasers* (Woodhead Publishing, 2013)
3. R. Paschotta, *Encyclopedia of Laser Physics and Technology* (Wiley-VCH, 2008)
4. W Koechner, *Solid-State Laser Engineering* (Springer, 2006)
5. V.V. Antsiferov, G.I. Smirnov, *Physics of Solid State Lasers* (Cambridge International Science Publishing Ltd, 2005)
6. A.A. Kaminskii, *Crystalline Lasers* (CRS Press, 1996)
7. A.A. Kaminskii, *Laser Crystals* (Springer, 1990)

Chapter 10

Semiconductor Lasers



Shortly after the realization of the first optically-pumped (ruby) laser, electrically-pumped lasing in the semiconductor gallium arsenide (GaAs) was reported by Robert N. Hall and others in 1962 using a diode structure. Initially, the operation was restricted to pulsed mode at low temperatures. With the invention of the double heterostructure (Sect. 10.3), continuous wave lasing at room temperature was achieved in 1970. Today, semiconductor diode lasers are of great economic importance and fabricated in large quantities, as they find numerous applications. Among other applications, they are employed in consumer goods such as CD, DVD and Blu-ray players, as well as in personal computers, laptops and laser printers. Besides, diode laser technology has become essential in telecommunication systems over the last decades, especially with the growth of the internet. Increasing interest is also emerging towards direct-diode applications in material processing like soldering and welding which is driven by the progressing development of high-power diode lasers. Furthermore, novel technologies like 3D printing in industry, medicine and architecture as well as 3D sensing and automotive lighting are expected to further increase the demand for semiconductor lasers.

The most important characteristics of semiconductor lasers compared to other laser types are:

- small dimensions in the micrometer- to millimeter-range (Fig. 10.1), allowing compact integration of the laser in various devices;
- laser operation at small injection currents and voltages, e.g. 10 mA at 2 V for output powers around 10 mW, so that conventional power supplies and electrical circuits can be used;
- high-power output power up to several 100 W delivered by broad-area diode lasers (1 cm wide bars) pumped at high injection currents, kW output if multiple bars are stacked together;
- high efficiency up to 80%;
- possibility to directly modulate the laser output via the pump current at frequencies above 25 GHz, which is important for the transmission of high data rates in glass fibers;

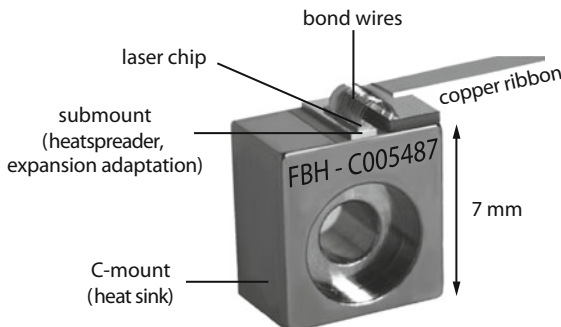


Fig. 10.1 Diode laser on a standard C-mount (courtesy of Ferdinand-Braun-Institut, Leibniz-Institut für Höchstfrequenztechnik (FBH Berlin))

- small beam diameters which facilitate direct coupling of the light into glass fibers, e.g. for optical communication purposes;
- easy integration with both electronic and optical components such as optical waveguides, thus enabling the design and manufacturing of complex opto-electronic circuits, e.g. based on polymers, glasses, InP layers, III-V compounds and silicon substrates;
- low-cost mass production in semiconductor fabrication processes.

One property of semiconductor lasers that is sometimes considered a disadvantage is the large beam divergence resulting from the small resonator cross-section. This issue can be readily solved by utilizing appropriate collimation optics (lenses) to produce nearly parallel beams. The frequency stability of simple diode lasers is rather poor. High frequency stability and narrow linewidth is achieved in more complex configurations, e.g. distributed feedback lasers (see Sect. 10.5). This yields large coherence lengths up to several tens of meters, so that such lasers can be employed for holography. However, the major application areas of frequency-stable diode lasers are information technology and metrology.

Diode lasers can be classified into the following four groups according to their material:

- Lasers based on III-V compounds such as GaAs, GaAlAs, InP, InGaAsP and GaSb emit in the yellow, red and near-infrared spectral range from 600 to 2200 nm. The lasers can operate in cw or pulsed mode at room temperature and are applied in optical communication, data storage on CDs and DVDs as well as in material processing.
- The second group is formed by InGaN diode lasers emitting in the green, blue and ultraviolet region. The last decade has seen a rapid advancement in the technology of these short-wavelength diode lasers which was primarily motivated by the development of the Blu-ray as storage devices as well as by the

growing interest in laser pico projectors and car head-up displays. Moreover, these sources are used in spectroscopic analytics. Kilowatt blue lasers are being developed for material processing.

- Lead-salt diode lasers emitting in the mid-infrared between 3 and 30 μm produce only powers of a few mW. They need to be operated at low temperatures $T < 200 \text{ K}$, particularly for continuous wave lasing and emission at longer wavelengths. Lead-salt lasers are mainly applied for spectroscopic measurements, e.g. for gas analysis.
- Quantum cascade lasers (QCLs) also generate infrared radiation beyond 100 μm and have thus largely replaced the lead-salt lasers. Efficiencies around 50% have been demonstrated, albeit only under cryogenic operation conditions. Important applications are THz generation and the spectroscopy of trace gas detection, e.g. for the detection of pollutants in the air.

The laser-active layers in semiconductor lasers are realized as

- homostructures,
- heterostructures or
- quantum wells and quantum dots.

These layers are, in turn, utilized for building various semiconductor laser types:

- edge-emitting lasers (laser propagates in the direction parallel to the wafer surface)
 - ridge waveguide lasers,
 - tapered amplifiers,
 - distributed feedback (DFB) lasers,
 - distributed Bragg reflector (DBR) lasers,
 - broad-area lasers,
 - one-dimensional laser arrays (bars),
 - two-dimensional laser arrays (stacks),
- surface-emitting lasers (laser propagates in the direction perpendicular to the wafer surface), also referred to as vertical cavity surface emitting lasers (VCSELs).

Apart from diode lasers with electron injection, there are semiconductor lasers that are excited by optical pumping or a beam of high-energy electrons. Optically-pumped semiconductor lasers (OPSLs) are of growing technical importance. Their design is similar to disk lasers (Sect. 9.5) and especially suited for intra-cavity frequency doubling and tripling, yielding output powers of several watts in the visible and ultraviolet spectral region.

Quantum cascade lasers are related to diode lasers in terms of their technology. However, population inversion is not realized in p-n diode structures between different electronic bands but between sub-bands resulting from a periodic series of thin semiconductor layers of varying material composition. QCLs are discussed in more detail in Sect. 10.7.

10.1 Light Amplification in p-n Diodes

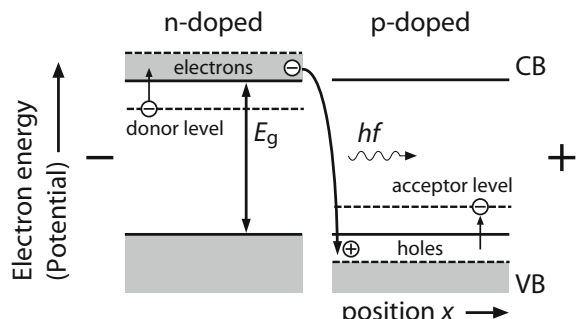
In contrast to the sharp energy levels in atoms and molecules, the electronic states in semiconductors are characterized by broad bands, as discussed in Sect. 1.6. As illustrated in Fig. 10.2, doping with donor and acceptor impurity atoms (typical concentration $>10^{18} \text{ cm}^{-3}$) creates electrons in the conduction band (CB) (n-type semiconductor) and positively charged holes in the material's valence band (VB) (p-type semiconductor), respectively. If two semiconducting regions with opposite doping type are connected, forming a p-n junction, and a voltage is applied (+ at the p-region, - at the n-region), the holes and electrons move towards the interface where they recombine. The released energy is emitted as photons (Fig. 10.2). In laser diodes, the photons are reflected from the end-facets of the semiconductor chip so that laser emission is built up which is partially transmitted by one end-face.

On closer inspection, it has to be considered that the bands are bent in the vicinity of the interface like in a rectifier diode (Fig. 10.3). The energy levels of the continuous bands are occupied with holes and electrons up to the (quasi-)Fermi levels F_c and F_v , respectively. In case of high doping concentrations, the Fermi levels are located inside the respective bands. Diffusion of holes into the n-region and electrons into the p-region at the p-n junction occurs until the space charge density and the resulting potential difference

$$V_D(E) \approx \frac{kT}{e} \ln\left(\frac{N_A N_D}{n_1^2}\right) \quad (10.1)$$

is large enough such that the Fermi levels F_c and F_v are equal. Here, N_A and N_D are the acceptor and donor density in the p- and n-region, respectively, while n_1 is the (relatively small) thermal electron density in the undoped semiconductor at the absolute temperature T . k denotes Boltzmann's constant and e is the elementary charge.

Fig. 10.2 Principle of a diode laser: Light emission is realized by transitions of electrons (grey shaded areas) from the conduction band (CB) to the valence band (VB)



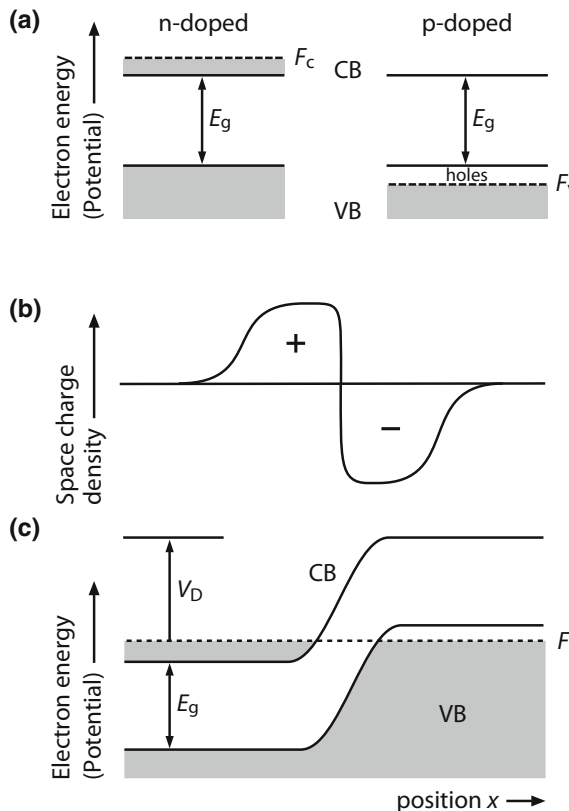


Fig. 10.3 Schematic of a (homostructure) diode laser as a p-n junction at high doping levels. **a** Energy bands of separated semiconductors with high n- (left) and p-type (right) (E_g - band gap energy, F_c , F_v - quasi-Fermi levels of the n- and p-type semiconductors, CB - conduction band, VB - valence band). **b** Connection of the n- and p-type semiconductors leads to diffusion of electrons into the p-region and diffusion of holes into the n-region, resulting in a space charge density and, in turn, an electric field which opposes the diffusion process. **c** Consequently, the electron energy is increased in the p-region by the potential difference V_D which limits the diffusion. A common Fermi energy F is established in the joint n- and p-type semiconductors

The spatial dependence of the space charge density ρ and the potential V , shown in Fig. 10.3b and c, follows from Poisson's equation with the vacuum permittivity ϵ_0 and the relative permittivity ϵ :

$$-\partial^2 V / \partial x^2 = \rho / \epsilon \epsilon_0. \quad (10.2)$$

Application of a forward voltage U leads to a reduction of the potential difference between the energy bands. Hence, electrons and holes are assisted in overcoming the potential barrier and flow into the p-region of the conduction band and into the n-region of the valence band, respectively. As a result, population inversion

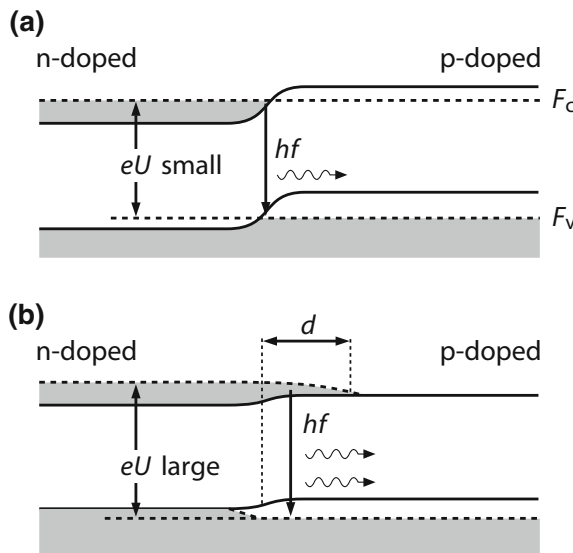


Fig. 10.4 Light emission (photons with energy hf) in diode lasers results from recombination of electrons and holes and can be achieved by applying a voltage across the p-n junction in the direction of easy current (forward-bias) which reduces the potential difference between the n- and p-region. At low voltages, only weak emission is observed (a), while strong recombination and intense radiation are obtained at higher voltages (b). The energy difference between the quasi-Fermi levels F_c and F_v is determined by the external voltage: $eU = F_c - F_v$

is established in a narrow zone, as shown in Fig. 10.4. As the mobility of the electrons is larger than that of holes, this zone mainly covers the p-region. The thickness d primarily depends on the diffusion constant D of the electrons in the p-region and the recombination time τ : $d = \sqrt{D \cdot \tau}$. For gallium arsenide (GaAs) with $D = 10 \text{ cm}^2/\text{s}$ and $\tau \approx 10^{-9} \text{ s}$, the thickness is $d \approx 1 \mu\text{m}$. Radiative recombination occurring in the so-called active zone forms the basis for laser operation in semiconductors. In heterostructures and quantum wells, the light-emitting zone is significantly smaller.

10.2 GaAlAs and InGaAsP Lasers

Gallium aluminum arsenide (GaAlAs), indium gallium arsenide phosphide (InGaAsP) and gallium indium nitride (GaInP) are the most widely used semiconductor laser materials. The elements Al, Ga and In belong to the third group of periodic table, while P and As belong to the fifth group. Therefore, compounds containing these elements are referred to as III-V semiconductors, as opposed to II-VI semiconductors such as CdS and ZnSe.

The emission wavelengths of laser diodes are determined by the band gap energy of the semiconductor in which the recombination of electrons and holes occurs. In binary semiconductors consisting of only two components the band gap is fixed, e.g. 1.43 eV in GaAs corresponding to 868 nm wavelength. In contrast, the band gap energy and thus the emission wavelength can be controlled by the mixing ratio in semiconductors composed of three or four components, as depicted in Fig. 10.5. Variation of the Ga and Al content in GaAlAs, indicated by the dashed line, results in a change in the band gap energy from 1.43 eV (GaAs) to 1.92 eV (AlAs), i.e. 868–646 nm. A larger spectral range from 564 to 3545 nm is covered by InGaAsP.

Laser diodes are almost always made of direct band gap materials (see Sect. 1.6), as indirect transitions involve the participation of phonons which reduces the recombination rate of carriers and hence inhibit the laser process. Indirect semiconductors are therefore not suitable as diode lasers and marked by jagged lines in Fig. 10.5. A further limitation arises from the different lattice constants of the used semiconductors which restricts the possibilities of combinations and the mixing ratios of the compound crystal. For this reason, $\text{Ga}_{1-x}\text{Al}_x\text{As}$ can be best grown on GaAs substrates, whereas $\text{In}_{1-x}\text{Ga}_x\text{As}_y\text{P}_{1-y}$ is preferentially grown on InP with $0 \leq x \leq 1$ and $y \approx 2.2x$. InGaAsP lasers can be produced for emission wavelengths ranging from 1000 to 1700 nm. Shorter wavelengths down to 650 nm, i.e. in the red spectral region, can be reached with InGaAsP on InGaP. Yellow diode lasers emitting around 570 nm are based on AlGaInP.

GaAlAs lasers suffer from oxidation of the aluminum which leads to optical damage of the end-faces by absorption of the laser light. This can be avoided by

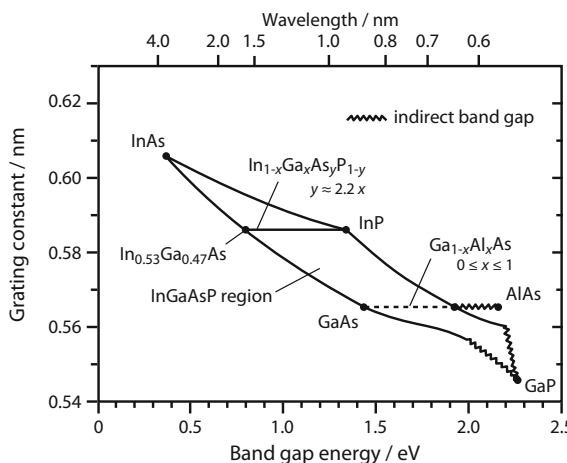


Fig. 10.5 Band gap energies, wavelengths and grating constants of GaAlAs and InGaAsP as a function of the atomic composition. For InGaAsP the values x and y which denote the atomic fractions span a parameter space indicated by area which is enclosed between the four semiconductors InAs, InP, GaP and GaAs. For GaAlAs the parameters for different values of x lie on the dashed line. Semiconductors having an indirect band gap (jagged line) are not suitable as diode lasers

using aluminum-free InGaAsP. During the fabrication process the laser wavelength can be controlled with an uncertainty of a few nanometers. For optical communication applications, wavelengths in the range from 1300 to 1600 nm are particularly suited, as optical fibers show minimal damping and dispersion in this spectral region. Consequently, InGaAsP lasers are mainly employed in this field (see Sect. 10.9). GaAlAs lasers emitting around 780 nm are produced in large quantities for optical scanning of data storage media, e.g. CDs.

10.3 Design of Diode Lasers

The schematic design of a diode laser is shown in Fig. 10.6. The resonator is formed by two plane-parallel end-faces of the semiconductor crystal, which can be produced simply by cleaving the crystal along a certain crystallographic plane and subsequent polishing. In Fabry-Pérot laser diodes (as opposed to DFB laser diodes), the end-faces of the structure are highly or partially reflecting the laser emission. Given the refractive index of GaAs of $n \approx 3.6$, the reflectance is calculated to $R = [(n - n')/(n + n')]^2 = 0.32$ for $n' = 1$ (air). Hence, additional coating of the end-faces for increasing the reflectance is usually not necessary, especially as the gain in diode lasers is very high. The other faces of the crystals are kept unpolished in order to prevent parasitic lasing or oscillations between them. Owing to diffraction at the narrow emission cross-section of the diode structure, the divergence angle of the emission in the plane perpendicular to the active zone (fast axis) is about 30°. The angle is smaller in the other direction (slow axis), as the width of the active zone (tens to hundreds of μm) is larger than its thickness d .

In homostructure diode lasers (Fig. 10.6) the p- and n-type semiconductor layers are made from the same material compound which is doped differently in the two regions. Index guiding of the laser beam is thus absent resulting in high losses, as the optical mode is not confined in the active layer but spreads into the lossy regions. Hence, the threshold current densities for laser operation are very high (about 100 kA/cm^2 at room temperature), so that cw operation is not possible.

Fig. 10.6 Schematic of a simple diode laser with homostructure

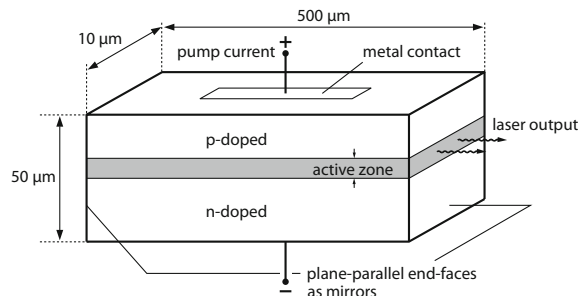
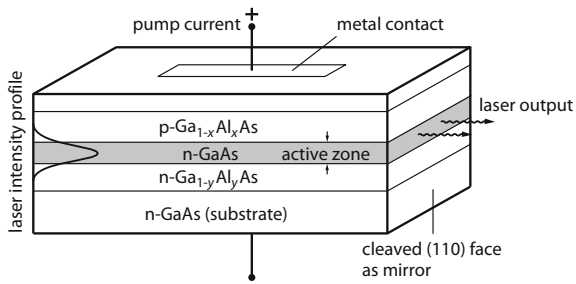


Fig. 10.7 Schematic of a double heterostructure laser. The active zone can also contain quantum wells (see Fig. 10.24)



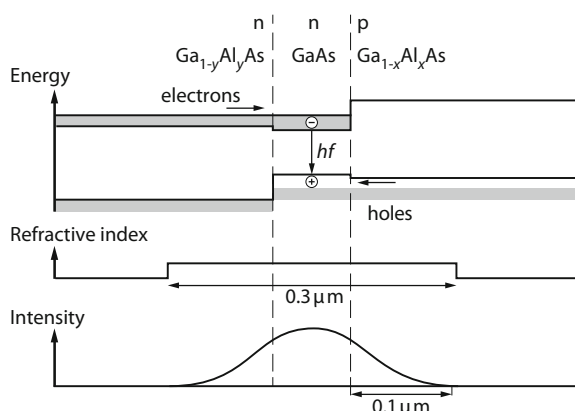
Double Heterostructure

A significant reduction of the threshold current densities and threshold currents is obtained in double heterostructure lasers. Here, the active layer is sandwiched between two (cladding) layers having a larger band gap. For instance, the active layer (GaAs) with a thickness of 0.1–0.5 μm is surrounded by n-doped and p-doped GaAlAs, as illustrated in Fig. 10.7. Injected electrons and holes move from the n- and p-region into the active GaAs zone where population inversion is created.

The resulting band structure is shown in Fig. 10.8. Due to the larger band gap of GaAlAs, the carriers are confined in the narrow active zone, as potential barriers prevent diffusion out of this region. Since the band gap energy is related to the refractive index of the material, a double heterostructure also provides a step in refractive index between the active layer and the adjacent cladding layers. Using the aforementioned example, the refractive index of GaAlAs is 5% smaller than that of GaAs. The refractive index profile acts as an optical waveguide (see Sect. 13.2), confining the optical mode closer to the active layer (Fig. 10.8).

The simultaneous carrier and photon confinement in the active zone greatly reduces the internal losses and, in turn, the threshold current densities from 100 to 1 kA/cm² which enables continuous operation at room temperature. The development of heterostructures for tailoring the band structure and the optical properties of

Fig. 10.8 Energy band structure of electrons and holes in a double heterostructure diode laser (top), spatial distribution of the refractive index (middle) and the light intensity (bottom)



layered semiconductor structures was a seminal advance in the field of high-speed- and opto-electronics. The two scientists Zhores I. Alferov and Herbert Kroemer who have enormously contributed to this achievement were awarded the Nobel Prize in Physics in 2000.

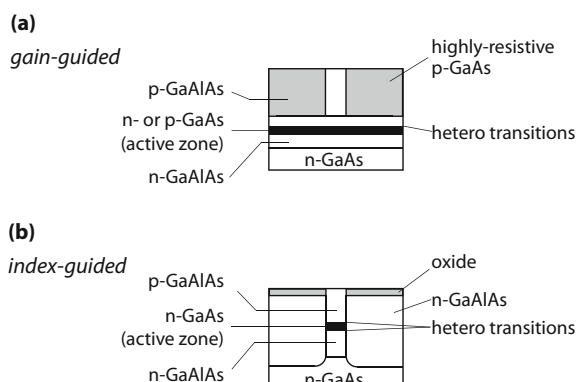
Single- and Multi-transverse Mode Operation

Further minimization of the required pump currents and improvement of the beam quality is achieved by lateral guiding of both the current and the radiation in the active layer. Adequate reduction of the width of the active layer ensures oscillation of the fundamental transverse mode only which increases the emission stability.

Narrowing of the active zone can be realized by restricting the current injection to a narrow region beneath a stripe contact while the adjacent regions are highly-resistive (Fig. 10.9a). Hence, lasing only occurs in a limited region of the active layer. These structures are called *gain-guided* diode lasers, as the optical intensity distribution in the lateral direction is determined by the gain profile produced by the carrier density distribution. The drawback of such lasers based on the strip geometry is that neither the current nor the radiation can be exactly confined in the active zone.

A more precise confinement is obtained in *index-guided* lasers, as is depicted in Fig. 10.9b. Here, the active zone is surrounded by materials with lower refractive indices in both the vertical and lateral transverse directions. It is thus buried in lower refractive indices layers which form a rectangular waveguide that confines the optical mode and determines the lasing characteristics. Such buried heterostructure configurations produce single transverse mode beams with high beam quality (Fig. 10.10), thus facilitating fiber coupling. Another important feature is the confinement of the injected carriers to the active region which leads to threshold currents as low as 10 mA at room temperature. However, the output power of these lasers is usually limited to only a few hundred milliwatts.

Fig. 10.9 Layer structure of
a gain-guided and
b index-guided diode lasers.
Fundamental transverse mode
output can be accomplished
by downscaling of the active
zone (black filled area)



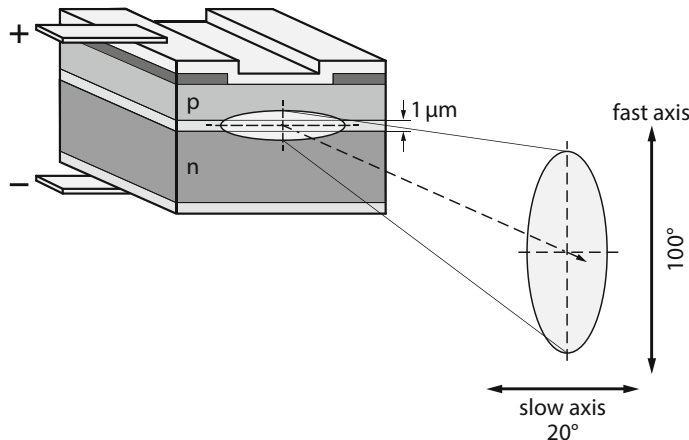


Fig. 10.10 Diode laser with single transverse mode output and elliptic beam profile

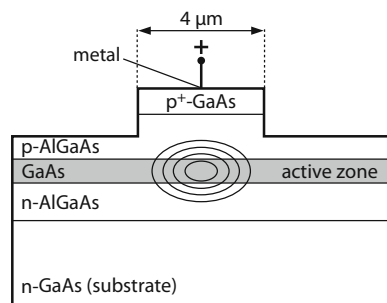
Ridge Waveguide Laser

Lateral guiding of the laser beam in the active region is also possible by a ridge-like structure, as shown in Fig. 10.11. The ridge having a width of a few μm acts as a waveguide, while the effective refractive index depends on the material thickness. Ridge waveguide lasers allow for fundamental transverse mode output at relatively large active layer cross-sections and thus high output powers of up to 1 W.

Horizontal-Cavity Surface-Emitting Laser (HCSEL)

An edge-emitting laser can be modified to a surface-emitting laser by building a structure according to Fig. 10.12. In a horizontal-cavity surface-emitting laser (HCSEL) the active layer is etched under an angle of 45°, so that the laser beam is

Fig. 10.11 Schematic cross-section through a ridge waveguide laser



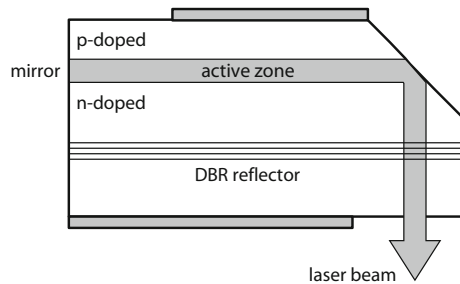


Fig. 10.12 Schematic of a horizontal-cavity surface-emitting laser (HCSEL) with a distributed Bragg reflector (DBR)

reflected by total internal reflection, resulting in vertical emission. The resonator is formed by a mirror on the left edge of the diode laser and a distributed Bragg reflector (see Sect. 10.5) that is oriented parallel to the active layer. This approach makes it possible to combine some of the advantages of edge-emitting and surface-emitting lasers such as improved cooling and easier assembly.

Tapered Amplifiers

Simultaneous realization of high output power and good beam quality is accomplished by master oscillator power amplifier (MOPA) systems (Fig. 10.13). A low-power diode laser operating in fundamental transverse mode is amplified in a tapered diode laser. The end-faces of the latter are anti-reflection coated in order to avoid lasing in this part of the structure. In this way, output powers of several watts are achieved. Tapered lasers combine the beam quality of a ridge waveguide laser with the high power known from broad-area lasers which will be outlined in the next section.

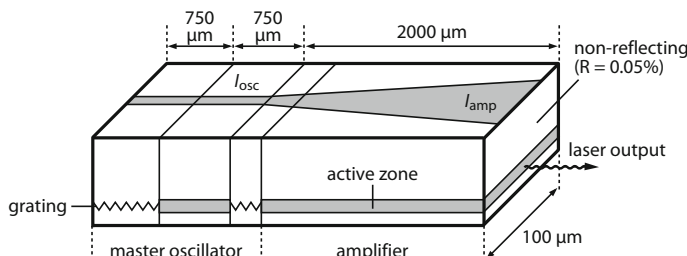


Fig. 10.13 Schematic of a diode laser master oscillator power amplifier (MOPA) configuration consisting of an DBR laser oscillator and a tapered amplifier (DBR: distributed Bragg reflector, I_{osc} : oscillator current, I_{amp} : amplifier current) (courtesy of Peuser, Daimler-Benz, Ottobrunn)

Broad-Area Diode Lasers, Laser Bars and Stacks for High Output Powers

Higher output powers of several tens of watts are also obtained with broad-area lasers (or broad-stripe lasers) where the emitting region at the front facet has the shape of a broad stripe with a width of up to 200 μm (Fig. 10.14). Due to the strong asymmetry of the edge emitter, the beam characteristics are completely different in the two emission directions. Whereas diffraction-limited beam quality and full angle divergence angles around 50° can be achieved in the vertical direction (fast axis), the light is distributed over many spatial modes in the slow axis direction and the beam profile may be multi-peaked in the horizontal direction. The achievable power increases with the width of the stripe, yet the slow axis beam quality in the direction becomes worse.

Combination of multiple broad-area emitters in a single device leads to a diode bar which can produce hundreds of watts or even 1 kW of optical power. The advantages and disadvantages of diode laser bars compared to single or multiple emitters are summarized in Table 10.1. Despite the higher output power, a diode bar has a lower brightness than a single emitter laser, as the beam quality is much lower.

Broad-area lasers and laser bars are often used for pumping of solid-state lasers, especially Nd lasers. Due to the better beam quality of single emitters, the design of a diode-pumped laser is generally simpler when using broad-area diodes. Moreover,

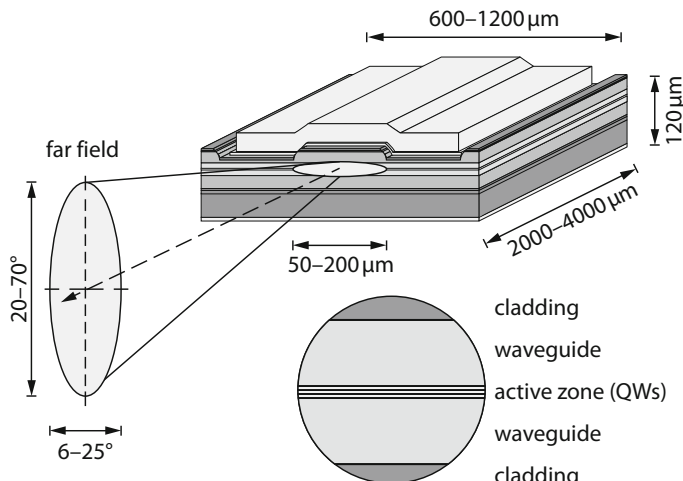


Fig. 10.14 Broad-area diode laser with far field beam profile and schematic of the layer structure (QWs: quantum wells). Due to the large width of the active zone, the beam divergence is smaller than in Fig. 10.10 (courtesy of Ferdinand-Braun-Institut, Leibniz-Institut für Höchstfrequenztechnik (FBH))

Table 10.1 Comparison of laser bars, single emitters and the combination of multiple emitters ($\uparrow \triangleq$ advantage, $\Rightarrow \triangleq$ neutral, definition of brightness see Sect. 11.5)

Parameter	Laser bar	Single emitters	Multiple emitters
Power	$\uparrow\uparrow$	\Rightarrow	\uparrow
Brightness	\Rightarrow	\uparrow	\uparrow
Efficiency	\Rightarrow	$\uparrow\uparrow$	\Rightarrow
Costs (module)	\Rightarrow	\uparrow	\Rightarrow
Costs (setup)	\uparrow	\Rightarrow	\uparrow

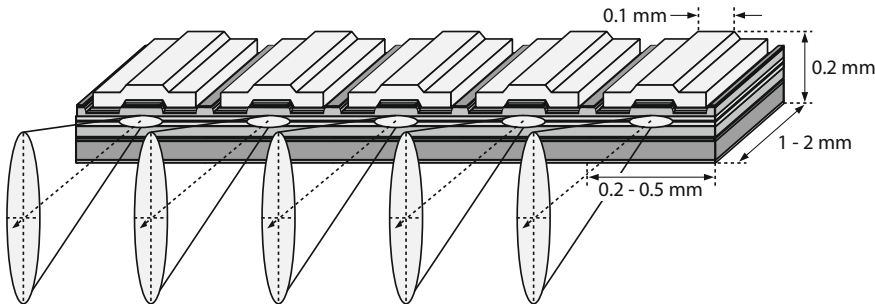


Fig. 10.15 Diode laser array consisting of multiple parallel arranged broad-area lasers (courtesy of Ferdinand-Braun-Institut, Leibniz-Institut für Höchstfrequenztechnik (FBH))

as opposed to laser bars, broad-area diode lasers can usually be switched on and off very often without shortening the lifetime.

The width of laser bars can reach a few centimeters, while the resonator length of the single broad-area lasers is typically 1–2 mm (Fig. 10.15). The distance between the emitters (pitch) is 0.2–0.5 mm. Such laser arrays can consist of up to 100 broad-area lasers with typical fill factors of 40% in continuous wave mode and 90% in pulsed mode, producing cw output powers exceeding 200 W.

Further power scaling is accomplished by combining several laser bars to a stack which provides cw output powers on the order of a few kW (Figs. 10.16 and 10.17). Although the beam quality is low, such devices can be employed for material processing, e.g. for welding applications with weld widths in the mm-range or hardening. High pulse peak powers are obtained in epitaxially grown stacks.

Another approach for reaching high cw output powers is the combination of multiple broad-area diode lasers by means of step mirrors. As shown in Fig. 10.18, several single emitters are stacked in a staircase arrangement. Each emitter has an individual fast axis collimation lens which is individually aligned. The diode emission is then optically stacked via a slow axis collimator consisting of a monolithic copper block with curved facets forming all laser beams. As a result, multiple stripes are emitted and aligned on top of each other. In a next step, the output radiation from multiple such modules can be combined by polarization or dense wavelength multiplexing (Fig. 10.19), boosting the output power to the kW-regime.

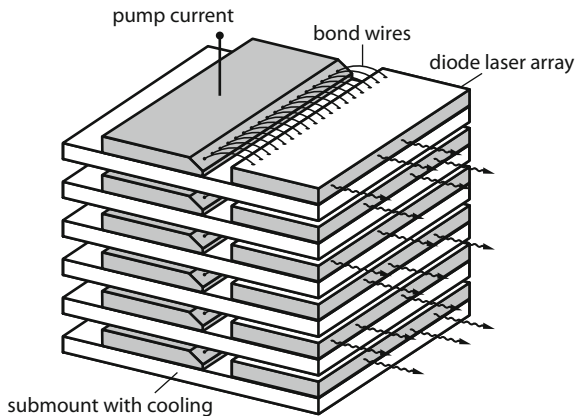


Fig. 10.16 Stack of diode laser arrays (courtesy of Peuser, Daimler-Benz, Ottobrunn)

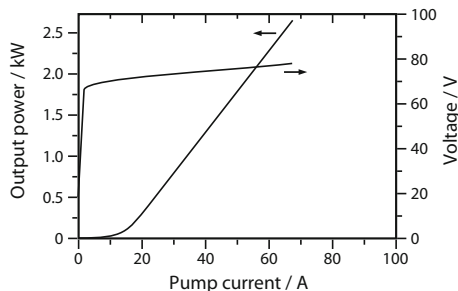


Fig. 10.17 Output power and voltage of a high-power diode laser stack depending on pump current (light-current-voltage or L-I-V curve). Power scaling up to 10 kW can be obtained

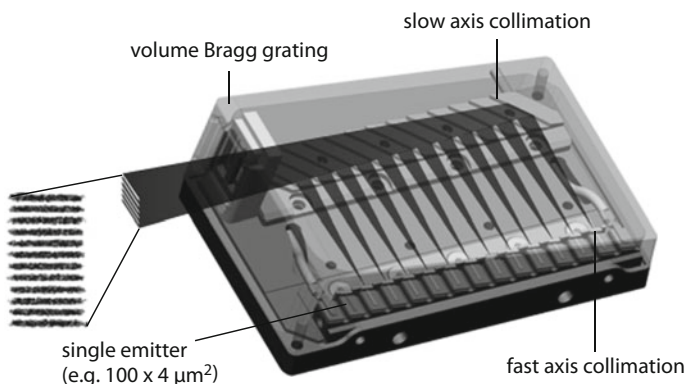


Fig. 10.18 Optical stacking of collimated laser beams from 12 laser emitters (courtesy of DirectPhotonics Industries, Berlin, 2015)

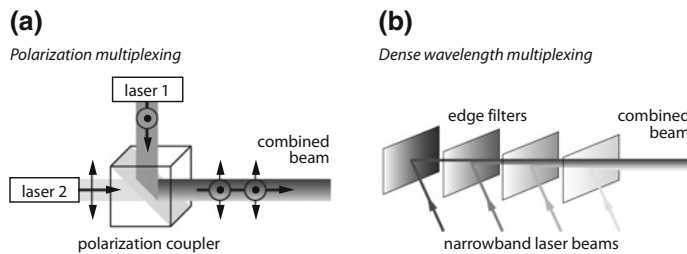


Fig. 10.19 **a** Polarization multiplexing and **b** dense wavelength multiplexing for beam combining of multiple diode lasers in order to increase the output power

Heat Management in High-Power Diode Lasers

A major challenge in the design and operation of high-power diode lasers is the dissipation of the heat that is generated in the semiconductor structure, because the electrical energy is not completely transformed into laser emission energy. The electrical-to-optical (or wall-plug) efficiency is on the order of 50%, while values around 80% are targeted.

The light-emitting semiconductor generally consists of multiple layers with a total thickness of several μm . The layers are applied on a substrate that is considerably thicker, e.g. 50 μm . For achieving good heat dissipation, the metallized side of the laser is soldered onto a metallic heat sink, e.g. a copper block, using an adequate solder material (indium or gold alloy). The heat sink has a much larger cross-sectional area compared to the laser structure, leading to a spreading of the heat flow and thus more efficient heat transfer to the environment. The latter can be improved by water cooling of the copper block through microchannels. Peltier elements are employed for heat removal as well. Heat spreading can be supported by burying a diamond layer between the laser structure and the copper heat sink. Diamond is characterized by an exceptionally high thermal conductivity and therefore rapidly increases the cross-section through which the heat flows. Semiconductor lasers can also be cooled from two sides. For this purpose, the substrate is removed. Following this approach, the company Jenoptik Laser GmbH has developed a single laser bar which provides 500 W of output power.

Reduction of the heat generation at high power levels is accomplished by operating the laser diodes in pulsed or quasi-continuous wave (qcw) mode. The ratio between pulse duration and pulse repetition interval is called duty cycle (on-off ratio) and is usually in the range from 1 to 20% at pulse durations from ns to ms. The average heat generation is thus minimized. During the pulse, the temperature does not reach the steady-state value that corresponds to the peak power. Operation in qcw mode thus allows for higher pump currents than achievable in cw mode. Consequently, pulse peak powers exceeding the maximum cw output power by a factor of 2 are obtained. However, this is only possible for pulses shorter 1 ms, as steady-state conditions like in cw mode are established at longer pulse durations.

Beam Shaping and Fiber Coupling

As explained in the previous sections, the small cross-sectional area of the active layer, the emission of diode lasers is usually characterized by a large divergence angle. In the idealized case of a diffraction-limited Gaussian beam, the half-angle divergence θ_0 in the far-field is simply given by the beam waist radius w_0 and the emission wavelength (see also Sect. 11.2):

$$\theta_0 = \frac{\lambda}{\pi w_0}. \quad (10.3)$$

For real laser beams, the divergence angle has to be multiplied by the so-called beam quality factor M^2 which represents a measure of the beam quality of a laser beam. While this factor is $M^2 = 1$ for lasers operating in fundamental transverse mode, it is $M_x^2 \approx 1$ and $M_y^2 \approx 10 \dots 100$ for the fast axis and slow axis, respectively (Fig. 10.20).

Collimation and focusing and fiber coupling of diode laser beams therefore requires beam shaping. The easiest way is to use spherical lenses (Fig. 10.21) or cylindrical lenses (Fig. 10.28). If the laser facet is located in the focal plane of the lens, the laser beam can be collimated in analogy to ray optics. In order to focus the laser beam, the laser facet has to be placed outside twice the focal length, to create a small image of the beam waist. The degree of focusing is determined by the numerical aperture of the used lens $NA = D/2f$, with D being the beam diameter at the

Fig. 10.20 Beam divergence of a diffraction-limited Gaussian beam ($M^2 = 1$) and a non-diffraction-limited beam ($M^2 > 1$)

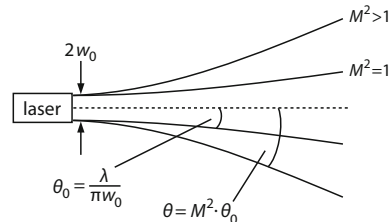
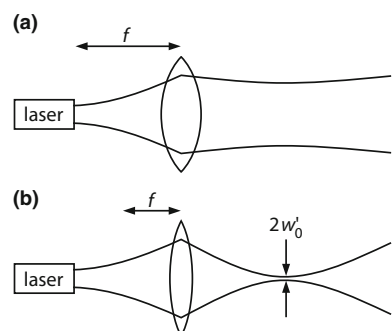


Fig. 10.21 Transformation of diode laser radiation using a lens: **a** collimation and **b** focusing



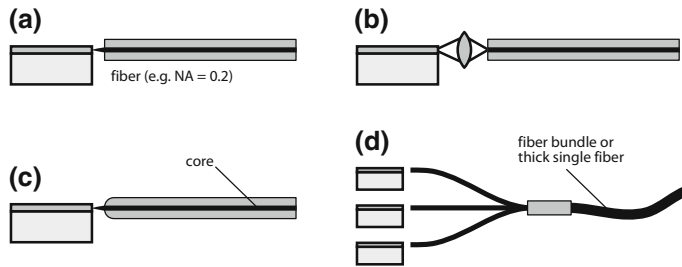


Fig. 10.22 Schemes for laser-to-fiber coupling: **a** direct coupling, **b** coupling by a lens, **c** coupling into a tapered fiber with a rounded end-face which acts as a lens, **d** combination of multiple single emitters in a fiber combiner. The single fibers can be combined to a fiber bundle or fused together to a thick single fiber

position of the lens and its focal length f , as well as the laser wavelength λ . The minimum beam radius after focusing (Fig. 10.21b) (see also Sect. 11.3) is

$$w'_0 \geq \frac{2f\lambda}{\pi D} = \frac{\lambda}{\pi NA}. \quad (10.4)$$

Different concepts are used for fiber coupling and are illustrated in Fig. 10.22. Single transverse mode lasers with small divergence angles can be directly coupled into the glass fiber by placing it close to the laser facet, such that the emission is within the acceptance cone of the fiber. At larger divergence angles, lenses are employed as explained above. Alternatively, cone-shaped fibers or fibers with attached (ball) lenses are utilized where beam shaping occurs at the entrance surface of the fiber. The radiation of multiple single emitters that are coupled into individual fibers by the described methods can be then combined in a single fiber by a fiber combiner. This allows for higher output power while maintaining good beam quality.

Quantum Well and Quantum Dot Lasers

Laser-active semiconductor materials can be produced with thicknesses down to $d \approx 10$ nm, e.g. by means of molecular beam epitaxy (MBE) or metal-organic chemical vapor deposition (MOCVD) (see Sect. 10.7). This thickness is comparable to the de-Broglie wavelength λ of the electrons ($\lambda = h/p$ with the momentum p and Planck's constant h). The injected electrons and holes are hence confined in a potential well and are regarded as standing matter waves. The energy states of the holes in the valence band and the electrons in the conduction band are therefore quantized. This leads to discrete energy levels E_1, E_2, E_3, \dots and $E_{h1}, E_{h2}, E_{h3}, \dots$, respectively (Fig. 10.23), while the density of states in the two bands can be

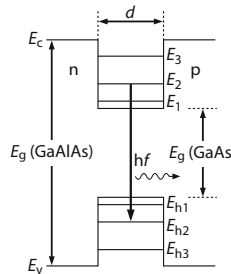


Fig. 10.23 Simplified energy level diagram of a quantum well laser. E_1, E_2, E_3 : energy levels of the electrons, E_{h1}, E_{h2}, E_{h3} : energy levels of the holes (see Fig. 10.8). The electrons are introduced from the n-region and recombine with the holes in the quantum well

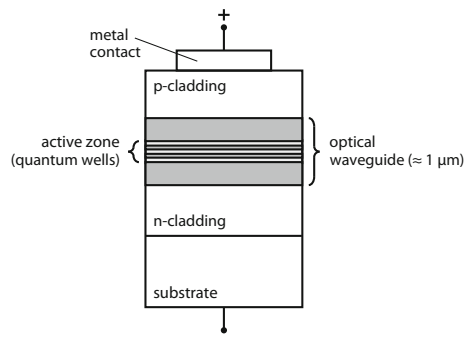
described by a staircase function. Laser emission originates from stimulated transitions between these levels.

Such quantum well lasers can be built from various semiconductor materials, many of them are based on gallium arsenide or indium phosphide wafers as substrates. A typical quantum well laser consists of a GaAs layer that is embedded between n- and p-doped GaAlAs with a larger band gap energy. Multiple quantum wells can be stacked in the active layer of a semiconductor structure (Fig. 10.24) to enhance the laser gain, e.g. in surface-emitting diode lasers (VCSEL, see Sect. 10.6).

The advantage of quantum well lasers is the two- to three-fold reduction of the threshold current that is also less temperature-dependent, so that continuous wave operation at powers up to 100 mW is possible at room temperature. The emission wavelength is determined by the width of the active region, the used material from which it is constructed as well as the strain between the active layers. The lifetime can reach 10^5 h. Quantum wells can also be implemented in broad-area lasers which, in turn, can be combined to form laser bars.

In a quantum wells, the movement of charge carriers is confined in one direction, while they are free to move in two dimensions in the plane parallel to the layer

Fig. 10.24 Vertical structure of a multiple-quantum-well laser where the active zone consists of three quantum wells. The thickness of the optical waveguide determines the fast axis divergence of the output laser beam. Single transverse mode can be obtained with thin waveguides



surface. Further restriction in dimensionality is present in quantum wires (1D) and quantum dots (0D) (see Fig. 1.16). The latter are realized as nanoparticles, e.g. cubes, spheres or pyramids, made of a semiconductor material. Here, the charge carrier movement is confined in all three spatial directions.

Large ensembles of quantum dots, embedded in a suitable matrix, form efficient laser materials that exhibit an electronic structure similar to atoms. The energy levels and hence the emission wavelengths can be adjusted by design, e.g. by controlling the quantum dot dimensions or the material composition. As the wavelength is insensitive to temperature fluctuations, quantum dot lasers are well-suited for use in optical data communication and optical networks. Moreover, devices based on quantum dot active media are of increasing interest for commercial application in medicine, e.g. for laser scalpels and optical coherence tomography, as well as for display technologies (laser projectors, laser television).

10.4 Characteristics of Diode Laser Emission

GaAlAs heterostructure lasers emitting at wavelengths between 640 and 870 nm are widely used in commercial products. The desired wavelength within this range is controlled by variation of the Al concentration which determines the band gap energy (see Fig. 10.5). Since GaAs is used as substrate material, lasers of this type are sometimes also referred to as GaAlAs/GaAs lasers or simply GaAs lasers. The maximum output power in fundamental transverse mode operation is 100 mW at an overall efficiency of 50%.

InGaAsP lasers based on InGaP substrates provide emission wavelengths in the red spectral region from 650 to 700 nm. If InP is used as substrate material, wavelengths from 900 to 1600 nm are obtained. InGaAsP lasers are often simply denoted as InP lasers. Semiconductor lasers based on InGaAs yield emission at 1.06 μm (see lower curve in Fig. 10.5) and can therefore be employed as a substitute or for simulation of Nd:YAG laser emission. Table 10.2 gives an overview of the emission wavelengths, typical output powers and applications of various semiconductor lasers. Some of the listed materials will be discussed later in the text.

The bandwidth of laser diodes is between 0.1 nm for single longitudinal mode lasers and 100 nm in broadband pulsed lasers. The wavelength shifts by about 0.25 nm/K for $\text{Ga}_x\text{Al}_{1-x}\text{As}$ and by about 0.5 nm/K for $\text{In}_x\text{Ga}_{1-x}\text{As}_y\text{P}_{1-y}$. Without applying spectral narrowing techniques, diode lasers mostly operate in multiple longitudinal modes, as the bandwidth can be much larger than the mode spacing which is on the order of $\Delta\lambda = \lambda^2/2nL \approx 0.6 \text{ nm}$ (n : refractive index, L : resonator length, λ : wavelength). In addition, mode-hops can occur due to temperature variations which introduce a change in resonator length. Operation of cw diode lasers requires a constant power supply which is protected against switching peaks, as the semiconductor can be destroyed by electrical overstress.

Table 10.2 Emission wavelength and exemplary cw output power of commercial semiconductor lasers operating in fundamental transverse mode and high beam quality

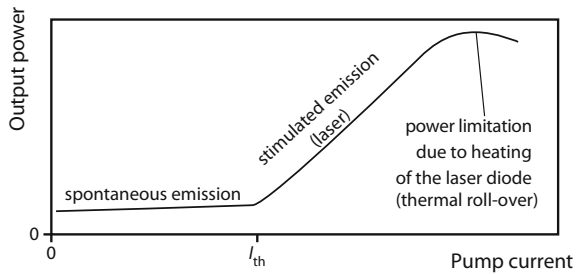
Laser type/ material	Wavelength (μm)	Output power (mW)	Applications
InGaN	0.38–0.53	200	Fluorescence excitation, Blu-ray, laser projectors
AlGaInP	0.63–0.69	500	Scanners, displays, DVD
InGaAsP on InGaP	0.65–0.73	100	Biophotonics
GaAlAs	0.65–0.87	100	Optical sensing, CD
InGaAs	0.88–0.89	500	Solid-state laser pumping
InGaAs	Around 1.06	500	Substitute for Nd:YAG laser, simulation of Nd:YAG laser emission
InGaAsP on InP	1.1–1.9	50	Metrology, communication
AlGaInAsSb on GaSb	1.9–3.0	50	Night vision
Quantum cascade lasers	3–300	1000	Lidar, metrology, gas detection, free-space communication
PbCdS	2.8–4.2	1	Metrology
PbSSe	4.0–8.5	1	Gas detection
PbSnTe	6.5–32	1	Gas detection
PbSnSe	8.5–32	1	Gas detection

The order of chemical elements in the material designations varies, e.g. GaAlAs $\hat{=}$ AlGaAs

Output Power

Semiconductor lasers show a characteristic relationship between the pump current and the optical output power which is plotted in Fig. 10.25. Below the laser threshold current I_{th} spontaneous emission occurs with a broad spectral bandwidth. Light-emitting diodes (LEDs) operate in this regime. At the threshold, the losses are compensated by the gain and stimulated emission sets in. Above the threshold, the output power increases linearly with the pump current. The power saturates at some point and then starts to decrease due to heating of the diode (thermal roll-over). The linear dependence can be explained with the fact that a constant portion of the injected charge carriers contributes to the emission of photons. The correlation between output power and voltage is more complicated, since even under idealized conditions the relationship between current and voltage is exponential. For this reason, power control of diode lasers is mostly realized by means of a current regulation circuit, while the voltage variation is kept low. In general, the output power is strongly temperature-dependent. Hence, characterization of the diode laser performance often involves the consideration of the increasing threshold current with temperature T according to

Fig. 10.25 Laser intensity of a diode laser in dependence on the pump current. The pump current at which maximum output power occurs can be much larger than the threshold current I_{th}



$$I_{\text{th}} \propto \exp(T/T_0), \quad (10.5)$$

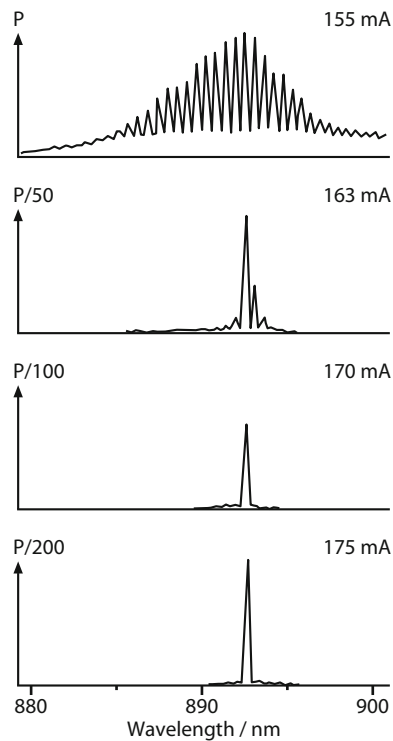
where T_0 denotes the characteristic temperature. This value is $T_0 \approx 200$ K for GaAlAs lasers and $T_0 \approx 50$ K for InGaAsP. The characteristic temperature is a measure of the temperature sensitivity of the diode laser. For higher values of T_0 the threshold current increases less rapidly with increasing temperature, i.e. the laser is more thermally stable. The development diode lasers with high thermal stability is subject of present research aiming at devices that do not require external temperature regulation.

Spectral Characteristics

The spectral output of a broad-area diode laser at different pump currents is depicted in Fig. 10.26. Spectral narrowing and ultimately single longitudinal mode (SLM) operation is observed when increasing the pump current. Although this behavior is typical for most diode lasers, SLM output is only achieved in some laser types. For improving the mode selection a diffraction grating structure with the period $\Lambda = m\lambda_0/2n_0$ can be etched into the active layer, with λ_0 , n_0 being the emission wavelength and the effective refractive index of the waveguide structure, while m is an integer ≥ 1 . Alternatively, the grating can be epitaxially grown on top of the active region, e.g. as corrugated waveguide. Reflection from that grating leads to constructive interference of waves with wavelength λ_0 that satisfy the above equation (Bragg's law), while waves with other wavelengths interfere destructively and are thus suppressed. Lasers of this type are called distributed feedback (DFB) lasers which allow for SLM operation at a desired wavelength within the gain bandwidth of the used semiconductor material (see also Sect. 10.5).

A similar approach is taken in distributed Bragg reflector (DBR) lasers where the grating structure is located outside of the active region and replaces one or both reflective end-faces, i.e. resonator mirrors (Fig. 10.12). SLM lasers have coherence lengths of up to 30 m, but temperature variations can cause the occurrence of mode-hops. In contrast to conventional Fabry-Pérot laser diodes (diode with plane

Fig. 10.26 Emission spectrum of a broad-area diode laser in dependence on the pump current (threshold current: 155 mA). At the onset of stimulated emission, the spectrum is narrowed down resulting in single longitudinal mode operation at 175 mA. Note the strong change in the laser power P while the current increases only slightly



parallel end-faces), DFB and DBR lasers offer wavelength tunability which is achieved by variation of the pump current or the operating temperature.

Spatial Properties

In case of large widths of the active region, the intensity distribution of broad-area diode lasers is characterized by filaments that dominate the lateral profile of the optical laser mode. Slightly above the threshold, the laser emission is not homogeneous across the active region. Instead, 2–10 μm wide, individually emitting filaments appear. With increasing pump current, more and more filaments are formed that change their positions. This leads to strong noise, as each filament emits at a different frequency and phase.

Moreover, the beam is expanded in the direction of the active zone (slow axis). The intensity distribution along the perpendicular direction (fast axis) can be approximated by a cosine function with exponential decay towards the outer regions of the beam. Higher-order Hermite-Gaussian modes, as described in Sect. 11.2, can be present as well. Restriction of the active region width to 10 μm

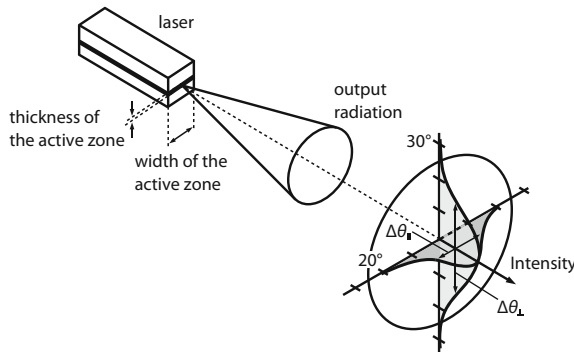


Fig. 10.27 Laser intensity of a diode laser parallel (slow axis) and perpendicular (fast axis) to the active zone. The FWHM divergence angles $\Delta\theta_{\parallel}$ and $\Delta\theta_{\perp}$ can vary significantly for different diode lasers (see Figs. 10.10 and 10.14)

ensures fundamental transverse mode operation, whereby this mode exhibits an elliptical cross-section due to the asymmetric waveguide structure.

The emission characteristics of diode lasers in the planes parallel and perpendicular to the active layer is described by the divergence angles $\Delta\theta_{\parallel}$ and $\Delta\theta_{\perp}$ (Fig. 10.27). In data sheets of laser diodes, it is common to use the full width at half-maximum (FWHM) divergence angle instead of referring to the points at which the intensity is $1/e^2$ of the maximum intensity, as it is done for the Gaussian beam radius. For Gaussian beams, this kind of full beam divergence angle is 1.18 times the half-angle divergence, e.g. used in (10.3). The slow axis divergence angle $\Delta\theta_{\parallel}$ depends on the width of the active layer and is typically on the order of 5° to 40° (FWHM). $\Delta\theta_{\perp}$ is given by the thickness d and the refractive indices of the active and surrounding layers. Typical values are between 40° and 80° . The divergent radiation of laser diodes can be collimated by lens systems. One example for fast-axis collimation of a laser bar using a cylindrical lens is shown in Fig. 10.28.

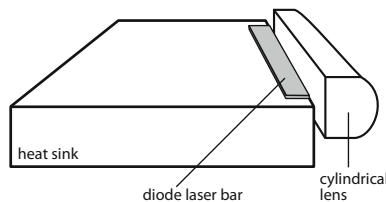


Fig. 10.28 The output radiation of a diode laser bar can be collimated by means of a cylindrical lens (fast axis collimation). Collimation along the other axis (slow axis collimation) can be accomplished by an additional lens system or a step mirror (see Fig. 10.18)

10.5 Wavelength Selection and Tuning of Diode Lasers

Spectral tuning of diode lasers is achieved by varying the refractive index of the gain medium via the temperature or the charge carrier density. In practice, this is accomplished by setting an appropriate combination of operating temperature and injection current. Typical temperature tuning rates are 0.2–0.3 nm/K for laser diodes in the visible spectral region.

Single longitudinal mode (SLM) emission at a desired wavelength can be obtained by employing wavelength-selective elements such as gratings, that are either integrated in the semiconductor structure (distributed feedback lasers and distributed Bragg reflector lasers) or placed outside of the laser diode chip, forming a so-called external cavity diode laser (ECDL). The two different methods are discussed in the following.

Distributed Feedback (DFB) and Distributed Bragg Reflector (DBR) Lasers

One way of generating narrow bandwidth emission is to integrate a grating structure directly inside the waveguide of the laser diode, leading to a compact and rugged design which is known as distributed feedback (DFB) laser. This approach allows for laser linewidths from 100 kHz to 5 MHz and moderate tunability over several nanometers. A schematic setup of a DFB laser is depicted in Fig. 10.29. Due to an etched grating structure on top of the active region, the electric field of the propagating wave experiences a periodic modulation of the effective refractive index n which follows from the average of the refractive indices of the adjacent layers. As

Fig. 10.29 Schematic of a distributed feedback (DFB) laser diode

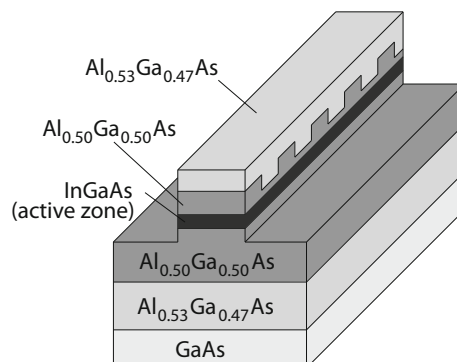
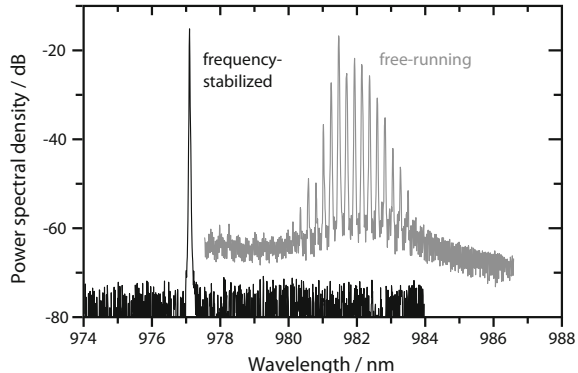


Fig. 10.30 Output spectrum of a free-running Fabry-Pérot laser diode and a frequency stabilized DFB laser (courtesy of Ferdinand-Braun-Institut, Leibniz-Institut für Höchstfrequenztechnik (FBH))



light propagates through the waveguide structure, only waves (wavelength λ_0) that satisfy Bragg's law

$$m \lambda_0 = 2n \Lambda, \quad (10.6)$$

undergo constructive interference, where Λ denotes the grating constant and m is an integer. Hence, only one longitudinal mode with wavelength λ_0 encounters positive optical feedback, while other modes with different wavelengths are suppressed by up to 60 dB, yielding single frequency operation and extremely small linewidth (Fig. 10.30). In contrast, free-running Fabry-Pérot diode lasers exhibit a multitude of longitudinal modes within the gain bandwidth.

In a different construction, the diffraction grating is incorporated in the passive region of the semiconductor structure, where it is, for instance, oriented parallel to the active layer (Fig. 10.12). Such a single-mode laser is called distributed Bragg reflector (DBR) laser. It can be used as the master oscillator in MOPA configurations, e.g. in combination with a tapered amplifier placed on the same semiconductor chip (Fig. 10.13). Such devices provide several watts of SLM output power.

Wavelength tuning of DFB and DBR lasers within the gain bandwidth is achieved by variation of the diode temperature which leads to a change of the resonator length and the grating constant of the structure. Moreover, the gain profile is shifted due to the temperature-dependent band gap energy of the semiconductor materials forming the p-n junction of the diode. Further wavelength (fine) tuning is obtained by varying the injection current which alters the refractive index via the volume charge density and additionally influences the temperature of the laser. As a result, stable SLM operation and tuning over a total range of a few nanometers is obtained without any moving mechanical parts (Fig. 10.31). This makes DFB an DBR lasers the most widely used lasers in optical communication applications. Moreover, the rugged and compact design qualifies such lasers for field deployable and space applications.

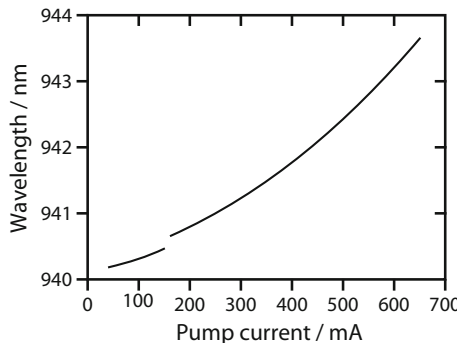


Fig. 10.31 Current-dependence of the output wavelength of a DFB laser. A mode-hop occurs at 150 mA

External Cavity Diode Laser (ECDL)

A more complex scheme is required to achieve wider tunability of SLM diode lasers. External cavity diode lasers (ECDL) are based on a laser diode chip which is incorporated into an external resonator. In case of the common Littrow configuration, this resonator is formed by the laser diode (with its highly reflective rear facet) in combination with a collimating lens and a diffraction grating which acts as an end mirror, as displayed in Fig. 10.32. The first-order diffracted beam provides optical feedback to the laser diode which is anti-reflection coated on the side facing the grating, while the zeroth order is coupled out of the cavity. Since the wavelength of the retroreflected light depends on the rotation angle of the grating, frequency selection is realized by slight tilting of the dispersive device, e.g. by means of a piezo actuator. The tuning range of the ECDL is limited by the gain bandwidth of the laser diode which can account for up to 150 nm, whereas the linewidth of the output radiation is determined by the resolution of the grating.

Fig. 10.32 External cavity diode laser in Littrow configuration

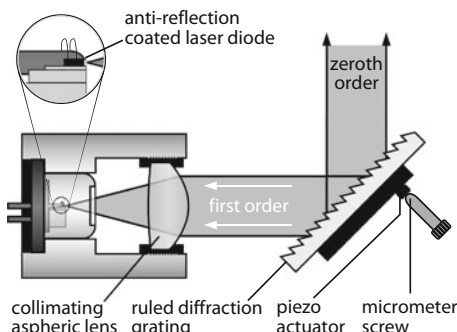
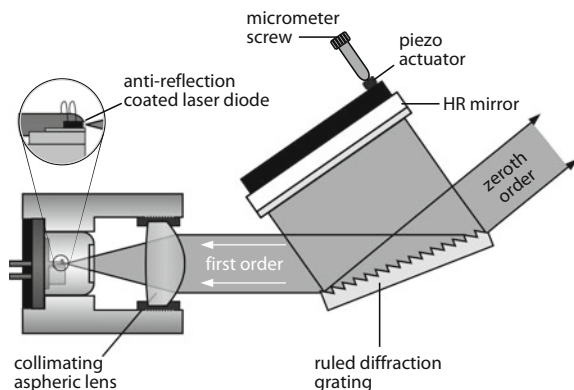


Fig. 10.33 External cavity diode laser in Littman–Metcalf configuration



A disadvantage of the Littrow configuration lies in the fact that rotation of the diffraction grating also changes the direction of the output beam. This problem can be avoided with the Littman-Metcalf configuration where an additional mirror is employed to reflect the first-order beam into the laser diode, while the grating orientation is fixed (see Fig. 10.33). Moreover, this design offers a smaller linewidth of the laser emission, as the wavelength-dependent diffraction occurs twice per resonator round-trip, thus enhancing the wavelength selectivity. However, the zeroth-order radiation of the beam reflected by the tuning mirror is lost, resulting in a lower output power compared to the Littrow design.

Apart from their use as transmitters in optical communication applications, SLM diode lasers are employed for laser cooling, optical metrology and sensing as well as high-resolution spectroscopy. They can also be used for injection-seeding of other lasers or optical parametric oscillators. Here, the low-power, single-mode light of the (seed) diode laser is injected into a high-power (slave) laser. If the seed radiation frequency is close to a resonance frequency of the slave cavity and the seed power is sufficient, the corresponding longitudinal mode lases first and suppresses other modes arising from spontaneous emission. As a result, narrowband high-power output is obtained.

10.6 Surface-Emitting Diode Lasers

A vertical cavity surface-emitting laser (VCSEL) is a laser diode where the optical resonator is vertically aligned and light emission occurs perpendicular from the top surface of the semiconductor chip, as opposed to conventional edge-emitting semiconductor lasers. VCSELs are formed by a thin active region, sandwiched by two distributed Bragg reflector mirrors that are oriented parallel to the wafer surface (Fig. 10.34). As the thin active region provides only low round-trip gain, high reflectance of the resonator mirrors is required for efficient operation.

The whole VCSEL structure is epitaxially stacked in vertical direction, e.g. starting with alternating n-doped AlAs and GaAs $\lambda/4$ -layers with a difference in refractive index. The layer stack acts as a dielectric multilayer mirror (see Sect. 14.2) or Bragg reflector reaching reflectances greater than 99.9%. The active zone consists of one or several quantum wells, e.g. InGaAs, which are embedded in confinement layers (AlGaAs) and quantum well barrier layers (GaAs). Another layer stack (p-doped AlAs/GaAs) at the top of the structure forms the second Bragg reflector. A single VCSEL has a diameter from 5 to more than 30 μm and a total height of a few μm . They can be designed as top emitters or as bottom emitters where the radiation is transmitted through the GaAs substrate which is transparent from 900 to 1000 nm.

After deposition of the single layers, for instance by molecular beam epitaxy, single VCSELs are structured on a wafer (Fig. 10.34). This is performed by photolithographic processes, wet chemical etching, proton implantation or an adequate combination of these techniques. The etching methods are applied to create so-called mesa (span. mesa = plateau) structures that are formed by selective removal of the top layers. Proton implantation is used for targeted generation of defects in the crystal lattice which reduce the electrical conductivity. In this way, the current is concentrated in the defect-free active zone (Fig. 10.35).

The emission wavelength of VCSELs depends on the material of the active zone, similar to edge-emitting diode lasers (see Table 10.2). Due to the very short resonator length, VCSELs operate in single longitudinal mode (Fig. 10.36). In case of small diameters of the structure, fundamental transverse mode is achieved as well. The relationship of the output power and the pump current measured for a relatively large VCSEL (20 μm diameter) is shown in Fig. 10.37. Thousands of VCSELs can be easily arranged in two-dimensional arrays, producing hundreds of watts of output power, albeit with poor beam quality.

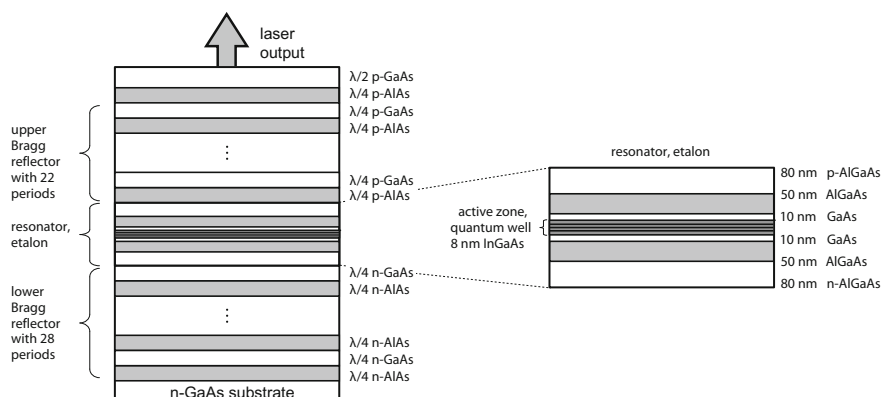


Fig. 10.34 Layer structure of a vertical-cavity surface-emitting laser (VCSEL). The layers adjacent to the active zone serve to adapt the resonator length to the wavelength

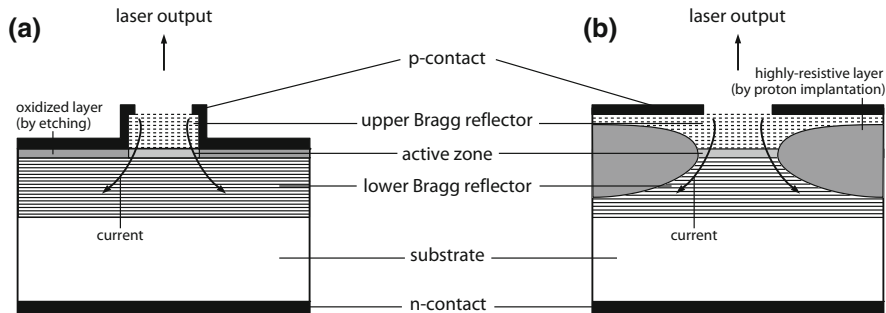


Fig. 10.35 Cross-section through two widely used VCSEL structures: **a** top-emitting mesa laser (TEMEL), **b** proton-implanted surface-emitting laser

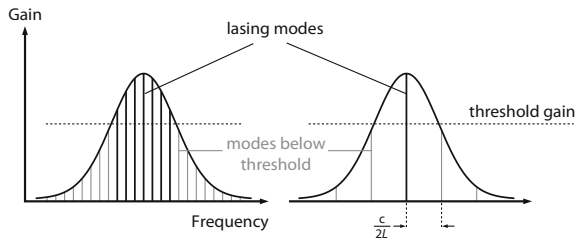
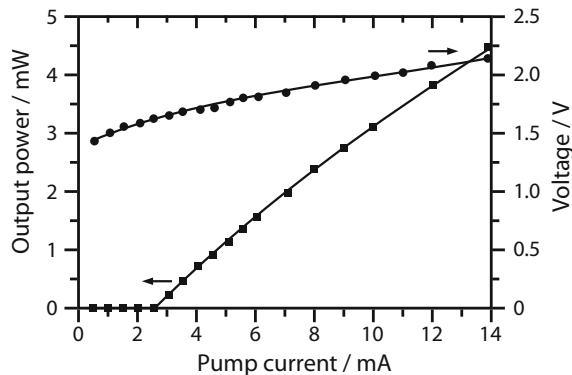


Fig. 10.36 Gain profile of a surface-emitting diode laser. Left: long resonator (L : resonator length) lasing at multiple longitudinal modes, right: VCSEL with a short resonator (larger mode spacing) and a single longitudinal mode above the threshold gain

Fig. 10.37 L-I-V
(light-current-voltage) curve
of a VCSEL with diameter of
20 μm and emission
wavelength of 850 nm



VCSELs have several advantages over edge-emitting diode lasers. Being surface-emitting emitters, they can be tested and characterized on the wafer directly after fabrication which reduces the process costs and allows for cheap mass production. The far-field divergence angle is usually between 15° and 25° , while the

emission is rotationally symmetric. This facilitates the coupling of the output radiation into glass fibers so that coupling efficiencies reach up to 90%. The threshold current of VCSELs can be as low as 100 μA . The low threshold involves a high overall efficiency and low heat deposition. Moreover, fast modulation in the GHz-range is possible at low bias currents which enables increased data transmission, e.g. for optical communication in data centers. Hence, multimode VCSELs emitting at 850 nm have been widely adopted by industry for short-and medium-range (<1000 m) optical networking applications. GaAlAs-VCSELs emitting from 750 to 980 nm are employed in smartphones and computer mice, exploiting the low power consumption which is especially important for battery-powered devices. Wavelength-tunable VCSELs are applied in (3D) gas sensing, particularly oxygen detection. For this purpose, VCSELs incorporating micro-electro-mechanical systems (MEMS) are used. MEMS-VCSELs have a separate output coupling mirror whose position can be tuned via thermal expansion or by means of a piezoelectric element. The global market for VCSELs has seen a strong growth in recent years.

10.7 Semiconductor Lasers for the Mid-IR and THz-Region

Lasers emitting in the mid- and far-infrared spectral range from 3 to 1000 μm wavelength, corresponding to radiation frequencies between 0.3 and 100 THz, are of interest for spectroscopic applications and gas analysis such as the detection of pollutants in the atmosphere. While lead-salt diode lasers reached their technological peak in the 1980s and early 1990s, quantum cascade lasers have superseded these devices in the last two decades.

Quantum Cascade Lasers

Quantum cascade lasers (QCLs) were first demonstrated by Federico Capasso and collaborators at Bell Laboratories, USA in 1994. Laser emission in QCLs is achieved through electron transitions between different states of a quantum well within the conduction band, so-called intersubband transitions (Fig. 10.38). This is in contrast to conventional semiconductor lasers where the emission originates from the recombination of an electron from the conduction band and a hole in the valence band (interband transition, Fig. 10.4). The position and the spacing of the energy levels in the QCL conduction band depends on the layer thickness of the quantum well. The latter can be precisely fabricated by means of molecular beam epitaxy (MBE) metal-organic chemical vapor deposition (MOCVD). By stacking multiple thin layers of varying material composition, cascades of up to 100 quantum wells

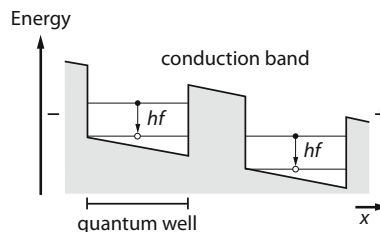


Fig. 10.38 Simplified schematic of the band structure of a quantum cascade laser (QCL). Laser transitions occur between different states of a quantum well within the conduction band (intersubband transitions). The transition frequencies increase with decreasing width of the quantum well. Scaling of the optical gain is achieved by using up to 100 quantum wells in a series (cascade) at the expense of a higher required electrical voltage. Miniband structures between the quantum wells enable the transport of electrons from one well to the next

heterostructures can be formed. After being injected into the gain region, an electron can undergo multiple intersubband transitions and thus produce multiple photons. Consequently, higher optical gain is obtained at the expense of a higher required electrical voltage. Between each transition, the electron tunnels from one quantum well to the next, as it moves through the cascade structure.

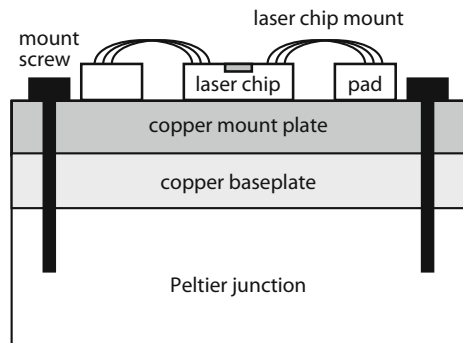
Fabrication Techniques

MBE is a physical deposition method for growing thin epitaxial structures made of semiconductors, metals or insulators. It offers precise control of film thickness, composition and doping. It is characterized by slow deposition rates (less than 1000 nm per h), which allows films to grow epitaxially. However, the slow rates require a higher vacuum to achieve the same impurity levels as obtained with other deposition techniques. MBE is a well-suited technology for small volume production of chips for QCLs.

MOCVD (sometimes also called metalorganic vapor phase epitaxy—MOVPE) represents an alternative technology for the realization of QCLs. Here, ultra-pure gases are injected into a reactor and finely dosed to deposit a very thin layer of atoms onto a semiconductor wafer. Surface reaction of organic compounds or metalorganics and hydrides containing the required chemical elements creates growth conditions for the epitaxy of materials and compound semiconductors. MOCVD typically has higher throughput and enhanced stability over long runs than MBE. It also does not require ultra-high vacuum which makes it cheaper and allows for high volume production of QCLs chips. On the other hand, MOCVD is less precise, whereas MBE can control the film thickness down to fractions of monolayers.

QCLs chips are usually soldered to a copper base and bonded with gold wire bonds to two aluminum nitride ceramic pads which are mounted on the same

Fig. 10.39 Typical laser chip mount of a quantum cascade laser with Peltier cooler. The setup is similar as for diode lasers shown in Fig. 10.1



copper base (see Fig. 10.39). The QCL mount is attached to a copper plate which lies on a Peltier junction for heat dissipation.

Apart from the creation of the active layers by means of MBE or MOCVD, the fabrication of QCL chips and semiconductor laser chips in general involves several additional process steps, as illustrated in Fig. 10.40. A key technology in this context is photolithography (Sect. 23.3) for patterning the active and passive layers and producing optical waveguides. Moreover, the manufacturing process includes the metallization of the semiconductor structure as well as the application of dielectric coating whose quality crucially affects the efficiency of the laser.

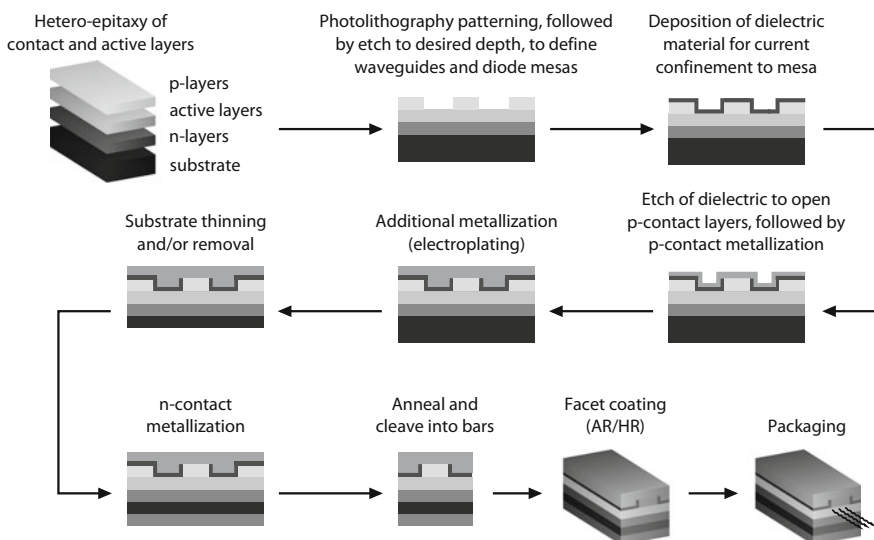


Fig. 10.40 Exemplary process flow for the fabrication of a diode laser bar

Output Characteristics of QCLs and Applications

The emission wavelength of QCLs can be designed by tailoring its electronic potential structure via the active region layer thickness. This process is referred to as band structure engineering which represents a key breakthrough in modern electronics and electro-optics. In this way, QCLs operating at wavelengths from a few to hundreds of μm can be produced. Apart from simple Fabry-Pérot structures, QCLs can also be realized as DFB, DBR or external cavity lasers, providing SLM output and linewidths down to 10 kHz.

Like in VCSELs, laser emission occurs perpendicular to the plane of the semiconductor layer which is mostly based on InP or GaAlAs. Continuous operation at room temperature is possible, albeit the output power is usually limited to a few watts. Higher power is obtained when cooling the device to nitrogen temperatures. Tuning ranges beyond 20% have been demonstrated. Typical output characteristics of commercially available high-power QCLs are presented in Table 10.3.

Spectroscopy and gas sensing are presently the major fields of application for QCLs. In particular, they are used for the detection of CH_4 , N_2O , NO, CO and other trace gases in the spectral range from 3 to 15 μm where most of the chemical compounds have fundamental vibration modes. The spectral regions from 3 to 5 μm and 8 to 12 μm are especially attractive, as the atmosphere shows high transmission. Moreover, Rayleigh scattering from dust and raindrops decreases dramatically in the long wavelength range (by a factor 10^4 from 1 to 10 μm). QCLs emitting at methane (CH_4) absorption lines are targeted for pipeline leak detection.

Further important application domains of QCLs are the detection of drugs and explosives, industrial process monitoring as well as life science and medicine. Although most QCLs operate in the mid-infrared spectral region, wavelengths of 300 μm , corresponding to 1 THz radiation frequency, can be reached. Hence, QCLs constitute very compact and simple sources of terahertz radiation (see Sect. 17.4). Since terahertz radiation is non-ionizing but can penetrate most non-conductive materials, it is used in a wide range of applications such as water content and tissue density mapping as well as the detection of metals, e.g. for security control at the airport.

Table 10.3 Typical output parameters of commercially available quantum cascade lasers

Parameter	Value
Average power	1–2 W
Peak power	1–10 W
Spectral width	$50\text{--}150 \text{ cm}^{-1}$
Central wavelength	4–10 μm
Wall-plug efficiency	10%
Beam quality (M^2)	1.5–3
Pointing error	6 mrad
Pulse width	From 20 ns to cw operation
Beam diameter	4 mm

Lead-Salt Diode Lasers

Before the development of quantum cascade lasers, laser output in the mid-infrared spectral region from 3 to 30 μm was provided by various types of lead-salt diode lasers. These lasers are based on lead compounds like $\text{Pb}_x\text{Sn}_{1-x}\text{Te}$ or $\text{Pb}_{1-x}\text{Sn}_x\text{Se}$, amongst others (see Table 10.2). The layer structure is similar to other semiconductor lasers whereby p-type and n-type conduction are determined by the stoichiometry, i.e. the relative quantities of the elements Pb, Sn, Se, etc. in the crystal. In this way, the band gap energy (typically well below 0.5 eV), and hence the emission wavelength is controlled by the element composition like in III–V semiconductors.

Additional wavelength tuning over several hundreds of cm^{-1} ($\approx 5 \text{ cm}^{-1}/\text{K}$) is achieved by setting the operation temperature. Fine tuning of the wavelength can be realized by variation of the injection current which introduces small temperature changes. Note that a tuning range of 100 cm^{-1} corresponds to 1 μm at a central wavelength of 10 μm (10% tuning range).

Operation of lead-salt diode lasers is only possible at cryogenic temperatures well below 200 K, typically at liquid nitrogen temperatures. This is especially required for continuous wave lasing and emission at longer wavelengths. Moreover, only low output powers of a few mW are obtained, and the overall efficiency is very low compared to that of shorter-wavelength semiconductor lasers. Lead-salt diode lasers were mainly applied in spectroscopy, particularly for the detection and analysis of molecular gases. However, for the above reasons, lead-salt diode lasers have been replaced by quantum cascade lasers for most applications.

10.8 Ultraviolet and Visible InGaAs Lasers

Two different material compounds were investigated for realizing green, blue and violet diode lasers: II–VI semiconductors based on ZnSe and III–V nitride semiconductors based on InGaAs. InGaN lasers, shortly called GaN lasers, have much longer lifetime, higher output power and are commercially available. Such semiconductors exhibit band gap energies that are large enough for providing short-wavelength emission. Typical output parameters are given in Table 10.4. Due to rapid progress in the development of GaN lasers, improvement of their performance is expected in the future.

Table 10.4 Comparison between ZnSe and InGaAs diode lasers (as of 2017)

Parameter	ZnSe (II–VI)	InGaAs (III–V)
Lifetime (h)	100	20,000
Color	Blue	UV, blue, green
CW output power (W)	0.1	>2
Shortest wavelength (nm)	474	240 (AlGaN)

III–V Nitride Lasers

GaN and GaInN LEDs were first introduced on the market by the Japanese company Nichia Chemical in 1993. The blue and green LEDs were about 100 times brighter than the blue SiC LEDs available at this time. In 1996, the company presented the first violet semiconductor laser emitting at 390 nm. The structures were fabricated by metal-organic chemical vapor deposition (MOCVD).

Initially, sapphire or SiC substrates having a very similar lattice constant were used. The changeover to quaternary systems such as boron aluminum gallium nitride (BAIGaN) enabled lattice-matching to SiC and AlN substrates. In addition, shorter emission wavelengths can be accessed. The processing, e.g. the epitaxial growth of hexagonal GaN on sapphire, and the fabrication of mirrors is relatively complicated. Hence, the production of GaN substrates was successfully pushed forward, while achieving a low defect density. Nevertheless, sapphire substrates are still used that are separated (or diced) after the layer deposition.

Despite the high threshold current densities of several kA/cm^2 , GaN lasers are very robust which can be traced back to the high hardness of the material. Therefore, these lasers are becoming increasingly commercially important. The same holds true for green InGaN laser diodes emitting at wavelengths to 550 nm. Laser diodes from 510 to 513 nm have an estimated lifetime of longer than 5000 h. During this time, the operating current increases by 30%.

In 2014, the Nobel Prize in Physics was awarded jointly to Isamu Akasaki, Hiroshi Amano and Shuji Nakamura for the invention of efficient blue light-emitting diodes which has enabled bright and energy-saving white light sources. Akasaki and Amano made breakthroughs in crystal growth by MOCVD, while Nakamura was involved in the development of the first blue laser in the mid-90s.

Applications

Optical storage represents by far the most important driver for the development of short-wavelength laser diodes. In particular, the Blu-ray format has gained increasing relevance over the last years, as it provides much larger storage capacities compared to CD (compact disc) and DVD (digital versatile disc), thus offering the recording of many hours of high-definition video. Blu-ray devices are based on GaN lasers producing violet light at 405 nm wavelength, as opposed to CD and DVD where 780 nm (AlGaAs) and 650 nm (AlGaInP) lasers are employed. The shorter wavelength can be focused to a smaller area which enables higher storage densities on the data medium (Sect. 25.1). Consequently, a Blu-ray disc is capable of holding about five times the amount of information that can be stored on a DVD.

Meanwhile, InGaN multidiode lasers are available with cw output powers of up to 50 W. Such systems are useful for cutting and joining plastic and polymer

materials. The short-wavelength emission also allows for higher resolution in imaging, so that blue and violet diode lasers are of great interest for biomedical applications such as flow cytometry (see Sect. 24.3) or laser microscopy as well as for spectroscopic measurements. Moreover, blue multidiode laser systems delivering kilowatt output power are currently being developed by several companies for material processing of gold and copper.

A further field of application for blue laser diodes is laser projection displays, e.g. laser pico projectors. Here, a raster-based image is projected by illuminating a screen with three laser sources emitting at the fundamental colors red, green and blue. The system works by scanning the picture pixel-by-pixel. This is accomplished by modulating the laser directly at a high frequency using a small mirror based on MEMS technology. Due to the tight focusing of the laser beam and the monochromatic fundamental colors, extremely brilliant images with high color purity are obtained that can be projected over large distances. The use of diode lasers (red: InGaAsP, green and blue: InGaN) is likely to provide a major advancement of these devices, especially for mobile projectors. Another family of projection applications where lasers provide a novel approach are head-up displays (HUDs), e.g. windshield displays in cars. In contrast to HUD systems currently used in vehicles, laser-based HUDs offer higher contrast and thus haze-free images. Furthermore, BMW and other companies developed headlights based on GaN lasers, which can deliver directional beams that are hard to create using LEDs.

II–VI Diode Lasers

Green and blue light-emitting diodes (LEDs) and laser diodes based on ZnSe have long been produced by molecular beam epitaxy. GaAs is mostly used as substrate material, as it is available with high surface quality and is nearly lattice matched to ZnSe. Moreover, compatible processing technology is available. Homoepitaxy on ZnSe-substrates has been demonstrated as well.

However, commercial utilization of ZnSe lasers has been hampered by the insufficient lifetime. Like in the early stages of the III–V lasers, the fast degradation is caused by defect (non-radiative recombination centers) that increase during operation.

10.9 Diode Lasers for Optical Communication

In modern telecommunication networks, data are transmitted via optical fibers. Consequently, lasers emitting in the spectral windows around $1.3\text{ }\mu\text{m}$ for medium ranges and $1.55\text{ }\mu\text{m}$ for long ranges are required. For this purpose, both edge-emitting and surface-emitting semiconductor lasers are employed. The latter are primarily used for short links ($<500\text{ m}$), e.g. at 850 nm wavelength.

Currently, InP and related compounds (InGaAsP, InGaAlAs) are suitable materials. Although the GaAs technology has made substantial progress, lasers based on this compound are only applicable for the spectral range below 1.3 μm . GaAs lasers at 800–900 nm wavelength are hence only suitable for short-range transmission.

Fabry-Pérot laser diodes find use in applications that have low requirements in terms of laser linewidth and wavelength stability. The simultaneous transmission of multiple wavelengths by means of wavelength division multiplexing (WDM) requires laser diodes operating in stable single longitudinal mode, so that DFB and DBR lasers (see Sect. 10.5) are deployed in this case. The wavelength spacing in a WDM transmission system can be coarse, e.g. ≈ 20 nm ($\hat{=}$ 2500 GHz at 1550 nm), or very dense, e.g. 0.4 nm ($\hat{=}$ 50 GHz at 1550 nm). Thus, lasers with a tuning range of more than 100 nm are demanded for this application.

This most simple method of data transmission using cw semiconductor lasers is based on the modulation of the diode current. Due to the finite photon lifetime in the resonator as well as parasitic capacities, the transmission frequency is limited to about 20 GHz for this technique. Alternatively, integrated modulators like electro-absorption modulators (EAM) or Mach-Zehnder modulators (MZM) offering frequencies above 40 GHz are applied.

Higher data rates in a single wavelength channel can be achieved by employing pulsed lasers. Here, interleaving trains of ultra-short pulses in the ps-range are used as input of the modulator, so that multiple data streams are transferred simultaneously, thus enhancing the data transmission capacities, e.g. 4×40 Gbit/s. This method is known as optical time division multiplexing (OTDM). The picosecond pulses are usually produced by mode-locking (Sect. 17.4). The transmission of data at rates of several 1 Tbit/s through a single glass fiber is obtained by wavelength division multiplexing. In 2014, researchers reported the successful transmission of a record high 255 Tbits/s over 1 km using a novel seven-core fiber, which allows much larger bandwidth than is currently available in communication networks.

Micro-lasers are studied for the generation of light at different wavelengths. Such devices can be integrated in silicon chips which also incorporate the electronic circuits and optical components for driving and modulating the laser as well as for coupling the light into the transmission fiber. Modulation is for instance realized by silicon electro-optic modulators based on p-i-n diodes, in which charge carrier modulation enables data rates exceeding 20 Gbit/s per wavelength channel.

The flourishing technology of integrated systems consisting of laser sources, optical waveguides including couplers, modulators, filters, etc. is referred to as silicon photonics. The different components are fabricated on silicon-on-insulator (SOI) wafers in CMOS technology, while the production of the laser sources requires additional materials such as InGaAsP.

The present growth in the diode laser market for optical communication mainly comes from the rapid expansion of data centers and the progressing replacement of copper by fibers related to the increasing demand for higher data rates. Here, diode lasers are primarily based on VCSEL architectures that can be easily integrated into optical communication systems.

In 2018, scientists from the Fudan University in Shanghai, China, claimed to have demonstrated the world's first optically-pumped all-silicon distributed-feedback laser which represents a key achievement in the field of integrated silicon photonics. Despite being an indirect semiconductor, stimulated emission of narrow-linewidth and low-divergence light was realized by exciting high-density silicon nanocrystals with intense femtosecond laser pulses. This breakthrough could also lead to the development of electrically-pumped silicon lasers.

Further Reading

1. B. Ismay (ed.), *Semiconductor Laser Diode Technology and Applications* (Scitus Academics LLC, 2016)
2. J. Jones (ed.), *Semiconductor Laser Diodes Handbook* (ML Books International, 2015)
3. T. Numai, *Fundamentals of Semiconductor Lasers* (Springer, 2015)
4. M. Yamada, *Theory of Semiconductor Lasers* (Springer, 2014)
5. R. Michalzik (ed.), *VCSELs* (Springer, 2013)
6. E. Bründermann, H.W. Hübers, M.F. Kimmitt, *Terahertz Techniques* (Springer, 2012)
7. F. Bachmann, P. Loosen, R. Poprawe (eds.), *High Power Diode Lasers: Technology and Applications* (Springer, 2010)
8. A. Krier, (ed.), *Mid-infrared Semiconductor Optoelectronics* (Springer, 2006)
9. S. M. Sze, K.N. Ng, *Physics of Semiconductor Devices* (Wiley-Interscience, 2006)
10. D. Mittleman (ed.), *Sensing with Terahertz Radiation* (Springer, 2003)
11. R. Diehl (ed.), *High-Power Diode Lasers* (Springer, 2000)
12. S. Nakamura, S. Pearton, G. Fasol, *The Blue Laser Diode* (Springer, 2000)
13. G.P. Agrawal, N.K. Dutta, *Semiconductor Lasers* (Springer, 1993)

Part IV

Free and Guided Light

Wave Propagation

Geometrical optics describes light in terms of rays that propagate in straight-line paths as they travel in vacuum or a homogeneous medium like air. This approximation is useful in cases when the wavelength of the light is small compared to the size of the structures in inhomogeneous media with which it interacts. However, owing to the wave nature of light, the simplification does not account for optical effects such as diffraction and interference, for example, when describing the propagation of narrow light beams as emitted by lasers. In the ideal case, laser radiation can be treated as so-called Gaussian beams that have minimum divergence for a given beam diameter. Real laser beams can be characterized by their beam quality. Guiding of laser radiation over long distances and on curved paths is accomplished through optical glass fibers, whereby the beam divergence and the losses introduced by absorption can be very low.

Chapter 11

Laser Beam Propagation in Free Space



Light is an electromagnetic wave which can be mathematically described by Maxwell's equations. Based on this set of differential equations, the wave equation is derived for the electric and magnetic field. The wave equation for the electric field E , reduced to the scalar form in Cartesian coordinates (x, y, z) , reads

$$\left(\frac{\partial^2}{\partial x^2} + \frac{\partial^2}{\partial y^2} + \frac{\partial^2}{\partial z^2} - \frac{1}{c^2} \frac{\partial^2}{\partial t^2} \right) E(x, y, z, t) = 0. \quad (11.1)$$

The electric field $E(x, y, z, t)$ (in V/m) is a function of the spatial coordinates x, y, z and the time t . The speed of light $c = c_0/n$ is given by the vacuum speed of light c_0 and the refractive index n of the medium through which the light propagates. The light intensity or power density I (in W/m²) is the power transferred per unit area and proportional to the square of the amplitude of the electric field: $I \propto |E|^2$. In the following, different solutions of the above wave equation are discussed.

11.1 Plane and Spherical Waves, Diffraction

A simple solution is the plane wave (see Fig. 1.1) that, e.g. travels in z -direction:

$$E(z, t) = E_0 \cos(\omega t - kz) = (E_0/2) \exp[-i(\omega t - kz)] + \text{c.c.}, \quad (11.2)$$

where c.c. means the complex conjugated expression of the first summand. The term c.c. is sometimes omitted for the sake of simplification. In the plane wave solution (11.2), E_0 is the amplitude of the electric field and ω is the angular frequency which is related to the (ordinary) frequency $f = c/\lambda$ by $\omega = 2\pi f$. The amount of the wave vector is $k = 2\pi/\lambda$. It is also referred to as spatial angular frequency. By inserting the solution into the wave (11.1), a relationship between the spatial and temporal angular frequency follows:

$$k^2 = \omega^2/c^2, \quad \text{i.e. } k = \pm\omega/c. \quad (11.3)$$

For plane waves, the locations of maximum amplitude are given by

$$\omega t - kz = -2\pi m \quad (m \text{ is an integer}) \text{ or } z = \omega t/k + 2\pi m/k = \pm ct + m\lambda. \quad (11.4)$$

The phase planes are spaced by the wavelength λ , oriented perpendicular to the wave vector \mathbf{k} and travel at the speed of light. The direction of \mathbf{k} is determined by the direction of propagation (see Fig. 1.2).

Spherical Waves

Another solution of (11.1) is the spherical wave:

$$E(r) = \frac{A}{r} \exp[-i(kr - \omega t)] + \text{c.c.} \quad \text{with } r = \sqrt{x^2 + y^2 + z^2} \quad (11.5)$$

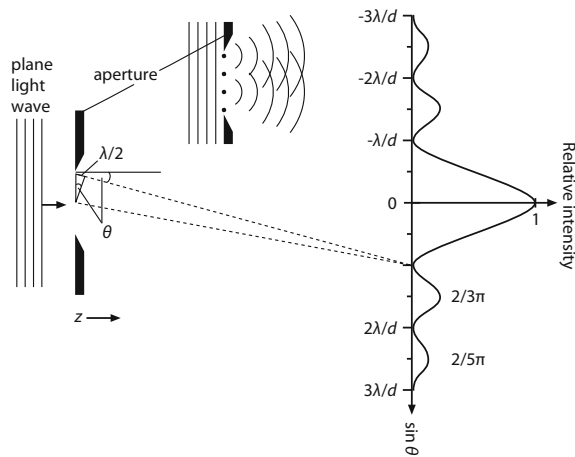
denoting the radius r from the center (origin) of the wave. The spherical phase planes (or fronts) are illustrated in Fig. 1.2 which shows a cross-section through the wave. The field amplitude A/r decreases with increasing radius. On the other hand, the amplitude diverges towards the origin which is not realistic for describing light sources. A better description is provided by the emission characteristic of an oscillating dipole (Fig. 2.8), as introduced in Sect. 2.6. Dipole radiation can be treated as a spherical wave at sufficiently large distance from the center.

Diffraction

The ideal plane and spherical waves, considered till now, are only useful to a limited extent for modelling laser beams. A plane wave is infinitely extended in space, while a spherical wave propagates in all directions. Both characteristics are in contrast to a laser beam that has a certain propagation direction and a finite beam cross-section. An improved model is developed by considering a plane wave whose phase fronts are laterally delimited by an aperture, as depicted in Fig. 11.1. This produces a light beam with constant intensity across the aperture cross-section. However, the rectangular intensity profile is not maintained behind the aperture. At large distances ($z > d^2/\lambda$), a broadened profile containing side lobes is observed.

The modification of the intensity profile of a light wave behind an aperture or other obstacle is called diffraction. In classical physics, diffraction is described by the Huygens–Fresnel principle, according to which each point of a wave front becomes a source of a secondary spherical wave, as shown on top of Fig. 11.1. The secondary waves superimpose with each other to form a new wave front of the wave propagating

Fig. 11.1 Intensity distribution for diffraction of light at a single slit of width d . A similar intensity distribution is observed for diffraction at a circular aperture



in the right half-space behind the aperture with a corresponding field distribution. Superposition of the waves involves constructive and destructive interference depending on the optical path difference of the spherical waves. If the path difference is zero, e.g. along the symmetry axis, constructive interference occurs (summation of the field amplitudes), leading to an intensity maximum. The top of Fig. 11.1. illustrates the interference of a pair of spherical waves emerging from two centers spaced by half the width of the aperture or slit $d/2$. If the path difference is $\lambda/2$, the waves extinguish each other, as the amplitudes are in opposite directions. This is the case for propagation directions at angles θ which satisfy the condition

$$\boxed{\sin \theta = k \frac{\lambda}{d}} \quad \text{with } k = \pm 1, \pm 2, \dots \quad (11.6)$$

A more comprehensive calculation results in the intensity distribution shown in Fig. 11.1. In conclusion, lateral restriction of a plane wave introduces changes of the intensity profiles, as it causes divergence of the propagating wave. The same occurs for laser beams which usually have a Gaussian intensity distribution. The latter also diverges as the laser beam travels but the divergence angle is smaller than that of a beam with a rectangular intensity profile. Due to this beneficial property, lasers are often designed to emit waves with Gaussian intensity profiles. The characteristics of such Gaussian beams are elaborated in the next section.

11.2 Gaussian Beams

Lasers can be excited and operated in various transverse field distributions (or transverse modes). The fundamental transverse mode TEM_{00} is characterized by a simple radially symmetric field distribution and is therefore suitable for many applications. For resonators based on spherical mirrors, the TEM_{00} mode features a

Gaussian intensity distribution. In the following, the propagation of Gaussian beams is described, showing that such beams can be treated as spherical waves with complex source point.

Spherical Waves with Complex Source Point

The center of a spherical wave according to (11.5) is arbitrary. It can also be located in the complex z -plane, even though this appears abstract at first. Hence, the coordinate z in (11.5) can be replaced by a complex parameter q :

$$z \rightarrow z + i z_R = q. \quad (11.7)$$

The quantity z_R is real, its physical meaning will be further discussed later in the text. The transformation (11.7) leads to spherical waves with complex centers:

$$E(r, z, t) = \frac{A}{\sqrt{q^2 + r^2}} \exp \left[-i \left(k \sqrt{q^2 + r^2} - \omega t \right) \right] \quad \text{with } r = \sqrt{x^2 + y^2}. \quad (11.8)$$

When restricting to the paraxial region, i.e. the region close to the z -axis, $r \ll |q|$, the electric field simplifies to

$$\begin{aligned} E(r, z, t) &\approx \frac{A}{q} \exp \left[-i \left(kq \left(1 + \frac{r^2}{2q^2} \right) - \omega t \right) \right] \\ &= \frac{B}{q} \exp \left(-i \frac{kr^2}{2q} \right) \exp [i(\omega t - kz)]. \end{aligned} \quad (11.9)$$

Like the parameter A , $B = A \exp(kz_R)$ represents some (initially) unspecified amplitude. The inverse complex (beam) parameter $1/q$ can be split into the real and imaginary part as follows:

$$\frac{1}{q(z)} = \frac{z - iz_R}{z^2 + z_R^2} = \frac{1}{R(z)} - i \frac{2}{kw^2(z)}. \quad (11.10)$$

The quantities $w(z)$ and $R(z)$ denote the beam radius and the radius of curvature of the light beam, as will be shown in the following sections. Inserting (11.9) into (11.10), the electric field reads

$$E(r, z, t) \approx \frac{B}{q} \exp \left(-\frac{r^2}{w^2(z)} \right) \exp \left(-i \frac{kr^2}{2R(z)} \right) \exp [i(\omega t - kz)]. \quad (11.11)$$

Aside from plane and spherical waves, (11.11) represents a further, albeit approximate, solution of the wave equation that is valid in the paraxial region. It is

referred to as Gaussian beam and describes the propagation of lasers operating in the fundamental transverse mode.

Beam Radius

The amplitude in the solution (11.11) is given by a Gaussian function that behaves as $\exp(-r^2/w^2(z))$ along the radial coordinate. The spatial intensity distribution $I \propto |E|^2$ can thus be expressed as

$$I/I_{\max} = \exp(-2r^2/w^2(z)). \quad (11.12)$$

The radial intensity distribution of a Gaussian beam is shown in Fig. 11.2. The beam travels in z -direction. $w(z)$ is the beam radius at which the intensity has decreased to $1/e^2$ times its peak value $I(r=w) = I_{\max}/e^2 \approx 0.135 \cdot I_{\max}$.

The intensity or power density is defined as the power dP that is transferred through an area dA : $I = dP/dA$. Integration of (11.12) yields a relationship between the laser power $P = \int I dA$ and maximum intensity I_{\max} :

$$P = \frac{\pi}{2} w^2 I_{\max}. \quad (11.13)$$

The power that is passing through a circular aperture with radius ρ , placed symmetrically in the center of the beam, is calculated to be

$$P(\rho) = P_{\text{total}} [1 - \exp(-2\rho^2/w^2)] \quad (11.14)$$

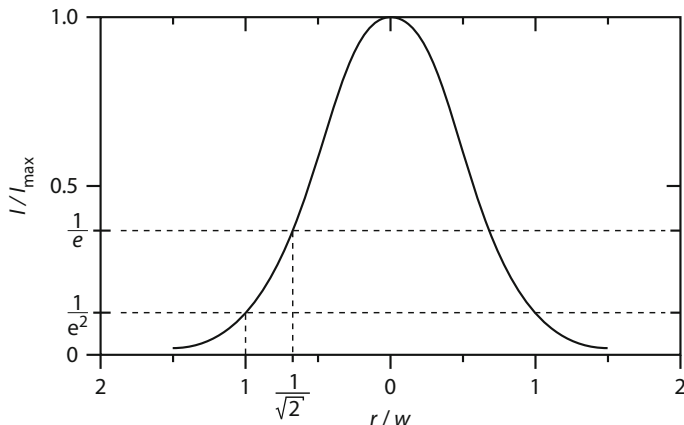


Fig. 11.2 Intensity distribution of a Gaussian beam perpendicular to the propagation direction. At the position of the beam radius w is $I/I_{\max} = 1/e^2$. For laser safety definitions, the beam radius $w' = w/\sqrt{2}$ is used with $I/I_{\max} = 1/e$

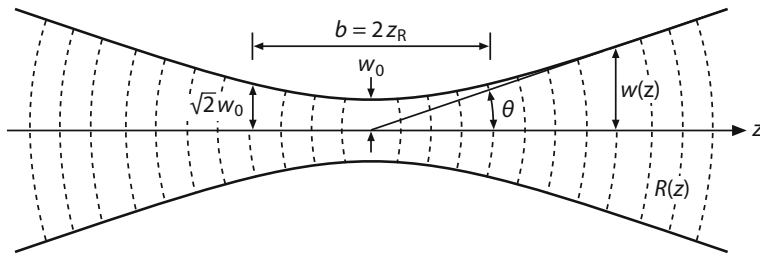


Fig. 11.3 Propagation of a Gaussian beam along the z direction with changing beam radius $w(z)$ and wave front curvature $R(z)$. At a distance from the beam waist (w_0) equal to the Rayleigh length z_R , the beam width is $\sqrt{2}$ larger than at the waist. At this position, the wave front curvature is greatest. The distance between the two points $z = \pm z_R$ is called confocal parameter b

For $\rho = w$, $P = P_{\text{total}}(1 - e^{-2}) \approx 0.865P_{\text{total}}$, i.e. 86.5% of the total power is enclosed within the $1/e^2$ -beam radius w .

The radius of a Gaussian beam $w(z)$ at any position along the z -axis can be derived from the beam waist w_0 . This is the beam radius at the point where it is smallest (at $z = 0$ for the above equations): $w_0 = w(z = 0)$:

$$w(z) = w_0 \sqrt{1 + z^2/z_R^2} \quad \text{with} \quad w_0 = \sqrt{\frac{z_R \lambda}{\pi}}. \quad (11.15)$$

The dependence of the beam radius upon the propagation coordinate z is depicted in Fig. 11.3. At $z = z_R$, the width w of the beam is $\sqrt{2}$ times larger than at the beam waist. The parameter z_R is called Rayleigh length and related to the beam waist as

$$z_R = \frac{\pi w_0^2}{\lambda}. \quad (11.16)$$

Hence, the shape of a Gaussian beam of a given wavelength λ along the propagation axis z is determined solely by the beam waist w_0 or the Rayleigh length z_R . Aside from the Rayleigh length, the confocal parameter, $b = 2z_R$, is often used to characterize laser beams.

Divergence Angle and Radius of Curvature

At large distances from the beam waist ($z \gg z_R$), the beam radius increases linearly with z :

$$w(z) = w_0 \frac{z}{z_R}. \quad (11.17)$$

This implies a divergence angle of the Gaussian beam (see Fig. 11.3) according to

$$\boxed{\theta = \lim_{z \gg z_R} \frac{w(z)}{z} = \frac{w_0}{z_R} = \frac{\lambda}{\pi w_0}}. \quad (11.18)$$

Illumination of a circular aperture with diameter $d = 2w$ with a plane wave would result in a diffracted light wave with divergence angle

$$\theta_k = 1.22 \lambda/d = 1.92\lambda/\pi w_0 > \theta \quad (11.19)$$

The angle θ_k denotes the angle for the first minimum of the diffraction pattern, as shown for a slit aperture in Fig. 11.1. The Gaussian beam is thus characterized by a lower divergence compared to other laterally delimited light beams, albeit this was only demonstrated at the example of a rectangular beam profile. For this reason, Gaussian beams are often called diffraction-limited.

The average intensity of a laser beam with radius w , $I_{av} = P/\pi w^2$ is only half of the maximum or peak intensity in the center of the beam which follows from (11.13): $I_{max} = 2P/\pi w^2$. Therefore, a smaller beam radius $w' = w/\sqrt{2}$ and divergence angle $\theta' = \theta/\sqrt{2}$ are commonly used in terms of laser safety regulations (see caption of Fig. 11.2 and Sect. 24.4).

The phase planes of a Gaussian beam are described by the parabolic relation

$$z = m\lambda - \frac{r^2}{2R(z)}, \quad (11.20)$$

with m being an integer. The radius of curvature of the parabola is given by

$$\boxed{R(z) = z + \frac{z_R^2}{z}}. \quad (11.21)$$

For $z \gg z_R$, the curvature is $R(z) \approx 0$, i.e. at large distances from the beam waist the phase planes are spheres with centers located at $z = 0$. In contrast, the curvature approaches infinity towards the beam waist ($R(z \rightarrow 0) \rightarrow \infty$), thus resulting in plane wave fronts. A Gaussian beam can therefore be considered as a mixture of a plane wave and a spherical wave (see Fig. 11.3).

The Complex Beam Parameter

As a Gaussian beam propagates, the beam radius $w(z)$ and the radius of curvature $R(z)$ change as a function of the distance z from the beam waist. Instead of considering these two quantities, it is often more convenient to use the complex beam parameter q which contains $w(z)$ and $R(z)$ according to (11.10). The parameter

$$q(z) = z + iz_R = z + q(0) \quad (11.22)$$

depends linearly on z and becomes purely imaginary at the beam waist:

$$q(0) = i z_R, \quad (11.23)$$

where z_R is the Rayleigh length as defined in (11.16). This again demonstrates that a Gaussian beam is solely governed by the position and the radius of its beam waist. The q -parameter is altered during the propagation of Gaussian beam and is also transformed upon propagation through lenses and other optical elements. These beam transformations can be described by means of ABCD matrices. However, in many cases the matrix formalism is not necessary; hence it is not used in the following discussion of basic concepts.

Higher-Order Hermite-Gaussian Beams

Apart from the Gaussian beam, there is a family of further solutions to the wave equation with the following x -component:

$$E_m(x) = H_m(\xi) \exp(-\xi^2/2) \quad \text{with } m = 0, 1, 2, \dots \quad (11.24)$$

where

$$H_0 = 1, \quad H_1(\xi) = 2\xi, \quad H_2(\xi) = 4\xi^2 - 2, \quad H_3(\xi) = 8\xi^3 - 12\xi \quad (11.25)$$

being the so-called (physicists') Hermite polynomials of degree m . From the above equations, it becomes clear that the Gaussian beam is the zero-order ($m = 0$) solution of the wave equation. The index m corresponds to the number of nodes along the x -axis. Comparison with (11.11) yields

$$\xi = x\sqrt{2}/w_0. \quad (11.26)$$

The field and corresponding intensity distributions of several Hermite-Gaussian TEM_{m0} modes calculated from (11.24) are depicted in Fig. 11.4. Such modes can for example occur in semiconductor lasers.

The Hermite polynomials form a complete orthogonal system of functions. The x -component of any function or field distribution can be represented by a sum of Hermite polynomials. Hence, for any field distribution along the x -axis, there is a solution for the wave equation in the entire space. In addition, the Hermite polynomials have the feature that the corresponding field distributions in x -direction are similar for every z -component and only differ in terms of the beam radius $w(z)$. In contrast, for other distributions along the x -axis, e.g. a rectangular function that is present behind a homogeneously illuminated slit (Fig. 11.1), the shape of the initial distribution changes during the light propagation. Additional examples of Hermite-Gaussian modes TEM_{mn} modes build by factorization $E_m(x)E_n(y)$ with m and n nodes along the x - and y -axis, respectively, are shown in Fig. 12.4.

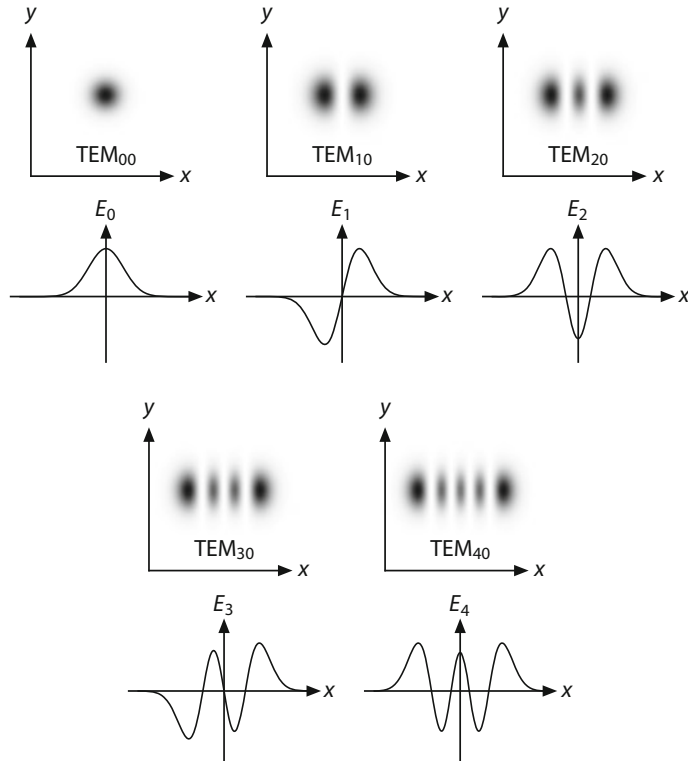


Fig. 11.4 Transverse intensity distribution and electric field $E(x)$ of different Hermite-Gaussian beams (TEM_{m0} modes). The field distribution along the y -axis is given by a Gaussian profile

Beam Radius and Divergence of Higher-Order Modes

Figure 11.4 reveals that higher-order modes extend over a broader range along the x -axis than the zero-order Gaussian mode. The distance x_m between the outermost maximum and the beam center can be approximated by

$$x_m \approx \sqrt{1+m} \cdot w_0, \quad (11.27)$$

where w_0 is the beam waist of the fundamental mode. A similar relation is found between the beam divergence of m th-order modes and the fundamental mode divergence θ :

$$\theta_m \approx \sqrt{1+m} \cdot \theta, \quad (11.28)$$

The increased divergence can be traced back to the modulation of the field along the x -direction which results in stronger diffraction.

11.3 Propagation of Gaussian Beams Through Lenses

The transformation of light rays traveling through lenses can be approximately described by the laws of geometrical optics. This approximation is especially suited when treating incoherent light sources where optical phenomena like interference and diffraction can often be neglected. On the contrary, diffraction effects play a major role in the propagation of laser beams, particularly Gaussian beams, due to their high coherence and limited beam diameter. Consequently, based on the laws of geometrical optics, modified transformation equations have to be formulated which are presented for Gaussian beams below.

Geometrical Optics

A lens or lens system is defined by its principal planes H and H' and its focal points F and F' , as illustrated in Fig. 11.5. If the same medium is present on both sides of the lens (e.g. air), the amount of the focal length f is the same on the object and image side. For thin lenses, the principal planes H and H' coincide with the lens center.

The following sign conventions have to be regarded for measuring distances during the formation of images by lenses: Distances from the respective principal planes are positive when measured in the direction of the incident rays (usually to

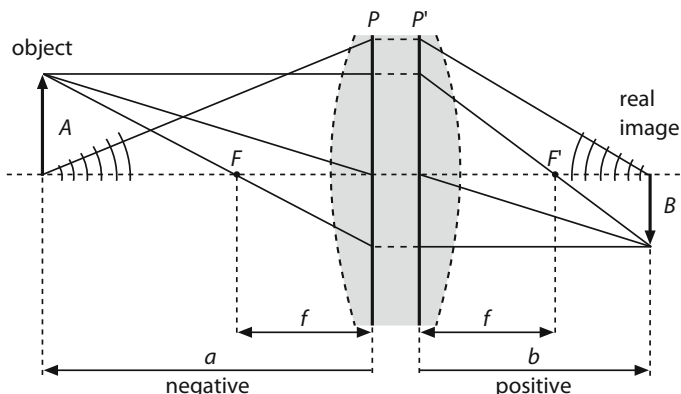


Fig. 11.5 Imaging with a thick lens according to geometrical optics. A : object, B : image, a : object distance, b : image distance, f : focal length, F, F' : focal points, P, P' : principal planes

the right, e.g. the image distance b), and negative when measured in the opposite direction (to the left, e.g. the object distance a). Likewise, the distances measured above the optic axis, e.g. the object size A , are positive, while those below the axis are negative, e.g. the image size B . In the latter case, the image is upside down.

The position and size of the image formed by a lens can be determined by the lens equation:

$$\boxed{\frac{1}{f} = \frac{1}{b} - \frac{1}{a}} \quad \text{or} \quad \boxed{\frac{1}{b} = \frac{1}{a} + \frac{1}{f}}. \quad (11.29)$$

The magnification of the lens is given by

$$\boxed{\beta = B/A = b/a}. \quad (11.30)$$

The relationship (11.29) can be proven by assuming that a spherical wave emerges from each point of the object. The radius of curvature of the wave belonging to a single point at the position of the (thin) lens is then $R_1 = -a$ (a is negative). The radius of curvature of the spherical wave directly behind the lens is $R_2 = -b$, where the negative sign is introduced as radii R are defined as positive for convex wave fronts (R_1) and negative for concave wave fronts (R_2).

Transformation of Gaussian Beams

Based on the lens equation derived from the laws of geometrical optics, the transformation of a Gaussian beam passing through a lens can be described. For this purpose, a beam with waist w_0 at a distance a from the lens being incident from the left is considered. The corresponding parameters of the transformed Gaussian beam behind the lens a' and w'_0 are determined in the following. Note that the distances measured from the beam waist towards the right are positive and negative to the left.

Starting from the conventional lens equation, the object and image distance in Fig. 11.5 are replaced by the radii of curvature $R_1 = -a$ and $R_2 = -b$ of the incident and transmitted spherical waves, respectively:

$$\frac{1}{R_2} = \frac{1}{R_1} - \frac{1}{f}. \quad (11.31)$$

The radii are positive for convex and negative for concave wave fronts, observed from the position of the lens. Since the radius w directly before and behind a (thin) lens is maintained for a Gaussian beam and according to (11.10), the above relation is transformed to

$$\frac{1}{q_2} = \frac{1}{q_1} - \frac{1}{f}. \quad (11.32)$$

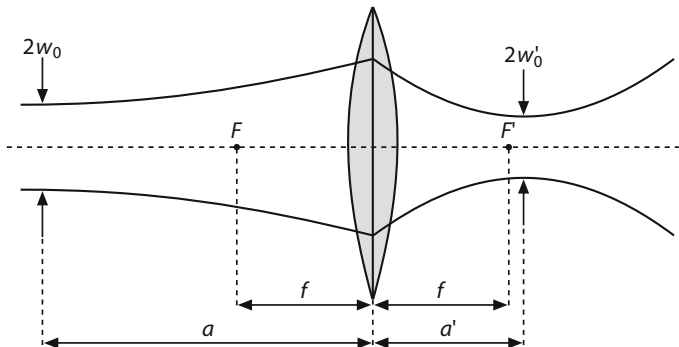


Fig. 11.6 Transformation of a Gaussian beam when propagating through a lens

The complex beam parameters q_1 and q_2 before and behind the lens follow from the respective Rayleigh lengths z_R , z'_R and beam waists w_0 , w'_0 under consideration of (11.7):

$$q_1 = a + i z_R, \quad q_2 = a' + i z'_R. \quad (11.33)$$

From (11.32) and (11.33), the beam parameters of the transformed Gaussian beam, as shown in Fig. 11.6, can be derived:

$$a' = -f + \frac{f^2(f-a)}{(f-a)^2 + z_R^2} \quad \text{and} \quad (11.34)$$

$$w'_0 = w_0 f / \sqrt{(a-f)^2 + z_R^2} \quad \text{with } z_R = \frac{\pi w_0^2}{\lambda}. \quad (11.35)$$

If the Rayleigh length is small compared to the distance $a - f$, the usual lens equation according to geometrical optics (11.29) is obtained. An interesting special case occurs when the beam waist of the incident beam coincides with the focal plane of the lens, i.e. $a = f$. In this case, $a' = -f$ and $w'_0 = \lambda f / \pi w_0$. Hence, the beam waist of the transmitted beam is located at the focal plane of the lens.

Focusing of Gaussian Beams

The minimum beam radius of transformed Gaussian beams has already been introduced in the context of fiber coupling of diode lasers, (10.4), in Sect. 10.3. Here, like in many other laser applications, it is crucial to focus the laser beam to a small spot with radius w'_0 . For this purpose, the Rayleigh length z_R , and hence w_0 should be as large as possible:

$$w'_0 = \frac{\lambda f}{\pi w_o}. \quad (11.36)$$

This equation is commonly used to determine the minimum beam radius w'_0 when focusing the beam by means of a lens, while assuming that $z_R \gg a - f$. Moreover, the diameter of the incident beam $2w_0$ has to be smaller than the lens diameter D to avoid clipping of the beam. The focus diameter is hence given by

$$\boxed{2w'_0 \geq \frac{4\lambda f}{\pi D}}. \quad (11.37)$$

Consequently, large incident beam and lens diameters are required to obtain small spot sizes of the focused beam. In practice, e.g. in material processing applications, laser beams are expanded before being focused to minimize the focus diameter. Since the focal length f of a bi-convex lens corresponds to its radius of curvature and is thus larger than its diameter, the smallest spot diameters that can be reached are on the order of the laser wavelength: $w'_0 \geq 2\lambda/\pi$. The confocal parameter or depth of focus $2z_R$ which represents another important parameter in the context of laser focusing can be calculated according to (11.15).

11.4 Telescopes and Spatial Frequency Filters

Expansion of laser beams is achieved by means of telescopes and involves a reduction in divergence which is relevant for the transmission of laser light over long distances.

Kepler Telescope

The Kepler telescope consists of a lens with short focal length f_1 (eyepiece) and a second lens with longer focal length f_2 that is referred to as objective (top figure in Fig. 11.7). The focal points of both lenses coincide in case the telescope is focused at infinity. After passing the telescope the diameter of an incident collimated beam is expanded from d to D , where the magnification follows from the laws of geometrical optics:

$$\boxed{D/d = f_2/f_1}. \quad (11.38)$$

In a more detailed treatment of the beam expansion, the wave nature of the light has to be considered. The situation for a Gaussian beam is depicted in Fig. 11.8. The original beam waist w_{01} is imaged by lens 1, leading to a second beam waist $w'_{01} = w_{02}$ slightly outside of the focal plane of this lens. The objective expands the

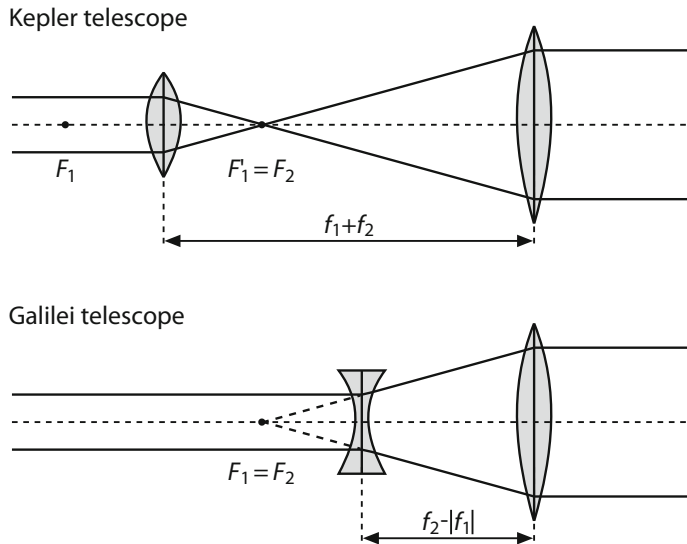


Fig. 11.7 Geometrical ray paths in a Kepler (top) and a Galilei telescope (bottom)

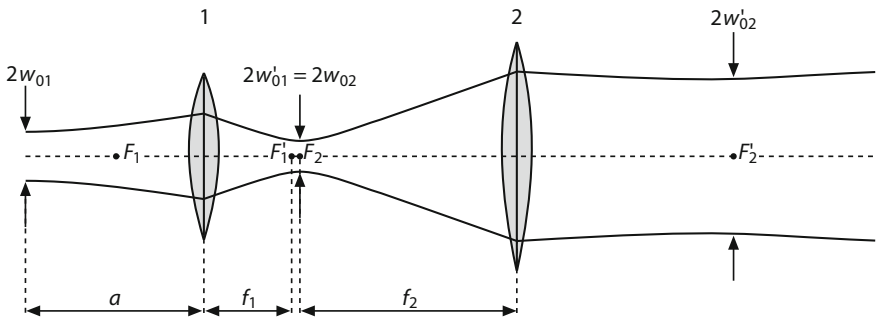


Fig. 11.8 Beam expansion of a Gaussian beam

beam to the radius w'_{02} which becomes maximal when the intermediate beam waist $w'_{01} = w_{02}$ falls into its focal plane. The expanded beam waist is then located in the right-side focal plane of the objective. Using the transformation equations for Gaussian beams, the expanded beam waist is

$$w'_{02} = w_{01} \frac{f_2}{f_1} \sqrt{\left((a - f_1)^2 + z_{R_1}^2 \right) / z_{R_1}^2}. \quad (11.39)$$

In the case that the first lens is located such that the beam waist w_{01} falls into its focal plane F_1 , and if additionally $F'_1 = F_2$, the equation is simplified to the relationship derived from geometrical optics [(11.38), Fig. 11.7]:

$$w'_{02} = w_{01} \cdot f_2/f_1 \quad \text{for } a = f_1. \quad (11.40)$$

As the beam radius is expanded, the divergence angle is reduced accordingly:

$$\boxed{\theta_2 = \theta_1 \cdot f_1/f_2.} \quad (11.41)$$

Galilei Telescope

Beam expansion using a Kepler telescope involves focusing of the radiation by the first lens which can lead to very high fluences and thus detrimental optical breakdown in the air. Hence, especially for high-power lasers, a Galilei telescope is favorable, as the beam expansion is realized by a concave lens with negative focal length, as shown in the bottom figure of Fig. 11.7. In case of coincidence of the two lenses' focal planes, (11.40) and (11.41) of the Kepler telescope apply, where f_1 has to be substituted by $|f_1|$.

Spatial Filter

The field distribution of real laser beams is often not given by the ideal fundamental transverse mode TEM_{00} . Instead, dust along the laser beam path and damage on optical components causes distortions and thus a modulation of the field distribution across the beam profile, as depicted in Fig. 11.9. A beam “cleanup” can be accomplished by using a spatial filter that consists of a focusing lens and a small aperture placed in the right-side focal plane of the lens. The diameter of the aperture is chosen to be slightly bigger than the focus diameter of the laser beam after propagation through the focusing lens. In this way, the Gaussian beam passes the aperture nearly without obstruction, whereas spherical waves, e.g. originating from

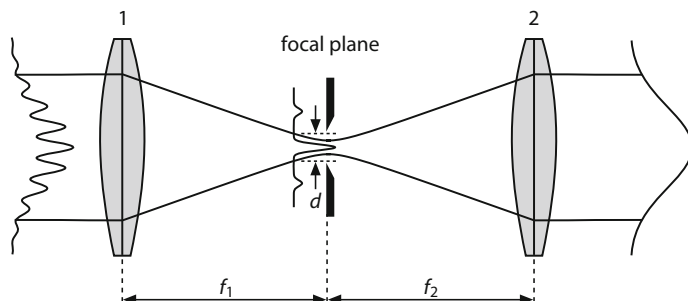


Fig. 11.9 Principle of a spatial filter

scattering from dust particles, are spatially separated from the Gaussian beam and hence blocked by the aperture. As a result, beam aberrations are filtered out of the transverse intensity profile of the beam. In many laser systems, it is convenient to integrate a spatial filter in a Kepler beam expander.

A more comprehensive description of the operating principle of a spatial filter is based on Fourier optics. It can be shown that the transverse intensity profile of the laser in the focal plane of the lens is the Fourier transform of the initial beam's intensity distribution. The central part of the profile corresponds to the ideal Gaussian beam, while outer parts of the profile correspond to contributions with higher spatial frequency arising from the distortions along the beam path. Thus, spatial filters are sometimes also called low-pass filters.

The diameter of the aperture d has to be larger than the beam waist of the ideal Gaussian beam to avoid undesired attenuation:

$$d > 2\lambda f / \pi w, \quad (11.42)$$

where w is the radius of the incident beam. On the other hand, d should be small enough to effectively block the side-lobes. This condition is met when d is smaller than the so-called first Fresnel zone:

$$d < 2\sqrt{\lambda f}. \quad (11.43)$$

In practice, the diameter is usually chosen as large as possible to facilitate the alignment. Typical values for spatial filters employed in holography are around $d \approx 40 \mu\text{m}$, when a microscope objective with a focal length of $f = 4 \text{ mm}$ is used.

11.5 Propagation of Multimode, Real Laser Beams

Most real laser beams are not perfect, i.e. diffraction-limited, Gaussian beams as described in the previous sections, but show intensity distributions that differ from the TEM_{00} mode profile. The reason can be the oscillation of higher-order transverse modes, amplitude and phase distortions due to an inhomogeneous gain distribution in the laser medium or the formation and superposition of partial beams. Hence, the formulas in the previous sections associated with the propagation of Gaussian beams are not applicable for non-diffraction limited beams. However, the relationships can be transferred by introducing the beam quality factor M^2 .

Beam Parameter Product and Beam Quality Factor

The propagation of an ideal Gaussian beam is determined by its beam waist radius w_0 and the wavelength λ . In the far-field of the beam, i.e. at large distances from the

beam waist, the beam radius grows approximately linearly and the divergence angle (half-angle) is given by (11.18)

$$\boxed{\theta = \frac{\lambda}{\pi w_0}.} \quad (11.44)$$

For quantifying the quality of laser beams, the beam parameter product (BPP) is commonly used in laser physics, as it is invariant under beam transformations, e.g. by lenses. It is defined as the product of the divergence angle and the beam waist radius:

$$\text{BPP} = \theta \cdot w_0. \quad (11.45)$$

The beam parameter product is given in the unit $\text{mm} \cdot \text{rad}$ and only depends on the wavelength for Gaussian beams: $\text{BPP} = \lambda/\pi$.

For real laser beams, the above-mentioned effects lead to deviations of the laser beam profile from the ideal Gaussian profile. This involves an increase both in the beam radius and the divergence angle by a factor of M . Hence, the beam parameter product reads

$$\theta \cdot w_0 = M^2 \frac{\lambda}{\pi}. \quad (11.46)$$

The parameter M^2 is called beam quality factor or beam propagation factor. It is minimal for Gaussian beams ($M^2 = 1$) and larger for real laser beams ($M^2 > 1$). Consequently, this quantity describes to what extent a laser beam deviates from an ideal TEM_{00} beam, as illustrated in Fig. 11.10. The figure compares the propagation characteristics of a diffraction-limited beam with that of a real laser beam with non-diffraction-limited beam quality, while assuming equal position and size of the beam waist. A different picture is obtained when comparing two collimated beams

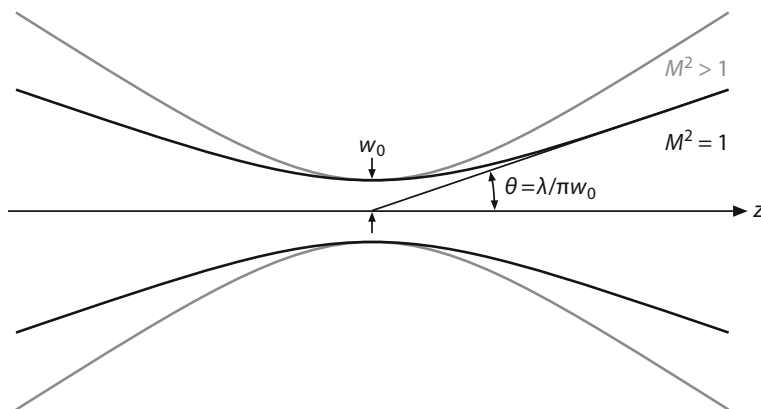


Fig. 11.10 Propagation of a diffraction-limited Gaussian beam with $M^2 = 1$ and a non-diffraction-limited beam with $M^2 > 1$ having the same beam waist diameter

with equal beam diameter D , but different M^2 , that are focused by the same lens (focal length f). The beam with the larger M^2 is focused to a larger beam waist and has higher divergence. This leads to a modification of (11.37) determining the smallest spot size of a focused laser beam:

$$\boxed{2w'_0 \geq M^2 \cdot \frac{4\lambda f}{\pi D}} \quad (11.47)$$

Hence, the smallest possible focus diameter scales with the beam quality factor M^2 .

Measurement of the Beam Quality Factor

The M^2 factor can be calculated from the measured evolution of the beam radius along the propagation direction. For this purpose, the laser beam is focused by a lens to form a so-called caustic, as depicted in Fig. 11.10. Then, according to a procedure defined by the ISO Standard 11146, the beam radius has to be determined at least at ten positions along the propagation axis z , where half of the data points should be within the Rayleigh length z_R on both sides of the beam waist. Fitting of the spatial evolution of the beam radius along the caustic $w(z)$ yields the beam waist w_0 and the divergence angle θ , so that the beam quality factor can be calculated:

$$\boxed{M^2 = w_0 \theta \frac{\pi}{\lambda}} \quad (11.48)$$

For obtaining correct results, several rules have to be followed, most importantly concerning the exact definition of the beam radius.

Definition of the Beam Radius

According to the ISO Standard 11146, the beam radius is defined by so-called moments of the spatial intensity profile. Here, a Cartesian coordinate system (x, y, z) is considered with z being the propagation direction. The first-order moments $\langle x(z) \rangle$ and $\langle y(z) \rangle$ describe the beam center which is also referred to as the beam's center of gravity:

$$\langle x(z) \rangle = \frac{\iint x \cdot I(x, y, z) dx dy}{\iint I(x, y, z) dx dy} \quad \text{and} \quad \langle y(z) \rangle = \frac{\iint y \cdot I(x, y, z) dx dy}{\iint I(x, y, z) dx dy}. \quad (11.49)$$

Calculation of the second-order moments

$$\begin{aligned}\langle x^2(z) \rangle &= \frac{\iint (x - \langle x \rangle)^2 \cdot I(x, y, z) dx dy}{\iint I(x, y, z) dx dy} \quad \text{and} \\ \langle y^2(z) \rangle &= \frac{\iint (y - \langle y \rangle)^2 \cdot I(x, y, z) dx dy}{\iint I(x, y, z) dx dy}\end{aligned}\quad (11.50)$$

produces the variances of the intensity distribution, while the square roots $\sqrt{\langle x^2(z) \rangle}$ and $\sqrt{\langle y^2(z) \rangle}$ are known as standard deviations.

The beam radius is then defined as twice the standard deviation σ :

$$w_x = 2\sigma_x = 2\sqrt{\langle x^2(z) \rangle} \quad \text{and} \quad w_y = 2\sigma_y = 2\sqrt{\langle y^2(z) \rangle}. \quad (11.51)$$

For the rotation-symmetric TEM₀₀ mode, the two radii are equal: $w_x = w_y$ and correspond to common definition as the distance from the beam center at which the intensity has fallen to $1/e^2 \approx 13.5\%$ of its peak value. The diameter $2w_{x,y}$ is also denoted as D4 σ width.

Laser Beams with $M^2 > 1$

The ISO Standard 11146 procedure allows for the determination of the M^2 factor for various Hermite-Gaussian or Laguerre-Gaussian beams (Sect. 12.2). For TEM _{m,n} beams with $m = 0, 1, 2, \dots$ and $n = 0, 1, 2, \dots$ the beam quality factors in x - and y -direction are given by

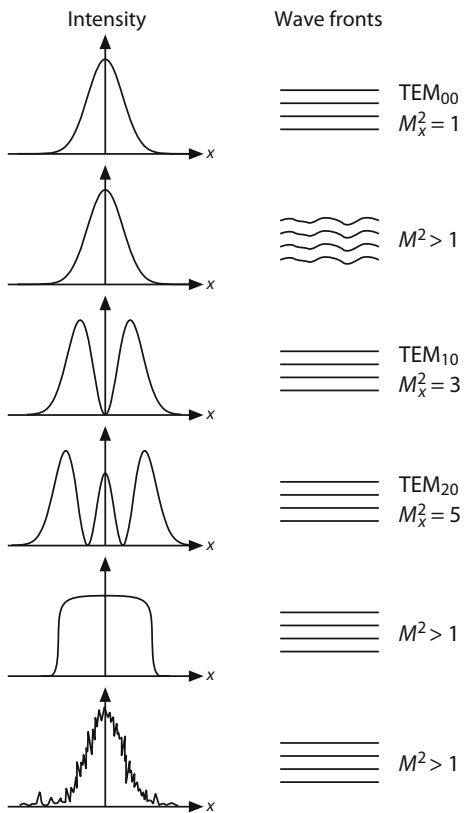
$$M_x^2 = 2m + 1 \quad \text{and} \quad M_y^2 = 2n + 1. \quad (11.52)$$

The intensity distributions of several TEM _{$m,0$} modes together with possible wave front profiles and the corresponding M_x^2 values are shown in Fig. 11.11. For undisturbed TEM _{$m,0$} beams, the wave fronts are plane at the beam waist. However, distortions of Gaussian-like beam profiles can occur, resulting in beam quality factors $M^2 > 1$.

Beam Profilers

Calculation of the beam radii according to (11.51) requires the knowledge of the two-dimensional intensity distribution of the laser $I(x, y, z)$ which can be attained by means of electronic cameras. There are commercially available beam profilers, e.g. from Ophir-Spiricon, which automatically perform beam quality measurements in short time. The systems incorporate both the hardware (focusing lens, translation

Fig. 11.11 Various beam profiles (transverse modes TEM_{m0} and other intensity distributions), wave fronts and corresponding beam quality factors M^2



stage, camera) for detecting the beam profile at different positions along the caustic and the software for calculating the beam parameters.

At high laser powers or at wavelengths where cameras are not available, the intensity distribution $I(x, y, z)$ is determined by scanning the beam profile with an aperture, slit or a knife edge, as explained in the following section. Alternative methods for quantifying the beam quality are based on wave front sensors, e.g. Shack–Hartmann sensors, which provide characterization of the spatial beam parameters from a measurement at only one position of the caustic.

Variable Aperture and Moving Slit Method

Apart from the determination of the beam radius via the second-order moments of the intensity profile, the ISO Standard 11146 provides three other simpler approaches for quantifying the beam radius. They are based on transmission measurements where one of the following objects is placed into the laser beam: a variable aperture, a moving slit or a moving edge.

The circular aperture with variable diameter allows the characterization of radial-symmetric intensity distributions. For this purpose, the aperture is placed in the center of the beam and the transmitted power is measured as the diameter is gradually increased. In case of a Gaussian beam, the aperture diameter is equal to the beam diameter, if 86.5% of the total laser power is transmitted. Using this relationship, the beam diameter of arbitrary intensity distributions can be defined. When a moving slit is employed, it is first placed such that the transmission is maximal. The slit whose width should be larger than 1/20 of the beam diameter is then laterally translated across the beam. The distance between the two positions at which the transmission through the slit is 13.5% of the total laser power defines the beam diameter. For beams with non-radially-symmetric intensity distributions, the procedure should be carried out along the two major axes. The moving edge technique is elaborated below, as it comparatively easy to perform.

Knife Edge Method

The edge method involves the translation of a knife edge, e.g. a razor blade, through the laser beam perpendicular to the propagation direction. The transmitted power of the clipped beam $T(x')$ is measured as a function of the razor position x' . Here, the area of the detector has to be large enough to also collect the diffracted radiation. The width of the beam is defined as the distance between the positions at which the transmission is 16% and 84%. In case of a Gaussian beam, the determined diameter corresponds to the $1/e^2$ -beam diameter of the intensity distribution.

For the case that the knife edge is pulled out of the beam, the transmission function $T(x')$ for a Gaussian beam with power P is given by

$$T(x') = \frac{1}{P} \int_{-\infty}^{x'} \int_{-\infty}^{+\infty} I(x, y) dx dy = \sqrt{\frac{2}{\pi}} \frac{2}{d} \int_{-\infty}^{x'} \frac{-2x^2}{w^2} dx = \frac{1}{2} \left[\operatorname{erf} \left(\sqrt{2} \frac{x'}{w} \right) + 1 \right]$$

with $I(x, y) = I_{\max} \exp \left[\frac{-2(x^2 + y^2)}{w^2} \right]$.

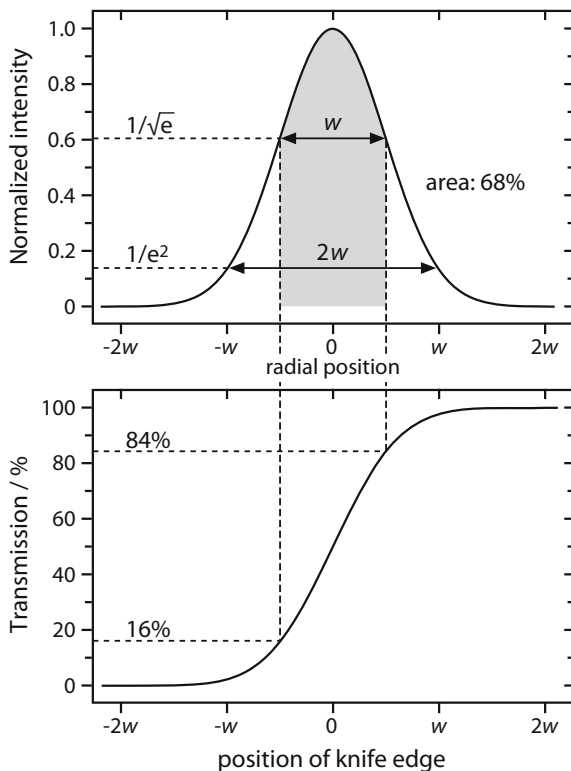
(11.53)

Evaluation of the error function yields

$$T\left(-\frac{w}{2}\right) \approx 0.16 \quad \text{and} \quad T\left(\frac{w}{2}\right) \approx 0.84. \quad (11.54)$$

The measurement of the beam radius according to (11.54) using the knife edge method is illustrated in Fig. 11.12. The razor is moved across the beam from the left to the right. Only for a Gaussian beam, the radius determined in this way is equal to the beam radius defined by the second-order moments in (11.49)–(11.51).

Fig. 11.12 Determination of the beam radius by the knife edge method. Top: radial intensity distribution of a Gaussian beam. Bottom: Transmission depending on the knife edge position. The $1/e^2$ -beam radius is given by the distance between the positions where 16% and 84% of the beam power are transmitted



It should be mentioned that the concept of the M^2 parameter has some limitations. First, the quantity can be difficult to be measured accurately. Background signals, e.g. from ambient light, can introduce large errors when measuring the M^2 factor based on the second moment method using a camera. Moreover, the M^2 of beams having an idealized rectangular (top-hat) intensity distribution is infinity, although this is not true of any physically realizable top-hat beam. For a pure Bessel beam, the beam quality factor cannot even be computed.

Brightness

The average power P and the beam quality of a laser source can be summarized in terms of the beam brightness L which describes the power per unit area and solid angle:

$$L = \frac{P}{A \cdot \Omega}. \quad (11.55)$$

For a given cross-sectional area at the beam waist, the solid angle is defined is determined by the M^2 factor and the radiation wavelength λ . Using $\Omega = \theta \pi$, the brightness can be expressed as

$$\boxed{L = \frac{P}{\lambda^2 (M^2)^2}} \quad (11.56)$$

Due to the quadratic dependence of the brightness on the beam quality factor M^2 , commercial lasers operating in transverse multimode ($M^2 > 30$) have comparatively low brightness, despite high average powers of several kW. In contrast, laser sources with nearly diffraction-limited beam quality and a few hundred watts of output power provide considerably higher brightness.

Further Reading

1. G.A.Reider, *Photonics: An Introduction* (Springer, 2016)
2. C. Velzel, *A Course in Lens Design* (Springer, 2014)
3. G. Laufer, *Intro Optics Lasers in Engineering* (Cambridge University Press, 2008)
4. M. Gu, *Advanced Optical Imaging Theory* (Springer, 2000)

Chapter 12

Optical Resonators



The transverse intensity distribution of a gas and solid-state laser beam is determined by the shape of the gain material as well as by the position and curvature of the mirrors forming the optical resonator. Light oscillating between the mirrors creates standing-waves corresponding to self-reproducing spatial distributions of the electric field. These discrete field distributions are called transverse electromagnetic modes of the optical resonator which are designated in the form TEM_{mnq} . The integers m and n denote the number of nodes of the field distribution in a rectangular or polar coordinate system perpendicular to the axis of the laser cavity, while q equals the number of field maxima between the mirrors along the cavity axis. Hence, laser modes with different q values are referred to as longitudinal (or axial) modes and differ in laser frequency. In case only the transverse field distribution is of interest, q is omitted in the mode designation and the intensity distribution across the laser beam is described by the term TEM_{nm} .

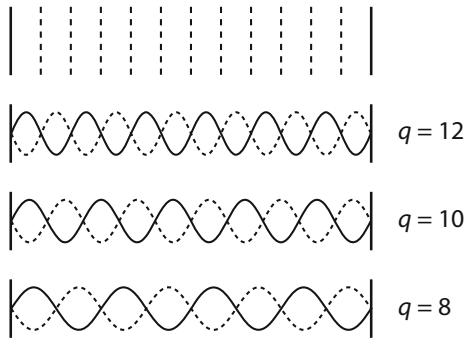
12.1 Plane-Mirror Resonators

The classic Fabry-Pérot resonator is formed by two plane-parallel mirrors and was for instance applied in the first ruby laser. In laser diodes, this scheme is realized by the two end-facets of the semiconductor chip which delimit the active zone. Fabry-Pérot resonators are also employed as interferometers or as etalons (Sect. 18.5).

Longitudinal Modes

When light bounces back and forth between the mirrors of an optical (laser) resonator, the superposition of the counterpropagating waves leads to the formation of a standing-wave pattern in the optical cavity which is associated to longitudinal (or

Fig. 12.1 Phase fronts (top) and electric field distributions of longitudinal modes (bottom) in a Fabry-Pérot resonator



axial) modes, as illustrated in Fig. 12.1. The allowed modes of the cavity are those where the mirror separation, i.e. the optical resonator length L , is equal to an exact multiple of half the wavelength $\lambda_q/2$:

$$\boxed{L = q \frac{\lambda_q}{2}}, \quad \text{with } q = 1, 2, 3, \dots \quad (12.1)$$

The radiation frequency $f_q = c/\lambda_q$ is hence given by

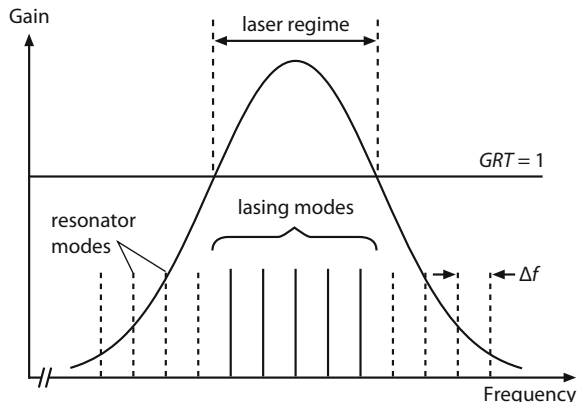
$$f_q = q \frac{c}{2L} \quad (12.2)$$

and the spacing between two adjacent longitudinal modes is

$$\boxed{\Delta f = f_q - f_{q-1} = \frac{c}{2L}}. \quad (12.3)$$

A portion of the frequency spectrum of an optical resonator with equidistant longitudinal modes is shown in Fig. 12.2 together with the gain spectrum $G(f)$ of a laser which is determined by the line shape of the laser transition and broadening

Fig. 12.2 Gain spectrum $G(f)$ and longitudinal modes of a laser



mechanisms (see Sect. 2.4). In a laser, only those modes for which the threshold condition $GRT \geq 1$ (2.27) is fulfilled, will oscillate. If the frequency-dependence of the mirror reflectance R and the transmission factor T are small, the range for which $GRT \geq 1$ is approximately given by the laser linewidth. For a He–Ne laser with a resonator length of $L = 30$ cm and a linewidth of $\Delta f_L = 1.5$ GHz, three longitudinal modes reach the laser threshold and thus simultaneously oscillate in the cavity: $\Delta f_L/\Delta f = 3$. In contrast, about 700 modes exist in a ruby laser of the same length but broader linewidth of $\Delta f_L = 330$ GHz.

The optical resonator length usually fluctuates due to mechanical vibrations, temperature and pressure variations or changes in the refractive index of the laser medium. Consequently, the frequency f of a laser mode is not constant, but varies over time, thus limiting the laser frequency stability to hundreds of MHz or even GHz. The frequency fluctuations can be diminished by active stabilization of the resonator length (Sect. 20.2). For instance, variations as low as $\Delta f' = 1$ MHz are achieved. For a 0.5 m-long resonator and a laser frequency of $f \approx 5 \times 10^{14}$ Hz, this frequency stability corresponds to a length stability $\Delta L = L \cdot |\Delta f'|/f < 1$ nm.

Resonator Losses

The excitation of standing-waves is also possible, if the light frequency does not exactly match the resonance frequency f_q of the optical resonator. The losses δ of the mode in the resonator can be expressed in terms of the resonator losses which can be split into reflection (R), absorption (A) and diffraction (D) losses:

$$\boxed{\delta = \delta_R + \delta_A + \delta_D}. \quad (12.4)$$

The losses upon reflection from the resonator mirrors are related to the mirror reflectance R :

$$\delta_R = 1 - R, \quad (12.5)$$

while the absorption losses are given by

$$\delta_A = 1 - e^{-L\alpha} \approx L\alpha. \quad (12.6)$$

Here, α is the absorption coefficient of the material between the resonator mirrors and L is the length of the material. The diffraction losses δ_D vanish for mirrors extending to infinity. For finite mirrors, δ_D denotes the ratio between the power of a wave traveling past the mirror with $R = 1$ and the incident power of a wave oscillating inside the resonator.

The total losses are related to a finite width (FWHM) of the mode as follows:

$$\boxed{df = \frac{c\delta}{2\pi L} = \frac{f}{Q}}, \quad (12.7)$$

where Q is the quality, or simply the “ Q ”, of the cavity and c is the speed of light. The finesse F describes the ratio of the mode spacing Δf and the FWHM df of the mode:

$$\boxed{F = \frac{\Delta f}{df} = \frac{\pi}{\delta}}. \quad (12.8)$$

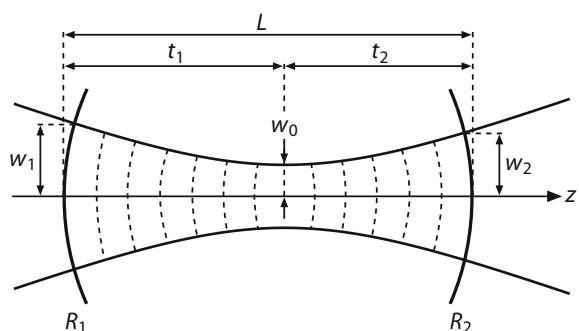
This relationship is, amongst others, important for the characterization of etalons used for frequency selection in lasers (Sect. 18.5). δ is in most cases dominated by the reflection losses so that only the mirror reflectances are considered for calculating the finesse.

12.2 Spherical-Mirror Resonators

Standing-wave laser resonators are mostly built with spherical mirrors, as outlined in Sect. 12.3. The field distributions formed in such resonators correspond to the Hermite-Gaussian modes that were discussed in Sect. 11.2. The fundamental mode TEM_{00} is fully determined by the position of the beam waist and its waist radius w_0 (see Fig. 12.3). The associated Gaussian beam generated in a spherical-mirror resonator is governed by the radii of curvature R_1 and R_2 of the two mirrors, as the curvature of the wave fronts at the position of the mirrors is adapted to the mirror surfaces. Note that the same holds true for plane-mirror resonators with infinitely large mirrors, where the fundamental mode is a plane wave, so that the infinite radius of curvature of the wave fronts corresponds to that of the mirror surfaces.

The radii w_1 and w_2 of the field distributions at the position of the mirrors can be calculated from the mirror curvatures R_1 and R_2 and the mirror spacing L using the complex beam parameters introduced in (11.10):

Fig. 12.3 Adaptation of a Gaussian beam to a spherical-mirror resonator



$$\frac{1}{q_1} = \frac{1}{R_1} - \frac{i\lambda}{\pi w_1^2} \quad \text{and} \quad \frac{1}{q_2} = \frac{1}{R_2} - \frac{i\lambda}{\pi w_2^2}. \quad (12.9)$$

R_1 and R_2 are positive, if the concave surface of the mirror faces the inner side of the resonator, and negative otherwise. According to (11.7), the beam parameters are connected by

$$q_2 = q_1 + L. \quad (12.10)$$

Elimination of the q -parameters leads to a complex equation which can be separated into real and imaginary part. Solving these equations yields the beam (or mode) radius at the first mirror

$$w_1^4 = \left(\frac{\lambda R_1}{\pi} \right)^2 \frac{R_2 - L}{R_1 - L} \left(\frac{L}{R_1 + R_2 - L} \right). \quad (12.11)$$

The beam radius w_2 at the other mirror is obtained by switching the indices 1 and 2. Instead of using the curvature radii, the so-called g -parameters are commonly employed for characterizing spherical mirrors:

$$g_1 = 1 - L/R_1 \quad \text{and} \quad g_2 = 1 - L/R_2. \quad (12.12)$$

Hence, the mode radius w_1 reads

$$w_1^4 = \left(\frac{\lambda L}{\pi} \right)^2 \frac{g_2}{g_1 - g_1^2 g_2}. \quad (12.13)$$

Similarly, the radius of the Gaussian beam at the beam waist inside the resonator can be derived considering that the phase fronts are plane at this position ($R_0 = \infty$):

$$w_0^4 = \left(\frac{\lambda L}{\pi} \right)^2 \frac{g_1 g_2 (1 - g_1 g_2)}{(g_1 + g_2 - 2g_1 g_2)^2}. \quad (12.14)$$

This equation has purely real solutions for $0 \leq g_1 g_2 \leq 1$. Outside of this region, the resonator is not stable, as discussed in detail in Sect. 12.3. The specification of a commercial laser often includes both the beam radius w_1 or w_2 at the end mirror and the divergence angle θ . The latter can be calculated from the beam waist radius w_0 using (11.18) for a diffraction-limited beam. In the general case of a non-diffraction-limited beam, the beam quality factor M^2 according to (11.48) has to be taken into account. In addition, the potential lensing effect of the output coupler must be considered.

The position of the beam waist is given by

$$t_1 = \frac{L(R_2 - L)}{R_1 + R_2 - 2L} = \frac{g_2(1 - g_1)L}{g_1 + g_2 - 2g_1 g_2}, \quad t_2 = L - t_1. \quad (12.15)$$

Fundamental and Higher-Order Modes

The fundamental transverse mode TEM_{00} is characterized by a Gaussian intensity distribution across the beam. In contrast, higher-order modes feature more complex intensity distributions with nodes perpendicular to the beam direction. The electric fields and, in turn, the intensity distributions of TEM_{mn} modes in an optical resonator can be regarded as solutions of the wave equation, as presented in Sect. 11.1, and depend of the shape of the mirrors. In case of a rectangular geometry, the indices m and n equal the number of nodes in x - and y -direction, respectively. If circular mirrors are used, the integers denote the number of nodes in radial (r) and azimuthal (φ) direction (polar coordinates). Here, p and l are often used as indices instead of m and n . The shapes of the transverse modes do not depend on the longitudinal mode index q .

A laser is expected to oscillate in the fundamental TEM_{00} mode if the average diameter $2w$ matches the diameter of the active material, e.g. a solid-state laser rod. In case the material diameter is larger, higher-order modes additionally oscillate. A specific mode can be selected, e.g. by arranging a thin wire into an intensity minimum of the desired mode. Oscillation of the fundamental mode can be ensured by inserting a circular aperture into the laser resonator.

The intensity distribution patterns of different TEM_{mn} modes for rectangular mirrors are depicted in Fig. 12.4. In accordance to (11.24), they are (in the two-dimensional case) given by the Hermite polynomials of degree m and n (see Sect. 11.2).

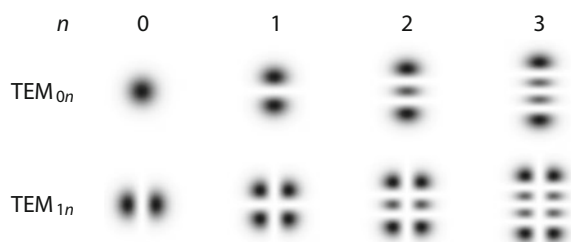
$$I_{mn}(x, y) \sim H_n^2(\xi) H_m^2(\eta) \exp(-(\xi^2 + \eta^2)). \quad (12.16)$$

The reduced coordinates $\xi = x\sqrt{2}/w$ and $\eta = y\sqrt{2}/w$ are defined by (11.26) for the two spatial dimensions across the beam. They are related to the effective mode radius of the TEM_{00} mode (Fig. 11.3).

In circular geometry, the intensity distributions I_{pl} of the TEM_{pl} modes are described by

$$I_{pl}(r, \varphi) = I_0 \rho^l \left(L_p^l(\rho) \right)^2 \cos^2(l\varphi) \exp(-\rho) \quad \text{with } \rho = 2r^2/w^2. \quad (12.17)$$

Fig. 12.4 Intensity distributions of different transverse (TEM_{mn}) modes in a rectangular geometry



The fundamental mode distribution I_{00} corresponds to the Gaussian profile with the beam radius w . $L_p^0(\rho)$ are the generalized Laguerre polynomials. The first three polynomials are

$$L_0^l(\rho) = 1, \quad L_1^0(\rho) = 1 - \rho, \quad L_2^0(\rho) = 1 - 2\rho + \frac{\rho^2}{2}. \quad (12.18)$$

The fundamental mode distribution I_{00} again corresponds to the Gaussian profile with the beam radius w . The intensity distributions of cylindrical modes TEM_{00} , TEM_{10} and TEM_{01}^* are depicted in Fig. 12.5. The asterisk indicates that the mode results from the superposition of two degenerate modes, TEM_{01} and TEM_{10} , one rotated by 90° about its axis relative to the other, thus forming a composite intensity distribution of circular symmetry, the so-called “donut mode”. Figure 12.6 shows the superposition of various transverse modes, as it occurs in lasers without transverse mode selection with zero intensity in the center. Laguerre-Gaussian beams are generated in resonators with cylindrical geometry.

A more detailed treatment of optical resonators shows that the frequencies of the modes depend not only on the longitudinal mode number q , but also on the transverse mode numbers m and n . In spherical-mirror resonators, the “resonator length” is shortened with increasing distance from the cavity axis, leading to a higher frequency of the higher-order modes.

Fig. 12.5 **a** Radial intensity distribution of the TEM_{00} , TEM_{10} and TEM_{01}^* modes. The radii are normalized to the beam radius of the fundamental mode. **b** Intensity distributions of selected cylindrical transverse modes

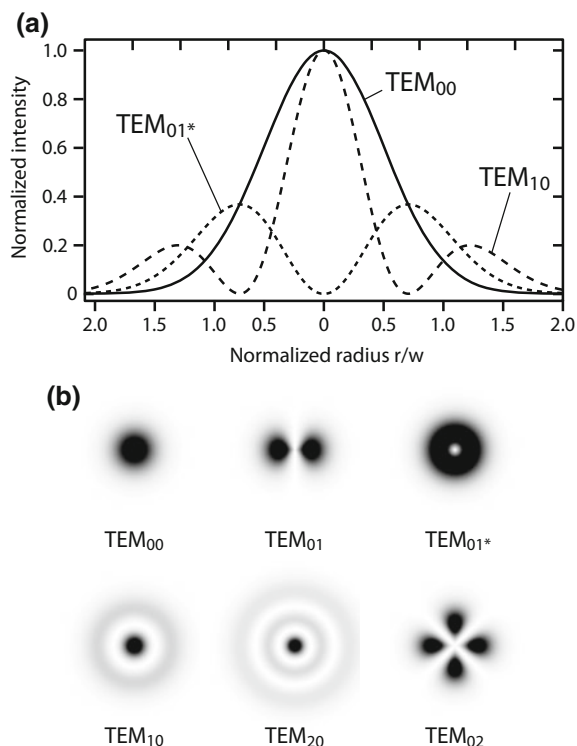
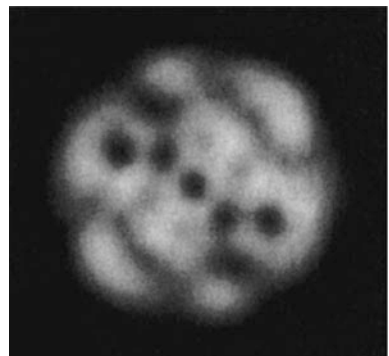


Fig. 12.6 Superposition of various transverse modes in a laser without mode selection. The diameter of the active laser material is much larger than the fundamental mode diameter. Then, it is also possible that a laser beam with a statistical intensity distribution with a Gaussian or top-hat average is generated



12.3 Resonator Configurations and Stability

In the following, different linear resonator configurations which are commonly used in practice are presented. Such optical resonators are characterized by the radii of curvature R_1 and R_2 of the two mirrors and their distance L (Fig. 12.7). The beam radii w_1 and w_2 of the TEM_{00} mode at the mirror surfaces can be calculated from (12.11), while the mode radius at the beam waist is given by (12.14).

Symmetric resonators are formed by mirrors with equal radii of curvature: $R = R_1 = R_2$, as shown in Fig. 12.7. For this special case, the mode radii at the mirrors surfaces read

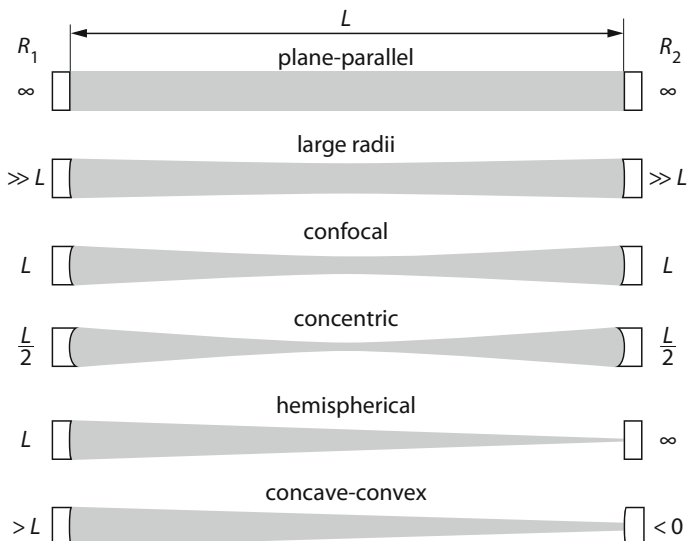


Fig. 12.7 Types of stable resonator configurations

$$w_1^2 = w_2^2 = \frac{\lambda R}{\pi} \sqrt{\frac{L}{2R - L}} \quad (12.19)$$

and the beam waist is located at the midpoint of the resonator with a beam radius of

$$w_0^2 = \frac{\lambda}{2\pi} \sqrt{L(2R - L)}. \quad (12.20)$$

For symmetric resonators with very large mirror curvatures ($R \gg L$), the mode radii are

$$w_1^2 \approx w_2^2 \approx w_0^2 \approx \frac{\lambda}{\pi} \sqrt{\frac{RL}{2}}. \quad (12.21)$$

Hence, the beam radius is nearly constant along the cavity. The frequency spacing of large-radius resonators is composed of longitudinal modes spaced by $\Delta f = c/2L$ that are each surrounded by a set of closely spaced transverse modes.

The *symmetric confocal resonator* is defined by the condition $R_1 = R_2 = R = L = 2f$. Here, the focal points of the two mirrors with focal length $f = R/2$ coincide at the midpoint of the cavity. For a given length L , the beam radii w_1 and w_2 are minimal compared to other resonator schemes:

$$w_1 = w_2 = \lambda L / \pi \quad \text{and} \quad w_0 = w_1 / \sqrt{2}. \quad (12.22)$$

In case multiple longitudinal and transverse modes are oscillating in the cavity, the frequency spectrum is characterized by a series of lines according to

$$f_{mnq} = (2q + m + n + 1)c/4L. \quad (12.23)$$

Consequently, all modes meeting the condition $2q + m + n + 1 = k$, where k is an integer, oscillate at the same frequency $kc/4L$. This means that the confocal resonator exhibits frequency degeneracy.

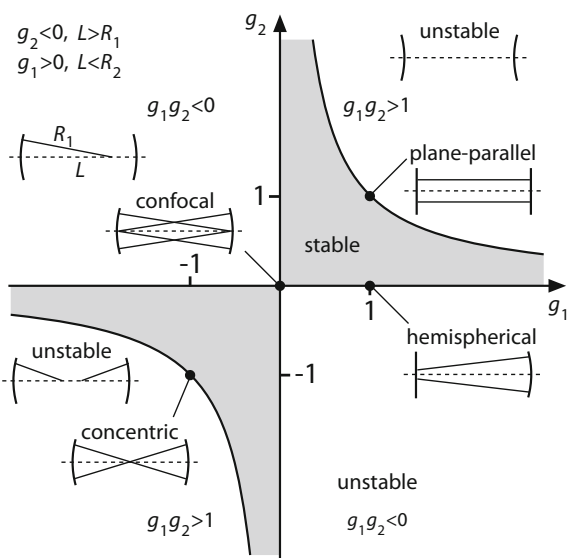
Confocal resonators can also comprise mirrors with different curvature radii. In this case, the resonator length is given by

$$R_1/2 + R_2/2 = f_1 + f_2 = L. \quad (12.24)$$

Asymmetric confocal resonators feature g -parameters g_1 and g_2 with different sign, i.e. $g_1 \cdot g_2 < 0$. Such resonators lie outside of the shaded region of the stability diagram (Fig. 12.8) and are thus unstable. The stability diagram will be introduced in the next section.

The *concentric resonator* is described by the condition $R_1 = R_2 = R = L/2$. The mirror surfaces are located on a common sphere so that their centers of curvature coincide. The fundamental mode corresponds to a spherical wave, where the mode radius is large at the position of the mirrors, whereas it is diffraction-limited at the beam waist.

Fig. 12.8 Stability diagram for a two-mirror cavity



For *plane-concave resonators* the beam waist lies on the plane mirror. This resonator type can be treated as an arrangement consisting of two identical spherical mirrors with length $2L$, which is built by extending the cavity by its mirror image.

The *hemispherical resonator* with $R_1 = L$ and $R_1 \rightarrow \infty$ represents a special case of the plane-concave resonator and is characterized by a diffraction-limited spot size ($w_2 \rightarrow 0$) at the plane mirror (see Fig. 12.7). However, the diffraction losses are large, as $w_1 \rightarrow \infty$. Therefore, it is favorable to select R slightly larger than L .

Concave-convex resonators with $R_2 < 0$ feature large fundamental mode volume, even at relatively short resonator length. In the limit of the concentric resonator, the centers of curvature of both mirrors coincide, when $R_1 > L$ and $R_2 = L - R_1 < 0$.

Plane-parallel or Fabry-Pérot resonators are mostly employed for laser media with high optical gain, since alignment of the cavity is rather challenging if the gain is low.

Stability Diagram

The relationship in (12.14) implies that a mode can only exist in a resonator, if the following stability condition is met:

$$[0 \leq g_1 g_2 \leq 1]. \quad (12.25)$$

The combinations of g -parameters for which (12.25) is fulfilled can be illustrated in a stability diagram by plotting g_2 against g_1 , as shown in Fig. 12.8. Resonators

within the shaded area are stable, as the formed modes are reproduced after every round-trip, whereas the mode grows without limits for cavities outside the stability region. The diagram includes the different resonator types discussed above: confocal resonator ($g_1 = g_2 = 0$), plane-concave resonator ($g_1 = 1$), hemispherical resonator ($g_1 = 1, g_2 = 0$), plane-parallel or Fabry-Pérot resonator ($g_1 = g_2 = 1$), symmetric resonator ($g_1 = g_2$) and concentric resonator ($g_1 = g_2 = -1$).

In stable resonators, the radiation power is concentrated in a small region around the resonator axis. Hence, only little energy is lost due to diffraction and the finite mirror size. In contrast, high diffraction losses occur in unstable resonators. Nevertheless, the radiation power ejected from the cavity by passing the mirror edges can be taken as the useful laser output, so that the actual losses are small. Unstable resonators are elaborated in the following section.

Unstable Resonators

Optical resonators with $g_1 \cdot g_2 > 1$ or $g_1 \cdot g_2 < 0$ are unstable, which means that very high diffraction losses occur, because a significant amount of the laser power leaks around the edges of the resonator mirrors. However, the attribute “unstable” should not be misinterpreted, as such configurations can be very robust and show low alignment sensitivity. In stable resonators, the realization of a fundamental mode with large diameter is complicated by its high sensitivity to disturbances like thermal lensing or misalignment. In contrast, unstable resonators can be used in lasers with large-diameter gain media for generating high-power output with high beam quality, while ensuring a homogeneous intensity distribution inside the resonator. Laser operation, however, requires high optical gain g_0 of the laser medium of length L_g , since only a few round-trips are performed by the laser beam. The following condition applies: $2g_0L_g > 1.5$.

The asymmetric confocal unstable resonator is of particular relevance. It produces a nearly parallel output beam with a “hole” in the center, as shown in Fig. 12.9. The field distribution inside the resonator can be approximated by a spatially limited spherical wave. Its diameter D is chosen such that it is slightly smaller than the diameter of the gain medium, while the latter is placed close to the mirror with radius R_1 . The diameter d of the output coupler with radius R_2 determines the geometric output coupling rate δ_g :

$$\delta_g = 1 - \frac{d^2}{D^2} = 1 - \frac{1}{M^2} \quad \text{with } M = \frac{D}{d}. \quad (12.26)$$

The parameter M denotes the magnification of the beam diameter introduced by the two-mirror system. For stable resonators comprising a partially transmissive output coupler, δ_g corresponds to the transmission rate $1-R$. The optimum output coupling depends on the properties of the laser medium, as outlined in Sect. 2.7.

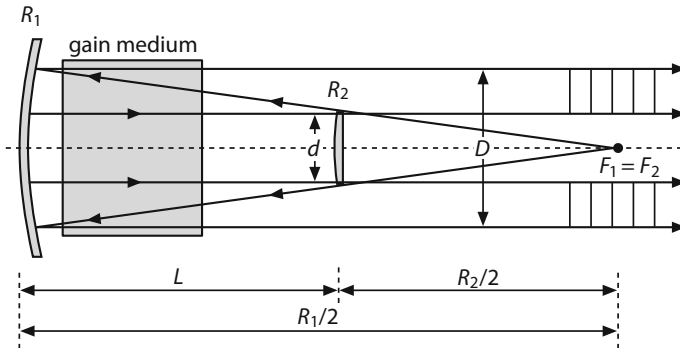


Fig. 12.9 Schematic of a confocal unstable resonator

The relationship between the mirror curvature radii and diameters of the confocal unstable resonator can be derived from geometrical considerations:

$$R_1 + R_2 = 2L \quad \text{and} \quad \left| \frac{R_1}{R_2} \right| = \frac{D}{d}. \quad (12.27)$$

From this follows that

$$R_1 = \frac{2ML}{M-1} \quad \text{and} \quad R_2 = \frac{-2L}{M-1}. \quad (12.28)$$

A more comprehensive wave-optical analysis of unstable resonators reveals that the geometric output coupling rate is actually lower than that given in (12.26), owing to diffraction effects. This can be considered by precise dimensioning of the resonator. Another result of wave-optical calculations is the existence of different transverse modes in unstable resonators, i.e. self-reproducing spatial distributions. As opposed to stable resonators, however, these field distributions cannot be clearly distinguished as low- and higher-order modes. Nevertheless, a homogenous “TEM₀₀-like” field distribution which is concentrated toward the beam axis experiences the lowest diffraction loss, so that this distribution is automatically established in a laser. This intrinsic mode discrimination facilitates fundamental transverse mode operation.

The concept of unstable resonators is primarily applied in high-gain lasers like flash lamp-pumped or diode-pumped Nd:YAG lasers, CO₂ lasers as well as in metal vapor lasers, excimer lasers and chemical lasers. The demand for high gain media also follows the fact that exact adjustment of low output coupling rates via the mirror diameter is challenging. Therefore, unstable resonators are especially suited for high-gain lasers where the output coupling rate is not critical and high diffraction losses can be tolerated. Although the output beam has a hole in the near field, the beam divergence of such lasers is usually quite small. In particular, when gain media with large cross-section are used, the beam quality of high-power lasers can be higher than achievable with stable resonators.

Fundamental Mode Operation and Fresnel Number

Lasers are mostly designed to operate in the fundamental transverse mode (TEM_{00}) or a similar intensity distribution. This requires the suppression of higher-order TEM_{mn} modes which can be achieved by exploiting the fact that the mode diameter, and hence the diffraction losses, increase with the mode order m, n (see Fig. 12.5).

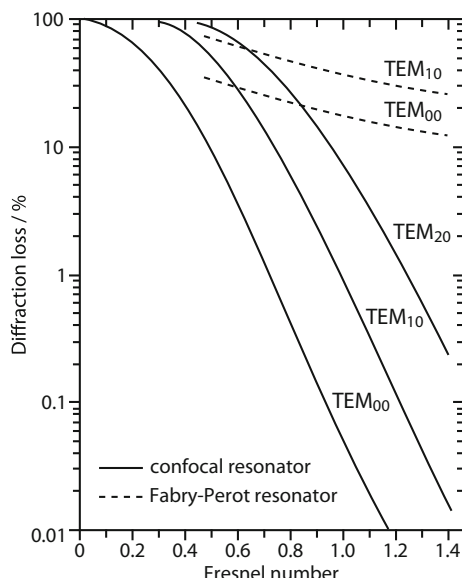
Fundamental mode output is often realized by inserting an aperture into the resonator whose diameter is slightly larger than the TEM_{00} beam diameter, but smaller than the diameter of the next higher transverse mode TEM_{10} . In this way, the losses for the TEM_{10} are increased, so that this mode and higher modes are prevented from oscillation in the resonator. However, this happens at the expense of reduced output power.

Figure 12.10 depicts the dependence between the diffraction loss and the so-called Fresnel number which is defined as follows:

$$\boxed{F = a^2/L\lambda}, \quad (12.29)$$

where, a is the mirror diameter or the diameter of an aperture placed close to one mirror, while L is the resonator length. Using (12.22), the Fresnel number of the confocal resonator can be written as $F = a^2/\pi w_1^2$. Consequently, low diffraction losses for the fundamental mode ($F > 1$, Fig. 12.10) are obtained, if the aperture area $\pi a^2/4$ is larger than the mode cross-section πw_1^2 . Higher-order modes TEM_{10} , TEM_{20} , etc. experience significantly higher losses. For the Fabry-Pérot resonator, $R_1 = R_2 \rightarrow \infty$ and thus also $w_1 = w_2 \rightarrow \infty$, resulting in higher diffraction losses compared to a confocal resonator with equal Fresnel number. Therefore, it is not

Fig. 12.10 Diffraction loss of selected transverse modes in dependence on the Fresnel number $F = a^2/L\lambda$ for a Fabry-Pérot and a confocal resonator



useful to insert small apertures into Fabry-Pérot resonators. Instead, the condition $F \gg 1$ should be met.

Since the confocal resonator offers the smallest mode diameter $w_1 = w_2$ for a given resonator length, the diffraction loss is minimal for a given Fresnel number. However, this does not mean that this resonator type is generally the best option when setting up a laser. When aiming at TEM_{00} mode operation, the resonator should be configured such that the fundamental mode diameter is similar to the diameter of the gain medium and nearly constant along the medium. This implies the use of mirrors with large radii of curvature, leading to high alignment sensitivity, since small tilting of the mirror results in large shifts of the resonance. An alternative is provided by unstable resonators, as presented in the previous section.

The considerations made above, and in particular the stability criterion formulated in (12.25), can be extended to more complex resonator configurations including optical elements like lenses. Moreover, thermal lensing of the gain medium can be taken into account. For this purpose, one considers an equivalent empty resonator of length L' that features the same complex beam parameters q_1 and q_2 at the mirror surfaces as the actual resonator. Using a matrix formalism, equivalent g-parameters g'_1 and g'_2 of the resonator can be derived for which the same stability condition applies:

$$0 \leq g'_1 g'_2 \leq 1. \quad (12.30)$$

The use of intra-cavity lenses or telescopes allows for the adaption of the mode diameter in resonators where the mirror spacing is considerably larger than the length of the gain medium. This is for instance the case in solid-state lasers.

Apart from apertures, transverse mode discrimination can also be accomplished with Gaussian mirrors, also known as variable reflecting mirrors (VRM). They are characterized by radially varying reflectance from the center to the edges of the mirror, so that the fundamental mode is favored, while higher-order modes suffer strong losses. The Gaussian reflectance profile also diminishes inhomogeneities in the transverse intensity distribution and thus improves the beam quality. Furthermore, the risk of optical damage is reduced when used in high-intensity lasers.

Further Reading

1. J. Heebner, R. Grover, T. Ibrahim, *Optical Microresonators* (Springer, 2008)
2. D.G. Rabus, *Integrated Ring Resonators* (Springer, 2007)
3. N. Hodgson, H. Weber, *Laser Resonators and Beam Propagation* (Wiley-VCH, 2005)

Chapter 13

Optical Waveguides and Glass Fibers



The transmission of laser light through fibers is essential in the fields of telecommunication, electrical engineering, material processing and medicine. This chapter discusses the basic principles of fiber coupling and light propagation in optical waveguides. It also presents different fiber materials as well as recent developments in terms of photonic crystal fibers.

13.1 Optical Materials

Lasers emit in the spectral range from the ultraviolet to the far-infrared. Thus, various optical materials are used for the fabrication of lenses, prisms, windows and mirrors. The transparency range of the materials is determined by the internal energetic structure. Absorption occurs when light causes a transition from one energetic state to a higher state (Chap. 2). There are no materials that are transparent at all frequencies or wavelengths. The transmission spectra of the most prominent optical materials are depicted in Fig. 13.1.

Fused silica is high-purity synthetic amorphous silicon dioxide (SiO_2) which combines a very low thermal expansion coefficient with excellent optical qualities and exceptional transmittance over a wide spectral range. It is available in a number of UV and IR grades for different applications. UV-grade fused silica has high transparency in the ultraviolet spectral region down to 0.15 μm , but has a strong OH-absorption band in the 2.6–2.8 μm wavelength range (Fig. 13.1). It is often used for vacuum viewports and sight glasses. On the contrary, IR-grade fused silica with low OH-content features high transparency from 0.2 to 3.5 μm wavelength.

In general, fused silica is widely employed for windows, lenses and prisms, as it is resistant to scratching and thermal shock and exhibits no bubbles or inclusions.

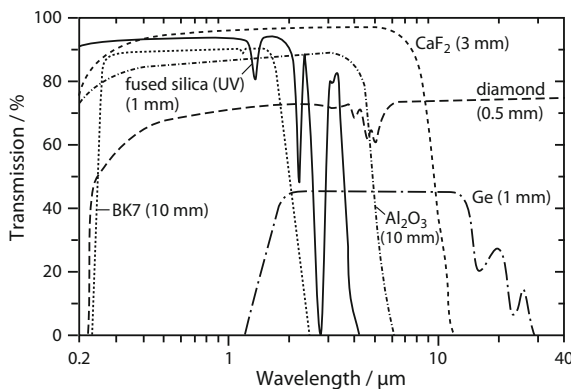


Fig. 13.1 Transmission spectra of selected optical materials used in laser physics

Table 13.1 Properties of selected optical materials

Material		Transparency range (μm)	Refractive index	Comments/field of application
Barium fluoride	BaF ₂	0.2–11	1.51–1.39	Applicable up to 800 °C
Borosilicate glass (BK7)	–	0.4–2.1	1.53–1.48	Standard glass
Cadmium telluride	CdTe	1–25	2.4–2.7	CO ₂ laser
Calcium fluoride	CaF ₂	0.17 – 10	1.5–1.3	UV, IR
Diamond	C	0.3–4, 7 to >100	2.5–2.3	Very high thermal conductivity
Fused silica (UV)	SiO ₂	0.15–2.5	1.5–1.4	High damage threshold, glass fibers
Fused silica (IR)	SiO ₂	0.2–3.5	1.5–1.4	
Gallium arsenide	GaAs	2.5–16	3.3–2.1	CO ₂ laser
Germanium	Ge	1.8–15	4.1–4.0	IR
Magnesium fluoride	MgF ₂	0.15–7	1.4	Coating material
Quartz	SiO ₂	0.15–2.5	–	Birefringent
Sapphire	Al ₂ O ₃	0.17–5.5	1.9–1.6	IR, optical fibers
Silicon	Si	1.1–7	3.5–3.4	IR
Zinc selenide	ZnSe	0.6–22	2.5–2.3	CO ₂ laser
Zinc sulfide	ZnS	0.3–13	2.7–2.3	Coating material

Moreover, due to its high damage threshold, fused silica is especially suited as material for both transmissive and reflective optics in high-energy laser applications. An overview of the optical properties of some more selected optical materials is given in Table 13.1.

Ultraviolet Spectral Range

The ultraviolet spectral region covers the wavelength range from 400 nm to a few tens of nanometers. Technically important, commercial laser sources exist with emission wavelengths down to about 150 nm, while lasers emitting at shorter wavelengths, e.g. X-ray lasers (Sect. 25.5), are operated only in a few laboratories.

There is a large number of optical glasses that are applicable for the near-ultraviolet range from 300 to 400 nm. Fluorides such as magnesium fluoride (MgF_2), calcium fluoride (CaF_2) or lithium fluoride (LiF) as well as UV-grade fused silica is transparent well below 200 nm. In general, material problems become more marked towards shorter wavelengths. As the photon energy rises, the probability for the excitation of electrons from inner shells increases, resulting in strong absorption. Oxygen molecules cause the air atmosphere to become opaque at about 185 nm. Hence, the spectral region below is referred to as vacuum ultraviolet (VUV). Noble gases with high ionization energy show higher transparency compared to air. Helium having the strongest electron binding energy (24.6 eV) is transparent down to about 50 nm. While there are no solids that are transparent for VUV radiation below 100 nm, X-radiation penetrates substantial thicknesses of many materials. Optical materials and coatings are damaged at high power densities. The damage threshold generally decreases with decreasing wavelength so that the probability for laser-induced damage is particularly high at violet wavelengths.

Visible Spectral Range

The visible spectral region spans the wavelength range from 400 to 700 nm. Here, silicate glasses, i.e. glasses based on the chemical compound silica (silicon dioxide, SiO_2), such as fused silica or borosilicate glasses are employed. They are characterized by high transparency (see BK7 in Fig. 13.1), high resistance, very low thermal expansion coefficient and low cost. The transparency range of silicate glasses also covers the near-infrared region up to 2 μm so that these materials can be used as optical elements for most solid-state lasers, e.g. the Nd:YAG laser emitting at 1.06 μm .

Infrared Spectral Range

Various materials have been developed for the infrared spectral region, particularly for those wavelengths where air is transparent, i.e. from 1 to 2 μm (near-IR), 3 to 5 μm (mid-IR) and 8 to 12 μm (thermal IR). As mentioned above, many conventional materials that are used in the visible are also applicable in the near-IR up to 2 μm . The mid-IR range from 3 to 5 μm exhibits a number of absorption bands

of air components like CO₂ and water. This range covers several emission lines of the CO laser (4.7–8.2 μm) and different chemical lasers (2.6–4.7 μm), while the CO₂ laser emits around 10.6 μm. Important materials for the infrared are fluorides and semiconductors like germanium, silicon, gallium arsenide (see Table 13.1) and others. Semiconductors are mostly opaque in the visible region. In addition to fluorides, other halides such as sodium chloride (NaCl) are employed. These materials can be more or less hygroscopic.

Particular requirements are demanded from materials that are used for IR optical fibers. Chalcogenide infrared (CIR) fibers are based on sulfides, selenides or tellurides, e.g. of arsenic (As) or germanium (Ge), like As₂S₃ or As₂Se₃ and typically transmit from 2 to 6 μm or even as far as 20 μm, depending on their composition. Alternatively, polycrystalline infrared (PIR) fibers, e.g. fabricated from silver halides like AgCl or AgBr, are commonly employed allowing transmission ranges from roughly 3 μm to 18 μm. Optical fibers can also be made of single crystalline sapphire (Al₂O₃) which provides transmission up to about 3.5 μm, low propagation loss and high robustness. Hence, sapphire fibers can withstand high optical average powers of more than 10 W and are for example applied for transmitting the output of Er:YAG lasers at 2.94 μm wavelength. The design and properties of optical fibers is further elaborated in Sects. 13.2 and 13.3.

13.2 Planar, Rectangular and Cylindrical Waveguides

Conventional fibers consist of a cylindrical core with a typical diameter of 3–1000 μm, surrounded by a cladding with lower refractive index. The core of fibers specified for the visible and adjacent spectral ranges is usually made from silica glass (either pure or doped with GeO₂) having a refractive index of $n_1 = 1.47$, while the lower refractive index of the cladding, e.g. $n_2 = 1.46$, is realized by using a different silica glass composition.

Laser light is coupled into fibers by focusing the radiation to a beam diameter that is smaller than the core diameter. Fiber coupling by means of a focusing lens is shown in Fig. 13.2. The lens can also be directly attached to the fiber end face, forming so-called ball lenses. Alternatively, cone-shaped fibers are used where the focusing occurs at the entrance surface of the fiber (see Fig. 10.22).

The light-guiding principle along the fiber is based on total internal reflection at the interface between the core and the cladding. This mechanism presumes that the incidence angle at the fiber entrance surface is small enough such that the corresponding incidence angle at the core-cladding interface is above the critical angle for total internal reflection (see Sect. 14.1). Otherwise, light is transmitted into the cladding, as indicated by the dashed ray in Fig. 13.2. The maximum incidence angle γ at the fiber surface, up to which total internal reflection occurs in the fiber term can be expressed in terms of the numerical aperture NA and is related to the refractive indices n_1 and n_2 of the core and cladding materials:

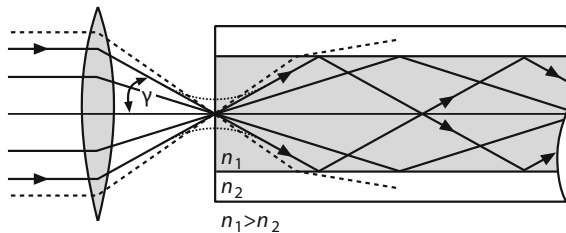


Fig. 13.2 Launching and propagation of light in an optical fiber. Guiding inside the fiber is due to total internal reflection on the interface between core and cladding. Frequently, the focus is located behind or in front of the entrance surface to prevent high power densities on the fiber end-faces (reflection at the glass fiber entrance surface is not shown)

$$\text{NA} = \sin \gamma = \sqrt{n_1^2 - n_2^2}. \quad (13.1)$$

For typical values of $n_1 = 1.47$ and $n_2 = 1.46$, a numerical aperture of $\text{NA} = 0.17$ is calculated. Larger values, e.g. $\text{NA} \approx 0.4$, are obtained when using silica core fibers that are surrounded by a plastic or polymer cladding. However, plastic-clad silica and polymer-clad silica fibers (PCS) have higher transmission losses and lower bandwidths than all-glass fibers and are mainly employed in industrial, medical or sensing applications where large core area are advantageous.

Propagation Modes in Planar Waveguides

The wave characteristics of light imply that only certain stationary field distributions (modes) can propagate in an optical fiber. This circumstance will first be discussed at the example of a planar waveguide where the field is confined in only one direction (here: in x -direction). If a plane wave is incident on such a waveguide, a zigzag wave is produced by total internal reflection. Figure 13.3 depicts the phase fronts of plane waves that are emitted into the waveguide under different angles. Reflection from the core-cladding interfaces leads to wave fronts traveling in two different directions, while a phase shift upon total internal reflection has to be considered. Constructive interference of the partial waves only occurs for discrete angles of incidence, as illustrated in Fig. 13.3, resulting in periodic field distributions in the transverse direction.

The integer mode index m indicates the number of nodes in the fiber core which increases with increasing angle between the wave normal and the fiber axis. Low-order modes are produced for small angles. For angles deviating from the described launch conditions, destructive interference takes place so that a stationary propagation of the incoming wave is not possible. Since the angle of incidence is further restricted by the critical angle for total internal reflection inside the fiber, the number of modes is limited.

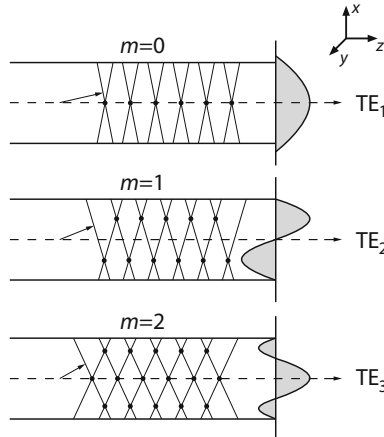


Fig. 13.3 Field distribution of different modes in planar waveguides. The modes originate from constructive interference of two planar waves propagating in two symmetric directions. According to a simple model of total internal reflection, the electric field has nodes at the waveguide boundaries. The more comprehensive theory shows the existence of an evanescent field outside the waveguide

To determine the light field distribution in the waveguide, Maxwell's equations have to be solved taking into consideration the boundary conditions. The waveguide structure is considered infinite in the y -direction, so that there are two separate groups of coupled electric and magnetic field components: E_y , E_x , and H_z described as transverse electric modes (TE modes) as well as H_y , E_x , and E_z described as transverse magnetic modes (TM modes).

Since only solutions propagating along the waveguide in the z -direction are of interest, the z -dependence of the wave has the form $\exp(ik_z z)$ with k_z being the z -component of the wave vector. Using Maxwell's equations in a non-magnetic, linear, isotropic medium with zero conductivity, one obtains wave equations which describe the transverse dependence of the electric and magnetic fields as follows:

$$\frac{\partial^2 \mathbf{A}}{\partial x^2} + (\epsilon_r \epsilon_0 \mu_0 \omega^2 - k_z^2) \mathbf{A} = 0, \quad (13.2)$$

where A stands for E and H , respectively. The angular frequency is denoted as ω , while μ_0 and ϵ_0 are the vacuum permeability and permittivity and ϵ_r is the relative permittivity. Using the dispersion relation $\omega = c \cdot k_0$ with the free-space wavenumber $k_0 = 2\pi/\lambda$ as well as $c^2 = 1/(\epsilon_0 \mu_0)$ and $n^2 = \epsilon_r$, the solution reads

$$\mathbf{A} = \mathbf{A}_0 \exp[i(k_z z - \omega t)] \exp(\pm i k_x x), \quad (13.3)$$

with

$$k_{1x} = \sqrt{n_1^2 k_0^2 - k_z^2} \quad \text{and} \quad (13.4)$$

$$k_{2x} = \sqrt{n_2^2 k_0^2 - k_z^2} = i\kappa. \quad (13.5)$$

For the case of total internal reflection, the waves in the different regions of the waveguide are shown in Fig. 13.4. Depending on whether the term $n^2(x) k_0^2 - k_z^2 = -\kappa^2$ is greater than or less than zero, the solutions in (13.3) are either sinusoidal or exponential functions of x . Inside the waveguide, i.e. within the higher refractive index medium, where $n_1^2 k_0^2 > k_z^2$, two plane waves with amplitudes A and B constitute the wave traveling in the z -direction. In contrast, outside the waveguide in the lower refractive index medium where $\kappa^2 > 0$, the field does not oscillate, but dies off exponentially from the waveguide interface. Such fields are denoted as evanescent.

Furthermore, the boundary conditions at the two interfaces, i.e. the continuity of the tangential field components, must be considered. Consequently, light guidance is only possible for certain values of k_z and k_x , leading to discrete modes supported by the waveguide, as shown in Fig. 13.3. For the transverse electric modes, the wave vector components are related to the width w of the waveguide as

$$\tan\left(\frac{k_{1x}w}{2} \pm \frac{m\pi}{2}\right) = \frac{\kappa}{k_{1x}} \quad \text{with } m = 0, 1, 2, \dots \quad (13.6)$$

denoting the mode index.

Equations (13.4) and (13.5), combined with (13.6), allow to calculate the propagation constant k_z for various modes in dependence of the frequency ω . The velocity of the modes is given by $c_{\text{eff}} = \omega/k_z$ which varies with the mode index. This is called modal dispersion of the waveguide in contrast to the material dispersion. An analytical calculation of the propagation constant k_z is not possible, so that numerical calculations are required resulting in graphical representations, as shown in Fig. 13.5 for different rectangular waveguides.

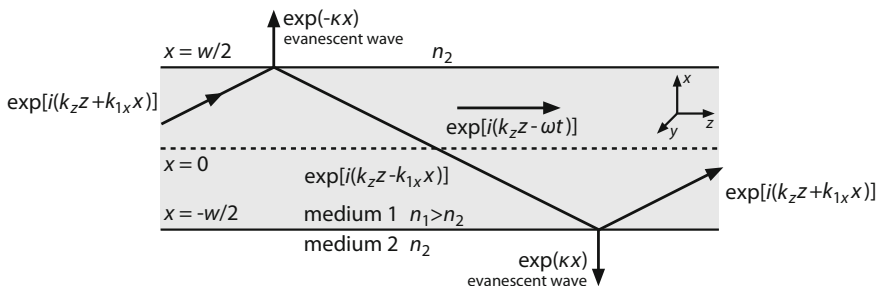


Fig. 13.4 Electric field components in a planar waveguide. The evanescent does not propagate in the x - but in the z -direction

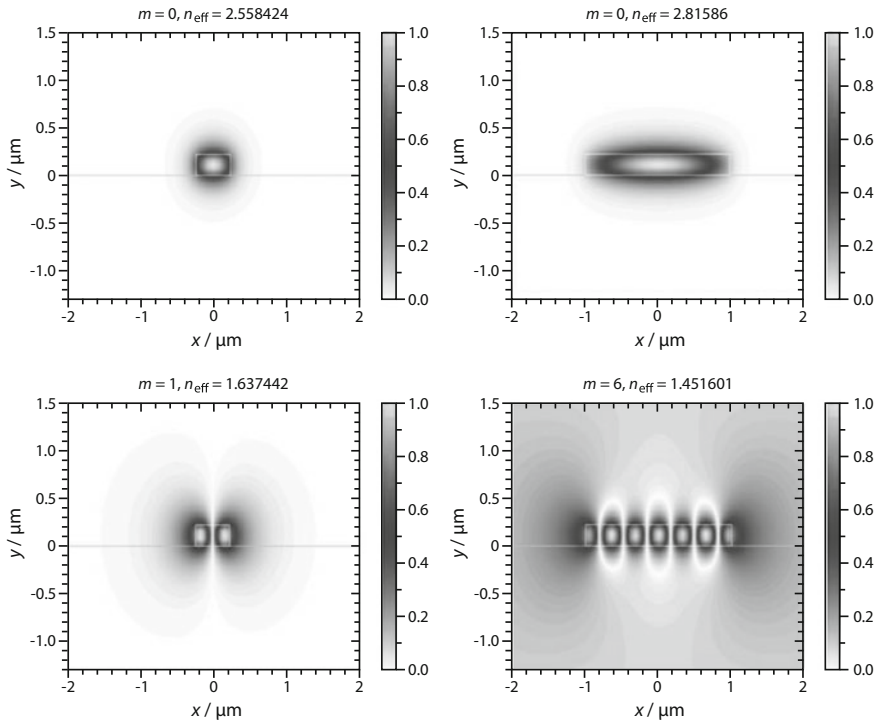


Fig. 13.5 Mode profiles (normalized electric field) in silicon waveguides with thickness of $0.22 \mu\text{m}$ and widths of $0.45 \mu\text{m}$ (left panels) and $2 \mu\text{m}$ (right panels), partially embedded in silicon oxide. The profiles were calculated by Shaimaa Mahdi using *Fullwave* software from RSoft, TU Berlin, 2013. Transverse TE_{mn} modes with maxima in two perpendicular directions also exist, if the waveguide thickness is larger

Transverse distribution of the electric field in the inside the planar waveguide becomes

$$E_{y,\text{in}} = E_e \cos(k_{1x}x) \quad \text{and} \quad E_{y,\text{in}} = E_o \sin(k_{1x}x) \quad (13.7)$$

for even and odd mode indices (symmetrical and asymmetrical TE modes), respectively. Outside the waveguide, the electric field for even and odd mode indices is given by

$$\begin{aligned} E_{y,\text{out}} &= E_e \exp(-|\kappa x|) \frac{\cos(k_{1x}w/2)}{\exp(-|\kappa w/2|)} \quad \text{and} \\ E_{y,\text{out}} &= E_o \frac{x}{|x|} \exp(-|\kappa x|) \frac{\cos(k_{1x}w/2)}{\exp(-|\kappa w/2|)}. \end{aligned} \quad (13.8)$$

Some field distributions given by (13.6) and (13.7) are depicted in Fig. 13.3. An analogous analysis yields the transverse magnetic modes.

Rectangular Waveguides

In rectangular waveguides, an additional confinement in the y -direction is introduced. Solving Maxwell's equations for the boundary conditions imposed by the waveguide again results in a finite number of modes that can propagate along the waveguide, see Fig. 13.5. A mode is then described by its propagation constant β (see below), corresponding to k_z in the calculations above, and by the electric and magnetic field distributions.

Rectangular optical waveguides are often used to confine the light in diode lasers close to the amplifying pn-junctions, e.g. in double heterostructure ridge waveguide lasers (see Sect. 10.3, Fig. 10.11). Silicon waveguides have been used in Raman lasers (Sect. 19.5).

Cylindrical Glass Fiber Waveguides

The structure of modes guided in fibers is more complicated compared to planar waveguides. A distinction is made between transverse electric (TE) modes, transverse magnetic (TM) modes and hybrid modes (HE and EH) where neither the electric nor the magnetic component is perpendicular to the propagation direction. In the latter case, the first letter denotes the dominant field component (E—electric, H—magnetic). The field and intensity distributions of the modes in a cylindrical waveguide are similar to that of laser beams with cylindrical symmetry, as described in Sect. 12.2. The lowest-order mode HE₁₁ is of particular importance, as it features an intensity distribution similar to the TEM₀₀ mode in free-space. The mode excited in the fiber depends on the incident field distribution which is decomposed into a number of fiber mode distributions such that the sum of the modes matches the incident field at the fiber entrance.

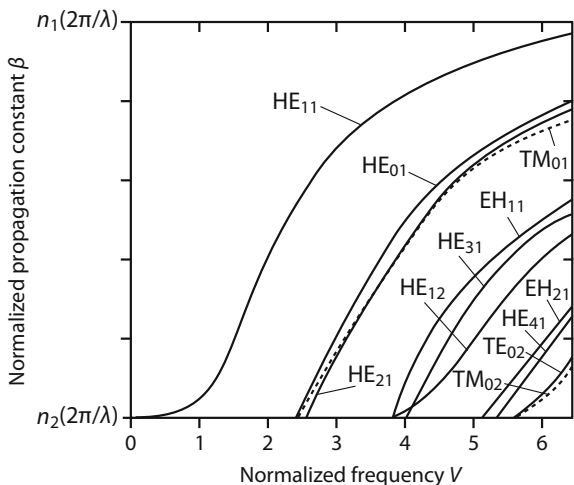
Two parameters are introduced for describing the propagation of modes in cylindrical fibers—the normalized frequency V and the normalized propagation constant β which are defined as follows:

$$V = \frac{2\pi}{\lambda} a \sqrt{n_1^2 - n_2^2}, \quad (13.9)$$

$$\beta = n_{\text{eff}} \frac{2\pi}{\lambda} = n_{\text{eff}} \frac{\omega}{c} \quad \text{with } n_{\text{eff}} = \frac{c_0}{c_{\text{eff}}}. \quad (13.10)$$

V depends on the wavelength λ (in vacuum), the core radius a and the refractive indices n_1 and n_2 of the core and cladding. The designation normalized frequency derives from the reciprocal wavelength in (13.9). The normalized propagation constant β corresponds to the amount of the wave vector k along the propagation direction (k_z in the above example) and is determined by the effective refractive index n of the fiber which describes the propagation speed c_{eff} of the mode in the fiber (c_0 —vacuum speed of light). n_{eff} varies between n_1 and n_2 , see Fig. 13.6.

Fig. 13.6 Propagation constant of various mode in a step-index fiber (cylindrical waveguide). TE: transverse electric, TM: transverse magnetic, HE, EH: longitudinal electric/magnetic. The fundamental mode HE₁₁ has a similar intensity distribution as the TEM₀₀ mode which occurs for propagation in free-space



The dependence of the normalized propagation constant β upon the normalized frequency V is plotted in Fig. 13.6 for different modes propagating in a step-index fiber (see next section). The graphic reveals that the following condition has to be fulfilled for single-mode guidance:

$$V = \frac{2\pi}{\lambda} a \sqrt{n_1^2 - n_2^2} < 2.405. \quad (13.11)$$

Hence, for given refractive indices and wavelength, the maximum core radius up to which a single mode is supported in the fiber can be calculated. Inserting, for instance, a wavelength of $\lambda = 630$ nm and refractive indices of $n_1 = 1.47$ and $n_2 = 1.46$, a maximum core diameter of $a = 1.4$ μm is obtained. For core diameters $a < 1.4$ μm , only the HE₁₁ mode is capable of propagation.

The maximum wavelength for which the condition $V = 2.405$ is met, is called cut-off wavelength. Above this wavelength, only one mode is transmitted. In telecommunication systems at 1.5 μm wavelength, single-mode fibers with core diameters around 8 μm are commonly used. The disadvantages of single-mode fibers are the power limitation and the difficulties of coupling light into the small fiber core area.

The maximum number of modes M increases with the core radius approximately according to

$$M \approx V^2 / 2. \quad (13.12)$$

For a fiber with $a = 50$ μm , $n_1 = 1.47$, $n_2 = 1.46$ and a wavelength $\lambda = 630$ nm, the number of modes accounts to $M \approx 3600$. Multimode fibers have the benefit that they can transmit much higher power than single-mode fibers and that coupling into the fiber is easily achieved due to the large core diameter. Therefore, multimode fibers are used if high powers are to be transmitted, for example for material processing or in medicine, as well as for signal transmission over short distances.

13.3 Fiber Types

The characteristics and applications of different types of glass fibers are outlined in the following. A more detailed overview of fiber-optic communication is provided in Sect. 25.2.

Step-Index Fibers

The relationship between normalized frequency and normalized propagation constant, plotted in Fig. 13.6, is valid for modes propagating in step-index fibers. Here, the refractive indices are constant within the fiber core and in the cladding, so that the index profile exhibits an abrupt step at the interface between the high-index and low-index layers (see Fig. 13.7a). The core diameter of such fibers is typically in the range from a few μm to 1 mm.

For small core diameters, only one mode is supported in the fiber which is beneficial in telecommunication applications, as the broadening of transmitted pulses through mode dispersion is diminished. The existence of multiple modes in fibers with large core diameters, on the contrary, involves different propagation speeds of the traveling modes, resulting in a delay between low-order and high-order modes. The differential mode delay strongly depends on the refractive index profile of the fiber and can be as high as 10 ps/m for step-index fibers which severely limits the achievable data transmission rate in fiber-optic communication systems.

On the other hand, launching of light into step-index fibers is facilitated by the high numerical aperture, so that they are employed for data transfer over short

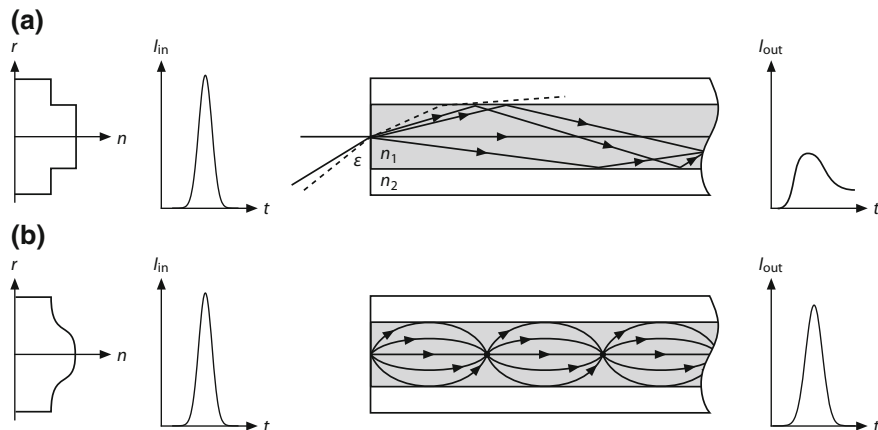


Fig. 13.7 Refractive index profiles of a step-index fibers and b graded-index fibers. The figure also shows the intensity distribution of a pulse (pulse shape) before and after propagation through the different types of fibers. The effect of pulse broadening can be diminished in graded-index fibers

distances, optical image transmission from body cavities in endoscopy as well as for the transmission of high laser powers in material processing applications. For instance, tens of kilowatts of output power can be efficiently transferred over several meters from a cw Nd:YAG laser to the site of operation by means of multimode step-index fibers.

Graded-Index Fibers

The simultaneous requirement for low mode dispersion and high numerical aperture has led to the development of graded-index fibers (sometimes also called gradient-index fibers). This fiber type is characterized by a continuously varying refractive index along the radial direction (Fig. 13.7b) The smooth transition of the index profile from the core to the cladding enables an effective compensation of the delay between modes of different order. In a simplified picture, low-order modes that mainly exist in the inner region of the fiber experience a higher refractive index than higher-order modes that predominantly travel in the outer regions where they “speed up” due to the lower refractive index. In this way, it is possible to realize nearly identical optical paths at varying geometrical paths of the modes. The most common refractive index profile for a graded-index fiber is nearly parabolic which results in sinusoidal paths of the light rays along the fiber, as illustrated in Fig. 13.7b. The minimization of mode dispersion can only be accomplished over limited wavelength ranges due to the wavelength-dependence of the refractive index.

Graded-index fibers with core diameters around 50 μm are mainly used for telecommunication purposes, as they offer easy coupling of light and the connection of different fiber pieces. Besides, large area fibers with core diameters of several hundred microns are applied for the transmission of high laser powers (power over fiber). Furthermore, graded-index fibers can be used in fiber-optic sensors or for guiding THz radiation.

Optically, graded-index fibers can be considered as a series of lenses reproducing the intensity distribution that enters the fiber. Hence, light is guided by refraction rather than by total internal reflection. As opposed to the sketch in Fig. 13.7b, the period length is much longer than the core diameter.

Fiber Fabrication

In general, glass fibers consist of silica (SiO_2). In order to increase the refractive index of pure silica in the core region or to decrease the refractive index in the cladding, dopants are added. Although the fiber can, in principle, be drawn directly from a crucible, additional process steps are required to ensure the purity needed for extremely low attenuation. Therefore, fibers are usually produced in two stages.

In the first stage, a model of the desired fiber on a larger scale, a so-called preform, is made. Having a typical diameter of 20–30 mm, the preform already exhibits the desired refractive index profile as well as the correct proportion of the core and cladding layers. In the second stage of the fabrication process the real fiber is drawn out of this preform.

The preform is produced by various vapor deposition techniques: outside vapor deposition (OVD), modified chemical vapor deposition (MCVD) or vapor axial deposition (VAD). In the MCVD process, SiO_2 is deposited by mixing SiCl_4 and O_2 inside a glass tube that rotates on a lathe at a temperature of about 1800 °C. The chemicals are fused and deposited layer by layer, while the temperature is controlled by a traveling burner that moves along the tube causing the chemical reaction to take place. One layer corresponds to one pass of the burner under the tube. In this manner, approximately 50 layers are deposited with the desired refractive index being adjustable by the flow of POCl_3 , GeCl_4 and BCl_3 . After deposition, the temperature of the burner is raised to collapse the tube into a solid rod – the preform. Using this process, highly-pure preforms can be fabricated.

Depending on the volume of the preform, some 10 km of fiber can be drawn. During the drawing process, the fiber is also coated to avoid micro-cracks which lead to a decrease of the mechanical strength. Organic materials are commonly used to build up the coating which is, in turn, protected against abrasion by an outer jacket, e.g. made of nylon. Before the fiber is used, a third step is usually carried out, the fiber cabling. This improves the mechanical properties of the fiber and protects it against severe mechanical stress. Depending on the operational field, diverse types of cabling are in use. For instance, a six-fiber cable often used in optical telecommunication systems can withstand a tensile force of about 5000 N, temperature variations from −50 °C to +60 °C, and it is moisture resistant.

Fiber Materials

Silica fibers are widely used for applications from the near-UV via the visible to the near-IR spectral region up to 2 μm wavelength. At longer wavelengths, strong absorption occurs (Fig. 13.10) which prevents their use in the mid-IR range. As outlined in Sect. 13.1, chalcogenide infrared (CIR) fibers, polycrystalline infrared (PIR) fibers as well as sapphire fibers are employed for guiding light at wavelengths from 2 up to 18 μm.

CIR fibers based on arsenic or germanium sulfides, selenides and tellurides like As_2S_3 or As_2Se_3 are suitable for the wavelength range from 2 μm up to 9 μm. However, these materials can exhibit strong absorption lines within that range, e.g. around 4 μm.

PIR fibers are fabricated from silver halides like AgCl or AgBr and provide high transmission from 3 μm to 18 μm. Here, a drawback lies in the crystalline nature of the fibers which can cause the formation of microcrystals and, in turn silver particles which increase the propagation loss.

Single crystalline sapphire fibers show high transmission up to about $3.5\text{ }\mu\text{m}$. In combination with their low propagation loss and high robustness, they are especially suited for guiding the output of erbium lasers, e.g. emitting at $2.94\text{ }\mu\text{m}$ wavelength. Sapphire can also be used to form hollow waveguides where most of the optical power propagates within an air core having a typical diameter of a few hundred micrometers. Apart from sapphire, silica glass, e.g. doped with PbO, can be utilized as cladding material. Since the mode has only little overlap with the cladding, strong absorption of the solid material can be tolerated without suffering high propagation loss. This enables long propagation lengths and a wide transmission range, while single-mode guidance is possible as well.

Another group of mid-IR fibers is given by heavy metal fluoride glasses such as ZBLAN with the composition $\text{ZrF}_4\text{--BaF}_2\text{--LaF}_3\text{--AlF}_3\text{--NaF}$. ZBLAN glass features an optical transmission window extending from $0.3\text{ }\mu\text{m}$ up to $7\text{ }\mu\text{m}$, but is rather fragile and sensitive to acids. Moreover, the optical quality of ZBLAN fibers is often degraded by the tendency for surface crystallization during the fabrication process (see also Sect. 9.5).

For several applications, e.g. in medicine, optical sensing or short-distance data transmission, plastic optical fibers (POF) are employed. These types of fibers are produced with core diameters larger than $500\text{ }\mu\text{m}$ which involves relaxed connector tolerances and allows for easy and efficient coupling of light sources including LEDs. Another advantage of POFs over glass fibers is their high robustness under bending and stretching.

Single-Mode Fibers

Excellent signal transmission characteristics, i.e. low pulse broadening, high beam quality and low propagation loss, are achieved by using single-mode fibers. The core diameter is only a few μm , so that a single mode propagates according to (13.11) and mode dispersion (see Sect. 13.4) is avoided. The same holds true for the dispersion of the refractive index, provided that laser emission with sufficiently narrow bandwidth is transmitted. Consequently, single-mode fibers allow for data transmission over hundreds of kilometers.

Single-mode fibers are also employed in fiber lasers and amplifiers for generating output radiation with diffraction-limited beam quality ($M^2 = 1$). For high-power fiber lasers and amplifiers, single-mode fibers with relatively large core diameters of tens of micrometers are required in order to mitigate unwanted nonlinearities and increase the damage threshold. This can be achieved either by making a large core with a small index difference (small numerical aperture), or by using a photonic crystal fiber, as explained below. However, large mode area (LMA) single-mode fibers generally tend to be more sensitive to bending losses compared with multimode fibers since the guiding is relatively weak.

Power scaling of fiber lasers while maintaining single-mode operation can be accomplished with gain-guided, index anti-guided single-mode fibers which were

proposed by A. E. Siegman. Here, the refractive index of the doped core is lower than that of the cladding, so that the unpumped fiber is anti-guiding. For sufficiently strong pumping, however, gain guiding can stabilize the leaky fundamental mode with high beam quality. Since the losses of this mode rapidly decrease for increasing core size, propagation with positive net gain is achieved if the core is large.

A similar and relatively novel concept is based on a fiber design where the cladding material has a refractive index which is lower than that of the core material at the pump wavelength, while the situation is reversed at the longer laser emission wavelength. As a result, the pump light propagates through the cladding as in a conventional index-guided fiber laser, while the laser emission is captured within the large area core as a gain-guided index anti-guided wave.

Photonic Crystal Fibers

The field of photonic crystal fibers (PCF) was first explored in the second half of 1990's and quickly evolved to a commercial technology. They are generally divided into index-guiding fibers with a solid core and photonic band gap fibers that have periodic micro-structured elements and a core of low index material, e.g. hollow core. An example for the first category is shown in Fig. 13.8, depicting a silica fiber whose core is surrounded by air-filled capillaries that are periodically arranged over the cross-section, thus forming a cladding that confines the light in the core. During the manufacturing process of index-guiding PCFs, an array of hollow capillary silica tubes is bundled around a pure silica rod replacing the center capillary, while a sleeving tube surrounds the entire assembly that forms the pre-form. Afterwards, the preform is heated to around 2000 °C and carefully pulled under the influence of gravity and pressure in a fiber draw tower. Compressed air is blown into the capillaries in order to prevent collapsing.

The resulting periodic arrangement of hollow channels is referred to as photonic crystal, as it resembles the periodic arrangement of atoms in a crystal. The effective refractive index of the cladding n_2 depends on the ratio between diameter d and distance Λ of the capillaries. The dispersion of n_2 is given by the normalized

Fig. 13.8 Photonic crystal fiber. The solid core is made of fused silica (refractive index n_1) which is surrounded by an array of air-filled capillaries with diameter d , resulting in an effective refractive index n_2 of the cladding

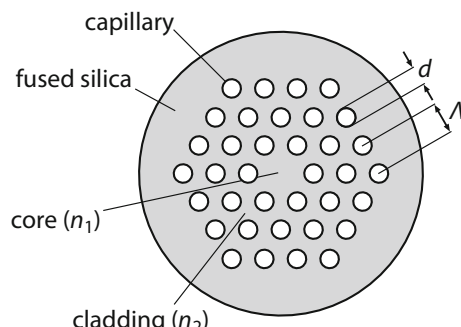
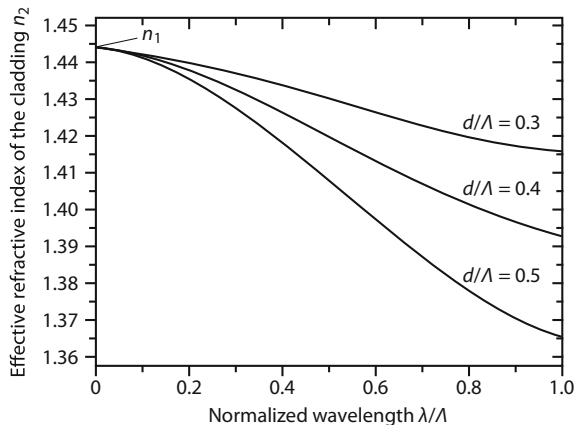


Fig. 13.9 The effective refractive index n_2 of a photonic crystal fiber depends on ratio between diameter and distance of the capillaries d/Λ as well as the normalized wavelength λ/Λ (see Fig. 13.8). The core which is free of capillaries has the refractive index n_1



wavelength λ/Λ , as shown in Fig. 13.9. In analogy to (13.9), a normalized frequency can be defined by substituting the core diameter a by the distance Λ between the capillaries. Similar to (13.11), only a single mode is supported in the PCF for $V > \pi$. For $\lambda/\Lambda > 0.45$, single-mode guidance is obtained regardless of the wavelength.

The major advantage of photonic crystal fibers is the large design flexibility in terms of the cladding refractive index, which enables a large range of novel characteristics. Apart from beneficial dispersion properties, PCF have the unique feature to support single-mode operation over a wide wavelength range from $0.3\text{ }\mu\text{m}$ to beyond $2\text{ }\mu\text{m}$, even for large mode field areas of several hundred μm^2 . This allows for the transmission of very high laser powers (up to several hundred watts) with high beam quality. Hence, applications of PCFs are found in various research fields like spectroscopy, metrology, telecommunication as well as biomedicine, imaging and industrial machining.

Furthermore, due to their special chromatic dispersion characteristics, PCFs are well-suited for supercontinuum generation. This term describes the formation of broadband continuous spectra by propagation of intense pulses through a strongly nonlinear medium. Supercontinua combine high brightness with broad spectral coverage which is of interest for many applications including fluorescence microscopy, optical coherence tomography and flow cytometry (Sect. 24.3). Moreover, supercontinua allow for the measurement of the carrier-envelope offset frequency of frequency combs (Sect. 22.6).

13.4 Fiber Damping, Dispersion and Nonlinearities

There are several physical mechanisms that affect the properties of the light guided in an optical fiber. The most relevant processes—damping, dispersion and nonlinear optical interactions—influencing the transmission, spectral bandwidth and polarization are discussed in the following.

Damping

The transmission T of a fiber with length L can be described by an exponential function

$$\boxed{T = \frac{P}{P_0} = e^{-\alpha L}}, \quad (13.13)$$

where P_0 and P are the incident and the transmitted power and α is the attenuation coefficient. In fiber optics, a logarithmic scale is commonly used to quantify the loss (rate) $\bar{\alpha}$ along the fiber as follows:

$$\bar{\alpha} = \frac{10\alpha}{\ln 10} = \frac{10}{L} \log_{10} \frac{P_0}{P} \quad \text{in dB/km.} \quad (13.14)$$

The damping D is then defined as

$$\boxed{D = 10 \log_{10} \frac{P_0}{P} = \bar{\alpha}L \quad \text{in dB}.} \quad (13.15)$$

Hence, the relationship between transmission T and damping D reads

$$\boxed{T = 10^{-D/10} = 10^{-\bar{\alpha}L/10}.} \quad (13.16)$$

The wavelength-dependence of the loss is depicted in Fig. 13.10 for a silica fiber. Maximum transmission, i.e. minimum loss of $\bar{\alpha} = 0.2 \text{ dB/km}$ is observed at $\lambda = 1.55 \mu\text{m}$. Using (13.16), the transmission is calculated to be $T = 1\%$ after a propagation length of 100 km, while the attenuation coefficient is $\alpha = 5 \cdot 10^{-7} \text{ cm}^{-1}$.

The global loss minimum around 1.55 μm wavelength results from the combination of different loss mechanisms and is the main reason why most optical communication systems and long-distance data transmission networks are operated at this wavelength. The three major reasons for light attenuation in the fiber are described in the following:

1. *Rayleigh scattering* arises from random density fluctuations and corresponding refractive index fluctuations in the fiber. The total scattered light decreases inversely with the fourth power of the wavelength, so that this process is the dominant loss mechanism in the UV to near-IR spectral region. Furthermore, scattering depends on the content of dopants, as they introduce inhomogeneities. Fibers with a difference in refractive index scatter less than those having a high refractive index difference between core and cladding. This is one reason for the use of low-index difference fibers in telecommunications.
2. *Intrinsic absorption* in the silica material, related to electronic transitions in the UV and vibrational transitions in the IR, lead to the dissipation of transmitted power as heat.

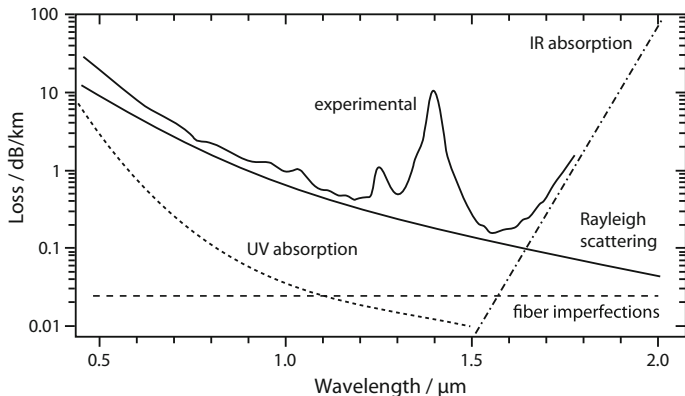


Fig. 13.10 Wavelength-dependence of the loss in a silica fiber. The strong absorption around $1.4 \mu\text{m}$ is due to impurities of the fiber such as water (OH^- groups)

3. *Bending losses* can be divided into two classes. Losses due to microscopic imperfections in the geometry of the fiber, such as core-cladding interface irregularities, bubbles, diameter fluctuations and axis meandering are called micro-bending losses. Micro-bends can also result from mechanical stress. The second class, macro-bending losses, are introduced by large fiber curvatures. In a multimode fiber, modes near the critical angle will be refracted out of the core. In a single-mode fiber, the outer parts of the field distribution will be converted into a radiation mode.

Figure 13.10 does not consider nonlinear optical processes which are briefly discussed below. The strong absorption peaks in Fig. 13.10 are due to impurities. This effect is also called *extrinsic absorption*. The most important impurity is the hydroxyl group OH^- which arises from water contamination during the manufacturing process. Hence, elaborate drying techniques are used to remove the water contamination as much as possible. Other contaminations increasing the fiber loss are ions of the transition metals, such as copper, iron, nickel, vanadium, chromium and manganese. The concentrations of the contaminants must be less than 1 ppb (10^{-9}) to avoid a severe increase in attenuation.

Despite the low loss around $1.55 \mu\text{m}$, fiber amplifiers are required in long-haul fiber transmission paths (Sect. 25.2). The erbium-doped fiber amplifier (EDFA) has revolutionized fiber communication, as it offers broadband, low-distortion optical amplification at this wavelength. It is realized by silica fibers of tens of meters in length that are doped with erbium at a concentration of 10^{18} to 10^{19} cm^{-3} . The EDFA works like a laser amplifier based on a three-level laser system. Pumping is performed using a laser diode with a pump power of 1–100 mW at a wavelength of 980 nm or alternatively at 1470 nm. The gain is around 30 dB, corresponding to a gain factor of 1000, while the amplifier is saturated at an output power of about 100 mW.

Dispersion

Fiber dispersion leads to a temporal pulse broadening which limits the data rate obtainable over a given telecommunication distance. There are three different dispersion mechanisms:

1. *Modal dispersion*, also called intermodal dispersion, only exists in multimode fibers. It results from the difference in the propagation constant of the modes supported by the fiber. Measurements show that, for long fibers, the modal dispersion increases with the square root of the fiber length. This is due to energy exchange between different modes, known as mode coupling. Mode coupling tends to average out the propagation delays among the modes, so that the modal dispersion increases less than linearly with the fiber length. Modal dispersion prevents broadband data transmission over long distances using multimode fibers, thus requiring single-mode fibers to eliminate this type of dispersion.
2. *Material dispersion* describes the wavelength-dependence of the refractive index of the fiber material. Different spectral components travel with different propagation speeds in the fiber. For instance, narrow-linewidth (0.1 nm) pulses emitted by a single longitudinal mode laser diode are less spread in time compared to pulses with broader linewidths, e.g. emitted from a LED (50 nm).
3. *Waveguide dispersion*: The field distributions of the fundamental mode HE₁₁ and any other mode are not confined to the fiber core but penetrate into the cladding. The propagation speed of a wave in the cladding is greater than in the core. Therefore, the propagation speed of a mode depends on the field distribution between the core and the cladding, and hence of the extension of the mode. For short wavelengths corresponding to small modal extensions, the propagation speed is nearly the same as in the core, whereas for long wavelengths the speed approaches the value in the cladding. The same mechanism causes a transit-time difference for different spectral components of one pulse.

Material and waveguide dispersion are important for single-mode fibers. They are often summarized under the term *chromatic dispersion*. A pulse of a spectral width Δf , measured in nanometers, undergoes a temporal broadening τ after traversing a fiber length L :

$$\tau = |D| \Delta f \cdot L. \quad (13.17)$$

This broadening is superimposed on the initial pulse width τ_0 . D denotes the chromatic dispersion parameter, considering both material and waveguide dispersion. Figure 13.11 depicts D for three different single-mode fibers.

The standard fiber is a step-index single-mode fiber. The dispersion parameter D is zero at a wavelength of about 1.31 μm. At this wavelength, the initial pulse width does not change, apart from higher-order dispersion effects and from the inherent spectral bandwidth which is related to the pulse duration via the uncertainty principle.

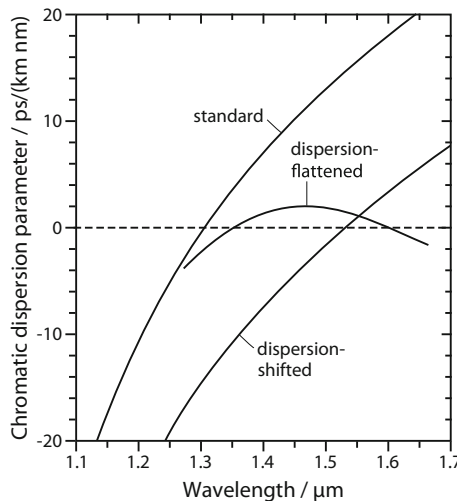


Fig. 13.11 Wavelength-dependence of the chromatic dispersion parameter D for three different single-mode fibers

Besides zero dispersion, light at $1.31 \mu\text{m}$ wavelength also experiences low attenuation in silica fibers, as shown in Fig. 13.10. Therefore, this wavelength is of great relevance for fiber-optic data transmission. Shifting the minimum of dispersion to the damping minimum at $1.55 \mu\text{m}$ would be even more effective. This is achieved in dispersion-shifted fibers by modelling the refractive index in such a manner that the waveguide dispersion cancels out the material dispersion. Additionally, by a special design of the refractive index profile, a dispersion-flattened fiber can be realized which features low dispersion over the whole wavelength interval from 1.3 to $1.6 \mu\text{m}$ (see Fig. 13.11).

The HE_{11} -mode is polarization-degenerate. Therefore, two modes can propagate in a single-mode fiber, which is thus not truly single-mode. Non-perfect manufacturing and mechanical stress induce birefringence in the fiber which removes the degeneracy. As a result, the two modes have different propagation constants, leading to a slow and a fast axis. The degree of this so-called modal birefringence increases linearly with the difference of the propagation constants and is not constant along the fiber but changes randomly. Light with linear polarization that is launched into the fiber quickly reaches a state of arbitrary polarization due to mode coupling between the two modes. An optical pulse is also broadened due to the different propagation constants along the fast and the slow axis. The effect is called *polarization mode dispersion*. For polarization-sensitive fiber applications such as interferometric sensors, polarization-maintaining fibers are used. Here, stress creates an azimuthal asymmetry resulting in strong birefringence. Consequently, the direction of polarization does not change if the initial polarization direction coincides with the fast or the slow axis, because mode coupling is suppressed.

Nonlinearities

The response of any dielectric becomes nonlinear at intense electromagnetic fields (Sect. 19.2). The second-order nonlinearity χ_2 [see (19.3)] in silica glass is zero because of the inversion symmetry at the molecular level. Hence, third-order nonlinear effects, corresponding to χ_3 , are dominant in silica fibers.

Inelastic scattering processes are of particular importance for the fiber transmission. As explained in Sect. 19.5, stimulated Raman scattering (SRS) describes the interaction of a light field with molecular vibrations, leading to an up- or downshifting of the wavelength. In the particle picture, an optical phonon is either created or annihilated during the interaction of an incident photon with the molecule, resulting in a lower (Stokes) or higher (anti-Stokes) photon energy of the scattered photon (Fig. 19.10). Stimulated Brillouin scattering (SBS) can be considered similarly; however, the interaction involves acoustic instead of optical phonons. The gain spectrum of SBS is noticeably narrower than that of SRS. Moreover, SBS shows a considerably higher gain and preferentially occurs in backward direction (Sect. 14.4). It is therefore the dominant process affecting narrowband light.

Important processes which result from the real part of the third-order susceptibility χ_3 are self-phase modulation (SPM) and cross-phase modulation (XPM). Both effects lead to an intensity-dependence of the refractive index. SPM result from the fact that the electric field of a wave affects the refractive index n of the medium through which it propagates. While traveling along the fiber, the modulation of the refractive index introduced by the wave itself results in nonlinear (self-induced) phase shifts. Since the time derivative of the phase is simply the angular frequency of the wave, SPM also appears as a frequency modulation, giving rise to spectral broadening. Likewise, XPM also leads to a nonlinear phase shift, but in this case one wave influences the refractive index seen by another wave. Another third-order nonlinear effect which is also associated with the real part of χ_3 is four-wave mixing (Sect. 14.4).

Owing to the small core diameter, especially for single-mode fibers, and the long effective interaction length in case of low attenuation, the power thresholds for nonlinear effects are comparably low in optical fibers. For instance, SBS limits the maximum power to be transmitted through a standard single-mode fiber to $P < 10$ mW. Above this value, new frequencies are generated which disturb the signal transmission in wavelength-multiplexed systems because of cross-talk between the channels.

However, nonlinear effects in fibers are also exploited in numerous applications. This includes, for instance, Raman and Brillouin laser and amplifiers. XPM is utilized for realizing ultra-short optical switches for the fs-regime (Kerr effect switches). For the generation of ultra-short laser pulses, SPM in fibers is used in fiber grating compressors. Moreover, nonlinear optical processes are exploited in photonic crystal fibers for supercontinuum generation, as stated above.

Another nonlinear phenomenon resulting from SPM is the formation of solitons. In the anomalous dispersion range (at wavelengths above 1.31 μm for a standard single-mode fiber, see Fig. 13.11), the frequency shift introduced by chromatic dispersion is opposite to that introduced by SPM. Chromatic dispersion leads to a blue shift at the leading edge of a pulse, whereas SPM leads to a red shift at the leading edge. Under certain circumstances, the two effects can exactly cancel each other, apart from a constant phase delay per unit propagation distance, so that the temporal and spectral shape of the waveform is preserved even over long propagation distances. Such a pulse is called a soliton.

Solitons are characterized by very high stability against changes of the properties of the medium, provided that these changes occur over distances which are long compared to the so-called soliton period. The latter is defined as the propagation distance in which the constant phase delay is $\pi/4$. Hence, solitons can adapt their shape to slowly varying parameters of the medium in order to re-establish the balance between chromatic dispersion and SPM.

Solitons can be used for data transmission. For a given fiber length, the bandwidth of data transmission is significantly increased, because neither dispersion nor SPM change the pulse form, but instead stabilize the pulse form. A 5 Gbit/s single channel soliton transmission over more than 15,000 km has been demonstrated experimentally.

Further Reading

1. M. Bertolotti, C. Sibilia, A. Guzman, *Evanescence Waves in Optics* (Springer, 2017)
2. O. Shulika, I. Sukhoivanov (eds.), *Contemporary Optoelectronics* (Springer, 2016)
3. G. Marowsky (ed.), *Planar Waveguides and other Confined Geometries* (Springer, 2015)
4. C. Yeh, F. Shimabukuro, *The Essence of Dielectric Waveguides* (Springer, 2008)
5. J.M. Lourtioz, H. Benisty, V. Berger, J.M. Gerard, D. Maystre, A. Tchelnokov, *Photonic Crystals* (Springer, 2008)
6. J. Hecht, *Understanding Fiber Optics* (Prentice Hall, 2005)
7. K. Okamoto, *Fundamentals of Optical Waveguides* (Academic Press, 2005)
8. K. Sakoda, *Optical Properties of Photonic Crystals* (Springer, 2005)
9. V. Lucarini, J.J. Saarinen, K.E. Peiponen, E.M. Vartiainen, *Kramers-Kronig Relations in Optical Materials Research* (Springer, 2005)
10. M.N. Islam (ed.), *Raman Amplifiers for Telecommunications 2* (Springer, 2004)
11. M.J. Weber, *Handbook of Optical Materials* (CRC Press, 2002)
12. E.G. Neumann, *Single-Mode Fibers* (Springer, 1988)
13. A.B. Sharma, S.J. Halme, M.M. Butusov, *Optical Fiber Systems and Their Components* (Springer, 1981)

Part V

Optical Elements for Lasers

Aside from the gain medium, mirrors are an essential part of almost every laser, as they form the resonator that provides the optical feedback, and hence, the amplification of the stimulated emission. The specification of laser mirrors, especially in terms of reflectance, is crucial for the laser performance. Other reflecting and refracting optical elements such as beam splitters or polarizers are important for guiding, separating, and combining the radiation, both inside and outside the laser cavity. Moreover, the utilization of passive and active optical devices enables the modulation of laser beams which is particularly relevant for generating short pulses. This part of the book gives an insight into the design and operation principle of different optics that are commonly employed in laser configurations. The focus is on different types of mirrors, polarization optics as well as diverse components used for deflecting and modulating laser beams.

Chapter 14

Mirrors



Simple laser mirrors are made of polished metals, e.g. copper for infrared CO₂ lasers, or metal layers, e.g. gold, silver, aluminum, on glass substrates for visible light. Reflection of light occurs at the mirror surface, while a portion of the radiation usually penetrates into the material where it is absorbed. Light can also be partially transmitted through the mirror which is especially important for laser output couplers.

Reflection also occurs at the surfaces of transparent media such as glass, water or other so-called dielectric, i.e. non-metallic, materials. In case of perpendicular (normal) incidence, the reflectance at the interface between air and glass is about 4%, but can reach 100% under grazing incidence angles when total internal reflection occurs. The physical laws governing reflection and refraction are discussed in Sect. 14.1.

Mirrors with desired degree of reflectance at arbitrary incidence angles are realized by dielectric multilayer systems. Here, multiple layers of two transparent materials with different refractive indices are alternately stacked, resulting in a series of interfaces with a pre-configured wavelength-dependent reflectance. Such multilayer mirrors are of significant importance in laser technology, as they allow for high flexibility in the design of laser resonators. Moreover, very low absorption is achieved since the power of the incident beam is distributed among the reflected and the transmitted beam almost without any losses. In this way, both highly reflective and highly transmissive optical components can be produced by the application of dielectric multilayer coatings. The configuration of multilayer mirrors is outlined in Sect. 14.2.

Coated plates that are tilted towards an incident beam are used as beam splitters (Sect. 14.3), where the division ratio depends on the light wavelength and polarization. It can be further adjusted via the thickness of the layers within the layer stack.

Phase conjugate mirrors are special reflecting devices that are characterized by the fact that light is always reflected straight back the way it came from, regardless of the angle of incidence. The underlying physical phenomenon, optical phase conjugation, is a nonlinear optical process which involves the generation of a light

wave that counterpropagates to the incident beam, but with reversed phase fronts. This principle is utilized for the compensation of phase distortions in high-power laser systems and will be explained in Sect. 14.4.

14.1 Reflection and Refraction

Light propagating through a medium with refractive index n travels at a speed

$$\boxed{c' = \frac{c}{n}}, \quad (14.1)$$

where $c = 2.998 \times 10^8$ m/s denotes the vacuum speed of light. When radiation is incident on an interface separating two materials, reflection and refraction occurs. While the law of reflection states that the angle θ_1 at which the ray is incident on the surface equals the angle θ'_1 at which it is reflected, the direction of the refracted ray θ_2 is given by Snell's law:

$$\boxed{n_1 \sin \theta_1 = n_2 \sin \theta_2}. \quad (14.2)$$

Here, n_1 and n_2 are the refractive indices of the two media, e.g. air and glass as shown in Fig. 14.1. Transparent materials have refractive indices ranging from $n = 1$ to about $n = 3$; glass has a value around $n = 1.5$ depending on the glass type and wavelength (see Table 14.1). The refractive index of air at 0 °C temperature, 1013.25 hPa = 1 atm. pressure and 589 nm wavelength is $n = 1.000292$.

Reflectance

The fraction of the incident power that is reflected from an interface is referred to as reflectance and can be derived from the Fresnel equations which describe the

Fig. 14.1 Reflection ($\theta_1 = \theta'_1$) and refraction of light at an optical interface (here: between air and glass)

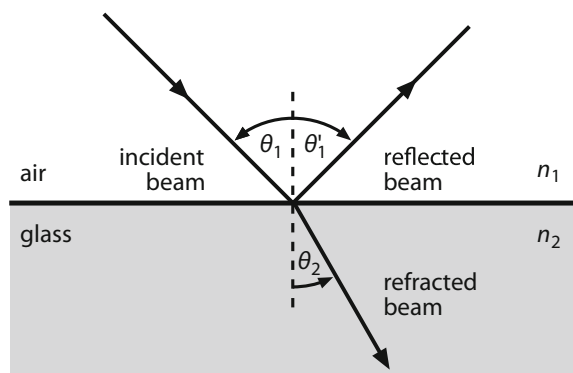


Table 14.1 Wavelength-dependence (dispersion) of the refractive index for different materials. The indices are related to certain spectral lines, e.g. D2 refers to the sodium D2-line at 589 nm

Material	n_C (red) (656 nm)	n_{D2} (yellow) (589 nm)	n_F (blue) (486 nm)	n_H (violet) (399 nm)
Water, 20 °C	1.331	1.333	1.337	1.343
Crown glass	1.516	1.519	1.525	1.535
Flint glass	1.614	1.619	1.631	1.653

behavior of light when traveling between media of differing refractive indices. The behavior depends on the direction of the electric field (polarization) of the incident light with respect to the plane of incidence, i.e. the plane that contains the incident, reflected and refracted rays. One distinguishes between the parallel (or p-polarized) component where the electric field is parallel to the plane of incidence and the perpendicular (or s-polarized) component. According to the Fresnel equations, the reflectances R_p and R_s are given as

$$R_p = \left(\frac{\tan(\theta_1 - \theta_2)}{\tan(\theta_1 + \theta_2)} \right)^2, \quad R_s = \left(\frac{\sin(\theta_1 - \theta_2)}{\sin(\theta_1 + \theta_2)} \right)^2. \quad (14.3)$$

For normal incidence ($\theta_1 = \theta_2 = 0$), the equations simplify to

$$R = R_p = R_s = \left(\frac{1 - n_1/n_2}{1 + n_1/n_2} \right)^2. \quad (14.4)$$

The angle-dependence of the reflectances R_p and R_s for an air-glass interface is shown in Fig. 14.2. For a particular angle of incidence, the so-called Brewster's angle, only the s-polarized component is reflected, while p-polarized light is completely transmitted through the material, i.e. $R_p = 0$. This is the case when $\theta_1 + \theta_2 = 90^\circ$, that is if

$$\boxed{\tan \theta_B = n_2/n_1}. \quad (14.5)$$

The vanishing reflectance for one polarization component can be explained by the fact that an oscillating electric dipole does not emit radiation in the direction of the oscillation (see Fig. 2.8).

Total Internal Reflection

In the situation described above, light traveled from a less optically dense medium, i.e. a medium with lower refractive index, to a more optically dense one ($n_1 < n_2$). If the situation is reversed ($n_1 > n_2$), the behavior is totally different. Light emanating from the interface between the two media is refracted away from the normal.

Fig. 14.2 Reflectance of a glass plate ($n_2 = 1.52$) for s- and p-polarized light being incident from air ($n_1 = 1$). At the Brewster angle θ_B , only one polarization component is reflected

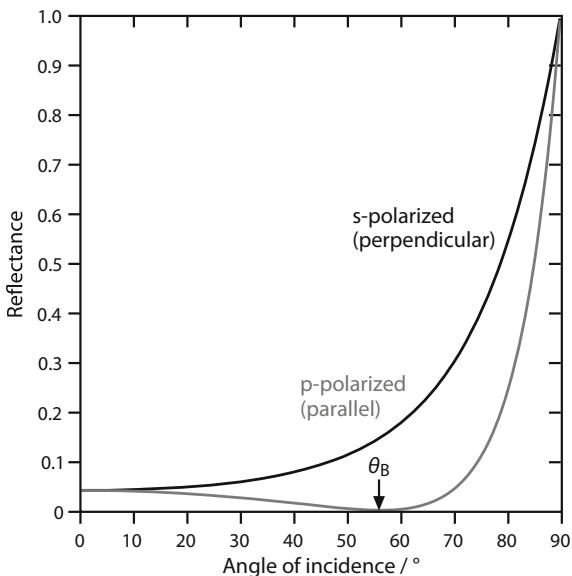
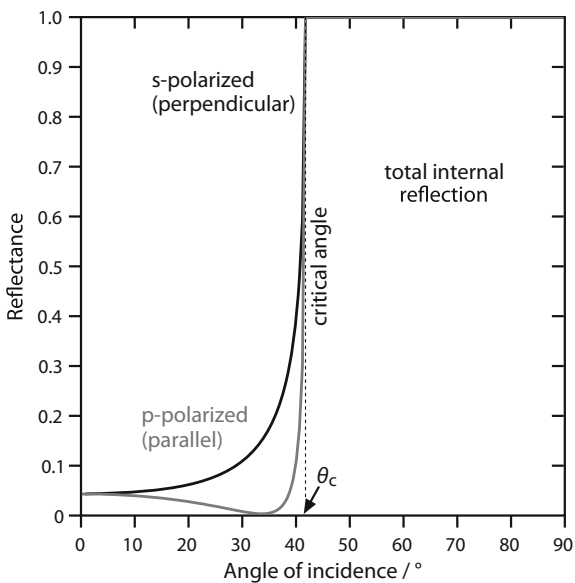


Fig. 14.3 Reflectance of a glass plate ($n_1 = 1.5$) for s- and p-polarized light being extracted to air ($n_2 = 1$). Above the critical angle θ_c , total internal reflection occurs



If the angle of incidence is increased beyond the critical angle θ_c , the wave will not cross the boundary, but will instead be totally reflected back into the denser medium (Fig. 14.3). This phenomenon is called total internal reflection. The critical angle can be derived from Snell's law (14.2) for $\theta_2 = 90^\circ$:

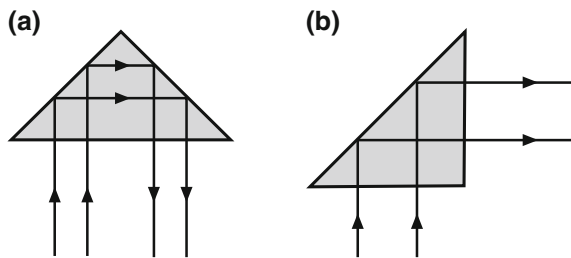


Fig. 14.4 Total internal reflection in a right-angle prism used for deviating the light path a by 180° (retroreflector) or b by 90° . For the retroreflector, the 180° deflection of the light path is independent of the angle at which the light enters the prism

$$\sin \theta_c = n_2/n_1. \quad (14.6)$$

For a glass-air interface, $\theta_c \approx 42^\circ$.

Total internal reflection is exploited for guiding light rays in optical fibers (see Sect. 13.2) and various prisms. Figure 14.4 shows a right-angle prism that can be used to deflect rays of light by 180° or 90° . When the input light is incident on the face of the hypotenuse, it undergoes total internal reflection twice at the sloped glass-air interfaces and exits again through the large rectangular face in a path parallel to that of the input beam (Fig. 14.4a). In this way, the element which is also known as Porro prism, acts as a retroreflector, where the 180° deflection of the light path is independent of the angle at which the light enters the prism.

When the incident light is incident on one of the prism's legs, total internal reflection occurs at the glass-air interface of the hypotenuse, leading to a ray that exits via the other prism leg (Fig. 14.4b). Like the retroreflector, the 90° -reflector represents a suitable alternative for a mirror, provided that the entrance and exit faces are anti-reflective coated.

Right angle deflection of a light ray or image is also obtained with roof prisms that are similar to the Porro prism, with the distinction that the hypotenuse of the prism consists of two faces meeting at a 90° angle, thus forming a roof edge. Hence, when passing through the roof prism, an image is deflected both right-to-left and top-to-bottom upon total internal reflection. In case light enters the prism at a slant angle with respect to the roof edge, the reflected ray is not parallel to the incoming ray, so that variations in the light direction are only compensated in one direction. In contrast, retroreflection with low alignment sensitivity is achieved with a corner cube reflector, as illustrated in Fig. 14.5. They are formed of three reflective prism faces each enclosing an angle of 90° , therefore returning an incident light ray in the opposite direction, regardless of the incidence angle. Unless the incident and reflected rays strike the exact center of the optic, they will not overlap but rather be displaced with respect to each other.

Corner reflectors are especially suited as highly-reflective, self-aligning laser mirrors. An array of retroreflectors has been set up on the lunar surface when

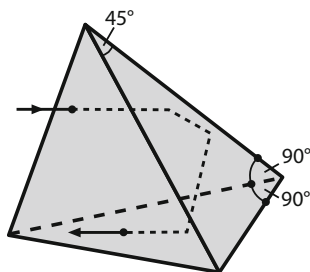


Fig. 14.5 Retroreflection in a corner cube. Light enters the tetrahedral prism through the indicated spot on the entrance plane which is defined by three face diagonals of a cube. The beam is then reflected from the three faces forming the corner of the cube. Thus, the direction of the exiting beam is antiparallel to the incident beam, while a displacement occurs. Refraction at the entrance surface is not shown in the picture

Apollo XI astronauts landed on the moon in 1969. Using laser ranging, the Earth-Moon distance can be determined with near millimeter accuracy from the time-of-flight of laser pulses aimed at the retroreflectors from the Earth. Corner reflectors are also applied in traffic and automotive engineering.

Dispersion

The refractive index of optical materials is dependent upon the wavelength of the incident light. In the visible spectral range, the refractive index increases with decreasing wavelength, i.e. blue light is refracted more strongly than red light (Table 14.1). Owing to dispersion, white light is split (dispersed) into a spectrum of colors in prisms, as the different wavelengths are refracted at different angles (see Fig. 18.5).

Metallic Mirrors

The description of reflection from metallic surfaces is more complicated compared to dielectrics. Although the polarization state is generally preserved upon reflection on metals, at very shallow incidence angles, a portion of the radiation can be absorbed in the material, resulting in elliptical polarization of the reflected light and potential damage of the mirror surface.

High backward reflectance of 99% is obtained in the infrared, whereas slightly lower values from 95 to 98% are common in the visible spectral region (Table 14.2). Metallic mirrors are usually produced by vapor deposition on glass substrates that are subsequently coated with protective layers, e.g. MgF_2 and SiO_2 .

Table 14.2 Reflectance of different metals

Wavelength (nm)	Reflectance R (%)		
	Al	Ag	Au
220	91.5	28.0	27.5
300	92.3	17.6	37.7
400	92.4	95.6	38.7
550	91.5	98.3	81.7
1000	94.0	99.4	98.6
5000	98.4	99.5	99.4
10,000	98.7	99.5	99.4

14.2 Dielectric Multilayer Mirrors

The reflection characteristics of optical surfaces can be strongly modified by the deposition of thin dielectric layers. Interference of light reflected from the different layers leads to an increased or decreased reflectance. By careful selection of the thickness and material of the dielectric layers, an optical coating with specified reflectance at different wavelengths can be designed. The refractive indices of different coating materials that are widely used for the fabrication of dielectric multilayer mirrors are listed in Table 14.3.

Anti-reflective Coatings

According to (14.4) and Fig. 14.2, about 4% of the light normally incident on an air-glass boundary is reflected. Coating of the glass surface with a dielectric layer with optical thickness

$$n d = \lambda/4. \quad (14.7)$$

reduces the reflectance for light with wavelength λ . The reduction is due to destructive interference of the waves reflected from the two surfaces of the quarter-wave (or $\lambda/4$) layer, as the wave reflected from the second surface travels exactly half its own wavelength further than the wave reflected from the first

Table 14.3 Refractive indices of selected coating materials. The values deviate from the refractive indices of the respective bulk materials and depend on the fabrication process

Wavelength (nm)	SiO_2	Ta_2O_5	HfO_2	MgF_2	ZnS	Al_2O_3
488	1.463	2.188	1.894	1.379	2.401	1.635
532	1.461	2.174	1.886	1.379	2.380	1.631
633	1.457	2.152	1.874	1.378	2.348	1.624
1064	1.450	2.117	1.861	1.376	2.296	1.615

surface. Since $n_1 < n < n_2$, reflection always occurs in the optically denser medium, while the waves undergo the same phase shift of π . If the two waves have equal amplitudes, they exactly cancel out each other. For this purpose, the refractive index of the $\lambda/4$ -layer must lie between that of air (n_1) and the glass (n_2). The reflectance in case of normal incidence reads

$$R = \left(\frac{n_1 n_2 - n^2}{n_1 n_2 + n^2} \right)^2. \quad (14.8)$$

Consequently, the condition

$$n = \sqrt{n_1 n_2}. \quad (14.9)$$

has to be met in order to achieve zero reflectance.

Lenses are often coated with $\lambda/4$ -layers of MgF_2 , where the requirement (14.9) is approximately fulfilled over the entire visible spectral range. In case the refractive index of the lens material is $n_2 = 1.6$, the reflectance is decreased to about 1%, almost independent on the wavelength.

For many optical materials, there is no ideal coating medium with appropriate refractive index that satisfies (14.9). Hence, the utilization of two different layers is necessary to realize anti-reflective coatings. Here, the layer facing the air has a lower (n) and the layer deposited on the substrate has a higher refractive index n' compared to the substrate material. The total reflectance vanishes if the field reflection coefficients r at the three surfaces add up to zero. The latter are given by

$$r_1 = \frac{n_1 - n'}{n_1 + n'}, \quad r_2 = \frac{n' - n}{n' + n}, \quad r_3 = \frac{n - n_2}{n + n_2}, \quad (14.10)$$

while the phase shifts Δ_1 and Δ_2 introduced by the two layers with different thickness have to be taken into account. Thus, the condition for zero total reflectance is

$$r_1 + r_2 \cdot e^{-i\Delta_1} + r_3 \cdot e^{-i(\Delta_1 + \Delta_2)} = 0. \quad (14.11)$$

This equation can be represented in the complex plane by a triangle with side lengths $|r_1|$, $|r_2|$ and $|r_3|$. The requirements imposed on the refractive indices n and n' of the two layers is therefore given by a set of inequalities as follows:

$$|r_1| < |r_2| + |r_3|, \quad |r_2| < |r_1| + |r_3|, \quad |r_3| < |r_1| + |r_2|. \quad (14.12)$$

These triangle inequalities are easily fulfilled in practice. With the knowledge of the different refractive indices, Δ_1 and Δ_2 are calculated from the angles of the triangle in the complex plane defined by (14.10) and (14.11). The relationship between the angles and the known side lengths is given by the law of cosines.

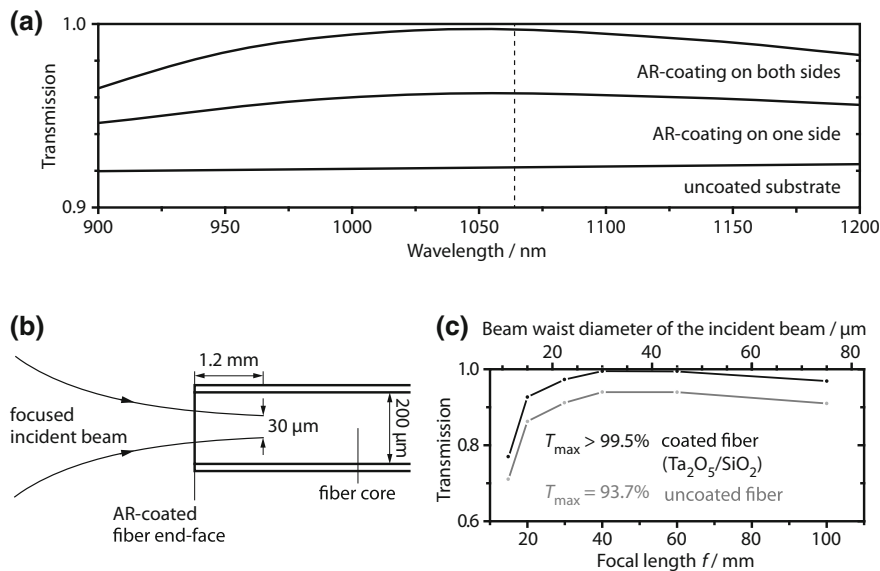


Fig. 14.6 **a** Transmission spectrum of a glass plate (BK7), uncoated and with a single- and dual-side anti-reflective coating consisting of SiO₂ ($n = 1.45$) and Ta₂O₅ ($n' = 2.1$). The residual reflection at 1064 nm is below 0.2%. **b** Anti-reflective (AR-) coating of a fiber end-face and **c** corresponding transmission spectrum

Using multiple layers also enables the realization of anti-reflective coatings for two or more wavelengths, e.g. 1064 and 532 nm. Moreover, such coatings can be applied to the end-faces of optical fibers to minimize coupling losses, as shown in Fig. 14.6b.

Laser Mirrors

The reflectance R of a partially transmissive mirror is related to its transmission T and absorption (including scattering) A via

$$R + T + A = 1. \quad (14.13)$$

Laser mirrors need to provide low absorption ($A \ll T$), as otherwise a portion of the laser power is lost during each round-trip. Furthermore, in case of high-power lasers, absorption involves the heating of the mirror that can ultimately lead to damage of the optic. Metallic mirrors feature high reflectance of up to 99% for infrared wavelengths (see Table 14.2), but since the absorption is significant in the visible spectral range, they are hardly used as laser mirrors.

Low-loss mirrors with high reflectance are instead realized by stacks of the $\lambda/4$ -layers, as defined in (14.7). Already a single layer deposited on a substrate can

considerably increase its reflectance. As opposed to anti-reflective coatings, the refractive index n of the layer has to be higher than that of the used substrate, e.g. glass:

$$n_1 < n > n_2. \quad (14.14)$$

In this way, the phase shift at the boundary between the layer and the substrate is avoided, while a phase shift of π is introduced at the air-glass interface. Hence, the total optical path difference between the two reflected waves is one wavelength, so that constructive interference occurs. For instance, a single high-index layer of ZnS ($n = 2.3$) enhances the reflectance of glass ($n_2 = 1.5$) at normal incidence from 4% to more than 30% in the wavelength range around 300 nm.

Higher reflectances exceeding 99% are obtained with multilayer mirrors that can be nearly loss-free. They consist of alternating layers of a low-index material like SiO₂ and a higher-index material like Ta₂O₅ that are deposited onto the substrate at an optical thickness of $nd = n'd' = \lambda/4$ (Fig. 14.7). Constructive interference between the numerous waves reflected from the interfaces results in a very high reflectance.

At normal incidence, it is approximately given by

$$R = \left[\frac{n^2(n/n')^{2m} - n_1 n_2}{n^2(n/n')^{2m} + n_1 n_2} \right]^2 \approx 1 - 4 \frac{n_1 n_2}{n^2} \left(\frac{n'}{n} \right)^{2m}, \quad (14.15)$$

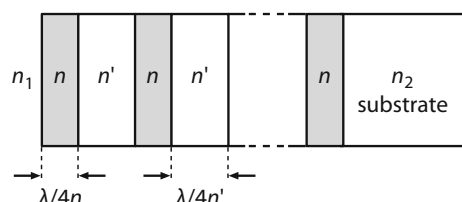
where n and n' are the refractive indices of the coated layers ($n > n'$), n_1 and n_2 denote the refractive indices of the air and the substrate and m is the number of low-index layers. The overall number of layers is uneven:

$$k = 2m + 1. \quad (14.16)$$

The reflectance of a multilayer mirror consisting of SiO₂ and Ta₂O₅ in dependence on the number of layers k is plotted in Fig. 14.8. Values of 99.99% are achieved in case of low absorption.

The reflectance is strongly wavelength-dependent, as shown in Figs. 14.9 and 14.10, depicting the transmission spectra of multilayer mirrors designed for different purposes. The first mirror is optimized for high reflectance at a center wavelength of $\lambda = 1064$ nm, for which the optical layer thickness meets the condition $nd = n'd' = \lambda/4$. Light at wavelengths that deviate from the center

Fig. 14.7 Layer composition of a dielectric multilayer mirror consisting of high- and low-refractive index layers ($n > n'$)



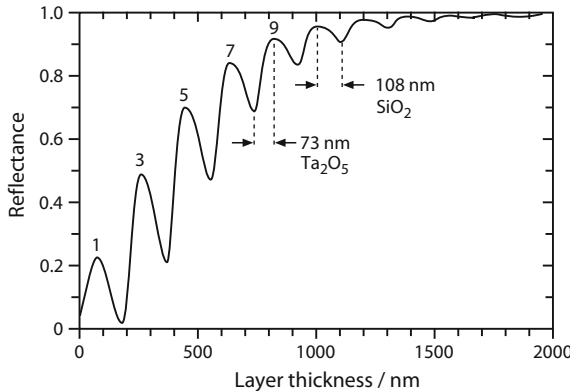


Fig. 14.8 Reflectance of a dielectric multilayer mirror for light at 633 nm wavelength depending on the layer thickness. The number of layers are indicated in the diagram (courtesy of C. Scharfenorth)

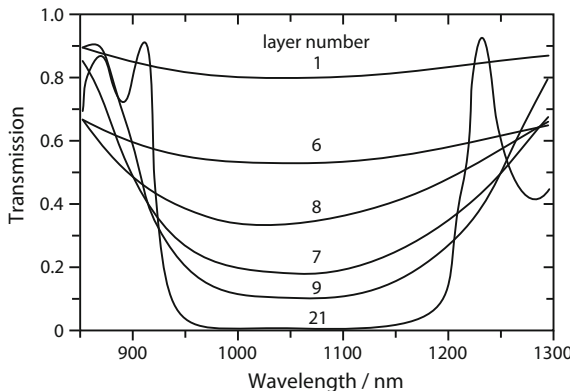
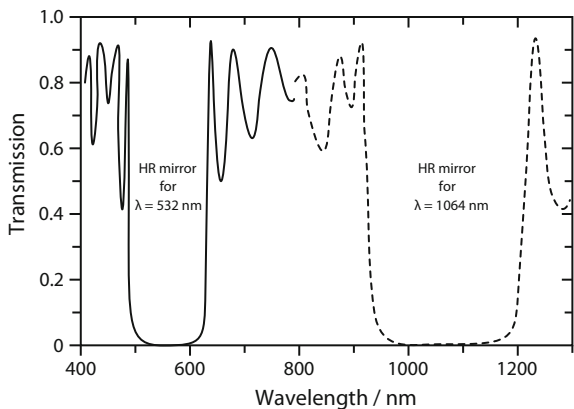


Fig. 14.9 Wavelength-dependent transmission $T \approx 1 - R$ of dielectric mirrors with different number of layers. The mirrors are designed for maximum reflectance at 1064 nm. Note that the eighth (low-refractive-index) layer reduces the reflectance compared to the seventh layer (see also Fig. 14.8)

wavelength experience lower reflectance. The second figure shows the transmission spectra of two highly-reflective (HR) mirrors specified for 1064 nm and 532 nm wavelength, respectively. Such mirrors are employed in (frequency-doubled) Nd: YAG lasers (Sect. 19.3).

The strong wavelength-dependence of the reflectance is also exploited in so-called dichroic mirrors that are used to separate light at different wavelengths. For instance, dichroic mirrors are essential in end-pumped lasers for injecting the pump light into the laser cavity (see, e.g. Fig. 9.21). Moreover, for the purpose of intra-cavity frequency-doubling, a dichroic end mirror may be used to couple out the frequency-doubled light while fully reflecting the fundamental radiation.

Fig. 14.10 Transmission of two different multilayer mirrors (each 21 layers of Ta_2O_5 and SiO_2) designed for high reflectance (HR) at 532 and 1064 nm wavelength, respectively. The HR region increases with wavelength



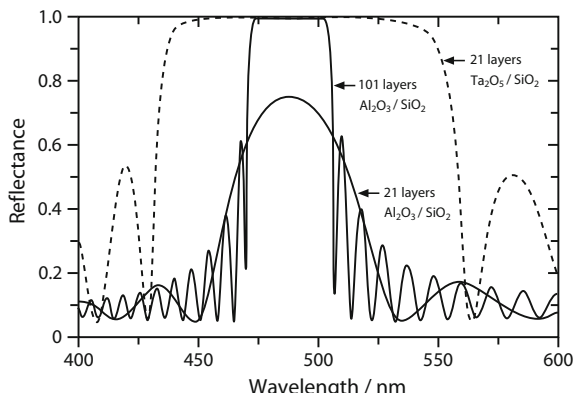
Likewise, optical parametric oscillators (Sect. 19.4) and Raman lasers (Sect. 19.5) for nonlinear frequency conversion are based on dichroic mirrors separating the pump from the frequency-converted radiation.

The direct quantification of mirror reflectances is complicated and often circumvented by measuring the transmission. If absorption and scattering can be neglected, the reflectance is given by $R \approx 1 - T$. The selection of coating materials with adequate refractive indices in combination with a sophisticated design of layer stacks allows for the fabrication of laser mirrors with desired reflectance at specific wavelengths for any incident angle and polarization state (see also Figs. 14.8 and 14.11).

14.3 Beam Splitters

Splitting of an incident light beam into two beams with different optical power is required in many applications, e.g. in interferometry or holography, as well as in autocorrelators and various laser systems. A beam splitter can be simply realized by

Fig. 14.11 Calculated reflectance R of dielectric mirrors consisting of Al_2O_3 , SiO_2 and $\text{Ta}_2\text{O}_5/\text{SiO}_2$. For large numbers of layers and small differences in refractive index (like for the material combination $\text{Al}_2\text{O}_3/\text{SiO}_2$), very narrow reflection bandwidths can be realized



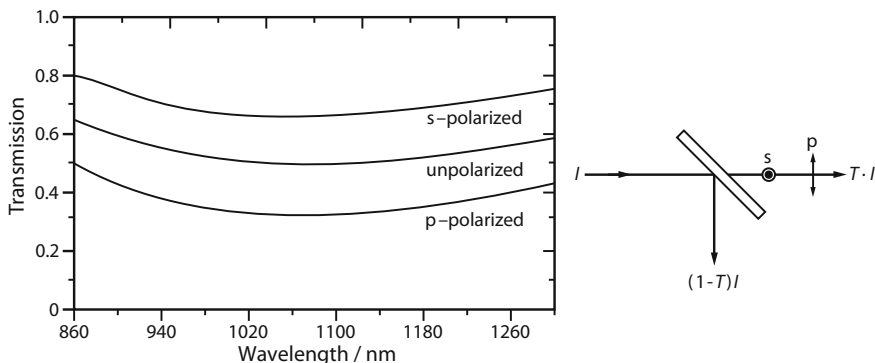


Fig. 14.12 Beam splitter with a calculated splitting ratio of 1:1 at an incidence angle of 45° for unpolarized radiation at 1064 nm wavelength. Other splitting ratios are obtained for s- and p-polarized light

a glass plate that is placed into the path of the laser beam at a certain angle (mostly at 45°). While one side is coated with a dielectric mirror with a specified reflectance $0 < R < 1$ according to the desired splitting ratio at a given incidence angle, the other side often has a broadband anti-reflective coating. The polarization- and wavelength-dependent transmission T of such a beam splitter is depicted in Fig. 14.12 together with a schematic showing the separation of the incident intensity I into two portions with intensities $T \cdot I$ and $(1 - T)I$. Dichroic mirrors, as described in the previous section, can also act as beam splitters. For instance, such a device can be employed after a frequency-doubling crystal (Sect. 19.3) for separating the harmonic radiation from the residual fundamental light (harmonic separator).

Other types of beam splitters are made of pellicles which are membranes, e.g. thin nitrocellulose foils, that can be coated with dielectric layers. As opposed to thicker glass plates, the membranes only introduce a negligible lateral displacement of the propagating beam and are sometimes used in cameras. However, such beam splitters are mechanically sensitive.

More practicable are cubic beam splitters consisting of two rectangular glass prisms that are assembled to a cube. Metallic or dielectric layers are positioned diagonally between the opposing base faces of the prisms. Since the incident and exit beams pass the air-glass interface perpendicularly, the lateral beam displacement is minimal. Depending on the design of the beam splitter cube, the different polarization components are reflected with equal or different intensity. Polarizing beam splitters serve as polarizers and are discussed in more detail in Sect. 15.3.

14.4 Phase Conjugate Mirrors

Over the last 35 years, phase conjugate mirrors (PCM) that rely on the nonlinear optical process of phase conjugation have been developed. These devices only reflect laser light if the incident optical intensity is sufficiently high. Moreover, PCMs have the interesting feature that the phase fronts of the reflected wave are

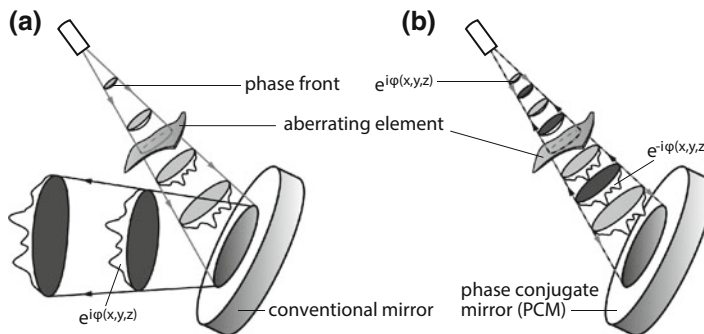


Fig. 14.13 Principle of a phase conjugate mirror: Reflection of a divergent beam with distorted phase fronts **a** by a conventional mirror and **b** by a phase conjugate mirror. Incident and reflected beams are indicated by light grey and dark gray color, respectively

inverted, i.e. they are identical to those of the incident wave, but the propagation direction is reversed. Consequently, in contrast to a conventional mirror where the law of reflection is obeyed, the beam reflected from a PCM can be regarded as a “time reversed” replica of the incident wave independent of the incidence angle. This leads to the compensation of phase distortions and a recovery of the original phase fronts after a double-pass through a phase-aberrating medium (Fig. 14.13). Therefore, the effect of phase conjugation is harnessed in high-power laser systems with double-pass amplifiers to eliminate thermally induced phase distortions, thus improving the beam quality of the output radiation. However, proper compensation presumes that the properties of the phase-aberrating medium remain constant in the time span between forward and backward propagation.

The term phase conjugation is derived from the fact that the optical field of the reflected light wave is related to the complex conjugate of the incident field. For a theoretical treatment, one considers a monochromatic wave of frequency f which is described by the electric field

$$E(x, y, z, t) = \frac{1}{2} E_0(x, y, z) \exp[i2\pi(ft + \varphi(x, y, z))] + c.c. \quad (14.17)$$

The amplitude E_0 and phase φ can be combined to the complex amplitude A :

$$A = (E_0/2) \exp(i2\pi\varphi). \quad (14.18)$$

In case of a plane wave propagating in z -direction, the phase is $\varphi = k \cdot z$, where $k = 2\pi/\lambda$ is the wave number and λ is the wavelength. The reflected wave has the same phase fronts, however the sign of the phase $\varphi(x, y, z)$ is inverted, so that the electric field is given by

$$E_{PC}(x, y, z, t) = \frac{1}{2} E_0(x, y, z) \exp[i2\pi(ft - \varphi(x, y, z))] + c.c. \quad (14.19)$$

Hence, the complex amplitude of the reflected wave is

$$A_{\text{PC}} = (E_0/2) \exp(-i2\pi\varphi) = A^*, \quad (14.20)$$

which is the complex conjugate of the incident amplitude. Therefore, the reflected wave E_{PC} is called the phase conjugate wave. It propagates with the same phase fronts, but in the opposite direction with respect to the incident wave. This becomes obvious at the example of a plane wave determined by the phase $\varphi = -k \cdot z$. The inversion of the sign corresponds to a reversal of the propagation direction. The elimination of phase distortions by means of a phase conjugate mirror is illustrated in Fig. 14.13. Such distortions can for instance be caused by discontinuous refractive index profiles in laser rods and are expressed by the term $\exp[i\varphi(x, y, z)]$. Since the phase fronts of the phase conjugate wave remain unchanged upon reflection, the distortions are compensated during the second pass through the aberrating medium.

Four-Wave Mixing

There are different methods for realizing optical phase conjugation. One common approach is the four-wave mixing (FWM) technique, while other nonlinear optical processes like stimulated Brillouin scattering can be used as well. Four-wave mixing can be understood as a special type of real-time holography. Here, materials are used whose refractive index or absorption coefficient depend on the incident light intensity, i.e. photorefractive crystals or saturable absorbers (see Sect. 16.4). Like in holography (Sect. 25.4), FWM involves the superposition of a signal beam A and a reference beam A_1 while the latter is called pump beam when describing FWM processes. Interference of the corresponding waves inside the medium leads to an intensity-dependent transmission that is, at the location $z = 0$, described by the function

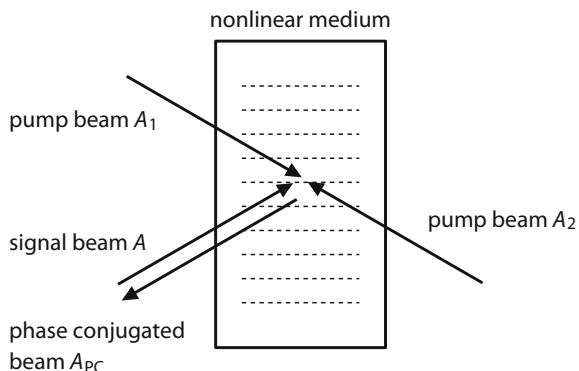
$$t(x, y) \sim |A_1(x, y, 0) + A(x, y, 0)|^2 = |A_1|^2 + |A|^2 + A_1 A^* + A_1^* A. \quad (14.21)$$

In contrast to the reconstruction of holograms, optical phase conjugation by FWM is realized by irradiating the nonlinear medium with a second pump beam $A_2 = A_1^*$ that counterpropagates the first pump beam, as shown in Fig. 14.14. The resulting light intensity in the plane $z = 0$ of the medium reads

$$A_1^* t(x, y) \sim |A_1|^2 A_1^* + |A|^2 A_1^* + |A_1|^2 A^* + A_1^{*2} A. \quad (14.22)$$

The term $A_{\text{PC}} = |A_1|^2 A^*$ can be identified with the phase conjugate wave propagating in the opposite direction to the signal wave. Since the imaginary part of the amplitude contains the phase of the wave (see (14.18)), the reflected wave A_{PC} in the

Fig. 14.14 Phase conjugation by four-wave mixing in a nonlinear medium. A transient diffraction grating is induced by two opposing pump waves A_1 and A_2 . Interference between one of the pump waves and a signal wave A generates a phase conjugated wave $A_{PC} = |A_1|^2 A^*$



“time-reversed” version of the signal wave A , scaled by the proportionality factor $|A_1|^2$ which can be interpreted as the reflectance of the phase conjugate mirror.

The process can be regarded as a real-time holographic process where the three incident beams interact in the nonlinear optical material to form a dynamic hologram or diffraction pattern from which the phase conjugate wave is read out. The other three contributions in (14.22) correspond to other waves that are of minor interest and are usually suppressed in thick materials by Bragg diffraction. One disadvantage of phase conjugation by FWM is the necessity of two pump beams to be generated by a laser and injected into the medium.

Stimulated Brillouin Scattering

A more practicable approach for producing phase conjugate beams relies on stimulated Brillouin scattering (SBS) which allows for the development of self-pumped phase conjugate mirrors. The used nonlinear materials are either liquids, e.g. carbon disulfide, acetone or heavy fluorocarbons, or gases like CH_4 , SF_6 and Xe . Multimode glass fibers were also found to be appropriate phase conjugators. A SBS-PCM can for example be realized by a cuvette filled with the nonlinear medium that is irradiated by an intense laser beam (Fig. 14.15).

Interaction of the pump wave with statistical density variations, i.e. acoustic waves, generates a counterpropagating wave that interferes with the pump wave. This process is called spontaneous Brillouin scattering. The resulting periodic spatial modulation of the material density induces a phase grating where the grating constant can be identified with the wavelength Λ of the acoustic wave. The induced grating, in turn, acts on the backscattered wave, as constructive interference only occurs if Bragg’s law

$$\lambda = 2\Lambda \cdot \sin \theta. \quad (14.23)$$

is satisfied, where λ denotes the wavelength of the incident wave and θ is the angle of incidence. Since the backscattered wave ($\theta = \pi$) exhibits the maximal overlap

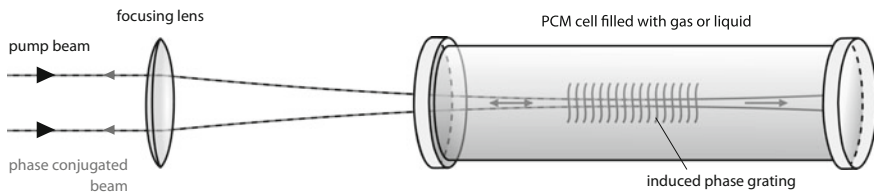


Fig. 14.15 Phase conjugation by stimulated Brillouin scattering (SBS) in a gas or liquid cell. The pump and phase conjugated beams are collinear but propagate in opposite directions

with the incident wave, constructive interference of both waves originates a comparably strong beat frequency equal to the sound wave frequency due to the Doppler effect. The beat gives rise to an acoustic wave by electrostriction which modulates the refractive index of the medium and couples both light waves. As a result, the original sound wave is amplified leading to an enhanced Brillouin scattering efficiency which reinforces the scattered wave. The positive feedback causes an energy transfer from the incident to the backscattered (or reflected) wave. At high pump intensities, Brillouin scattering becomes a stimulated process and the ratio between reflected and incident power, i.e. the SBS reflectance, can reach more than 90%.

Compensation of Phase Distortions in Laser Amplifiers

Optical phase conjugation is exploited in master oscillator power amplifier (MOPA) systems, as illustrated in Fig. 14.16. A laser beam produced in the oscillator is amplified before being incident on the phase conjugate mirror (PCM) which is realized by a SBS cell. The reflected beam performs a second pass through the two amplifiers, thus boosting the output power again. Since the amplifier chain includes a Faraday rotator (Sect. 16.4), the polarization direction is rotated by 90° after the double-pass, so that the reflected beam is coupled out of the amplifier via a polarizer. The use of the PCM thus results in a doubling of the effective amplifier length, while simultaneously compensating for phase distortions, e.g. introduced by thermal lensing in the amplifier medium. In this way, efficient power scaling of the oscillator beam is obtained without deterioration of its good beam quality (Fig. 14.17).

Phase conjugate mirrors are especially suited for pulsed solid-state lasers. A commercial Nd:YAG MOPA system incorporating a PCM, for instance provides, 40 W of average power at a pulse repetition rate of 100 Hz and pulse duration of 4 ns. More than 200 W of output power with near-diffraction-limited beam quality were achieved in the laboratory with a two-stage Nd:YALO MOPA configuration operating at repetition rates of about 1 kHz and pulse duration around 100 ns.

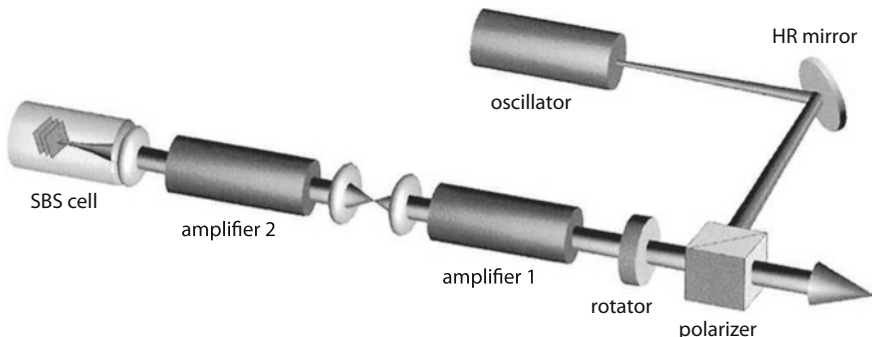


Fig. 14.16 Master oscillator power amplifier (MOPA) system including a stimulated Brillouin scattering (SBS) cell as phase conjugate mirror (PCM), which realizes a double-pass through the amplifier stage. The lens system between the two amplifiers compensates the thermal lens introduced by amplifier 1 and thus prevents focusing of the beam in amplifier 2, while an additional quartz rotator between the amplifiers (not shown) allows for birefringence compensation and minimizes depolarization of the amplified laser radiation. The MOPA system generates more than 200 W output power (courtesy of A. Haase, O. Mehl, Institute of Optics and Atomic Physics, TU Berlin)

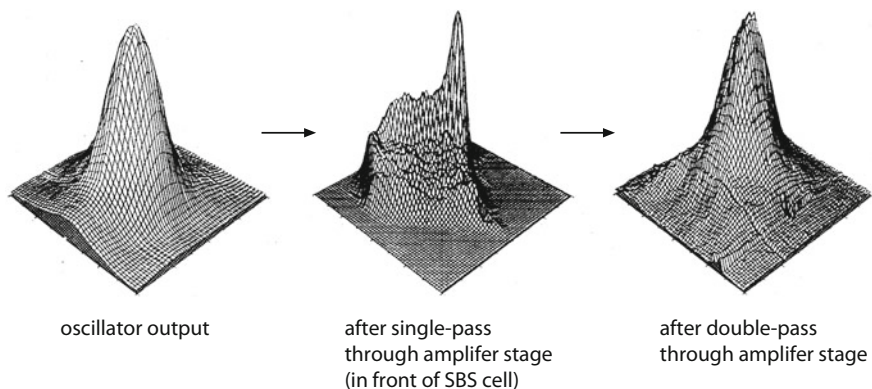


Fig. 14.17 Transverse intensity distribution of a laser beam generated in a MOPA system. While the oscillator output shows a “clean” TEM_{00} profile, phase distortions occur during the first pass through the amplifier stage. After reflection from the phase conjugate mirror and second pass through the amplifier stage, a high-energy beam with excellent beam quality is produced

PCMs can also be employed as laser mirrors to compensate for phase distortions occurring in laser resonators introduced, e.g. by thermal effects in laser crystals or gas discharges. At the same time, the alignment sensitivity of the mirrors is reduced. It should be noted that the application of PCMs in resonators or MOPA systems is not simply realized by substituting a conventional dielectric mirror. Instead, it requires careful adaptation of the laser parameters to the characteristics of the phase conjugate medium.

Further Reading

1. V.V. Apollonov, *High-Power Optics* (Springer, 2015)
2. S. Meister, *Functional optical coatings on fiber end-faces* (Mensch & Buch Verlag, 2009)
3. N. Kaiser, H.K. Pulker (eds.), *Optical Interference Coatings* (Springer, 2003)
4. J. Sakai, *Phase Conjugate Optics* (McGraw-Hill, 1992)
5. B.Y. Zel'Dovich, N.F. Pilipetsky, V.V. Shkunov, *Principles of Phase Conjugation* (Springer, 1985)

Chapter 15

Polarization



Light can be considered as a transverse electromagnetic wave if it propagates in vacuum or infinite isotropic media. The electric and magnetic field oscillate perpendicular to each other and perpendicular to the propagation direction. The oscillation direction is referred to as polarization. Three types of polarization are usually distinguished: linear, circular and elliptical polarization. Light with randomly and quickly varying polarization is said to be unpolarized. In birefringent materials, the propagation speed of light depends on its polarization state. This characteristic is utilized in many optical devices such as polarizers, beam splitters, polarization rotators and wave plates. Light propagation in anisotropic media also gives rise to longitudinal components of the electric or magnetic field.

15.1 Types of Polarization

In the normal case of transverse oscillation of the electric and magnetic field, a distinction is made between three different polarization states.

Linear Polarization and Unpolarized light

If the electric field or magnetic field vector is confined to a plane perpendicular to the direction of propagation, it is called linearly polarized. Any polarization direction perpendicular to the direction of motion of the light is possible. The direction of polarization is defined by the electric field vector.

The light emitted from the sun, light bulbs as well as gas discharge lamps and LEDs is *unpolarized*, meaning that it is composed of many randomly oriented linearly polarized waves that are not correlated to each other. Consequently, although there is a definite direction of the electric and magnetic field vector at a

certain time and location, the polarization state changes so rapidly in time and space, and in an unpredictable manner, there is no preferred polarization direction.

Unpolarized light can be considered as two mutually perpendicular linearly polarized beams with equal magnitude. Hence, when unpolarized light is transmitted through an ideal polarizer, 50% of the optical power is transmitted, while the other half is extinguished in the process of conversion to polarized light.

Circular Polarization

In general, any field vector can be separated into two perpendicular components that oscillate independently, as shown in Fig. 15.1. In case of linearly polarized light, the two components are in phase, so that the tip of the resulting vector moves along a straight line during the oscillation. In contrast, circular polarization is present, if the two components are equal in amplitude, but have a phase difference of $\pi/2$, i.e. a quarter of the radiation wavelength ($\lambda/4$). At a given location of a circularly polarized wave propagating in z -direction, the two components can be described as follows:

$$\mathbf{E}_x(t) = E_0 \cos(2\pi f t) \text{ and } \mathbf{E}_y(t) = E_0 \sin(2\pi f t). \quad (15.1)$$

The resulting field vector \mathbf{E}_0 rotates in a circle around the direction of propagation at the angular frequency $\omega = 2\pi f$, leading to a corkscrew pattern in space with one complete revolution during each wavelength.

Elliptical Polarization

The superposition of mutually perpendicular linearly polarized component with differing and/or a phase difference other than $\pi/2$ results in elliptically polarized light. This is the most general description of polarized light, as linearly and circularly polarized light can be regarded as special cases of elliptically polarized light. This is illustrated in Fig. 15.2, depicting the resulting field vector for phase

Fig. 15.1 Any field vector can be separated to two mutually perpendicular components. Circularly polarized light consists of two perpendicular, linearly polarized waves of equal amplitude and 90° ($\lambda/4$) difference in phase

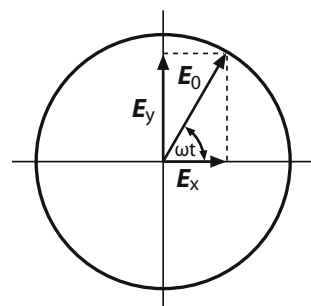
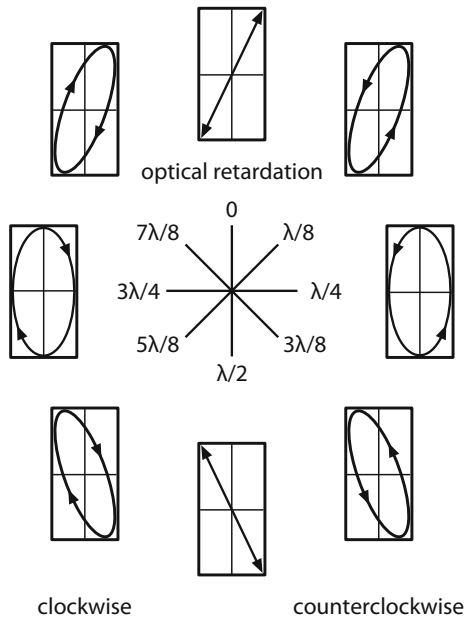


Fig. 15.2 Superposition of linearly polarized waves of different amplitude results in elliptically or linearly polarized light depending on their phase difference (optical retardation)



differences of $\pi/4$, $\pi/2$, $3\pi/4$, etc. which corresponds to path differences of $\lambda/8$, $\lambda/4$, $3\lambda/8$, etc. At a phase difference of 0, $\lambda/2$ (or in general $n\lambda/2$, $n = 0, 1, 2, \dots$), linear polarization is obtained, while two different polarization directions occur. Elliptically polarized light with opposing rotation direction appears for phase differences $\lambda/4$, $3\lambda/4$, etc., while circular polarization is present in case of equal amplitudes.

A linearly polarized wave can be transformed into any other polarization state using a birefringent crystal plate which shows different refractive indices for the two linearly polarized components. Hence, a phase shift is introduced between the components, so that the behavior of the resulting field vector behind the plate is different from that of the incident wave. Depending on the thickness of the so-called retardation plate, elliptically or circularly is produced. Likewise, rotation of the linear polarization direction can be realized as well. The operation principle of retardation plates is elaborated in Sect. 15.3. Prior to that, the phenomenon of birefringence is explained in the following.

15.2 Birefringence

Isotropic, i.e. amorphous or cubic crystalline, materials are characterized by an equivalent arrangement of atoms or ions along all directions, so that optical properties like the refractive index are the same in any orientation. Thus, refraction in isotropic media can be simply described by Snell's law according to (14.2). On

the contrary, anisotropic materials exhibit birefringence (double refraction), meaning that the refractive index experienced by the propagating light depends on its polarization direction with respect to the crystallographic axes. Birefringence can also be induced in optically isotropic media by mechanical stress as well as by electric or magnetic fields, hence breaking the original symmetry.

A simple type of birefringence is present in *uniaxial* optical materials where optical anisotropy is encountered in a single direction, defined by the so-called optic axis, whereas all directions perpendicular to this axis are optically equivalent. Consequently, light traveling along the optic axis does not suffer birefringence, as the direction of the electric field, i.e. the polarization, is perpendicular to it. The light experiences the same refractive index for any polarization direction, which is referred to as ordinary refractive index n^o . However, light whose propagation direction is perpendicular to the optic axis sees an extraordinary refractive index n^e which changes with the polarization direction. As a result, when light is incident on a birefringent material, it is split into two orthogonal linearly polarized components, an ordinary and an extraordinary ray, that travel through the medium at different speeds. One distinguishes between positive and negative uniaxial crystals depending on whether the extraordinary index is higher or lower than the ordinary index. The refractive indices of a positive uniaxial crystal are illustrated in Fig. 15.3.

While the refractive index of the ordinary ray, like in an isotropic material, is independent of the propagation direction in the crystal, the extraordinary index depends on the propagation direction, indicated by the ellipse in Fig. 15.3. The polar diagram is rotationally symmetric about the optic axis. The plane defined by the optic axis and the direction of incidence is called principal plane. The ordinary ray is perpendicularly polarized to the principal plane, whereas the extraordinary ray is parallelly polarized to it.

The situation is more complicated in *biaxial* materials, since there are three mutually orthogonal principal axes associated with different refractive indices (see Table 15.1). However, in most cases, the orientation of the birefringent medium is

Fig. 15.3 Refractive indices $n^o(\theta)$ and $n^e(\theta)$ of ordinary and extraordinary polarized light in dependence on the propagation direction with respect to the optic axis in a uniaxial crystal

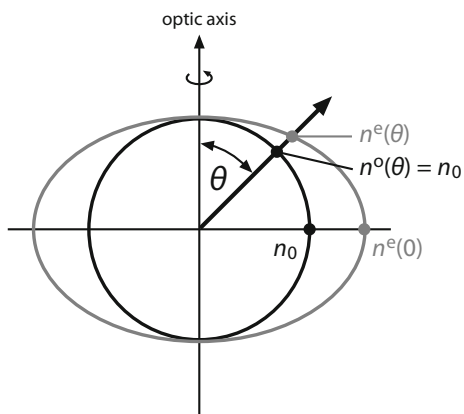


Table 15.1 Principal refractive indices of selected crystals at the sodium D-Line (589 nm)

Crystal	n_1	n_2	n_3	Type of birefringence
Calcite	1.6584	1.4864	–	Uniaxial negative
Corundum	1.7682	1.6598	–	Uniaxial negative
Quartz	1.5442	1.5533	–	Uniaxial positive
Ice	1.309	1.313	–	Uniaxial positive
Sucrose	1.5382	1.5658	1.5710	Biaxial
Mica	1.5612	1.5944	1.5993	Biaxial

chosen such that the propagation direction lies in one of the planes spanned by the principal axes, so that the calculation is considerably simplified.

At the interface between air and a uniaxial birefringent material, the ordinary ray is refracted according to Snell's law. For the extraordinary ray, the wave fronts are not perpendicular to the propagation direction, but slightly skewed. Hence, the direction perpendicular to the wave fronts, which is called the wave normal direction, is no longer collinear with the ray direction, i.e. the direction of the energy of the electromagnetic field. Instead, the wave normal includes an angle with the propagation direction which is up to 6° for calcite (CaCO_3) depending on the wave normal direction. Regarding the refraction of the extraordinary ray, it turns out that Snell's law is obeyed for the wave normal direction.

In case of light propagation parallel or perpendicular to the optic axis, the ray direction coincides with the wave normal direction. If, in contrast, unpolarized light enters a birefringent material at an angle to the optic axis, the different refractive indices will cause the two orthogonal linearly polarized rays to split and travel in different directions, as shown in Fig. 15.4. In the depicted example, the wave normal direction of the extraordinary ray coincides with the propagation direction of the ordinary ray.

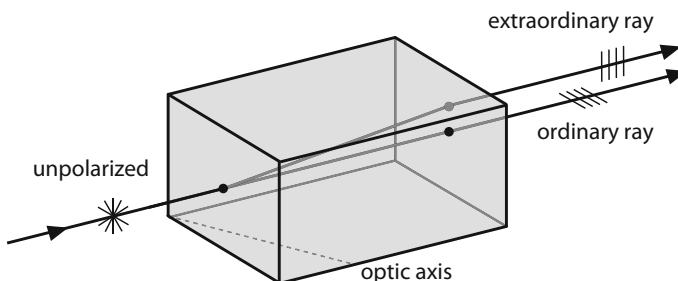


Fig. 15.4 Birefringence in calcite. The two emerging (ordinary and extraordinary) rays have orthogonal polarization states

The deviation between ray direction and wave normal direction leads to a beam walk-off which is detrimental in the context of second harmonic generation in nonlinear crystals. However, as long as the walk-off is small compared to the beam diameter, this effect can be neglected.

15.3 Polarizers and Retardation Plates

Linear polarized light can be produced from unpolarized or elliptically polarized light by absorption, birefringence or reflection. Birefringent quarter-wave plates are used for the transformation between linear and circular polarization, while rotation of the polarization plane is accomplished with half-wave plates.

Dichroic Polarization Filters

Certain materials show selective absorption of light which is polarized in particular directions. This characteristic is called dichroism and can be exploited for generating linearly polarized light. Dichroic polarization filters used in low-power applications are often made of elongated organic molecules, e.g. doped polymers. Stretching of a polymer sheet during the fabrication process causes the polymers chains to align in one particular direction. Hence, light polarized along the polymer chain is strongly absorbed (nearly 100%), while perpendicular polarized light is partially transmitted. An alternative type of dichroic polarizers is based on silver or copper nanoparticles embedded in thin ($<500\text{ }\mu\text{m}$) glass plates. Such filters are more durable than sheet polarizers and show considerably higher polarization efficiencies of up to 100,000:1, yet they are also much more expensive and only available in small sizes. Nevertheless, as they are especially suited for near-infrared wavelengths, glass polarizers are widely used in fiber-optic communication.

Polarizing Prisms

Birefringent prisms are the most common polarizing devices in laser system, as they offer several benefits including high polarization efficiency, high transmittance over a wide spectral range and high damage threshold. Instead of absorbing one polarization component which introduces heat in the material and thus limits the manageable optical power, the desired polarization component is spatially separated from the rejected component due to birefringence. Hence, most prisms are made of highly birefringent materials such as quartz or calcite, while usually two right-angled pieces of the material with different orientations of the optical axis are

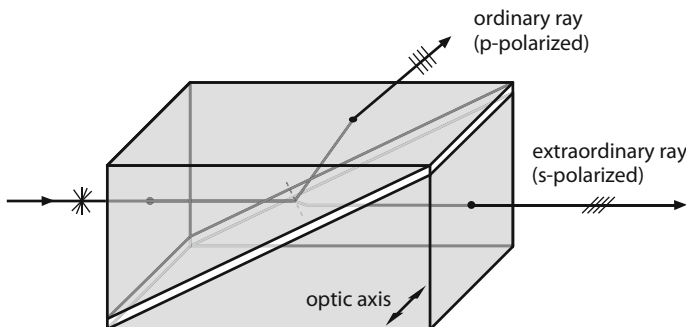


Fig. 15.5 Operation principle of a Glan-Thompson polarizer

either cemented together or joined leaving a small air gap between them. If calcite is used, polarization prisms can be employed at wavelengths from 0.3 to 2.3 μm .

There is a number of distinctive designs which can be classified into two groups depending on the physical phenomenon that leads to the separation of the two polarization components. The first type of polarizers relies on total internal reflection (Sect. 14.1). In a *Glan-Thompson polarizer* (Fig. 15.5), unpolarized light is split at the intersection of the two crystals which allows s-polarized light (extraordinary ray) to continue, while p-polarized light (ordinary ray) experiencing a higher refractive index in the prism compared to the material between the crystals is totally reflected. Originally, Canada balsam was used for assembling the two prisms, but has now largely been replaced by synthetic polymers.

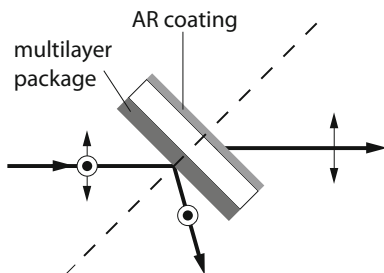
Higher damage threshold at the expense of lower acceptance angle is obtained with the *Glan-Foucault polarizer* where the prisms are separated by an air space. In the *Glan-Taylor polarizer* (Fig. 15.9), the optical axes of the birefringent crystals are aligned parallel to the plane of reflection, so that p-polarized light is transmitted, whereas total internal reflection occurs for the s-polarized component. Hence, as the angle of incidence at the gap can be close to Brewster's angle, unwanted reflection of p-polarized light is minimized, yielding higher transmission and better polarization of the reflected light.

Other types of polarizers such as the *Wollaston prisms* are not based on total internal reflection, but make use of slightly different refraction angles due to birefringence, resulting in two spatially separated output beams. Here, the angle of divergence between the beams is determined by the prisms' wedge angle and the wavelength of the light. Typical divergence angles are between 15° and 45°.

Brewster Windows and Thin-Film Polarizers

A plate made of glass or another transparent material acts as a polarizer, if it is inserted into a light beam at a certain angle. As described in Sect. 14.1, the

Fig. 15.6 Schematic of a thin-film polarizer having a reflection coating on the front side and an anti-reflective coating on the back side



reflectance of the plate surface is different for the parallel (p) and the perpendicular (s) polarized component with respect to the plane of incidence. In particular, when light is incident at Brewster's angle, the p-polarized component is not reflected at all (Fig. 14.2), so that the reflected light is fully s-polarized. However, since the reflectance for s-polarized light at this angle is far below 100% (only 16% for normal glass and visible light), the efficiency of such a polarizer is rather low. Nevertheless, due to the low loss for p-polarized light, Brewster windows are often used as polarizers in laser oscillators, e.g. in He–Ne lasers (see Fig. 4.2). In the low-gain regime, the incomplete s-transmission is sufficient to suppress s-polarized oscillation in the laser resonator, resulting in p-polarized emission.

Increase of the polarizing efficiency is achieved by using a stack of multiple Brewster plates placed behind each other, so that the s-polarized portion is successively diminished. A similar but much more compact approach is taken in thin-film polarizers (TFPs) which are based on dielectric multilayers the are coated on a glass substrate. Like for a dielectric mirror (Sect. 14.2), strongly polarization-dependent reflectance is obtained for a range of incidence angles. The coating of TFPs is often designed such that the angle of incidence is at Brewster's angle in order to avoid reflection loss of the transmitted (p-polarized) light on the back side of the substrate. For other angles of incidence (e.g. 45°), an anti-reflective coating is required (Fig. 15.6).

Quarter-Wave and Half-Wave Plates

The polarization state of light can be altered by means of retardation plates (or wave plates) made of quartz or mica whose optic axis is parallel to the plate surface. Quarter-wave plates ($\lambda/4$ -plates) are used for the conversion between linearly polarized and circular polarized light, whereas half-wave plates ($\lambda/2$ -plates) allow to rotate the polarization direction of linearly polarized light.

Circularly polarized light is produced by passing linearly polarized light through a $\lambda/4$ -plate with its optic axis oriented at 45° with respect to the incident polarization direction. A line indicating the orientation of the optic axis is usually engraved on the housing of the wave plate. Due to birefringence, the ordinary and

Fig. 15.7 Conversion of linearly polarized light to circularly polarized light by a quarter-wave plate. The incident polarization direction makes a 45° angle with the optic axis of the plate. Elliptically polarized light is produced for other angles

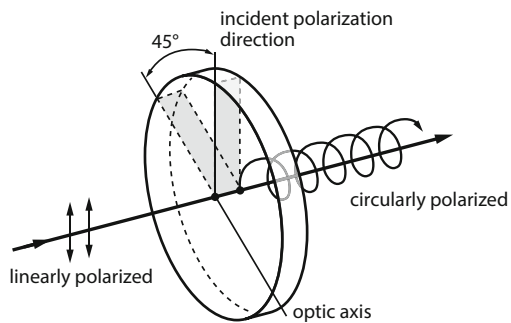
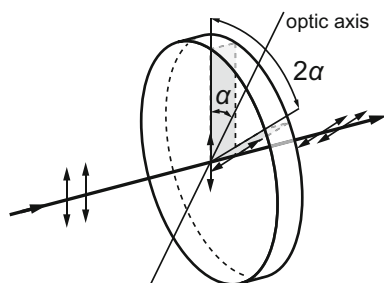


Fig. 15.8 Polarization rotation of linearly polarized light by a half-wave plate. The angle of optical rotation is twice the angle of the optic axis of the half-wave plate with respect to the plane of polarization of the incident light



extraordinary component of the propagating light experience different refractive indices, so that they travel through the plate at different speeds. Consequently, a phase difference is introduced between the two components. The thickness of the plate is chosen such that the phase difference is $\lambda/4$, resulting in circularly polarized light exiting from the retarder (Fig. 15.7).

Since the phase difference varies strongly with the wavelength of the light, retardation plates are generally manufactured for a specific range of wavelengths. This is especially true for so-called multi-order wave plates, where the phase difference is larger than $\lambda/4$ by an integer multiple of 2π for the sake of better mechanical stability. The wavelength-dependence can be reduced by stacking two multi-order wave plates with slightly different thickness and orthogonal optic axes. By adjusting the difference in thickness, a net phase shift of $\lambda/4$ is obtained, thus ensuring larger operating bandwidth and lower temperature-dependence.

In half-wave plates, a phase shift of π is introduced between the polarization components. As a result, the polarization direction of light passing through the plate is rotated by an angle 2α , where α is the angle between the optic axis of the plate and the incident polarization direction, as shown in Fig. 15.8.

The configuration consisting of a $\lambda/2$ -plate and a polarizer (see Fig. 15.9) is often employed as loss-free variable attenuator in laser systems and many experimental setups. Linearly polarized light propagating through the polarizer, e.g. a Glan-Taylor polarizer, is separated into two orthogonal polarized beams. By

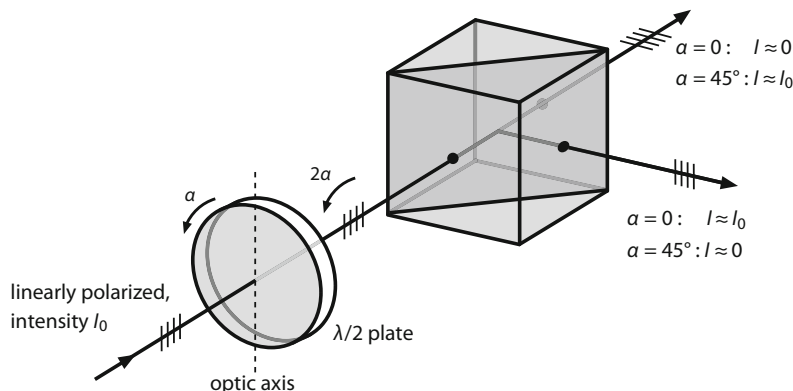


Fig. 15.9 Schematic of a variable attenuator consisting of a half-wave plate and a Glan-Taylor polarizer

rotating the waveplate around the beam axis, the polarization direction and, in turn, the amount of optical power rejected by the polarizer can be continuously varied. This principle is especially convenient for attenuating high-power lasers. A second $\lambda/2$ -plate can be additionally placed behind the polarizer to restore the original polarization state.

Further Reading

1. S. Zhang, W. Holzapfel, *Orthogonal Polarization in Lasers* (Wiley, 2013)
2. S. Huard, *Polarization of Light* (Wiley, 1997)

Chapter 16

Modulation and Deflection



In many laser applications, it is necessary to modulate or deflect the laser beam. Apart from mechanical devices, acousto-optic and electro-optic elements are mainly employed for this purpose. In particular, acousto-optic and electro-optic modulators, beam deflectors, Pockels and Kerr cells are widely applied in laser physics. Moreover, magnetic Faraday rotators are important for optical isolation, while saturable absorbers are used for the generation of ultra-short pulses. Laser beam deflectors are important in a wide range of scientific and industrial applications such as fluorescence microscopy, laser material processing, optical storage, sensing and laser printers.

16.1 Mechanical Modulators and Scanners

Amplitude modulation of light can be simply achieved by mechanical interruption of the light beam, e.g. with photographic shutters. Optical choppers that are realized as rotating discs with slits or as oscillating tuning fork-like devices are used to periodically modulate the light intensity, providing switching times on the order of milliseconds, or frequencies of several kHz, respectively. Higher frequencies and smaller switching times are challenging due to the large forces required for acceleration of the interruptor.

Mechanical deflection systems are based on rotating prisms with multiple facets, wedges or mirrors operating according to the galvanometer principle. Such systems are characterized by low losses at the reflecting surfaces and high resolution; however, the response times are rather slow. The resolution of commercial deflection devices (scanners) ranges from 10^2 to 10^4 spots per line at response times from 0.1 to 1 ms. Two-dimensional deflection is accomplished by serial combination of two scanners.

Modulators relying on frustrated total internal reflection (FTIR) were specifically developed for Q-switching of solid-state with high average output powers or long

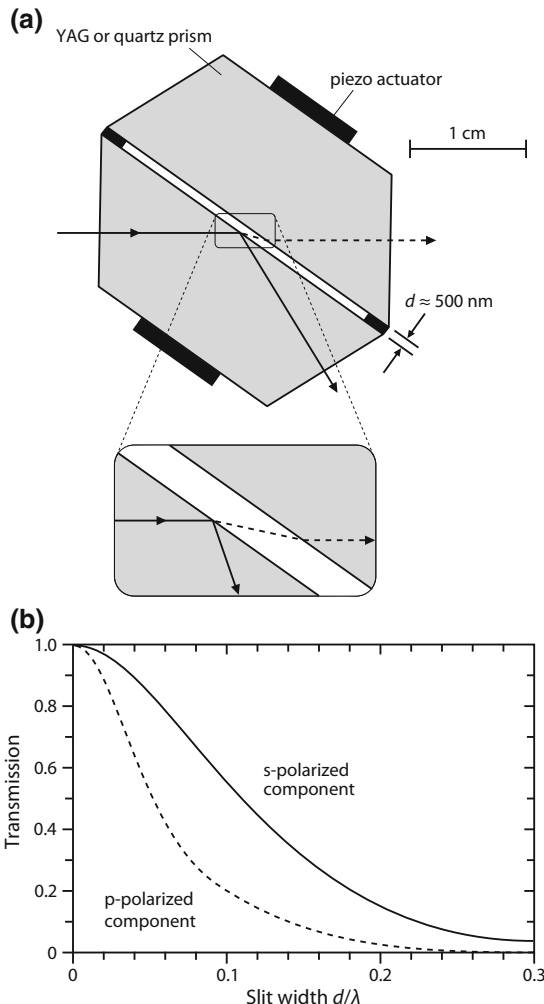


Fig. 16.1 Frustrated total internal reflection (FTIR) Q-switch. **a** At large slit widths d , an incident light beam is totally reflected from the first surface of the slit, while it is transmitted by the optical tunnel effect at small slit widths. The slit width is controlled by applying voltage pulses to piezo actuators producing shock waves in the prisms made of YAG or other materials, **b** calculated transmission of the FTIR Q-switch in dependence on the slit width

wavelengths, e.g. around $3 \mu\text{m}$. Here, two prisms made of YAG or quartz are sandwiched back-to-back while leaving a small air gap between them, as shown in Fig. 16.1a. The spacing or slit width between the two prisms can be piezoelectrically altered. If the slit width is sufficiently large, total internal reflection occurs at the interface so that an incident beam is deflected. At small spacings, energy may flow across the gap into the second prism and the beam path is no longer blocked.

This effect is referred to as frustrated total internal reflection or “optical tunneling” in analogy to the quantum mechanical phenomenon. The transition from total to no reflection occurs gradually, resulting in a continuous variation of the transmitted optical power depending on the slit width. The dependency is plotted in Fig. 16.1b for p- and s-polarized light.

16.2 Acousto-optic Modulators

Ultrasound waves are periodic density variations. When propagating through a medium, the waves induce spatially periodic changes in the refractive index of the material. The resulting refractive index modulation produced by a sound wave, in turn, interacts a light wave traveling through the medium, giving rise to refraction, diffraction and interference (Debye-Sears effect). In terms of diffraction, one distinguishes between thin and thick refractive index gratings. For thin gratings, Raman and Nath developed a model describing diffraction in dependence on the diffraction angle φ (see Fig. 16.2):

$$\boxed{\sin \varphi = \frac{\lambda}{\Lambda n}} \quad (16.1)$$

In this equation, λ/n is the light wavelength in the medium with refractive index n (under unperturbed conditions), while $\Lambda = v/f$ denotes the wavelength of the sound wave which corresponds to the grating constant of the induced grating. The latter depends on the sound frequency f (typically 50–500 MHz) and the speed of sound $v \approx 5 \times 10^5$ cm/s. The maximum diffraction efficiency of a thin sinusoidal ultrasound grating is calculated to be 33.8%. For a grating with thickness l , multiple diffraction orders are observed in the so-called Raman-Nath regime which is defined by the condition $\lambda l < \Lambda^2$.

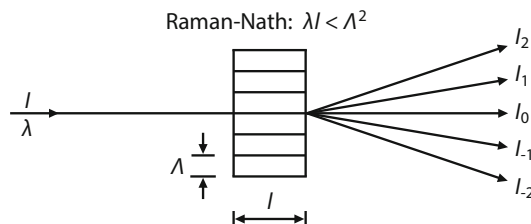


Fig. 16.2 Diffraction at a thin ultrasonic grating. C. V. Raman and N. S. N. Nath have developed a general theory considering multiple diffraction orders in the regime $\lambda l < \Lambda^2$

Bragg Configuration

If the grating is thick compared to the grating constant Λ , the diffracted intensity in Fig. 16.2 decreases, as destructive interference occurs among the diffracted waves. Hence, for obtaining constructive interference in gratings with $\lambda l > \Lambda^2$, Bragg's condition needs to be fulfilled depending on the angle of incidence θ :

$$\boxed{\sin \theta = \frac{\lambda}{2\Lambda n}}. \quad (16.2)$$

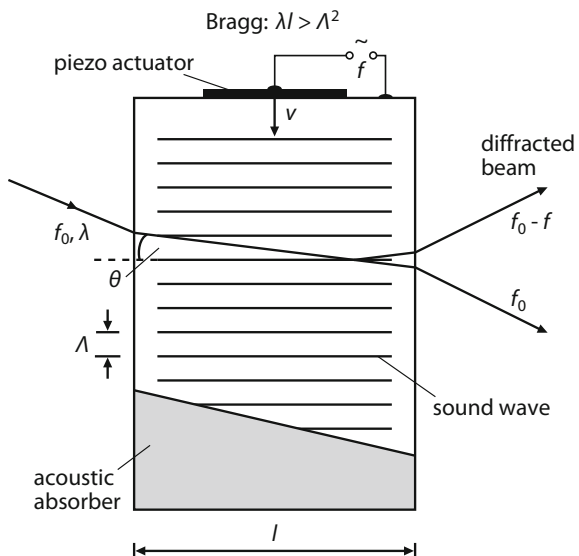
This principle is used in acousto-optic modulators (AOMs), as illustrated in Fig. 16.3. They consist of an acousto-optic crystal to which a transducer, usually a piezo-electric actuator, is attached. Driven by an amplifier, the transducer launches acoustic waves of frequency f (typically 80 MHz to 1 GHz) into the crystal, thus producing the diffraction grating.

The transmission T of an AOM can be described by the relation

$$T = T_0 \cos^2(MP^{1/2}/\lambda), \quad (16.3)$$

where T_0 is the normal transmission, M is a material- and geometry-dependent constant and P is the injected acoustic power. At powers $P \approx 10$ W, the transmission is nearly zero, i.e. the diffraction efficiency can reach up to 100%. Another advantage of the Bragg configuration is the fact that only one diffraction order is usually generated, as higher-order diffraction orders undergo destructive interference.

Fig. 16.3 Diffraction at a thick acousto-optic modulator (AOM) in Bragg configuration



Traveling and Standing Ultrasound Waves

In the arrangement shown Fig. 16.3, the ultrasound wave is absorbed after propagation through the modulator to avoid reflection, so that a standing-wave is not established in the crystal. Light diffracted from the moving grating experiences a frequency shift due to the Doppler effect. While the original frequency f_0 is maintained for the transmitted light, the frequency of the diffracted light is $f_0 \pm f$, with f being the ultrasound frequency. For a propagation direction of the sound wave according to Fig. 16.3, the frequency is down-shifted (negative sign), whereas a positive frequency shift is introduced if the sound waves travels in the opposite direction.

Standing-waves are produced by reflection of the ultrasound wave. The diffracted light is then amplitude modulated at the frequency $2f$, which is for instance exploited in mode-locked lasers (see Sect. 17.4). Standing-wave modulators are primarily used for high-frequency modulation of light. If light modulation with an arbitrary amplitude distribution is desired, traveling-wave modulators are preferred.

Modulators

Configurations operating with traveling sound waves, as depicted in Fig. 16.3, can be utilized both as modulators or as beam deflectors. Amplitude modulation of the propagating light beam is realized by switching the acoustic power on and off. The switching time is mainly limited by the transit time $\tau = v/d$ of the ultrasound wave through the beam diameter d , and thus, by the speed of sound v in the acousto-optic crystal. Consequently, the modulation bandwidth is inversely proportional to the beam diameter. For a typical beam diameter of $d = 0.8$ mm, the bandwidth is about 3 MHz at ultrasound frequencies around 100 MHz. Higher bandwidths are achieved by focusing the light beam. However, as this leads to higher beam divergence, Bragg's condition is no longer fully satisfied, hence reducing the diffraction efficiency.

Acousto-optic modulators (AOMs) are used for Q-switching and cavity-dumping of solid-state lasers (Sects. 17.2 and 17.3). Being integrated in the laser resonator, the AOM serves to block the resonator in order to generate ultra-short pulses. Since the required electric drive power is lower compared to electro-optic modulators, higher repetition rates up to 100 kHz are obtained. However, the switching times are relatively long, e.g. 300 ns for the above example.

Beam Deflectors

Acousto-optic devices for beam deflection are based on the variation of the ultrasound frequency or wavelength, respectively. According to Bragg's condition (16.2), each wavelength Λ is associated with a particular incidence angle θ for

which constructive interference occurs. Hence, if the incidence angle θ is fixed and the ultrasound frequency is varied, the direction of the deflected laser beam changes. However, maximum diffraction efficiency is only obtained when the incidence angle equals the deflection angle and thus the Bragg angle. Consequently, as the ultrasound frequency is increased, Bragg's condition is increasingly violated, resulting in lower optical efficiency of deflection. This effect can be counteracted by faceted and phase-shifted transducers that adapt the orientation of the sound wave with respect to the light beam. In this way, the frequency bandwidth and, in turn, the maximum deflection angle can be increased.

Despite this technique, the number of resolvable spots ($N = 10^2 \dots 10^3$) is relatively small compared to mirror-based deflectors. Nevertheless, much faster response times on the order of a few μs are possible. Moreover, due to the lack of moving parts, acousto-optic deflectors are free of drawbacks associated with mechanical scanners such as wear, mechanical noise and drift. The combination of an optical deflector and a mechanical scanner in series allows to exploit the advantages of both deflection technologies.

Acousto-optic Materials

Modulators and beam deflectors are realized in standing-wave or traveling-wave geometry using either thick or thin diffraction gratings. Owing to their low absorption in the visible and adjacent spectral regions as well as their robustness, fused silica and crystalline quartz (SiO_2) are often used for commercial acousto-optic devices. Another common material is tellurium dioxide (TeO_2) which can be operated at lower electric drive powers due to the higher elasto-optic coefficient.

The piezoelectric actuator (Fig. 16.3) is mostly made of lithium niobate (LiNbO_3), where typical voltages of 7–10 V are required at high-frequency (HF) powers around 1 W. This material is also suited for building integrated-optical devices, such as tunable optical filters or optical switches, containing one or more AOMs on a chip. Taking advantage of the piezoelectricity of LiNbO_3 , acoustic waves can be generated via metallic electrodes on the chip surface.

Longitudinal and Shear Mode

The interaction between the light wave and the sound wave described above refers to the so-called isotropic or longitudinal mode interaction. Here, the acoustic wave travels longitudinally in the crystal and the incident and diffracted laser beams experience the same refractive index, so that the incidence angle is equal to the diffraction angle. Furthermore, there is no change in polarization associated with the interaction. This leads to high diffraction efficiencies which, however, depend on the polarization state of the incident laser beam.

Polarization-independent operation is accomplished by using acoustic shear waves, where the acoustic movement is in the direction of the laser beam. This anisotropic interaction involves a drastic reduction in the propagation speed of the sound wave, especially in case tellurium dioxide is used as acousto-optic material. Hence, AOMs operating in shear mode are generally much slower than longitudinal mode devices. In addition, the polarization state of the diffracted light beam is rotated by 90° with respect to the incident beam. Nevertheless, the deflection angles are considerably larger due to the broader frequency bandwidth.

16.3 Electro-optic Modulators

The phase of a light wave can be modulated by modifying the refractive index through electro-optic effects in nonlinear optical materials. The phase modulation is utilized in electro-optic devices such as Pockels or Kerr cells to control the polarization state of a light beam. In combination with polarizers, the modulation can also be imposed on the light intensity. Electro-optic modulators (EOMs) offer fast switching times down to 100 ps and modulation frequencies up to the microwave region. A drawback is the necessity of high (kV) voltages required for operation.

Pockels Cells

Electro-optic modulators predominantly rely on the Pockels effect (named after the German physicist Friedrich Pockels) which describes the influence of electric fields on the refractive index in non-centrosymmetric crystals. Application of an electric field leads to a slight deformation of the crystal lattice, thus inducing or modifying the birefringence (Sect. 15.2) of the material. As a result, the ordinary and extraordinary component of a propagating light wave experience different refractive indices, where the difference Δn is linearly proportional to the electric field, and hence, on the applied voltage U (linear electro-optic effect):

$$\Delta n = n^3 r E = n^3 r U / d. \quad (16.4)$$

Here, r is a material constant that depends on the orientation of the electric field with respect to the crystal axes (Table 16.1). d is the distance between the (capacitor) electrodes producing the electric field $E = U/d$.

The change in refractive index introduces a phase difference between the two orthogonal polarized components of the light wave with wavelength λ . If the optical path difference is $\Delta nl = \lambda/2$, the phase difference is $\delta = \pi$, with l being the interaction length of the light wave in the crystal. The corresponding voltage $U_{1/2}$ is called half-wave voltage and can be calculated from $\Delta nl = \lambda/2 = n^3 r U_{1/2} l / d$. In the

Table 16.1 Electro-optic properties of selected materials used in Pockels cells at $\lambda = 0.63 \mu\text{m}$ (from Koechner (2006)). The voltages given for ADP, KDP and KD*P refer to longitudinal cells. They can be calculated from (16.5) with $d = l$. The value for LiNbO₃ refers to a transverse device with $d/l = 9/25$

Material	$n = n_0$	$r ((\mu\text{m}/\text{V}) \times 10^6)$	$U_{1/2} (\text{kV})$
Ammonium dihydrogen phosphate (NH ₄ H ₂ PO ₄ , ADP)	1.522	$r_{63} = 8$	11
Potassium dihydrogen phosphate (KH ₂ PO ₄ , KDP)	1.512	$r_{63} = 11$	8
Potassium di-deuterium phosphate (KD ₂ PO ₄ , KD*P = DKDP)	1.508	$r_{63} = 24$	4
Lithium niobate (LiNbO ₃)	2.286	$r_{22} = 7, r_{33} = 31$	2
Cadmium telluride (CdTe)	2.60	$r_{41} = 6.8$ (at 10.6 μm)	12

general case, the phase difference δ between the ordinary and extraordinary polarized component after propagation through the electro-optic crystal reads

$$\boxed{\delta = \pi U / U_{1/2} \quad \text{with } U_{1/2} = \lambda d / 2n^3 rl.} \quad (16.5)$$

A device consisting of an electro-optic crystal with electrodes attached to each side is called Pockels cell. By varying the voltage applied to the electrodes, the phase difference and, in turn, the polarization state of a light beam traveling through the medium can be modulated. Pockels cells can thus be regarded as voltage-controllable retardation plates (Sect. 15.3). For instance, if linearly polarized light is incident whose polarization direction is at angle of 45° with respect to the two principal polarization directions (s and p), the two orthogonal components have the same amplitude inside the birefringent crystal (see birefringent filter, Sect. 18.6). After propagation through the crystal, both components have a phase difference according to (16.5), so that the polarization state of the transmitted light wave depends on the applied voltage (see also Fig. 15.2). In general, elliptically polarized light is obtained. For $\Delta nl = 0, \lambda, 2\lambda$, etc., the polarization state remains unchanged, whereas the polarization direction is rotated by 90° if the applied voltage is chosen such that $\Delta nl = \lambda/2, 3\lambda/2$, etc.

When the Pockels cell is placed between crossed polarizers, as shown in Fig. 16.4, only a portion of a linearly polarized light wave incident on the configuration is transmitted. The transmission T is then given by

$$T = T_0 \sin^2 \left(\frac{\pi}{2} \frac{U}{U_{1/2}} \right), \quad (16.6)$$

where T_0 denotes the maximal transmission of the system, i.e. if the introduced phase difference is $\Delta nl = \lambda/2$ ($U = U_{1/2}$), so that the polarization direction of the wave emerging from the Pockels cell is parallel to the transmission axis of the second polarizer which is also referred to as analyzer.

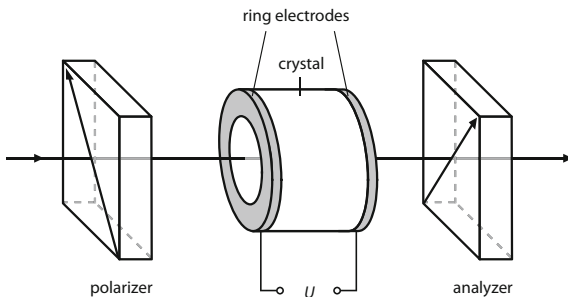


Fig. 16.4 Electro-optic modulator containing a Pockels cell in longitudinal configuration

There are two different types of Pockels cells which are distinguished by the direction of the applied electric field with respect to the direction of the light beam. In *longitudinal* devices, the electric field is oriented along the light propagation direction (Fig. 16.4). In this case, the electrode separation can be identified with the crystal length $d = l$, so that $U_{1/2}$ is independent of the crystal dimensions. For adequate crystal orientations, the electric field can also be applied through electrodes at the sides of the crystal, so that the electric field perpendicular to the light beam (*transverse* Pockels cell). Here, the half-wave voltage $U_{1/2}$ depends on the ratio l/d . According to (16.5), low operating voltages are obtained for long and thin transverse Pockels cells. This enables their application as broadband modulators with bandwidths up to 100 MHz. However, as the capacity increases with the length l , the operation is complicated at higher modulation frequencies.

Common materials for Pockels cells specified for the visible and near-infrared spectral region are potassium dihydrogen phosphate (KH_2PO_4 , or short KDP) and lithium niobate (LiNbO_3). KDP crystals are transparent in the range from 0.4 to 1.3 μm . The lengths and thicknesses are typically on the order of a few centimeters, while the losses $1 - T_0$ account for a few percent. The electrodes of longitudinal devices are usually realized as metallic rings or transparent layers on the end-faces with metallic contacts. Sometimes deuterated KDP (KD_2PO_4 , short KD*P or DKDP) is used instead of KDP, as this material allows for lower operating voltages. Moreover, optical peak powers of the modulated light as high as $40 \text{ MW}/\text{cm}^2$ at pulse durations of 10 ns can be handled in KD*P.

LiNbO_3 crystals exhibit higher electro-optic coefficients and thus offer lower half-wave voltages than KDP (Table 16.1). However, the damage threshold is considerably lower. As for acousto-optic devices, LiNbO_3 is especially suited for small integrated optical modulators. Cadmium telluride (CdTe) is used for the spectral range from 1 to 30 μm . Due to the long wavelengths, the required voltages are relatively high. Apart from nonlinear optical crystals, poled polymers with specifically designed organic molecules are increasingly employed as electro-optic materials. They feature very high nonlinearity which exceeds that of highly-nonlinear crystals by one order of magnitude.

Kerr Cells

Birefringence can be induced in isotropic materials by applying an electrical voltage. As opposed to the Pockels effect, the refractive index change Δn is proportional to the square of the electric field E :

$$\Delta n = K \cdot \lambda \cdot E^2. \quad (16.7)$$

Therefore, this phenomenon is called quadratic electro-optic effect, or Kerr effect (named after the Scottish physicist John Kerr). In the above equation, K is the Kerr constant which is e.g. $K = 245 \times 10^{-14} \text{ m/V}^2$ for nitrobenzene ($\text{C}_6\text{H}_5\text{NO}_2$) at 20°C and $\lambda = 589 \text{ nm}$ wavelength. In Kerr cells, the voltage is usually applied perpendicular to the light beam and the operating voltages are much higher compared to Pockels cells. They are mainly employed as photographic shutters providing very fast shutter speeds down to nanosecond level.

The Kerr effect can also be initiated by the electric field of intense laser pulses (optical Kerr effect), i.e. by the light propagating through the medium itself. When a short optical pulse travels through a nonlinear medium, the Kerr effect leads to a variation in the refractive index which scales with the intensity $I \propto |E|^2$ according to (16.7). Due to the non-uniform transverse intensity distribution of the (e.g. Gaussian) laser beam, the change in refractive index is larger on the beam axis compared to the outer parts of the beam. Consequently, the Kerr medium acts as a lens, resulting in so-called self-focusing which is utilized in passively-mode-locked lasers (Sect. 17.4).

The optical Kerr effect is also used for measuring short pulse durations in the ps-regime which cannot be resolved electronically. For this purpose, a short light pulse is sent through a Kerr cell shutter, while a train of preferably even shorter pulses is injected into the medium to open the shutter at separate times. In this way, the intensity of the pulse to be measured is determined, thus enabling a reconstruction of the pulse shape and duration.

16.4 Optical Isolators and Saturable Absorbers

Light modulation is also possible by exploiting magneto-optical effects which are especially important for building optical isolators which transmit light in one direction while blocking it in the opposite direction. Fast optical switching is accomplished with saturable absorbers which are passive optical devices that are characterized by an intensity-dependent transmission.

Faraday Rotators

The Faraday effect describes the magneto-optical interaction between a light wave and a magnetic field. As linearly polarized light passes through a transparent medium that is exposed to a homogeneous magnetic field, the polarization direction is continuously rotated. The degree of rotation is nearly proportional to the component of the magnetic field in the direction of the light wave, while the rotation direction corresponds to the direction of the current in the coils that generate the magnetic field. Hence, the rotation angle β of a Faraday rotator is related to the magnetic flux density B in the direction of propagation:

$$\boxed{\beta = l \cdot V \cdot B}. \quad (16.8)$$

V is the Verdet constant which is e.g. $V = 0.07$ arcmin/A for lead silicate glass, and l is the propagation length in the material. If a long coil with N turns and length l is used for producing the magnetic field and the current in the coil is I , the rotation angle can be calculated as follows:

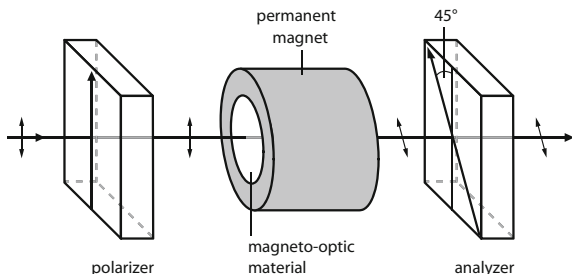
$$B = N \cdot I / l \Rightarrow \beta = V \cdot N \cdot I. \quad (16.9)$$

Since the rotation direction depends on the propagation direction with respect to the orientation of the magnetic field, the polarization changes experienced by linearly polarized light traveling forth and back through a Faraday rotator add up instead of canceling each other. This non-reciprocal optical propagation is fundamentally different to the behavior of electro-optic and acousto-optic modulators as well as of optical elements like wave plates or polarizers.

Faraday rotators are the key element of optical (Faraday) isolators which are important devices in many laser configurations, particularly if operating at high power levels. They are formed by a Faraday rotator that is placed between an input polarizer and an output polarizer (analyzer), as depicted in Fig. 16.5. The transmission axis of the analyzer is oriented at 45° with respect to that of the input polarizer. Light propagating from left to right is s-polarized when entering the Faraday rotator which rotates the polarization direction by 45° . Consequently, the light is transmitted by the analyzer. In contrast, light traveling in the backward direction is polarized at an angle of 45° after passing the analyzer. The rotator again changes the polarization direction by 45° , but in the same direction as in the first case, so that the light is blocked by the polarizer. Hence, Faraday isolators act as an optical diode, thus preventing detrimental and potentially damaging optical feedback in laser systems. Such devices are for instance used in master oscillator power amplifier systems to protect the low-power oscillator against back-reflections from the amplifier (Fig. 14.16).

Due to the high required currents, Faraday rotators employed for pulsed lasers are also operated in pulsed mode. In a commercial system, the magnetic field is generated by discharging an $80 \mu\text{F}$ -capacitor at a voltage of 500 V into a coil to

Fig. 16.5 Optical isolator using a Faraday rotator



induce 500 A of coil current. Nowadays, Faraday rotators used in optical isolators are mostly based on permanent magnets.

Faraday rotators can also be utilized for amplitude modulation. However, owing to the large inductance of the magnetic coil, the achievable modulation frequencies are considerably lower compared to electro-optic modulators. Polarization rotation is also accomplished with ferroelectric crystals that do not require an external magnetic field. Such crystals are applicable for optical isolation in the low-power regime, e.g. in semiconductor lasers.

Saturable Absorbers

Saturable absorbers are optical elements whose transmission characteristics depend on the incident light intensity. The absorption coefficient α , and hence, the losses introduced by the material decreases with the incident intensity I as

$$\boxed{\alpha = \frac{\alpha_0}{1 + I/I_s}}, \quad (16.10)$$

with α_0 being the maximum absorption coefficient at $I = 0$. I_s is the material-dependent saturation intensity for which α is reduced to $\alpha/2$. The transmission $T = \exp(-\alpha x)$ through a medium with thickness x thus increases with the incident intensity.

Saturable absorption can be explained with the depletion of the ground state of the absorbing atoms or molecules. At high optical intensities, the population density of an upper state becomes equal to that of the ground state, so that the number of absorbed photons equals the number of emitted photons. Consequently, the absorption saturates, i.e. the absorption coefficient vanishes ($\alpha \rightarrow 0$, $T \rightarrow 1$), at least theoretically, according to (16.10).

Regarding laser technology, saturable absorbers are applied as passive, i.e. self-acting, switches that automatically open once a certain incident intensity is reached. This results in the generation of ultra-short (nanosecond) pulses by Q-switching, as elaborated in the next chapter. Even shorter pulses in the picosecond to fs-regime are produced by mode-locking. Here, absorbers with short

recovery times are of particular relevance, as fast re-establishment of the initial transmission T_0 after switching off the incident light enables high repetition rates.

Dye solutions were used as saturable absorbers in earlier times, where the initial transmission was adjusted by the dye concentration and the absorber thickness. For example, cryptocyanine solved in methanol, employed as passive Q-switch in ruby lasers, has a saturation intensity of $I_s \approx 5 \text{ MW/cm}^2$.

For passive Q-switching of solid-state lasers emitting in the spectral region around 1 μm , e.g. Nd lasers, YAG crystals doped with Cr⁴⁺-ions are preferably used. Here, the saturation intensity is on the order of a few kW/cm². Gases like SF₆ can be employed in CO₂ lasers.

Passive mode-locking is usually performed by using semiconductor saturable absorber mirrors (SESAMs) or layers of graphene sheets or carbon nanotubes (CNT). The latter can exhibit very broadband absorption features and are therefore well-suited for broadband lasers. For instance, fiber lasers can be passively-mode-locked by applying thin layers of CNTs to the fiber ends, enabling short recovery times and, in turn, high repetition rates of tens of MHz.

Further Reading

1. R. Paschotta, *Encyclopedia of Laser Physics and Technology* (Wiley-VCH, 2008)
2. W. Koechner, *Solid-State Laser Engineering* (Springer, 2006)

Part VI

Laser Operation Modes

Lasers are operated in various modes. While continuous wave (cw) lasers produce a continuous, uninterrupted light beam, ideally with stable (and in some cases high) output power, pulsed operation is usually motivated by the need for high laser peak power, i.e., high energy emitted in a short period of time. Depending on the pulse energy, duration, and repetition rate required for a particular application, different techniques are utilized for the production of laser pulses and will be explained in this part of the book. Laser emission properties cannot only be modified in the temporal, but also in the spectral domain. Wavelength tuning and the control of longitudinal modes is, amongst other methods, achieved by means of frequency-selective elements such as etalons, gratings, or filters. The emission spectrum of lasers can be considerably expanded by nonlinear optical processes that are initiated at high laser intensities, as elastic and inelastic interactions of light with matter give rise to the generation of new laser wavelengths. In Chap. 20, important laser characteristics in terms of stability and coherence as well as their assessment are discussed.

Chapter 17

Pulsed Operation



Many types of gas, dye and solid-state lasers including semiconductor lasers are operated in continuous wave (cw) mode, i.e. they are continuously-pumped and continuously emit light. However, in some lasing media, particularly in three-level systems, uninterrupted maintenance of population inversion is impractical or even impossible, as the required pumping levels would exceed the damage threshold of the laser material. Hence, such lasers can only be operated in pulsed mode. The first ruby laser realized in 1960 and other lasers such as atomic metal vapor and excimer lasers fall into that category.

In other cases, laser pulses are produced in order to obtain high peak powers and consequently higher focused intensities compared to cw operation, thus enabling nonlinear optical effects that are exploited in a wide range of various scientific and technical applications. Apart from pulsed excitation, e.g. by gas discharge, flash lamps or pulsed pump lasers, pulsed laser emission can be accomplished by a number of different techniques comprising Q-switching, cavity dumping, mode-locking and chirped-pulse amplification. This allows for pulse durations ranging from a few microseconds down to the as-regime (10^{-18} s) depending on the laser material and excitation method which will be elaborated in the following sections:

- free-running flash lamp or diode-pumped solid-state laser
(laser spike width): 10 µs
- Q-switched solid-state laser: 1 ns
- diode laser (pulsed excitation): 5 ps
- discharge-pumped nitrogen laser: 100 ps
- mode-locked argon ion laser: 100 ps
- mode-locked dye laser: 25 fs
- mode-locked titanium-sapphire laser: 5 fs
- mode-locked titanium-sapphire laser + chirped-pulse amplification: >1 fs
- attosecond laser (X-ray pulses by higher harmonic generation): 50 as

Lasers producing ultra-short pulses are versatile tools for studying physical or chemical processes that occur on extremely short time scales. Pulsed laser output allows for maximizing nonlinear optical interactions such as second-harmonic generation, optical parametric oscillation or stimulated Brillouin and Raman scattering.

17.1 Laser Spiking

The pulsed laser emission of flash lamp-pumped solid-state lasers is often characterized by strong fluctuations of the laser power. As shown for a ruby laser in Fig. 9.3, the laser power exhibits numerous spikes, i.e. short intense pulses with random amplitude, duration and temporal distance. In cw solid-state lasers, for example Nd:YAG lasers, laser spiking occurs when the laser is switched on (see Fig. 17.1 with regular spikes). A similar behavior is caused by disturbances of continuously-pumped lasers, e.g. by pump power fluctuations. The observed spikes are the result of relaxation oscillations that arise from the rate equations introduced in Sect. 2.8.

Qualitatively, relaxation oscillations can be understood as follows. After initiation of the pumping process the population density N_2 of the upper laser level in the gain medium increases, but does not immediately stabilize to its steady-state value $N_{2,s}$. Instead, since the photon density in the resonator is still low and stimulated emission is at first negligible, the population density N_2 strongly exceeds the steady-state value $N_{2,s}$, as depicted in Fig. 17.2.

Due to the high population inversion, the photon field builds up rapidly and the photon flux φ (photons per area and time) overshoots the steady-state value. Consequently, the upper laser level is quickly depleted by stimulated emission so that the population inversion falls below the laser threshold and the laser power decreases. As the pump power is further increased, the population density of the upper laser level grows again and the cycle repeats, resulting in multiple spikes that are more and more damped until stationary conditions are reached.

Fig. 17.1 Relaxation oscillations (“spiking”) of a Nd:YAG laser

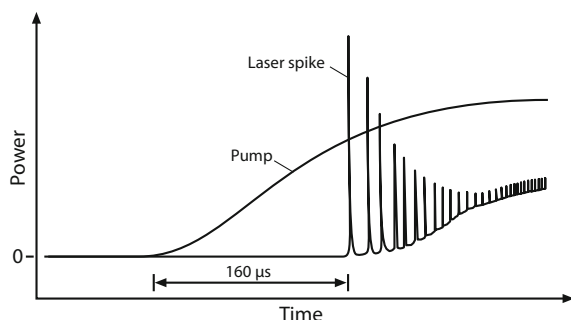
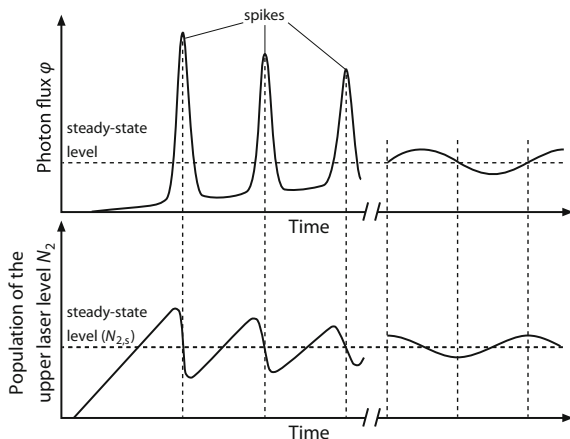


Fig. 17.2 Power (photon flux) and upper-state population of a laser oscillator showing spiking behavior (from Koehner (2006))



While the behavior illustrated in Figs. 17.1 and 17.2 is typical at low pump levels, pumping with intense pulses usually involves the generation of single laser pulses, as the population inversion drops so much that the laser emission stops after the first spike. In continuously-pumped solid-state lasers, small perturbations lead to relaxation oscillations that manifest as damped sinusoidal oscillations around the steady-state value (typically in the kHz region) with a certain decay time. Strongly damped oscillations with much higher frequencies in the GHz-regime are observed in semiconductor lasers.

The oscillatory behavior can be modelled using rate equations which describe the coupling between the upper level population density N_2 and the intra-cavity photon flux φ . The solutions derived from a numerical analysis are plotted in Fig. 17.2, showing a phase shift of $\pi/2$ between the two quantities due to the interaction of the radiation in the resonator with the energy stored in the gain medium.

Regular relaxation oscillations, as depicted in Figs. 17.1 and 17.2, are observed in single-mode lasers. Multimode lasers show irregular or chaotic spike trains (see Fig. 9.3). Although numerical simulations suggest regular relaxation oscillations, rather chaotic and undamped dynamics are observed in practice with spikes being random in amplitude and spacing. This can partially be traced back to low damping so that stationary conditions are not reached during the pump pulse. In addition, the simultaneous oscillation of multiple longitudinal and transverse modes in the resonator has to be considered. Since the dynamics of each mode affect the population density, they are coupled among each other, resulting in a complex set of coupled equations. Hence, both regular and chaotic solutions are found already for the case that two modes exist in the resonator. The random occurrence of laser spikes is thus an example for chaotic behavior in nonlinear systems.

If regular spiking is required for a particular application, e.g. in material processing, it has to be ensured that the laser operates in a single longitudinal and

transverse mode, preferably the TEM₀₀ mode. The pulse peak power in a spike can then be several orders of magnitude higher than the average output power. Emission of a single spike is achieved by using sufficiently short pump pulses. Typical output pulse durations of the first spike are on the order of a few tens of nanoseconds, while subsequent spikes become increasingly longer (up to tens of microseconds).

17.2 Q-Switching

Generation of shorter pulses, and thus, higher pulse peak powers, is accomplished by Q-switching which involves the modulation of the quality described by the Q factor of the laser resonator. The quality of an optical resonator is inversely related to the internal losses due to transmission of laser power through the output coupler or intra-cavity optical elements.

As opposed to laser spikes which occur regularly or randomly during the pump pulse while the population inversion is periodically built up and depleted, Q-switched laser pulses (sometimes also called giant pulses) are produced by suppressing the laser oscillation until the maximum population inversion is reached. This is the case at the end of the pump pulse, provided that the upper state lifetime is long compared to the pump pulse duration. In order to prevent the onset of laser emission during the pumping process, the resonator is blocked by increasing the resonator losses, e.g. by an electro-optic modulator or switch. Then, after the pump energy stored in the gain medium has approached the maximum possible level, the Q factor is rapidly increased to a high value (at time t_Q), so that the laser power in the resonator builds up very quickly during only a few round trips. As a result, an intense short laser pulse with high peak power is generated. The temporal sequence of this process is depicted in Fig. 17.3.

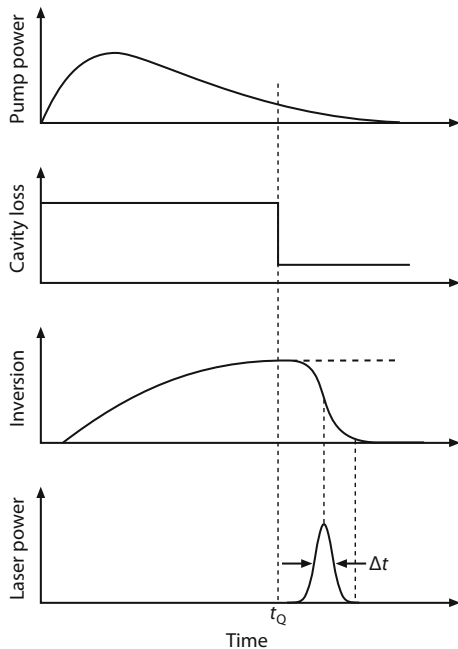
Strong enhancement of the pulse peak power by Q-switching requires the upper state lifetime to be longer than the pump pulse duration. The output pulse duration, in turn, is typically in the nanosecond region, corresponding to several round-trips in the resonator. The round-trip time Δt is given by the resonator length L and the propagation speed of the light c :

$$\boxed{\Delta t = \frac{2L}{c}}. \quad (17.1)$$

Depending on the pulse energy which is limited by the number of excited laser atoms or ions in the gain medium, pulse peak powers in the kW-, MW- or even GW-range are obtained. Due to additional losses introduced by the intra-cavity elements required for Q-switch operation, the pulse energy is generally slightly lower than the total energy extracted in free-running mode of the laser.

Generation of short laser pulses by Q-switching is done also with cw-pumped lasers, e.g. Nd:YAG lasers, using acousto-optic switches.

Fig. 17.3 Temporal evolution of a Q-switched laser pulse (from Koechner (2006)). Pump power (e.g. current of a flash lamp), cavity loss (e.g. introduced by a Pockels cell), inversion or population difference of the upper and lower laser level (curve shape is determined by the integral of the pump power up to the Q-switch), laser power (Δt in ns-regime, power in the MW-regime)



Electro-optic Switches

Q-switching can be realized by active control elements such as acousto-optic or electro-optic modulators (Sects. 16.2 and 16.3). In the latter approach, a Pockels cell (e.g. based on KDP) is used to control the polarization state of the radiation in the laser resonator by applying an electric field. Typical configurations of Q-switched laser oscillators are shown in Fig. 17.4.

In the first setup, the Pockels cell is placed between crossed polarizers. The crystal axes of the Pockels cell and the applied voltage are adjusted such that a phase difference of $\lambda/2$ is introduced between the ordinary and extraordinary component of the propagating light, resulting in a rotation of the polarization direction by 90° . As long as the Pockels cell is switched off, light generated in the laser rod is deflected out of the resonator at one of the crossed polarizers. The resonator losses are thus high, and the laser does not start to oscillate. During this low-Q period, energy is accumulated in the lasing atoms or ions building up a high population inversion. Once the Pockels cell is switched on, the resonator quality increases immediately and a short laser pulse is emitted (*on Q-switching*, Fig. 17.4a).

Fewer optical elements and lower operating voltages are required in the configuration depicted in Fig. 17.4b. Here, a $\lambda/4$ -voltage is applied to a Pockels cell to transform linearly polarized light into circularly polarized light. After reflection from the resonator rear mirror and a further pass through the Pockels cell, the light is linearly polarized again, but the plane of polarization has been rotated by 90° . Hence,

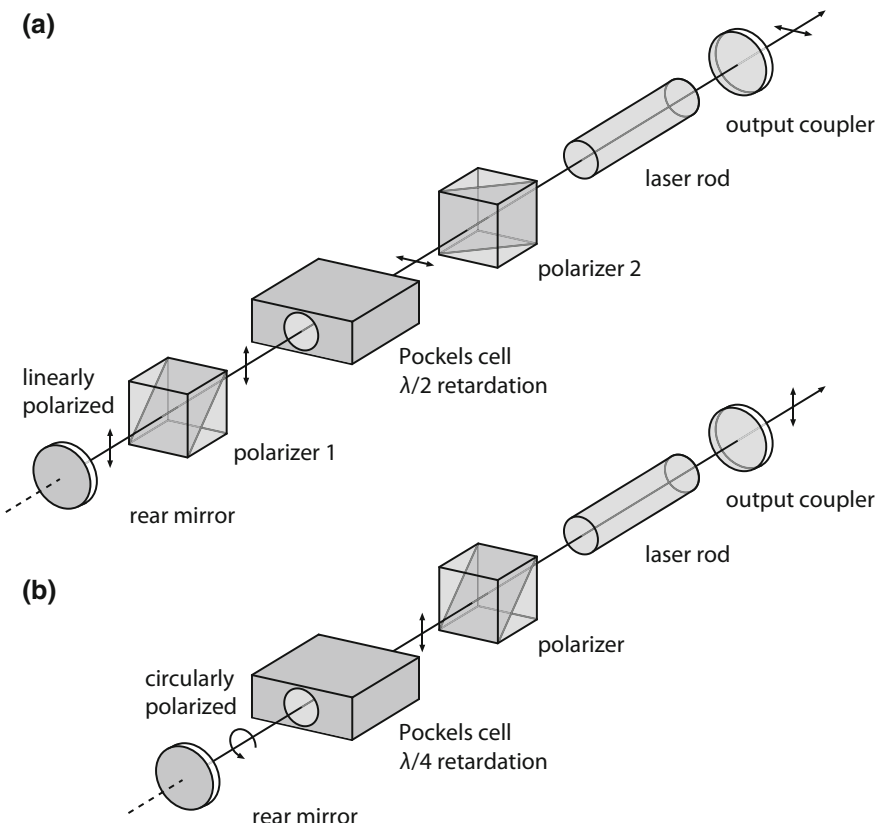


Fig. 17.4 Electro-optic Q-switching: **a** Configuration using a Pockels cell in $\lambda/2$ mode. The resonator is transparent when the Pockels cell is switched on (“on Q-switching”), **b** configuration using a Pockels cell in $\lambda/4$ mode, leading to circularly polarized light incident on the rear mirror. After double-pass through the Pockels cell, the plane of polarization is rotated by 90° and the light is deflected out of the resonator. Once the Pockels cell is switched off, the resonator losses are low and a short laser pulse is generated (“off Q-switching”)

the resonator is blocked when the Pockels cell is switched on. At the moment the maximum storage capacity of the gain medium has been reached, the $\lambda/4$ -voltage is switched off so that laser action can take place (*off Q-switching*). Electro-optic modulators offer fast switching times of less than 1 ns.

Other Switches

Commercial electro-optic switches for Q-switching are not readily available for the infrared spectral ($>3 \mu\text{m}$) and the ultraviolet spectral region. Therefore, mechanical switches such as spinning mirrors or prisms are employed for this purpose. As the

mirror or prism is quickly rotated, proper alignment is only realized in a very short period of time during which the giant pulse is produced. This approach requires precise synchronization of the rotation with the pump pulse emission. Pulse generation in lasers emitting around $3\text{ }\mu\text{m}$ is accomplished with Q-switches based on frustrated total internal reflection (FTIR) (see Sect. 16.1, Fig. 16.1).

Q-switching can also be achieved with acousto-optic modulators (AOMs) which serve to block the laser resonator by diffraction. When a high-frequency voltage is applied to an AOM placed in the laser cavity, the laser beam is diffracted from the grating introduced by an ultrasound wave (see Fig. 16.3). If the caused diffraction losses are higher than the laser gain, laser oscillation is suppressed, and population inversion can build up. Once the AOM is switched off, the stored energy is extracted as a short pulse. The switching times are generally larger compared to Pockels cells; however, higher modulation frequencies, and hence, higher pulse repetition rates can be achieved. AOMs are used for active Q-switching of continuously-pumped solid-state lasers providing pulse repetition rates of several kHz and pulse peak powers that are 1000 times higher than the average power.

Saturable absorbers are utilized as passive Q-switches. As outlined in Sect. 16.4, the transmission properties of these elements depend on the incident light intensity. As the intensity increases, more and more electrons are pumped into an excited state from which they relax into the ground state by stimulated emission. At high intensities, the excitation rate becomes comparable to the relaxation rate, so that the population densities of the excited state and the ground state are nearly equal. Thus, the absorption saturates, and the material appears transparent.

For the purpose of Q-switching, the absorption of the passive switch material is chosen such that the initial loss in the resonator is high, while still permitting some weak lasing once the stored energy in the gain medium approaches its maximum. At this point, the intra-cavity intensity and, in turn, the transmission of the saturable absorber rapidly increases. This allows for efficient generation of an intense laser pulse. After extraction of the pulse, the absorber recovers to its initial transmission and the resonator is blocked again. The repetition rate is hence determined by the recovery time of the absorber. While dye solutions (e.g. malachite green, DODCI) were originally employed as saturable absorbers, nowadays it is more common to use semiconductor elements (SESAMs), ion-doped crystals ($\text{Cr}^{4+}\text{:YAG}$, $\text{V}^{3+}\text{:YAG}$, $\text{Co}^{2+}\text{:MgAl}_2\text{O}_4$, $\text{Co}^{2+}\text{:ZnSe}$) or carbon nanotubes and graphene layers.

Passive Q-switches offer the realization of very compact microchip lasers, as the need for a modulator and its electronics is eliminated. For instance, a thin absorber layer ($100\text{ }\mu\text{m}$ of $\text{Cr}^{4+}\text{:YAG}$) can be epitaxially deposited on a thin Nd:YAG substrate (1 mm) (Fig. 17.5). The end-faces are polished and coated with dielectric mirrors. Cutting of the substrate produces a multitude of micro cavities with dimension of only 1 mm^3 . Diode-pumped, passively-Q-switched solid-state microchip lasers generate pulses with high repetition rates and excellent beam quality. Depending on the absorber thickness and dopant concentration, pulses with energy from 1 to $100\text{ }\mu\text{J}$ and duration of about 1 ns are obtained. In larger systems, passive Q-switches have the disadvantage that the pulse energies are typically lower compared to active devices. Moreover, external triggering of the pulses is not possible, so that the emission shows temporal fluctuations (jitter).

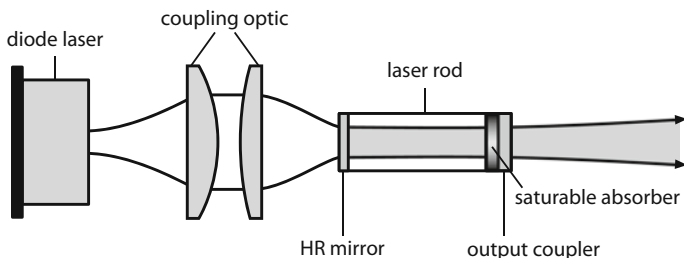


Fig. 17.5 Passive Q-switching of a diode-pumped microchip laser using a saturable absorber (e.g. Cr⁴⁺:YAG)

17.3 Cavity-Dumping

Another method for generating nanosecond laser pulses is cavity-dumping. As opposed to Q-switching where the laser energy is stored in the gain medium, this technique is based on energy storage in the optical cavity. For this purpose, the resonator contains only highly reflective mirrors and no partially transmissive output coupler, so that a strong intra-cavity light field builds up when the gain medium is pumped. Output coupling is realized by an optical modulator, usually an acousto-optic modulator, which is placed inside the resonator and rapidly switched on to eject a short pulse out of the cavity.

Cavity-dumping is for instance utilized in continuously-pumped argon or krypton lasers for producing short pulses with high peak power. Here, Q-switching is not applicable due to the short upper state lifetime. In cavity-dumped argon lasers, the peak pulse power exceeds the cw output power by a factor of 30–50, while the average output power is comparable to the cw output power. The pulse repetition rate is controllable via the modulator and can be varied from single pulse operation to several tens of MHz.

Provided that the switching time of the cavity-dumper is shorter than the resonator round-trip time, the laser pulse is extracted without only one round-trip. Hence, the pulse duration is determined by the resonator length, resulting in very short pulses of a few nanoseconds, even at high repetition rates. This is the main advantage over Q-switching where the pulse duration increases with the repetition rate due to the lower gain stored in the laser medium.

17.4 Mode-Locking

The longitudinal modes existing in a free-running multimode laser oscillate independently at slightly different frequencies (Sect. 12.1). Their mutual phase relationships are not fixed and vary randomly, e.g. due thermal changes in the gain medium. If only a few modes are supported in the cavity, constructive and

destructive interference of the field amplitudes causes strong intensity fluctuations that are amplified while the light circulates in the resonator. Such a spontaneous coupling of modes results in a fast and random modulation of the laser output power which occurs for example in gas lasers and can be avoided by ensuring single longitudinal mode operation.

However, it is also possible to enforce constructive superposition of multiple longitudinal modes. By suppressing the phase differences between the oscillating modes such that the field amplitudes constructively interfere during each round-trip, very short pulses with high intensity are produced. The time-dependent field amplitude at a certain location in the resonator with length L is composed of the sum of N adjacent longitudinal modes defined by their respective amplitudes E_q , frequencies f_q and phases φ_q :

$$E(t) = \sum_{q=q_0}^{q_0+(N-1)} E_q \cos(2\pi f_q t + \varphi_q) = \sum_{q=q_0}^{q_0+(N-1)} E_q \cos\left(2\pi q \frac{t}{T} + \varphi_q\right), \quad (17.2)$$

considering that the frequency of a longitudinal mode q is given as $f_q = q \cdot c/2L = q/T$ (12.2) with the resonator round-trip time $T = 2L/c$. q_0 describes the lowest laser frequency.

The intensity $I \propto |E|^2$ according to (17.2) is plotted in Fig. 17.6. When the longitudinal modes are oscillating in phase ($\varphi_q = 0$), i.e. the phases of the modes are locked, there are certain times and locations in the cavity at which all the modes constructively interfere with each other. This leads to pronounced peaks of the field amplitude with a period $T = 2L/c$ that corresponds to the resonator round-trip time. Hence, an intense pulse is produced which circulates in the resonator.

During each round-trip, one pulse is transmitted through the output coupler of the mode-locked laser, resulting in a train of ultra-short pulses separated by the round-trip time T or the inverse of the mode spacing frequency $1/T$, correspondingly (Fig. 17.7).

The pulse duration τ is determined by the number of oscillating (and phase-locked) modes N . It is much shorter than the cavity round-trip time, typically

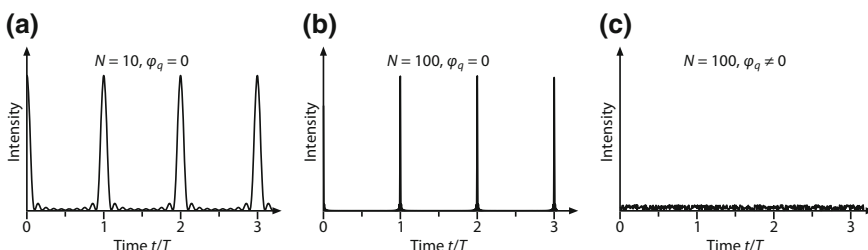
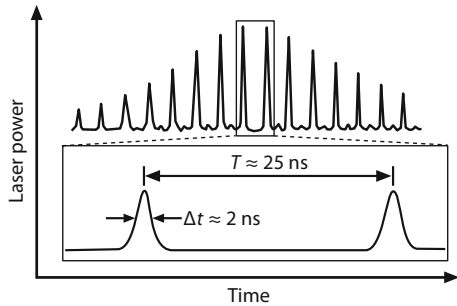


Fig. 17.6 Temporal evolution of the laser intensity $I(t) \propto E^2(t)$ in case of superposition of N longitudinal modes with (a, b) and without (c) a fixed phase relationship. The ordinate scaling is different for the three plots

Fig. 17.7 Mode-locked pulse train of a flash lamp-pumped solid-state laser. The lower plot depicts a portion of the pulse train at 10-fold higher temporal resolution. Typical pulse durations are much shorter (ps to fs)



ranging from tens of picoseconds down to a few femtoseconds. The more modes, i.e. the wider the spectral bandwidth of the laser, the shorter the pulse duration (see Fig. 17.6). In practice, the actual pulse duration is governed by the exact amplitude and phase relationship of each longitudinal mode which also influence the pulse shape.

The relationship between the bandwidth Δf and the pulse duration τ can be expressed in terms of the so-called time-bandwidth product which follows from the Fourier transform between the temporal evolution of the electric field $E(t)$ and its frequency distribution (spectrum):

$$\boxed{\tau \cdot \Delta f \geq K}. \quad (17.3)$$

The two parameters τ and Δf are specified as the full width at half-maximum (FWHM) in the time and frequency domain, respectively. The constant K depends on the shape of the pulse which is regarded as a wave packet. Typical values are $K \approx 0.44$ for Gaussian-shaped and $K \approx 0.31$ for sech^2 -shaped pulses.

The number N of oscillating modes within the laser bandwidth Δf is

$$N = \Delta f \frac{2L}{c}. \quad (17.4)$$

Thus, according to (17.3), the pulse duration reads

$$\boxed{\tau \geq \frac{K}{N} \frac{2L}{c}}. \quad (17.5)$$

In broadband laser media, more than $N = 10^5$ longitudinal modes can be coupled, yielding laser pulses with durations in the fs-regime. When the pulse duration is only a small multiple of the optical cycle (few-cycle pulses), the shape depends on the phase of the electric field (Fig. 17.8).

Such ultra-short pulses show certain characteristics when traveling through a medium. Due to the broad spectral bandwidth, the wavelength-dependence of the refractive index (dispersion) becomes significant and influences the propagation of the pulse. In case of normal dispersion, i.e. the refractive index decreases with

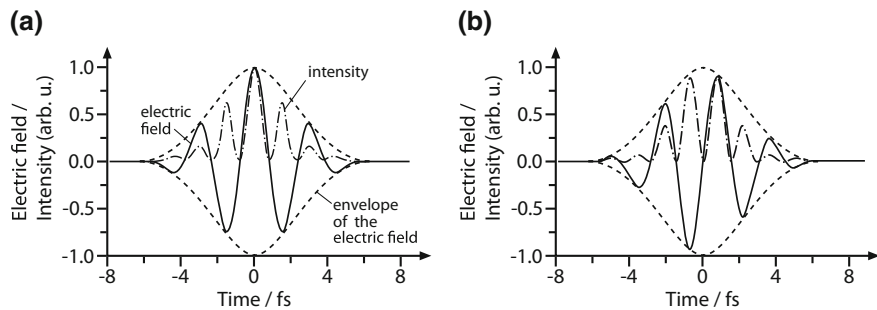


Fig. 17.8 The maximum intensity of ultra-short few-cycle laser pulses depends on the phase of the oscillation. **a** Cosine-like oscillation with maximum intensity, **b** sine-like oscillation with lower maximum intensity

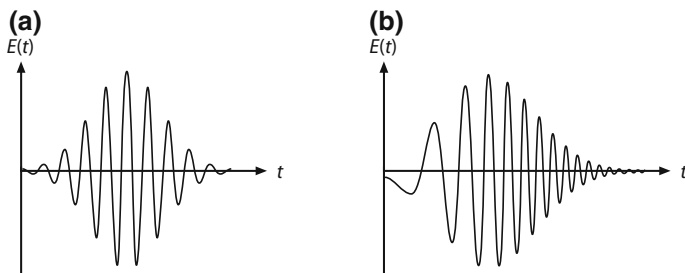


Fig. 17.9 Temporal evolution of the electric field of an ultra-short pulse **a** Before and **b** after propagation through a dispersive medium. Due to dispersion the instantaneous frequency increases with time (up-chirp)

increasing wavelength, the higher-frequency portions of the pulse experience a larger refractive index and are thus retarded with respect to the lower-frequency portions. This group velocity dispersion (GVD) involves a temporal broadening of the pulse and a variable *instantaneous frequency* which is referred to as chirp. The latter is illustrated in Fig. 17.9, where the frequency of the electric field increases with time (up-chirp).

Additionally, owing to the high peak intensities, ultra-short pulses can also give rise to nonlinear optical effects in the medium such as self-phase modulation. Here, the phase of the electric field φ is altered by the intensity-dependent refractive index $n \propto I$ (see Kerr effect, Sect. 16.3) which is relevant at intensities beyond 10^{14} W/m^2 . The modulation of the phase introduced by its own intensity results in a time-dependent phase change which is associated with spectral broadening of the pulse, since $f = d\varphi/dt$.

Mode-locking is achieved by different techniques which rely on the principle that unlocked modes suffer higher losses than locked modes. In general, a distinction is made between passive and active mode-locking methods. The latter are

based on external modulation of the resonator losses, whereas passive mode-locking involves loss modulation by the pulse intensity itself.

Saturable Absorber Mode-Locking (Passive)

Mode-locking can be accomplished by incorporating a saturable absorber into a laser resonator. Saturable absorbers were already introduced in the context of passive Q-switching (Sect. 17.2) and also allow for generating mode-locked laser pulses. Initially, pumping of the gain medium gives rise to weak lasing without saturating the absorber. The intensity inside the resonator fluctuates, as many unlocked modes independently oscillate (Fig. 17.6c). However, since fluctuations with higher intensity experience weaker absorption, they are preferentially transmitted by the absorber. Hence, randomly occurring intensity peaks corresponding to phase-locked modes are selectively amplified during each round-trip, while modes with different phase are suppressed. Eventually, due to phase distortions, these modes also get in phase with the already locked modes, so that they constructively contribute to the formation of the pulse, and thus to the saturation of the absorber. In this way, the pulse becomes shorter with each round-trip until a steady-state has been reached. Since the modulation of the resonator losses is realized by the generated pulse itself, it is much faster than achievable with an active modulator. Therefore, provided that the absorber has a sufficiently short recovery time, the pulse durations of passively-mode-locked lasers are shorter compared to configurations based on active mode-locking.

As outlined in Sect. 16.4, semiconductor saturable absorber mirrors (SESAMs) are usually applied for passive mode locking. These compact devices allow for flexible adjustment of the saturation properties over broad ranges and are employed in solid-state and semiconductor lasers. In earlier times, liquid absorbers, filled in flow cells, were used as resonator mirrors. The pulse train produced in a passively-mode-locked solid-state laser based on this design is shown in Fig. 17.7. The envelope of the emitted laser output is determined by the population density of the upper laser level. In case of pulsed pumping, the emission ends when the pump power falls below the laser threshold. Since the pulse train originates from initial intensity fluctuations, stochastic variations of the output dynamics occur. For instance, the intensity-dependent transmission characteristics of the absorber can lead to the so-called Q-switched mode-locking regime where the intra-cavity pulse energy undergoes strong oscillations. Here, several weak (secondary) pulses are emitted between the intense mode-locked pulses.

Colliding Pulse Passive Mode-Locking (Passive)

Another passive mode-locking technique relies on two ultra-short pulses that counterpropagate in a ring laser and meet in an absorber medium, e.g. a liquid jet.

Amplification of the intra-cavity laser field occurs in a continuously-pumped dye jet where a population inversion is created. The distance of the absorber jet and the amplifier jet is chosen such that the population inversion is re-established in a period shorter than half of the round-trip time $T/2$. Mode-locking is achieved by the simultaneous propagation of the two pulses through the absorber medium which is only a few hundreds of a millimeter thick. The colliding pulses form an interference pattern with enhanced peak intensity that fully saturates the absorber. In this way, the leading edges of the pulses become steeper, while the trailing edges are cut by gain saturation (see Sect. 2.5). The interplay of these mechanisms enables pulse durations of a few picoseconds.

In order to obtain femtosecond pulses, dispersion effects have to be taken into account. The colliding pulse mode-locked (CPM) laser depicted in Fig. 17.10 incorporates a prism sequence where higher-frequency portions of the pulse travel further towards the tip of the prisms, so that group velocity dispersion is compensated. As a result, the configuration generates ultra-short dye laser pulses with duration of 27 fs at 620 nm wavelength (Valdmanis und Fork 1986).

Mode-Locking with a Modulator (Active)

Active mode-locking involves electro-optic or acousto-optic modulation of the intra-cavity losses at the frequency $c/2L$ which corresponds to the inverse of the cavity round-trip time. As a consequence, only light that travels through the modulator at times when the transmission is high is circulating in the resonator and thus amplified in the gain medium. Hence, a single pulse bounces back and forth in the cavity, leading to the emission a mode-locked pulse train. Active mode-locking is utilized for both pulsed and continuously-pumped lasers. The output dynamics are more reproducible compared to passively-mode-locked system; however, the obtained pulse durations are usually longer. In hybridly-mode-locked configurations (Fig. 17.11), the advantages of both techniques are combined, thus enabling stable emission of ultra-short pulses.

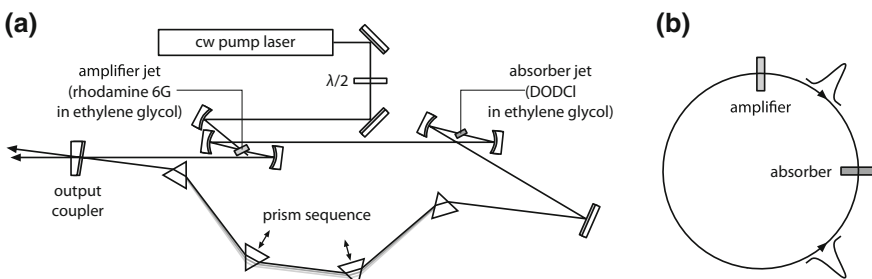


Fig. 17.10 **a** Experimental setup and **b** pulse sequence scheme of a colliding pulse mode-locked (CPM) dye ring laser with two counterpropagating femtosecond pulses

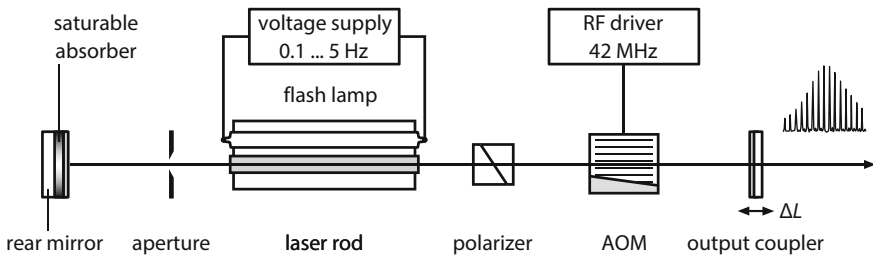


Fig. 17.11 Hybrid mode-locking of a Nd:YAG laser using a saturable absorber and an acousto-optic modulator (AOM). The output coupler can be precisely translated in order to adjust the cavity length, and thus, the longitudinal mode spacing and pulse repetition frequency with the modulator frequency

Synchronous Pumping (Active)

When a mode-locked laser is used as a pump source for another laser, the latter can also produce mode-locked pulses, provided that the resonator lengths of both systems are matched so that the round-trips are synchronized. This approach is based on a periodic modulation of the gain, as opposed to the loss modulation present in the previous methods. The duration of the output pulses generated in synchronously-pumped lasers can be considerably shorter than the pump pulse duration. For instance, dye lasers provide pulses with duration of only 100 fs when pumped by a mode-locked noble gas ion laser (100 ps). The principle of synchronous pumping is also utilized in optical parametric oscillators (OPOs) (Sect. 19.4).

Kerr-Lens Mode-Locking

Apart from the presented classic active and passive mode-locking techniques, femtosecond pulse generation is often realized by means of Kerr lens mode-locking. For this purpose, the intensity-dependent refractive index of a material is exploited. Besides self-phase modulation which causes spectral broadening, self-focusing occurs when a highly-intense laser beam propagates through a medium (Kerr effect, Sect. 16.3). Since the intensity of a (e.g. Gaussian) laser beam is higher on the beam axis compared to the outer parts of the transverse intensity profile, the resulting spatial distribution of the refractive index in the medium acts as a lens.

Mode-locking is passively achieved by the self-induced reduction of the beam size, whereby two different approaches are used. In the first case, the Kerr lens optimizes the spatial overlap of the resonator mode with the pump beam, and hence the gain. This method which is referred to as soft aperture Kerr lens mode-locking, is thus based on gain modulation. In contrast, hard aperture Kerr lens mode-locking

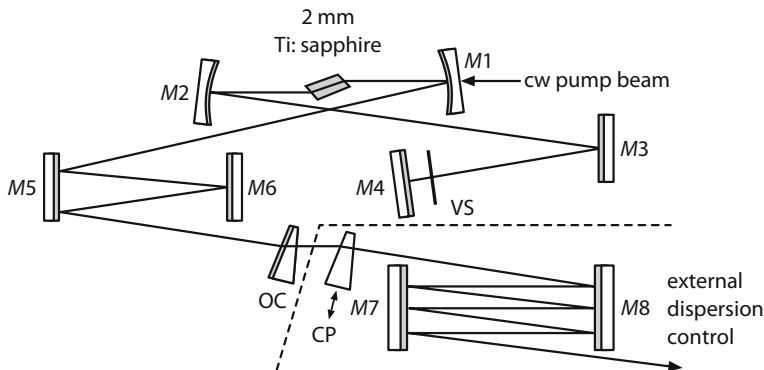


Fig. 17.12 Titanium-sapphire femtosecond laser (8 fs) with dispersion compensation (mirrors M_5 , M_6) and vertical slit (VS) used as aperture for Kerr-lens mode-locking (Stingl, Lenzner, Spielmann and Krausz, Wien, 1995). The generated ultra-short pulse extracted from the output coupler (OC) is further compressed by means of an external dispersion control realized my mirrors M_7 and M_8

relies on loss modulation. Here, an aperture is placed inside the cavity, so that unlocked modes which are associated to a weaker self-focusing are suppressed during each round-trip.

Both techniques are employed in solid-state lasers. In particular, gain materials with vibronically broadened transitions such as titanium-sapphire (Sect. 9.4) are well-suited for ultra-short pulse generation, as they exhibit a large nonlinear refractive index n_2 , aside from their broad emission spectrum. The Kerr lens is produced in the laser crystal itself which has a typical thickness of a few millimeters. This allows for rather simple laser configurations, as shown in Fig. 17.12. Such systems produce laser pulses as short as 5–8 fs at wavelengths around 800 nm, if special dispersion-compensating mirrors are used. The latter are dielectric multilayer mirrors with a frequency-dependent optical penetration depth which even enable higher-order chirp compensation.

Femtosecond Fiber Lasers

Femtosecond pulses can also be generated in stable and compact fiber lasers. A common approach is based on an Yb-doped glass fiber which is pumped by a diode laser emitting at 980 nm wavelength. As depicted in Fig. 17.13, the pump laser is launched into a double-clad fiber (see Fig. 9.27) by a wavelength division multiplexer (WDM) which couples the pump light into the inner cladding, while the Yb:glass laser emission around 1030 nm (linewidth: 40 nm) propagates in the fiber core. The laser travels through a single-mode fiber (SMF) before being incident on a configuration of free-space polarization optics. The latter comprises a quarter-wave

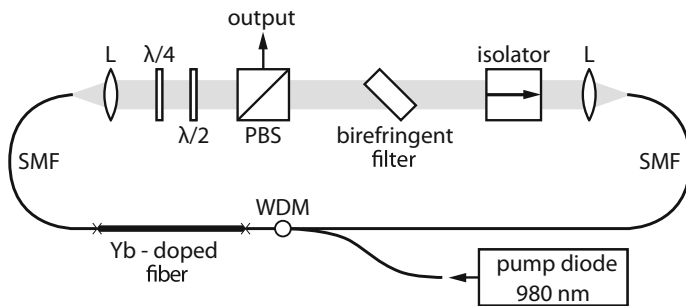


Fig. 17.13 Schematic of an all-normal-dispersion (AND) fiber laser (L lens, PBS polarizing beam splitter, SMF single-mode fiber, WDM wavelength-division multiplexer)

plate, a half-wave plate for rotating the polarization direction, a polarizing beam splitter (PBS), a birefringent plate as well as an optical isolator that ensures unidirectional propagation of the light.

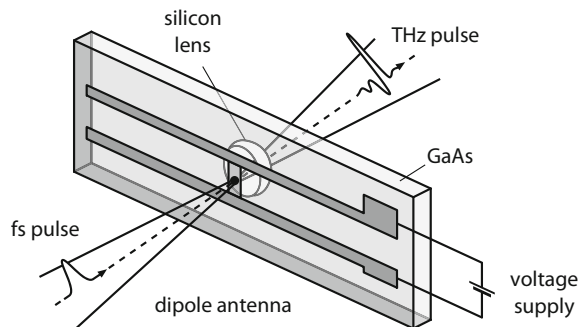
Mode-locking relies on the modification of the polarization properties in the fiber depending on the laser intensity. Similar to the Kerr effect, the generated light in the fiber causes laser-induced birefringence. In case that the free-space optical elements are properly adjusted to the laser intensity, the free-space path becomes optically transparent once a certain intensity is reached, thus producing a train of ultra-short pulses with energy of several tens of nJ and duration of 100 fs. Multi-stage amplification of the pulses in fibers with larger core diameters boosts the average output power to the kW-regime, so that these femtosecond fiber laser systems are well-suited for high-precision material processing (Sect. 23.2).

Terahertz Generation in Photoconductive Antennas

Radiation in the THz-range between 10^{11} and 10^{12} Hz can be generated by various techniques, for instance by quantum cascade lasers (Sect. 10.7) or by ultra-short pulses, as illustrated in Fig. 17.14. Here, a femtosecond pulse is focused into a photoconductive switch made of a semiconductor material, e.g. GaAs, with two metallic stripes (contacts) deposited onto it. The laser radiation generates free carriers in the region between the contacts which are accelerated by an electric field induced by applying a voltage to the stripes. The short current pulse which is about as long as the laser pulse gives rise to a short electromagnetic pulse that is emitted from the stripe structure acting as a dipole antenna. According to (17.3), a pulse with duration of $\tau = 100$ fs contains frequency components up to $f = K/\tau = 4$ THz, if the pulse shape is such that $K = 0.4$.

Continuous wave THz-radiation can be produced through difference frequency generation (Sect. 19.4). In this approach, a photoconductive antenna is irradiated with two single-frequency laser diodes, e.g. at about 850 nm wavelength, whose

Fig. 17.14 Terahertz generation from femtosecond pulses in a photoconductive antenna. A silicon lens is used for focusing the THz-radiation



difference in emission frequency is in the THz-range. As a result, the photo current is modulated at THz frequencies and, consequently, an electromagnetic wave in the THz-range is emitted. Photoconductive antennas operating in cw mode are also referred to as THz-photomixers.

17.5 Amplification and Compression

The energy of laser pulses can be increased in amplifiers. For this purpose, energy is stored in the amplifier gain medium by creating population inversion that is then depleted by the propagating pulse. Higher amplification is obtained by realizing multiple passes through the gain medium. A major problem that arises during pulse amplification is amplified spontaneous emission (ASE) which leads to undesired depletion of the inversion density in the amplifier medium and an incoherent background. Spatial filters, saturable absorbers and synchronous pumping are utilized to suppress ASE.

A laser amplifier incorporating six passes of the pulse through the gain medium (dye or titanium-sapphire crystal) is shown in Fig. 17.15. The final two passes are separated by means of a telescope together with a saturable absorber. The pump pulse from a frequency-doubled Nd:YAG laser is synchronized to the femtosecond (or picosecond) pulse which was generated in a CPM laser (see Fig. 17.10), thus enabling amplification factors up to 10^6 .

Regenerative Amplifiers

In case of low single-pass gain of the amplifier medium, like for titanium-sapphire crystals, regenerative amplifiers are employed. Here, the pulse to be amplified is injected into a resonator containing the gain medium using an electro-optic switch (e.g. a Pockels cell). Then, the pulse performs several tens to hundreds of round-trips increasing the pulse energy to a high level. After a fixed period, the

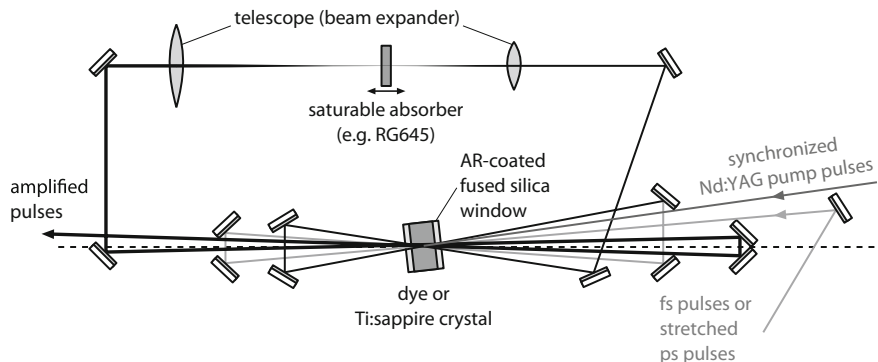


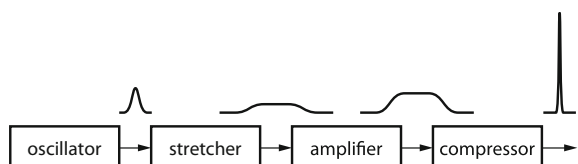
Fig. 17.15 Pulse amplifier in a six-pass configuration using a dye or titanium-sapphire crystal as amplifying medium

amplified pulse is released from the cavity by the same or a second switch. Employing amplifiers of moderate size, this allows for pulse energies in the mJ-range, while even higher energies are possible with larger systems. The repetition rate is typically on the order of 1 kHz, although the (seed) laser source producing the initial weak pulses may have a much higher pulse repetition rate, e.g. tens of MHz. Hence, only a small fraction of the seed pulses is used for amplification.

Chirped-Pulse Amplification

At very high optical peak intensities, distortion of the pulse or, even more problematic, optical damage of the laser material and other optical elements may occur. In order to avoid these detrimental effects during the amplification process, ultra-short pulses are often temporally stretched before being amplified and compressed afterwards. This technique is called chirped-pulse amplification (CPA) and was developed by Donna Strickland and Gérard Mourou in 1985 (Fig. 17.16). Pulse stretching can be accomplished by propagating the pulse through a dispersive medium, e.g. a glass block, which also causes a strong chirp, thus reducing the pulse peak intensity to a level where the deleterious effects are prevented. Temporal re-compression of the amplified pulse relies on the same principle as the prism

Fig. 17.16 Principle of chirped-pulse amplification (CPA) (Strickland and Mourou (1985))



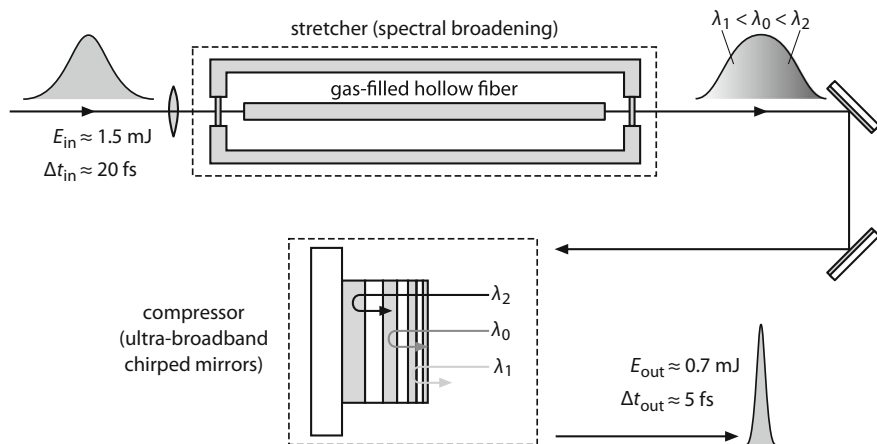


Fig. 17.17 Schematic experimental setup of a hollow-fiber chirped-mirror high-energy pulse compressor. The chirp of the broadened pulse is removed upon reflection off broadband chirped mirrors (Brabec and Krausz, T.U. Wien, 2000)

sequence in CPM lasers and uses an element with opposite dispersion which also removes the chirp, so that the pulse has a duration similar to the initial pulse duration. In 2018, Strickland and Mourou were awarded the Nobel Prize in Physics for their method of generating high-intensity, ultra-short optical pulses.

The schematic of a high-power pulse compressor is depicted in Fig. 17.17 where spectral broadening of the pulse is obtained by a chirp which is induced in a hollow fiber filled with a noble gas. Subsequent chirp compensation of the broadband pulse is achieved with chirped mirrors. Another common method for compressing amplified laser pulses is the use of diffraction gratings, exploiting the fact that different frequency components of the pulse undergo different path lengths (Fig. 17.18). Compression ratios of more than 1000 can be achieved which, in combination of titanium-sapphire lasers, results in 100 fs-pulses with energy exceeding 1 J. This corresponds to peak powers of more than ten terawatt (10^{13} W). For even higher peak powers, amplifier systems consisting of several regenerative and/or multi-pass amplifiers are used. In this way, peak powers in the PW-range ($1 \text{ PW} = 10^{15} \text{ W}$) can be reached in large-scale facilities (Sect. 25.6).

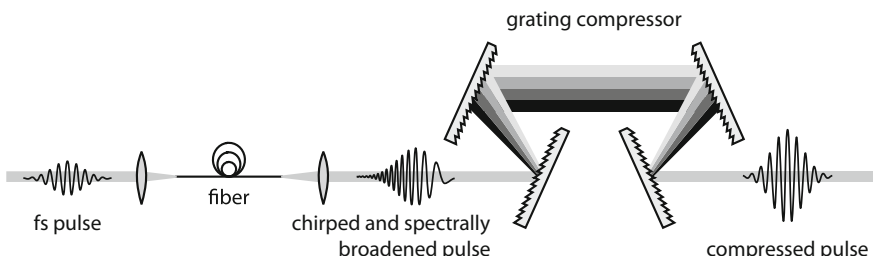


Fig. 17.18 Pulse compression after propagation through a fiber using a grating compressor

Pulse compression at lower power, e.g. directly behind a fs-laser, can be easily obtained by focusing the ultra-short pulse into a glass fiber. Aside from standard optical fibers, photonic crystal fibers (see Sect. 13.3) or gas-filled hollow fibers (Fig. 17.17) can be used. Due to nonlinear effects such as self-phase modulation, the pulse is spectrally broadened. At the same time, the dispersion in the fiber results in a strong chirp. After re-compression the pulses are shorter than before entering the fiber, as the spectral bandwidth has been increased. For instance, 27 fs-pulses from a CPM laser are compressed down to 6 fs. In special fibers with anomalous dispersion, chirp and compression can be simultaneously realized. If such a fiber is incorporated into the feedback loop of a mode-locked color-center laser, a so-called soliton laser can be built.

Pulse compression also occurs during nonlinear frequency conversion. Optical parametric oscillators (Sect. 19.4) and Raman lasers (Sect. 19.5) often emit pulses which are significantly shorter than the pump pulses. Moreover, when a high-intensity femtosecond pulse is injected into a gas jet, higher harmonic generation (Sect. 19.3) occurs which, under certain conditions, enables the generation of attosecond pulses.

Further Reading

1. S. Nolte, F. Schrempel, F. Dausinger (eds.), *Ultrashort Pulse Laser Technology* (Springer, 2016)
2. V. Protopopov, *Practical Opto-Electronics* (Springer, 2014)
3. L. Plaja, R. Torres, A. Zaïr (eds.), *Attosecond Physics* (Springer, 2013)
4. A.W. Weiner, *Ultrafast Optics* (Wiley, 2009)
5. K.E. Oughstun, *Electromagnetic and Optical Pulse Propagation 2* (Springer, 2009)
6. R. Paschotta, *Encyclopedia of Laser Physics and Technology* (Wiley-VCH, 2008)
7. S. Watanabe, M. Katsumi (eds.), *Ultrafast Optics V* (Springer, 2007)
8. K.E. Oughstun, *Electromagnetic and Optical Pulse Propagation 1* (Springer, 2007)
9. J.C. Diels, W. Rudolph, *Ultrashort Laser Pulse Phenomena* (Academic Press, 2006)
10. W. Koechner, *Solid-State Laser Engineering* (Springer, 2006)

Chapter 18

Frequency Selection and Tuning

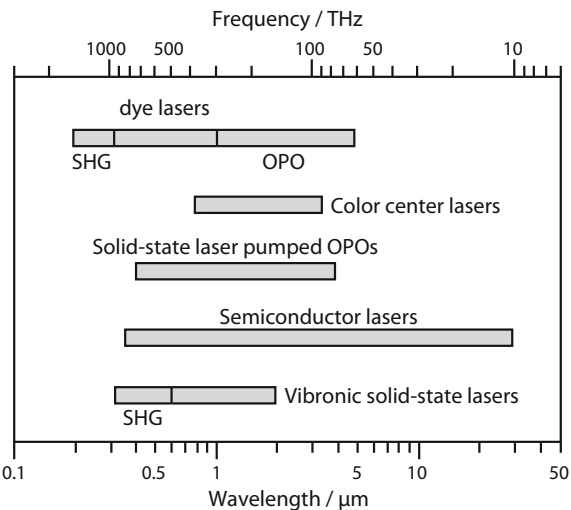


In general, multiple longitudinal and transverse electromagnetic modes simultaneously oscillate in a laser resonator. Hence, lasers emit a range of frequencies or wavelengths, determined by the linewidth of the laser transition, e.g. 1.5 GHz (2 pm) for the He–Ne laser at 633 nm or several THz (hundreds of nm) for the titanium-sapphire laser around 800 nm. The number of oscillating modes, and thus, the emission range of a laser can be reduced by the use of frequency-selective elements that are inserted into the laser resonator, ultimately enabling single longitudinal and single transverse mode operation. Moreover, alteration of the intra-cavity elements, e.g. tilting of a prism, grating, etalon or birefringent filter, allows for continuous tuning of the emission wavelength within the laser bandwidth.

18.1 Frequency Tuning

The tuning ranges of widely-employed, continuously wavelength-tunable laser systems are illustrated in Fig. 18.1. Dye lasers are available at emission wavelengths from 0.3 to 1.0 μm depending on the used dye and wavelength-selective element. This range can be extended to the UV spectral region (down to 0.2 μm) by means of second harmonic generation (SHG) in nonlinear crystals (Sect. 19.3). Extension to the mid-infrared region (up to about 5 μm) is possible with optical parametric oscillators (OPOs) or Raman lasers. Lasers based on color centers (Sect. 1.5) complement the emission spectrum of dye lasers in the near-infrared. Over the last twenty years, dye and color center lasers have been almost completely replaced by more practicable and more stable vibronic solid-state lasers and OPOs which are discussed in more detail in Sect. 19.4. Although the tuning bandwidth of semiconductor lasers is relatively small, the large variety of possible material compositions allows for a

Fig. 18.1 Emission ranges of continuously tunable lasers



wide range of emission wavelengths from 0.35 to 30 μm , according to the designed band gap energy (see Fig. 10.5). In addition to the continuously tunable laser sources shown in Fig. 18.1, there are further systems and techniques for increasing the spectral range of laser wavelengths that are, however, only rarely applied in commercial devices: third and fourth harmonic generation, frequency mixing in gases for the generation of VUV radiation at 20 nm and high-pressure gas lasers (infrared molecular lasers and excimer lasers). A more detailed overview of available laser wavelengths is given in Fig. 3.1.

In some gain media, laser emission is obtained from multiple transitions at different center wavelengths. CO₂ and other molecular gas lasers, for instance, emit at a range of closely spaced spectral lines. Using a frequency-selective element, the output wavelength is either discretely tuned between the single lines, or continuously tuned within the bandwidth of one line.

18.2 Longitudinal Mode Selection

Laser operation at the fundamental transverse mode (TEM₀₀) is in most cases readily achieved by the use of a mode aperture inserted into the resonator. When the diameter of the aperture is chosen to be slightly larger than the TEM₀₀ beam diameter, but smaller than the diameter of higher transverse modes, the losses for the latter are high enough to prevent them from oscillating in the resonator (Sect. 12.2).

The selection of longitudinal modes and the realization of single longitudinal mode (SLM) operation is generally more challenging. In this context, a distinction is made between homogeneously and inhomogeneously broadened gain media (see Sect. 2.4).

Spectral Hole Burning

In the case of inhomogeneous line broadening (e.g. collisional broadening in gas lasers), the effect of spectral hole burning occurs. Here, the population inversion, and thus the gain, is selectively depleted for the individual longitudinal modes. As a result, the gain spectrum features several minima (“holes”), as depicted in Fig. 2.7, with the width of each “hole” being on the order of the natural linewidth. The modes oscillate independently from each other and there is no competition between them. Consequently, multiple modes can independently exist above the laser threshold.

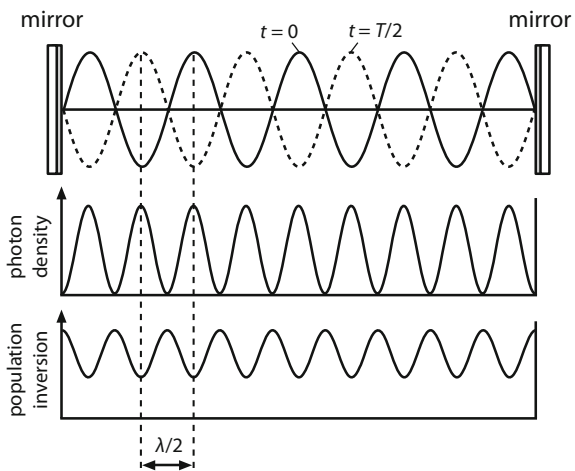
Spatial Hole Burning

The situation is different for homogeneous line broadening where the mode with the highest gain first oscillates, yet without creating a “hole” in the gain spectrum, as the mode simultaneously interacts with all the laser-active atoms or molecules. Instead, due to the homogeneous (uniform) saturation, the gain profile is flattened (see Fig. 2.6). Since the gain is saturated by the first oscillating mode exactly balancing its losses, any other mode experiences a negative net gain and will be suppressed. Therefore, in the absence of other effects, the laser will operate at a single longitudinal mode.

However, in standing-wave laser resonators, multimode operation and mode instabilities are usually observed which can be explained by the phenomenon of spatial hole burning as follows. An oscillating mode forms a standing-wave interference pattern in the laser resonator with the period being half of the emission wavelength. The gain is preferentially saturated in the anti-nodal regions of the pattern where the photon intensity is high, leading to a spatial modulation of the population inversion along the laser medium, as shown in Fig. 18.2. The nodal regions where the gain is less saturated, can hence be occupied by another longitudinal mode which has a different wavelength and thus forms a different interference pattern. Due to spatial hole burning, multiple modes can simultaneously oscillate, as they have their anti-nodal regions at different locations along the gain medium.

The effect can be eliminated in ring lasers where the generated light field may not form a standing-wave, but a traveling-wave, provided that the ring cavity contains an optical isolator that ensures unidirectional propagation of the wave in the resonator. Spatial hole burning is also reduced by placing a thin gain medium with a short absorption depth at one end of the resonator where the anti-nodal points of nearby longitudinal modes are relatively close. Further approaches for overcoming or circumventing spatial hole burning can be classified into schemes involving short-cavity lasers, the twisted-mode technique, intra-cavity frequency-selective elements and injection seeding. These methods are discussed in the following sections.

Fig. 18.2 Spatial hole burning in a standing-wave laser cavity. The population inversion is spatially modulated by one longitudinal mode, giving rise to the oscillation of additional longitudinal modes



Short Resonators

Shortening of the resonator length L leads to an increase in the longitudinal mode spacing according to $\Delta f = c/2L$. If the mode spacing becomes larger than the gain bandwidth of the laser medium, SLM operation is achieved. For a helium-neon laser with a bandwidth of 1.5 GHz (due to collisional broadening), SLM output is obtained at lengths below $L = 10$ cm. The frequency of the mode is tuned by fine adjustment of the cavity length. In this way, the mode can be placed in the center of the gain profile. In solid-state lasers with much broader gain bandwidth of several 100 GHz, the resonator length has to be in the sub-mm-range. This is accomplished with microchip lasers consisting of thin gain materials which are directly contacted to the resonator mirrors (see Fig. 17.5). The short resonator length of such monolithic lasers additionally facilitates the generation of sub-nanosecond pulses. However, these lasers are not capable of generating high average output power above a few watts due to the limited volume of the gain material.

Twisted-Mode Technique

Another approach to circumvent the perturbing spatial hole burning effect, especially in linear resonators with large gain bandwidth, is provided by the so-called twisted-mode technique. It involves the utilization of two quarter-wave plates which are placed at each end of the gain medium. The optic axes of both plates are rotated by 90° with respect to each other and by 45° with respect to the polarization state of the light in the resonator governed, e.g. by an intra-cavity polarizer or the laser crystal itself. As a result, the forward and backward propagating waves are circularly polarized when passing through the gain medium, whereas they are

linearly polarized in the rest part of the resonator. The superposition of the counterpropagating waves leads to a helical interference pattern which exhibits no electric field nodes. Consequently, the optical intensity is not spatially modulated between the two quarter-wave plates and the intra-cavity optical intensity becomes longitudinally uniform inside the gain medium. Spatial hole burning is hence eliminated and SLM operation is facilitated.

Injection Seeding

A method which is often applied to obtain SLM output in pulsed lasers and OPOs is injection-seeding. Here, low-power radiation from a narrowband (seed) laser is injected into a high-power (slave) laser. In case the seed radiation frequency is close to a resonance frequency of the slave cavity and the injected power is sufficient, the corresponding longitudinal mode first saturates the gain medium and suppresses further growth of other modes from spontaneous emission. Different methods are used to stabilize the slave laser frequency to the seed frequency. For instance, it is possible to adjust the resonator length so that the build-up time of the Q-switched laser pulse is minimized. Alternatively, the resonator length is scanned by translating one mirror and the Q switch is fired once a resonance is detected (ramp-hold-fire technique, see Fig. 20.3).

Frequency-Selective Elements

SLM operation can be also achieved by inserting an optical element into the laser resonator which acts as a frequency filter. One example of such an element is the Fabry-Pérot etalon, which is formed by a transparent plane-parallel plate, usually with highly-reflective surfaces. The etalon has transmission peaks spaced by the free spectral range $\Delta f_{\text{FSR}} = c/2nd$, with n and d denoting the refractive index and the thickness of the plate, respectively. The width of the transmission peaks δf is determined by the so-called finesse F : $\delta f = \Delta f_{\text{FSR}}/F$ (Sect. 18.5).

A longitudinal mode oscillates when the gain G exceeds the threshold $1/TR$ (see (2.27)) which is given by the reflectance of the (identical) resonator mirrors R and the resonator transmission T . The latter is primarily defined by the transmission properties of the etalon. As illustrated in Fig. 18.3, the quantity $1/TR$ is strongly frequency-dependent. In order to obtain SLM operation, the thickness and finesse of the etalon have to be chosen such that first, Δf_{FSR} is larger than half of the gain bandwidth, and second, δf is smaller than the longitudinal mode spacing. The finesse F is related to the reflectance of the two etalon surfaces (Sect. 18.5). By tilting the etalon, one of its transmission peaks can be adjusted to the maximum of the gain profile.

Fabry-Pérot etalons are also employed as reflectors (Fig. 18.4a, b). However, due to the higher frequency selectivity, it is often more convenient to use it in

Fig. 18.3 Frequency selection using an intra-cavity etalon. Only the central mode with frequency f_L reaches the threshold which is determined by the resonator mirror reflectances R and modulated by the etalon transmission function T

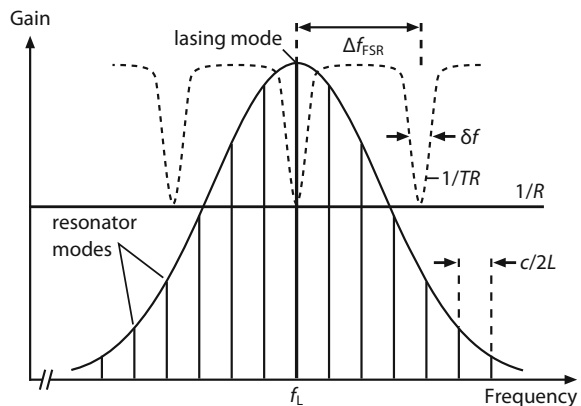
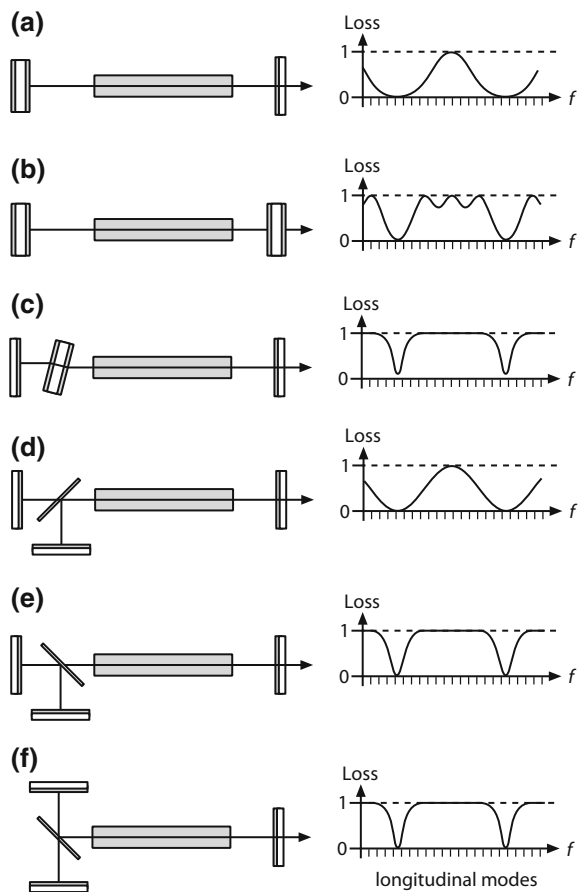


Fig. 18.4 Different interferometer configurations for longitudinal mode selection: **a, b** Fabry-Pérot reflectors, **c** intra-cavity Fabry-Pérot etalon, **d** Michelson interferometer, **e, f** Fox-Smith interferometer (from Kneubühl and Sigrist (2008))



transmission configurations (Fig. 18.4c). Aside from solid or air-spaced etalons (with some air gap between the parallel surfaces), other interferometer arrangements can be applied for longitudinal mode selection. Their transmission characteristics are shown in Fig. 18.4d–f. In the following sections, other optical elements used for wavelength tuning and selection are described.

18.3 Prisms

Light traveling through a prism is refracted (Fig. 18.5a), whereby the deviation angle α during (symmetric) propagation depends on the prism base angle γ and the wavelength λ according to

$$\boxed{\sin \frac{\alpha + \gamma}{2} = n(\lambda) \sin \frac{\gamma}{2}}, \quad (18.1)$$

with $n(\lambda)$ being the wavelength-dependent refractive index of the prism material.

When a prism is placed into a resonator, only light within a narrow wavelength range $d\lambda$ is maintained in the cavity and thus amplified, whereas light outside this range suffers high losses. The range $d\lambda$ can be estimated from the angular dispersion $d\alpha/d\lambda$ of the prism which describes the amount of change in diffraction angle per unit change in the wavelength:

$$\boxed{\frac{d\alpha}{d\lambda} \approx 2\alpha \frac{dn}{d\lambda}}. \quad (18.2)$$

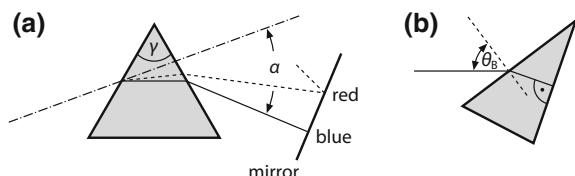
The $dn/d\lambda$ is the dispersion, i.e. the wavelength-dependence, of the refractive index. The deviation angle α can be related to the divergence angle θ of the laser beam:

$$d\alpha \approx \theta. \quad (18.3)$$

The emission bandwidth of the laser containing an intra-cavity prism is hence given by

$$\boxed{d\lambda \approx \frac{\theta}{d\alpha/d\lambda} \approx \frac{\theta}{2\alpha dn/d\lambda}}. \quad (18.4)$$

Fig. 18.5 **a** Prism for frequency tuning of a laser. **b** Brewster reflection prism (θ_B : Brewster's angle)



Fused silica with $dn/d\lambda \approx 1000 \text{ cm}^{-1}$ in the visible spectral region has an angular dispersion of $d\alpha/d\lambda = 2000 \text{ rad cm}^{-1} = 200 \mu\text{rad nm}^{-1}$. Assuming a typical divergence angle of a laser operating in fundamental transverse mode of $\theta = \lambda/\pi w_0 = 2 \cdot 10^{-4} \text{ rad} = 200 \mu\text{rad}$ (e.g. for $\lambda \approx 500 \text{ nm}$, $w_0 = 0.8 \text{ mm}$), the bandwidth is calculated to be $d\lambda = 1 \text{ nm}$. The actual emission range of the laser can significantly differ from this value, as it also crucially depends on the spectral characteristics of the laser gain.

Further narrowing of the bandwidth is achieved by inserting additional prisms into the resonator. Prisms are often used for frequency selection in noble gas ion lasers, where one surface acts as a mirror, as depicted in Fig. 18.5b. The prism is then cut such that the laser beam is incident at Brewster's angle (Sect. 14.1). In this way, the laser wavelength can be tuned by rotating the prism.

18.4 Gratings

Wavelength selection is often realized by using reflection gratings which exhibit a periodic surface relief formed by ridges or grooves, as illustrated in Fig. 18.6a. Light incident on this structure is diffracted into different angles depending on its wavelength and the grating periodicity (or grating constant d). The operation principle of a reflection grating can be understood by considering a plane wave of monochromatic light (wavelength λ) that is incident on the grating surface. According to the Huygens–Fresnel principle, each groove in the grating acts as a point source from which spherical waves are emitted. Constructive and destructive interference of the diffracted waves emanating from each groove lead to the formation of new wave fronts. When the path difference between the light from adjacent grooves is equal to $\lambda/2$, the waves will be out of phase and cancel each other, while a path difference of λ results in constructive interference and high

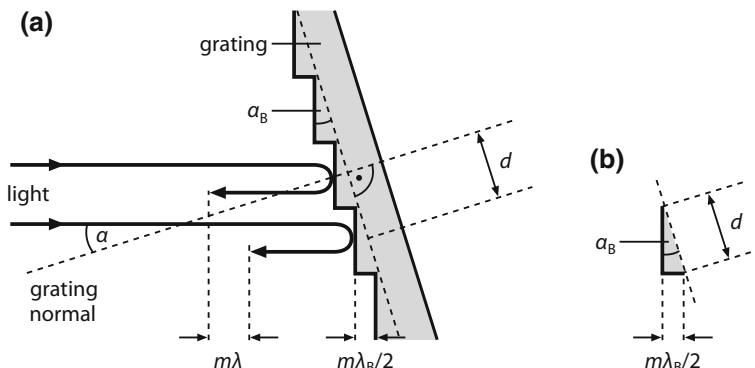


Fig. 18.6 **a** Schematic of a blazed reflection grating, **b** detail illustrating the relationship $\lambda_B = (2d \sin \alpha_B)/m$

intensity of the diffracted light. The latter condition is expressed by the grating equation:

$$\sin \alpha_{\text{in}} + \sin \alpha_{\text{diff}} = m \cdot \lambda/d \quad \text{with } m = 0, 1, 2, 3, \dots \quad (18.5)$$

Here, α_{in} and α_{diff} are the incidence and diffraction angle, respectively, while d is the grating constant. According to (18.5), the grating equation is satisfied for a set of diffraction angles corresponding to multiple diffraction orders enumerated by the integer m . Hence, multiple beams are emitted from the grating and the optical power is distributed over the different diffraction orders.

In a blazed grating (or echelle grating from the French word échelle = ladder), the grating grooves have a sawtooth-shaped cross-section forming a step structure. The steps are tilted at the angle α_B (blaze angle) with respect to the grating surface and are chosen such that light of a given wavelength is diffracted into the same direction as light that is reflected from the steps. In this way, the grating efficiency in a given diffraction order (usually the first order) is maximized, albeit for a specified wavelength. Blazed gratings are mostly employed in the so-called Littrow configuration, where the diffracted beam travels back along the incident beam, i.e. $\alpha_{\text{in}} = \alpha_{\text{diff}} = \alpha$. Consequently, the grating equation becomes (see Fig. 18.6b)

$$|2d \sin \alpha = m\lambda| \quad \text{with } m = 0, 1, 2, 3, \dots \quad (18.6)$$

Light with the blaze wavelength $\lambda_B = (2d \cdot \sin \alpha_B)/m$ experiences the highest diffraction efficiency. If the grating is slightly tilted, reflection at the grating steps occurs at an angle that is no longer identical to the diffraction angle according to (18.6). In other words, the angle between the incident light beam and the grating surface defines the wavelength that is reflected from the grating. This enables wavelength tuning by rotating the grating with respect to the incident light beam. The angular dispersion is given by

$$\frac{d\alpha}{d\lambda} = \frac{\tan \alpha}{\lambda}. \quad (18.7)$$

In analogy to the considerations made for a prism in the previous section, the deflection angle can be approximated with the divergence angle of the laser beam $d\alpha \approx \theta$ (18.3) to estimate the spectral bandwidth of a laser containing a diffraction grating:

$$d\lambda \approx \frac{\theta}{d\alpha/d\lambda}. \quad (18.8)$$

For a grating with $m = 1$, $d = 500$ nm (2000 grooves per mm), $\lambda = \lambda_B = 500$ nm and $\alpha = 30^\circ$, the angular dispersion is $d\alpha/d\lambda = 10^4$ rad cm $^{-1}$ = 1000 μ rad nm $^{-1}$. Hence, assuming the same laser beam parameters as above ($\theta = 200$ μ rad, $w_0 = 0.8$ mm), such a grating allows for a fivefold narrowing of the spectral emission

range ($d\lambda = 0.2$ nm) compared to the prism discussed in the previous section. The spectral resolving power is thus $\lambda/d\lambda = 2500$.

In general, the resolving power of a grating can be approximated by the product of the grating order m and the number of illuminated grating grooves N :

$$\boxed{\frac{\lambda}{d\lambda} \approx N \cdot m.} \quad (18.9)$$

Considering the above grating with 2000 grooves/mm and laser beam with radius of $w_0 = 0.8$ mm, the illuminated length is on the order of 1.6 mm, leading to a first-order resolution ($m = 1$) of $\lambda/d\lambda = 3200$. This value is in fair agreement with the result obtained from (18.8).

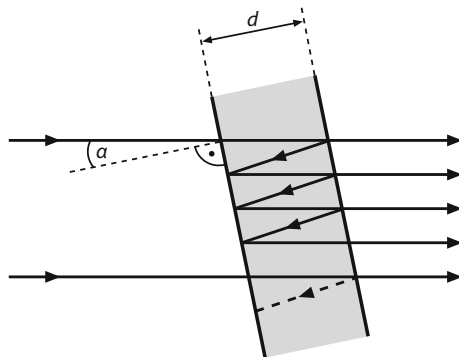
In order to enhance the resolving power of a grating, beam expanders (see Fig. 11.8) are often placed into the laser resonator. Besides the increased number of illuminated lines, this has the benefit that the energy density on the grating is reduced, thus diminishing the hazard of optical damage. For instance, increasing the illuminated length of the grating from 16 to 50 mm results in a resolving power of 10^5 for the first diffraction order.

Reflection gratings are applied in a wide range of laser systems to tune the emission wavelength via rotation. The tuning range is determined by the diffraction efficiency of the grating which, in turn, depends on the reflectance of the grooves and their cross-sectional profile. High reflectance is obtained with metallized gratings. In the visible spectral range, tuning ranges of several 100 nm can be achieved at diffraction efficiencies of about 90% depending on the grating layout.

Besides the conventional diffraction gratings discussed above where the surface relief is usually mechanically imprinted on a glass or metallic surface (ruled diffraction grating), there are also holographic surface gratings which are fabricated by means of photolithographic techniques offering finer grating structures. Furthermore, there are so-called volume Bragg gratings (VBGs) where diffraction occurs inside a transparent bulk material. VBGs are emerging as bandpass and notch filters with diffraction efficiencies exceeding 99.9%. These optics are realized by a refractive index modulation fabricated into the volume of a photosensitive material, mostly photo-thermo-refractive (PTR) glass, and are increasingly applied for longitudinal and transverse mode selection in diode, fiber and solid-state laser resonators (see Fig. 10.18). PTR glass provides a large transparency window (0.35–2.7 μm), low thermo-optic coefficient and high damage threshold. Thus, VBGs are especially suited for lasers with high intra-cavity intensity.

18.5 Fabry-Pérot Etalons

A Fabry-Pérot etalon is formed by two parallel, partially transmitting mirrors that are, for instance, deposited on both sides of a plane-parallel glass substrate with refractive index n and thickness d (solid etalon, Fig. 18.7). Alternatively, the

Fig. 18.7 Fabry-Pérot etalon

mirrors can be coated on two separate glass plates leaving an air gap in between (air-spaced etalon). Due to its parallel surfaces, the etalon acts as an optical resonator. An incoming wave passing through the etalon is multiply reflected to produce many transmitted partial waves, as depicted in Fig. 18.7. In case of constructive interference of the circulating waves, the etalon shows high transmission, whereas high reflection losses occur if the partial waves are not in phase. The former case is present when the following condition is fulfilled:

$$2d\sqrt{n^2 - \sin^2 \alpha} = m\lambda \quad \text{with } m = 1, 2, 3, \dots \quad (18.10)$$

The angles α at which maximum transmission is obtained is hence related to the wavelength λ of the incident light. Correspondingly, at a fixed incidence angle, the transmission spectrum of the etalon exhibits several peaks corresponding to multiple resonances. The etalon is usually inserted into a laser cavity at some tilt angle in order to avoid parasitic resonators that are potentially formed by the laser mirrors and the etalon surfaces. Provided that the tilt angle is small enough to ensure sufficient spatial overlap of the counterpropagating waves inside the etalon, the resonance wavelength can be controlled via the tilt angle. This provides an adjustable optical filter for tuning the laser emission wavelength.

Assuming an air-spaced etalon ($n = 1$), the angular dispersion is given by

$$\frac{d\alpha}{d\lambda} = \frac{1}{\lambda \tan \alpha}. \quad (18.11)$$

At small tilt angles, the angular dispersion is considerably larger than that of prisms or gratings, yielding a much better wavelength selection. Aside from tilting, the laser wavelength can be tuned by changing the spacing of the etalon mirrors (wedge filter) or by altering the refractive index of the medium in between, e.g. by varying the pressure of the gas between the two mirrors.

Since the condition (18.10) is satisfied for multiple wavelengths (at fixed d , n and α), the transmission spectrum shows equidistant peaks (for $\alpha = 0$), spaced by the so-called free spectral range

$$\boxed{\Delta f_{\text{FSR}} = \frac{c}{2nd}}. \quad (18.12)$$

This relationship corresponds to (12.3) describing the spacing of longitudinal modes in an optical resonator. An intra-cavity Fabry-Pérot etalon can thus be thought of as an additional cavity that only transmits those modes of the laser that are also modes of the etalon. This implies that SLM operation is only accomplished if the free spectral range of the etalon is larger than half of the spectral bandwidth of the laser. For this reason, one or more additional thinner etalons are used for mode preselection in broadband lasers. SLM operation further requires that the spectral width δf of the etalon transmission peak is smaller than the laser mode spacing. In the idealized case of a plane wave and an infinitely large diameter of the etalon, the spectral width reads

$$\boxed{\delta f = \frac{\Delta f_{\text{FSR}}}{F}}, \quad (18.13)$$

with F denoting the finesse of the etalon. It is defined by the reflectance R of the etalon surfaces:

$$\boxed{F = \frac{\pi\sqrt{R}}{1-R}}. \quad (18.14)$$

For $R = 10\%$, the finesse is $F = 11$, while it is $F = 100$ for $R = 97\%$. The resolving power $\lambda/d\lambda = -f/\delta f$ is much larger compared to prisms and gratings, if d and R take large values. However, in practice, the resolving power of an etalon is significantly lower due to the limited diameter and finite divergence of the laser beam. Etalons are available over a broad range of thicknesses, and hence spectral bandwidths δf . Very thin etalons with $d \approx \lambda$ and $\delta f/f = 0.01$ are also referred to as interference filters. Thicker etalons with d on the order of a few millimeters feature much narrower linewidths. The combination of multiple etalons with different thickness enables continuously frequency-tunable SLM output, even for tens of centimeters long laser resonators.

18.6 Birefringent Filters

Light propagating through a birefringent crystal, e.g. quartz, is split into two orthogonal linearly polarized components, an ordinary and an extraordinary ray (Sect. 15.2). As the two components experience different refractive indices n^o and n^e , they travel through the medium at different speeds, leading to a phase difference between them. Superposition of the waves results in elliptically polarized light which is attenuated when passing through a polarizer (Fig. 18.8b). Maximum transmission is only obtained when the polarization state remains unchanged upon

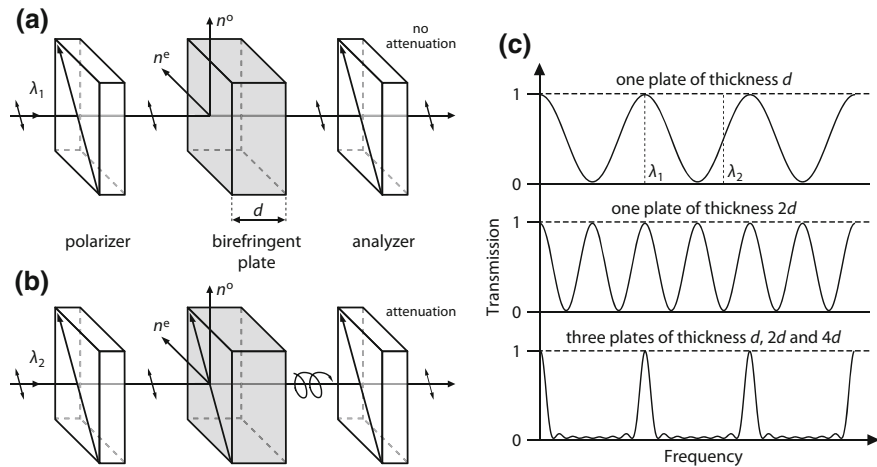


Fig. 18.8 Lyot filter. Depending on the wavelength of the incident light, the plane of polarization is changed after propagation through a birefringent plate. If the wavelength satisfies (18.15), the polarization state remains unchanged (a) and the light passes the second polarizer (analyzer) without attenuation, while other wavelengths lead to elliptically polarized light and are (partially) filtered out (b). The combination of multiple birefringent plates of different thickness results in sharper transmission functions (c). The plates are usually inserted at Brewster's angle to minimize reflection loss for p-polarized light

propagation through the birefringent crystal, i.e. when the phase difference is an integer multiple of the wavelength λ :

$$|n^o - n^e|d = m\lambda \quad \text{with } m = 1, 2, 3, \dots \quad (18.15)$$

The combination of a birefringent plate and a polarizer forms a birefringent filter. Wavelength tuning is realized by tilting the plate, as this alters the effective thickness d and thus the phase difference according to (18.15). Alternatively, the filter can be rotated about its surface normal to change the extraordinary refractive index n^e which depends on the angle between the optic axis of the plate and the polarization direction of the incident light. Variation of the refractive indices can also be introduced by applying an electric field, similar to a Pockels cell (Sect. 16.3).

In analogy to a Fabry-Pérot etalon, the free spectral range of a birefringent filter is defined as

$$\boxed{\Delta f_{\text{FSR}} = \frac{c}{|n^o - n^e|d}}. \quad (18.16)$$

The transmission range of a single birefringent filter is half of the free spectral range Δf_{FSR} which is relatively broad. Hence, a sequence of multiple plates with different thickness and polarizers is usually employed to achieve a better frequency selection, as shown in Fig. 18.8c. Such an arrangement is called a Lyot filter,

named after its inventor Bernard Lyot. The main advantage over (coated) Fabry-Pérot etalons is the absence of surfaces with strongly wavelength-dependent reflectance. Lyot filters are thus applicable over a broader wavelength range and generally show lower losses. This is especially true for Lyot filters that do not contain polarizers and purely rely on the Fresnel losses experienced by s-polarized light.

Further Reading

1. Y.K. Sirenko, S. Ström (eds.), *Modern Theory of Gratings* (Springer, 2010)
2. H. Venghaus (ed.), *Wavelength Filters in Fibre Optics* (Springer, 2006)
3. F.J. Duarte, *Tunable Laser Optics* (Academic Press, 2003)
4. E.G. Loewen, E. Popov, *Diffraction Gratings and Applications* (Marcel Dekker, 1997)
5. L.F. Mollenauer, J.C. White, C.R. Pollock (eds.), *Tunable Lasers* (Springer, 1992)
6. J.M. Vaughan, *The Fabry Perot Interferometer* (Institute of Physics Publishing, 1989)
7. H.J. Eichler, P. Günter, D.W. Pohl, *Laser-Induced Dynamic Gratings* (Springer, 1986)
8. R.L. Byer, E.K. Gustafson, R. Trebino (eds.), *Tunable Solid State Lasers for Remote Sensing* (Springer, 1985)

Chapter 19

Frequency Conversion



The spectral emission range of lasers can be greatly extended by various frequency conversion techniques. Nonlinear optical effects such second harmonic generation, optical parametric generation and stimulated Raman scattering are of particular importance for generating laser radiation at wavelengths that are not easily accessible with conventional laser gain media. Prior to the discussion of nonlinear optical phenomena, this chapter briefly outlines the Doppler effect which leads to small frequency shifts and which is widely exploited for metrological applications.

19.1 Doppler Effect

When a light wave is reflected from a moving mirror (Fig. 19.1), it experiences a frequency shift

$$\Delta f = -\frac{2v}{c}f_0 \cos \alpha, \quad (19.1)$$

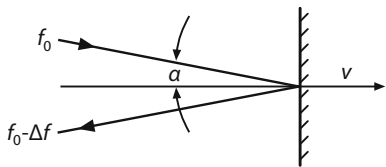
where f_0 is the frequency of the wave incident on the mirror at the angle α and c is the speed of light. If the mirror moves towards the light wave with velocity v , the frequency shift is negative. Assuming a mirror velocity of $v = 1.5$ m/s and normal incidence of the light wave, the relative Doppler frequency shift is $\Delta f/f_0 = 10^{-8}$.

Larger changes in frequency are obtained by light diffraction at ultrasonic waves. Here, the frequency shift of the light wave Δf is given by the frequency of the ultrasonic wave f_S :

$$\Delta f = n f_S, \quad n = \pm 1, \pm 2, \pm 3, \dots, \quad (19.2)$$

with n denoting the diffraction order. In most cases the first diffraction order is used for ensuring optimum diffraction efficiency. Sound frequencies in the range

Fig. 19.1 Doppler frequency shift introduced by reflection of light from a moving mirror with velocity v



of $f_S = 10^9$ Hz can be achieved realizing relative Doppler frequency shifts of $\Delta f/f_0 = 2 \times 10^{-6}$ in case of red light with frequency of $f_0 = 5 \times 10^{14}$ Hz. Higher sound frequencies and thus larger frequency shifts are introduced by the nonlinear optical effect of stimulated Brillouin scattering which has been introduced in the context of phase conjugate mirrors in Sect. 14.4. However, unlike stimulated Raman scattering, this scattering process is only rarely employed for laser frequency conversion. Very large, relativistic Doppler shifts occur in free-electron lasers (see Sect. 25.5). The Doppler shift of light is exploited in a wide range of applications. Amongst others, it is used in astronomy for measuring the speed at which galaxies are approaching or receding from the observer. Furthermore, wind measurements by light detection and ranging (Sect. 25.3) and particle velocimetry (Sect. 25.4) are based on the Doppler effect.

19.2 Nonlinear Optical Effects

The electric field E of an electromagnetic wave propagating through some medium causes electron oscillations and thereby induces dipole moments. The dipole moment density is referred to as (electric) polarization P (not to be confused with the polarization state of the electromagnetic field). The time-varying polarization of the oscillating atoms involves the emission of radiation. At low light intensities, the relationship between polarization and incident electric field is linear (regime of classical optics). However, at high light intensities, nonlinear optical effects occur which can be derived from a Taylor series expansion of the polarization in terms of the electrical field as follows:

$$P = \epsilon_0(\chi_1 E + \chi_2 E^2 + \chi_3 E^3 + \dots) \quad (19.3)$$

with the vacuum permittivity $\epsilon_0 = 8854 \times 10^{-12}$ As/Vm. The coefficients χ_i are called i -th order susceptibilities of the medium and have to be considered as tensors. Typical values for solids are $\chi_1 \approx 1$, $\chi_2 \approx 10^{-12}$ m/V, $\chi_3 \approx 10^{21}$ m²/V². Second-order nonlinearities are only present in crystals, liquid crystals and other anisotropic materials. Based on (19.3), various nonlinear effects involving frequency conversion of the interacting electromagnetic radiation can be derived.

When two plane waves of the form

$$E_i = \frac{A_i}{2} \exp[i(\mathbf{k}_i \cdot \mathbf{r} - \omega_i t)] + \text{c.c.} \quad (i = 1, 2) \quad (19.4)$$

with angular frequencies $\omega_i = 2\pi f_i$ and wave vectors $|\mathbf{k}_i| = 2\pi n_i / \lambda_i = n_i \omega_i / c$ propagate through a nonlinear crystal with non-vanishing second-order susceptibility (Fig. 19.2), the second order nonlinear polarization according to (19.3) reads

$$P_2(\omega, \mathbf{k}) = \epsilon_0 \chi_2 E_1(\omega_1, \mathbf{k}_1) E_2(\omega_2, \mathbf{k}_2). \quad (19.5)$$

Insertion of (19.4) and expansion of (19.5) yields plane polarization waves defined by the sum and difference frequencies and wave vectors

$$\boxed{\omega = \omega_1 \pm \omega_2, 2\omega_1, 2\omega_2} \text{ and } \boxed{\mathbf{k} = \mathbf{k}_1 \pm \mathbf{k}_2, 2\mathbf{k}_1, 2\mathbf{k}_2} \quad (19.6)$$

The cubic term in (19.3) provides, in the case of three different incident waves, the following frequencies ω' and wave vectors \vec{k}' :

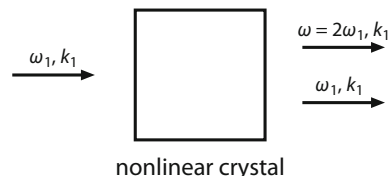
$$\boxed{\omega' = \omega_1 \pm \omega_2 \pm \omega_3, 3\omega_1, 2\omega_1 \pm \omega_2, \text{ etc.}} \text{ and } \boxed{\mathbf{k} = \mathbf{k}_1 \pm \mathbf{k}_2 \pm \mathbf{k}_3, 3\mathbf{k}_1, 2\mathbf{k}_1 \pm \mathbf{k}_2, \text{ etc.}} \quad (19.7)$$

The various frequency components given in (19.6) and (19.7) are also present in the light waves emitted by the induced oscillating dipoles responsible for the nonlinear polarization. Consequently, irradiation of nonlinear materials with intense laser radiation leads to new emission frequencies, thus enabling laser frequency conversion to other spectral regions.

19.3 Second and Higher Harmonic Generation

Irradiation of a crystal with only one light wave having angular frequency $\omega_1 = 2\pi f_1$ results in a nonlinear polarization oscillating at the double frequency $\omega = 2\omega_1$. As a result, a light wave with this frequency is emitted, the so-called second harmonic wave. In order to obtain maximum intensity of the second harmonic radiation, the induced polarization wave ($2\omega_1, 2\mathbf{k}_1$) and the generated light wave

Fig. 19.2 Second harmonic generation of light in a nonlinear crystal



$(\omega = 2\omega_1, \mathbf{k})$ have to propagate through the medium with the same phase velocity. Hence, the following condition must be satisfied:

$$|\mathbf{k}| = \frac{n\omega}{c} = |2\mathbf{k}_1| = 2 \frac{n_1\omega_1}{c}. \quad (19.8)$$

Phase-matching is ensured if the refractive indices n, n_1 of the two waves are equal. This index-matching can be achieved by exploiting birefringence in anisotropic media (Sect. 15.2).

An optically uniaxial crystal shows different refractive indices for light being linearly polarized perpendicular (ordinary) and parallel (extraordinary) to the principal plane (=plane defined by the incident direction and optic axis of the crystal). For optimum phase-matching the fundamental and second harmonic waves have to be ordinary and extraordinary polarized, respectively, leading to different refractive indices n_1^o and n^e . While n_1^o is independent of the incidence angle θ , measured with respect to the optic axis, $n^e(\theta)$ is strongly angle-dependent. Thus, proper choice of the incidence angle, e.g. $\theta \approx 50^\circ$ (Fig. 19.3), allows for the exact matching of the refractive indices (type-I phase-matching).

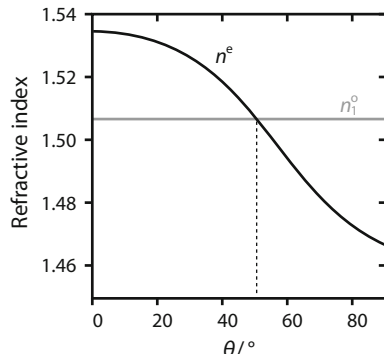
Phase-matching can also be achieved by periodic modulation or “poling” of the crystal nonlinearity along the propagation direction of the light. The period Λ is chosen such that

$$\frac{2\pi}{\Lambda} = k = k - 2k_1 = \frac{\omega_1}{c}(n - n_1). \quad (19.9)$$

This technique is known as quasi-phase-matching and does not require a birefringent medium, yet its preparation is much more elaborate. Periodic poling is often realized using the strongly nonlinear material LiNbO₃. PPNL (periodically-poled lithium niobate) is widely employed for second harmonic generation (SHG) of low-power solid-state and diode lasers to produce visible radiation, e.g. in green laser pointers.

In principle, the SHG conversion efficiency can be up to 100% if exact phase-matching is accomplished. Values of 90% have been demonstrated with

Fig. 19.3 Refractive indices n_1^o and n^e of KDP for ruby laser light and its second harmonic as a function of the angle between propagation direction and optic axis of the crystal



intense lasers. However, the conversion efficiency is much lower in most applications. Since the efficiency scales quadratically with the intensity of the incident radiation, the latter is usually focused into the nonlinear crystal while considering its laser damage threshold. In the low efficiency regime (<20%) and for ideal phase-matching, the second harmonic intensity I is related to the fundamental intensity I_1 and the crystal length L as follows:

$$\boxed{I = \frac{2\omega_1^2 d_{\text{eff}}^2}{c^3 \epsilon_0 n_1^2 n} I_1^2 L^2.} \quad (19.10)$$

The nonlinear coefficients $d_{\text{eff}} \approx \epsilon_0 \chi_2$ of the most common SHG crystals are given in Fig. 19.4. At high conversion efficiencies and exact phase-matching, the relationship reads:

$$I = I_1 \tanh^2 \sqrt{\frac{2\omega_1^2 d_{\text{eff}}^2 I_1 L^2}{c^3 \epsilon_0 n_1^2 n}}. \quad (19.11)$$

Crystals

The most prevalent optical materials for nonlinear frequency conversion are KDP (potassium dihydrogen phosphate, KH_2PO_4) and similar crystals (ADP, RDA, CDA) which are transparent from 0.2 to 1.9 μm and show high laser-induced damage threshold above 400 MW/cm² for 10 ns pulses at 1.06 μm . Table 19.1 provides the threshold value for shorter pulse duration. Lithium niobate (LiNbO_3) is

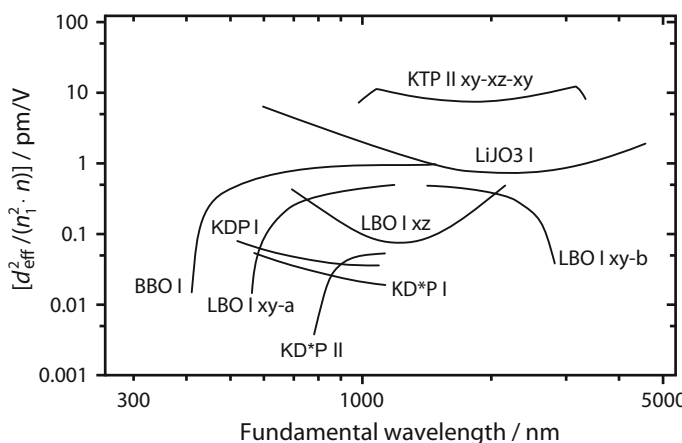


Fig. 19.4 Effective nonlinear coefficient d_{eff} of different crystals for phase-matched second harmonic generation of various wavelengths (I = type I, II = type II). n and n_1 are the refractive indices experienced by the fundamental and second harmonic wave, respectively (courtesy of Gsänger, Optoelektronik, Planegg)

another common material useful in the spectral range from 0.4 to 5.2 μm . Its nonlinear coefficient is much larger than that of KDP; however, its damage threshold is significantly lower. The same holds true for lithium iodate (LiIO_3) and lithium tantalate (LiTaO_3). Very high conversion efficiencies can be obtained using KTP (potassium titanyl phosphate, KTiOPO_4) which offers high optical nonlinearity and is suitable for periodic poling. A drawback is its comparatively low damage threshold. Frequency-doubling is possible for fundamental wavelengths in the range from 1.0 to 3.4 μm , thus allowing for the generation of second harmonic wavelengths down to 500 nm. Further crystals of this type are KTA (KTiOAsO_4), RTP (RbTiOPO_4) and RTA (RbTiAsPO_4). Shorter wavelengths down to 186 nm are reached using BBO (beta barium borate, $\beta\text{-BaB}_2\text{O}$) which also provides very high damage thresholds, exceeded only by LBO (lithium triborate, LiB_3O_5). SHG in the infrared region is achieved using proustite (Ag_3AsS_3) or cadmium selenide (CdSe).

The SHG conversion efficiency scales quadratically with the intensity of the fundamental radiation. Hence, for low-power lasers, the nonlinear crystal is often placed into the laser resonator where the incident power is enhanced by the factor $1/T$, with T being the mean transmission of the cavity mirrors. In addition to cavity enhancement, intra-cavity frequency-doubling has the advantage that the fundamental radiation that has not been converted in one pass through the crystal remains in the resonator and can be converted in the following round-trip. Insertion of the SHG crystal into the cavity often causes temporal instability of the laser, yet this problem can be largely prevented by careful design and construction of the laser resonator. Commercial diode-pumped and frequency-doubled Nd:YAG lasers are mostly realized as intra-cavity SHG cavities.

Second harmonic generation is also observed without phase-matching in second harmonic microscopy of biological material. Here, a signal arises only from molecules without inversion symmetry, e.g. chiral molecules like collagen (see Sect. 24.3).

Higher Harmonic Generation

The generation of higher harmonic waves from a fundamental wave follows from higher-order terms in (19.3). As discussed above, the cubic term in the Taylor expansion is responsible for third harmonic generation. Due to the small third-order susceptibility χ_3 , high conversion efficiencies are difficult to achieve. Therefore, sum frequency mixing (see next section) of the fundamental and the second

Table 19.1 Laser damage threshold of different nonlinear crystals at 1.053 μm and pulse duration of 1.3 ns

Crystal	Fluence (J/cm^2)	Intensity (GW/cm^2)
KTP	6.0	4.6
KDP	10.9	8.4
BBO	12.9	9.9
LBO	24.6	18.9

harmonic wave is more convenient for generating third harmonic radiation. Even higher harmonics are produced by subsequent SHG and sum frequency mixing processes. For instance, higher harmonic generation of a Nd:YAG laser at 1064 nm results in emission wavelengths at 532 nm (second harmonic), 355 nm (third harmonic), 266 nm (fourth harmonic) and 213 nm (fifth harmonic), as shown in Fig. 19.5. Lasers emitting at these wavelengths are commercially available. Harmonic generation of Ti:sapphire lasers is employed for developing tunable laser sources in the visible and UV spectral range.

In the late 1980s, the generation of high harmonics up to the 17th order was observed in noble gases (Xe, Kr, Ar, Ne, He) upon irradiation with intense laser radiation ($>10^{15} \text{ W/cm}^2$). Owing to the inversion symmetry of the gases, only harmonics of odd order were produced. A more recent experimental setup used for high harmonic generation (HHG) is depicted in Fig. 19.6, while Fig. 19.7 shows a characteristic spectral intensity distribution of the output radiation. The peak intensity of the individual orders is nearly constant in the central part of an HHG spectrum (plateau region), but drops rapidly to zero towards lower and higher orders. The highest order is called cut-off harmonic which can be approximated as follows:

$$W_p = I_p + 3.17 \frac{e^2 E^2}{4m\omega^2}. \quad (19.12)$$

Here, I_p is the ionization potential of the gas, E and ω describe the electric field and angular frequency of the incident radiation, e and m are the charge and mass of the electron.

Since lighter atoms have a higher ionization energy, they offer higher maximum photon energy. More crucially, they provide a higher saturation intensity for ionization which allows for stronger electric fields and, in turn, results in higher cut-off energies and shorter wavelengths. Heavier (larger) atoms, however, show higher

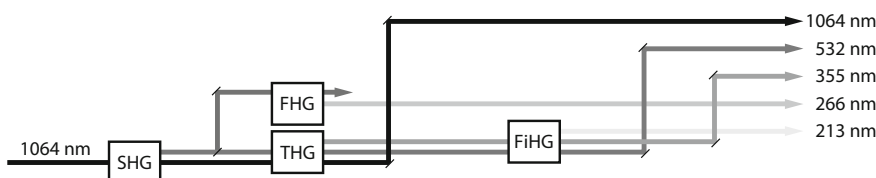


Fig. 19.5 Schematic diagram illustrating higher harmonic generation of a fundamental wave at 1064 nm: SHG—second harmonic generation (1064 nm → 532 nm), THG—third harmonic generation by sum-frequency mixing of the fundamental and SHG wave (1064 nm + 532 nm → 355 nm), FHG—fourth harmonic generation by frequency-doubling of the SHG wave (532 nm → 266 nm), FiHG—fifth harmonic generation by sum-frequency mixing of the SHG and THG wave (532 nm + 355 nm → 213 nm)

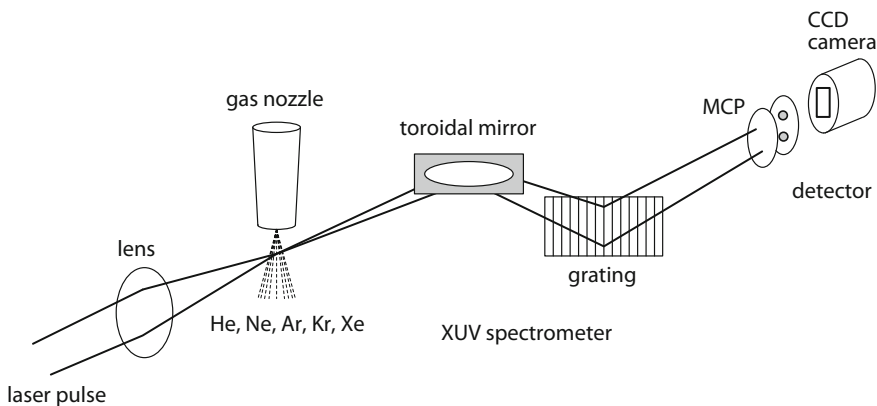


Fig. 19.6 Experimental setup for high harmonic generation in noble gases (MCP = micro-channel plate (Sect. 21.3) and fluorescence screen) (courtesy of G. Sommerer and W. Sandner, Max-Born-Institute Berlin)

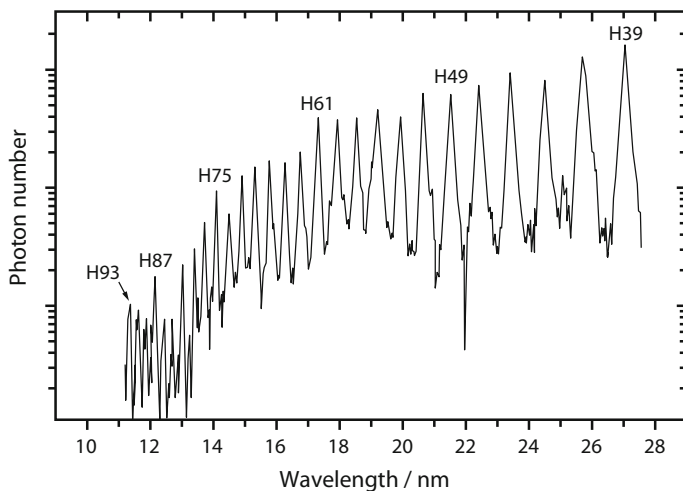


Fig. 19.7 High harmonic spectrum generated in neon by 800 fs pulses at 1053 nm wavelength which were focused to a spot radius of $60 \mu\text{m}$, realizing pump intensities on the order of 10^{14} W/cm^2 . The relative photon numbers of the different orders strongly depend on the experimental parameters. The linewidth of the peaks is limited by the resolution of the spectrometer (courtesy of D. Schulze, G. Sommerer and W. Sandner, Max-Born-Institute Berlin)

polarizability and thus larger nonlinear dipole moments than smaller atoms, leading to higher photon numbers at lower harmonic orders.

The HHG conversion efficiency in argon was determined to be 10^{-5} in the range from 10 to 40 eV. For photon energies between 43 and 73 eV, efficiencies on the order of 10^{-10} have been reported when using a Nd:glass laser with 650 fs pulse

duration. Conversion to the range from 40 to 150 eV shows efficiencies from 10^{-6} to 10^{-8} . These comparatively large values refer to different femtosecond lasers, e.g. Cr:LiSAF ($\lambda = 825$ nm), Ti:sapphire ($\lambda = 790$ nm) with pulse durations below 100 fs.

High harmonic generation provides a coherent light source in the VUV/XUV region reaching the water window which is defined as the spectral range between the K-absorption edge of oxygen at 2.34 nm and the K-absorption edge of carbon at 4.4 nm. Thus, the radiation is absorbed by carbon atoms while water is transparent for these wavelengths. Radiation in this range can be used for studying biological substances in aqueous solution.

The HHG process involves significant pulse shortening. In the year 2000, researchers succeeded in generating soft X-ray pulses of 90 eV and 1.8 fs duration by focusing 770 nm (≈ 1.6 eV) pulses of 7 fs duration into a neon gas cell. The resulting pulses were even shorter than the oscillation cycle of the driving laser (2.6 fs). Eight years later, similar experiments yielded pulses as short as 80 attoseconds. Demonstration of attosecond pulses generated from a UV supercontinuum (see Sect. 19.6) in the range from 55 to 130 eV was accomplished in 2012.

Apart from high harmonic generation of laser pulses, VUV/XUV sources can be provided by synchrotron or undulator radiation, free-electron lasers (FEL), XUV lasers, X-ray lasers and laser plasma emission (see Sect. 25.5). These sources show very different physical properties and differ significantly in terms of their technical effort so that the appropriate source has to be chosen for each particular application. For some applications, however, the different techniques are in direct competition. For instance, certain experiments which used to be done using synchrotron radiation can nowadays also be carried out utilizing HHG radiation. The latter approach is advantageous, as it provides ultra-short pulse duration while offering much lower costs and requiring less space.

19.4 Parametric Amplifiers and Oscillators

When two light waves with different angular frequencies ω_1, ω_2 are coupled into a crystal with second-order nonlinearity, polarization components are generated which oscillate at the sum and difference frequencies $\omega_1 \pm \omega_2$ giving rise to new electromagnetic waves at those frequencies according to (19.6). Difference frequency generation can be exploited for *parametric amplification*. Here, an intense pump wave with frequency ω_p and a weak signal wave with frequency ω_s are incident on a nonlinear medium where the so-called idler wave is generated at the difference frequency

$$\boxed{\omega_i = \omega_p - \omega_s}. \quad (19.13)$$

Exact matching of the refractive indices is required to ensure high efficiency of the process:

$$n_i \omega_i = n_p \omega_p - n_s \omega_s. \quad (19.14)$$

The produced idler wave itself interacts with the pump and signal wave via the second-order nonlinearity of the crystal. Difference frequency generation involving the pump and idler wave, in turn, gives rise to a wave at frequency $\omega_s = \omega_p - \omega_i$, where the phase-matching according to (19.14) is automatically satisfied. Hence, the signal wave experiences gain (parametric amplification), while the pump is depleted. Gain factors of up to $G \approx 100$ can be obtained using LiNbO₃ or KTP crystals with lengths of several cm.

Difference frequency generation is applied in optical parametric amplifiers (OPAs) to produce wavelength tunable output at a fixed pump frequency. Here, a weak tunable signal wave is coupled into a nonlinear crystal together with the strong pump wave (Fig. 19.8a). Parametric amplification under consideration of the phase-matching conditions then yields different pairs of signal and idler wave frequencies depending on the refractive indices experienced in the crystal. Variation of the refractive index is realized by rotating the crystal (Fig. 19.9) or changing its temperature. Hence, accurate control and stabilization of the crystal temperature are required for efficient operation.

An optical parametric oscillator (OPO) is built by an optical resonator which contains a nonlinear crystal (Fig. 19.8b). When an intense pump wave is incident on the crystal, the wave whose frequency satisfies the phase-matching condition (19.14) will be parametrically amplified from the quantum noise of the electromagnetic field. The cavity mirrors are designed to resonate the signal wave, thus providing multiple round-trips through the OPO crystal and, in turn, large gain for the desired output wave which compensates the round-trip losses. When steady-state conditions are reached, the output power of the resonated wave scales with the pump power. The amplification process involves the generation of an idler wave at frequency $\omega_i = \omega_p - \omega_s$. Some OPOs are configured to resonate both the signal and idler wave (doubly-resonant OPO). In this case, the differentiation between both waves is irrelevant.

Parametric amplifiers and oscillators are widely used as continuously tunable laser sources in the UV to MIR spectral range and of particular importance in regions which cannot be accessed by conventional tunable lasers. OPOs which are synchronously-pumped by picosecond or femtosecond lasers can reach conversion

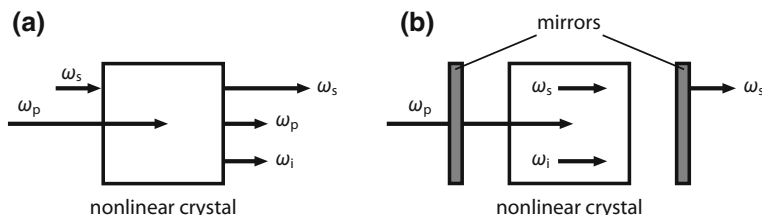


Fig. 19.8 Schematic of **a** an optical parametric amplifier (OPA) and **b** an optical parametric oscillator (OPO)

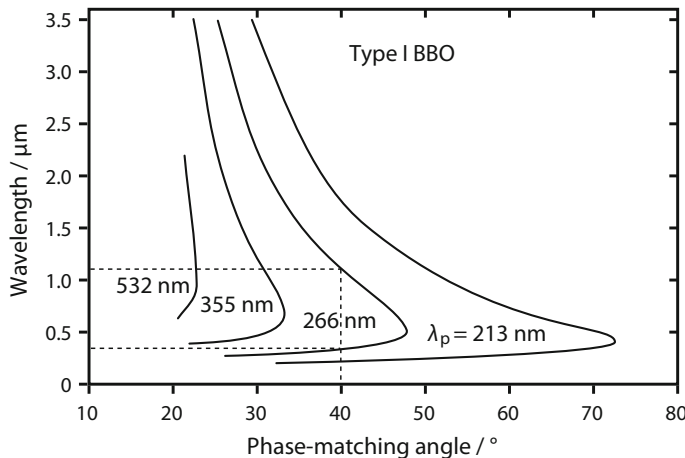


Fig. 19.9 Tuning curve of an optical parametric oscillator based on BBO. The phase-matching angle denotes the propagation direction with respect to the optic axis of the crystal. For instance, at an angle of 40° and a pump wavelength of 266 nm, two waves at 0.3 and 1.1 μm are generated (courtesy of A. Fix, German Aerospace Center, DLR)

efficiencies in the range of 30 to 50%. If operated in cw mode, e.g. using periodically-poled lithium niobate, the efficiencies are usually much lower.

Due to their wavelength versatility, OPOs are attractive for remote sensing of chemical species in the atmosphere like pollutants or greenhouse gases (water vapor, carbon dioxide, methane, etc.). The latter affect the Earth's climate, as they absorb incoming solar radiation and outgoing thermal radiation which are part of the planet's energy balance. The German-French satellite mission MERLIN, scheduled for launch in 2024, aims at the global observation of atmospheric methane (CH_4) concentrations employing a spaceborne light detection and ranging (Sect. 25.3) system. It is based on a pulsed OPO which is tuned to a CH_4 absorption line at 1645 nm delivering 9.5 mJ of pulse energy at 20 Hz repetition rate. Narrowband emission is realized by the injection-seeding technique (Sect. 18.2).

19.5 Stimulated Raman Scattering and Raman Lasers

The generation of novel laser frequencies is also possible by Raman scattering. The Raman effect describes the inelastic scattering of photons from atoms or molecules which leads to a transfer of vibrational energy to or from the interacting medium (Fig. 19.10a). An incident pump photon hf_p is converted into a Stokes photon hf_s while the difference energy $hf_R = hf_p - hf_s$ is absorbed by the scattering medium. The frequency of the emitted Stokes photon is therefore determined by the pump frequency f_p and the Raman shift f_R :

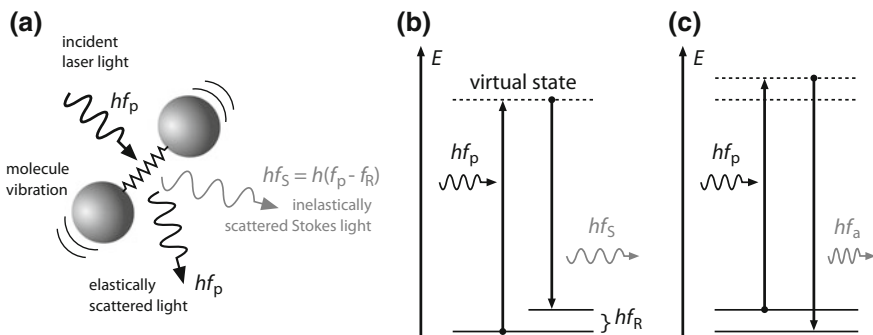


Fig. 19.10 **a** Principle of Raman scattering and energy level diagram for **b** Stokes and **c** anti-Stokes Raman scattering

Table 19.2 Raman shifts of selected gases and solids

Medium	H ₂	HF	CH ₄	N ₂	Diamond	Ba (NO ₃) ₂	SiO ₂ glass
Raman shift (cm ⁻¹)	4155	3962	2914	2330	1332	1048	200–600

$$f_S = f_p - f_R, \quad (19.15)$$

where the latter depends on the energy levels of the Raman medium (Table 19.2). Figure 19.10b illustrates the Stokes Raman scattering process in which the scattered photon has lower energy (and hence lower frequency) than the incident photon. If the interaction involves a molecule (or atom) which is in an excited state, the scattered photon gains energy as the molecule relaxes to its ground state (Fig. 19.10c). Consequently, the scattered photon has a larger frequency than the incident photon according to

$$f_{AS} = f_p + f_R. \quad (19.16)$$

This process is referred to as anti-Stokes Raman scattering. The upper energy levels shown in Fig. 19.10b and c are in most cases virtual levels with lifetimes on the order of a few picoseconds. When the frequency of the incident photon is near the frequency of an allowed electronic transition of the molecule, the Raman process involves real energy levels and the Stokes or anti-Stokes intensity can be greatly enhanced (resonance Raman scattering).

Spontaneous Raman scattering, which has been discussed so far, is a very weak interaction. Only one out of 10 million photons that interact with the medium is scattered inelastically. However, at high pump intensities, a considerable number of Stokes photons is generated which, in turn, stimulate the transition from the virtual level to the ground state. As a result, the Stokes radiation is amplified by stimulated

emission, leading to directional and powerful output which is frequency-shifted relative to the pump.

In the regime of stimulated Raman scattering (SRS), the gain $G = \exp(g_R \cdot L_p \cdot L)$ grows exponentially with the pump intensity I_p , the interaction length L with the Raman medium and a wavelength-dependent gain coefficient g_R . The latter is specific for the molecular vibrational mode that interacts with the pump radiation and also scales with the density of scattering molecules. Therefore, solid-state materials such as barium nitrate ($\text{Ba}(\text{NO}_3)_2$) ($g_R \approx 11 \text{ cm/GW}$ at $\lambda_p = 1064 \text{ nm}$) or diamond crystals ($g_R \approx 10 \text{ cm/GW}$ at $\lambda_p = 1064 \text{ nm}$) are mostly used for Raman frequency conversion. The gain coefficients of selected Raman crystals are given in Table 19.3 together with their transparency ranges and Raman shifts.

At very high pump intensities, the Stokes field becomes strong enough to initiate the SRS process itself, giving rise to cascaded Stokes generation and additional emission lines at lower frequencies (longer wavelengths). Frequency mixing of the pump, Stokes and anti-Stokes waves interacting in the Raman medium produces further spectral components including higher-order anti-Stokes lines at higher frequencies (shorter wavelengths). The spectrum of the scattered radiation thus shows a comb of emission lines separated by the Raman shift f_R , as shown for diamond in Fig. 19.11.

Amplification of one particular spectral component can be achieved by placing the Raman material into a resonator whose optical feedback is selective for a certain Stokes or anti-Stokes component, thus providing efficient conversion to a desired output wavelength. Figure 19.12 depicts an external $\text{Ba}(\text{NO}_3)_2$ Raman laser. Depending on the mirror reflectances the first ($\lambda_{S1} = 1198 \text{ nm}$), second ($\lambda_{S2} = 1369 \text{ nm}$) or third Stokes wave ($\lambda_{S3} = 1599 \text{ nm}$) is amplified and coupled out of the cavity.

In the case of first-order Stokes generation, the maximum (quantum-limited) conversion efficiency η_{\max} from the pump wave at frequency f_p to the Stokes wave at f_S accounts for

$$\eta_{\max} = (f_p - f_R)/f_p. \quad (19.17)$$

Table 19.3 Optical and nonlinear properties of selected Raman crystals. $\text{KGd(WO}_4)_2$ (KGW) shows different Raman shifts depending on the pump polarization with respect to the crystal orientation

Crystal	Transparency range (μm)	Raman shift (cm^{-1})	Raman gain coefficient (cm/GW)
$\text{Ba}(\text{NO}_3)_2$	0.35–1.8	1048	11
$\text{KGd(WO}_4)_2$	0.35–1.8	768 and 901	4.4 and 3.5
CaCO_3 (Calcite)	0.21–2.3	1087	4.3
GdVO_4	0.35–5.5	882	4.5
BaSO_4	0.21–4.2	985	2.7
Diamond	0.23–2.5	1332	10

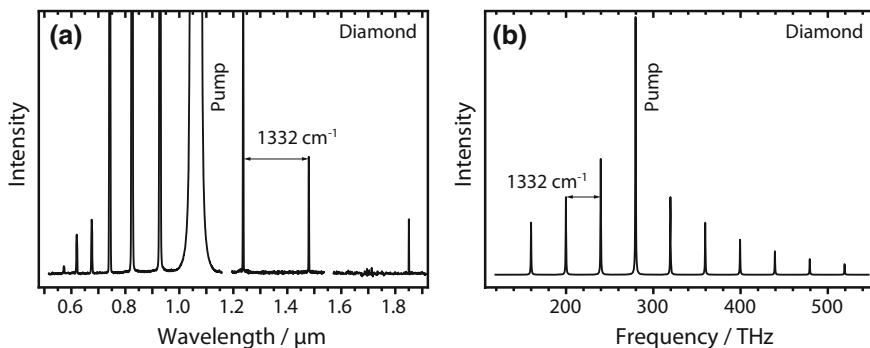


Fig. 19.11 Stimulated Raman scattering (SRS) spectrum of a diamond single crystal, plotted versus **a** wavelength and **b** frequency (calculated spectrum). The incident pump pulses (1064 nm wavelength, 120 ps pulse duration) were focused into the crystal to a spot diameter of 160 μm . The Raman shift of 1332 cm^{-1} corresponds to a frequency of 40 THz

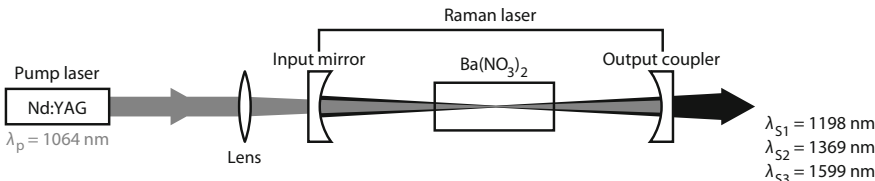


Fig. 19.12 Experimental setup of a Raman laser. Intense pump radiation is focused into a Raman medium that is placed into an external resonator. Optical feedback provided by the cavity mirrors ensures high gain for a chosen Stokes component, generating laser output at the desired Stokes wavelength. Using a Nd:YAG pump laser at 1064 nm and barium nitrate as Raman crystal results in wavelengths at 1198, 1369 or 1599 nm, depending on the mirror specifications

Inserting the Raman shift for diamond (Table 19.2) and a pump wavelength of $\lambda_p = 1064 \text{ nm}$ results in $\eta_{\max} \approx 86\%$ for first Stokes generation at $\lambda_S = 1240 \text{ nm}$. Conversion efficiencies near the quantum limit have been achieved in diamond Raman lasers. This material is characterized by high thermal conductivity and robust mechanical properties. Using other Raman crystals, the efficiency is typically lower due to thermal lensing which affects the Raman laser stability, especially in the regime of high average or cw output powers.

Apart from external cavity configurations, various Raman laser designs have been explored over the years. In intra-cavity Raman lasers, the Raman material is placed within the optical cavity of the pump laser crystal. The resonator mirrors are specified to ensure low losses for the pump wavelength, while the desired Stokes component is partially transmitted through the output coupler. This concept is well suited for lower power pump sources, such as cw-pumped and repetitively-Q-switched lasers, as it utilizes the high intra-cavity power leading to low threshold operation and very high overall conversion efficiencies.

A special case is given by self-Raman lasers where the pump laser crystal acts a Raman-active medium itself. For instance, Nd³⁺-doped vanadate crystals, such as GdVO₄ and YVO₄ have been employed to realize high power laser sources emitting in the near-infrared or visible spectral range. The latter is achieved by integrating a frequency-doubling crystal into the laser resonator.

If a weak Stokes wave is injected into the Raman medium together with a strong pump wave, energy is transferred from the pump to Stokes through SRS as the two signals co- or counterpropagate in the medium (Raman amplification). This principle is mainly applied in optical waveguides and fibers, e.g. in fiber transmission lines where diode-pumped SiO₂ fibers are used as Raman amplifiers.

In Raman fiber lasers, Bragg gratings are usually inscribed into the fiber core to realize narrowband reflectors which act as the cavity mirrors. This provides low-loss resonators and delivers output powers on the order of tens of watts in cw operation. In 2004, researchers from Intel demonstrated Raman laser operation in silicon waveguides which was referred to as “silicon laser”. However, since the underlying laser process is based on SRS, it may not be confused with a conventional semiconductor (inversion) laser where the laser process involves transitions between energy bands. As a consequence of the fundamentally different laser process without energy storage in the gain medium, there is no simple equivalent to spatial hole burning (Sect. 18.2) in Raman lasers. Hence, longitudinal mode instabilities are avoided and SLM operation is facilitated in such devices.

19.6 Supercontinuum Generation

An intense light pulse traveling through a medium alters the refractive index by its high electric field via the optical Kerr effect (Sect. 16.3). The variation in refractive index introduces a phase modulation as different parts of the pulse (leading edge, maximum, trailing edge) propagate through the medium at different speeds (self-phase modulation). Since the phase varies temporally, the instantaneous frequency across the pulse is different from the carrier frequency. This effect is called chirp (see Sect. 17.4) which produces new frequency components and thus spectral broadening of the incident radiation. Self-phase modulation can be exploited for the generation of very broad spectra which are often referred to as (white light) supercontinua spanning the entire visible spectral range (Fig. 19.13) or even the ultraviolet to infrared region. Although self-phase modulation is the dominant effect which causes spectral broadening of the incident radiation, other nonlinear processes such as four-wave mixing and stimulated Brillouin and Raman scattering play an important role in the broadening mechanisms, especially at longer pulse durations in the ps- and ns-regime. Femtosecond lasers are usually employed as pump sources, providing pulse energies in the μJ-range which is sufficient to produce broad spectra after propagation lengths of a few millimeters.

While water and other liquids as well as different glasses and crystals were used in the early investigation of supercontinuum generation, research has focused on

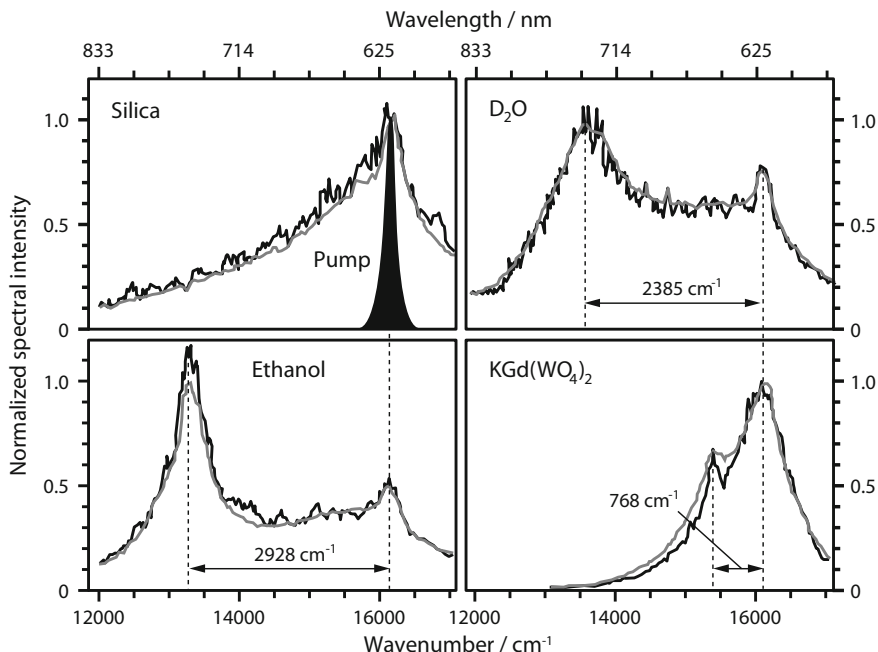


Fig. 19.13 Supercontinuum spectrum generated by focusing a 100 fs pulse at 625 nm wavelength and 0.5 mJ pulse energy into different materials (thickness: 1 cm). The spectral intensity distribution is shown for a single pulse and for an average over 50 pulses (smoother spectrum). Raman lines are observed for D₂O, ethanol and KGW resulting in further spectral broadening. The spectrum of the pump pulse is indicated in the top left figure (courtesy of B. Jähnig and R. Elschner, TU Berlin)

optical fibers and photonic crystal fibers (see Sect. 13.3) in the last decades. The latter are characterized by a high nonlinear refractive index n_2 , thus offering efficient spectral broadening at moderate input pulse energies. In addition, the tight spatial confinement of the mode in the fiber core (few μm) introduced by the microstructure of the fiber allows for strong nonlinear interaction over a significant length of fiber. The interaction length can be further increased by appropriate design of the structure in order to realize propagation with zero group velocity dispersion (GVD) in the spectral range of the pulse.

Supercontinuum white light sources are commercially available providing ultra-short pulses at up to 100 MHz repetition rate. The spectra typically range from 400 to 2500 nm while the spectral power density can be up to 10 mW/nm, resulting in output powers of up to 20 W. These light sources are employed for spectroscopic material characterization as well as for studying fast biological and chemical processes, e.g. by means of time-resolved fluorescence spectroscopy. A further application is optical coherence tomography (OCT) which allows non-invasive imaging of cells or other structures in living tissue with penetration depths of several millimeters and micrometer resolution (Sect. 24.3).

Further Reading

1. Y. Feng (ed.), *Raman Fiber Lasers* (Springer, 2017)
2. R.A. Ganeev, *Nonlinear Optical Properties of Materials* (Springer, 2013)
3. O. Lux, *Laser Frequency Conversion by Stimulated Raman Scattering in the Near Infrared Spectral Region* (Mensch & Buch Verlag, 2013)
4. H. Rhee, *Stimulated Raman Scattering Spectroscopy in Crystalline Materials and Solid-State Raman Lasers* (Mensch & Buch Verlag, 2012)
5. J. Yao, Y. Wang, *Nonlinear Optics and Solid-State Lasers* (Springer, 2012)
6. T. Brabec (ed.), *Strong Field Laser Physics* (Springer, 2009)
7. R.W. Boyd, *Nonlinear Optics* (Elsevier Ltd, 2008)
8. R.R. Alfano, *The Supercontinuum Laser Source* (Springer, 2006)
9. R.L. Sutherland, *Handbook of Nonlinear Optics* (CRC Press, 2003)
10. Y.R. Shen, *The Principles of Nonlinear Optics* (Wiley-Interscience, 2002)
11. V.G. Dmitriev, G.G. Gurzadyan, D.N. Nikogosyan, *Handbook of Nonlinear Optical Crystals* (Springer, 1999)

Chapter 20

Stability and Coherence



Laser properties such as frequency, power, beam profile, pointing direction and polarization generally show variations which can have a disturbing effect on many applications. For instance, fluctuations in the frequency or wavelength of a helium–neon laser employed for interferometric length metrology lead to a limitation in the measurement accuracy. Instabilities in the energy and beam profile of pulsed high-power lasers applied for material processing diminish the precision of the workpiece, e.g. the diameter or shape of a drilled hole. The methods for monitoring and reduction of laser instabilities are versatile and thus only briefly outlined in this chapter. The focus is on the explanation of the main terms that are used to describe the stability of laser characteristics and the magnitude of their variations. Moreover, the stability limits are discussed.

High stability is predominantly obtained in lasers operating in continuous wave mode. The stabilization of pulsed lasers is more elaborate, as it requires fast electronic circuitry. Hence, although the stability of cw and pulsed laser sources is affected by the same effects, reaching the fundamental stability limits is more challenging for pulsed lasers.

20.1 Power Stability

This section presents several technical problems that give rise to variations in the output power of lasers. The inevitable shot noise is discussed in Sect. 20.3.

In electrically-pumped lasers, power variations are caused by the limited stability of the electrical power supply. One can distinguish between long-term fluctuations with time constants of several minutes to hours that are e.g. introduced by temperature changes; variations occurring at the power frequency of 50 Hz or integer multiples (higher harmonics); and high-frequency instabilities on the order of 10 kHz that are related to internal switching frequencies of the power supply.

Another source of power fluctuations is the imperfect mechanical stability of the laser setup. Temperature changes, mechanical shocks and acoustic vibrations can lead to a misalignment of the laser mirrors, thus affecting the beam path inside the resonator. Furthermore, the gain medium itself can cause instabilities, for instance, by plasma oscillations in discharge lasers or thermally-induced phase distortions in optically-pumped solid-state lasers. The magnitude of the power fluctuations depends on the operating conditions, e.g. the discharge current, gas pressure or magnetic field in ion lasers.

In multimode lasers without phase locking, random modulations of the output power occur at the difference frequencies of the oscillating longitudinal and transverse modes. The frequencies are typically in the range of 10–100 MHz for common gas and solid-state lasers. The resulting power instabilities are referred to as mode distribution noise.

For characterizing laser power fluctuations, different specification parameters are provided by laser manufacturers. Amplitude stability is often quantified by the variation in laser output power within the time frame of one hour after the laser has reached its steady-state regime. Typical values of a commercial noble gas ion laser are around 2–3%. Reduction by a factor of 10 can be accomplished by means of a feedback loop for stabilizing the power. Power fluctuations in the frequency range from about 10 Hz to a few MHz are called optical noise. Noble gas ion lasers exhibit root mean square variations of below 1%. A comparable quantity is the so-called maximum ripple which shows similar values.

Pointing Stability

Besides intensity fluctuations, variations in the beam pointing direction are observed in many lasers. They are for instance caused by changes in the position of the gain medium and are tackled by an appropriate opto-mechanical laser design. The pointing stability can be assessed with quadrant detectors which allow to accurately measure the displacement of an incident beam relative to a calibrated center. Pointing variations are usually smaller than the beam divergence.

Polarization Stability

The polarization direction of the radiation produced by a laser is governed by intra-cavity polarizing elements (Sect. 15.3) such as Brewster windows, thin-film polarizers, polarizing prisms or the gain medium itself. The fraction of the radiation that is polarized is quantified by the degree of polarization (DOP). A perfectly polarized wave has a DOP of 100%, whereas DOP = 0% for an unpolarized wave. Polarized He–Ne lasers show DOP values exceeding 99.99%. An unpolarized laser beam can be linearly polarized by using a polarizer outside of the laser cavity.

However, the radiation behind the polarizer often shows an intensity modulation at the fundamental resonator frequency $c/2L$. In addition, optical power is lost at the polarizer. Hence, the use of intra-cavity polarizing optics is more convenient to produce stable polarized laser emission.

20.2 Frequency Stability

Frequency-stable lasers are used in a wide range of spectroscopic and metrological applications. The spectral bandwidth (FWHM) of a single longitudinal mode laser is fundamentally limited by spontaneous emission. This lower limit is expressed by the Schawlow–Townes equation:

$$\boxed{\delta f = \pi h f (\delta f_p)^2 \mu / P.} \quad (20.1)$$

Here, f is the center frequency, P is the output power and $h = 6.626 \times 10^{-34}$ Js is Planck's constant. The spectral bandwidth of the passive resonator δf_p is related to the free spectral range Δf_{FSR} and finesse F of the cavity [see (18.13) and (18.14)]:

$$\delta f_p = \frac{\Delta f_{\text{FSR}}}{F} = \frac{c}{2nL} \cdot \frac{(1-R)}{\pi\sqrt{R}} \quad (20.2)$$

and is thus determined by the optical cavity length $n \cdot L$ (n : refractive index) and the mirror reflectances $R = (R_1 + R_2)/2 \approx \sqrt{R_1 R_2}$. The factor

$$\mu = N_2 / (N_2 - N_1)_{\text{thr}} \quad (20.3)$$

quantifies the spontaneous emission rate where N_2 is the population density of the upper laser level and $(N_2 - N_1)_{\text{thr}}$ is the difference in population density between the upper and lower level at the laser threshold.

For a He–Ne laser with $\lambda = 633$ nm, $f = 5 \times 10^{14}$ Hz, $hf = 3.3 \times 10^{-19}$ Ws, $P = 1$ mW, $n \cdot L = 10$ cm, $R = 99\%$ and $\mu = 1$, the minimum linewidth is $\delta f(\text{He–Ne}) = 0.05$ Hz. However, due to thermal instabilities and mechanical vibrations affecting the resonator length, the Schawlow–Townes limit is difficult to reach in practice and the laser linewidth is usually much higher.

For a GaAs diode laser with $\lambda = 850$ nm, $f = 3.5 \times 10^{14}$ Hz, $P = 3$ mW, $n \cdot L = 3.5 \cdot 300$ μm, $R = 30\%$ and $\mu = 3$ (diode lasers are operated far above threshold), $\delta f(\text{GaAs}) = 1.5$ MHz. Linewidth measurements of diode lasers show values that are higher by the so-called linewidth enhancement factor (or Henry factor) which is on the order of 10–100, even when the influence of technical noise is very low. The increased linewidth was found to result from a coupling between intensity and phase noise caused by a refractive index modulation in the semiconductor gain medium. The modulation is, in turn, originated from fluctuations of the electron density due to spontaneous emission.

The exact center frequency is defined by the resonance frequency f of the laser cavity which is given by

$$f = \frac{mc}{2nL} \text{ with } m = 1, 2, 3, \dots \quad (20.4)$$

Differentiation of this equation yields a relationship between the laser frequency fluctuations Δf and the variations in the optical resonator length L :

$$\frac{\Delta f}{f} = -\frac{\Delta L}{L}. \quad (20.5)$$

In general, the frequency fluctuations introduced by length changes are considerably larger than the theoretical linewidth limit according to (20.1). Short-term (<1 s) frequency instabilities are caused by acoustic or mechanical disturbances of the resonator or current variations in gas discharges. Temperature changes result in long-term variations (>1 s).

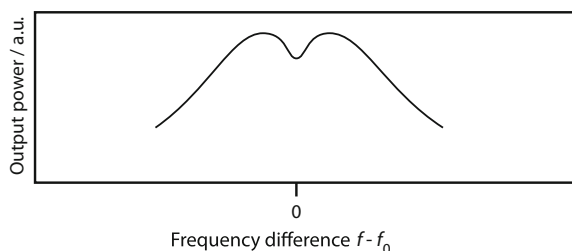
Passive stabilization of the laser frequency is accomplished by the use of mechanical components (optical bench, mirror spacers, etc.) made of materials with small expansion coefficients like the nickel–iron alloy Invar. Moreover, protection of the laser against mechanical vibrations and air flow using damping elements and laser housings increases the laser stability. Further improvement is obtained by active stabilization techniques such as the Lamb-dip method.

Lamb-Dip Frequency Stabilization

When the resonance frequency of the laser cavity is stabilized to the maximum of the gain profile, maximum output power is expected. However, due to spectral hole burning in gas lasers with inhomogeneously (Doppler-) broadened spectral lines (Sect. 18.2), this is not the case. Instead, the spectral distribution of the output power features a dip at the center, as depicted in Fig. 20.1. This effect can be exploited for actively stabilizing the laser to the center frequency.

The Lamb-dip relies on the Doppler effect (Sect. 19.1) occurring when thermally moving atoms emit radiation. If light emitted along the z -direction has the

Fig. 20.1 Output power of a Doppler-broadened single longitudinal mode gas laser (e.g. helium–neon laser) in dependence on frequency, depicting the Lamb-dip for $f = f_0$



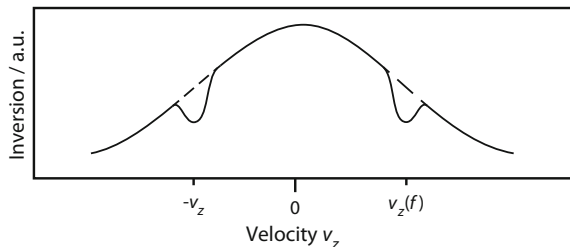


Fig. 20.2 Distribution of the population inversion in a gas laser in dependence on the axial velocity of the gas atoms. The dips at $|v_z| = c/f(f - f_0)$ are due to stimulated emission of photons with frequency f along the laser axis (in both directions). Laser operation at the center frequency $f = f_0$ ($v_z = 0$) results in a Lamb-dip (see Fig. 20.1)

frequency f , it was originated from atoms with the velocity component v_z . On the contrary, if light with the same frequency propagates in the opposite direction ($-z$), it can be traced back to atoms with the velocity component $-v_z$. Consequently, two dips (or “holes”) are observed in the velocity distribution shown in Fig. 20.2, as two classes of atoms contribute to the laser output power. At the line center, the atoms have zero velocity. Hence, if the laser frequency is tuned to the center, the Lamb-dip according to Fig. 20.1 is obtained and the laser emission is produced only by the class of atoms with $v_z = 0$.

Owing to the Lamb-dip, the line center of the gain profile is more pronounced. Deviations from the local minimum can be detected and used to actively control the length of the laser cavity. A common approach is to translate one of the resonator mirrors using a piezoelectric actuator. In the “inverse Lamb-dip” technique, a gas cell is incorporated into the resonator and a specific absorption line of the gas is used as a reference frequency. Since there are less absorbing atoms at the line center ($v_z = 0$) compared to the adjacent regions, the absorption line features a minimum at the central frequency, resulting in a maximum of the laser power. Monitoring of the laser power thus allows to stabilize the laser resonator. In this manner, a frequency stability on the order of $\Delta f/f = 10^{-13}$ is obtained in laboratory configurations, while commercial stabilized He–Ne lasers are available with $\Delta f/f = 10^{-8}$. Iodine (I_2) cells are commonly used as absorption cells for He–Ne and ion lasers. He–Ne lasers emitting at $3.39\ \mu\text{m}$ are stabilized using methane (CH_4), whereas CO_2 , OsO_4 or SF_6 is employed for CO_2 lasers.

Other Active Stabilization Methods

Single longitudinal mode operation of pulsed solid-state lasers and optical parametric oscillators (OPOs) can be achieved by injecting a continuous wave, narrow-linewidth and low-power seed laser into the laser cavity (injection seeding, see Sect. 18.2). To obtain high frequency stability, the slave cavity has to be

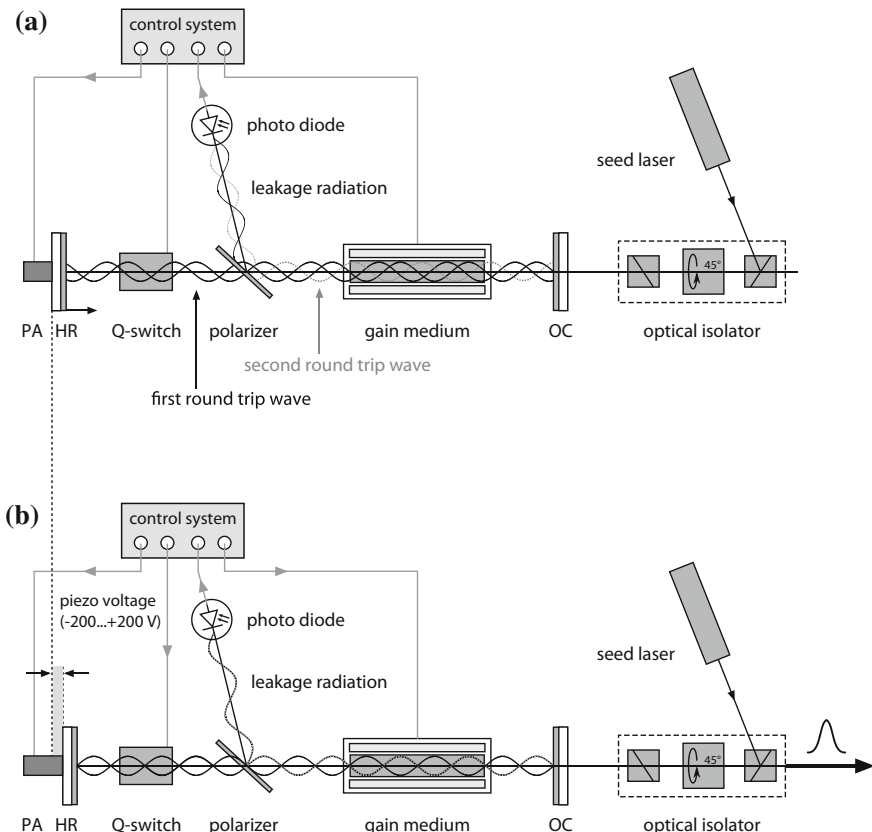


Fig. 20.3 Schematic principle of the ramp-hold-fire stabilization technique: **a** The seed radiation is coupled into the slave cavity via the output coupling mirror (OC) while the highly-reflective resonator mirror (HR) is translated by a piezo actuator (PA). **b** When the cavity is in resonance with the seed radiation, the PA is held, the gain medium is pumped, and the Q-switch is fired generating a narrowband laser pulse

controlled in length to ensure resonance with the seed laser wavelength during the pulse build-up.

Various techniques are employed for active cavity control of Q-switched, injection-seeded lasers. One approach is based on the minimization of the *pulse build-up time* which depends on the detuning between the seed laser frequency and the slave cavity resonance. Adaptation of the cavity length to the injected wave is obtained by a feedback loop using the build-up time of the Q-switch pulse as an error signal that is minimized by translating a piezo-mounted resonator mirror. Since the feedback occurs after the pulse is generated, this method is rather inappropriate at low repetition rates and in mechanically noisy environment. Furthermore, there is no way of measuring the direction of deviation from the optimum cavity length.

High frequency stability even in case of significant amplitude noise is achieved with the *Pound-Drever-Hall technique* where a phase-modulated seed radiation consisting of a carrier frequency and two side bands is coupled into the slave cavity. Heterodyne detection (Sect. 22.5) of the seed light reflected from the cavity yields an electronic (beat) error signal which is a measure of how far the carrier frequency is off-resonance with the cavity. This mechanism involves a decoupling of amplitude and frequency noise, thus enabling precise adjustment of the resonator length independent from laser power fluctuations. A drawback of this technique lies in its high complexity.

Reliable frequency stabilization with a comparatively simple experimental setup is provided by the ramp-hold-fire (RHF) technique which utilizes the Fabry-Pérot property of the slave cavity. As illustrated in Fig. 20.3, the seed radiation is coupled into the laser oscillator, e.g. via output coupler, while leakage radiation reflected from an intra-cavity polarizer is monitored by a photodiode. The latter measures an interference signal resulting from the superposition of seed radiation portions which have performed a different number of round-trips inside the slave cavity. A ramp voltage is applied to a piezo actuator attached to one of the resonator mirrors to change the cavity length. Once the resonator is in resonance with the injected wave, the photodiode signal shows a maximum due to constructive interference. At this point the ramp is stopped, holding the cavity length constant until the pump laser is triggered and the Q-switch is fired. Since the RHF procedure is carried out for each consecutive pulse, this system works on a shot-to-shot basis while offering the capability of suppressing high environmental disturbance.

20.3 Shot Noise and Squeezed States

An ideal laser with stable frequency and amplitude emits a light wave with a field amplitude whose temporal evolution at a fixed location is described by an ideal sinusoidal oscillation. Consequently, the temporal mean of the amplitude, and hence the laser intensity should be constant. However, as light can also be considered as a stream of discrete photons that are emitted at random times, the number of emitted photons per unit time varies, giving rise to intensity fluctuations. The standard deviation of the photon number ΔN which is also referred to as signal-to-noise ratio is equal to the square root of the photon number N :

$$\boxed{\Delta N = \sqrt{N}}, \frac{\Delta N}{N} = \frac{1}{\sqrt{N}}. \quad (20.6)$$

For small photon numbers, the relative deviation becomes large, whereas high signal-to-noise ratios and small relative deviations are present for large photon numbers.

When measuring the average power with a detector having a frequency bandwidth B , the detector signal shows fluctuations with a characteristic period $T = 1/(2B)$,

as can be confirmed by a Fourier transformation. Therefore, using $N = PT/hf$, one obtains

$$\Delta P = \sqrt{2 hf PB}. \quad (20.7)$$

This power fluctuation is called shot noise, as it originates from the quantized nature of light. Shot noise limits the accuracy of experiments that are based on the measurement of small power changes, e.g. for trace gas detection or in interferometric applications.

Shot noise can also be quantified by interpreting the optical power of a light beam as a random sequence of pulses represented by single photons. Spectral analysis of such a pulse yields a so-called white spectrum having a constant amplitude distribution, i.e. all the frequencies contribute with the same amplitude. The average noise level per frequency interval is then given by (20.7). Shot noise is especially pronounced at high frequencies, while the noise sources described in Sect. 20.1 dominate at low frequencies.

Squeezed States

Aside from power instabilities, shot noise also involves phase and frequency fluctuations, as illustrated in Fig. 20.4a. Due to the photon nature of light, it cannot be described by an ideal sinusoidal oscillation as mentioned above. Nevertheless, over the last three decades, it was demonstrated in various experiments that the intensity fluctuations can be significantly reduced, even below the shot noise level:

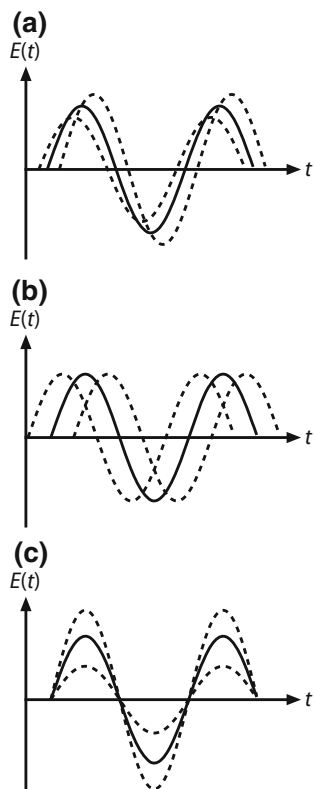
$$\Delta N < \sqrt{N}. \quad (20.8)$$

As a trade-off, the phase fluctuations $\Delta\varphi$ are increased (Fig. 20.4b). The resulting light is said to be in a “squeezed state”, referring to the representation of a quantum state in the so-called phase space. Likewise, squeezed states with reduced phase or frequency noise can be obtained at the expense of increased amplitude noise in accordance with the uncertainty principle

$$\Delta N \cdot \Delta\varphi > 1. \quad (20.9)$$

Squeezed laser light can be applied in a number of sensitive measurement techniques, since amplitude or frequency noise can be largely eliminated. Besides the improvement of optical communication technologies, squeezed light enables ultra-precise measurement of lengths for the detection of gravitational waves with large-scale interferometers (Sect. 25.6). However, as the methods for producing squeezed light are very complicated and the suppression of amplitude noise is rather low, the utilization of squeezed light is more or less limited to fundamental quantum optics research and has not yet found widespread applications.

Fig. 20.4 Electric field for three different states: **a** normal coherent state with amplitude and phase fluctuations, **b** squeezed state with stabilized amplitude. The illustrated complete amplitude stabilization has not been demonstrated yet, **c** squeezed state with stabilized phase. The average electric field is depicted as the solid line, while the dashed lines show the fluctuation ranges



20.4 Coherence

In the context of electromagnetic waves, the term coherence describes to what extent an electric field with stochastically varying amplitude and phase resembles an ideal wave with exactly defined amplitude and phase. An ideal plane or spherical wave is called coherent. The same holds for an ideal Gaussian beam emitted from a laser.

Conventional light sources and real lasers emit light waves that behave as ideal waves only in a small spatio-temporal domain. Hence, they are referred to as partially coherent. In this sense, a stabilized laser is a nearly coherent light source, whereas the light emitted from a bulb or the sun is considered incoherent. The quantitative description of (partial) coherence is based on the so-called cross-correlation function which will not be introduced here.

The coherence properties of light are especially important for applications that rely on interference effects such as holography. The superposition of coherent light leads to constructive and destructive interference producing an interference pattern. In contrast, interference is not observed when incoherent waves are superimposed, as the field intensities simply add up. For partially coherent light sources, the contrast of the interference pattern is reduced. Coherence can thus also be understood as the ability of light to exhibit interference effects.

Temporal Coherence

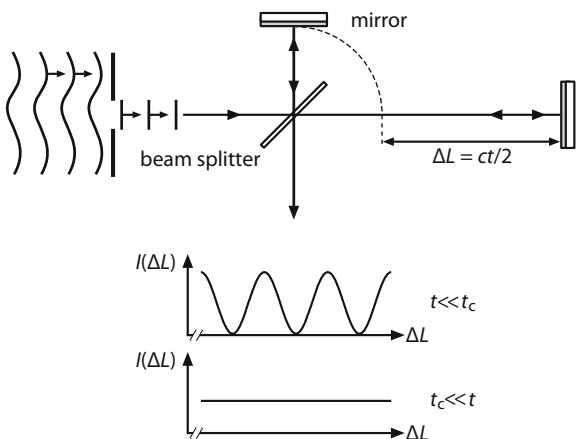
A distinction is made between spatial and temporal coherence. Quantification of the latter involves the comparison (or correlation) of the electric field of a light wave at a fixed point in space but at different times. Over short periods of time, the phase difference of the electric field between two instances is nearly constant, i.e. the phase can be predicted from one point in time to another. However, for periods longer than the so-called coherence time t_c , the phase difference shows random fluctuations. Hence, the wave is no longer correlated with a copy of itself delayed by $t > t_c$ and hence does not show interference effects when being superimposed with itself after a delay longer than the coherence time.

The coherence time of a laser can be experimentally measured using a Michelson interferometer consisting of two mirrors and a beam splitter, as depicted in Fig. 20.5. The laser beam is first separated into two portions by the beam splitter. The two partial beams are then reflected back toward the beam splitter where they are recombined at a slight angle to produce an interference pattern that is incident on a detector. The length of one interferometer arm can be adjusted to introduce a variable delay t between the two partial beams. Measurement of the time-averaged intensity of the superimposed light exiting the interferometer allows to derive the interference visibility in dependence on the delay $t = 2\Delta L/c$. In this way, the coherence time t_c is determined from the decrease in the interference contrast, i.e. the modulation depth, of the function $I(\Delta L)$, as shown on the bottom of Fig. 20.5.

The light from conventional sources originates from the spontaneous emission of photons or wave packets with a duration τ , corresponding to the lifetime of the involved energy levels. As a result, the phase varies randomly from one wave packet to the other and the coherence time is

$$t_c \approx \tau. \quad (20.10)$$

Fig. 20.5 Michelson interferometer for measuring the temporal coherence of light and the coherence time t_c . The contrast of the intensity distribution $I(\Delta L)$ in the observation plane depends on the delay t between the two partial beams produced by the beam splitter



According to Sect. 2.4, the lifetime τ is related to the spectral bandwidth Δf as follows:

$$t_c \approx 1/\Delta f. \quad (20.11)$$

Although lasers are based on stimulated emission and therefore emit waves with nearly constant amplitude, (20.11) can be used to estimate the coherence time from the spectral bandwidth. The exact mathematical relationship follows from the Wiener-Khintchine theorem and depends on the spectral shape of the laser emission.

The coherence length is the distance the light travels in the coherence time t_c :

$$l_c = ct_c \approx c/\Delta f = 132 \text{ m MHz}/\Delta f, \quad (20.12)$$

where c is the speed of light.

White light containing the whole visible spectrum has a very short coherence length of about 1 μm . Spectral lamps can feature lengths of up to 1 m, albeit at very low intensity. The coherence length of lasers ranges from sub-millimeters up to several kilometers depending on the gain medium and applied stabilization method (Table 20.1).

The coherence length l_c can be shortened by expanding the spectral bandwidth. In diode lasers, this is accomplished by fast modulation of the injection current, leading to linewidths from 1 MHz to 1 GHz. Conversely, diode lasers can be stabilized to 0.5 Hz, resulting in coherence length of thousands of kilometers according to (20.12). Free-running laser modules, e.g. at 405 nm, exhibit bandwidths on the order of 1000 GHz = 1 THz, corresponding to coherence lengths of about 130 μm . Broader linewidths are obtained with superluminescent LEDs having coherence lengths around 10 μm . Such diodes are used for optical coherence tomography (OCT) in medical applications (see Sect. 24.3) to investigate the structure of biological tissue. Irradiation of liquids, crystals or optical fibers with ultra-short pulses generates supercontinuum radiation (Sect. 19.6) with coherence lengths shorter than 1 μm .

Table 20.1 Typical coherence lengths of selected commercial lasers

Laser type	Coherence length
Diode laser without stabilization	<1 mm
Diode laser with external resonator (ECDL, Fig. 10.32)	100–1000 m
Nd:YAG laser (continuous wave)	1 cm
Microchip Nd:YAG laser	10 m
He–Ne laser without stabilization	20 cm
He–Ne laser with stabilization	1 km
Argon laser with intra-cavity etalon	1 m
Fiber laser without stabilization	50 μm
Fiber laser with stabilization	100 km

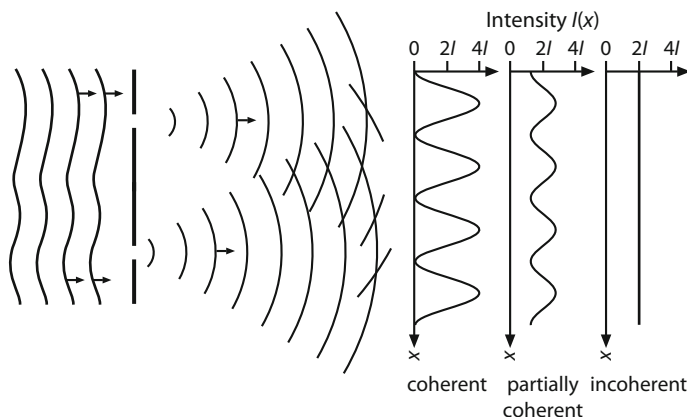


Fig. 20.6 Experimental setup for measuring the spatial coherence. An incident wave is guided through a double pinhole, defining two points at distance x . Spherical waves emanate behind the pinholes and interfere in the observation plane. The contrast of the resulting intensity distribution $I(x)$ is a measure of the degree of coherence. For incoherent light the intensity is constant ($I(x) = 2I$), corresponding to the sum of the single intensities. For coherent light $I(x)$ varies between 0 and $4I$

Spatial Coherence

In analogy to temporal coherence, spatial coherence describes the correlation of the electric field of a wave at a fixed time but different points in space. It can be assessed by means of a double-slit interferometer (Fig. 20.6) to analyze the correlation of the electric field at two different locations across the beam profile. For a perfectly spatially coherent wave, an interference pattern with maximum contrast is obtained. In case of partial coherence, the modulation depth is reduced. A laser operating in single transverse mode, e.g. the TEM_{00} mode, shows total spatial coherence, whereas multimode lasers have lower spatial coherence, as the different transverse modes have different frequencies, and thus, temporally varying phase differences.

Further Reading

1. Z. Ficek, S. Swain, *Quantum Interference and Coherence* (Springer, 2005)
2. L. Mandel, E. Wolf, *Optical Coherence and Quantum Optics* (Cambridge University Press, 1995)

Part VII

Laser Metrology and Spectroscopy

Lasers are as versatile as their application domains. Proper specification of a laser source is important to assess its performance and suitability for a particular application. After presenting relevant photometric and radiometric quantities, the measurement techniques and devices for the determination of major laser parameters are discussed in this part of the book. Aside from various types of photodetectors and cameras for measuring the output power, pulse energy, and spatial properties of a laser beam, autocorrelators are necessary for the analysis of ultra-short pulses. The spectral characteristics of a laser are quantified using different spectrometers and interferometers as well as heterodyne detection and optical frequency combs.

Chapter 21

Photodetectors



One of the most important parameters of a laser is its output power. For pulsed lasers, it is necessary to differentiate between the average output power and the peak power, so that other quantities like the pulse repetition rate, the pulse energy and the pulse duration need to be assessed to characterize the laser beam. While thermal detectors and photodiodes are used to determine these laser parameters, the spatial intensity distribution across the beam cross-section is measured using CCD or CMOS line sensors and arrays. Pulse shapes and widths less than 100 ps are evaluated by means of autocorrelators exploiting nonlinear optical effects.

21.1 Radiometric and Photometric Quantities

Electromagnetic radiation is usually measured in terms of radiometric units according to the International System of Units (SI). When a light source is characterized in terms of its perceived brightness to the human eye, photometric SI quantities are used. A comparison between the most relevant radiometric and photometric quantities which can be regarded as two parallel systems is given in Table 21.1. The lumen is defined as the amount of light that is emitted into one steradian by a point source of one candela strength ($1 \text{ lm} = 1 \text{ cd} \cdot \text{sr}$). The candela is a base SI unit, and defined as the luminous intensity of a monochromatic light source at 555 nm with a radiant intensity of $I_\Omega = 1/683 \text{ W/sr}$ (Watt/steradian). Hence, for light at this particular wavelength in the green spectral region where the human eye is most sensitive, 1 W of radiant power corresponds to a luminous flux of 683 lm.

At other wavelengths, the radiant power has to be weighted by a luminosity function that models the brightness sensitivity of the human eye, as depicted in Fig. 1.3.

The output power of continuous wave (cw) lasers can be simply measured using semiconductor diodes where the radiation produces a photocurrent that is

Table 21.1 Comparison of selected radiometric and photometric quantities

Radiometric quantity		Photometric quantity	
Name	Unit	Name	Unit
(Radiant) energy E	Joule (J)	Luminous energy Q	Lumen · s (lm · s)
Power (Radiant flux) P	Watt (W)	Luminous flux Φ	Lumen (lm)
(Radiant) intensity I_Ω	Watt/steradian (W/sr)	Luminous intensity I_v	Candela (cd = lm/sr)
Irradiance or intensity I	Watt/m ² (W/m ²)	Illuminance E_v	Lux (lx = lm/m ²)
Radiant fluence or exposure H	Joule/m ² (J/m ²)	Luminous exposure H_v	Lux · s (lx · s)

proportional to the power of the incident light due to the inner photoelectric effect. The relatively strong wavelength-dependence of the photocurrent is unfavorable and can be avoided by employing thermal detectors showing a largely wavelength-independent spectral sensitivity.

For pulsed lasers, the temporal evolution of the power $P(t)$ is recorded with fast diodes and oscilloscopes, or in case of ultra-short pulses, with a streak camera. Integrating devices are used to measure the average power P_{av} . When the pulse repetition rate f_p and pulse duration τ are known, the pulse energy E_p and pulse peak power P_p can be calculated according to (3.1) and (3.2). The pulse energy $E_p = \int P(t) dt$ is directly assessed using devices that integrate over only one pulse. The detection of weak optical powers is achieved with photomultipliers or channel plates.

21.2 Thermal Detectors

The operation principle of thermal photodetectors integrated in power and energy meters relies on the measurement of temperature changes introduced by the incident radiation. Heating of the electrical device can be caused either by single light pulses (ballistic mode) or continuous irradiation resulting in a steady-state temperature increase. The temperature measurement is carried out with thermocouples and thermopiles, temperature-sensitive resistors (bolometer) or by exploiting the pyroelectric effect.

Thermocouples and Thermopiles

The principle setup of a thermocouple for the measurement of laser pulse energies is shown in Fig. 21.1. It consists of two dissimilar electrical conductors, e.g. wires of different materials, that form electrical junctions. Light is incident on a sample cone

Fig. 21.1 Schematic of a thermocouple for measuring the energy of laser pulses

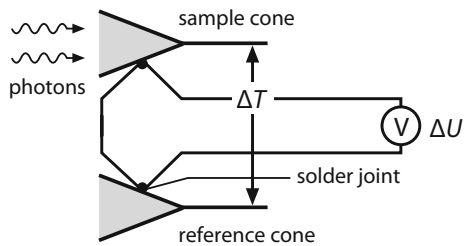
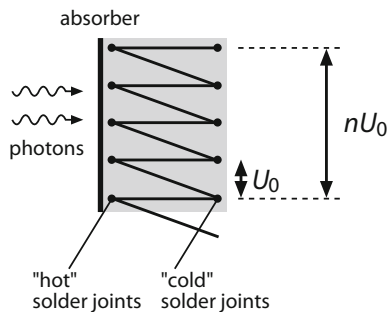


Fig. 21.2 Schematic of a thermopile for measuring the laser output power. U_0 —thermo voltage, n —number of thermocouples



where it is absorbed after multiple reflections, while a reference cone measures the background radiation.

The temperature increase at the sample cone leads to a temperature difference ΔT between the two different solder joints which scales with the incident pulse energy E_p . Due to the so-called Seebeck effect, the temperature gradient ΔT is converted into a voltage $\Delta U = S \cdot \Delta T$. The thermoelectric power (or Seebeck coefficient) S depends on the material (or alloy) combination, e.g. iron-constantan or chromel-alumel, and is on the order of $S \approx 10^{-5}$ V/K.

Measurement of the laser average output power is carried out with a thermopile laser sensor. As illustrated in Fig. 21.2, it consists of several sequentially connected thermopiles with one junction being exposed to an absorber ("hot" junction) and the other junction at lower temperature acting as a reference ("cold" junction). The latter is sometimes attached to a heat sink. High sensitivity is obtained by using an absorber material with low heat capacity.

The voltage produced by the temperature gradient between the hot and cold junction in each thermocouple is directly proportional to the power of the incoming radiation. Due to the large number of thermopiles, voltages of a few μ V to V are reached. In this way, laser powers ranging from a few μ W to several W can be measured. Depending on the thickness of the absorption layer, thermopile sensors can be classified into surface absorbers (up to 100 μ m) for cw or long-pulse lasers and volume absorbers (mm thickness) for short intense pulse lasers. Unlike photodiodes, thermopile sensors can be used for a broad spectrum of wavelengths from the ultraviolet to the mid-infrared spectral region.

Pyroelectric Detectors

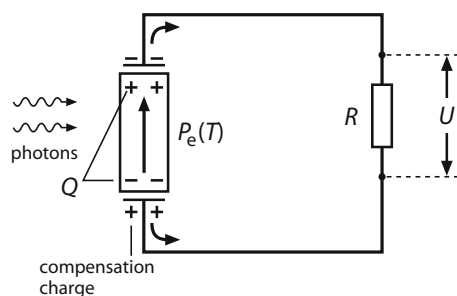
Pyroelectric detectors, as schematically depicted in Fig. 21.3, are made from materials that exhibit spontaneous polarization, i.e. dielectric polarization which occurs due to internal processes even in the absence of an external electric field. Examples are (deuterated lanthanum α -alanine doped) triglycine sulfate (DLa-TGS), barium titanate (BaTiO_3) or lithium tantalate (LiTaO_3). At a constant temperature, the polarization P_e causes effective surface charges $Q = P_e \cdot A$ in the pyroelectric crystal (area A). The surface charges are neutralized by mobile charge carriers. When the temperature T of the crystal changes upon the absorption of light, the spontaneous polarization and thus the effective surface charge are altered. Hence, the original charges are no longer neutralized, leading to a voltage across the resistor with resistance R according to

$$U(t) = R \frac{dQ}{dt} = AR \frac{dP_e}{dT} \frac{dT}{dt}. \quad (21.1)$$

Consequently, as opposed to thermoelectric devices where a permanent voltage is generated as a result of a temperature gradient within the material, pyroelectricity involves the creation of a temporary voltage due to a temporal temperature change in the medium. The quantity dP_e/dT is a material-specific parameter.

Pyroelectric detectors are primarily used for measuring the pulse energy or the average power of pulsed lasers, particularly in the infrared spectral region. They are also becoming more and more attractive for the emerging field of THz (Terahertz) radiation. Commercial devices are capable of detecting light pulse energies even below 1 μJ . Pyroelectric sensors show higher photo sensitivity and better temporal resolution than thermocouples and thermopiles which are, however, simpler in design and more robust. The latter have typical rise times of 10^{-5} s, compared to 10^{-9} s of pyroelectric detectors. In general, thermal detectors have the advantage that the spectral sensitivity is largely constant over a wide range of wavelengths. Hence, they are mainly employed for the quantification of absolute radiant powers and energies. Their major drawbacks are a relatively low sensitivity and slow response compared to photoresistors and photodiodes (Sect. 21.4).

Fig. 21.3 Principle of a pyroelectric detector



21.3 Vacuum Photodetectors

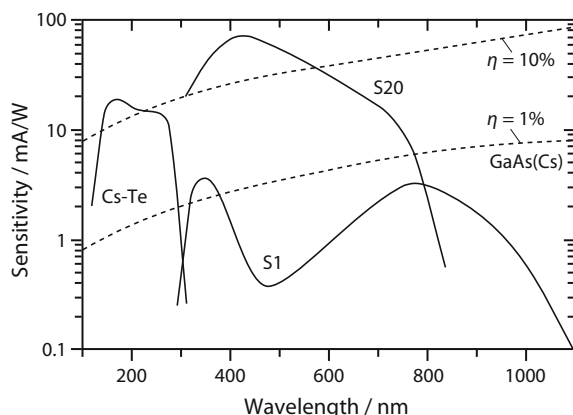
Vacuum tube diodes, photomultipliers, image converters and streak cameras rely on the outer photoelectric effect, i.e. the emission of so-called photoelectrons from an irradiated material (photocathode) into vacuum. The number of electrons ejected per incident photon is referred to as quantum efficiency η . The spectral sensitivity is then given by $\eta e/hf$, with e denoting the electron charge and hf being the photon energy. Quantum efficiency and spectral sensitivity are strongly material- and wavelength-dependent (see Fig. 21.4).

Materials used as photocathodes are sometimes designated with an internationally agreed S number, e.g. S1 or S20, as specified by the Electronic Industries Association. In other cases, the material composition is given, e.g. GaAs(Cs). The latter is characterized by a flat sensitivity curve. The specification of the sensitivity often depends on the window material onto which the cathode is deposited. The photoelectric effect requires a minimum photon energy or, respectively, threshold frequency to emit electrons from the cathode. Since the minimum energy (often referred to as work function) is on the order of a few eV, the application of vacuum detectors is limited to the near-infrared, visible and ultraviolet spectral region where the photon energy is sufficient.

Vacuum Tubes

The simplest device based on the photoelectric effect is the vacuum tube diode whose electrical circuit is shown in Fig. 21.5. Here, the photoelectrons liberated from the cathode are accelerated towards an anode producing a photocurrent. Vacuum tubes diodes feature rise times of about 100 ps and photocurrents of up to several amperes over short periods. By adding one or more control grids within the

Fig. 21.4 Spectral sensitivity of selected photocathodes (e.g. employed as vacuum photodiodes or photomultipliers)



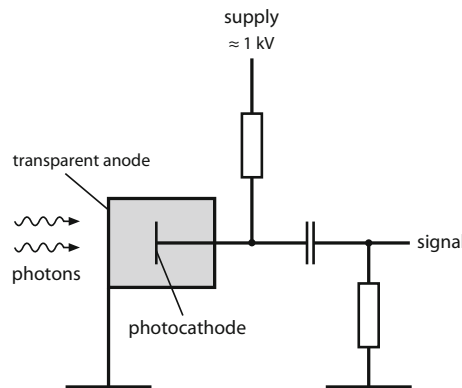


Fig. 21.5 Electrical circuit of a vacuum photodiode

vacuum tube, the current between the cathode and anode can be controlled which allows for amplification, rectification, switching and oscillation of the signal.

Photomultipliers

Photomultipliers (PMTs) offer much higher sensitivity compared to vacuum tubes, as the photocurrent produced by the incoming light is multiplied by as much as 100 million times through the generation of secondary electrons. This is accomplished in multiple dynode stages, as depicted in Fig. 21.6. A photoelectron is accelerated by an electric field between the photocathode and the first dynode, where it knocks out multiple secondary electrons. Those electrons are subsequently accelerated to a second dynode where each electron knocks out additional electrons. Repetition of this acceleration and multiple electron emission process on about 10–20 dynodes yields gain factors of up to 10^8 . The avalanche process is very fast, so that the rise

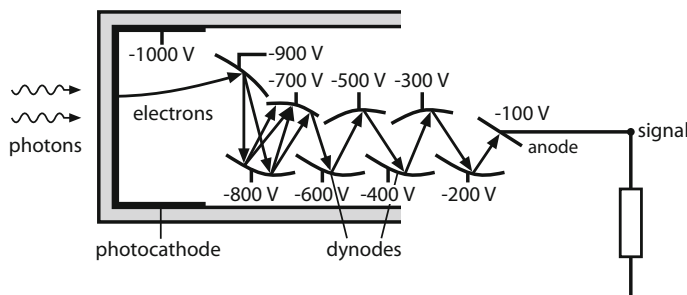


Fig. 21.6 Schematic of a photomultiplier

times are in the ns-regime. The combination of high gain, large bandwidth and low noise is unsurpassed by any detection system and allows single photon counting.

There are also avalanche photodiodes exhibiting a similar amplification mechanism, however occurring in a semiconductor material rather than in a vacuum tube (see Sect. 21.4). An array containing many avalanche diodes is referred to as silicon photomultiplier.

Microchannel Plates

A much more compact design of a secondary electron multiplier is provided by a microchannel plate (MCP). It is formed by a specially fabricated thin plate (1 mm) which contains a multitude of independent small-diameter glass capillaries (channels) each working as an independent electron multiplier. The inner wall of the channels (inner diameter 10–30 μm) is coated with a material having a high secondary emission coefficient, while a voltage of about 1 kV is applied across both ends of the plate. An electron entering a channel ejects several secondary electrons from the channel wall which are accelerated by the electric field along the channel. Like in a photomultiplier, more and more secondary electrons are produced by subsequent collisions with the walls, resulting in millions of electrons emerging from the rear of the plate.

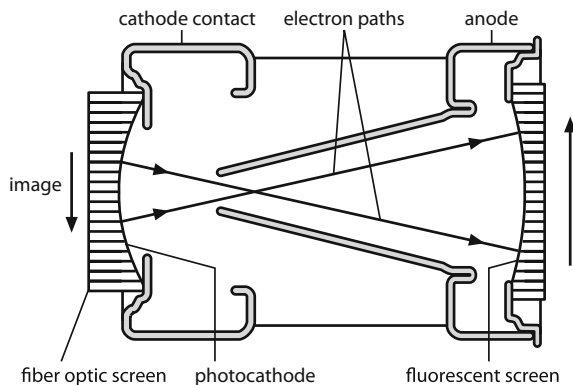
MCPs offer a combination of favorable properties like high gain and high spatial and temporal resolution. Furthermore, the assembly of numerous individual microchannels allows to increase the electron current density incident on the front surface, while preserving its spatial pattern at the rear of the plate. Hence, such devices can be used in a large variety of applications including imaging spectroscopy and microscopy.

Image Converter

Image converters are employed to transform a given light intensity distribution from one spectral range (e.g. infrared) to another (e.g. visible). In this way, the transverse beam profile of an infrared laser can be conveniently observed by the naked eye. For this purpose, the beam is projected onto a photocathode screen to liberate electrons whose number is proportional to the incident light intensity at the corresponding position on the screen. The electrons are accelerated towards a fluorescent screen under the action of an intense electric field between the cathode and a conical anode (Fig. 21.7). When hitting the rear screen, the electrons, in turn, cause the emission of photons, thus displaying the transverse intensity distribution of the laser beam.

The conversion can be combined with an intensification of the image using a microchannel plate which increases the number of electrons before re-converting

Fig. 21.7 Schematic of an image converter



them into photons. Hence, the image on the fluorescent screen is brighter than the original image. In laser technology, image converter tubes are, for instance, used in infrared scopes for aligning beam paths of infrared lasers at up to 1500 nm wavelength.

Streak Camera

The temporal intensity variation of ultra-short laser pulses can be measured with a streak camera whose principle design is illustrated in Fig. 21.8. An incoming pulse hits a photocathode within a vacuum tube and generates electrons that are accelerated by a high voltage, forming a pulsed electron beam. The beam intensity scales approximately linearly with the optical intensity and is increased by means of an MCP before the electron beam falls on a fluorescent screen. The photocathode is illuminated through an entrance slit leading to a slit image on the screen. While traveling towards the MCP, the electron beam is rapidly deflected by a pair of electrodes perpendicular to the slit axis, to which a fast ramp voltage is applied. As a result, the spatial intensity distribution of the slit image on the screen (streak image) reflects the temporal evolution of the optical power in the light pulse. Precise triggering of the deflection mechanism is required so that the ramp voltage is applied just before the light pulse hits the photocathode.

Since the detection and deflection systems are integrated in one device, streak cameras offer a much higher temporal resolution (<200 fs) compared to the combination of photodetector and oscilloscope. Shorter pulses are resolved using autocorrelators and FROGs (Sect. 21.5). Instead of illuminating the slit with a spatially constant intensity (single-channel mode), a streak camera can also be operated in the so-called multi-channel mode where the incident light distribution varies along one direction, e.g. representing a spectrum. The streak image then reveals the temporal evolution of a one-dimensional intensity field. In 2011, researchers from the Massachusetts Institute of Technology used a streak camera in

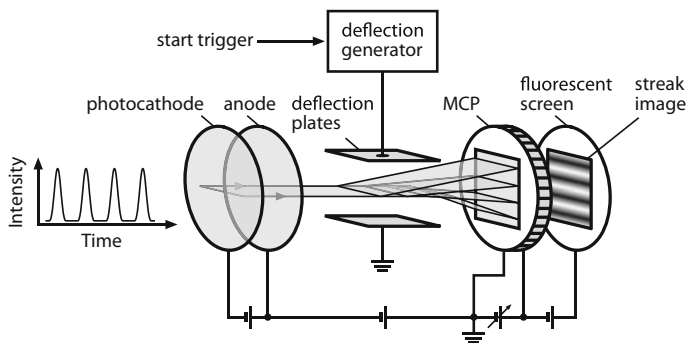


Fig. 21.8 Schematic of a streak camera (MCP- microchannel plate)

combination with repeated femtosecond laser pulses to visualize the propagation of light with a frame rate of 10^{12} frames per second. This technology is referred to as femto-photography.

21.4 Semiconductor Detectors

Light detection using semiconductor materials mostly relies on the inner photoelectric effect which generates mobile charge carriers through electromagnetic radiation. When the energy of an absorbed photon is equal to or greater than the band gap of the material, an electron is lifted from the valence band to the conduction band, thereby creating a mobile electron and a positively charged mobile hole. The produced electrons are detected by a variety of electronic devices which are increasingly used instead of thermal and vacuum photodetectors.

Photoresistors

Light irradiated onto a homogeneously doped semiconductor generates mobile charge carriers. Thus, the resistance of the material is reduced which can be exploited for light detection. While the resistance of a photoresistor is typically on the order of several megaohms in the dark, it can be as low as a few hundred ohms when the photoresistor is exposed to light. The spectral sensitivity of such photoresistors is determined by the band gap or energy spacing of the donor and acceptor energy levels, respectively (see Sect. 1.6). The wavelength of maximum sensitivity is 0.5 μm for cadmium sulfate (CdS), 2.5 μm for lead sulfate (PbS), 6 μm for indium antimonide (InSb) and 20 μm for copper-doped germanium (Cu:Ge). Hence, photoresistors are primarily used for the detection of infrared light. In most cases, cooling is required to prevent thermal generation of carriers and thus

ensure a low dark current (current generated in the absence of light). The temporal resolution is often very low, but can reach 10^{-10} s with special designs.

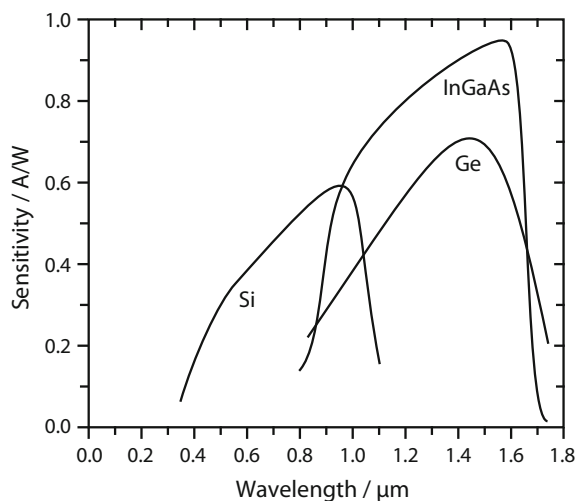
Photodiodes

Good spectral sensitivity in the visible and near-infrared spectral region is obtained with photodiodes (Fig. 21.9). Typical materials are silicon for the range between 350 and 1100 nm, germanium (from 800 to 1800 nm) and InGaAs (from 800 to 1700 nm or even 2500 nm).

A photodiode is simply fabricated by a p-n junction in reverse-bias, i.e. the p-type region is connected to the negative terminal and the n-type region is connected to the positive terminal of the power supply. When a photon of sufficient energy is absorbed in the junction's depletion region, an electron-hole pair is created. The charge carriers are swept away from the junction by the electric field in the depletion region. While the electrons move towards the n-type region, the holes move towards the p-type region, thus producing a photocurrent. The dark current of photodiodes is significantly lower compared to homogeneous photoresistors.

In case of low penetration depth of the light into the semiconducting material, the depletion layer, and hence the volume where electron–hole pairs are generated, can be extended by inserting an undoped (intrinsic) region between the p- and n-doped region. This structure is called PIN photodiode (see Fig. 21.10). The intrinsic region is flooded with charge carriers from the adjacent highly-doped regions. Due to this high-level injection, the electric field extends deeply into the intrinsic region, which accelerates the transport of charge carriers between the p-type and the n-type region, resulting in faster response of the diode. For instance,

Fig. 21.9 Spectral sensitivity of a silicon, germanium and InGaAs photodiode



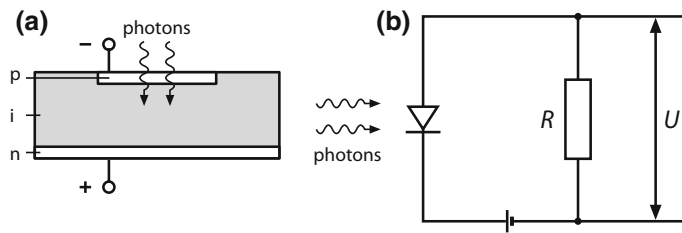


Fig. 21.10 Schematic (left) and electrical circuit (right) of a PIN photodiode

a silicon PIN diode with an intrinsic layer of $700\text{ }\mu\text{m}$ thickness allows for light detection at wavelengths up to $1.1\text{ }\mu\text{m}$.

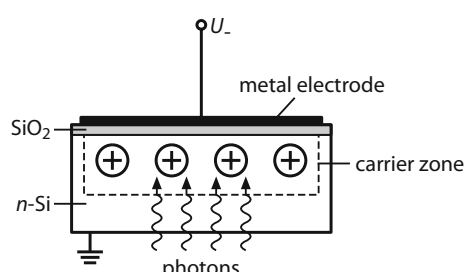
In avalanche photodiodes (APDs), the structure is optimized for operating with high reverse-bias, approaching the reverse breakdown voltage. As a result, in analogy to a photomultiplier tube, each created carrier is multiplied by avalanche breakdown caused by carrier impact ionization, leading to internal gain within the photodiode. The higher the reverse voltage, the higher the gain. APDs offer high effective responsivity (ratio between generated photocurrent and incident optical power) and are therefore well-suited for long-range optical fiber communication, range finding and imaging. They are also increasingly applied in high-speed laser scanners and laser microscopes.

Photodiode arrays (PDAs) consist of multiple equally spaced diodes of the same size forming a linear arrangement with a pixel size of e.g. $25\text{ }\mu\text{m} \times 2500\text{ }\mu\text{m}$. The single diodes are subsequently read out. PDAs are employed in a wide range of applications such as laser beam position detection or spectrophotometry where the pixel size is adapted to the dimensions of the spectrometer slit.

CCD and CMOS Sensors

A charge-coupled device (CCD) is a microelectronic system that serves as a one- or two-dimensional photodetector. It consists of an array of individual, closely spaced pixels represented by metal-oxide-semiconductors (MOS) capacitors. The structure

Fig. 21.11 Schematic of a single silicon n-type MOS capacitor. Positive charge carriers are produced close to the semiconductor-oxide interface through the photoelectric effect



of an n-type MOS (or nMOS) capacitor is shown in Fig. 21.11. It is obtained by growing a layer of silicon dioxide (SiO_2) on top of a silicon substrate and depositing a layer of metal or polycrystalline silicon. Since SiO_2 is a dielectric material, the MOS structure is equivalent to a planar capacitor, with one of the electrodes replaced by a semiconductor.

Before the single pixels are exposed to light, the MOS capacitors are forced into depletion. For this purpose, a negative voltage is applied to the metal electrode, so that the majority charge carriers, in case of an nMOS capacitor the electrons, are swept away from the semiconductor-oxide interface, creating a depletion layer of immobile, positively charged donor ions. The depth of this layer is then reduced by the generation of electron-hole pairs through the photoelectric effect. In contrast to a photodiode where the carriers produce a photocurrent, the electrons drift deep into the substrate due to the applied voltage, while the holes accumulate in a carrier zone at the interface (see Fig. 21.11). In this way, the optical information is stored as electrical charge in the MOS capacitor. Ideally, the charge is proportional to the intensity of the light incident on the individual pixels.

In one-dimensional CCD arrays, as used in line-scan cameras, the MOS capacitors are linearly arranged, whereas a two-dimensional array, e.g. in digital or video cameras, captures a 2D image corresponding to the scene projected onto the focal plane of the sensor. For the read-out of the optical information, a control circuit acts as a shift register and causes each capacitor in the array to transfer its charge packets to its neighbor, as depicted in Fig. 21.12. The charge is finally dumped into a charge amplifier where it is converted into a voltage. Repeating this process creates a digitizable signal that is stored in memory to create an image.

The MOS capacitor has a typical dimension of $10 \times 10 \mu\text{m}$, the semiconductor is a few tenths of a mm thick, while the thickness of the oxide layer is only $0.1 \mu\text{m}$. A common chip integrated in a video camera consists of 2048×2048 pixels, corresponding to a chip size of a few cm. For some applications, e.g. in optical

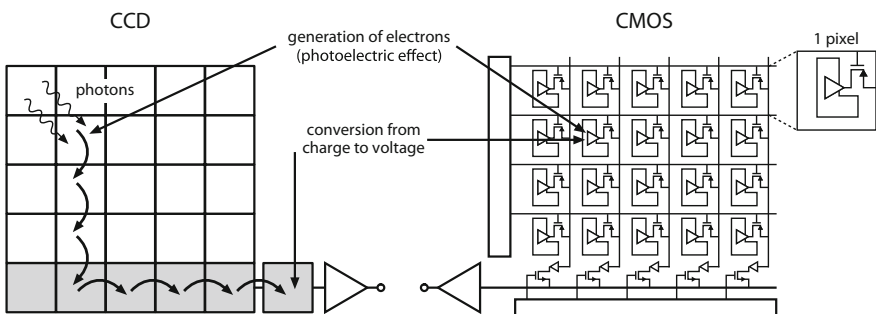


Fig. 21.12 In a charge-coupled device (CCD) (left), the charge generated by photons is transferred between neighboring capacitors to a charge amplifier where it is converted into a voltage. In contrast, in a CMOS sensor (right), the voltage is read out in every single pixel individually. The CMOS sensor contains pixels with an amplifier circuit

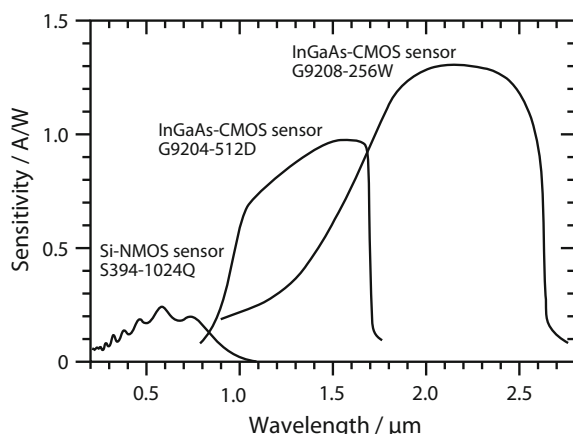
multichannel analyzers, it is beneficial to combine the charges from multiple adjacent pixels (pixel binning). This offers faster read-out speeds and improved signal-to-noise ratios at the expense of reduced spatial resolution.

The spectral sensitivity of CCD sensors is determined by the band gap energy of the semiconductor material and the transparency range of the layer materials. Figure 21.13 shows the spectral sensitivity of a silicon-based n-type MOS CCD sensor together with two different CMOS sensors discussed below. In the region of maximum sensitivity (600–800 nm), the quantum efficiency of a Si CCD is about 50%, the detection limit is on the order of 4 fJ/cm^2 and the saturation limit is 250 pJ/cm^2 . This corresponds to a dynamic range of 16 bit. The signal-to-noise limit is around 900:1. As the dark current increases with temperature, cooling of the sensor using a Peltier element or liquid nitrogen improves its performance.

Apart from the operation principle described above, there are other variants of CCD detectors. For instance, a p-doped silicon substrate can be used in combination with a positive bias applied to the metal electrode (n-channel CCD). In this case, the optical information is stored as electrons instead of holes, providing higher read-out speeds. In a buried-channel CCD, the charge carriers are not stored directly at the semiconductor-oxide interface, but deeper in the material, thus reducing the probability for the recombination of stored charge carriers. Enhancement of the sensitivity is achieved by optically connecting a CCD with a microchannel plate. In 2009, the invention of the CCD concept by George E. Smith and Willard Boyle was awarded with the Nobel Prize in Physics.

The serial transfer of charges from one pixel to another in a CCD detector requires external clocks and drivers which increase the size and power consumption of the device. Moreover, the leakage of charges into adjacent pixels (blooming) may occur, especially at high light intensities. These limitations are overcome in active pixel sensors where each pixel incorporates a photodetector and active amplifier, hence combining the sensing function and image processing function within the same integrated circuit (see Fig. 21.12). From the many types of

Fig. 21.13 Spectral sensitivity of different Si-NMOS and InGaAs-CMOS sensors (data taken from Hamamatsu datasheet)



integrated circuit active pixel sensors, the complementary metal-oxide-semiconductor (CMOS) sensors are most common and also widely used in cell phone and web cameras. Using CMOS technology, the fabrication of complete cameras on a single chip is possible and typically less expensive than the production of a CCD sensor. Moreover, the image processing is more flexible since arbitrary sections of the image can be read out individually. However, as the active circuitry in CMOS pixels covers some area on the surface, the fill factor, i.e. the ratio of light sensitive area versus total area, is reduced. This problem is mitigated in back-illuminated sensors.

21.5 Autocorrelation and FROG

Ultra-short laser pulses with durations of only a few femtoseconds (10^{-15} s) are too short to be resolved by means of a photodiode or streak camera. In order to gain information on the temporal evolution of an ultra-short laser pulse, it can be sampled by a second identical pulse. This technique is known as autocorrelation. The principle configuration of an autocorrelator is shown in Fig. 21.14.

The pulse $I(t)$ to be measured is first divided into two identical copies by a beam splitter. The relative timing of the two pulses is mechanically adjusted via a variable delay stage. The pulses are then focused into a nonlinear medium, e.g. a second harmonic generation crystal. Provided that the pulses have temporal overlap, sum-frequency generation (Sect. 19.2) occurs in the crystal, generating light at a shorter wavelength. The intensity of the sum-frequency (or autocorrelation) signal $A(\tau)$ is a function of the delay τ between the two pulses and can be measured using a slow detector, e.g. a photodiode. The autocorrelation function is given by

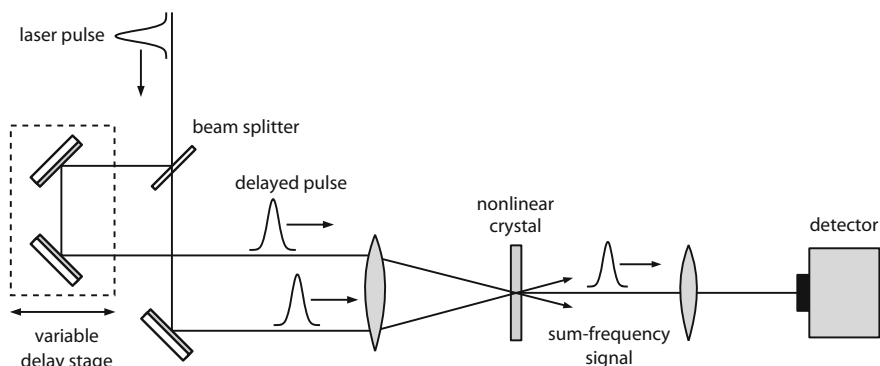


Fig. 21.14 Configuration of an autocorrelator for measuring the duration of ultra-short laser pulses. The superposition of two time-delayed versions of the same pulse in a nonlinear crystal generates a sum-frequency signal whose intensity depends on the time delay

$$A(\tau) = \int_{-\infty}^{+\infty} I(t)I(t - \tau)dt. \quad (21.2)$$

For a Gaussian pulse with pulse width Δt_p (full-width at half maximum, FWHM)

$$I(t) \sim \exp \left[-\left(\frac{2\sqrt{\ln 2}t}{\Delta t_p} \right)^2 \right], \quad (21.3)$$

the autocorrelation function also has a Gaussian shape:

$$A(\tau) \sim \exp \left[-\left(\frac{2\sqrt{\ln 2}\tau}{\Delta t_A} \right)^2 \right], \quad (21.4)$$

while the autocorrelation width Δt_A is broader by a factor of $\sqrt{2}$:

$$\Delta t_A = \sqrt{2} \cdot \Delta t_p. \quad (21.5)$$

For a Lorentzian pulse shape, the width of the autocorrelation function is twice the pulse width. The ratio of the autocorrelation width and the pulse width is sometimes called the deconvolution factor. Since the factor depends on the pulse shape, the latter has to be known or assumed in order to determine the pulse duration.

Hence, autocorrelation only estimates the duration of an optical pulse, as it does not provide information on its shape or the spectral distribution. Complete characterization of a laser pulse requires knowledge about both the intensity and the phase of the pulse. This is accomplished by using frequency-resolved optical gating (FROG). Here, the autocorrelation signal is spectrally resolved by replacing the photodetector of an autocorrelator with a spectrometer. A FROG measurement thus involves recording a multitude of spectra for different delays between the two pulses, producing a two-dimensional signal in the time-frequency domain. Using an iterative algorithm, the full time-dependent electric field can be retrieved from this FROG trace. Hence, the exact pulse duration as well as the chirp of the pulse can be derived.

Further Reading

1. G. Gagliardi, H.P. Loock (eds.), *Cavity-Enhanced Spectroscopy and Sensing* (Springer, 2014)
2. R. Trebino, *Frequency-Resolved Optical Gating* (Springer, 2012)
3. P. Seitz, A.J.P. Theuwissen (eds.), *Single-Photon Imaging* (Springer, 2011)
4. K.E. Peiponen, R. Myllylä, A.V. Priezzhev, *Optical Measurement Techniques* (Springer, 2009)

5. H.H. Schneider, H.C. Liu, *Quantum Well Infrared Photodetectors* (Springer, 2007)
6. J.C. Diels, W. Rudolph, *Ultrashort Laser Pulse Phenomena* (Academic Press, 2006)
7. R.H. Kingston, *Optical Sources, Detectors, and Systems* (Academic Press, 1995)
8. R.H. Kingston, *Detection of Optical and Infrared Radiation* (Springer, 1978)

Chapter 22

Spectrometers and Interferometers



The most common devices for the spectral dispersion of light are prism and grating spectrometers as well as diverse types of interferometers such as Fabry-Pérot, Fizeau or Michelson interferometers. Spectrometric instruments are characterized in terms of their linear dispersion and spectral resolving power. The linear dispersion is a measure of the spatial separation between two spectral lines at the image plane of the detector (unit: nm/mm). The spectral resolving power $\lambda/\Delta\lambda$ describes the instrument's ability to distinguish between two spectral lines separated by a small wavelength difference $\Delta\lambda$ at a wavelength of λ . Precise determination of optical frequencies is also achieved with optical heterodyne detection and frequency combs.

22.1 Prism Spectrometers

Light dispersion in a prism (Sect. 18.3) is caused by the fact that different wavelengths experience different refraction in the prism material and therefore propagate at different speeds. Moreover, since the angle of refraction at the surfaces depends on the refractive index according to Snell's law (14.2), each wavelength bends at a different angle when entering and leaving the prism. As the refractive index decreases with increasing wavelength (in normally dispersive media), blue light is bent more than red light, as illustrated in Fig. 18.5.

This principle is utilized in a prism spectrometer where a narrow entrance slit is illuminated with the light to be spectrally analyzed (Fig. 22.1). The slit is placed in the focal plane of a lens or a concave mirror, so that a nearly collimated beam is incident on the prism. When passing through a prism with a highly-reflective coating on the back, the light is refracted twice, whereby the angle of refraction depends on its wavelength. The light is then focused by a second lens or mirror to produce an image of the entrance slit. This results in a number of thin spectral lines, each being observable at a different angle.

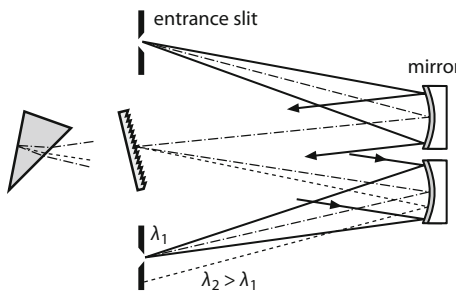


Fig. 22.1 Principle of a prism and grating spectrometer

Table 22.1 Parameters of different spectrometric instruments at a wavelength around 500 nm

Instrument	Order m	Number of interfering beams N	Spectral resolving power $\lambda/\Delta\lambda$
<i>Prism spectrometer</i>			
$dn/d\lambda = 1730 \text{ cm}^{-1}$, base $t = 10 \text{ cm}$	–	–	17,300
<i>Grating spectrometer</i>			
16.5 mm, 600 grooves/mm	3	100,000	300,000
<i>Fabry-Pérot interferometer</i>			
$R = 95\%$, 1 cm thick	40,000	60	2,400,000
$R = 95\%$, 10 cm thick	40,000	60	24,000,000

Prism spectrometers are relatively easy to construct; however, the spectral resolving power $\lambda/\Delta\lambda$ is only on the order of 10^4 – 10^5 , as it is limited by diffraction. Due to its finite size, the prism acts as an aperture clipping the incoming light beam. Hence, diffraction causes divergence even in a parallelized and monochromatic beam which limits the spectral resolving power. The latter depends on the length of the base t and the dispersion of the prism material:

$$\boxed{\lambda/\Delta\lambda = t dn/d\lambda.} \quad (22.1)$$

Heavy crown glass has a dispersion of $dn/d\lambda = 530 \text{ cm}^{-1}$, while light and heavy flint glass show values around 960 and 1730 cm^{-1} , respectively. Thus, a prism made of heavy flint glass with a base length of $t = 10 \text{ cm}$ features a spectral resolving power of $\lambda/\Delta\lambda = 17,300$ (see Table 22.1). Increasing the resolving power is challenging because of the practical limitation on the size of prism. Another disadvantage is the nonlinear dispersion function which depends on the prism material. Consequently, for a quantitative spectral analysis, the prism spectrometer has to be calibrated by reference to various known wavelengths.

22.2 Grating Spectrometers

In a grating spectrometer, the prism is replaced by a diffraction grating, while the principle setup shown in Fig. 22.1 remains the same. The physical basics of diffraction are elaborated in Sect. 18.4. The relationship between the wavelength λ of a light beam that is normally incident on a grating and the deflection angle α is given by

$$2d \sin \alpha = m\lambda, \quad (22.2)$$

with $m = 0, 1, 2, 3, \dots$ enumerating the multiple diffraction orders. The grating constant d is typically on the order of a few μm . As discussed in Sect. 18.4, the resolving power of a grating scales with the grating order and the number of illuminated grating grooves N :

$$\lambda/\Delta\lambda \approx N \cdot m. \quad (22.3)$$

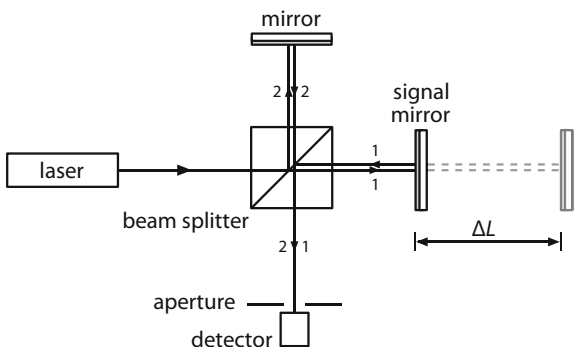
In case of small grating constants, the grating order is limited to $m \approx 3$, while the number of illuminated grooves is usually around $N \approx 10^5$, leading to a resolving power of 300,000 (Table 22.1). Typical values for $\lambda/\Delta\lambda$ lie between 10^5 and 10^6 . If the grating constant is known, a grating spectrometer allows measuring the absolute wavelength of a light source.

Ruled diffraction gratings are manufactured by physically forming grooves into a reflective surface utilizing a fine diamond tool. In contrast, holographic gratings are produced by exposing a polished and photoresist-coated substrate to an interference pattern formed by two laser beams from the same laser (photolithography). Both fabrication techniques involve a replication process where a highly accurate master grating is copied many times, thus facilitating the mass production. This copying process has led to a wide distribution of gratings in general and grating spectrometers in particular. Apart from the cheaper price and higher resolving power, gratings are easier to calibrate compared to prisms due to their linear dispersion function.

22.3 Double Beam Interferometers

Spectral analysis of light can also be performed using different types of interferometers. In a double beam interferometer, the light to be analyzed is separated into two portions by a beam splitter. The partial beams are then reflected back to the beam splitter by two mirrors where they are recombined and superimposed, producing an interference pattern that is imaged onto a photodetector. Constructive interference and thus maximum intensity of the detected signal occurs if the optical path difference $2\Delta L$ between the two beams is equal to an integer multiple of the wavelength $k\lambda$. By scanning the length of one interferometer arm, e.g. by moving

Fig. 22.2 Michelson interferometer for measuring wavelengths, distances and coherence lengths. The two mirrors are often slightly tilted so that an interference pattern consisting e.g. of parallel fringes appears on the screen. The fringes move when ΔL changes



one of the two mirrors, separation of wavelengths is achieved. Moreover, the absolute wavelength of a light source can be retrieved. Among the various designs of double beam interferometers, the configuration according to Michelson (Figs. 22.2 and 20.5) is most common.

Michelson interferometers are also used for measuring small lengths. Here, the change in the length of one of the two interferometer arms ΔL introduces a phase shift between the two partial beams. Consequently, the interference pattern which is imaged on an aperture in front of the detector is altered, resulting in an intensity modulation of the detected signal. As the pattern crosses the plane of the aperture, the number of intensity maxima (fringes) k registered by the detector are counted which allows determining the length change according to

$$\Delta L = k \frac{\lambda}{2}. \quad (22.4)$$

Due to the generally long coherence length of laser light, this technique can be used to measure lengths from dozens of meters down to fractions of the laser wavelength. Since interference only occurs for relative mirror displacements ΔL that are smaller than the coherence length, the latter can be quantified using a Michelson interferometer (see Sect. 20.4). Although much more sophisticated, the principle design of the two installations of the Laser Interferometer Gravitational-Wave Observatory (LIGO) used for gravitational wave detection is based on Michelson interferometers. As discussed in Sect. 25.6, LIGO is capable of measuring relative length changes as small as 10^{-21} .

Fourier Transform Spectrometer

Measuring the signal intensity as a function of the time delay between the two beams in a Michelson interferometer yields an interferogram in the time-domain. In case of a narrowband light source, the signal is a simple sinusoidal oscillation, whereas a complicated superposition of many different oscillations is obtained when a

broadband source is coupled into the interferometer. Using a Fourier transformation, the actual spectrum in the frequency domain is retrieved. This method is called Fourier transform spectroscopy and is primarily applied in the infrared spectral region where it is referred to as Fourier transform infrared (FTIR) spectroscopy.

Fourier transform spectrometers offer several significant advantages over prism and grating, i.e. dispersive, spectrometers. Most importantly, they provide higher signal-to-noise ratios (SNRs), since all wavelengths are simultaneously detected for each delay setting between the partial beams. Moreover, interferometers do not require the incoming light to pass through a narrow entrance slit in order to achieve high spectral resolution. The improvement in the SNR, which is known as Fellgett's advantage, is offset if the detector noise is dominated by shot noise (Sect. 20.3), as it is usually the case in photomultiplier tubes. For this reason, Fourier transform spectroscopy is not well-suited for analyzing UV or visible light.

22.4 Fabry-Pérot and Fizeau Interferometers

Fabry-Pérot interferometers (FPIs) have a simpler design than double beam interferometers. They are formed by two parallel, partially transmitting mirrors spaced by a distance d of typically several millimeters to centimeters. (see also Sect. 18.5). A light beam passing through the FPI is multiply-reflected between the two mirrors to produce many transmitted partial waves. If the optical path difference is an integer multiple m of the light wavelength λ , constructive interference occurs, resulting in a transmission peak in the signal detected behind the FPI:

$$m\lambda = 2d\sqrt{n^2 - \sin^2\alpha} = 2nd \cos\beta \quad \text{with } m = 1, 2, 3, \dots \quad (22.5)$$

Here, n is the refractive index of the medium filling the gap between the two mirrors, α is the angle of incidence measured outside the interferometer and β denotes the corresponding angle measured between the mirrors.

For a fixed mirror spacing, light of different wavelength is transmitted under different incidence angles. Such a device is equivalent to a Fabry-Pérot etalon as described in Sect. 18.5. A spectrum is obtained by illuminating the FPI with slightly divergent light. The divergence angle can be adjusted using a configuration according to Fig. 22.3. It incorporates a lens system L_1, L_2 which also acts as a beam expander. Light passing through the interferometer is collected by a third lens L_3 and focused onto screen. The resulting interference pattern is a set of concentric rings (fringes). In case of a single-frequency laser, the pattern is characterized by a small number of fringes, as shown in Fig. 22.4a, whereas multimode laser output manifests in a multitude of rings (Fig. 22.4b, c).

The spacing between adjacent FPI interference orders, i.e. equivalent sets of rings, is called free spectral range (FSR) and is determined by the mirror spacing d and refractive index n of the medium between the mirrors according to (18.12). The

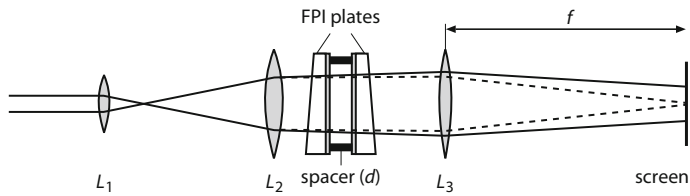


Fig. 22.3 Fabry-Pérot interferometer. The solid and dashed lines indicate ring patterns of different order k

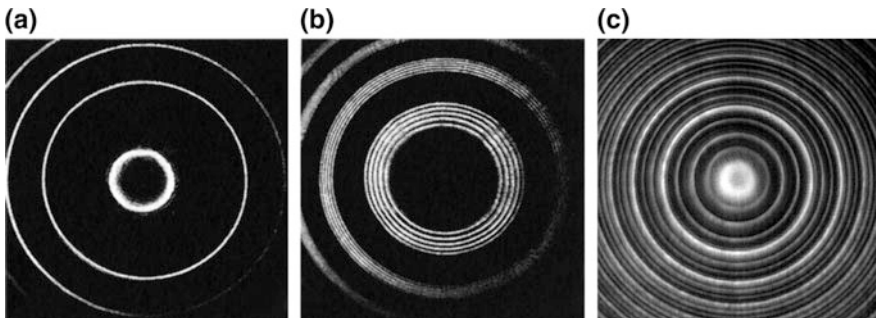


Fig. 22.4 Interference (ring) pattern of a laser produced by a Fabry-Pérot interferometer. **a** single mode, **b** 5 modes, **c** spectral bandwidth larger than free spectral range of the FPI ($c/2d = 1.6$ GHz)

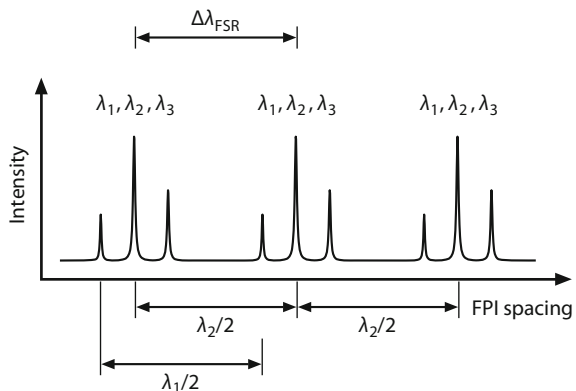
sharpness of the rings, or the spectral width of the transmission peaks correspondingly, is related to the finesse (18.13) which is, in turn, determined by the mirror reflectance [see (18.14)]. For a typical FSR of 2 GHz and a mirror reflectance of $R = 95\%$, the finesse is $F \approx 61$, yielding a spectral width of the transmission peaks of 33 MHz. The spectral resolving power of a FPI interferometer is then given by

$$\boxed{\frac{\lambda}{\Delta\lambda} = \frac{4rF}{\lambda}}, \quad (22.6)$$

where r is the radius of curvature of the mirrors. For a confocal FPI with a mirror curvature of $r = 50$ mm and a laser wavelength of $\lambda \approx 1 \mu\text{m}$, the resolving power is about 12×10^6 . Even higher values of up to $\lambda/\Delta\lambda = 10^8$ can be reached by using mirrors with higher reflectance. However, since the highly-reflective (HR) region of dielectric multilayer mirrors typically spans over only tens to a few hundreds of nm (Sect. 14.2), the applicable spectral range of a FPI interferometer is limited to this range.

FPI interferometers can also be operated in scanning mode where one mirror is translated, e.g. by a piezoelectric actuator driven by a sawtooth voltage. The spectrum of the incoming light is then obtained from the temporal variation of the transmitted intensity which can be recorded with an oscilloscope. For a given wavelength λ_1 , a transmission peak is detected when (22.5) is satisfied at a certain

Fig. 22.5 Interference pattern produced by a scanning Fabry-Pérot interferometer. As the spacing of the FPI is varied, different wavelengths are transmitted. $\Delta\lambda_{\text{FSR}}$ -free spectral range



mirror spacing d . For a different wavelength λ_2 , maximum transmission occurs at a different spacing. The temporal distance between the transmission peaks can be translated into a wavelength difference by relating it to the free spectral range $\Delta\lambda_{\text{FSR}}$ of the interferometer (Fig. 22.5). Likewise, the spectral width of the emission lines can be determined.

Fizeau Interferometers

A modified version of the FPI is the Fizeau interferometer where one of the two mirrors is slightly tilted with respect to the other and exhibits different reflectance. In general, this is realized by dielectrically coated glass wedges with a small angular mismatch of a few arcseconds. Superposition of the partial beams produced by multiple reflection of an incident light beam leads to an interference pattern with a wavelength-dependent periodicity. The measured pattern can be imaged onto CCD photodiode arrays by a cylindrical lens and compared to a previously recorded calibration pattern in order to determine the absolute wavelength and linewidth of the incoming light. This measurement principle is, for instance, applied in wavelength meters which are widely used to characterize the spectral properties of single-frequency laser sources with an accuracy of a few MHz. In addition to the broader applicable spectral range, a significant advantage of Fizeau interferometers is the absence of mechanical moving parts which makes them very robust and reliable.

22.5 Optical Heterodyne Detection

Optical heterodyne detection involves the superposition of the light to be analyzed (frequency f_1) with the light from a reference source (frequency f_2) which is referred to as local oscillator (Fig. 22.6). The total intensity of the combined optical signal is

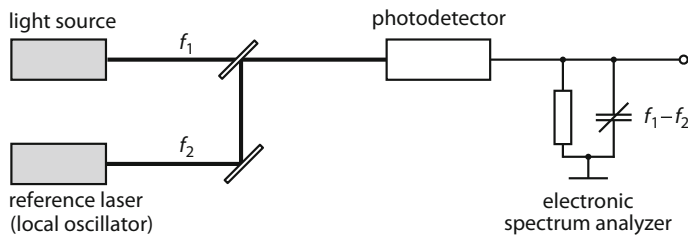


Fig. 22.6 Heterodyne detection technique for measuring optical frequencies

detected by a detector, typically a photodiode, whose response is linear in intensity, and hence quadratic in the amplitude of the electromagnetic field. The superposition of the two light waves leads to a modulation of total intensity at the difference frequency (the beat note $f_1 - f_2$). Provided that the two frequencies are not too far apart, the oscillating part of the signal is slow enough to be processed with electronic means. Hence, if f_2 is known, f_1 can be determined from the beat note. By using a powerful local oscillator, the heterodyne signal resulting from a weak input signal can be considerably stronger than for direct detection.

The resolving power of the heterodyne detection technique is better than 10^{10} and enables the measurement of frequency differences well below 1 Hz. A spectral width of 1 Hz corresponds to a coherence length of 300,000 km (Sect. 20.4). Heterodyne detection is utilized in laser Doppler velocity measurements, e.g. in wind lidar systems (Sect. 25.3). Furthermore, the method allows measurement of length changes as small as 10^{-15} m. For this purpose, the length variation has to be transferred into a displacement of one of the laser mirrors, as this leads to a corresponding change in the laser frequency. The frequency change is then detected as an alteration of the frequency difference after superposition of the laser with the local oscillator.

22.6 Optical Frequency Combs

An optical frequency comb represents a spectrum consisting of equidistant spectral lines, whereby the intensity of each frequency component can vary substantially. Frequency combs are useful for measuring optical frequencies by comparing them with the known comb frequencies, e.g. by optical heterodyne detection, as described in the previous section. Hence, frequency combs are often referred to as “optical rulers”. Today, they are commercially available and widely used for metrology purposes. Apart from scientific applications like the precise measurement of electronic transitions in atoms to test advanced quantum theory, frequency combs are also technologically important, for instance, in the Global Positioning System (GPS) or space projects.

The interest in frequency combs has been boosted after Theodor W. Hänsch received the Nobel Prize in Physics in 2005 for demonstrating that a regular train of

femtosecond laser pulses can be used as a frequency comb. Such a pulse train has a frequency spectrum of equidistant spectral lines, as outlined in the context of mode-locking in Sect. 17.4.

The frequency spacing between the comb lines is given by the pulse repetition rate f_{rep} of the laser (Fig. 22.7) which is typically in the radio- or microwave-regime of 10^{10} Hz = 10 GHz. Consequently, the beat note frequencies produced by optical heterodyning are on the same order and can be measured with high precision of 10^{15} using cesium atomic clocks which represent the primary standard of time and frequency. The spectral bandwidth of a frequency comb is related to the pulse duration according to (17.3). For a Gaussian-shaped pulse with a duration of 100 fs and a center wavelength of 1064 nm, the bandwidth is 4.4 THz, corresponding to 16.6 nm.

Spectral broadening can be achieved by exploiting nonlinear optical effects outside the laser resonator, realizing frequency combs that span more than one optical octave while preserving the integrity of the comb lines. A frequent approach is to send a pulse train from a Kerr-lens mode-locked titanium-sapphire (see e.g. Fig. 17.12) into a micro-structured silica fiber or photonic crystal fiber (Sect. 13.3, Fig. 13.8). As the tightly focused, high-intensity laser beam is guided through the fiber, self-phase modulation (Sect. 17.4) and other nonlinear effects occur, so that the pulse spectrum is considerably broadened (supercontinuum generation, see Sect. 19.6). Since the nonlinear processes are highly reproducible, successive pulses of the train remain correlated upon the broadening. As a result, they can interfere with each other, producing a frequency comb of several hundred thousand spectral lines. Meanwhile, other laser-based systems are also available for frequency comb generation, e.g. those relying on stimulated Raman scattering (see Fig. 19.11).

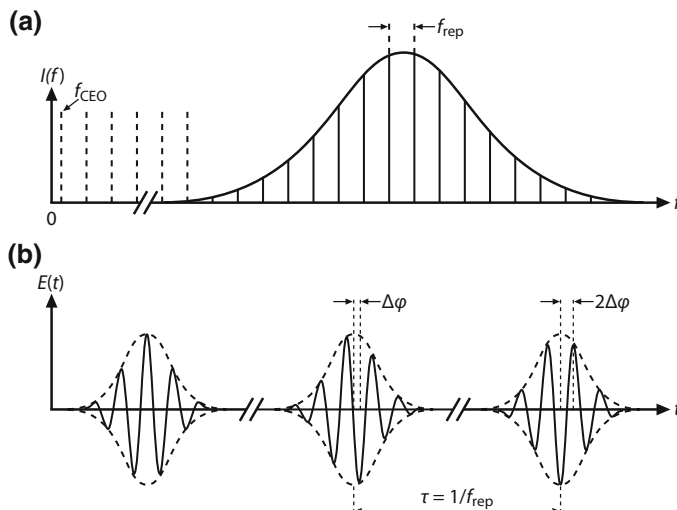


Fig. 22.7 Optical frequency comb **a** in the frequency domain and **b** in the time domain

As shown in Fig. 22.7a, the absolute frequency f_n of a comb line with integer n is given by

$$f_n = n \cdot f_{\text{rep}} + f_{\text{CEO}}, \quad (22.7)$$

where f_{CEO} is the carrier-envelope offset frequency. The latter is related to the phase difference $\Delta\varphi$ between two successive pulses (Fig. 22.7b):

$$f_{\text{CEO}} = f_{\text{rep}} \frac{\Delta\varphi}{2\pi}. \quad (22.8)$$

If f_{CEO} and f_{rep} are known, all frequencies of the comb are determined according to (22.7), and any optical frequency within the range of the frequency comb can be precisely measured using optical heterodyne detection.

While f_{rep} is easily quantified by means of a photodiode, the determination of f_{CEO} is often more challenging. In case that the frequency combs span over more than one octave, the $f - 2f$ self-referencing scheme can be applied. Here, a few thousand comb lines from the lower-frequency end of the spectrum are frequency-doubled in a nonlinear crystal and superimposed with lines from the higher-frequency end of the comb. Since the frequency-doubled lines are displaced by twice the offset frequency f_{CEO} , the resulting beat note directly reveals the offset frequency. Once the offset is known, it can also be actively controlled, e.g. by adjusting the pump power or the dispersion of the laser cavity. In particular, f_{CEO} can be set to zero, so that comb line frequencies become precise integer multiples of the laser repetition frequency f_{rep} .

Further Reading

1. S. Musazzi, U. Perini (eds.), *Laser-Induced Breakdown Spectroscopy* (Springer, 2014)
2. Y.K. Sirenko, S. Ström (eds.), *Modern Theory of Gratings* (Springer, 2010)
3. V.V. Protopopov, *Laser Heterodyning* (Springer, 2009)
4. W. Demtröder, *Laser Spectroscopy* (Springer, 2008)
5. R. Paschotta, *Encyclopedia of Laser Physics and Technology* (Wiley-VCH, 2008)
6. T.W. Hänsch, Passion for precision (Nobel lecture). *ChemPhysChem* 7, 1170 (2006)
7. E.G. Loewen, E. Popov, *Diffraction Gratings and Applications* (Marcel Dekker, 1997)
8. J.M. Vaughan, *The Fabry Perot Interferometer* (Institute of Physics Publishing, 1989)

Part VIII

Material Processing, Medicine and Further Applications

The final part of the book addresses the importance of lasers in scientific and industrial applications in addition to laser metrology discussed in the previous chapters. First, the focus is on material processing where lasers are used, among others, for cutting, welding, and hardening of various materials. Additionally, emerging technologies like laser cladding and additive manufacturing are presented.

Chapter 24 is concerned with lasers in medicine and biophotonics. After introducing the operating regimes of medical lasers, selected techniques applied in surgery and other therapies as well as diagnostics are outlined. Finally, the vital role of lasers in everyday life and modern technology is highlighted. Here, major application fields like optical communication, light detection and ranging, and holography are discussed as well as recent developments regarding gravitational wave detection and extreme high-power laser systems dedicated to laser fusion. The last chapter also reviews laser types that have not been covered in the first parts of the book, as they rely on concepts which differ from conventional laser sources. This comprises free-electron lasers, X-ray, and XUV lasers as well as so-called atom lasers. The book closes with an outlook on the perspectives of lasers in the near future and an overview of the economic relevance of different laser applications.

Chapter 23

Material Processing



The flexibility and unique properties of the laser make it a versatile tool for material processing in a wide range of industries. Aside from well-established applications such as hardening, welding, cutting and drilling, novel technologies for laser cladding and additive manufacturing have gained great attention over the past years. Revenues for laser material processing (including lithography) systems exceeded four billion US dollars in 2016, making it the largest segment of the total laser market. This chapter discusses the mechanisms of action that are exploited in laser material processing and provides an overview of the most common industrial applications.

23.1 Laser Interaction with Materials

When a laser beam is incident on a metal or other material, the radiation energy is absorbed, and the material heats up. Depending on the amount of absorbed energy and interaction time, the material is even melted or vaporized. The thermal processes are utilized in various material processing applications from which a selection is listed in Table 23.1.

Hardening of ferrous materials, e.g. steels, is accomplished by heating the workpiece to just under the melting temperature in order to alter its crystal structure. Laser-induced melting is used for welding purposes. For laser cutting of (metallic) materials, the workpiece is heated to the melting point, while a focused gas jet blows the molten material out of the kerf. Drilling involves local vaporization of the material. As opposed to the subtractive manufacturing methods mentioned above, vaporized material can also be deposited on other workpieces for applying thin layers of precious metals, for passivating materials or for creating corrosion-resistant surfaces. Such laser cladding processes can also be performed in the liquid or gaseous phase and play an increasingly vital role in microtechnology. The same holds true for additive manufacturing based on selective laser melting where a three-dimensional workpiece is produced layer by layer using a laser beam which

Table 23.1 Physical processes for material processing as well as advantages and disadvantages over other techniques

Heating	Hardening, surface modification
Melting	Welding, alloying, cutting, rapid prototyping
Vaporizing	Drilling, marking, deposition
Advantages	Fabrication of arbitrary shapes (Rapid) processing of hard materials Absence of tool wear Micromachining Flexible beam guiding through optical fibers Application in computer-aided manufacturing (CAM) systems
Disadvantages	High costs (decreasing) (Partially) strict requirements in terms of design, materials, handling

fuses metal powder particles. In general, laser-assisted 3D printing is emerging as a versatile technology, as it is easily combined with computer-aided designing (CAD) and computer-aided manufacturing (CAM), thus enabling rapid prototyping of arbitrary structures.

When using laser light for material processing, the power density and exposure time have to be adapted to the desired mechanism of action. At low power densities and long exposure times, a large volume of material is warmed by heat conduction. Conversely, irradiation of the material with (ultra-)short intense laser pulses limits the heat-affected zone to the region where the laser beam is absorbed, hence reducing the losses introduced by heat conduction into the volume.

The penetration depth d can be estimated from the pulse duration τ according to

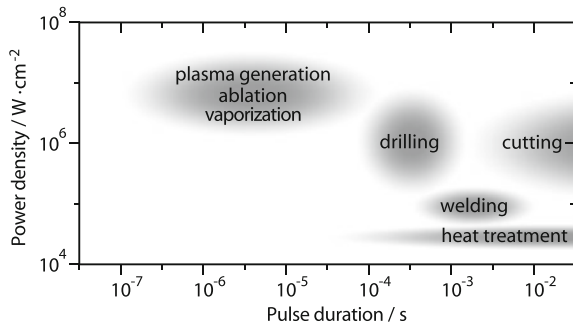
$$d \approx \sqrt{4\alpha\tau}, \quad (23.1)$$

where $\alpha = k/c_p \cdot \rho$ is the thermal diffusivity of the material which is determined by the thermal conductivity k , the specific heat capacity c_p and the density ρ . For steel containing 1% of carbon with $\alpha = 0.12 \text{ cm}^2 \text{ s}^{-1}$, the penetration depth is $d \approx 1 \times 10^{-4} \text{ cm} = 1 \mu\text{m}$. The optical penetration depth of laser radiation into metals, i.e. the inverse of the absorption coefficient, is on the order of $10^{-6} \text{ cm} = 10 \text{ nm}$.

Glasses and semiconductors are characterized by weak (linear) absorption in the visible and near-infrared spectral region, provided that the incident intensity is low. At high intensities, multi-photon processes occur leading to nonlinear absorption which reduces the penetration depth down to a few nanometers comparable to metals. Consequently, picosecond or femtosecond lasers with high peak pulse power are employed for precise ablation, drilling and cutting of transparent materials.

Typical power densities and pulse durations of lasers used for different material processing tasks are illustrated in Fig. 23.1. The boundaries are blurred, as the laser parameters required for a particular application also depend on the laser type and the material to be processed.

Fig. 23.1 Typical power densities and pulse durations of lasers for different material processing applications

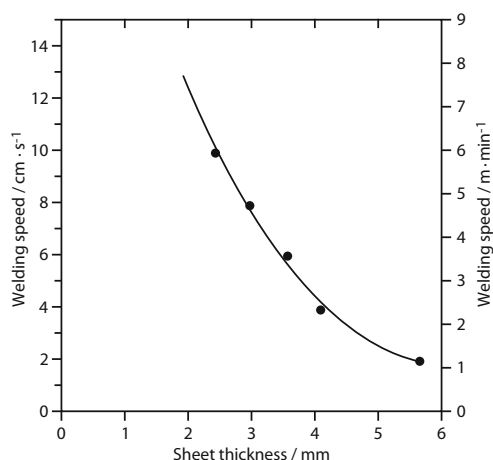


23.2 Lasers for Material Processing

CO_2 lasers are primarily deployed for cutting, welding and drilling of medium-size and large workpieces. In the early stage of laser machining, these were large-scale devices with a volume of several cubic meters. With the development of segmented, e.g. quadratically arranged, discharge tubes, compact configurations were realized (see Fig. 6.8). One advantage of laser material processing over other methods is the possibility to cut arbitrary profiles into metal sheets. Using conventional techniques, it is necessary to build complicated punching tools or to apply thermal separation processes which require reworking. In contrast, the laser is a universal tool which can be easily modified and adapted to a variety of tasks.

Some data on the welding speed achieved with a CO_2 laser is depicted in Fig. 23.2. For steel sheets, welding speeds of several meters per minute are obtained depending on the sheet thickness. For instance, 6 cm-thick sheets are welded using 20 kW fiber lasers. The use of lasers with output powers exceeding 100 kW is envisaged.

Fig. 23.2 Welding speed of a CO_2 high-power laser at 3.6 kW output power for unalloyed steel



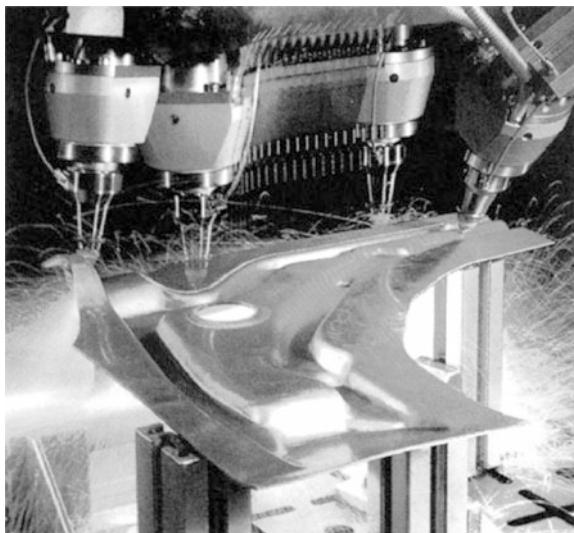
In the advent of solid-state lasers, they were employed for micromachining applications, e.g. for drilling holes with diameters of a few microns, for manufacturing and machining integrated electronic circuits as well as for trimming electrical resistors and welds of conductive tracks on printed circuit boards of electronic devices. By now, solid-state lasers reach output powers of several tens of kilowatt, making them well-suited for spot and seam welding of car bodies. For this purpose, the near-infrared laser radiation is delivered via glass fibers which is not possible for the output of the CO₂ laser due to its longer wavelength.

The advantages of laser material processing over conventional technologies are summarized in Table 23.1. Lasers offer the possibility to fabricate arbitrary shapes and to machine practically all metallic materials from soft to hard and brittle, glasses, ceramics and plastics. The laser beam is ideal for micromachining and does not wear out like mechanical tools used for turning and milling. Laser processing is in many ways superior to methods involving other light sources, such as gas burners, electric arcs as well as plasma or electron beams. The laser beam can be focused down to the micrometer scale, to be easily be guided by mirrors or optical fibers and thus coupled with industrial robots for beam delivery. Because of these and other reasons, lasers are increasingly employed in industrial manufacturing. The limits are set by the expenditure on equipment and the associated costs. Today, around 50,000 laser systems are in use for manufacturing worldwide. The full potential of the laser in this application domain is, however, far from exhausted. The annual growth rates exceed 10%, so that the global laser processing market is expected to reach more than 20 billion US dollars by 2025.

Complete laser systems providing output powers ranging from 100 W to 100 kW are offered by various companies. The motion of the laser is usually controlled by Computerized Numerical Control (CNC) which guides the laser beam to the workpiece via a processing head, as depicted in Fig. 23.3. Here, the laser beam is focused while the distance to the workpiece is monitored and actively controlled by adjusting the position of the focusing lens. A gas flow prevents the condensation of vaporized material on the lens. During the machining process, vapors and dusts are generated which must be extracted, filtered and disposed of properly. Moreover, the process is often carried out in a safety cabin with inspection windows, so that the operator cannot be harmed by direct or reflected laser radiation.

At the turn of the millennium, CO₂ lasers represented the most important sources for laser material processing. In particular, flowing-gas CO₂ lasers dominated the market for machining applications such as welding, cutting and marking due to their high efficiency of more than 20%, high output power (tens of kilowatts) and high reliability. A major drawback of the CO₂ laser, however, is the fact that guiding of the 10 μm radiation by means of flexible fibers cannot be achieved in a technically satisfactory manner. Hence, over the past two decades, other laser technologies have emerged including direct diode lasers and diode-pumped solid-state lasers, especially fiber lasers. These have the advantage that the infrared

Fig. 23.3 Partial view of a facility for cutting and welding of metal sheets. The processing head moves to different positions which are depicted by multiple exposure



radiation at wavelengths around $1 \mu\text{m}$ can be transmitted through quartz fibers, thus enabling flexible beam delivery and easy coupling to industrial robots. Furthermore, the wall-plug efficiency, i.e. the electrical-to-optical conversion efficiency, of direct diode and diode-pumped solid-state lasers is considerably higher compared to CO_2 lasers.

Fiber lasers additionally feature very high beam quality, rugged and compact design as well as minimum maintenance. They can be installed within a few hours without the need for special mounting surfaces required by many conventional solid-state lasers. While single-mode fiber lasers typically provide a few kilowatts of output power, multimode systems deliver up to several tens of kilowatts. This enables high processing speeds at low cost per watt. With the development of new fiber lasers offering additional wavelengths, higher peak powers and cost advantages, the material processing market will continue to shift from CO_2 lasers and classical solid-state lasers to the fiber laser technology.

A key advantage of direct diode laser systems is their very high wall-plug efficiency of up to 50% which directly translates into low operating cost since less electricity is required to produce a given amount of output power. Furthermore, they are much more compact and lightweight compared to most other industrial lasers. Diode lasers, e.g. emitting at 808 or 940 nm wavelength, can provide tens of kilowatts of output power in continuous wave mode.

Precise drilling and milling is accomplished using pulsed solid-state lasers with pulse durations in the picosecond to fs-range. Laser systems with repetition frequencies from 50 to 100 MHz and average power of up to 200 W are available for this task. A selection of material processing applications using different types of lasers is described in the following sections.

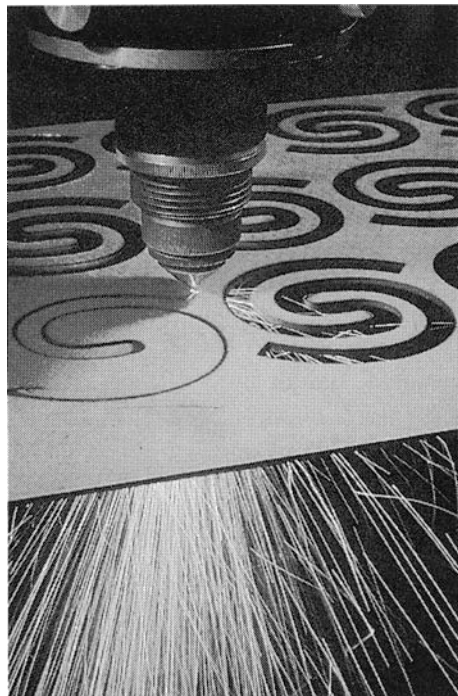
23.3 Processing Applications

Lasers are employed in a very broad range of industrial material processing applications. In the early years of the laser, it was primarily used as a tool in microtechnology, e.g. for drilling small holes in the jewel bearings of mechanical watches, or for soldering thin wires in electronics. With the development of more and more powerful, efficient and reliable laser sources, they have been increasingly applied for machining larger workpieces, e.g. in the automotive and aircraft industry.

Cutting of Metal Sheets, Foils and Glasses

Laser cutting of sheets, e.g. for fabricating metal housings, involves melting of the material. The molten material is ejected from the workpiece by a focused gas jet. When using oxygen, the cutting speed is considerably increased due to the additional oxidation heat. The laser beam can be guided along complicated paths in three-dimensional space, and even hard materials, that can otherwise only be cut linearly using a diamond grinding wheel, are easy to machine (Fig. 23.4). There are advantages of using lasers in the cutting of coated sheets, organic fiber materials,

Fig. 23.4 Laser cutting. The focused laser beam is directed at the material which vaporizes away in the form of small particles (courtesy of Spectra Physics)



plastics, ceramics, glass or wire-reinforced rubber parts. In the automotive industry, cutting lasers are particularly used in the development of new body parts, as the contours can be easily and quickly changed.

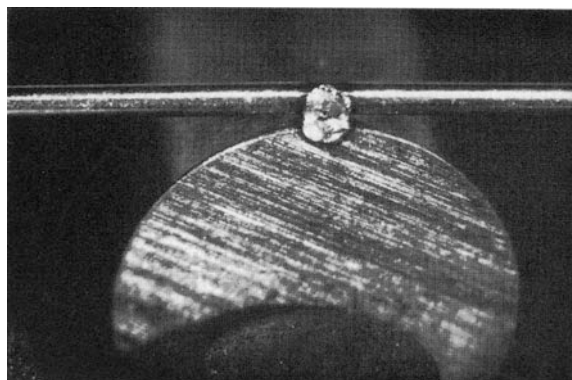
Welding of Metals and Plastics

Thin sheets are welded together by so-called *heat conduction welding*. Here, the laser beam is scanned over the surface of the mating parts along the common joint. The laser power and interaction time are chosen such that the temperature of the liquid remains below the boiling point and evaporation hardly occurs. Hence, the molten materials flow together and solidify to form the weld as they cool off. The depth of the weld seam is typically only about 1.5 times larger than its width. Figure 23.5 shows a spot weld. Heat conduction welding is the method of choice for hose connections which can be made more quickly and with lower material distortion than with usual welding methods. Moreover, this technique allows for smooth and pore-free welding seams that do not need any post-processing.

In *deep welding*, the temperature is above the boiling point, so that the local melt pool is displaced by the pressure of the created vapor in the weld. The melt thus circulates and is even partially lifted over the material surface creating a weld bead. Deep welding offers high process speed and low material distortion. The weld seam is characterized by a low content of impurities as well as by a narrow, fine-grained structure with a depth gauge that is often bigger than its width. Sometimes the evenly structured seam is even harder than the material itself.

In automotive industry, laser welding enables material saving by up to 5 kg per car, due to the high precision of the process which reduces the overlap of the weld beads. Advantages arise when welding has to be performed in places that are difficult to access such as corners or pipes where conventional welding tools cannot be used because of their size. Laser welding techniques are also used in the electrical industry for joining various materials.

Fig. 23.5 Laser welding.
A wire is bonded onto a metal rod (courtesy of S. Smernos, Standard Elektrik Lorenz AG)



Diode lasers with output powers of 50–200 W and 940 nm wavelength are suitable for welding thermoplastic materials. In so-called *transmission welding*, a permeable film is placed on an absorbent film. The laser beam passes through the permeable film and melts the absorbent film so that the two plastics are welded together at their interface. Waterproof seams in laminated fabrics can be produced using this technique.

Laser Hardening and Cladding

For the manufacturing of mass-produced articles, the surfaces of certain components are often heat-treated to improve their mechanical and chemical properties or visual appearance. In this context, lasers are utilized for the purpose of hardening, coating and alloying surfaces. Figure 23.6 shows the cross-section of a surface that has been hardened using an intense CO₂ laser beam on an approximately 4 mm wide track. A considerable increase in hardness is achieved. For instance, steel components can be hardened from about 25–28 HRC to 50–60 HRC (hardness according to the Rockwell C scale), corresponding to a Vickers hardness of about 500–700 VH.

Surface alloying has become an industrially accepted technology only through the use of lasers. A powdery substance, e.g. boron carbide, is applied on the

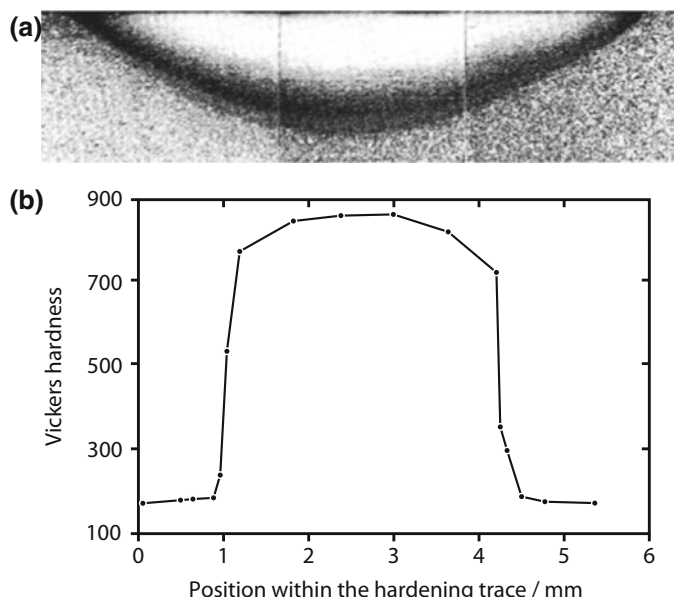


Fig. 23.6 Laser hardening of a metal surface. **a** Cross-section the surface with different structural conditions. **b** Vickers hardness along the cross-section (courtesy of S. Smernos, Standard Elektrik Lorenz AG)

workpiece where it is fused with the surface by the laser radiation. The result is a new alloy that can be very fine-grained and hard in case of rapid cooling (quenching) of the material. This type of surface treatment is, for instance, used for improving the mechanical properties of valve seats in car engines.

Laser cladding is a similar technology which has emerged in material processing over the past two decades. The laser is used to heat the workpiece and to melt a powdered cladding material that is deposited onto the surface without forming an alloy. For this purpose, the powder is either blown into the interaction zone between the laser beam and the workpiece or pre-deposited on the substrate. In many industries, this process serves to refine the surface and to enhance the wear, corrosion or heat resistance of a workpiece. Besides the commonly used CO₂ and Nd: YAG lasers, fiber and diode lasers are increasingly being used because they are easy to integrate, have low total cost of ownership and provide very good processing results without thermal deformation of the workpiece.

Laser quenching, which represents a further development of classical heat treatment procedures, is a somewhat simpler process. It involves laser heating of the surface to just below the melting temperature. The material, usually steel, is then cooled at a very fast rate by heat conduction into the bulk material. This process is referred to as self-quenching which causes a transformation from the austenite to the martensite phase. The latter is harder and usually has a finer-grained structure (Fig. 23.6a).

The region where the phase transformation occurs should not be too deep in order to prevent the workpiece from becoming too brittle. Hence, lasers are ideal tools for rapid and precisely localized heating of the material. Applications are found in the hardening of gears as well as valves and cylinder walls of internal combustion engines. Irradiation with high energy densities and short exposure times, followed by rapid cooling, leads to the formation of a glassy, amorphous phase. This surface-melting technique is referred to as *laser glazing*.

Processing of Transparent Materials

Most glasses are transparent in the visible and near-infrared spectral region and show only weak absorption at low intensities. Strong linear absorption, however, occurs at wavelengths longer than 3 μm. Hence, CO₂ lasers emitting at 10 μm can be used to heat glasses, so that they can be cut similar to metal sheets. As opposed to the conventional separation of glasses by scoring and breaking, laser processing does not leave sharp-edged corners.

Transparent materials can also be machined using short-wavelength lasers, provided that the laser intensity is sufficiently high. When the material, e.g. quartz glass, is irradiated with ultra-short pulses in the femtosecond to ps-regime, the nonlinear absorption increases strongly with the pulse energy and the penetration depth of the light is drastically reduced to a few nanometers. The absorbed energy is

thus concentrated in a small volume, so that the atoms in the material are ionized, i.e. broken up into ions and electrons. The resulting plasma rapidly expands, and the hot ions and electrons are ejected from the irradiated volume. This removal of solid material by laser radiation is referred to as laser ablation. Due to the short pulse duration, the ablation process occurs so quickly that the surrounding material absorbs very little heat. Successive irradiation of the material with many laser pulses therefore allows very precise micromachining of transparent materials. Femtosecond lasers are for example used to produce repeatable, accurate features down to 10 µm in size, like holes and grooves on surfaces or structures. One application is the production of Bragg gratings in glass fibers which act as filters (see Fig. 9.26). Furthermore, ultra-short lasers enable the fabrication of 3D structures in transparent materials with far greater simplicity than lithography.

Marking

Lasers are widely used for labeling and marking purposes. Typical applications include the manufacturing of scale marks on precision optical instruments, the marking of electronic and other components, the writing of barcodes or simply the labeling of pens. Different companies offer such systems which are controlled by computers and can produce various types of labels with high flexibility. Marking inside transparent materials like glass is possible by using pulsed laser beams that are focused into the material, resulting in small cracks, discoloration or refractive index changes. In this way, durable 2D and 3D images or information like serial numbers, barcodes, security and identification marks are written inside the object without damaging the surface.

Marking systems based on fiber lasers have gained attraction over the past years, as they require little space and have very low maintenance requirements. Moreover, the excellent beam quality of fiber lasers is especially useful in high precision marking applications. Single-mode fibers with attached termination modules for beam collimation and integrated zoom optics provide easy beam delivery over a distance of several meters.

Production of Semiconductor Devices

Lasers find numerous applications in semiconductor technology, from which a small selection is presented here. *Laser annealing* is a widespread technique which is applied to heal crystal defects in wafers formed by the implantation of ions. The method includes injection of the required dopant ions into the semiconductor crystal, followed by laser-induced heating in order to remove the produced lattice imperfections. The annealing temperature is controlled via the exposure time and

the power density of the laser beam which moves over the wafer. The power density is, in turn, related to the width of the beam along its moving direction and the scan speed.

The deposition of various layers of materials on semiconductor surfaces can be accomplished with lasers as well. For this purpose, the deposited metal or a semiconductor material is incorporated into a gaseous compound which is then decomposed at the semiconductor surface upon irradiation with a laser beam, forming the desired layer. A particular advantage of this method is that the focused radiation enables the production of conductive tracks and other two-dimensional structures on the surface.

The standard procedure for structuring semiconductor surfaces is *photolithography* (see Fig. 10.40). Here, the surface is first coated with a photo-sensitive lacquer (called photoresist). Then, a mask with the pattern of the structure to be produced is applied to the surface, so that only unmasked regions of the material will be exposed to light. Through a series of chemical treatments, the photoresist structure is developed in analogy to photography. In the case of a positive photoresist, the photosensitive material is degraded by the light, so that a solvent (developer) will dissolve away regions that were exposed to light, leaving a coating where the mask was placed. In contrast, application of a negative photoresist leads to strengthening of the photosensitive material and a selective dissolving of regions that were not exposed to light. In both cases, the desired structure is transferred to the semiconductor as a geometric pattern of the photoresist. In subsequent process steps, the uncoated parts of the wafer can be etched, chemically doped, metallized or coated with other materials, resulting in complex structures required for integrated circuits.

The integrated circuit feature size is determined by the wavelength of the radiation that is used for the exposure of the wafer. In the past, mercury vapor lamps with wavelengths of about 250 nm were used. With the progressing miniaturization of functional elements in integrated circuits, excimer lasers, e.g. ArF lasers at 193 nm, have become the state-of-the-art in photolithography. Such lasers are, for example, employed by Intel to produce integrated circuits with minimum feature sizes of only 40 nm. This technology also requires new types of photoresists with specific exposure thresholds. The fabrication of even smaller structures down to 13 nm wavelength is envisaged by utilizing VUV or X-ray lithography. Hence, lasers have been playing a vital role in the continued increase of the packing density of integrated circuits according to Moore's law which states that the number of transistors in a dense integrated circuit doubles approximately every two years.

In the context of manufacturing integrated circuits, *wafer dicing* is another application that can be performed using lasers. In the stealth dicing process, defect regions are introduced into the wafer by scanning a laser beam along intended cutting lines, before an underlying carrier membrane is expanded to induce fracture. *Laser scribing* and cutting of semiconductor chips are firmly established techniques in electronics mass production. The same holds for *laser soldering* and *laser trimming* of resistors or other passive circuit elements by material removal which are routinely performed with lasers.

Selective Laser Melting

Additive manufacturing of complex structures is accomplished by selective laser melting (SLM) where laser radiation is utilized to selectively melt successive layers of a powder material (metals like copper, aluminium, chrome, titanium or metal alloy compositions) in order to build up a three-dimensional workpiece. In contrast to sintering, the metal powder is fully molten during the SLM process, so that very dense parts with properties comparable to conventionally manufactured ones are produced. The manufacturing costs are almost independent of the part complexity, since time and effort needed for production only depend on the component volume. This allows the realization of innovative products with integrated functionalities.

Due to the high flexibility and packing density of the three-dimensional objects, additive manufacturing techniques like SLM are already applied commercially in the field of rapid prototyping. The benefits of SLM are for example exploited for building lightweight parts for aerospace. In particular, novel designs of components are possible, e.g. including internal complex cavities, that cannot be produced with traditional methods due to constraints in terms of tooling and the physical access to the surfaces to be machined.

Future Technologies

Laser material processing is a technology with interesting perspectives and ever-growing opportunities. Mutual adaptation between the product and the production lines is, however, required for the benefits to come to fruition. Laser-compatible design and materials as well as online control of the fabrication processes play a crucial role compared to alternative technologies involving electron or plasma beams.

Novel applications may result from the exploitation of special effects induced by laser irradiation. The past decades have shown that nonlinear optical effects open up new possibilities in material processing, such as highly localized ablation without thermal damage of surrounding material or microstructuring of semiconductor devices by laser-induced crystal modification.

Major advances are expected from the development of high-power diode and fiber lasers. Multimode fiber lasers with 50 kW of output power and single-mode lasers with 10 kW are currently available. The applicability of these lasers is improved by their robustness, compact size and high wall-plug efficiency of 30%. This allows cost-effective implementation of material processing applications that were previously uneconomic. For example, the beam adaptation of a high-performance fiber laser to various welding tasks (homogeneous intensity distribution in laser soldering, dynamic beam oscillation in thick-plate welding) ensures a significant increase in productivity.

Fiber-coupled high-power direct diode lasers have equally promising prospects. In comparison to conventional lasers, they are characterized by low acquisition and operating costs and will therefore become dominant in various areas of industrial material processing up to the multi-kW-range in the near future. High-power diode lasers based on GaAs, which are tunable in the spectral region around 1000 nm, are for example used for separating glass sheets, silicon wafers and other semiconductors as well as for welding aluminum. The emission wavelength within the tuning range is selected depending on the machined material so that process optimization with respect to the absorption efficiency is achieved.

Further applications of high-power lasers are found in the fabrication of efficient solar cells at high processing speed. Laser-based processing steps include separation of silicon wafers, production of insulation areas in thin-film solar cells and drilling holes for the passage of contact wires from front to back. Mode-locked UV lasers offer the fabrication of solar cells with narrow surface contacts which enables low-loss conduction of the generated photocurrent and, in turn, higher efficiency of the solar cells.

The excellent controllability of the optical power in space and time, combined with the possibilities of online process control, makes the laser a multifunctional tool for flexible and automatic material processing. Since further optimization in terms of compactness, efficiency and cost-effectiveness is ongoing, the number of commercially viable laser applications in production technology will continue to increase steadily.

Further Reading

1. H. Hügel, T. Graf, *Laser in der Fertigung* (Springer Vieweg, 2014)
2. W. M. Steen, J. Mazumder, *Laser Material Processing* (Springer, 2010)
3. C. Phipps (ed.), *Laser Ablation and its Applications* (Springer, 2007)
4. M. Kozlowski, J. Marciak-Kozlowska, *Thermal Processes Using Attosecond Laser Pulses* (Springer, 2006)
5. R. Iffländer, *Solid-State Lasers for Material Processing* (Springer, 2001)

Chapter 24

Medical Applications and Biophotonics



Lasers are used in various medical applications both in therapy and diagnosis. Common diagnostic methods including optical tomography, spectroscopy and Doppler velocity measurements largely correspond to the methods which are also employed in other fields such as biophotonics and sensing. Depending on the application domain, different mechanisms of action of the laser radiation are exploited. While spectroscopic and imaging techniques for diagnostics purposes rely on lasers operating at low power levels, high-power lasers with output power of several watts and/or pulse energies in the joule-range are employed for laser surgery and other therapeutic treatments. After an overview of the different operating regimes of medical lasers and their related application areas, this chapter presents selected laser techniques used in the field of medicine, particularly surgery and other therapies, medical diagnostics and biophotonics. Laser surgery is widely used for skin treatment and vision correction and many other medical applications. It is expected that laser therapies and optical methods for rapid diagnostics will be combined into so-called theranostic systems that allow medical treatment directly guided by diagnostic results. This will make medical treatment safer and less time consuming. In the last part of the chapter, biological aspects of laser safety are discussed. Here, the focus is on the interaction of laser radiation with the human eye and skin. Depending on the laser wavelength, different penetration depths in tissue and different damage mechanisms occur. This leads to corresponding exposure limits and safety precautions that have to be observed when working with lasers.

24.1 Operating Regimes of Medical Lasers

In therapeutic applications, the thermal effect of laser radiation is predominantly utilized for minimally invasive surgical procedures. When tissue is irradiated by a laser, the temperature rises due to absorption of energy by the tissue. At about

Medical terms contained in Chapter 24 are explained by Google or Wikipedia.

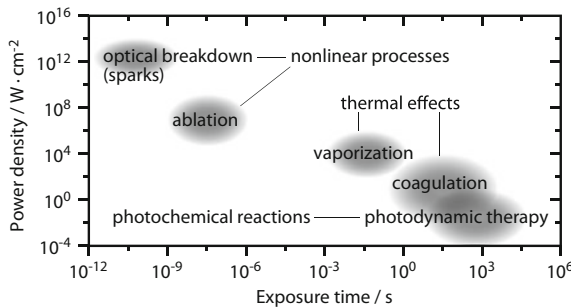


Fig. 24.1 Typical power densities and exposure times for different medical laser applications

60 °C proteins coagulate, at about 100 °C tissue water evaporates and the tissue carbonizes with further temperature increase. The gradual effects of light on biological material are depicted in Fig. 24.1, and can be used for sclerotherapy, ablation and cutting, amongst others. The rise of temperature and volume of the affected tissue depends on its physical properties (absorption and scattering coefficient, thermal conductivity) and on the laser parameters (wavelength, power density and pulse duration). Laser surgery offers high-precision, contact-free and aseptic treatment. Moreover, due to the vascular occlusion by coagulation, it allows almost bloodless incision, even when the tissue is strongly perfused. The thermal effects are determined by the depth of the wavelength-dependent penetration in the tissue (Fig. 24.2).

Aside from the thermal effects of laser radiation, there are various other mechanisms that are exploited for medical purposes, depending on the irradiation duration and power density (Fig. 24.1). Photoablation requires short pulses of high

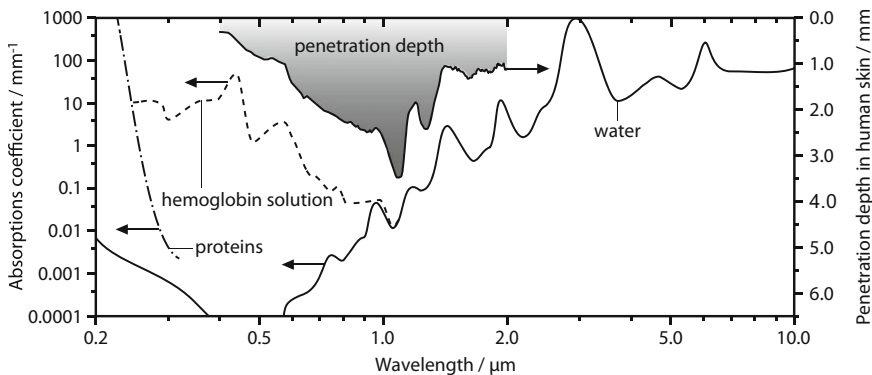


Fig. 24.2 Wavelength-dependence of the absorption coefficients of water, hemoglobin (7 g/dl in H₂O, desoxygenized) and proteins. The latter determine the penetration depth of light in human skin in the UV spectral range, while water and hemoglobin dominate the absorption in the visible and infrared range. Apart from absorption, scattering of light in skin tissue must be considered (data taken from A.N. Bashkatov, E.A. Genina, V.I. Kochubey, and V.V. Tuchin, J. Phys. D: Appl. Phys. 38, 2543 (2005) as well as G.M. Hale and M.R. Querry, Appl. Opt. 12, 555 (1973))

power. The effect occurs when the penetration depth of the radiation in the tissue is in the range of micrometers and the pulse duration is sufficiently short that no substantial heat conduction occurs during this period. The pulse duration for which heat conduction is negligible can be estimated from (23.1) by inserting the penetration depth for the parameter d . Hence, tissue is removed by short pulses without thermally damaging the surrounding tissue through heat conduction. Photoablation is performed using excimer lasers (ArF , XeCl) or frequency-converted solid-state lasers emitting in the ultraviolet spectral region. Another possibility is provided by the erbium laser operating in the infrared at $2.9\ \mu\text{m}$. In the ultraviolet spectral range, the ablation can also be achieved by direct breaking of chemical bonds (photochemical ablation).

The removal of (fatty) deposits in blood vessels, so-called arterial calcifications, by means of angioplasty involves a laser beam introduced into the artery via glass fiber catheter to carry the deposits away. A further application of photoablation is the photorefractive corneal surgery. Using an excimer laser (ArF , $193\ \text{nm}$) or frequency-quadrupled solid-state laser, the curvature of the cornea can be changed by ablation, thus providing a long-lasting alternative to eyeglasses or contact lenses. This procedure is known as laser-assisted in-situ keratomileusis (LASIK). Furthermore, lasers are also offered for photoablation in dentistry. For instance, the erbium laser is used for drilling to remove caries.

With further increase of the laser peak power, i.e. at higher power and shorter pulse durations, occurs optical breakdown (plasma generation), producing a pressure wave which can lead to photodisruption. This effect is used in ophthalmology to destroy the cataract membrane and in urology to destroy kidney and bladder stones (lithotripsy). An interesting photochemical application is the so-called photodynamic therapy of tumors. A drug is selectively attached to the tumor tissue by intravenous injection. Irradiation of the tissue with a diode or dye laser at $630\ \text{nm}$ wavelength leads to the decomposition of the drug into radicals that destroy the tumor. For instance, small scattered bladder tumors can be treated this way. The underlying mechanism of biostimulation has not yet been fully understood. Here, a weak laser (mW) is used to accelerate the growth of cells or to initiate other medical effects.

The most important medical lasers are listed in Table 24.1. Aside from semiconductor lasers listed in Table 24.2, which become more and more prevalent, the classical and well-established Nd:YAG and CO_2 lasers are still widespread. While the conventional laser sources are characterized by high radiance or brightness (power per unit area and per solid angle) and therefore well-suited for ablation and cutting processes, diode lasers are more compact, more efficient and operate at specific wavelengths that are not accessible with solid-state or gas lasers. Diode lasers emitting at wavelengths around $1.5\ \mu\text{m}$ are of particular interest, as radiation in this spectral range is strongly absorbed by water-containing tissue. This opens new applications in urology and thoracic surgery. Diode laser emission from 1.5 to $2.0\ \mu\text{m}$ wavelength can be transmitted through standard optical fibers, hence providing a promising alternative to CO_2 , erbium and holmium lasers previously used

Table 24.1 Specifications and application domains of selected medical lasers

Laser type/ operation mode	Wavelength/ power or pulse energy	Penetration depth in tissue/mechanism of action	Application examples
Excimer laser (ArF) pulsed (ns)	193 nm 10 mJ	Penetration depth: 1 μm Photochemical ablation	Corneal surgery on the eye by refractive corneal surgery (LASIK procedure)
KTP laser (SHG-Nd:YAG) quasi-cw/ pulsed (ns)	532 nm 1–200 W/ 1 J	Penetration depth: 0.5 mm (absorption by hemoglobin) Coagulation, selective photothermolysis	Retinal surgery, urology, dermatology (tattoo removal), ENT (ear, nose, throat), surgery, cosmetics
Dye laser cw pulsed	400–800 nm 5 W	Penetration depth: a few mm Coagulation, photochemistry	Dermatology, photodynamical therapy
Alexandrite laser pulsed (ns)	700–800 nm 0.1 J	Penetration depth: a few mm Photodisruption, thermal effects	Lithotripsy, removal of hair and tattoos
Titanium-sapphire laser/ Nd:YLF laser pulsed (fs)	800 nm/ 1053 nm few mJ	Photodisruption (opto-mechanical effects)	Corneal surgery on the eye (femto-LASIK, cutting of flaps)
Diode laser cw (see Table 24.2)	around 900 nm or 630 nm 10–100 W around 1500 nm	Penetration depth: several mm Coagulation Penetration depth: sub-mm	Surgery, urology, gynecology, ENT, photodynamical therapy
Nd:YAG laser cw/ pulsed (ns)	1064 nm 10–50 W/ 10–100 mJ	Penetration depth: several mm Coagulation, photodisruption (opto-mechanical effects)	Surgery, gynecology, urology, stone fragmentation, dermatology, removal of inner eye posterior membrane
Holmium laser/ Thulium fiber laser quasi-cw	around 2.0 μm 200 W	Penetration depth: 0.1 mm (absorption by water) Thermal effects	Urology
Erbium laser pulsed	2.9 μm 10 mJ	Penetration depth: 2 μm (absorbed by water) Thermal photoablation	Dermatology, dentistry
CO ₂ laser cw or pulsed	10.6 μm 50 W	Penetration depth: 10 μm (absorption by water) Thermal effects	Surgery, dermatology

Table 24.2 Wavelengths of diode lasers for specific medical applications (source: M. Schulze, Coherent Inc., 2018)

Medical field	Applications	Wavelength (nm)
Aesthetics	Acne treatment	450, 1470
	Hair and wrinkle removal	766, 810, 915, 1064, 1210
	Laser skin resurfacing	810, 915
	Lipolysis	1064, 1210,
	Pigmented lesions	810, 940, 980,
	Tooth whitening	810, 980,
Diagnosis	Varicose vein removal	940
	Spectroscopy (Fluorescence, Raman)	405, 532, 670, 690, 785, 830, 1064
Photodynamic therapy	Age-related macular degeneration	689, 752
	Cancer treatment	635, 652, 670
	Wound healing	405, 980
Surgical treatment	Dental treatment	980
	Endovenous treatment	940
	General surgery	980, 1064, 1320, 1470, 1550,
	Micro surgery	1940
	Urology	980, 1064 980, 1320, 1470

due to their low penetration into biological tissue. However, replacement of conventional laser types requires re-validation of established surgical techniques.

Excimer, diode and so-called KTP lasers are primarily employed for eye surgery. The latter represents the frequency-doubled Nd:YAG laser at 532 nm wavelength where second harmonic generation is realized in a KTP crystal. Using a laser beam, the doctor can easily penetrate the eye lens to treat the interior of the eye. Retina treatments based on this technique have become a standard procedure.

In general, femtosecond lasers are increasingly attractive for medical applications. The very high peak power and extremely short exposure time results in sharp ablation borders due to nonlinear absorption, thus offering broad deployment opportunities and a high marketing potential.

The major advantages of lasers for medical purposes include the possibility to perform sharp and non-bleeding incisions into tissue by the coagulation of blood vessels as well as precise tissue removal by photoablation. Moreover, the use of the laser allows to access body cavities via glass fibers and the interior of the eye and the eye lens area. Microsurgery is facilitated by the simple combination of the laser source with microscopes and other optical devices.

Disadvantages of lasers in medicine were considered to be high equipment complexity and resulting high cost. However, compact solid-state and fiber laser as well small and reliable diode lasers (Table 24.2) make medical systems cheaper and more stable at reduced costs so that medical laser applications become increasingly widespread. With the rapid development of laser technology, particularly in the fabrication of tailored semiconductor diode lasers, considerable progress in terms of practicability is expected in the coming years.

24.2 Laser Surgery

Medical therapies with (laser) light have a long history. The treatment of skin diseases by light therapies, the promotion of vitamin D production by irradiation with UV light and the use of sun radiation for the treatment of eye diseases are just as important as the first applications of a ruby laser in 1961 and 1963 in ophthalmology and dermatology, respectively. With the development of the various laser types like the argon ion, helium-neon and CO₂ lasers, more and more applications were being discovered over the following years. In 1971, it was finally possible to couple Nd:YAG laser radiation into an optical fiber, making endoscopic interventions possible. To date, a large variety of laser surgical systems for different indications has been developed. New advancements are being made in eye surgery, photodynamic therapy, lithotripsy in the bladder and kidney, laser-induced interstitial thermotherapy (LITT) for the destruction of tumors, and, not least, aesthetic and cosmetic surgery.

The treatment of diseased tissue using lasers is used in various medical disciplines:

- Aesthetic/cosmetic surgery
- Dentistry
- Dermatology
- Eye surgery
- Gastroenterology
- Gynecology, urology
- Neurosurgery
- Oncology
- Otorhinolaryngology
- Pulmonology
- Proctology
- Thorax surgery
- Vascular surgery
- Visceral surgery.

A selection of laser techniques and applications in different medical fields is presented below.

Laser-Induced Interstitial Thermotherapy (LITT), Laser Coagulation

In the last few years, LITT has emerged as an effective minimally invasive procedure for the treatment of certain cancer diseases. It focuses on the thermal treatment of malignant tissue by means of laser light. The therapeutic effect is based on the conversion of the light absorbed by the tissue into heat, with the absorption

characteristics varying greatly with the type of tissue. In contrast to healthy tissue, tumor cells show a different sensitivity to hyperthermic exposure. Hence, proper regulation of the temperature during the LITT allows for targeted destruction of diseased tissue, while preserving healthy tissue. A frequent application of LITT is the obliteration of liver tumors. For this purpose, a glass fiber is injected into the tumor to deliver the output of a cw Nd:YAG laser to the carcinogenic tissue which selectively absorbs the light and is thus heated up. At about 60 °C, the protein coagulates, leading to the death of the malignant cells which are later decomposed by the body. In ophthalmology, this principle is utilized for transpupillary thermotherapy (TTT), employing a near-IR cw diode laser at 810 nm wavelength as an additive to ¹⁰⁶Ruthenium-brachytherapy for choroidal melanoma (sandwich technique). Low Level Laser Therapy (LLLT) is possible also below 60°C.

Removal of Skin Lesions

In aesthetic surgery, cosmetically disturbing skin lesions are precisely removed by laser irradiation. Here, it must be ensured that the laser radiation is restricted to the desired regions so that the affected skin is selectively removed (ablated) while the neighboring faultless skin areas remain unaffected as much as possible during the treatment. Hence, it is necessary to control the temperature in the vicinity of the applied laser beam and to keep it low by a suitable choice of the laser parameters.

Ablation of Tumor Precursors and Tumors

Similar requirements have to be met in the treatment of skin alterations in body cavities. Examples are the resection of cancerous tissue on vocal cords in otorhinolaryngology (ear, nose and throat surgery, ENT), on the cervix in gynecology or on the urethra in urology.

Removing Deposits in Vessels

A highly local application of laser in medicine is the removal of deposits in blood vessels. This task necessitates accurate temperature control, both to avoid damage of the vessel wall, and to regulate the convection of heat through flushing liquids.

Tissue Cutting

Lasers are widely used for tissue cutting based on vaporization and thermal ablation. Again precise regulation of the temperature is necessary to prevent

carbonization and coagulation of tissue regions adjacent to the cut. Applications are found in various fields of surgery.

Medical and Surgical Treatment of Eye Diseases

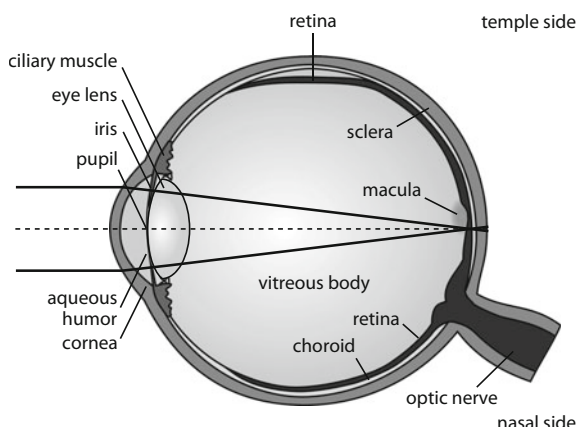
In 1949, Gerhard Meyer-Schwickerath used the sun light and the emission of xenon lamps to treat precursors of retinal detachment and thus one of the causes of blindness after having found that small scars in the retina limit such detachments. Following this approach, intense light is focused on the retina (Fig. 24.3) by an optical system such that the absorbing pigment epithelium is locally heated and scarred after coagulation. The nutrition and function of the neighboring outer layers of the retina comprising the light-sensitive rods and cones remain intact. The latter are responsible for the transmission of light information (brightness, color) to the brain. Likewise, the signal transmission through the nerve fibers located in the inner layer of the retina is unaffected.

Light coagulation in the eye, predominantly performed using solid-state lasers in the visible (532 nm) and infrared spectral range (810 and 1064 nm), is also used for the treatment of diabetic eye changes, occlusions of the eye fundus, degeneration of the macula (yellow spot on the retina in the middle of the eye background) as well as for pressure reduction in glaucoma.

The macula is essential for detailed fine vision tasks such as reading and recognizing faces and colors. The rest of the retina has lower local resolution but is very important for the peripheral field of vision, and hence for orientation and motion detection.

Lasers are widely employed to treat defective vision which, in most cases, is caused by irregular length of the eyeball resulting in a mismatch between the focal length of the optical system and the lens-retina distance. Defective vision can be

Fig. 24.3 Horizontal cross-section of the human right eye. The cornea and lens focus light onto the retina which transmits an electrical signal to the brain via the optic nerve



corrected with spectacles or contact lenses. An eye with normal visual acuity has refraction tolerance within the diopter range of -0.50 to $+0.50$. Near-sightedness (or myopia, eyeball too long, negative diopters) leads to blurring in the distance and can reach extreme proportions, e.g. -25.00 diopters, far point: 4 cm.

Laser treatment involves ablation (flattening) of the corneal surface and offers correction by up to about 6 diopters. When the surface is ablated directly from the surface using an excimer laser at 193 nm, the technique is called photorefractive keratectomy (PRK). During the procedure, the epithelial layer of the cornea has to be removed or pushed back. Although the layer grows back in a few days, the recovery phase is usually painful. In laser in-situ keratomileusis (LASIK), a thin lamella (flap) (diameter about 9 mm, thickness between 100 and 160 μm) is cut into the cornea using a microkeratome (corneal planer) or femtosecond laser (femto-LASIK). This flap maintains a connection to the remaining cornea serving as a “hinge”. After the cut, the flap is lifted to allow the excimer laser beam access to the exposed corneal tissue for ablating it according to the required correction. When the flap is folded back, it immediately adheres, while the change in curvature proceeds to the corneal surface. As the LASIK procedure is usually painless and involves short rehabilitation after the surgery, it is becoming more and more prevalent. This is especially true for femto-LASIK due to fewer complications compared to the use of a microkeratome.

A cataract describes the partial or complete turbidity (“clouding”) of the eye lens resulting in reduced visual acuity as well as diminished contrast and color vision. The clouded lens can almost always be surgically replaced by an artificial lens implant. For this purpose, a femtosecond laser can fulfill two tasks within the surgery: the opening of the anterior capsule and the dissection (fragmentation or pre-fragmentation) of the lens. Advantages of the femtosecond laser are the much more precise cutting in the capsule opening procedure and the small-scale disassembly of the lens, offering a much weaker additional ultrasound radiation than usual. The latter is harmful to the corneal endothelium. As a late consequence of the cataract surgery, a hazy membrane may form just behind the intraocular lens implant (posterior capsule) with a corresponding loss of vision. For the treatment of the so-called after-cataract, the pupil is medicamentously dilated and the rear lens capsule is opened using pulses from a Q-switched Nd:YAG laser, thereby eliminating the turbidity in an ambulatory and painless manner.

Different laser sources are employed for laser-assisted glaucoma treatment for lowering the eye pressure. In trabeculoplasty, the emission of a cw frequency-doubled Nd:YAG laser at 532 nm is focused to approximately 100 spots ($50 \mu\text{m}$, 0.2 – 1.0 W, 100 ms exposure time) in the area of the outflow paths of the aqueous humor (trabecular mesh of the chamber angle) in order to reduce the drainage resistance, and in turn, the intraocular pressure. Alternatively, pulsed lasers in the green spectral region with much shorter exposure time (3 ns) are used, while fewer and larger spots are illuminated, e.g. $40 \times 400 \mu\text{m}$. This method is referred to as Selective Laser Trabeculoplasty (SLT).

Cyclophotocoagulation involves the reduction of the intraocular pressure by obliteration of the ocular water-forming structures of the eye (secreting epithelium

of the ciliary body). Using infrared cw lasers (usually diode lasers at 810 nm, or Nd:YAG lasers at 1064 nm), the pigmented ciliary epithelium is coagulated externally on the conjunctival sclera surface without opening the eyeball, since the sclera is transparent at the laser wavelength (about 20 spots, 0.5–2.0 W, 2 s exposure time). However, because of the proliferation of the ciliary epithelium, the effectiveness is limited to short periods.

Urology

Lasers are especially suited for the treatment of the benign enlargement of the prostate. The laser beam is directed to the affected area via a fiber optic endoscopic system, the cystoscope, to vaporize prostate tissue. Frequency-doubled Nd:YAG lasers (532 nm), diode lasers (900–1300 nm), holmium lasers (2300 nm) as well as thulium fiber lasers (1900–2000 nm) with powers of up to 200 W are used for this purpose. Another application is the destruction of stones (lithotripsy) in the urinary tract and gall bladder. Here, pulsed laser emission is guided to the stone through an optical fiber. Due to the high power density (e.g. 10^{11} W/cm²), a plasma is formed on the stone surface, creating a pressure wave in the stone due to plasma expansion. This crushes the stone and enables the removal of the small fragments. Nd:YAG lasers are often deployed in a double-pulse process using both the fundamental and frequency-doubled emission at 1064 and 532 nm with pulse durations of around 1 μs, pulse energies of 200 mJ and repetition rates of up to 20 Hz. Other lithotripsy devices are based on holmium or alexandrite lasers.

ENT Surgery

The CO₂ laser is traditionally used for the treatment of ear, nose and throat pathologies due to its good precision in cutting combined with the excellent coagulation effect. For instance, it is used for the surgery of soft tissue tumors where the beam is coupled into surgical microscopes and directed to the areas to be treated without contact. Larger and smaller tumors can be vaporized or coagulated, e.g. inside the larynx (see Fig. 24.4). Furthermore, constrictions of the trachea can be widened. Typical laser powers are in the range of several tens of watts.

Fiber-coupled infrared lasers with wavelengths around 1 μm are used for nasal cavity surgery in chronic nasal obstruction. In the so-called conchotomy, parts of the turbinate are coagulated or evaporated, to reduce their swelling. Furthermore, superfluous mucous membrane of the soft palate can be removed to solve snoring problems. Compact Nd:YAG lasers and diode lasers are mainly applied, as they offer rechargeable battery operation with about 10 W laser power.

Alternatively, the frequency doubled Nd:YAG laser at 532 nm wavelength is employed whose emission is strongly absorbed by red tissue such as blood vessels

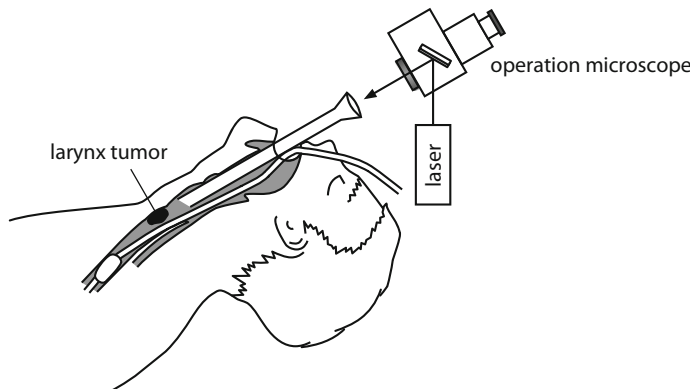


Fig. 24.4 Laser microsurgery of the larynx e.g. for the removal of tumors on the vocal cords

or skin pigments. Therefore, in addition to applications in the nasal cavity, it is well-suited for treating spider veins or blemishes of the epidermis.

Pulsed Er:YAG lasers at $2.9\text{ }\mu\text{m}$ are used to process bones through the process of photoablation. The penetration depth of the radiation in tissue and bone is around $1\text{ }\mu\text{m}$, thus allowing very precise surgical interventions in the middle ear.

Laser in Dentistry

Photoablation of hard tissue using erbium lasers (Er:YAG at $2.94\text{ }\mu\text{m}$ or Er:Cr^{3+} : YSGG at $2.78\text{ }\mu\text{m}$) also forms the basis for many dentistry applications where the conventional dental drill can (at least partially) be replaced. The removal of caries, for example, can be performed with considerably lower temperature than during drilling and thus reduced risk of cracks, due to the short exposure time and low penetration depth of the pulsed erbium laser emission in the tooth substance. Moreover, the treatment is less uncomfortable for the patients.

Using the infrared radiation of a CO_2 laser, tissue can be coagulated, cut or vaporized in the oral cavity, enabling high efficiency and effectiveness of a variety of treatments. Reduction of heat conduction is achieved by generating so-called “superpulses” in the ms- and μs -range. Examples are the correction and removal of lip and tongue ligaments or the treatment of sensitive tooth necks. Aphthous and cold sores (herpes simplex) can be irradiated for a few seconds, resulting in immediate relief of pain.

Nd:YAG and diode lasers are used for root canal treatment, the treatment of gum diseases (periodontitis) and for surgical interventions where significant germ reduction in infected root canals or periodontal pockets is achieved. Germ removal can be also accomplished by means of photodynamic therapy using diode lasers, e.g. at 810 nm .

Dermatology

Pulsed lasers emitting in the visible spectral region are particularly suitable for the therapy of extended veins (telangiectasia), port-wine stains (nevus flammeus), rosacea and spider veins. For instance, 595 nm radiation is mainly absorbed by hemoglobin (selective photothermolysis), so that a scar-free, selective removal of blood vessels can be achieved while preserving the surrounding tissue. Typical pulse widths are between 0.4 and 40 ms with energy densities around 10 J/cm^2 . The radiation penetrates about 1.5 mm into the tissue. Other applications include the removal of warts, scars, eczema and others. Similar tasks are undertaken with the frequency-doubled Nd:YAG laser at 532 nm which has a slightly smaller tissue penetration depth. Deeper penetration for the therapy of deeper lying vessels is accomplished with the Nd:YAG laser at 1064 nm.

The CO₂ laser has a penetration depth of only 10 μm so that treatment on the surface is possible. The erbium laser at 2.9 μm has an even shorter penetration depth of only 1 μm, offering more accurate removal of tissue without thermal damage of the skin regions underneath. The UV radiation of the excimer laser at 308 nm is, amongst others, used to treat psoriasis and vitiligo.

Aesthetic Surgery

In aesthetic surgery and cosmetics lasers are predominantly used for hair and tattoo removal and wrinkle smoothing as well as for the correction of superficial cosmetic damage of the skin. For the removal of tattoos, Q-switched ns pulses of a Nd:YAG laser (1064 or 532 nm) or alexandrite laser (755 nm) are used. Since the latter can be also employed as pump source for the Nd:YAG crystal, simultaneous operation at all three wavelengths is optionally available with only one laser system. The multi-wavelength approach allows destruction of tattoo pigments of different color with a few joules of pulse power.

In addition to flash lamps laser pulses in the range of 50 ms are utilized for hair removal. Diode lasers at 810 nm or Nd:YAG lasers are particularly applicable. At typical energy densities on the order of 10 J/cm^2 , the melanin absorbing the laser emission is thermally altered causing more or less permanent destruction of the hair follicles. Since light hair contains little or no melanin, the laser process works poorly in this case. In wrinkle smoothing, thermal effects on the production of collagen in the dermis are stimulated by laser pulses with duration of about 50 ms in the infrared range (Nd:YAG or diode laser).

Another method involves removal of the upper layers of the skin using a pulsed CO₂ laser to create skin rejuvenation. Spider veins and other skin anomalies can also be removed with the laser as mentioned above. Port-wine stains, for instance, can be treated with pulsed (few ms) dye lasers emitting in the orange spectral range (595 nm)

or red diode lasers. The absorption of the light by the hemoglobin molecules raises the temperature, thereby closing the blood vessels. Other laser applications can eliminate age spots, couperose, erythema, sebaceous cysts and fibroids.

24.3 Biophotonics and Spectroscopic Diagnostics

Biophotonics deals with the interaction of light with biological substances such as tissue and cells. This field is of great interest in medical, biological and biochemical research and diagnostics. Over the last decades, a number of optical methods, using lasers as light sources, have become much more powerful or even the only possible procedures in this domain. Spectroscopic and imaging techniques that have found wide application in medical diagnostics and biophotonics are outlined below.

Absorption and Fluorescence

When light of suitable wavelength is incident on biological molecules, it can be absorbed, resulting in a transition of the molecule from the ground state S_0 into an electronically excited state S_1 or S_2 (Fig. 24.5, also Figs. 1.9b and 1.10). The absorption often takes place in the so-called singlet system, where the total spin of the molecule is zero (molecules usually have an even number of electrons and if the electron spins are anti-parallel the total spin is zero). When a sample of molecules is examined the absorption leads to a characteristic minimum in the spectrum of the light passed through sample, a fact that can be used to determine the nature of the molecules in the sample.

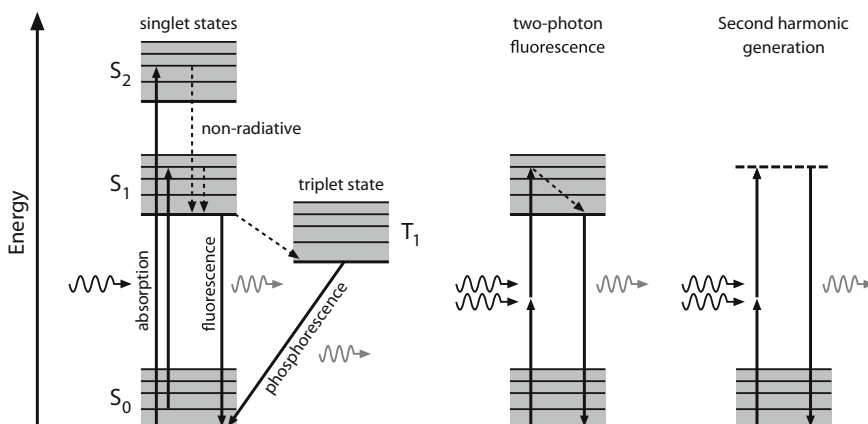


Fig. 24.5 Energy level diagrams for fluorescence, two-photon fluorescence and second harmonic generation (the phosphorescence process is only shown in the fluorescence diagram)

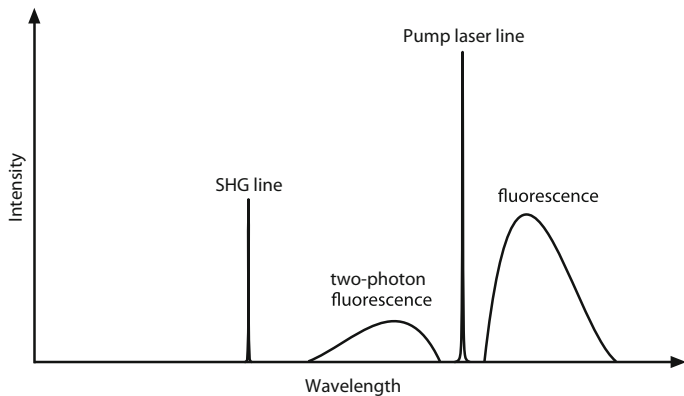


Fig. 24.6 Qualitative emission spectra for fluorescence, two-photon fluorescence and second harmonic generation

After absorption, the excited molecule is quickly transferred (within ps) to the lowest rotational-vibrational level of the singlet state S_1 . From there, fluorescence transitions to the ground state S_0 take place, resulting in the emission of photons with specific wavelengths that can be analyzed, e.g. to study the molecular composition of organic compounds or to differentiate between malignant and benign tissue. The lifetime of S_1 is typically in the ns-range. Since the transition can terminate in different overlapping rotational-vibrational levels of S_0 , the fluorescence spectrum is continuous with wavelengths longer than the excitation wavelength (see Fig. 24.6).

The spectral analysis of biological samples is often performed in combination with so-called fluorophores (dyes) which enable the detection of biological macromolecules or pathogens. The fluorophores are introduced into the biological tissue and anneal with pathogens thereby labeling them. Fluorescence methods are generally more sensitive compared to spectroscopic techniques based on absorption. However, not all molecules and biological samples show fluorescence. According to Fig. 24.5, a part of the excited molecules is transferred from the singlet state S_1 to the long-lived triplet state T_1 via intersystem crossing rather than radiation. Triplet states are characterized by parallel spin of electron pairs in the molecule. Therefore, relaxation to the singlet ground state can only occur with a spin-flip through the process of phosphorescence which takes place on slow time scales (up to several seconds or even hours) and thus is rarely used for spectroscopic applications.

Fluorescence Microscopy and Imaging Techniques

In fluorescence microscopes, fluorescence is exploited for imaging of biological tissues, cells or subcellular structures. For this purpose, the laser beam is coupled

into the beam path of a microscope via a selective mirror. In most cases ultraviolet lasers, e.g. frequency-multiplied solid-state lasers, are used. The part of the sample within the field-of-view of the microscope is excited to produce fluorescence. In the regime of weak fluorescence, scanning microscopes are used where a diffraction-limited laser beam is focused onto the sample by a lens. Scanning of the laser beam or sample creates an image. Fluorescence is also used in flow cytometry to identify cells (see below).

More specific and meaningful investigation of biological samples is possible by recording fluorescence (or emission) spectra for a range of different excitation wavelengths. In this way, a two-dimensional emission map is obtained by plotting the emission intensity as a function of excitation and emission wavelengths. This method is particularly suitable for studying the autofluorescence, i.e. fluorescence without dyes or exogenous fluorophores, in living tissue (*in vivo* analysis). The absorption and emission spectra of several endogenous fluorophores are depicted in Fig. 24.7.

A variety of microscopic techniques based on fluorescence has been established over the years and two of these techniques are briefly presented here.

Fluorescence Lifetime Imaging Microscopy (FLIM): The lifetime of the fluorescent radiation from a molecule provides additional information about the nature of that and its interaction with the environment. FLIM measures the spatial distribution of the lifetime of excited molecules in a sample using a microscope. This distribution can be color-coded and hence be used to construct an image of a biological sample and its composition.

Total Internal Reflection Fluorescence Microscopy (TIRF): Total reflection occurs when light travels from a more optically dense medium, i.e. a medium with higher refractive index, to a less optically dense one and the angle of incidence (with respect to the surface normal) is larger than the so-called critical angle (Sect. 14.1). During the process, light partially enters the region of lower refractive index, where the penetration depth is on the order of the light wavelength and depends on the angle of incidence. This effect is exploited to excite fluorescence in

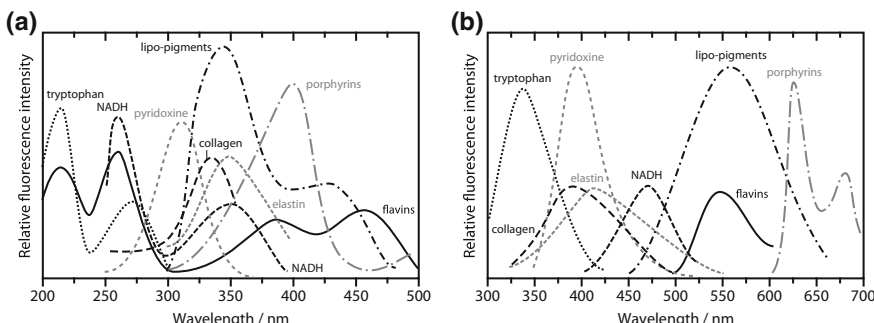


Fig. 24.7 **a** Absorption and **b** emission spectra of various endogenous tissue fluorophores (data taken from G.A. Wagnières, W.M. Star and B.C. Wilson: *In Vivo Fluorescence Spectroscopy and Imaging for Oncological Applications*, Photochem. Photobiol. 68(5), 603–632 (1998))

a very thin layer of the sample. As a result, the undesired background radiation is significantly reduced so that the fluorescence of individual molecules can be detected.

Immunofluorescence

An interesting feature of fluorophores is that they attach to very specific biological structures. This specificity is utilized in the well-known immunofluorescence to visualize the distribution of target biomolecules in the sample. For the detection of a certain antigen, e.g. a foreign protein, a suitable antibody is specifically manufactured. Antibodies (immunoglobulins) are proteins that are used by the immune system to neutralize pathogens such as viruses or bacteria. Antibodies are produced by leukocytes (white blood cells) able to recognize certain types of pathogens.

In immunofluorescence, specific antibodies are labeled with fluorophores before being introduced to the sample, where they couple with the desired antigen (protein). Thus, the protein can be detected by fluorescence. This antibody-antigen reaction allows the accurate identification of proteins, DNA, chromosomes and cell structures. Up to now, only a few fluorophores have been approved for medical *in vivo* use. The development of green fluorescent proteins (GFP) and variants by O. Shimomura (Japan), M. Chalfie and R. Y. Tsien (both USA) enabled the observation of complex biochemical structures and processes to gain extraordinary knowledge and insights into biological pathways. The three scientists were awarded the Nobel Prize in Chemistry in 2008.

Two-Photon Fluorescence and Second Harmonic Imaging Microscopy

The excitation of (normal) fluorescence is usually achieved with blue or ultraviolet radiation around 400 nm, according to the typical spacing of the involved electronic levels. At high intensities, however, nonlinear optical effects become significant and the excitation of the electrons to the upper singlet states can also be achieved by two photons of half the transition frequency, as depicted in Fig. 24.5. This corresponds to excitation wavelengths in the near-infrared spectral region around 800 nm. In contrast to normal fluorescence, the emission spectrum of two-photon fluorescence is at wavelengths shorter than the excitation wavelength (Fig. 24.6). The near-IR excitation radiation has a greater penetration depth into tissue (in the mm-range), which is advantageous for many applications. Furthermore, the quadratic dependence of the fluorescence signal intensity on the excitation intensity allows for a more precise focusing of the scanning microscope and thus a better image resolution.

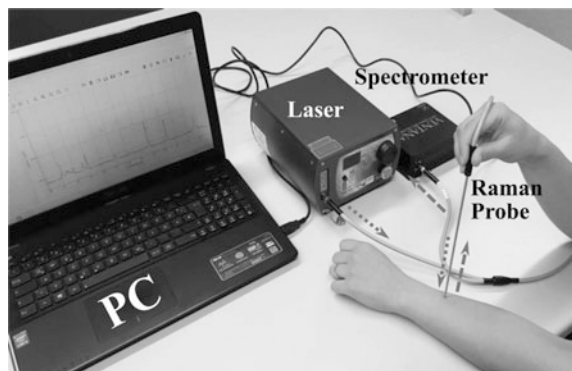
Nearly every physical effect can be used for imaging, including the nonlinear effect of second harmonic generation (SHG). For example, pulsed excitation at 800 nm produces a signal at 400 nm (Figs. 24.5 and 24.6). SHG only occurs in non-centrosymmetric molecules such as collagen having a helical structure. Consequently, the spatial distribution of collagen in biological samples can be visualized under a scanning microscope based on SHG.

Raman Spectroscopy and CARS

Raman scattering is described in Sect. 19.5. Here, (pump) light with frequency f_p is inelastically scattered from atoms or molecules involving a transfer of vibrational energy to or from the interacting medium. When energy is absorbed by the medium, the scattered light is called Stokes emission and has the frequency $f_s = f_p - f_R$ (see Fig. 19.10a), where f_R is the Raman (frequency) shift which depends on the excited vibrational mode of the interacting molecule. Hence, the Raman shift is characteristic of the molecules contained in a given sample. The Raman spectrum of biologically relevant molecules is often much more complex than the fluorescence spectrum. Therefore, it enables the detection of specific molecules in complex systems and additionally provides information on the structure of tissue. An example is the detection of β -carotene and antioxidants in the skin, where resonance enhancement of the Raman line is achieved by appropriate choice of the excitation wavelength.

The (spontaneous) Raman scattering effect is very weak and thus generally leads to very low scattering intensities. Nevertheless, using intense lasers as excitation sources, Raman spectra can be obtained in practicable measuring times (Fig. 24.8). Another difficulty of Raman spectroscopy that follows from the weak inelastic scattering process, involving as few as 10^{-7} photons, is separation of the Raman signal from the much stronger Rayleigh signal resulting from elastic scattering. Hence, notch filters are used to single out the frequency range around the pump

Fig. 24.8 Photo of a Raman measurement setup: PC with analysis software, Raman diode laser (785 nm, 400 mW maximum power), Raman spectrometer and specially designed Raman fiber-optic probe (TU Berlin)



frequency. However, this prevents the detection of low-frequency Raman modes, e.g. with $f_R < 100 \text{ cm}^{-1}$.

Higher Raman intensities are reached by means of surface-enhanced Raman scattering (SERS) or stimulated Raman scattering (SRS) spectroscopy. In coherent anti-Stokes Raman scattering (CARS), two lasers are employed emitting at the pump and Stokes frequency, respectively. As a result, the difference frequency $f_R = f_p - f_s$ coincides with the frequency spacing of two vibrational levels of the sampled molecule, thus driving the molecular vibration very efficiently. Due to four-wave mixing and the enhancement of the Raman resonance, a very intense (blue-shifted) anti-Stokes line with $f_{AS} = f_p + f_R$ is produced which is sensitive to the vibrational signatures of the investigated molecules.

Optical Biosensors

Biosensors are used to detect analytes, i.e. a substances or chemical constituents in a biological sample. The analyte may be a macromolecule, enzyme, DNA, virus or any other biological element. It can also be an antigen to which an antibody may bind with high specificity. In a biosensor, this antibody is applied to a layer such that it only reacts with a single antigen. If this antigen is present in a biological sample, selective antibody-antigen binding occurs. This interaction can involve various optical effects, for instance change in the excitation wavelength through linear or two-photon fluorescence, Raman scattering and CARS, frequency doubling, or change in refractive index. In this fashion, biosensors offer the direct, real-time and label-free detection of many biological and chemical substances. Compared to conventional analytical techniques they provide high specificity, sensitivity, small sensor size and cost-effectiveness. A few variants of biosensors are explained in the following.

Optical biochip: A planar waveguide is coated with a matrix of different antibodies. The matrix can contain many hundreds of elements, each binding a different antigen. The latter is located on a biological sample which is brought in contact with the coated waveguide. The binding, for instance, alters the fluorescence signal. The read-out is performed by introducing a laser beam which propagates through the waveguide due to total internal reflection. As described for TIRF above, the radiation enters slightly into the coating where it produces a fluorescence pattern. The matrix is projected onto a two-dimensional detector array, e.g. an electronic camera. Using the optical biochip technology, a sample can be analyzed for hundreds of substances. In contrast, only one or more substances can be detected with a fiber-optic biosensor.

Interferometric biosensors: Protein structures and cells are often almost transparent in the optical spectral range often, which makes them difficult to detect by absorption measurements. Nevertheless, since the refractive index of the sample solution depends on the cell concentration, a precise measurement of changes in the refractive index allow for the detection of such cells. This is accomplished with

sensitive interferometers. For instance, compact Mach-Zehnder interferometers are employed to measure refractive index changes introduced by antibody-antigen binding in antibody-coated waveguides.

Surface Plasmon Resonance: So-called plasma oscillations occur in metal layers in which the valence electrons oscillate collectively with respect to the crystal lattice. Plasma oscillations are optically excited and exhibit a strong dependence on the exciting beam's angle of incidence. The excitation is hence detected by an increased absorption of a laser beam by the sample's surface. In a biosensor based on this principle, a thin metal film applied to a glass plate is coated with an antibody. In case of antibody-antigen binding, the frequency of the plasma resonance is altered. Consequently, the absorption minimum occurs at a different angle of incidence.

Flow Cytometry

Cytometry is the automatic detection and measurement of various attributes of cells, particularly blood components. In flow cytometry, a thin stream of fluid, e.g. blood, containing cells to be analyzed is produced. So-called hydrodynamic focusing is applied where the thin sample beam is forced out from a thicker sheath flow, as shown in Fig. 24.9. The small diameter of the laminar sample beam of about $20\text{ }\mu\text{m}$ ensures that the distance between the individual cells is large enough to only examine one cell at a time. A focused laser beam is directed across the sample beam. Cells passing by the laser beam change the scattered light optical properties which are analyzed to measure the characteristics of the cells. Amongst other physical and chemical characteristics, angle-dependent scattering efficiencies and fluorescence signals of up to thousands of particles per second can be registered. Fluorescence exhibits an isotropic angular distribution and is usually examined at an angle of 90° in combination with different color filters or a spectrometer.

Flow cytometry can also utilize fluorophores and immunofluorescence and be combined with an automated cell sorting system. In many applications, two different antibodies labeled with fluorophores are simultaneously investigated. Flow cytometry represents an important technology in the fields of biophotonics and medical diagnostics.

Optical Coherence Tomography

Medical X-ray fluoroscopy is associated with radiation exposure that increases the chance of cancer or genetic damage. This problem is avoided in magnetic resonance tomography (MRI), where high-frequency radiation is deployed in combination with strong magnetic fields to image internal organs and structures. Alternatively,

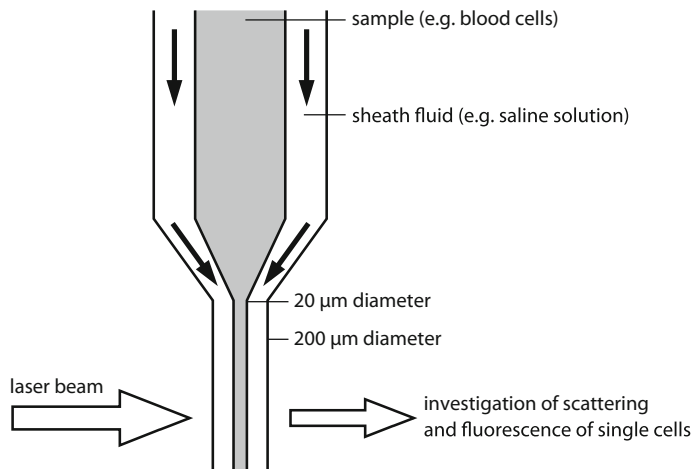


Fig. 24.9 Principle of flow cytometry. A liquid stream (sheath fluid) encompasses and thereby confines the investigated sample cells (hydrodynamic focusing). The cells are guided to a narrow channel where the liquid is illuminated by a focused laser beam. The angular distribution of the scattered light is analyzed to determine the shape and size of the cells, while the fluorescence spectrum provides information on the molecular composition

visible light and THz radiation is increasingly used for imaging internal structures in tissue. For example, an optical fluoroscopy device based on a near-infrared laser has been developed to transilluminate finger joints for rheumatic diagnostics.

Strong light scattering in tissue can be partially eliminated by irradiation with ultra-short pulses in the fs-range. During transillumination, only photons with the shortest transit time, i.e. photons that did not undergo scattering, are registered. The same can be achieved by using amplitude-modulated laser beams in the MHz-range (photon density waves) in conjunction with phase-sensitive detection. Another application example is optical mammography.

Optical coherence tomography (OCT) involves the illumination of tissue with focused broadband light from a superluminescent diode or supercontinuum laser having a very short coherence length in the μm region. The light is coupled into a Michelson interferometer where one arm contains the examined tissue while the length of the other (reference) arm can be varied by a translatable mirror. Constructive interference occurs if the path lengths in both arms are equal. Due to the short coherence length of the light source, only a very thin tissue layer contributes to the interference signal. As a result, the intensity of the interference signal can be used for high-resolution imaging. By scanning the mirror in the reference arm, a reflectance profile of the sampled tissue is obtained, thereby providing depth information about the structure of interest (A-scan). Lateral combination of a series of depth scans permits cross-sectional reconstruction of the sample (B-scan), yielding a three-dimensional tomographic image of the sample. An OCT device for the tomography of the retina and optic nerve is available on the market.

Optical Tweezer

The energy and momentum of a photon is related to the frequency f by $E = hf$ and $p = hfc$, respectively, where c is the speed of light. Momentum is a vector quantity with p describing its magnitude. When light is refracted, the momentum direction is changed while its magnitude remains invariant. Due to momentum conservation, the change in light momentum introduced by refraction causes an equal but opposite momentum change on the refracting medium, leading to a reaction force (momentum per unit time). This principle is exploited in optical tweezers to trap and move microscopic dielectric objects similar to conventional tweezers.

Here, a dielectric particle, e.g. a cell, is placed in the vicinity of an intense laser beam, which is usually tightly focused by a microscope objective. Owing to polarized electric field interactions, forces are exerted on the particle, particularly along the gradient to the region of maximum electric field, i.e. at the beam waist. Once the particle is trapped in the beam center, it can be translated in any direction by moving the focus. This enables the precise micromanipulation of cells and cell components as well as the measurement of the forces at piconewton (pN) levels. Amongst others, optical tweezers allow pulling apart of DNA clusters, analysis of molecular motors and the study of protein-protein bonds.

In many cases, the optical tweezer is combined with a so-called optical scissor. The latter is realized by a focused ultraviolet laser beam which can drill and cut precisely by photoablation. The combination of an optical scissor with an optical tweezer is, for instance, employed for the union of an egg cell with a specific sperm (in vitro fertilization). In 2018, the physicist Arthur Ashkin was awarded the Nobel Prize in Physics for the invention of optical tweezers and their application to biological systems.

Opto-acoustic Imaging

X-ray and ultrasound medical imaging are used for the diagnosis of breast cancer. Novel opto-acoustic systems enable clinicians to diagnose cancer promising a greater degree of specificity than ever before. The technology involves the generation of acoustic waves which are excited by laser pulses emitted into tissue. Strong absorption of the pulses leads to local tissue expansion and the emission of acoustic waves which are then detected on the tissue surface by an acoustic probe producing electrical pulses. By scanning the probe over the tissue surface, the acoustic intensity distribution is measured and the acoustic field in the tissue volume is calculated. Hence, opto-acoustic imaging allows to determine the source position, namely the strongly light absorbing region. Increased absorption may be due to different blood properties in benign or malignant tumors compared to normal blood so that tumors might be localized.

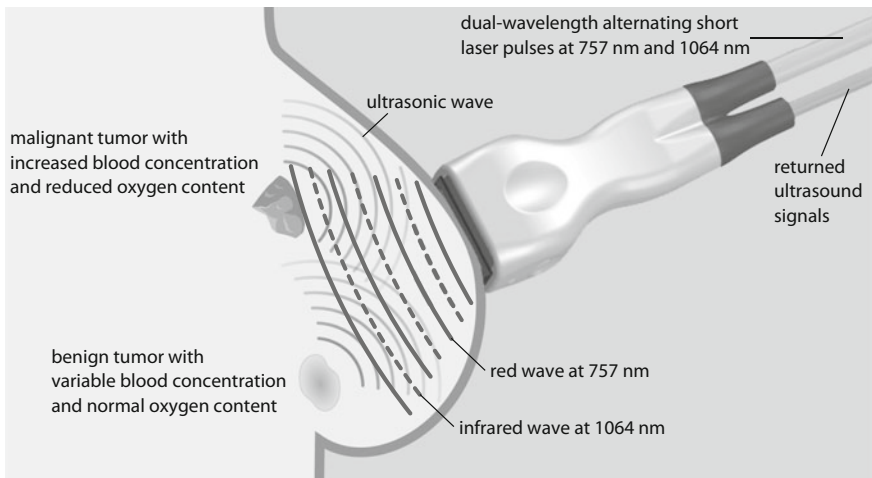


Fig. 24.10 Optoacoustic detection of breast cancer being developed by Seno Medical Instruments Inc. The system delivers pulsed laser radiation at two different wavelengths via fiber optic cables. When the two optical pulses impinge through a handheld probe upon the breast tissue, thermoelastic expansion of the tissue causes ultrasound pulses to be emitted from it. The two wavelength-specific backscattered acoustic signals are then detected by a transducer in the probe. While light at 757 nm wavelength is absorbed primarily by deoxygenated hemoglobin in the malignant tumor, light at 1064 nm wavelength is absorbed primarily by oxygenated hemoglobin. The two images created by processing of the opto-acoustic signals highlight the locations in the breast tissue where the hemoglobin is oxygenated or deoxygenated

It is expected that malignant tumors can be better distinguished from benign tissue using exciting laser pulses at different wavelengths. These are specifically chosen to enable the system to determine the relative amount of oxygenated and deoxygenated hemoglobin within blood vessels in the breast and surrounding tissue. For that reason, the handheld unit emits short pulses of laser light at two wavelengths: light at 757 nm wavelength is absorbed primarily by deoxygenated hemoglobin, whereas light at 1064 nm wavelength is absorbed primarily by oxygenated hemoglobin. The two images created by processing the opto-acoustic signals highlight the locations in the breast tissue where the hemoglobin is oxygenated or deoxygenated. While the presence of a malignant tumor may be highlighted by increased hemoglobin concentration and relatively decreased oxygen content, benign growths can be identified by a variable hemoglobin concentration with relatively more oxygenation. If the necessary imaging methods and technologies are well developed, the system will be able to determine both hemoglobin concentration and its relative oxygenation, so that clinicians have a better chance of making an accurate diagnosis.

A third set of ultrasonic signals is created by the excitation of the breast tissue in response to the additional ultrasound pulses emitted by the probe. By combining opto-acoustic imaging and traditional ultrasonic imaging, the system can employ just one ultrasonic transducer to detect all three ultrasound pulses and use the same

set of analog and digital electronics for signal acquisition and processing. The processed signals generated from, and then acquired by the transducer, are used to create a functional image of the breast similar to those seen on a traditional ultrasound, while the two opto-acoustic signals also captured by the transducer are processed to create functional images of the vessels within the breast.

Figure 24.10 sketches the operation of a device which uses the combination of light and ultrasonic pulses. The transducer in the probe detects both the morphologic ultrasonic signals reflected from various tissue structures in and around the lesions and the functional opto-acoustic signals. The signals are then processed and co-registered to produce both functional and anatomical images of the breast. The breast imaging system from Seno is currently CE-marked in Europe and being processed through the US FDA's Office of Device Evaluation. The new system should provide a more effective tool to help radiologists confirm or rule out malignancies than current diagnostic imaging approaches, all without exposing patients to the potentially harmful ionizing radiation from X-rays used in mammography systems, or the contrast agents used in MRI systems.

24.4 Biological Aspects of Laser Safety

When using lasers, the eyes and skin may be exposed to significantly higher irradiances compared to normal light sources. Therefore, working with lasers involves special hazards that, without taking proper safety precautions, can lead to serious accidents and damage to health. Most accidents involving lasers affect the eye. In the visible (VIS) and in the near-infrared (IR-A) spectral range, the retina is mainly damaged, while the anterior portions of the eye, such as the eye lens and cornea may be injured when operating in the ultraviolet (UV-A, UV-B, UV-C) and infrared (IR-B, IR-C) regions. There are also accidents caused by unintentional irradiation of the skin. The endangerment of the eye and skin comes from both direct laser beams and intense laser radiation reflected or diffusely scattered from other objects.

Absorption and Scattering

The absorption of laser light depends strongly on the nature of the tissue and the wavelength of the radiation. It is largely determined by the absorption of water, the blood pigment hemoglobin and, in the ultraviolet range, by proteins. The wavelength-dependence of the absorption coefficient for the three components is plotted in Fig. 24.2. Besides absorption, the propagation of light in tissue is also governed by scattering. Hence, the distribution of the laser radiation is commonly described in terms of the penetration depth, which also partly considers scattering properties of the tissue. As can be seen from Fig. 24.2 (right scale) and Table 24.3, radiation in the visible and in the near-infrared range (VIS and IR-A) penetrates

Table 24.3 Typical penetration depths ($1/e$ values) of laser radiation in human skin for different wavelengths

Wavelength (nm)	Penetration depth in skin
193 (UV-A)	1 μm
308 (UV-B)	50 μm
450–590 (VIS)	0.5–2 mm
590–1500 (VIS, IR-A, IR-B)	2–8 mm
2127 (IR-B)	0.2 mm
2940 (IR-B)	3 μm
10,600 (IR-C)	20 μm

several millimeters into human skin. However, there are considerable differences depending on the tissue type. In case of very strong absorption, the penetration depth can be calculated from the reciprocal absorption coefficient (penetration depth = $1/\text{absorption coefficient}$). This relationship is especially valid in the ultraviolet and infrared (IR-B and IR-C) spectral regions.

Strong absorption in the ultraviolet range is due to organic molecules such as proteins, resulting in a short penetration depth of several micrometers (Table 24.3). The absorption maximum of the nucleic acid DNA is around 260 nm. Irradiation in this range causes double-strand breaks and thus genetic defects (see below). In the visible region, various pigments, e.g. hemoglobin and melanin, are mainly responsible for the absorption. The penetration depth is a few 0.1 mm in the blue-green range. In the red and near-infrared spectral region (IR-A), the radiation penetrates deeper (a few mm) into the tissue (see Fig. 24.2). At infrared wavelengths above 2 μm , the absorption of human tissue is essentially determined by that of water. For instance, the penetration depth of laser radiation at a wavelength of 10.6 μm (CO_2 laser) is about 20 μm (Table 24.3). However, the infrared range features several characteristic absorption peaks at about 2 μm and 3 μm , where the penetration depth is 0.1 mm and 1 μm , respectively (Fig. 24.2).

Tissue contains numerous scattering centers which deflect the light in different directions. In case of elastic scattering, the wavelength remains unchanged during the scattering process. The radiation is thus transported through the tissue more or less diffusely in all directions. For molecules and very small structures whose dimensions are less than one tenth of the wavelength of the light, the scattering is weak and approximately spherically symmetric (Rayleigh regime). When the scattering centers are about the size of the wavelength, the scattering is stronger and primarily occurs in the forward direction. In the regime of Mie scattering, where the size of the scattering centers exceeds that of the light wavelength, strong forward scattering is observed. Although both Rayleigh and Mie scattering are present when light propagates through tissue, the latter predominates due the high abundance of larger structures.

Due to the low penetration depth of ultraviolet light in tissue, scattering is small and can hence be neglected in most cases (Table 24.4). In the visible spectral range, the radiation penetrates deeper into tissue, so that scattering processes are more frequent and just as relevant as absorption processes. This is especially true in the

Table 24.4 Comparison of absorption and scattering in tissue for different spectral regions

Spectral range	Comparison of absorption and scattering
Ultraviolet (UV)	absorption \gg scattering
Visible (VIS)	absorption \approx scattering
Infrared (IR)	absorption \ll scattering
Infrared beyond 2 μm	absorption \gg scattering

blue-green region. The penetration depth further increases to the mm-range towards the red and infrared (IR-A) region, where scattering dominates over absorption. In this regime, light is also transported in areas lateral to the incident laser beam. The diffusely backscattered radiation can amount to up to 50% of the radiation entering the tissue. Thus, the irradiance at the tissue surface can be significantly enhanced by scattering. Since absorption is very strong at wavelengths beyond 2 μm , scattering is negligible in this part of the infrared spectral range (Table 24.4). In regions where absorption predominates, the portion of light which is diffusely reflected at the tissue surface is about 5%.

Interaction of Laser Radiation with Tissue

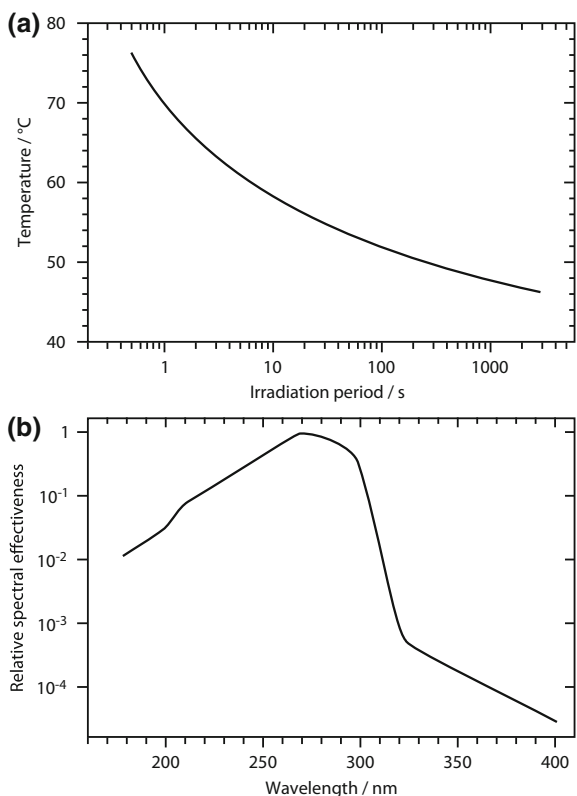
The absorbed laser radiation has diverse effects on tissue. To avoid accidents, it is important to understand the causes and extent of possible damage. Depending on the wavelength, power density and duration of the irradiation various interactions occur which can be classified as follows: thermal effects, photochemical effects, photoablation and photodisruption (Fig. 24.1).

Most laser damage is caused by thermal effects involving mechanisms that are summarized in Table 24.5. When the temperature rises only by a few degrees, reversible damage occurs. Figure 24.11a shows that the critical temperature for irreversible tissue damage depends on the irradiation period. For example, a temperature increase to 60 °C over a period of 10 s leads to coagulation.

Table 24.5 Thermal effects of laser radiation on tissue (from H.-P. Berlien and G. Müller: Angewandte Lasermedizin, Ecomed, Landsberg München Zürich (1989))

Temperature	Damage
37 °C	No irreversible damage
40–45 °C	Shrinkage of collagen, formation of edema, membrane loosening, cellular death (depending on exposure time)
50 °C	Reduction of the enzymatic activity
60 °C	Denaturation of proteins, onset of coagulation, formation of necrosis
80 °C	Denaturation of proteins, coagulation of collagen, membrane defects
100 °C	Drying
>150 °C	Carbonization and vaporization

Fig. 24.11 **a** Critical temperature for permanent tissue damage depending on irradiation period. **b** Relative spectral effectiveness describing the hazard of UV radiation. The maximum is around 270 nm where the carcinogenic potency is especially high



At temperatures above 100 °C, the tissue water evaporates. The tissue thus dries out and ultimately carbonizes. As the temperature increases further, tissue evaporates. The evaporation zone is surrounded by a charring and coagulation zone. If the temperature remains below 100 °C, only a coagulation zone is formed with an adjacent zone where reversible damage occurs. Due to heat conduction and scattering of the laser radiation, tissue outside the irradiated volume is also heated more or less quickly and potentially damaged.

The photon energy increases with decreasing wavelength. Therefore, photons in the blue and ultraviolet spectral regions have a higher energy than those in the red region, giving rise to photochemical damage. The photon energy absorbed by biological molecules such as DNA can cause alterations in the molecular structure. For instance, double-strand breaks occur, in which both strands in the double helix are severed, as depicted in Fig. 24.12. A photochemical damage is most likely when tissue is exposed to ultraviolet light and less pronounced in the visible spectral range from 400 to 600 nm.

DNA damage is particularly hazardous to the cell, as it can lead to genome rearrangements thus preventing the replication mechanism from functioning properly. Although there are cellular repair mechanisms that can correct individual

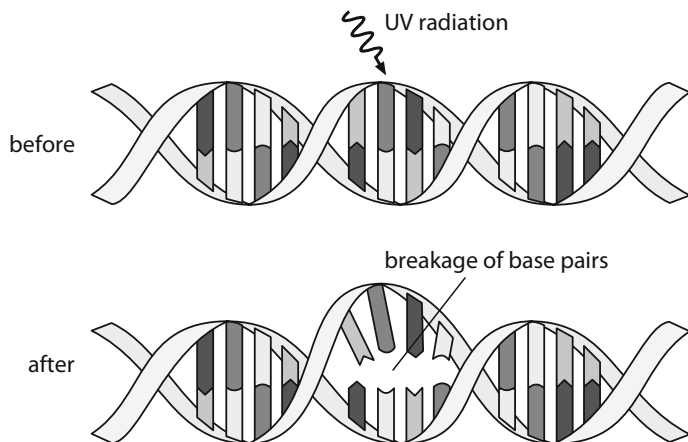


Fig. 24.12 Damage of the DNA helix (double-strand break) after exposure to UV radiation

damage to DNA, this is not possible in case the damage is too severe. The affected skin cells then die and are replaced by younger cells that emerge from deeper layers. If errors occur during the repair process, the cells can degenerate leading to skin cancer in the worst case.

In addition to these long-term effects, there are also short-term effects such as sunburn as well as photoallergic and photochemical reactions which can be aggravated by drugs or cosmetics (photosensitization). As described below, typical eye damages caused by ultraviolet light include, for example, keratitis, conjunctivitis or clouding of the eye lens (cataract). Furthermore, so-called blue light damage of the retina occurs in the wavelength range of from 300 to 600 nm.

The exposure limits for photochemical damage to the eye and skin are similar and very low. The maximum irradiation is 1 mW/m^2 for continuous wave lasers emitting at wavelengths below 315 nm and an irradiation period of one working day. This limit is about 10,000 times smaller compared to the visible spectral range. The relative spectral effectiveness of ultraviolet radiation, also known as hazard weighting function, is shown in Fig. 24.11b. The hazard is maximum in the UV-C spectral region around 270 nm.

The low exposure limit for ultraviolet radiation is due to the fact that the effects of individual irradiation doses add up. Hence, the repeated exposure to UV light increases the risk of skin cancer even if the doses are low. In this sense, tissue “remembers” every damage caused by natural and artificial ultraviolet sources, so that every sun bath and solarium visit have a long-term effect. It is important to note that DNA damage also occurs when no redness of the skin is visible. People who often expose themselves to ultraviolet radiation have an increased risk of damage to the genome of the cells, and hence skin cancer. Because of the long-term effects of ultraviolet radiation, hazard assessments for this type of radiation must be kept for 30 years.

When tissue is irradiated with short laser pulses in the range of nanoseconds to microseconds and intensities of about 10^9 W/cm^2 , it is evaporated. In case of strong absorption, the radiation penetrates only a few micrometers into the tissue, so that a very thin layer of tissue is heated and immediately evaporated within the pulse duration. Since the process is too fast for heat conduction to act, the surrounding tissue is only slightly heated. This process of removing a thin layer without heating adjacent material is called photoablation (Fig. 24.1).

For ultraviolet radiation, photoablation is predominantly based on a photochemical effect. Here, the energy of the photons is large enough to break molecular bonds. The resultant molecular fragments then escape from the material. Photoablation is for instance used in corrective eye surgery such as LASIK (see Sect. 24.2).

At even higher intensities, i.e. higher laser power and/or shorter pulse durations, a plume of plasma is formed consisting of free electrons and ions. In this regime, the electric field of the light wave is so high that a “laser spark” is generated, forming an intense pressure or shock wave around the spark which mechanically destroys the tissue. This process is called photodisruption. It is for example exploited for cataract extraction. Accidents during the treatment causing eye damage through the process of photodisruption are unknown.

Eye Hazards

The eye is at particular risk when working with lasers. Laser-induced damage of the eye has serious consequences, especially when the beam hits the yellow spot (macula) (see Fig. 24.3). The macula has a diameter of about 3 mm and contains about 4 million of the total of about 6.8 million photoreceptors (cone cells) which are responsible for color vision. In the center of the macula lies the fovea, a small indentation with 1.5 mm diameter containing the highest cone density, thus representing the site with the highest visual acuity.

When a laser beam in the visible or infrared spectral region (IR-A) is incident along the visual axis of the eye, it is focused onto the retina by the optical system of the eye (cornea and eye lens). The focus then lies exactly in the region of the fovea, and the focused radiation can coagulate and destroy retinal tissue (Fig. 24.13). This severe damage is perceived as a blind spot in the field of vision. Drastic consequences can also occur when the laser beam is focused onto the blind spot where the optic nerve exits the eye transmitting the visual information from the retina to the brain (Fig. 24.3). Here, the radiation can destroy the nerve tracts leading to considerable loss of vision. For other incidence directions of the laser beam, the focus is located in the peripheral areas of the retina. If the exposure limit is exceeded, the retina is coagulated at the focus position. At low power levels around 10 mW, the damage might not even be noticed. However, at higher levels, serious retinal damage occurs also outside the yellow and blind spot region resulting in severe visual disturbances.

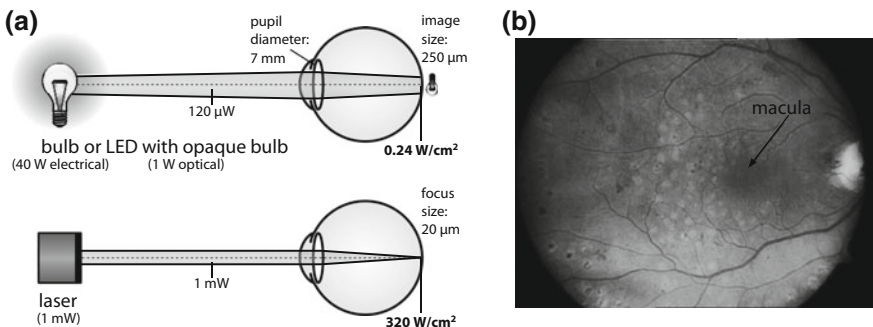
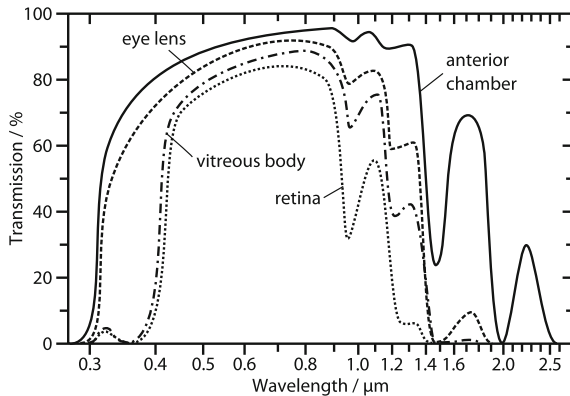


Fig. 24.13 **a** Imaging of a normal light source and a laser beam onto the retina. While the light from a normal source, e.g. a light bulb, produces a relatively large image, a laser beam is focused on a small spot of only a few tens of μm . **b** Photograph of retinal damage after laser treatment (laser power <100 mW, exposure time 0.1 s). The bright spots indicate already scarred tissue that was damaged by laser radiation. Aside from the macula, the blind spot with outgoing blood vessels is visible on the right edge (courtesy of Augenklinik Greifswald)

Fig. 24.14 Transmission of the human eye depending on wavelength. Laser radiation in the visible and near-infrared spectral region (IR-A) is focused onto the retina



The human eye is transparent for wavelengths in the visible spectral range between 400 and 700 nm. Thus, for visible laser sources, almost the entire laser power which is incident on the eye reaches the retina. The transparency range extends to the near-infrared (IR-A) region up to about 900 nm. At longer wavelengths, the transmission curve exhibits several dips, dropping to nearly zero at 1400 nm. Aside from retinal damage, IR-A radiation close to this wavelength additionally causes clouding of the eye lens. The transmittance of different components of the eye is displayed in Fig. 24.14. The minima are related to the absorption maxima of water (Fig. 24.2).

Infrared radiation (IR-B) from 1400 to 2500 nm is fully absorbed by the anterior areas of the eye, the cornea and lens. Hence, in case of an accident, the laser beam does not reach the significantly more sensitive retina. For this reason, lasers emitting at wavelengths longer than 1400 nm are often called “eye-safe”.

Nevertheless, corneal injuries can be very painful. Moreover, in contrast to the outer surface of the cornea (epithelium), the inner part (endothelium) cannot heal after damage.

At wavelengths above 2500 nm, the penetration depth in the cornea is well below 0.1 mm, especially around 3 μm (erbium lasers) and around 10 μm (CO_2 lasers). Consequently, laser radiation is absorbed in a very thin layer increasing the risk of corneal damage. As opposed to ultraviolet light, the damage is not due to photochemical but due to thermal effects for which the exposure limits are higher.

UV-A and UV-B radiation at wavelengths below 400 nm is absorbed in the anterior part of the eye and only partially reaches the eye lens potentially injuring the cornea and/or the crystalline lens. In contrast, at wavelengths below 280 nm, complete absorption takes place in the cornea, so that corneal damage occurs in case of accidental exposure of the eye to UV-C laser radiation.

A particular danger to the eye arises from the fact that the lens system formed by the cornea and the eye lens focuses visible and IR-A laser radiation onto the retina, as depicted in Fig. 24.13a. Due to the low divergence of lasers, the light is focused on a very small spot whose diameter is substantially smaller compared to normal light sources. The spot diameter is typically about 20–25 μm when directly looking into a laser beam.

In laser safety calculations an average pupil diameter of 7 mm is usually assumed. For a laser beam with the same diameter, focusing reduces the beam width by a factor of $\approx 10^5$, and the irradiance on the retina is hence increased by the same factor. This explains why even very low laser powers below 1 mW exceed the exposure limits and can cause retinal damage. When looking into a normal light source, a relatively large image of the source is produced on the retina. The radiation is thus distributed over a broad area. In addition, normal light sources radiate in all directions, and only a small portion of the radiation falls into the eye. This is fundamentally different for lasers where the entire output power may enter the pupil.

In a thought experiment, the eye is to be irradiated with a laser pointer having an output power of 1 mW. The focus diameter on the retina is assumed to be 20 μm . From these values one calculates an irradiance or power density of approximately 320 W/cm^2 (see Fig. 24.13a). This value should now be compared with the corresponding irradiance when looking into the sun. Here, a relatively large image of the sun is created on the retina with a diameter of 250 μm . The power density of the sun on the Earth (solar irradiance) is known as the so-called solar constant of about 1360 W/m^2 . Hence, considering the given image diameter, the power density on the retina is determined to be below 30 W/cm^2 . A glance into a laser with power of 1 mW thus produces a more than 10 times higher irradiance on the retina than when looking into the sun. The factor is much larger when comparing a laser to a light bulb (Fig. 24.13a), pointing out the hazard of lasers to the eye even at low powers as provided by laser pointers.

The considerable risk to the eye is also shown in Fig. 24.13b, which depicts a photograph of the retina after clinical treatment using a laser with power of less than 100 mW. Small coagulation areas are formed on the retina within a tenth of a second. Since these are located in the peripheral regions of the yellow spot and the

blind spot, they are hardly perceived as disturbing by the patient. In the event of an accident, however, severe damage can occur in the macula. While the retinal damage in Fig. 24.13b was caused by a green laser beam, similar tissue alterations are observed for IR-A laser sources. On the contrary, eye damage induced by infrared radiation in the IR-B and IR-C region manifests in the cornea and partially in the eye lens. The exposure limits for corneal damage are higher, as the anterior portions of the eye are less sensitive than the retina.

As stated above, ultraviolet radiation also does not reach the retina (Fig. 24.14), so that UV lasers primarily cause damage of the cornea and conjunctiva (UV-B and UV-C) as well as of the eye lens (UV-A). For instance, increased UV exposure may lead to keratitis and conjunctivitis which describe (often painful) inflammations of the cornea and conjunctiva, respectively. Usually, the cornea regenerates within two days, but strong or long-term irradiation causes scars and permanent damage to the eyes. Keratitis is mainly induced by UV-B radiation, whereas UV-C light is often responsible for conjunctivitis. Typical fluences causing keratitis and conjunctivitis are 100 and 50 J/m². UV-A and UV-B radiation can also provoke the formation of cataracts, i.e. the clouding of the eye lens which impairs the vision. Cataracts are most commonly due to the denaturation of proteins in the eye lens which is accelerated by exposure to ultraviolet light. The effects of laser radiation on the human eye and the resulting damages depending on the laser wavelength are summarized in Table 24.6.

Table 24.6 Damage of the human eye and skin caused by radiation of different wavelengths

Wavelength range (nm) and effect	Eye damage	Skin damage
100–280 (UV-C) photochemical effects	Keratitis and conjunctivitis	Erythema (sunburn), tissue alterations, skin cancer
280–315 (UV-B) photochemical effects	Keratitis and conjunctivitis, cataract	Increased pigmentation, erythema (sunburn), accelerated skin aging, tissue changes, skin cancer
315–400 (UV-A) photochemical effects	Cataract	Increased tanning (pigment darkening), skin aging, skin cancer, skin burn
400–700 (VIS) thermal effects	Retinal damage, photochemical damage (in case of prolonged exposure)	Skin burn, photosensitive reactions
700–1400 (IR-A) thermal effects	Retinal damage, cataract	Skin burn
1400–3000 (IR-B) thermal effects	Aqueous flare, corneal damage, cataract	Skin burn
>3000 (IR-C) thermal effects	Corneal damage	Skin burn

Skin Damage Risks

In addition to the eye, excessive exposure to laser radiation will result in biological damage of the skin. In general terms, the skin can tolerate higher irradiances to laser beam energy than the eye, so that severe laser skin injuries are less common and minor accidents do not have serious long-term effects. Nevertheless, the protection of the skin against laser radiation must also be taken seriously and the corresponding exposure limits must be observed.

In the ultraviolet range (UV-B and UV-C), the radiation is completely absorbed in the epidermis, whereas UV-A radiation reaches a bit deeper into the dermis (Fig. 24.15a). In the visible spectral range, the penetration depth is even larger, especially in the red region where the light reaches the subcutis. The penetration is deepest for IR-A radiation, where scattering processes become dominant (Fig. 24.15b; Table 24.4) leading to a diffuse distribution of light in the tissue that extends beyond the boundaries of the incident beam. In the IR-B range, the radiation only reaches the epidermis, and in the IR-C region, it is strongly absorbed at the surface of the epidermis.

The penetration depth in human skin for different wavelengths is provided in Table 24.3. The given data are typical mean values. More detailed information depends strongly on the skin type. For short or long wavelengths in the UV-C and IR-C range, the penetration depths are on the order of micrometers. Much larger penetration depths of several millimeters occur in the spectral region between 600 and 1500 nm.

Powerful lasers can cause considerable thermal damage to the skin. The biological effects vary from a mild erythema to severe blisters. Due to heat conduction, damage can also occur in deeper tissue layers leading to serious injuries and inflammations that heal very slowly. If the basal layer (stratum germinativum) is affected, the process of skin regeneration is strongly hindered.

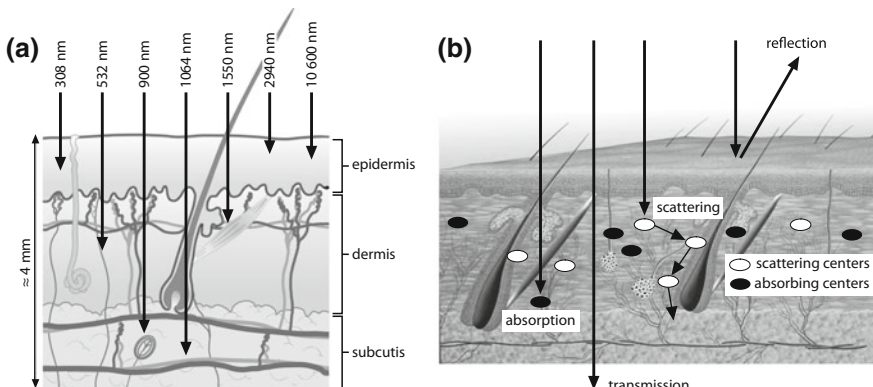


Fig. 24.15 **a** Penetration depth of radiation in human skin for selected typical laser wavelengths. **b** Interaction processes of light with skin

For the visible and near-infrared (IR-A) spectral range, the exposure limits for the skin are significantly higher compared to the eye where the radiation is focused onto the retina. In other spectral regions, the exposure limits for skin and eye are nearly the same because the cornea and normal skin respond similarly to the radiation resulting in comparable damage mechanisms. However, eye damage has much more severe consequences than skin damage.

Ultraviolet radiation can destroy important cellular components which, in the worst case, can lead to skin cancer. Since the doses from multiple individual exposures are added, the exposure limits in the UV region are particularly small. Table 24.6 lists the effects of laser radiation on skin for various wavelengths. The optical damage is related to the penetration depth and primarily results from thermal and photochemical processes.

Maximum Permissible Exposure

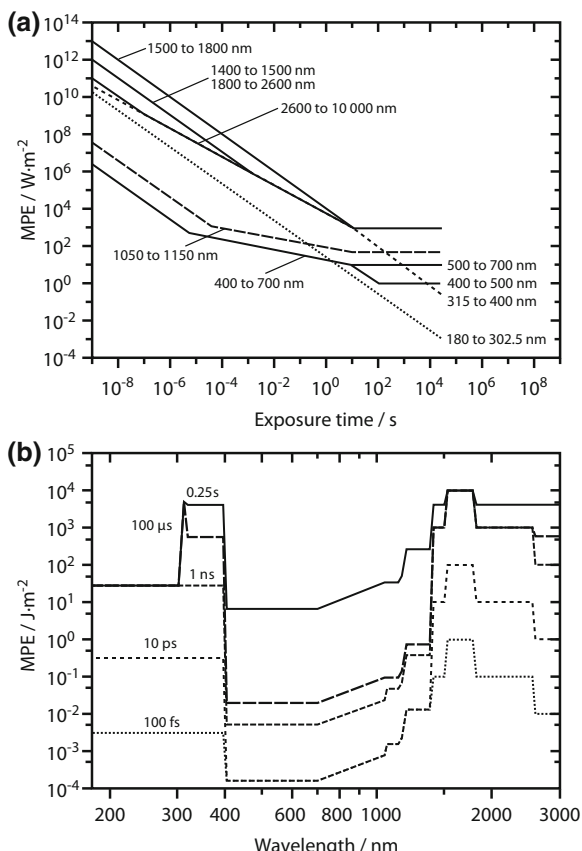
In order to prevent laser damage of the eye and skin, the lowest laser power suitable for the specific purpose or application should be used. Lasers should be operated such that individuals are not exposed to levels in excess of the so called maximum permissible exposure (MPE) levels, in Europe: exposure limit values. The latter represent the maximum levels to which the eye or skin can be exposed without consequential injury immediately or after a long time. Following the above considerations, the levels depend on the wavelength of the radiation, the pulse duration or exposure time, the tissue at risk and, for visible and near-infrared (IR-A) radiation in the range from 400 to 1400 nm, the size of the retinal image. Figure 24.16 shows simplified diagrams indicating the MPE levels of the cornea depending on exposure time and wavelength. More detailed information is provided in the international standard IEC 60825 and the European directive 2006/25/EC which are applicable to lasers emitting in the wavelength range from 180 nm to 1 mm. In the US, guidance on safe laser use is given in the ANSI Z136 series of standards. These documents also include MPE levels of the skin.

Laser Classes and Safety Precautions

Depending on the hazard potential, lasers are classified into laser classes 1, 1C, 1 M, 2, 2 M, 3R, 3B and 4 according to the IEC 60825 and ANSI Z136 standards as follows:

- Class 1: The laser is safe under all conditions of normal use. This means that the MPE cannot be exceeded when viewing the laser with the naked eye or with the aid of magnifying optics. Continuous wave lasers emitting in the red to green spectral region with an accessible

Fig. 24.16 Maximum permissible exposure (MPE) levels of the cornea as per IEC 60825 (simplified): **a** MPE in terms of power density versus exposure time for various wavelengths. In the spectral ranges from 302.5 to 315 nm, 700 to 1050 nm and 1150 to 1400 nm, the MPE levels are wavelength-dependent and thus not shown. **b** MPE in terms of energy density versus wavelength for various exposure times. Data taken from “Safety of laser products—Part 1: Equipment classification and requirements” (IEC 60825-1:2014)



emission limit (AEL) of up to $390 \mu\text{W}$ and blue-violet lasers with an AEL of up to $39 \mu\text{W}$ fall under this category.

- Class 1 M: The laser is safe unless it is viewed through typical *magnifying* optics such as telescopes or microscopes. These are often lasers with highly-divergent beams or beam cross-sections that are larger than the eye’s pupil.
- Class 1C: The laser is intended to be applied in *contact* with skin or internal body tissues for medical procedures. It has safeguards that prevent leakage of laser radiation in excess of the AEL of Class 1. Hence, there are no limitations in power or energy.
- Class 2: The laser is considered safe due to the body’s involuntary defense response for eye protection (also known as corneal reflex or “blink reflex”) which limits the exposure time to 0.25 s. Consequently, this class only applies to visible lasers from 400 to 700 nm. The power limit for continuous wave lasers is 1 mW. Meanwhile, it is assumed

that the blink reflex does not occur for low-power laser beams, probably because the focus on the retina is too small.

- Class 2 M: The laser is safe because of the blink reflex, provided it is not passed through optical instruments which decrease the beam diameter.
- Class 3R: The laser is potentially hazardous under direct and specular reflection viewing condition if the eye is appropriately focused and stable, but the probability of an actual injury is small. In the visible spectral range, the AELs are five times higher than for a Class 2 laser (5 mW for continuous wave operation). For the other spectral regions and exposure times of less than 100 s, the values are up to five times higher than for a Class 1 laser. Compared to Class 3B lasers, the safety measures for Class 3R lasers are *relaxed*.
- Class 3B: The laser is hazardous if the eye is exposed directly, but specular reflections are normally not harmful. The AEL for continuous wave lasers in the range from 315 nm to the far-infrared is 0.5 W. For pulsed lasers in the visible region, the limit is 30 mJ.
- Class 4: The laser exceeds the AELs for Class 3B and is thus dangerous for the eye and skin. Even diffuse reflections are hazardous and may cause injuries. Moreover, the laser constitutes a fire risk as it may ignite combustible materials. Continuous wave lasers with output powers exceeding 0.5 W (at wavelengths longer than 315 nm) belong to Class 4

When Class 3 or 4 lasers are being used in an institution, a laser safety officer (LSO) has to be appointed who is responsible for the implementation of the requirements according to the IEC 60825 or ANSI Z136 standard, thus ensuring that laser safety regulations are followed by all other employees. The LSO also assists with the preparation of risk assessments to identify the hazards related to laser use and to specify the measures for eliminating or controlling those hazards. Furthermore, all employees are to be instructed once a year.

An area in which the exposure limits are exceeded is called laser area. It must be marked with appropriate warning signs and, if possible, by warning lights above the entrance doors. For Class 3B and 4 lasers, the access to the laser area must be restricted to authorized personnel. Additional control measures include, amongst others, the use of a low-power He-Ne or diode alignment laser for a preliminary alignment, the removal of watches and reflective jewelry before any alignment activities and the restriction of the beam path at a safe height (below eye level). Furthermore, technical measures can be applied to prevent laser accidents such as safety interlocks, beam shutters, beam dumps and emission indicators.

Most importantly, whenever there is a risk of laser exposure to levels above the specified MPEs, safety eyewear must be used. Protection by laser safety eyewear is afforded by incorporating optical filters to reduce the level of exposure to the eye to below the limiting MPE. The latter is specified for the wavelength and power or pulse energy of the used laser source in the IEC 60825 or ANSI Z136 standards (see Fig. 24.16). For the proper choice of the eyewear, the required optical density

(OD) which quantifies the degree of attenuation on a logarithmic scale needs to be determined. For instance, safety eyewear with OD7 reduces the beam power in the specified wavelength range by a factor of 10^7 .

In the European Community, laser safety eyewear is specified in terms of the so-called scale number according to the EN 207 standard. The scale number ranges from LB1 to LB10, where LBn means that $OD > n$. Hence, laser goggles specified as LB6 reduce the beam power by a factor of at least 10^6 . Apart from sufficient attenuation, the eyewear has to withstand a direct hit from the laser without breaking or melting. In this respect, the European standard is more demanding than the American norm ANSI Z136 that only regulates the required OD. Moreover, the EN 207 standard specifies four laser working modes: continuous wave (D) with pulse durations longer than 0.25 s, pulsed mode (I, 1 μ s to 0.25 s), giant pulsed mode (R, 1 ns to 1 μ s) and mode-locked mode (M, <1 ns).

Aside from the hazards posed by the laser beam itself, there are additional non-beam hazards associated with use of laser systems. This includes risks from electrical equipment, e.g. high-voltage power supplies; chemical hazards (beryllium oxide in argon ion laser tubes, halogens in excimer lasers, organic dyes dissolved in toxic or flammable solvents in dye lasers) as well as hazards associated to the use of flammable and cryogenic liquids, vacuum pumps, plasma tubes, etc.

Further Reading

1. H.J. Lewerenz, *Photons in Natural and Life Sciences* (Springer, 2012)
2. A. Zoubir (ed.), *Raman Imaging* (Springer, 2012)
3. J. Popp, V.V. Tuchin, A. Chiou, S.H. Heinemann, *Handbook of Biophotonics* (Wiley-VCH, 2012)
4. M. Niemz, *Laser-Tissue Interactions* (Springer, 2007)
5. P. Török, F.J. Kao (eds.), *Optical Imaging and Microscopy* (Springer, 2007)
6. T. Moseley, G. Zabierek, *Guidance on the Safe Use of Lasers in Education and Research* (Association of University Radiation Protection Officers (AURPO), 2006)
7. R. Henderson, K. Schulmeister, *Laser Safety* (Institute of Physics Publishing, 2004)
8. P. Berlien, G.J. Müller, *Applied Laser Medicine* (Springer, 2003)
9. P.N. Prasad, *Introduction to Biophotonics* (Wiley-VCH, 2003)
10. D. Bičanić (ed.), *Photoacoustic and Photothermal Phenomena III* (Springer, 1991)
11. V.P. Zharov, V.S. Letokhov, *Laser Optoacoustic Spectroscopy* (Springer, 1986)
12. Y. LeGrand, S.G. ElHage, *Physiological Optics* (Springer, 1980)
13. R. Pratesi, C.A. Sacchi, *Lasers in Photomedicine and Photobiology* (Springer, 1980)
14. G. Bally (ed.), *Holography in Medicine and Biology* (Springer, 1979)

Chapter 25

Further Applications and Future Potential



When the first laser was realized about sixty years ago, it was considered a solution looking for its problem and only a few people were aware of the application potential offered by this new type of light source. Today, laser technology has become indispensable in science, industry and everyday life. Besides material processing and medicine, presented in the preceding chapters, lasers play a key role in optical communication, sensing and metrology. Scientific applications are primarily related to interferometric, holographic and spectroscopic techniques, the investigation of nonlinear optical phenomena as well as light detection and ranging (lidar) experiments. The unique properties of the laser, particularly its high coherence, monochromaticity and ability to reach extremely high power densities, have been paving the way for major advances in the fields of biology, chemistry, physics and astronomy over the past decades.

A recent breakthrough was the detection of gravitational waves using laser interferometers with unprecedented precision. This seminal experiment was realized by the Laser Interferometer Gravitational-Wave Observatory (LIGO) in the United States. The European X-ray free-electron laser (XFEL), inaugurated in Hamburg, Germany in 2017, generates high intensity pulses at wavelengths down to 0.05 nm which allows exploring ultra-fast dynamics occurring at atomic length scales. Another challenging goal which is currently being pursued is laser fusion. Here, the world's largest and most powerful laser system located at the Lawrence Livermore National Laboratory (LLNL) in Livermore, California, is used to heat and compress a small amount of hydrogen fuel to the point where nuclear fusion reactions take place. Apart from these complex and prestigious large-scale research projects where existing laser technologies are pushed to their limits, much simpler laser systems are widespread in a variety of mass-produced articles. Many everyday objects such as CD, DVD and Blu-ray players, laser printers and barcode readers rely on lasers to function, enabling faster and better performance than their predecessors.

The present chapter describes the working principles and applications of selected laser-based systems employed in research and industry. First, the use of lasers in consumer goods is presented, followed by brief reviews of optical communication,

lidar applications as well as holography and interferometry. Afterward, high-brightness lasers including free-electron, extreme ultraviolet (XUV) and X-ray lasers are discussed more comprehensively. The next section deals with the major international projects treating gravitational wave detection and laser fusion mentioned above. The last section of this chapter outlines potential future developments of laser technology. Other applications of specific lasers are described in Parts II and III.

25.1 Lasers in Everyday Life and Consumer Goods

In addition to the major applications in optical communication, material processing, medicine and metrology, lasers are employed for a variety of purposes in everyday life. Laser beams are used ubiquitously in electronic devices for reading and writing information. Laser printers produce high-quality text and graphics; barcode readers at supermarket checkouts have streamlined the payment process and laser turntables provide significantly improved playback quality compared to mechanical devices, with less wear and more compact sound carriers.

Laser-based displays, e.g. in laser television and laser projectors, represent a more recent technology which utilizes multiple individually modulated laser beams of different colors that are scanned and projected across an arbitrary surface, producing images with very high contrast and wide color spectrum. Lasers in combination with beam distribution optics and movable deflection systems can be found in nightclubs and music shows where they are used for decoration and advertising purposes. Lasers are used in art and architecture conservation projects as well as purely artistic endeavors such as light sculptures. Some of the most widespread devices relying on lasers are presented below.

Laser Pointer

The straight-line propagation and low divergence of laser beams is exploited in laser pointers which are widely used in educational or business presentations. High-quality laser pointers are also employed in the construction of roads, canals, tunnels, buildings as well as for precise alignment of parts in the production of engines and other machines. The least expensive laser pointers are simply based on a battery-powered laser diode emitting red light near 650 nm wavelength. Due to the much higher sensitivity of the human eye in the green spectral region, diode-pumped solid-state lasers producing green light at 532 nm have become most common recently. Yellow-orange (594 nm), blue (473 nm) and violet (405 nm) laser pointers are also available.

As sketched in Fig. 25.1, green laser pointers typically consist of an aluminum gallium arsenide (AlGaAs) laser diode which generates light at 808 nm wavelength

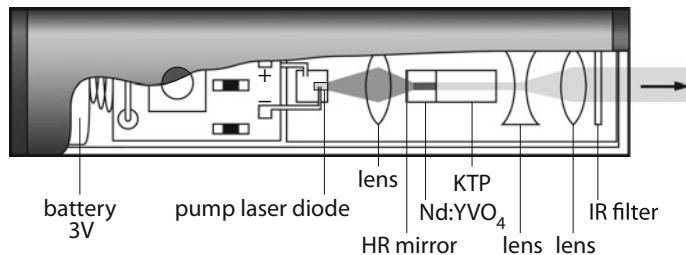


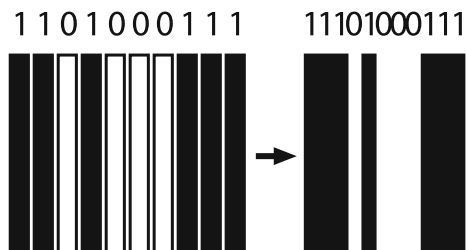
Fig. 25.1 Schematic of a green laser pointer. A Nd:YVO₄ crystal is pumped by a laser diode at 808 nm, generating radiation at 1064 nm wavelength which is frequency-doubled to 532 nm in a KTP crystal

with an output power of several hundreds of mW. The infrared output of the laser diode is coupled into a Nd:YVO₄ (or Nd:YAG) crystal to produce radiation at 1064 nm wavelength. The latter is converted into green light at 532 nm by second harmonic generation in a potassium titanyl phosphate (KTP) crystal. In order to ensure high conversion efficiency, phase-matching (see Sect. 19.3) must be performed by proper orientation of the two anisotropic crystals. The Nd-doped gain medium and the frequency-doubling crystal are contained in a resonator which is formed by dielectric mirrors that are coated directly on the crystal end-faces. The mirror on the Nd-doped crystal transmits the pump light at 808 nm and reflects the 1064 nm radiation, while the output coupler on the KTP crystal reflects the infrared light at 1064 nm and transmits the green light at 532 nm. Residual infrared radiation is rejected by an additional IR filter. Collimation of the green laser beam is obtained by a lens system which is also integrated into the laser pointer.

Barcode Reader

Barcode readers or scanners are widely used for identifying goods and prices in shops and for encoding ISBN numbers on books. The goods are marked with a barcode consisting of several parallel bars of varying width and spacing (Fig. 25.2). Among the multitude of barcode symbologies, the Universal Product Code (UPC) and the

Fig. 25.2 Barcode: a binary sequence is represented by a series of bright and dark lines. Neighboring bars can be grouped together



related European Article Number (EAN) are prevalent in most English-speaking countries like the United States, Canada, United Kingdom, Australia, New Zealand as well as in continental Europe and other countries. The information, e.g. about a trade item, is encoded in a 12-digit or 13-digit number, whereby each digit is represented by a unique pattern of bars and spaces. Aside from linear or one-dimensional barcodes, two-dimensional codes based on rectangles, hexagons and other geometric patterns are increasingly employed. A special variant is the so-called Quick Response (QR) code which has recently become very popular due to its fast readability and greater storage capacity compared to the standard UPC. Reading a barcode is performed with a laser beam that is moving back and forth across the code using either a reciprocating mirror or a rotating prism. The intensity of the reflected light is measured with a photodiode which registers a sequence of pulses that corresponds to the geometrical pattern of the code. The electrical signal is then evaluated to retrieve the information stored in the barcode.

CD, DVD and Blu-Ray Disc

The technology of the compact disc (CD) started in the research laboratories of Philips (Eindhoven, The Netherlands) and Bosch (Berlin, Germany) at the end of the 1960s. As early as 1972, the first optical video disc player was presented incorporating a He–Ne laser at 633 nm for reading.

In a CD, the information (speech, music, video signals) is stored digitally as a series of indentations (so-called pits) that are molded into the top of a polycarbonate layer along a spiral track. The areas between pits are referred to as lands. Each pit is approximately 0.6 μm wide and 0.1 μm deep, while the length varies from 0.83 to 3.5 μm (Fig. 25.3).

The pits are scanned by a focused diode laser beam which is a contactless and wear-free process, as opposed to conventional records. In order to ensure high read-out quality, a reflective layer of aluminum or gold is applied to the surface of the polycarbonate plate. The thin metal layer is protected by a film of lacquer that is usually coated directly onto it. A standard CD is 1.2 mm thick, weighs 15–20 g and has a diameter of 120 mm.

The binary information (logic zero or logic one) is not directly encoded as pits and lands. Instead, the change from pit to land or vice versa represent a logic one, while no change indicates a series of logic zeros (non-return-to-zero encoding), as illustrated in Fig. 25.4. When the focused laser beam is incident on a land, the beam is reflected from the flat surface and detected by a photodetector. If, however, the beam is positioned over a pit edge (technically called a ridge), a portion of the light is reflected from the bottom of the pit, while the rest is reflected from the level outside the pit. The depth of the pit is designed to be $\lambda/4$ of the laser wavelength so that the path difference of the two beam portions is $\lambda/2$. Consequently, destructive interference occurs at the transition between pit and land, resulting in a lower signal on the photodetector. The sequence of high and low intensities is converted into a

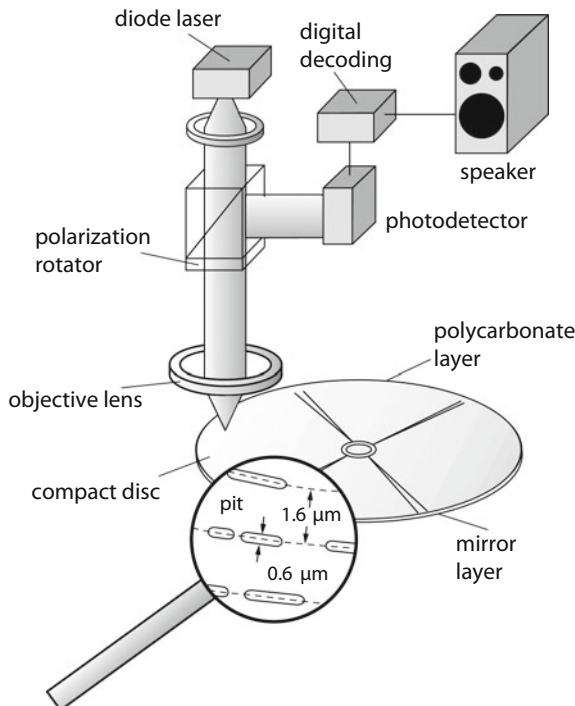


Fig. 25.3 Data storage on a compact disc. The data are stored as a series of tiny indentations known as pits, encoded in a spiral track which is molded into the top of a polycarbonate layer

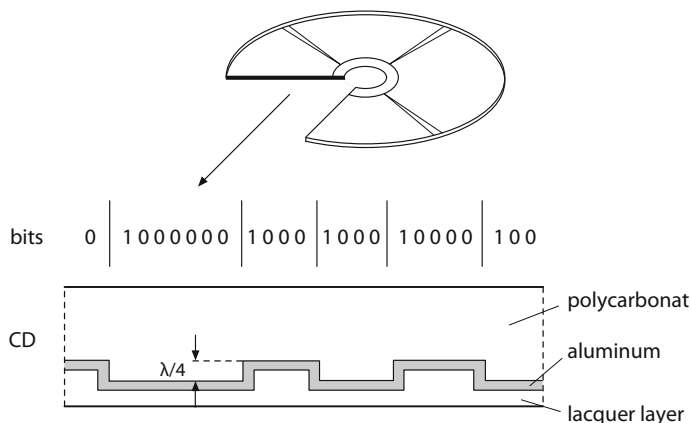


Fig. 25.4 Layer structure of a compact disc. A change from pit to land or land to pit indicates a logic one, while no change indicates a series of logic zeros (non-return-to-zero encoding)

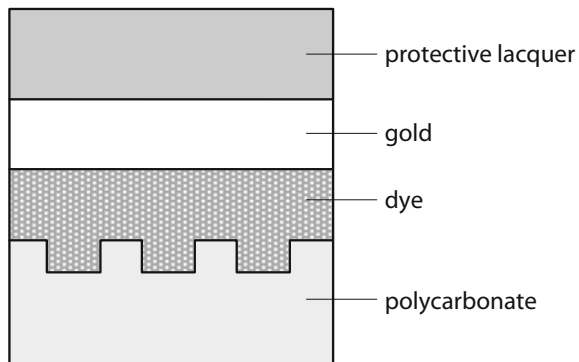
digital signal consisting of zeros and ones. It can then be decoded, amplified and, in case of an audio CD, fed into a speaker for sound reproduction.

As discussed in Sect. 10.8, different types of laser diodes with output powers below 1 mW are employed for reading the data encoded on optical storage media. While AlGaAs lasers at 780 nm and AlGaInP lasers at 650 nm wavelength are used for the CD and DVD (digital versatile disc) format, short-wavelength laser diodes based on GaN which emit at 405 nm are incorporated in Blu-ray devices. The shorter wavelength enables the reduction of the pit length from 0.83 μm (CD) and 0.4 μm (DVD) to 0.15 μm, thus allowing more information to be stored in the same area. CDs and DVDs have a storage capacity of only 0.65 GByte and 5 to 17 GByte respectively, depending on the data format. In contrast, conventional Blu-ray discs contain 25 GByte per layer, while dual-layer discs (50 GByte) are the industry standard for feature-length video discs. Ultra-High-Definition (UHD) Blu-ray discs with a capacity of 100 GByte, supporting 4K videos with a resolution of 3840×2160 pixels and very broad color spectrum, are expected to supersede the conventional Blu-ray format. 4 K Blu-ray discs and players became available in the first quarter of 2016.

Lasers are used not only for reading but also for fabricating optical storage devices. Short-wavelength solid-state lasers are employed in the mastering process where a light-sensitive material (photoresist) is selectively illuminated to create the desired pit pattern on the master blank CD (laser beam recording). When exposed to the laser light, the photoresist undergoes a chemical reaction which either hardens it (negative photoresist) or makes it more soluble (positive photoresist). Afterward, the exposed layer is then soaked in a developer solution which removes the exposed positive photoresist or the unexposed negative photoresist. In a subsequent process step, the master is electroplated to produce a durable stamper that can be used to replicate thousands of CDs. Molten polycarbonate is then injected onto a stamper to transfer the pit pattern, and hence the digital information. The polycarbonate layer is metalized and protected against damage by a 5–10 μm thick layer of lacquer. In this way, scratches, dust or fingerprints on the surface do not disturb reproduction as much as those in the pit plane, into which the laser beam is focused. On the surface of the polycarbonate carrier, the beam is widened and therefore only insignificantly influenced by scattering losses introduced by small dust particles.

Pre-pressed compact discs, as depicted in Fig. 25.4, are read-only media (CD-ROM). The layer structure of a recordable CD-R that can be written once and read arbitrarily many times is shown in Fig. 25.5. The bottom side of the polycarbonate layer, which faces the laser beam in the player or drive, is flat and smooth, while the top side contains a spiral groove, called pre-groove, to guide the laser beam upon writing and reading information. The pre-groove is molded into the top side of the polycarbonate layer, where the pits and lands would be in a non-recordable CD-ROM. The pre-groove side is coated with a thin layer of organic dye, followed by a reflective metal layer (silver, silver alloy or gold) and a protective lacquer coating. The recording is carried out by a semiconductor laser of much higher power (>10 mW) than the reading laser, which heats (“burns”) the dye, creating a sequence of burned and non-burned spots. The transitions between

Fig. 25.5 Layer structure of a one-time writable compact disc (CD-R). A diode laser is used for sequential writing (from bottom) by changing the absorption and refraction properties of the dye



burnt and unburnt areas are recognized by the reading laser due to the different reflection and absorption characteristics in a similar way as the pits and lands of replicated ROM-discs.

In rewritable optical discs (CD-RW), the information layer consists of a phase-changing metal alloy film, e.g. made of GeSbTe, which is heated up by the writing laser. The local heating at the exposed spot induces a phase change from the crystalline to the amorphous state and vice versa, controlled by the burning temperature of the writing laser. Rapid cooling is achieved by dielectric layers on both sides of the metal alloy. The amorphous areas reflect the light of a reading laser with lower intensity than the crystalline regions, allowing the transition between the two states to be registered. Data can thus be erased and rewritten by up to 1000 times.

The pervasiveness of the CD and DVD technology has remained for more than two decades, despite progressively declining sales. Nevertheless, the era of the CD is drawing to an end, as indicated by the fact that the multinational consumer electronics corporation Best Buy announced plans to end CD sales in 2018. Despite the much larger storage capabilities, the (UHD) Blu-ray technology faces strong competition from video-on-demand services and solid-state storage devices.

Laser Printer

Parallel to the tremendous progress of electronic data processing, the printing technology has been experiencing significant development. Starting from the traditional typewriter with type bars, dot-matrix, thermal, inkjet and electrophotographic printers were established. In the course of the development, the characters were first printed serially, then line-by-line and finally page-by-page, allowing for increasing printing speeds.

Among the different page printing technologies which are based on electrophotographic effects as explained below, laser printers are most common, although light-emitting diodes (LEDs) are used as light sources as well. The operating principle of a laser printer is illustrated in Fig. 25.6. The printing process

first involves charging a photoconductive cylinder called imaging drum (Fig. 25.6a). Afterward, a laser beam, e.g. from an AlGaAs semiconductor laser, is repeatedly passed over the rotating drum to selectively neutralize negative charges, thus creating an electrostatic image of the page to be printed (Fig. 25.6b). For this purpose, the laser beam is guided onto the photoconductive drum via a rotating polygonal mirror and through a system of lenses and mirrors, writing up to 65 million pixels per second. Powdered ink (toner) particles from a developer roll are then electrostatically attracted to the neutralized areas of the imaging drum that were exposed to the laser beam (Fig. 25.6c). The toner particles are transferred onto the paper which is subsequently passed to a finisher where the particles are permanently fused onto the paper by heat and pressure (Fig. 25.6d). Finally, the drum is homogeneously discharged by light irradiation in order to clean it of excess toner, so that the printing process can start again at the first step after a full rotation of the drum.

Laser printing requires a raster image processor which converts the page image into a raster of dots which is stored in the printer's memory. A typical resolution is 300 dpi (dots per inch), corresponding to about 8 million dots per A4 page. In the printing industry, a resolution of over 1200 dpi is common. Since all steps of the printing process can be completed in rapid succession during one revolution of the

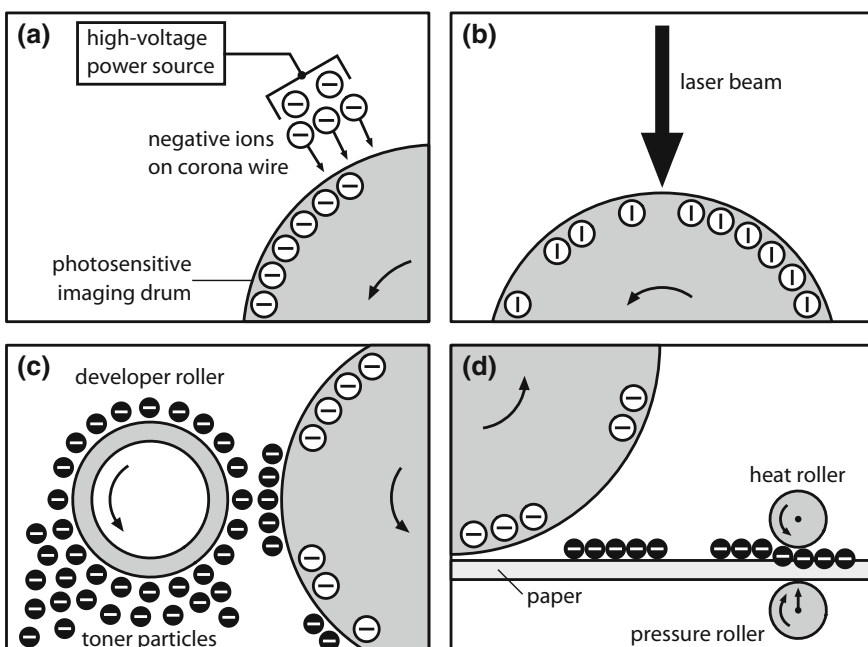


Fig. 25.6 Operating principle of a laser printer. **a** Charging of the imaging drum, **b** production of an electrostatic image by exposure of the imaging drum to a laser beam and selective neutralization of negative charges, **c** developing of the image by applying toner particles, **d** transfer of the toner particles onto the paper

drum, the printer can be built as a very compact unit and achieve printing speeds of 200 monochrome pages per minute. Color laser printers are based on multiple colored toners, typically cyan, magenta, yellow, and black (CMYK), which are engaged sequentially.

Laser Projectors

Laser projectors represent a more recent technological development. These devices are able to generate images with deep and rich colors and have only recently entered the home entertainment market. Here, a raster-based image is generated from three different laser sources emitting at the fundamental colors red, green and blue (red: InGaAsP, green and blue: InGaN). Galvanometers or MEMS devices are used to scan the RGB laser beams across the projection surface, pixel-by-pixel, with up to 60 thousand points per second, producing a smooth and flicker-free image. Due to the tight focusing of the laser beam and the fundamental monochromatic colors, extremely brilliant images with high color purity and wide spectrum are obtained. With the progressing development of (green) diode lasers, a major advancement of these devices is expected in the future, especially for portable and handheld pico projectors. In 2015, the Chinese company Lenovo introduced a smartphone incorporating a laser projector.

Besides the better picture quality, laser projectors offer additional advantages over conventional lamp projectors. While a traditional projector lamp loses half of its brightness during the first 2500–5000 h of operation, laser projectors feature consistent brightness over more than 15,000 h. Moreover, lamp projectors exhibit color shifts which deteriorate the image quality and necessitate re-calibration every 500–1000 h. On the contrary, laser projectors show constant color balance over very long periods and fast on/off switching without the necessity to warm-up or cool down the device.

25.2 Optical Communication

Today, digital data transmission has become an essential and integrated part of modern society. Optical communication systems, where light is used as the transmission medium, generally consist of a transmitter which encodes a message into an optical signal, an optical fiber which carries the signal to its destination, and a receiver which retrieves the information from the received optical signal (Fig. 25.7). Semiconductor laser transmitters represent key components of broad-band communication systems. With the ever-increasing demand on bandwidth, speed and efficiency, the diode laser technology is continuously evolving to provide optical communication systems with higher speed, lower production costs, smaller size and lower power consumption.

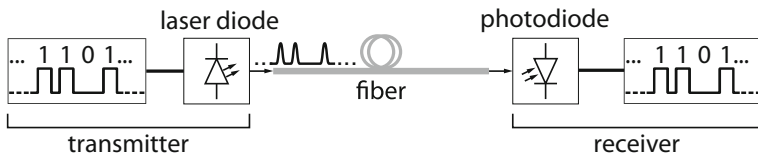


Fig. 25.7 Optical communication via glass fibers. Multiple data channels can be coupled in one fiber

While edge-emitting lasers such as Fabry-Pérot (FP) laser diodes are commonly used in short-range and low-speed applications, distributed feedback (DFB) lasers with narrower spectral bandwidth are well-suited for long-range applications. Vertical cavity surface-emitting lasers (VCSELs) are characterized by much higher efficiency compared to FP or DFB lasers. However, the maximum achievable single-mode output power of VCSELs is lower so that amplifiers are required to boost their power. Hence, multimode VCSELs emitting at 850 nm wavelength are primarily employed in short-range (<100 m) and medium-range (<1000 m) fiber-optic communication systems like Gigabit Ethernet and Fibre Channel, where they allow for data rates beyond 100 GBit/s. More information on diode lasers for optical communication can be found in Sect. 10.9.

Optical data transmission is in most cases done via optical fibers which allow for the low-loss transmission of light over several hundreds of kilometers without alignment issues or disturbing influences of the atmosphere. Land and underwater connections all over the world, e.g. submerged in the Atlantic Ocean, link countries and continents through a network of fiber-optic cables, carrying optical signals for the majority of the world's telecommunication and Internet traffic.

About thirty years ago, the first submarine optical fiber cable was installed between Europe and the east coast of the United States transmitting light at $1.3 \mu\text{m}$ wavelength over a length of more than 5000 km. The transatlantic and transpacific connection provided data rates of less than 280 Mbit/s. Only shortly after that, 560 Mbit/s were reached using fiber-optic systems with DFB laser operating at $1.55 \mu\text{m}$ wavelength. Despite the lower losses of about 0.2 dB/km (see Fig. 13.10) compared to $1.3 \mu\text{m}$ systems, the optical signals had to be regenerated every 50 km using opto-electronic repeaters. The latter transformed the optical signal into an electrical signal and amplified it before converting it back to the optical form. Opto-electronics repeaters were soon replaced by erbium-doped fiber amplifiers (EDFAs) which amplified the optical signal at $1.55 \mu\text{m}$ directly without converting it to an electrical signal. A submarine cable installed in the mid-1990s that was based on EDFA technology thus no longer required signal recovery every 50 km and already worked with a data rate of 5 Gbit/s. This was also possible by using single-mode fibers with core diameters of only $8 \mu\text{m}$ which minimized pulse-spreading due to dispersion.

A major advance in optical communication was the development of wavelength division multiplexing (WDM) which boosted the available data capacity of optical fibers by utilizing parallel channels in a single fiber, each channel carrying

independent information at a dedicated wavelength. Multiplexing and demultiplexing are commonly achieved using arrayed waveguide gratings (AWGs) having both imaging and dispersive properties. Here, light is coupled into an array of waveguides with a constant length increment thus introducing a constant phase shift. The diffracted light interferes constructively and gets refocused at the output of the AWG with the focus position depending on the wavelength. In this way, different wavelengths are separated (demultiplexed) or combined (multiplexed) if the AWG is used in the opposite direction. Aside from WDM, more complex modulation formats, including polarization-division multiplexing (PDM) and quadrature phase-shift keying (QPSK), have been developed over the last decades, further increasing the data rates. Currently, transatlantic cables can hold up to eight fiber pairs each containing 100 channels. Each channel, in turn, is capable of transmitting a 100 Gbit/s signal, so that overall data rates of 80 Tbit/s are obtained. That is seven orders of magnitude larger than the capacity of the first submarine telephone cable that went into service about 60 years ago.

The idea of using glass fibers for the transmission of information in the form of optical signals was already known in the 1960s. However, excessively high losses in the optical fibers due to scattering prevented their practical use at that time. Following the theoretical work of Chinese-British-American scientist Charles Kao, who attributed the losses to impurities in the glass, fibers with much higher purity were manufactured enabling optical transmission over long distances with minimal signal attenuation. In 2009, Kao was awarded the Nobel Prize in Physics. He shared the prize with the Canadian physicist Willard S. Boyle and the American scientist George E. Smith, who invented the charge-coupled device (CCD) which is used to convert optical information into an electrical signal (Sect. 21.4).

Due to much lower attenuation, fiber-optic transmission has large advantages over existing telecommunication systems based on copper wires, particularly when data is transferred over long distances. As the prices for fiber-optic communication have considerably dropped over the last two decades, short-distance optical networks are also expanding to support the increasing growth of bandwidth-rich Internet video applications along with traditional voice and data services. More and more fibers run directly onto customers' premises (Fiber-to-the-Premises, FTTP), providing new products and services that can be activated remotely. Compared to copper, FTTP delivers higher speeds for both upload (100 Mbit/s) and download (200 Mbit/s) with higher reliability, is less susceptible to harsh weather and easier to maintain. The German telecommunication company Deutsche Telekom is hence accelerating the construction of the fiber-optic infrastructure, having laid 40,000 km of new fiber-optic cables in 2017.

In this context, silicon photonics is a relevant technology for the further development of optical communication, as it offers the realization of energy-efficient, high-speed optical interconnects at high volumes and low costs. Since silicon is both semiconducting and transparent at telecommunication wavelengths around $1.55\text{ }\mu\text{m}$, it is well-suited for opto-electronic integration. Due to the high refractive index difference between silicon and oxide, small footprint integrated circuits can be designed with mode field diameters in the sub- μm regime. For these reasons, hybrid

devices can be created in which the optical and electronic components including the laser source, modulator and photodiodes are integrated on the same microchip. In addition, the use of microelectronic complementary metal-oxide-semiconductor (CMOS) fabrication lines facilitates low-cost mass production of photonic integrated circuits. The German company Sicoya has developed the world's smallest silicon modulator that allows for the implementation of more than 10,000 high-speed modulators per square millimeter. This reduction in size directly translates into higher energy efficiency of the control electronics and the usage of the light from the laser source. Very recently, a 100 Gbit/s transceiver chip featuring integrated electronics and optics on a single chip was demonstrated.

Lasers are also increasingly used for free-space optical transmission without fibers enabling the data exchange between satellites (inter-satellite communication) or from satellites to Earth. Moreover, lasers enjoy increasing interest in the communication with aircraft and unmanned aerial vehicles. Free-space optical data links between metropolitan buildings (LAN-to-LAN connections) are technologically less challenging and can be much simpler and more cost-effective than installing a fiber cable. Such connections are for instance used to obtain fast Internet access for multiple buildings, even if only one of them has direct access to a fiber network. However, atmospheric disturbance such as rain, fog, snow or strong wind needs to be handled. Laser transmitters emitting in the infrared spectral region, particularly in the eye-safe region around $1.5\text{ }\mu\text{m}$, are employed for this purpose. For distances up to a few kilometers and moderate data rates, light-emitting diodes (LEDs) can be used instead of lasers as well.

25.3 Light Detection and Ranging

Being originally a portmanteau for the words light and radar, lidar is now used as an acronym for light detection and ranging. In a narrower sense, it describes a method for measuring the distance from a target by illuminating it with a pulsed laser and detecting the reflected pulses with a sensor. Beyond the ranging capability, additional information about the target can be retrieved by analyzing the changes in the intensity, frequency or phase of the return signal compared to the transmitted laser pulse. This allows, for example, measuring the speed of an object or inferring various physical properties of the atmosphere with high spatial resolution. For instance, spectral analysis of light backscattered from a distant volume is utilized for remote detection of pollutants, e.g. from industrial sources (Fig. 25.8).

Depending on the type of measurement, lidar systems are either ground-based or operated from ships, aircraft or satellites. Over many years, lidar has been used for range-finding and aerial mapping as well as three-dimensional scanning of objects and locations, amongst other applications. With the growing interest and rapid development in autonomous vehicles, lidar devices are also becoming increasingly applicable to obstacle detection and in avoidance systems for ensuring safe navigation in outdoor environments. Primarily because of this emerging application, the

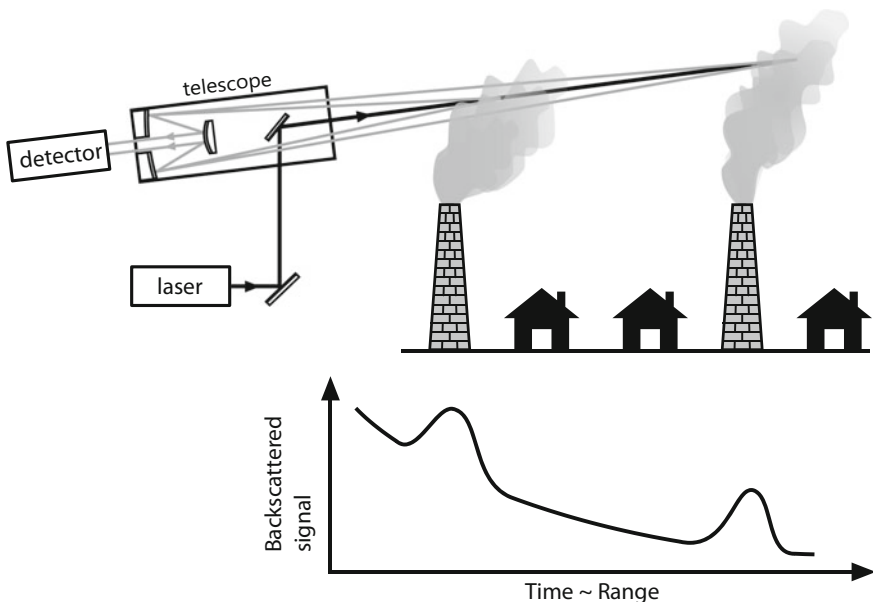


Fig. 25.8 Principle of a lidar system for air pollution analysis. Short light pulses are transmitted through the atmosphere, backscattered from exhaust fumes, collected by a telescope and detected by a receiver. The distance to the pollution source is determined from the travel time of the pulse, while the spectroscopic investigation of the backscattered light yields information on the chemical composition of the fumes

market for lidars is projected to double in size between 2018 and 2022. For geographic, geodetic or archaeological purposes, lidar is used to map the landscape by means of airborne laser scanning (ALS) to create highly-accurate three-dimensional maps of land surfaces. Being one of the first applications of laser technology, lidar is also employed for a variety of meteorological purposes such as profiling clouds, studying aerosols, quantifying atmospheric components or measuring winds. ALS and Doppler wind lidar applications are presented in the following section.

Airborne Laser Scanning

In ALS systems, a laser onboard an aircraft sends pulses towards the ground and the light reflected from different objects along the beam path is detected by a receiver. The use of a laser scanning unit enables the acquisition of three-dimensional information about the Earth's surface at high-speed acquisition rates. There are two types of commercial ALS systems: discrete echo and full-waveform sensors. While the former detects a relatively small number of discrete trigger signals in real-time, each representative of multiple echoes, full-waveform systems register the complete temporal variation of the received signal intensity with a typical resolution of

1 ns. Hence, in contrast to discrete echo systems, additional parameters such as the signal amplitude or the echo width can be retrieved from the stored waveform in post-processing adapted to the individual needs.

The immediate output from an ALS system is a point cloud, consisting of the coordinates of unequally spaced return signals which are associated with objects from which sufficient laser light has been reflected. The raw data is then processed using various algorithms treating the distribution and intensity of the return signals. Classification is performed to distinguish between vegetation, human-engineered structures and the bare ground (Fig. 25.9).

To reach high data coverage and accurate processing, lasers with high pulse repetition rates of typically 100 kHz are used. Moreover, the so-called multi-pulse technology allows detecting the echoes of multiple laser pulses traveling through the atmosphere simultaneously. In addition, multiple scanners can be employed on one airborne platform to enable side-, forward- or backward-looking views. The scan pattern usually consists of parallel mutually overlapping stripes with lengths of a few kilometers and widths of several hundred meters depending on the altitude of the aircraft and the maximum scan angle.

ALS is utilized to create high-resolution digital elevation models (DEMs) of archaeological sites revealing subtle topographic features that are hidden by vegetation. Recently, 60,000 previously unknown structures from a vast Mayan megalopolis were discovered in a deep forest in Guatemala using an ALS system

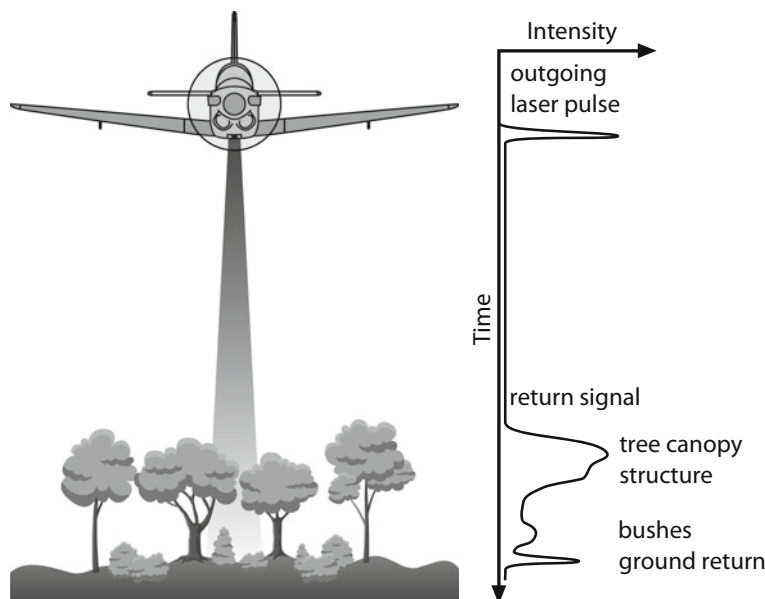


Fig. 25.9 Airborne laser scanning. Laser pulses are emitted towards the ground and diffusely reflected from various objects. The temporal signature of the return signal detected by a sensor onboard the aircraft is analyzed yielding information about the Earth's surface

without having to cut down a single plant. The discovery was a major breakthrough that showed that the Maya civilization was much larger than previously thought. Apart from archeological purposes, ALS devices are employed in forestry to determine canopy heights (Fig. 25.9), biomass and leaf areas.

Doppler Wind Lidar

Wind lidar systems are used in a variety of applications. For instance, they are employed at airports to detect atmospheric disturbances such as strong wind shears, gusts or wake vortices which are hazardous to airliners, particularly during take-off or landing phases. Moreover, the performance of wind turbines can be improved by measuring the wind speed and direction ahead of the turbine blades, so that the blade parameters can be optimized. Wind measurements are also highly-important in terms of weather prediction and climate studies, as the wind carries heat, moisture and particles around the globe.

Most wind lidar systems rely on the Doppler effect (Sect. 19.1). When light is scattered from moving particles (cloud particles, aerosols or molecules), it experiences a frequency shift Δf which scales linearly with the wind velocity v according to (19.1). Hence, the wind speed, i.e. the collective motion of aerosols, cloud particles and molecules within the air, can be retrieved by measuring the frequency difference between an outgoing laser pulse and the backscattered signal.

Different methods are applied for determining the frequency shift which is typically on the order of only a few MHz. Coherent wind lidar systems are based on optical heterodyne detection to derive the Doppler frequency shift from a beat signal, as described in Sect. 22.5. Alternatively, the shift can be quantified by measuring the amount of backscattered light transmitted through band-pass filters in so-called direct-detection Doppler wind lidar (DWL) systems.

Due to the random, thermal motion of the molecules and particles in the air, Doppler broadening occurs when a laser pulse is backscattered in the atmosphere. For molecular backscattering, the broadening is in the GHz-range, whereas it is four to six orders of magnitude smaller for cloud particles or aerosols due to their much larger mass (see 2.24). Consequently, the line shape of the backscattered light represents a convolution of broadband and narrowband signals. The latter is called Mie signal, as the size of the aerosols and cloud particles is typically on the same order as the laser wavelength ($0.1\text{--}1 \mu\text{m}$), while molecular signals are associated with Rayleigh scattering where the laser wavelength is much longer than the dimension of the scatterer. Coherent DWL systems rely entirely on the narrowband Mie backscatter return, although recent studies have shown that the broadband Rayleigh signal can be analyzed by heterodyne detection as well.

In 2018, the satellite Aeolus was launched carrying the first ever satellite-borne DWL instrument ALADIN (Atmospheric LAser Doppler INstrument). ALADIN provides profiles of one component of the horizontal wind vector in the line-of-sight (LOS) direction of the laser beam and telescope which are tilted by 35° from nadir, as

depicted in Fig. 25.10. Since Aeolus is polar-orbiting and the LOS pointing direction is perpendicular to the satellite ground track, the speed along the west-east (zonal) direction of the wind vector is predominantly derived, except for high latitudes.

The system comprises a frequency-tripled Nd:YAG laser at 355 nm, a 1.5 m-diameter telescope and a very sensitive receiver. Owing to the large difference in spectral width of the Mie (~ 50 MHz) and Rayleigh (~ 3.8 GHz at 355 nm and 293 K) atmospheric backscatter signals, the receiver consists of two complementary channels to separately analyze the return signals from both molecules (Rayleigh channel) and clouds and aerosols (Mie channel).

The measurement principle of the Rayleigh channel is illustrated in Fig. 25.11. It relies on the double-edge technique and involves two band-pass filters (A and B) which are placed symmetrically around the frequency of the emitted laser pulse. The width and spacing of the filter transmission curves are chosen such that the maxima are close to the inflection points (edges) of the Doppler-broadened molecular line. The transmitted signal through each filter is proportional to the convolution of the respective filter transmission function and the line shape function of the atmospheric backscatter signal. Consequently, the contrast between the return

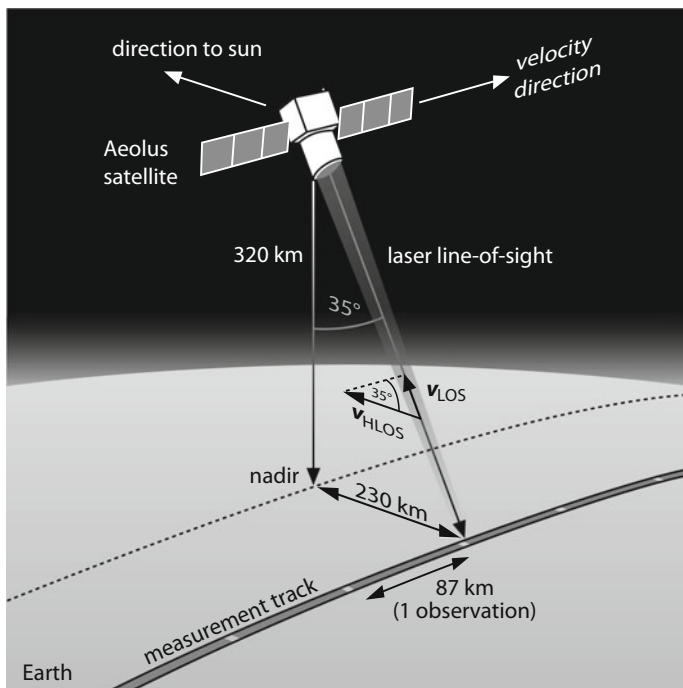


Fig. 25.10 Measurement geometry of the satellite-borne wind lidar system ALADIN onboard the polar-orbiting satellite Aeolus at 320 km altitude. The pointing direction of the telescope at 35° off-nadir involves a separation of the satellite and measurement tracks by 230 km. Line-of-sight wind profiles are obtained after averaging over 90 km, corresponding to one observation

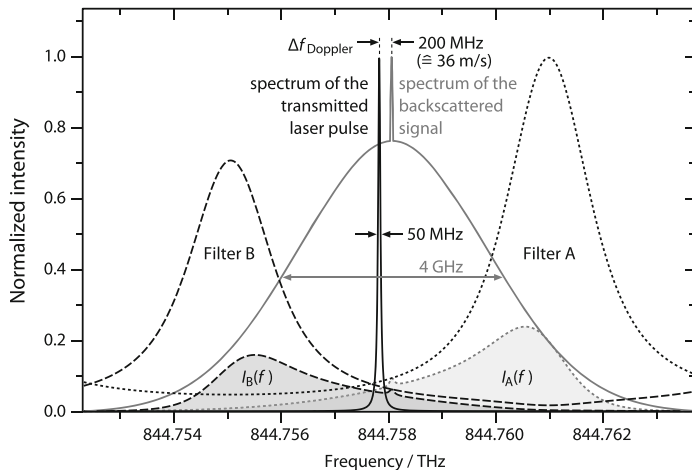


Fig. 25.11 Wind measurement using the double-edge technique as utilized for the Aeolus mission: spectral distribution of the transmitted laser pulse (black) and the backscattered signal (grey) which is composed of the narrowband Mie and the broadband Rayleigh component. The transmission spectra of the two Fabry-Pérot interferometer filters A and B of the Rayleigh channel are shown as dotted and dashed lines, while the filled areas illustrate the respective transmitted intensities $I_A(f)$ and $I_B(f)$ for determining the Doppler shift

signals I_A and I_B transmitted through filters A and B represents a measure of the Doppler shift.

The band-pass filters are realized as Fabry-Pérot interferometers with slightly different length (Sect. 22.4). Using this principle, frequency differences as small as 5 MHz can be resolved despite the large bandwidth of the Rayleigh signal. This corresponds to a wind speed accuracy of 1 m/s.

ALADIN is the most sophisticated laser instrument ever put into orbit, delivering wind information from the ground up to altitudes of 30 km with a vertical resolution of 0.25–2 km depending on altitude. The data from Aeolus contributes to the improvement in numerical weather prediction, as it closes the gaps in the global wind data coverage, especially over the oceans and the tropics. It thus improves the quality of weather forecasts as well as the understanding of atmospheric dynamics and climate processes.

25.4 Holography and Interferometry

Holography is a method for recording and reconstructing the information of light fields and for storing three-dimensional images. For this purpose, the laser light reflected or scattered from an illuminated object (object wave) is superimposed with a reference wave on a recording medium, e.g. a photosensitive layer. As opposed to a photograph, the produced hologram contains the information not only about the

amplitude but also about the phase of the object wave. The holographic image generally bears no resemblance to the object and is unintelligible when viewed under diffuse ambient light. However, the object wave can be reconstructed from the hologram by suitable illumination, so that a three-dimensional image of the object is produced.

The schematic configuration for recording a hologram is depicted in Fig. 25.12a. The holographic process is described by considering the electric fields of the object and reference wave as defined in (14.17). In analogy to (14.18), the amplitudes $E_{A,R}^0(x,y,z)$ and phases $\varphi_{A,R}(x,y,z)$ of the fields can be combined to the complex amplitudes of the object and reference wave $A(x,y,z)$, $R(x,y,z)$ as follows:

$$A = (E_A^0/2) \exp(2\pi i \varphi_A), R = (E_R^0/2) \exp(2\pi i \varphi_R). \quad (25.1)$$

The intensity of the superimposed waves at the plane of the recording medium ($z = 0$) is given by $|A(x,y,0) + R(x,y,0)|^2$. Illumination of the photosensitive medium results in an amplitude modulation $t(x,y)$ which is approximately proportional to the intensity and exposure time:

$$t(x,y) \propto |A + R|^2 = |A|^2 + |R|^2 + AR^* + A^*R. \quad (25.2)$$

Here, A^* and R^* denote the complex conjugate amplitudes. The information about the amplitude and phase of the object wave is recorded in the interference terms $A(x,y,0) \cdot R^*(x,y,0)$ and $A^*(x,y,0) \cdot R(x,y,0)$, respectively. The exposed and developed medium, e.g. photographic plate, is called hologram.

When the hologram is, in turn, illuminated by a wave that is identical to the reference wave R , reconstruction of the original object wave front is obtained (Fig. 25.12b). The field amplitude directly behind the medium reads

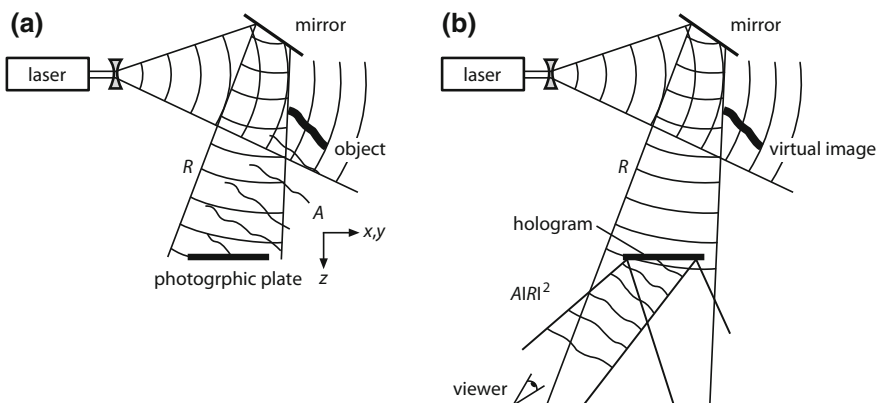


Fig. 25.12 Principle of holography: **a** scheme for recording a hologram, **b** reconstruction of a hologram

$$Rt(x, y) \propto R \left(|A|^2 + |R|^2 \right) + A|R|^2 + A^*R^2. \quad (25.3)$$

Provided that the intensity $|R|^2$ of the reference wave is constant at the hologram plane, the summand $A|R|^2$ in (25.3) represents a field amplitude that is identical to that of the object wave $A(x, y, 0)$. Hence, the reconstructed wave that emerges from the hologram is a replica of the original object wave $A(x, y, z)$.

Note that the whole complex wave front is given in all planes if amplitude and phase of a wave front are known in one plane. The other summands in (25.3) describe additional waves produced behind the hologram which, however, propagate in directions other than the reconstructed wave. A viewer or a camera located in the reconstructed beam thus perceives exactly the same scene as it would be seen by viewing the original object.

The above considerations describe the principle of amplitude holograms where the information is recorded in the form of an interference pattern consisting of bright and dark fringes. Since this pattern absorbs most of the light, the reconstruction efficiency of amplitude hologram is rather low. Therefore, photographic bleaching processes are carried out to produce phase holograms in which the differences in transmission are converted into refractive index variations.

Aside from the classical transmission holograms according to Fig. 25.12, reflection holograms are usually applied for demonstration purposes. The images of these holograms can also be reconstructed using light sources other than lasers, such as light-emitting diodes. Volume reflection holograms are recorded in photographic layers, with the preparation technique similar to transmission holograms described above.

Most holograms like bleached silver halide, photoresist or photopolymers have surface relief patterns which conform with the illumination intensity. In an embossing process, the surface relief pattern can be copied by impressing it onto another material, thus allowing for mass production of the hologram. The material used to make embossed copies usually consists of a polyester base film, a resin separation layer and a thermoplastic film constituting the holographic layer. Additional metallization of the surface, e.g. with aluminum, results in high reflectance, and hence good reconstruction efficiency. Embossed holograms are widely employed on credit cards, banknotes as well as passports, ID cards and other articles used for authentication purposes.

Holographic Interferometry

Holographic interferometry is a powerful optical technique for high-accuracy detection of changes in the shape of three-dimensional objects, e.g. introduced by temperature shifts or mechanical stress. For this purpose, a hologram is illuminated in such a way that the reconstructed wave interferes with the wave that is directly diffracted by the object to be investigated. The interference pattern then characterizes the changes that have occurred in the time between the recording of the

hologram and the observation of the interference. Changes in the state of the object, for instance, as a result of deformation or displacement, will alter the relative phase of the waves, and hence the holographic interference pattern. This allows for nondestructive testing or strain and vibrations analysis in real-time with spatial resolution on the order of the light wavelength.

The technique can be carried out using traditional photographic plates or digital sensor arrays (digital holography). In a variant of holographic interferometry, two (or even more) holograms corresponding to different states of the object are successively recorded on the same medium (double- or multi-exposure holographic interferometry). By simultaneous illumination, the reconstructed waves representing object states existing at different times will interfere, yielding a “frozen fringe” hologram that can be analyzed. A similar approach is the so-called sandwich holography where the interfering waves are recorded on separate holograms.

Time-averaged holography involves creating a hologram while the object is subjected to a periodic vibration or stress. This produces a visual image of the vibration pattern. Since other interferometric methods like speckle interferometry offer several advantages over holographic techniques, the latter is more of historical interest.

Laser Doppler Velocimetry

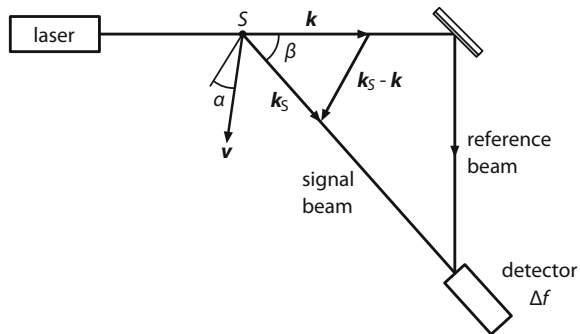
Light scattering from particles can be used in various ways for metrological purposes, e.g. for determining the number and size of dust grains or aerosols in the air. Measurement of the velocity of transparent or semi-transparent fluids and gases also exploits scattering from particles that either occur naturally as impurities or introduced into the medium to be analyzed.

When light is scattered from a moving particle, the frequency of the light is shifted due to the Doppler effect (see Sect. 19.1). The Doppler frequency shift Δf is proportional to the velocity v of the scatterer entrained in the flow. This velocity can be quantified using a configuration as depicted in Fig. 25.13. The scatterer S is illuminated with coherent light from a laser characterized by its wave vector \mathbf{k} . The magnitude of the wave vector is related to the wavelength: $|\mathbf{k}| = k = 2\pi/\lambda$. The wave vector of the light scattered from the particle under an angle β is denoted \mathbf{k}_S . The frequency difference between the incident and the scattered light then reads

$$\Delta f = \frac{1}{2\pi} (\mathbf{k}_S - \mathbf{k}) \cdot \mathbf{v} = \frac{1}{2\pi} (\mathbf{k}_S - \mathbf{k}) \cdot v \cdot \cos \alpha, \quad (25.4)$$

where α is the angle between $(\mathbf{k}_S - \mathbf{k})$ and \mathbf{v} . Since the speed of light is large compared to the flow speed, $|\mathbf{k}_S| \approx |\mathbf{k}|$, so that the frequency shift is approximately given by

Fig. 25.13 Velocity measurement using the reference beam method. The flow velocity v of a particle (scatterer S) is determined from the Doppler frequency shift between scattered and unscattered laser light



$$\Delta f = (2v/\lambda) \cos \alpha \sin(\beta/2). \quad (25.5)$$

This shift can be detected by superposition of the scattered beam with a second (reference) beam that passes outside the flow. Interference of the two beams on a photodetector produces an electric beat signal at the difference frequency Δf which can be analyzed by optical heterodyne detection (Sect. 22.5). Using this technique, flow velocities from 10^{-5} to 10^3 m/s can be measured.

In a different method which is commonly used nowadays, two laser beams are guided through the flow. The beams are usually obtained by splitting a single beam in order to ensure high coherence between them. Visible lasers, e.g. He–Ne, Argon ion or diode lasers, are mostly employed allowing the beam path to be observed. Using lenses, the two beams are focused such that they intersect at their beam waists, producing an interference pattern consisting of straight fringes. Scattering from particles moving through the focal plane leads to a variation of the fringe pattern at a frequency which is equivalent to the Doppler shift between the incident and scattered light. The scattered light is collected by receiving optics and focused onto a photodetector, typically an avalanche photodiode (Sect. 21.4). The Doppler shift, and hence the flow velocity, is then retrieved from the measured amplitude modulation.

Doppler flow velocimetry is used in wind tunnels for testing aerodynamics of vehicles like aircraft, cars or trains. Other applications include velocity measurements of flows in pipes, channels, inside engines or through nozzles as well as the quantification of blood flow in human tissue. The technique is also applied in the fields of environmental research, automation and navigation.

25.5 Free-Electron Lasers, X-Ray and XUV Lasers, Atom Lasers

This section discusses three scientifically interesting laser types relying on physical concepts which differ from the conventional laser types described in the other chapters:

- *Free-electron lasers* (FELs) are based on light emission from electron beams traveling in a periodic magnetic field. This leads to coherent radiation from the infrared to the X-ray spectral region (50 pm to 10 nm), which by far surpasses the spectral range covered by other lasers.
- *Coherent XUV* (100–10 nm) and *X-ray lasers* can also be generated by stimulated emission from ions in laser-induced plasmas.
- *Atom lasers* describe a coherent state of propagating atoms. The term is however misleading since this physical object is not related to the emission of an electromagnetic wave, but to a coherent beam of atoms.

The three concepts, as well as the beam characteristics, are fundamentally different. They are presented here to show future perspectives in the field of laser physics.

Synchrotron Radiation

When charged particles such as electrons move close to the speed of light and are accelerated radially, e.g. by a magnetic field, synchrotron radiation is emitted in a narrow cone tangentially to the particle's orbit. After studying the characteristics of synchrotron radiation in so-called first-generation machines in the late 1960s, second- and third-generation synchrotron sources were built all over the world towards the end of the last century. These conventional synchrotron radiation sources like BESSY I and II in Germany usually consist of an injector, a storage ring and beamlines with experimental stations. The synchrotron radiation produced in such sources is incoherent, as the electrons radiate independently, and the electromagnetic waves emitted from randomly distributed electrons interfere constructively and destructively in time. The intensity of this spontaneous synchrotron radiation thus scales only linearly with the number of electrons.

Much higher intensities are reached in FELs, which are also referred to as fourth-generation synchrotron sources. Here, the electron beam interacts with its own radiation which results in a coherent oscillation of electrons, so that the radiation fields superimpose in phase. Hence, the radiation intensity is proportional to the number of electrons squared, leading to highly-intense optical pulses.

The FEL FLASH (Free-electron Laser Hamburg) of the German Electron Synchrotron research center (Deutsches Elektronen-Synchrotron, DESY) is the world's first soft X-ray FEL. It has been available for experiments since 2005, producing X-ray pulses shorter than 30 fs at wavelengths ranging from 52 to 4 nm. Even shorter wavelengths down to 0.05 nm with pulse durations of less than 100 fs are generated with the European X-ray free-electron laser (European XFEL) which is a European project (TESLA) in collaboration with DESY. The first X-ray pulses were emitted in September 2017 allowing scientists to explore ultra-fast dynamics with ultra-high resolution. For instance, the details of atomic and molecular

nanostructures such as viruses and cells become discernible and chemical reactions happening in the fs-regime can be observed.

A quantity which is often used in the context of synchrotron radiation sources is the spectral brightness (or spectral brilliance) B . It is defined as the number of photons N that are emitted per unit time τ , area A , and solid angle Ω , normalized to the spectral bandwidth $\Delta\nu$:

$$B = \frac{N}{\tau \cdot A \cdot \Omega \cdot \Delta\nu}. \quad (25.6)$$

The unit of the spectral brightness is photons/(s mm² mrad² 0.1% bandwidth). The term “0.1% bandwidth” takes into account that only a portion of the overall bandwidth, e.g. of a continuous spectrum, is used. This portion can, for instance, be extracted by band-pass filters.

Conventional (second- and third-order) synchrotron sources are characterized by a peak spectral brightness from 10^{19} to 10^{25} photons/(s mm² mrad² 0.1% bandwidth). FELs reach even higher values. The European XFEL provides up to 5×10^{33} photons/(s mm² mrad² 0.1% bandwidth), as shown in Fig. 25.14. Synchrotron pulses, however, feature higher repetition rates around 500 MHz, while FELs emit bursts of pulses at a rate of a few Hz. Each burst typically consists of hundreds to thousands of pulses. The XFEL can produce up to 2700 pulses every 0.1 s, corresponding to an effective repetition rate of 27 kHz.

Free-Electron Lasers

In FELs, the radiation is generated by fast electrons that move along curved trajectories through a spatially periodic transverse magnetic field and hence oscillate. The accelerated electrons emit radiation perpendicular to the oscillation direction. The directed radiation thus does not originate from stimulated emission involving transitions between atomic energy levels. Nevertheless, due to the high coherence of the emitted radiation, the term laser is commonly used.

The schematic configuration of a FEL is illustrated in Fig. 25.15. A beam of electrons is accelerated to very close the speed of light. The electron energies are on the order of hundreds of MeV to a few GeV. The ultra-relativistic electron beam passes through a periodic arrangement of magnets with alternating poles which create a static, transverse and spatially periodic magnetic field. Such an arrangement of magnets is called undulator. Owing to the Lorentz force, the electrons travel along a sinusoidal path about the axis of the undulator. The transverse acceleration of the electrons results in the generation of a polarized electromagnetic wave of a specific frequency that is preferably emitted and amplified along the direction of the electrons.

In case of infrared or visible radiation, mirrors are placed at each end of the undulator to form an optical resonator, as depicted in Fig. 25.15. The electron beam

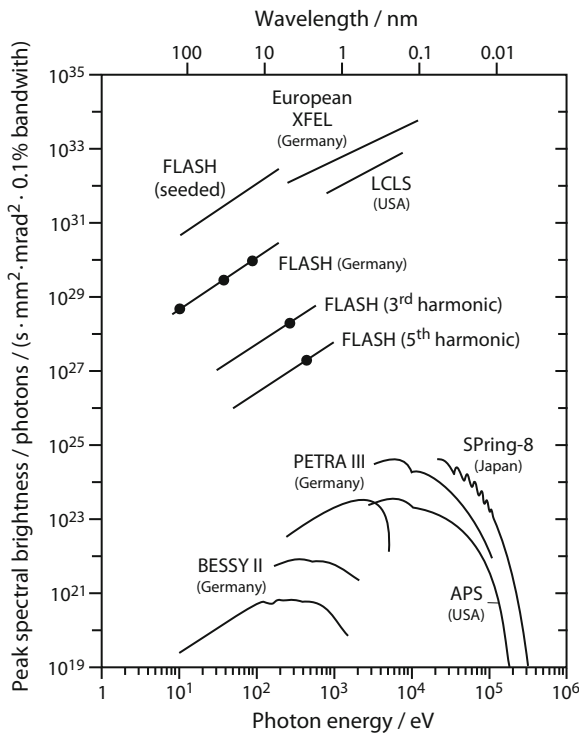


Fig. 25.14 Photon energy and peak spectral brightness of short wavelength FELs (top) and third-generation synchrotron sources. The spots indicate the experimental performance of the FLASH FEL at the fundamental, 3rd and 5th harmonics. Picture adapted from W. Ackermann, Nature Photon. 1, 336 (2007). The highest brightness and shortest wavelength are reached with the European X-ray free-electron laser (European XFEL) which started operation in 2017

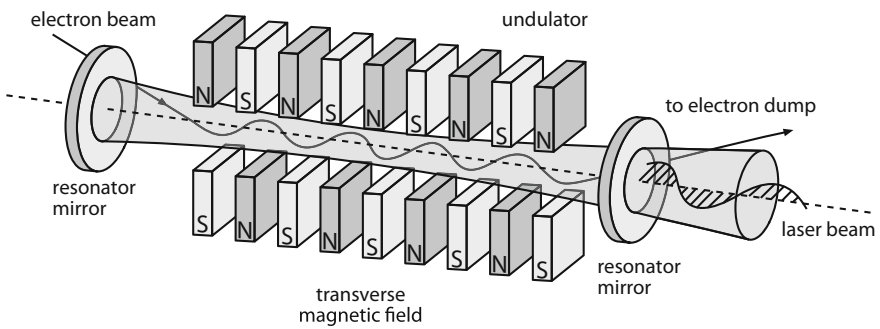


Fig. 25.15 Schematic of a long wavelength free-electron laser (FEL) with undulator, resonator and mirrors. The generation of shorter wavelengths in the VUV or X-ray region is usually achieved without the use of mirrors, e.g. SASE-FEL (self-amplified spontaneous emission free-electron laser). There are also seeded FELs where the shown configuration without a mirror is employed as an amplifier, e.g. FERMI-FEL in Trieste, Italy with photon energies up to 60 eV or the Linac Coherent Light Source (LCLS) in Stanford, USA with 250–9.5 keV

is then injected into the magnetic field structure laterally past the mirrors. FELs emitting shorter wavelengths are operated in a single-pass mode without mirrors due to the lack of low-absorption and highly-reflective mirrors for XUV or X-ray radiation. Here, long undulators are used in order to achieve high single-pass gain, and hence an adequately bright laser beam (superradiance).

For the description of the radiation emitted from the electron, a coordinate system is used which moves with the electron along the beam direction. In this system, the electron performs a sinusoidal oscillation, as shown in Fig. 25.16. The emission wavelength is derived using special relativity, as the electron propagates at a speed of, e.g. $v = 0.99993 c$. Due to length contraction, the undulator period L in the moving system is shortened by the factor $1/\gamma$ with

$$\gamma = \frac{1}{\sqrt{1 - v^2/c^2}} = \frac{E}{mc^2} \quad (25.7)$$

being the relativistic Lorentz factor. E denotes the total energy of the electron, while $mc^2 = 0.511 \text{ meV}$ is the rest energy with the electron mass m and the speed of light c .

In the system moving close to the speed of light, oscillation of the electrons produces a linearly polarized, monochromatic wave with the wavelength

$$\lambda_e = L/\gamma. \quad (25.8)$$

Transformation to the laboratory system leads to a strongly deformed, very narrow radiation lobe (Fig. 25.17). As for synchrotron radiation, emission occurs almost exclusively in the forward direction, with a divergence angle

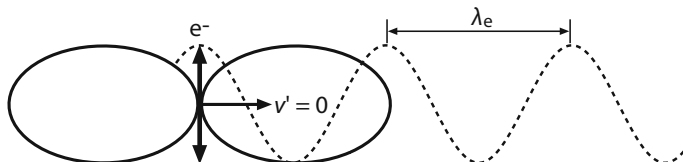
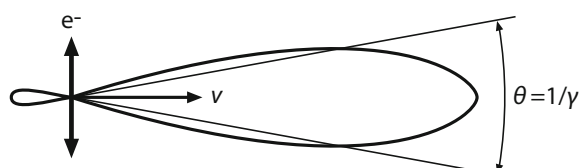


Fig. 25.16 Radiation distribution of an electron observed from an inertial system moving with a relative velocity $v' = 0$. The electron radiates like a dipole (see also Fig. 2.8), λ_e : electron wavelength

Fig. 25.17 Radiation lobe of an electron in the laboratory system. The distribution corresponds to spontaneous emission. $\theta = 1/\gamma$



$$\theta = 1/\gamma. \quad (25.9)$$

In the forward direction, the wavelength is shortened due to the relativistic Doppler effect, so that the wavelength of the radiation observed in the laboratory reads

$$\lambda_l = \lambda_e \cdot \frac{\sqrt{1 - v^2/c^2}}{1 + v/c} = \frac{L}{(1 + v/c)\gamma^2} \approx \frac{L}{2\gamma^2} \quad \text{for } v \approx c. \quad (25.10)$$

For undulator periods of $L = 2$ cm, wavelengths λ_l down to the X-ray spectral region are obtained, as listed in Table 25.1.

Since the initial energy of the electron is partially converted into oscillation energy by the magnetic field B , the right-hand side of (25.7) is not exactly correct. Consequently, the so-called undulator factor K has to be taken into account in (25.10), leading to (e = elementary charge):

$$\lambda_l(k) = \lambda_l \left(1 + \frac{K^2}{2}\right) = \frac{L}{2\gamma^2} \left(1 + \frac{K^2}{2}\right) \quad \text{with } K = \frac{eBL}{2\pi mc}. \quad (25.11)$$

The emission wavelength can thus be tuned by changing the undulator magnetic field in a wide spectral range set by the electron beam energy. The spectral bandwidth depends on the number N of undulator periods, as the electron emits an electromagnetic wave packet with N oscillation cycles. Fourier analysis yields the spectral width (full-width at half maximum):

$$\frac{\Delta\lambda}{\lambda_l} \leq \frac{1}{2N}. \quad (25.12)$$

Equality holds in case of undulator radiation generated in a conventional synchrotron, whereas the spectral bandwidth $\Delta\lambda$ is generally much smaller in FELs.

Undulators should not be confused with wigglers. The latter are characterized by a stronger magnetic field and a longer spatial period of the magnets which are typically arranged in a so-called Halbach array. As a result, the oscillation amplitude is larger, so that the radiation lobes form larger angles with the wiggler axis. Thus, the contributions from each field period thus do not interfere and sum up independently, leading to a much broader energy spectrum compared to undulators. Wigglers were preferentially used in the first synchrotron sources, whereas only undulators are employed in modern third- and fourth-generation synchrotron facilities.

Table 25.1 Wavelengths of a free-electron laser with an undulator period of $L = 2$ cm

Electron energy (meV)	γ	Wavelength λ_l (μm)	Divergence θ (mrad)
10	20	25	25
50	100	1	10
500	1000	10	1

Coherent Synchrotron Radiation by Self-amplified Spontaneous Emission (SASE)

Up to now, only incoherent spontaneous emission was considered. Coherent emission is achieved by the interaction between the light wave and the electrons. Figure 25.18 shows the trajectory of the electron (dashed line) in the undulator together with an incident light wave with wavelength λ . Depending on the relative phase between the electron oscillation and the optical field, the electron is either accelerated or decelerated. If the electric field vector of the light wave E is parallel to the transverse component of the electron velocity v , energy is transferred from the light wave to the electron (Fig. 25.18a). The electron is thus accelerated, and absorption occurs. Conversely, the electron is slowed down, as it transfers energy to the optical field when E and v point in opposite directions. The latter case can be interpreted as light amplification by stimulated emission.

The relative phase between the electron oscillation and the electromagnetic wave varies along the propagation direction since the electrons and the light have slightly different velocities. If the light wave slips exactly by half an optical wavelength in a half-period of the electron oscillation, the relative phase remains constant over the entire undulator. This resonance condition is met if the light wave is exactly one optical wavelength ahead of the electron after one oscillation period:

$$\frac{L}{v} = \frac{L + \lambda}{c} \Leftrightarrow \lambda = \left(\frac{c}{v} - 1\right)L \approx L\left(1 - \frac{v}{c}\right) = \frac{L}{2\gamma^2} = \lambda_l \quad (25.13)$$

Consequently, synchronization only occurs at a certain wavelength λ_l which equals the maximum of the spontaneous emission spectrum in the forward direction according to (25.10) (see Fig. 25.19). At shorter or longer wavelengths, absorption

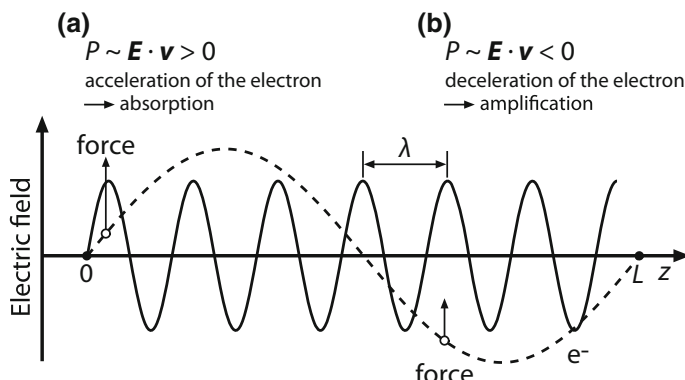


Fig. 25.18 Interaction of a light wave with an electron in an undulator. **a** absorption ($P > 0$), **b** amplification by stimulated emission ($P < 0$). E : electric field, v : transverse electron velocity, P : power transferred to the electron

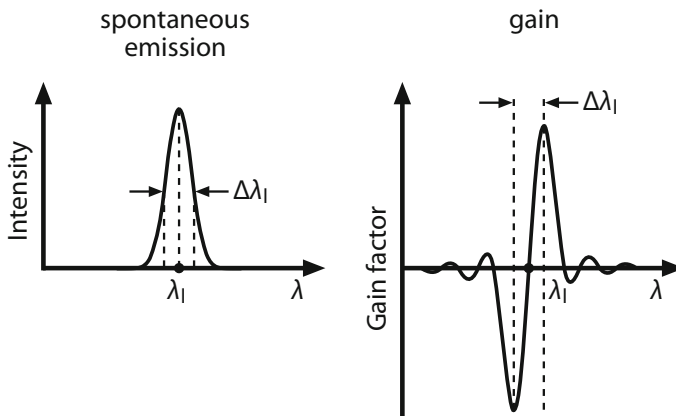


Fig. 25.19 Spectral distribution of spontaneous emission (left) and gain distribution of a free-electron laser (right)

or amplification occurs. The resonance condition is also fulfilled for other multiples of the wavelength ($2\lambda_l, 3\lambda_l, \dots$), giving rise to higher harmonics of the FEL radiation (Fig. 25.14). Even harmonics are generally much weaker than odd harmonics for symmetry reasons.

The equality in (25.13) between the spontaneous undulator emission wavelength and the wavelength fulfilling the resonance condition is the physical basis of self-amplified spontaneous emission (SASE). This term describes the phenomenon that the interaction between the electrons and the electric field of the radiation beam leads to coherent amplification, when the synchrotron radiation becomes sufficiently strong, e.g. in an optical resonator or after a certain propagation length in the undulator. Injected electrons that are initially uniformly distributed along the beam axis are either accelerated or decelerated depending on their phase. This leads to a modulation of the electron density with a period of one wavelength of the optical field. The electrons are thus concentrated in very narrow regions separated by λ_l (microbunching). These microbunches are close to the positions where maximum energy transfer to the optical field takes place. Moreover, the radiation emitted by the bunched electrons is in phase, so that the emitted optical fields add coherently. As the intensity of the radiation field grows, the microbunching is reinforced, so that the radiation intensity increases exponentially as a function of the length of the undulator. This process continues until the radiation reaches a saturation intensity which is several orders of magnitude higher than that of the spontaneous undulator radiation (see Fig. 25.14).

The regime of stimulated synchrotron radiation with very high beam intensities and laser-like properties distinguishes FELs from conventional synchrotron radiation sources. Examples for extreme spectral brightness X-ray SASE-FELs are the Linac Coherent Light Source (LCLS) at the Stanford Linear Accelerator Center (SLAC) in the USA and the XFEL in Europe. The latter facility has a total length of 3.4 km comprising 91 undulator segments each 5 m long.

FELs are often seeded with a laser tuned to the resonance of the FEL in order to improve the temporal coherence and the pulse-to-pulse stability or to synchronize the FEL output with an external signal. For wavelengths down to the XUV spectral range, the coherent seed can be provided via high-harmonic generation of an optical pulse, whereas seeding at X-ray wavelengths is possible by using the FEL output itself which is filtered through a diamond monochromator. This self-seeding technique is utilized in the SASE-FEL at the LCLS facility.

XUV and X-Ray Lasers from Highly-Ionized Plasmas

Common lasers operating in the ultraviolet to infrared spectral region rely on transitions between electronic or vibrational states creating photons with energies up to only about 5 eV ($\lambda = 248$ nm). XUV and X-ray wavelengths correspond to photon energies exceeding 100 eV ($\lambda = 12.4$ nm) which cannot be reached by outer-shell transitions of neutral atoms and molecules. Such high energy differences, however, occur in the outer shells of highly-charged ions. Using Bohr's theory, transitions in the Balmer series ($n = 3 \rightarrow 2$) can be calculated for the hydrogen atom as well as for the He^+ and C^{5+} -ions. According to (5.1) and Fig. 5.1, one obtains $\lambda = 656$ nm for H, $\lambda = 164$ nm for He^+ and $\lambda = 18$ nm for C^{5+} . Highly-ionized plasmas are hence suitable gain media for X-ray lasers, and a number of such lasers emitting from 60 nm down to 1 nm have been produced over the last decades (Table 25.2).

In principle, short-wave X-ray radiation can also be generated by transitions to unoccupied electronic states of inner shells. For instance, K_{α} radiation of copper at 0.15 nm wavelength (8 keV) is produced when a K-shell electron is ejected, and the vacancy is subsequently filled by an electron from the outer L-shell. The excitation of such transitions requires pump sources at even shorter wavelengths. Moreover, the population inversion is influenced by the Auger effect where the filling of the inner-shell vacancy is accompanied by the emission of an electron. This non-radiative relaxation process typically occurs on time scales of 10^{-14} s, thus requiring femtosecond pump pulses in order to achieve stimulated emission at the K_{α} line. While the latter has not been accomplished yet, femtosecond laser radiation at 1.46 nm (849 eV) was demonstrated by inner-shell excitation of Ne 1s using a FEL in 2012.

An overview of short-wavelength lasers realized in highly-ionized ions is provided in Table 25.2. Characteristic beam parameters of plasma-based X-ray lasers are summarized in Table 25.3.

The peak spectral brightness is lower compared to FELs which are, however, also much more complex.

Currently, there are three promising development directions for plasma-based X-ray lasers: collisional-pumped X-ray lasers, particularly in the transient regime, recombination lasers and electrically pumped systems. The three concepts are presented below.

Table 25.2 Selected XUV and X-ray laser transitions (λ wavelength, g gain coefficient, L gain medium length)

Laser transition	Inversion process	λ (nm)	g (cm $^{-1}$)	L (cm)	Pump intensity (W/cm 2)
Kr $^{8+}$ (4d \rightarrow 4p)	Electron collision	32.8	80		
Ti $^{12+}$ (3p \rightarrow 3s)	Electron collision	32.6	35		
Zn $^{20+}$		21.2			
Sc $^{24+}$ (3p \rightarrow 3s)	Electron collision	21.0	30		
Ge $^{22+}$ (3p \rightarrow 3s)	Electron collision	19.6	1.5	10	10^{14}
Mo		18.9			
C $^{5+}$ ($n = 3 \rightarrow 2$)	Recombination	18.2	4.1	0.7	5×10^{13}
Pd $^{22+}$ (4d \rightarrow 4p)	Electron collision	14.7	65		
Ag $^{23+}$ (4d \rightarrow 4p)	Electron collision	13.9	10		
Sn		13.5			
Mo $^{32+}$ (3p \rightarrow 3s)	Electron collision	13.1	4	3.5	4×10^{14}
Yb $^{42+}$ (4d \rightarrow 4p)	Electron collision	5.0	1	3.5	1.4×10^{14}
Al $^{12+}$ ($n = 3 \rightarrow 2$)	Recombination	4.24	10	0.4	
Au $^{51+}$ (4d \rightarrow 4p)	Electron collision	3.56	2		
Ne $^+$ (2p \rightarrow 1s)	Inner-shell photoionization	1.46	65	0.3	

Table 25.3 Characteristic beam parameters of plasma-based X-ray lasers

Laser parameter	Value
Linewidth $\Delta\lambda/\lambda$	$\sim 10^{-3} \dots 10^{-4}$
Divergence	≥ 3 mrad
Pulse duration	$\sim 10 \dots 100$ ps
Pulse energy	$\mu\text{J} \dots \text{mJ}$
Efficiency	$10^{-5} \dots 10^{-7}$
Pulse separation	few min to s (excitation at low pump energy)
Peak spectral brightness	$\sim 10^{28}$ (for Zn $^{20+}$ laser at 21.2 nm)

Electron Collision Excitation

Highly-charged ions for generating X-ray laser emission are produced by exposing a solid material to short pulses from high-power lasers. Excitation of the ions is then achieved by electron collision. Commonly used targets are foils or solid-state surfaces that are irradiated with a line focus on one or both sides over a width of 100 μm and a variable length of up to 5 cm, as shown in Fig. 25.20. Due to the lack of suitable mirrors in the X-ray spectral region, plasma-based X-ray lasers are usually operated without mirrors, so that the beam is generated in a single pass through the high-gain medium. In most cases, a long and weak pre-pulse first creates a pre-plasma at the surface of the target. Afterward, a shorter and more

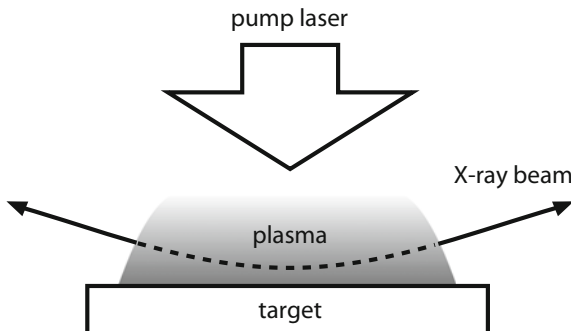


Fig. 25.20 Principle of an X-ray laser. Irradiation of a target with a short laser pulse generates a plasma which acts as an active medium. The gain region has a typical length of 10 to 20 mm and a diameter of 0.1 mm. The X-ray beam is slightly curved inside the active medium, as the electron density decreases with distance to the target

energetic main pulse is used to produce optimum plasma conditions, preferentially at the most stable electron configurations with ten electrons remaining (neon-like) or with 28 electrons remaining (nickel-like). The main pulse also excites the plasma to achieve population inversion between the involved energy levels of the ions.

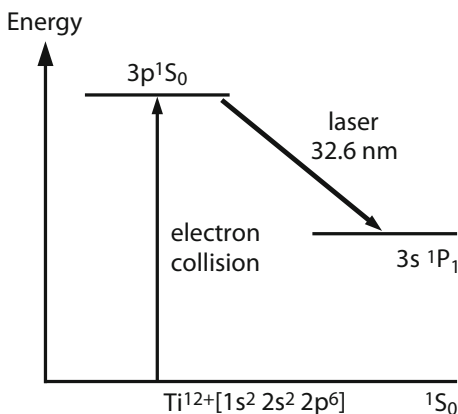
The time window between the pre-pulse and the main pulse is typically on the order of tens of nanoseconds. Generation of the pre-plasma allows for more efficient coupling of the main pulse into the plasma and thus a larger and more homogeneous gain volume. Successful experiments were conducted in several laboratories in the United States, Japan, Great Britain, France and Germany.

Electron collisions in neon-like ions lead to the population of $2s^2 2p^5 3p$ states from which laser transitions to the $2s^2 2p^5 3s$ level occurs. The $3p \rightarrow 3s$ transitions involve the emission of radiation at 32.6 nm for Ti^{12+} or 19.6 nm for Ge^{22+} . Even shorter wavelengths are obtained with the nickel-like Au^{51+} -ion, emitting at 3.6 nm. The used excitation intensities range from 10^{13} to 10^{15} W/cm^2 and the created plasma has a temperature of more than 10^7 K which translates to an electron temperature of 1 keV. The population inversion is determined by the lifetime of the lower laser state which should be as short as possible. The gain coefficient g is usually around a few cm^{-1} .

Originally, plasma-based X-ray lasers required large pump laser systems providing pulse energies of several tens of joules or even kilojoules. A major advance towards table-top configurations was the demonstration of the so-called transient gain regime in neon-like ions in 1995. After creation of a pre-plasma by a nanosecond pre-pulse, a picosecond pulse is used for fast heating of the plasma via electron collision. Additionally, the picosecond pulse initiates the laser process, as it excites electrons preferentially to the upper laser level. The resulting laser transition is illustrated for neon-like Ti^{12+} in Fig. 25.21.

The transient excitation mechanism is characterized by very high gain coefficients of $g > 30 \text{ cm}^{-1}$ as well as short X-ray pulses in the ps-range. In contrast to the previously described quasi-stationary gain regime, the population inversion

Fig. 25.21 Electron collision excitation of a titanium X-ray laser. Neon-like Ti^{12+} -ions are generated in a plasma by a nanosecond pulse, while a picosecond pump pulse excites the upper laser level ($3p$). The laser transition from $3p$ to $3s$ results in X-ray radiation at 32.6 nm wavelength



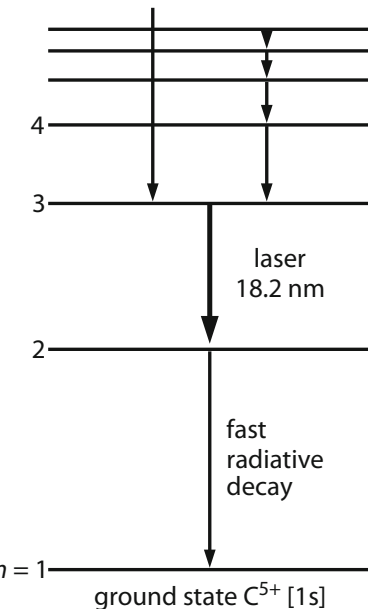
does not depend on the lower level lifetime. Instead, it is governed by the dynamics of the electron collision excitation. Transient X-ray lasers can be operated at significantly lower pump energies of few joules, and hence provide higher efficiencies of better than 10^{-6} .

Recombination Excitation and Electrically-Pumped X-ray Lasers

Pumping of X-ray lasers is also possible by exploiting recombination processes. For this purpose, small fibers, e.g. carbon fibers, with diameters of several μm and lengths of 1–2 cm are vaporized by transverse irradiation from a CO_2 or Nd:glass laser, resulting in a nearly fully ionized plasma. Fast cooling of the plasma involves recombination and the formation of hydrogen-like atoms, whereby excited $n = 3$ states are primarily populated, either directly or through cascading processes from higher electronic states, as shown in Fig. 25.22. The lower laser state $n = 2$ is rapidly depleted by radiative transitions to the ground state $n = 1$, so that population inversion between $n = 3$ and $n = 2$ is achieved. For five-fold ionized carbon (C^{5+}) the laser emission wavelength is 18.2 nm, while gain coefficients from 3 to $6\ \text{cm}^{-1}$ have been demonstrated at pulse durations of up to 100 ns. Recombination-pumped lasers can also be realized for helium- and lithium-like atoms, such as Mg^{9+} , Al^{10+} and S^{13+} . Laser wavelengths as short as 4.2 nm were generated in helium-like Al^{11+} using a Nd-based pump laser with 60 J of pulse energy and pulse duration of 100 ps. The gain was $G = I/I_0 = 50$ at a plasma length of 4 mm, which has to be further increased to be viable for practical applications. In general, recombination lasers offer better energy scaling than X-ray lasers relying on the collisional-excitation pumping scheme described above.

Another interesting pumping mechanism for X-ray lasers, especially for the soft X-ray region, is based on capillary plasma-discharge. Here, a high-current and

Fig. 25.22 Recombination excitation of a carbon X-ray laser at 18.2 nm. The upper laser level of the C^{5+} -ion ($n = 3$) is populated directly or via cascades from higher levels, while the lower level ($n = 2$) has a very short lifetime



ultra-fast (sub- μs) electrical pulse creates a plasma by electron collision in a capillary made of resistant material, e.g. alumina. The capillary is typically 10–20 cm long and has a diameter of several mm. Besides the required ionization state, the electrical pulse also produces a population inversion. In some cases, pre-ionization of the medium is created by means of additional electrical or optical pulses. Gain values of $g \cdot L \sim 15$ have been demonstrated in neon-like Ar^{8+} lasers emitting at 46.7 nm. The beam divergence of such X-ray lasers is very small, ranging from 5 to 10 mrad.

Perspectives of X-ray Lasers

The generation of X-ray laser emission is often accomplished in a single-pass configuration. Since all material show low reflectance in the soft X-ray spectral range, the fabrication of mirrors for X-ray lasers is challenging. In recent years, multi-layer mirrors with reflection coefficients around 50% were developed and successfully employed in half-resonators producing a double-pass through the gain medium. Another approach is the utilization of Bragg reflection in crystals where reflection coefficients above 50% are expected, albeit only for hard X-ray radiation below 1 nm.

X-ray lasers are of particular interest for applications which require high penetration depth and high coherence, such as X-ray holography for three-dimensional imaging of biological structures or X-ray interferometry for material surface

research. Moreover, the short pulse durations enable time-resolved investigations. In lithographic applications, there is a growing demand for compact and coherent extreme ultraviolet (EUV) sources which are employed for the production of computer chips with structure sizes <20 nm. Although ArF lasers at 193 nm wavelength are capable of fabricating such small structures now, table-top plasma-based X-ray lasers emitting around 13 nm offer further miniaturization. While xenon was originally used, tin-based plasmas have become the established EUV light sources lately due to their higher efficiency. Here, Sn droplets are heated to several 10^5 K by CO₂ laser pulses to create a plasma that emits EUV radiation at 13.5 nm wavelength. The radiation is collected by a concave mirror with silicon-molybdenum multi-layer coatings. The mirror selectively reflects the EUV radiation and guides it to the illumination optics for the EUV process. A major problem arises from the fact that the 13 nm radiation is strongly absorbed by air and all materials, so that EUV lithography requires vacuum. Average output powers of 250 W at pulse repetition rates of 100 kHz are pursued. Enhanced performance is achieved by using a pre-pulse at 1064 nm wavelength which heats the Sn droplet so that it expands from 20 to 300 μm , thus improving the absorption of the CO₂ laser pulse.

Coherent Atom Beams

Particle beams, e.g. electron, atomic and molecular beams, have long been used in science and technology. They are streams of particles that move in one direction at approximately uniform speed. Their trajectories are straight lines in the field-free space and form a bundle of particle rays, similar to a bundle of light rays. According to quantum mechanics, every particle has wave-like properties and can be described in terms of a wave function. The squared modulus of the wave function represents the probability density of finding the particle at a given point in space and time. The same principle also applies to particle beams. Because of statistical or thermal variations in particle velocity, the wavelengths and propagation directions of the single particles are slightly different. The individual wave functions are thus uncorrelated, and the particle beam generally shows low coherence. However, by cooling of free atoms to near absolute zero, coherent atom beams can be produced. Heisenberg's uncertainty principle dictates that the position of an atom with mass m is smeared out over a distance given by the thermal de-Broglie wavelength:

$$\lambda = h / \sqrt{2mk_B T}, \quad (25.14)$$

where h and k_B are Planck's and Boltzmann's constants, respectively, and T is the temperature of the gas containing the atoms. At room temperature, λ is much shorter than the average distance between two atoms. Their de Broglie wavelengths are thus uncorrelated. When the gas is cooled down, λ increases according to (25.14), so that the wave functions of adjacent atoms overlap, resulting in a

coherent wave. Below a critical transition temperature, the behavior of the entire system can hence be described by a single macroscopic wave function. This state of matter is referred to as Bose-Einstein condensate (BEC). The condensation is only possible for particles with integer spin (bosons), but not for half-spin particles (fermions) like electrons, as the latter are not allowed to share a quantum state due to the Pauli exclusion principle.

Creation of a BEC traditionally involves the two-step cooling of a cloud of atoms contained in a magnetic trap. In a first step, laser cooling is used to reach temperatures on the order of mK. Here, the atom cloud is irradiated with a laser that is tuned to a frequency slightly below that of an electronic transition of the atom to be cooled. Owing to the Doppler effect, the red-shifted light will be preferentially absorbed by atoms that move towards the light source. Hence, by applying lasers from two opposite directions, the atoms will preferentially absorb photons from the laser beam which points opposite to their propagation direction, so that the momentum of the atoms is decreased. The photon absorption also excites the atoms to a higher energy state. Relaxation to the ground state then leads to the spontaneous emission of photons with the same amount of momentum, but in random directions. Moreover, the frequency and hence the energy of the emitted photons is higher compared to that of the absorbed red-shifted photons. Consequently, the result of the absorption and emission process is a reduction in the momentum and the energy of the atoms, so that the gas cools down and becomes denser.

As the density of the gas rises, it becomes more and more likely that a photon emitted by one atom is absorbed by another atom. Thus, instead of cooling the gas, the photon only moves the heat around. Furthermore, the atom that absorbs the photon recoils in the opposite direction from the atom that emits it, hence creating a repulsive force between the atoms that prevents the gas from reaching a sufficiently high density for a BEC. Therefore, evaporative cooling is utilized in a second step. Here, the fast, high-energy atoms are selectively removed from the atom cloud by allowing them to leave the magnetic trap. Although this process is time-consuming and 99% of the atoms are lost, the ensemble comprising the remaining lower-energy atoms reaches temperatures of a few nK which is below the BEC transition temperature.

The condensation of atoms in the lowest energy state in a magnetic trap is analogous to the formation of a standing-wave in a laser resonator by stimulated emission of photons. Therefore, the trap can be considered as an atomic resonator with magnetic mirrors. Output coupling of a coherent atom beam is achieved by a short high-frequency pulse that changes the direction of the magnetic moment of the atoms, so that some or all atoms can escape from the trap. The coherence of the produced atomic wave was demonstrated by interference experiments with coherent beams originating from two separate condensates. In order to distinguish a BEC confined in a trap from a propagating atomic wave obtained by extraction from a previously realized BEC, the latter is often referred to as atom laser although it is not related to the emission of an electromagnetic wave. The current experimental research aims at the creation of an atom laser directly from a hot beam of atoms without creating a trapped BEC first.

25.6 Gravitational Wave Detection and Extreme High-Power Lasers

The detection of gravitational waves is a milestone in modern science, as it confirmed Einstein's theory of general relativity opened a path for new insights into cosmic events. Gravitational waves are ripples in spacetime that are caused by the acceleration of masses during highly-energetic processes in the universe such as the birth of supernovae or the merging of black holes or neutron stars. The waves deform the spacetime as they travel through the cosmos at the speed of light. On Earth, these distortions are manifested through extremely small length changes which are below the dimensions of elementary particles. Hence, although the existence of gravitational waves was already predicted by Albert Einstein in 1916, about a century passed until they were first observed by the Laser Interferometer Gravitational-Wave Observatory (LIGO).

The LIGO experiment consists of two installations based on Michelson interferometers (Fig. 22.2) which are located at widely separated sites in the United States. The basic measurement principle is explained in Sect. 22.3 and rather simple. However, the LIGO detectors are much more complex than classical Michelson interferometers and represent the largest and most sensitive interferometers in the world. In general, the length sensitivity of an interferometric device increases with the propagation length of the laser beam between source and detector. Therefore, each of the two 4 km-long interferometer arms of LIGO additionally includes a Fabry-Pérot cavity where the light from a Nd:YAG laser performs approximately 280 round-trips before the two beams are superimposed. This results in an effective arm length of 1120 km and enables the detection of relative length changes as small as 10^{-21} . When a gravitational wave passes through the interferometer, both the lengths of the two interferometer arms and the wavelength of the circulating laser light are altered, thus changing the interference pattern. The resulting phase shift is measured as a tiny intensity variation in the detected interference signal which is resolved with an accuracy of about one femtosecond.

The unprecedented sensitivity of the LIGO detector is also possible by ensuring extremely high frequency, power and beam pointing stability of the laser which emits about 200 W of output power at 1064 nm wavelength. Furthermore, variations in the interference pattern that are introduced by sources other than gravitational waves, e.g. thermal or seismic noise, have to be separated from the signal to be detected. Apart from earthquakes, LIGO is capable of sensing vibrations from traffic on nearby roads, ocean waves crashing on shores as well as weather patterns on the other side of the continent. The reduction of noise sources is accomplished by passive and active vibration isolation components. The latter involves the use of position- and vibration-sensors tuned to different frequencies of environmental vibrations, along with actuators that counteract the ground movements, so that the instrument is kept motion-free.

As of the end of 2017, LIGO has made five detections of gravitational waves related to colliding black hole pairs as well as to the collision of two neutron stars.

In the same year, Rainer Weiss, Barry C. Barish and Kip S. Thorne were awarded the Nobel Prize in Physics for their decisive contributions to the LIGO detector and the observation of gravitational waves.

Laser Fusion

The sun gains its energy from nuclear fusion reactions in which four hydrogen nuclei (protons) fuse to form one helium nucleus, releasing energy in the process. Since the 1950s, laboratories in various countries have been attempting to exploit fusion processes on Earth for the controlled generation of energy. A breakthrough towards technical applicability has not yet taken place. In order to initiate fusion processes, it is necessary to sufficiently heat the hydrogen gas so that it passes over into the plasma state. Temperatures exceeding one hundred million degrees are required to reach energies of the hydrogen nuclei that are high enough to overcome the mutual Coulomb repulsion and thus cause fusion. At such extreme temperatures, special devices are necessary to confine the hot plasma. In several fusion experiments, magnetic fields are used for this purpose. In order to achieve higher temperatures and longer periods of confinement, ever larger and more complex fusion plants are being built. However, the technical realization of fusion power plants with magnetic plasma confinement is only foreseen in the next decades.

An alternative approach is provided by laser-induced fusion. The basic idea here is to use a pulsed laser for heating and compressing a target, typically in the form of a solid pellet, which contains a few milligrams of frozen fusion fuel. The latter is usually a mixture of the hydrogen isotopes deuterium and tritium. Using an ultra-short laser pulse, the outer layer of the pellet is heated so that it explodes. As a result, a reaction force is produced that is directed towards the center of the target, thus compressing it. Ideally, a series of powerful shock waves is created which travel through the target and heat the fuel up to point where fusion reactions occur. The resulting plasma is thus not confined by an external field, but by its own inertia. Therefore, the approach is referred to as inertial confinement fusion (ICF). The ICF process requires extreme lasers with energies in the MJ-range to reach the fusion temperatures. Moreover, the energy has to be injected into the target within a few nanoseconds so that the reactions take place before the plasma expands.

Laser-based ICF is currently performed at the National Ignition Facility (NIF), located at the Lawrence Livermore National Laboratory (LLNL) in California. The facility whose layout is sketched in Fig. 25.23 employs the world's largest and most powerful laser. The parameters are summarized in Table 25.4. Since its completion in 2009, the delivered energy and peak power have steadily increased to more than 2 MJ and 500 TW, respectively. The laser is composed of 192 beamlines which are housed in a 200 m-long building consisting of several floors. The laser systems are operated in parallel and driven by a single laser oscillator which ensures the synchronization of the numerous laser amplifiers.

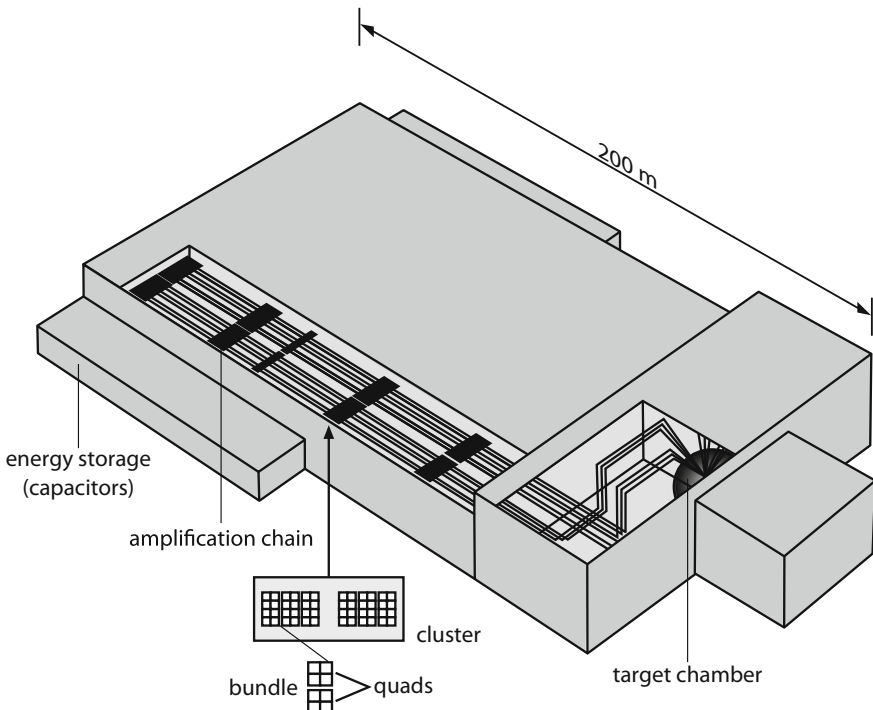


Fig. 25.23 Simplified layout of the National Ignition Facility (NIF) at the Lawrence Livermore National Laboratory (LLNL) in Livermore, California

Tab. 25.4 Laser beam parameters of the NIF laser used for inertial confinement fusion

Laser parameter	Value
Energy per pulse	up to 2.0 MJ
Pulse duration	0.5–20 ns
Pulse peak power	Up to 500 TW
Wavelength	351 nm (frequency-tripling from 1053 nm)
Material	Nd:glass
Costs	3.5 billion USD (constructed 1998–2009)

The weak laser pulse from an ytterbium-doped fiber laser is split and guided to 48 preamplifiers that increase the pulse energy by a factor of 10^{10} to a few joules. The 48 beams forming one cluster are then grouped into four beamlines which are further organized into bundles and quads (Fig. 25.23). Each bundle passes through an array of flash lamp-pumped Nd:glass amplifier slabs, where the injected energy of each beam is amplified to the MJ-range. The use of Nd-doped phosphate glass limits the operation of the laser to one or fewer firings per day due to cooling

requirements. In the future, diode-pumping and alternative solid-state or fiber lasers are envisioned in order to obtain higher repetition rates.

Implosions of the target generate hot electrons which are detrimental to the process, as they preheat the fusion target fuel, and hence hinder its compression. Since the number of electrons is significantly lower at shorter wavelengths, the laser wavelength of each beam is converted from 1053 to 351 nm by a pair of nonlinear KDP and DKDP crystals (Sect. 19.3). The ultraviolet laser beams with a cross-section of $40 \times 40 \text{ cm}^2$ and energy of almost 2 MJ are finally focused from different directions onto the target contained in a concrete-shielded chamber (10 m diameter).

For reaching the required energy densities, accurate beam pointing and precise synchronization of the 192 laser pulses has to be achieved to ensure proper spatial and temporal overlap when irradiating the fuel target which has a diameter of only a few mm. Beam timing is achieved by using delay lines in the individual optical paths, enabling timing accuracy of a few picoseconds. In addition, pulse shaping is crucial for the spherical implosion of the pellet as is desired for ignition. Another important aspect of the fusion process is the preparation of the target which has to be made with extremely high sphericity and surface aberrations of less than a few μm , so that the shock wave from the implosion is focused exactly on the center of the target.

An important milestone towards the commercialization of laser fusion was achieved in 2013, when the NIF demonstrated, for the first time, that a fuel target produced more energy than being supplied to. However, many technical challenges need to be solved to readily achieve ignition at a higher repetition rate. Hence, it is expected that several more decades will pass until the almost inexhaustible supply of nearly pollution-free energy will be available. ICF will soon also be studied in Europe at the Laser Mégajoule (LMJ) facility being built near Bordeaux in France. The LMJ plans to deliver about 1.8 MJ of laser power. At the end of 2014, the first beamline was put into operation. Two more are to be added annually, so that full power will be available around 2025.

Extreme Light Infrastructure (ELI)

The Extreme Light Infrastructure (ELI) project is a multi-sited research infrastructure aiming to host the most intense laser systems worldwide. The infrastructure comprises three facilities being implemented in Eastern Europe each providing several laser sources with extreme pulse energies, pulse durations and repetition rates, thus offering many possibilities for interdisciplinary research and applications in plasma physics, material research as well as medical diagnosis and therapies.

The main objective of the ELI-Beamlines facility in Prague, Czech Republic, is the development of multiple highly-intense lasers which can be used for generating X-radiation for particle acceleration. The ELI Attosecond Light Pulse Source (ELI-ALPS), located close to Szeged in Hungary, represents a unique facility which

provides ultra-short light pulses between THz (10^{12} Hz) and X-ray (10^{18} to 10^{19} Hz) frequency range with high repetition rate. Laser-induced nuclear experiments will be performed at ELI-NP (nuclear physics) to be built in Măgurele near the Romanian capital Bucharest. The location of a fourth research institute devoted to nonlinear quantum electrodynamics and laboratory astrophysics has yet to be decided. The first three facilities are outlined in the following.

ELI-Beamlines close to Prague operates four primary lasers systems to drive different secondary lasers and particle sources. The pulsed laser emission is converted to a femtosecond X-ray beam by nonlinear high harmonic generation which can then be used to accelerate electrons or positrons over a distance of several mm to GeV energies. The generated particle beams can, in turn, be applied for medical cancer therapies.

Three of the four lasers of ELI-Beamlines employ diode-pumped solid-state lasers for pumping broadband amplifiers, while the fourth one uses advanced flash lamp technology. The first laser system generates <20 fs pulses with energy exceeding 100 mJ per pulse at 1 kHz repetition rate. The peak power is thus on the order of 5 TW (5×10^{12} W). Even higher pulse peak powers around 1 PW (10^{15} W) are achieved in the second laser which operates at a lower repetition rate of 10 Hz, but higher energies of about 1 J. This is accomplished by means of optical parametric chirped-pulse amplification (CPA, Sect. 17.5). The third laser uses a titanium-sapphire power amplifier to deliver PW pulses with energy in excess of 30 J and durations <30 fs at a repetition rate of 10 Hz. Extremely high and unprecedented peak power of 10 PW during pulse duration of about 130 fs is provided by the fourth laser. The uncompressed energy can reach almost 2 kJ with a shot rate of 1/min, which represents a milestone in the field of kJ-class lasers. The architecture is based on direct compression of a broadband beam amplified by a combination of different Nd:glass slabs. By focusing the output beam of the fourth laser to a spot area of $10 \mu\text{m}^2$, power densities of up to 10^{23} W/cm 2 are realized, thus offering unique research opportunities for dense-plasma and high-field frontier physics.

ELI-ALPS in Hungary intends to deliver attosecond laser pulses at short ultraviolet and X-ray wavelengths and repetition rates up to 100 kHz. These ultra-short pulses can be used to study electron transfer and other fast processes in atoms, molecules, plasmas and condensed matter. Moreover, dynamic charge distributions in molecular bonds and ionization processes can be investigated. The laser sources of ELI-ALPS are also used to generate surface plasmas on solid materials on nanoscales. In addition, ELI-ALPS aims to generate highly energetic laser pulses with 200 PW peak power.

The research infrastructure at ELI-ALPS is based on four main laser sources: three operating in the regime of 100 W average power in the near-infrared (800–900 nm and 1030 nm) and one at 10 W in the mid-infrared at 3.1 μm wavelength. These systems are designed to deliver ultra-short pulses with unique parameter combinations of pulse duration, repetition rate and pulse energy. Characteristic for this next generation laser architecture is the use of sub-ps fiber oscillators, pulse

amplification in fibers as well as white light-generated seeding pulses which exhibit passive carrier-envelope phase stability.

The *ELI-NP* institute in Romania is devoted to investigating nuclear reactions with innovative laser technology. Laser beams will be used to generate ion and electron beams as well as brilliant gamma radiation to interact with atomic nuclei for the study of nuclear reactions at high energies in short time periods. Gamma radiation will be generated by the interaction of short laser pulses with a relativistic electron beam. This process is called inverse Compton scattering producing brilliant gamma rays similar to a laser beam. The gamma rays with energies about 19 meV are then used to initiate a nuclear reaction.

25.7 Perspectives of Laser Development

Over the past decades, lasers have evolved from complicated laboratory equipment into reliable components that can be integrated into complex opto-electronic systems. This development will continue, as more stable and compact laser systems with improved efficiency and reduced costs are to be expected. The major goals of further laser development are listed in the following and discussed below:

- more compact, efficient and cost-effective diode and solid-state lasers,
- extension of the spectral range, particularly towards shorter wavelengths,
- power scaling to the MW-range (cw) and
- generation of ultra-short pulses in the attosecond-regime.

Dramatic advances are currently being made in the field of semiconductor lasers emitting from the infrared to the near-ultraviolet spectral range. These have replaced low-power gas, solid-state and dye lasers for many applications. The small size, high efficiency, long lifetime and easy handling of diode lasers allow the large-scale production of electro-optical devices for various measurement and analysis techniques as well as for consumer electronics. The combination of semiconductor technology with solid-state lasers will also enable more efficient and compact designs of lasers in the medium- to high-power range which are employed in laser surgery and material processing, thereby promoting the adoption of these applications.

Another development direction of laser technology is the generation of shorter wavelengths in the X-ray spectral range using FELs and plasma-induced X-ray lasers. Work in this direction is not only scientifically motivated but such lasers are also excellent tools for the investigation, manipulation and production of very small structures in nanotechnology. Shortening of the laser wavelength thus allows advancing to submicroscopic, molecular levels.

Further progress is also expected in the field of high-power lasers. As discussed in Chap. 23, power scaling of material processing lasers is ongoing. Over many years, CO₂ lasers delivering cw output powers of several tens of kW have been

available, which is sufficient for many manufacturing applications. Nevertheless, high-performance solid-state lasers represent adequate alternatives, as they allow more flexible beam guiding through optical fibers. Moreover, much more compact and efficient diode laser arrays or stacks with cw powers in the multi-kW-range are increasingly employed for material processing, especially as the beam quality of these devices is continuously being improved. More recent laser applications in complex manufacturing systems, such as rapid prototyping, as well as in microstructure and thin-film technology, are also gaining growing interest. The same holds true for military lasers with applications ranging from gun sights and rangefinders to imaging and communication devices, directed-energy weapons and drones for surveillance and security. In addition, high-power lasers planned for ICF experiments discussed above are also intended to secure the know-how for defense technology in the longer term.

The generation of ultra-short laser pulses represents another topic of current research. In 2017, the world's shortest laser pulse with a duration of only 43 as (1 as = 10^{-18} s) was produced at the Swiss Federal Institute of Technology (ETH) in Zurich, Switzerland. Such short optical pulses pave the way for understanding or even directly manipulating the dynamics during a chemical reaction. Since short optical pulses are necessary to excite X-ray lasers (Sect. 25.5), the developments of short-wavelength and short-pulse lasers are closely interrelated. Short-wavelength and short-pulse laser sources will also become more important for material processing and medicine, as they enable non-thermal material removal via photoablation.

Future Scientific Laser Applications

The laser is a measuring device with unprecedented accuracy which refines our understanding of the universe. Spectroscopic investigations of atoms are used to test fundamental physical theories, while the construction of huge laser facilities has enabled the detection of gravitational waves emitted by very strongly accelerated masses in space. The recent discovery of such waves has marked a milestone in 21st-century science, as it confirmed Einstein's theory of general relativity. At the other end of the length scale, lasers are employed to study physical, chemical and biological phenomena on microscopic spatial and temporal scales. Further advances in the generation of ever-shorter light pulses and X-ray lasers will allow even smaller spatial structures to be analyzed.

Aside from being an accurate measuring device, the laser represents a precise tool. Single atoms can be significantly cooled down by lasers enabling experiments of quantum physics. It is expected that, apart from capturing atoms, lasers will also become capable of manipulating individual atoms so that chemical reactions with isolated atoms can be investigated.

Since the electric fields of intense lasers beams can be much stronger than the electric attraction between nuclei and electrons, nonlinear optical properties of

matter and laser-induced plasmas can be studied. Moreover, advances in ultra-fast lasers open up new possibilities for nanomaterials research. Many interesting effects have been discovered over the last decades and many more are expected in the future.

Future Technical Laser Applications

Material processing, medicine and telecommunication are domains in which lasers are already well-established, and the continuous advance in laser technology will lead to even more intensive use in the future (Table 25.5). For instance, lasers are still relatively rarely employed for manufacturing purposes compared to conventional techniques, so that there is still tremendous potential for expansion of laser applications and associated optics. The evolving field of photonics is anticipated to have the same impact on science and technology in the 21st century as electronics had in the 20th century. Lasers represent key components in photonic devices, very much like integrated circuits in computers or other electronic devices. Thus, it is expected that lasers will become just as relevant for commercial devices as electronic components. Some examples of products that are already encountered in everyday life are laser pointers, Blu-ray players, laser printers and barcode scanners as presented at the beginning of this chapter. Additional consumer goods will be developed and widely disseminated. Laser video displays and projectors have already proven to be successful on the market.

The expanding field of photonics also covers optical computing. This technology involves replacing current computer components with optical equivalents, i.e. using photons instead of electrons for computation. Although optical computers have the prospect to process larger amounts of information than high-speed electronic computers, it is not expected that they will completely supersede electronic devices in the near future. Instead, optical components are likely to be integrated into traditional computers to produce an optical-electronic hybrid with increased performance. The further development of photonic circuits and components will be

Table 25.5 Some current and future laser applications

Current	Material processing Medicine Optical communication Information technology Metrology Sensor technology Entertainment
Future	Optical computing Quantum information technology Laser fusion Gravitational wave detection

additionally driven by the demand for high-bandwidth fiber-optic communication systems.

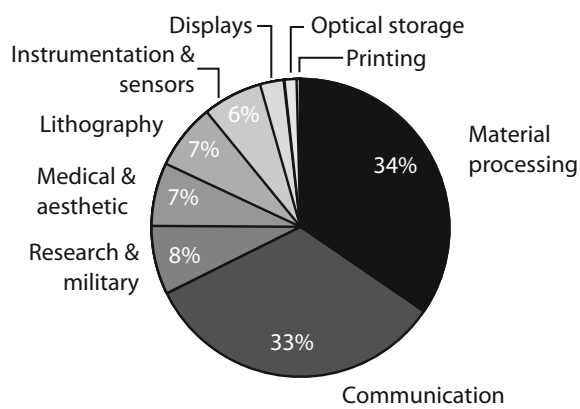
Like optical computing, other laser applications and technologies will only become viable in the long term. For instance, numerous technical challenges have to be overcome in order to realize energy-efficient inertial confinement fusion based on lasers. For this purpose, extensive research is required to develop novel solutions based on physical principles that are yet to be discovered.

25.8 Economic Aspects

In its annual laser market review, the journal Laser Focus World estimated the worldwide laser revenue for 2017 to be 12.3 billion USD. This is an increase of 18% over 2016 which is in large part driven by the material processing sector, where revenues rose by 26%, for fiber lasers alone by 34%. The recent growth can be primarily attributed to the increasing use of lasers and optics in consumer devices, and the fabrication of those devices. For instance, assembly of smartphones involves a number of laser-based processes, including cutting glass, engraving parts and drilling circuit boards. Moreover, many smartphones contain VCSELs for 3D sensing and ranging applications, leading to increased sales of such lasers.

Industrial lasers for material processing represent the largest segment, accounting for more than one-third of the total revenues (Fig. 25.24). Here, high-power fiber lasers experience the biggest growth, followed by diode and excimer lasers used for the manufacture of displays. Disk lasers are also gaining market share, while CO₂ laser sales have declined over the past few years.

Fig. 25.24 Global revenues by laser market segments in 2017 (source Laser Focus World)



Diode lasers account for about half (44%) of the total laser revenue and are particularly important for optical communication and optical storage applications. While the telecommunication sector grows in accordance with bandwidth demand, the sales of optical storage devices like DVD, CD, and Blu-ray media continue to drop, as cloud-based solutions are eliminating the need for large local storage. Regarding the military and defense sector, the laser market is brisk with most lasers being used for gun sights, imaging, ranging and communication applications. The laser business for scientific purposes is especially boosted by China which has been one of the biggest contributors in terms of laser sales for research and development. Spending on medical lasers is highest for beauty and aesthetic applications including tattoo, wrinkle, and hair removal, skin resurfacing, and skin lightening. Another strong area is laser surgery, most markedly for the heart, oral and prostate surgery, where lasers offer better outcomes at less total cost.

There is an enormous growth of the instrumentation and sensing segment which is largely driven by lidar applications of all types (Sect. 25.3) as well as by the emerging facial recognition technology being incorporated in smartphones. Other prominent applications in this domain include spectroscopy, flow cytometry and UV inspection. The fastest growth of all non-material processing areas in terms of laser revenue is seen for the display and entertainment segment, since lasers are becoming the preferred light source for display devices, particularly in cinema projection. Furthermore, the number of lasers being used for laser light shows has exploded over the last few years, primarily due to the availability of efficient high-power diode lasers that have replaced more expensive solid-state lasers.

Finally, it should be noted that the laser itself constitutes only a small part of the total costs of a laser-based device. The costs for beam guidance, safety devices and other peripherals often far exceed that of the laser. Taking this in account, optical and photonic devices and systems for over 100 billion USD are produced annually.

Summary

The invention of the laser in 1960 led to the rapid development of coherent and powerful light sources which enabled the discovery of surprising optical effects. Thanks to the unique properties of laser light, numerous new scientific and industrial applications have become possible, giving rise to the field of photonics which has become an important part of the economy. Comparison of microscopic semiconductor lasers incorporated in smartphones with large-scale laser facilities developed for inertial confinement fusion experiments and gravitational wave detection illustrates the range in size and complexity of modern laser systems. Apart from such prestigious projects as gravitational wave detection, lasers are increasingly ubiquitous in everyday life, to such an extent that people use them without realizing it. With the further advances in photonics technology, the laser will continue to influence our world in the future.

Further Reading

1. M. Maggiore, *Gravitational Waves* (Oxford University Press, Oxford, 2018)
2. A. McGurn, *Nanophotonics* (Springer, 2018)
3. K.J. Kim, Z. Huang, R. Lindberg, *Synchrotron Radiation and Free-Electron Lasers* (Cambridge University Press, Cambridge, 2017)
4. O. Shulika, I. Sukhoivanov (eds.), *Advanced Lasers* (Springer, 2015)
5. I. Kaminow, T. Li, A. Willner (eds.), *Optical Fiber Telecommunications* (Academic Press, St. Louis, 2013)
6. M. Atef, H. Zimmermann, *Optical Communication over Plastic Optical Fibers* (Springer, 2013)
7. H.P. Freund, *Principles of Free-Electron Lasers* (Springer, Berlin, 2013)
8. H. Zimmermann, *Integrated Silicon Optoelectronics* (Springer, 2013)
9. H. Bjelkhagen, D. Brotherton-Ratcliffe, *Ultra-Realistic Imaging* (CRC Press, 2013)
11. H. Venghaus, N. Grote (eds.), *Fibre Optic Communication* (Springer, 2012)
12. W. Hergert, T. Wriedt (eds.), *The Mie Theory* (Springer, 2012)
13. M.K. Kim, *Digital Holographic Microscopy* (Springer, 2011)
14. G.K. Ackermann, J. Eichler, *Holography—A Practical Approach* (Wiley-VCH, Weinheim, 2007)
15. P. Günter, J.P. Huignard (eds.), *Photorefractive Materials and Their Applications 3* (Springer, 2007)
16. P. Jaeglé, *Coherent Sources of XUV Radiation* (Springer, 2006)
17. L. Pavesi, G. Guillot (eds.), *Optical Interconnects* (Springer, 2006)
18. C. Weitkamp (ed.), *Lidar* (Springer, Berlin, 2005)
19. H.J. Coufal, D. Psaltis, G.T. Sincerbox (eds.), *Holographic Data Storage* (Springer, 2000)
20. P.K. Rastogi (ed.), *Holographic Interferometry* (Springer, 1994)
21. R.C. Elton, *X-Ray Lasers* (Academic Press, 1990)

Index

A

Ablation, 410, 429
Absorption, 29, 435, 445
Absorption coefficient, 29, 410
Acceptors, 24, 168
Additive manufacturing, 420
Aeolus, 473
Aesthetic surgery, 434
Airborne laser scanning, 471
Alexandrite laser, 152, 426
Alkali vapor laser, 86
Ammonium Dihydrogen Phosphate (ADP), 306
Amplified spontaneous emission, 331
Amplifier, 331
Annealing, 418
Anti-reflective coating, 275
Anti-Stokes Raman scattering, 360
Argon ion laser, 32, 36, 80
Atmospheric LAser Doppler INstrument (ALADIN), 473
Atomic metal vapor laser, 71
Atom laser. *See* Coherent atom beams
Atoms, 8
Attosecond pulses, 334, 499
Autocorrelation, 394
Avalanche photodiode, 391
Average output power, 53

B

Band gap, 17, 169
Band structure, 20
Barcode reader, 461
Barium fluoride, 246
BBO, 354

Beam deflectors, 303
Beam expander, 220
Beam parameter product, 222
Beam profiler, 225
Beam quality factor, 222
Beam radius, 211, 215, 224
Beam shaping, 181
Beam splitter, 280
Beam waist, 212
Beam walk-off, 294
Beer-Lambert Law, 29
Biophotonics, 435
Biosensors, 440
Birefringence, 291
Blu-ray, 200, 464
Bolometer, 382
Boltzmann distribution, 34
Bose-Einstein condensate, 493
Bragg configuration, 302
Brewster's angle, 271, 341
Brewster window, 69, 295
Brightness, 228, 481
Brillouin scattering, 284
Broad-area diode laser, 177

C

Cadmium selenide, 354
Cadmium telluride, 246, 306
Calcite, 293, 361
Calcium fluoride, 246
Candela, 381
Carbon nanotube, 311, 321
Carrier-envelope offset frequency, 260, 406
Cataract, 431, 449
Cavity-dumping, 322

- CCD. *See* Charge-coupled device
 CD. *See* Compact disc
 Chalcogenide Infrared (CIR) fibers, 248
 Charge carrier injection, 24
 Charge carriers, 23
 Charge-coupled device, 391
 Chirp, 325
 Chirped mirror, 333
 Chirped-pulse amplification, 332, 498
 Chopper, 299
 CMOS sensor, 394
 Coagulation, 424, 428
 Coherence, 375
 - spatial, 378
 - temporal, 376
 Coherence length, 377
 Coherent Anti-Stokes Raman Scattering (CARS), 439
 Coherent atom beams, 492
 CO₂ laser, 32, 36, 92, 104, 411, 426
 - axial gas flow, 98
 - frequency tuning, 103
 - gasdynamic, 103
 - sealed-off, 99
 COIL. *See* Iodine laser
 Collisional broadening, 37
 Collision of the second kind, 67
 Color centers, 19
 Compact disc, 200, 462
 Complex beam parameter, 210, 213
 Computer-aided designing, 410
 Conduction band, 20, 168
 Confocal parameter, 212
 Cornea, 430, 450
 Corner cube reflector, 273
 Corundum, 18, 293
 Critical angle, 272
 Cr:LiSAF laser, 159
 Cross-phase modulation, 265
 Cross-section, 31, 32, 147
 Cr⁴⁺:YAG, 321
 Crystal field, 18
 Crystals, 306, 353
 - biaxial, 292
 - uniaxial, 292
 Cutting, 411, 414, 429
- D**
- DBR laser. *See* Distributed Bragg Reflector
 De-Broglie wavelength, 182, 492
 Debye-Sears effect, 301
 Dense wavelength multiplexing, 180
 Density of states, 22
 Dermatology, 434
- DFB laser. *See* Distributed Feedback laser
 Diamond, 246, 360, 361
 Dielectric multilayer mirrors, 275
 Diffraction, 208, 342
 Diffraction-limited beam, 181, 213
 Digital versatile disc, 200, 464
 III-V diode laser, 200
 II-VI diode laser, 201
 Diode laser. *See* Semiconductor laser
 Dipole radiation, 42, 483
 Direct diode laser, 413, 421
 Disk laser, 161
 Dispersion, 271, 342, 343, 345
 Distributed Bragg reflector, 189
 Distributed feedback laser, 189, 468
 Divergence, 212, 215
 DKDP, 306, 497
 DLa-TGS, 384
 DNA damage, 448
 Donors, 24, 168
 Doping, 18, 24, 168
 Doppler broadening, 37
 Doppler effect, 349, 473, 478
 Doppler wind lidar, 473
 Drilling, 411
 DVD. *See* Digital Versatile Disc
 Dye laser, 32, 36, 121, 426
 - lamp-pumped, 124
 - laser-pumped, 124
 Dynode, 386
- E**
- EDCDL. *See* External Cavity Diode Laser
 Economic aspects, 502
 EDFA. *See* Erbium-Doped Fiber Amplifier
 Einstein coefficient, 31
 Electron collision, 67, 488
 Electronic levels, 13
 Energy density, 6
 Energy level diagram, 8
 Energy levels, 8
 Energy meter, 382
 ENT surgery, 432
 EOM. *See* Modulators
 Erbium-doped fiber amplifier, 164, 262, 468
 Erbium laser, 147, 426
 Er:YAG laser. *See* Erbium laser
 Etalon. *See* Fabry-Pérot etalon
 European XFEL, 480
 Evanescent wave, 251
 Excimer laser, 32, 36, 114, 426
 External cavity diode laser, 191
 Extraordinary refractive index, 292, 352
 Extreme Light Infrastructure, 497

- Eye, 430, 451
Eye hazards, 450, 453
- F**
Fabry-Pérot etalon, 339, 344, 401
Faraday effect, 309
Faraday rotator, 309
Far-infrared laser, 89
 electrically-pumped, 91
 optically-pumped, 90
Fast axis, 172
Femto-LASIK. *See* LASIK
Femto-photography, 389
Fermi distribution, 22
Fermi level, 23, 168
Few-cycle pulse, 324
Fiber laser, 162, 329, 413
Fibers, 468
 coupling, 181, 248
 damping, 261
 dispersion, 263
 fabrication, 256
 graded-index, 256
 materials, 257
 modes, 253
 nonlinearities, 265
 photonic crystal, 259, 364
 single-mode, 258
 step-index, 255
Finesse, 234, 346, 402
FLASH, 480
Flash lamps, 145
Flow cytometry, 441
Fluorescence, 435
Fluorescence microscopy, 436
Fluorescence spectroscopy, 437
Fluorophores, 436, 437
Four-level laser, 45
Four-wave mixing, 265, 283
Free-electron laser, 479, 481
Free spectral range, 345, 401
Frequency comb, 404
Frequency conversion, 349
Frequency-Resolved Optical Gating (FROG), 395
Frequency stabilization, 370
 lamb-dip, 370
 Pound-Drever-Hall, 373
 pulse build-up time, 372
 ramp-hold-fire, 373
Frequency tuning, 57, 335
 of CO₂ lasers, 103
 of semiconductor lasers, 189
 of solid-state lasers, 151
Fresnel equations, 271
Fresnel number, 243
Frustrated total internal reflection, 299
Fundamental transverse mode, 209, 336
Fused silica, 245, 246
- G**
GaAlAs laser, 184
Gain, 39
Gain coefficient, 39, 147, 361
Gain factor, 33
Gain-guided, 174
Galilei telescope, 221
GaN laser, 200, 464
Gas discharge, 69, 102
Gaussian beam, 209
 focusing, 218
 transformation, 217
Gaussian mirrors, 244
Gaussian profile, 38
Geometrical optics, 216
Germanium, 246, 390
Giant pulse, 318
Glan-Foucault polarizer, 295
Glan-Taylor polarizer, 295, 298
Glan-Thompson polarizer, 295
Glasses, 245, 344, 410, 414
Glazing, 417
Gold vapor laser. *See* Atomic metal vapor laser
Gradient mirrors. *See* Gaussian mirrors
Gratings, 342
 arrayed waveguide, 469
 blazed, 343
 holographic, 344
 reflection, 343
 ruled, 344, 399
 volume, 344
Grating spectrometer, 399
Gravitational wave detection, 494
Group velocity dispersion, 325, 364
- H**
Half-wave plate, 296
Hardening, 416
Heat-affected zone, 410
Heat management, 180
Helium-neon laser, 32, 36, 65
He-Se laser. *See* Metal vapor ion laser
Heterodyne detection, 403, 473
Heterostructure, 173
HF laser, 106
Higher harmonic generation, 334, 354
High-power laser, 158, 494
Holes, 20

Holmium laser, 150, 426

Holography, 475

Homogeneous saturation. *See* Saturation

Homostructure, 169, 172

Horizontal-Cavity Surface-Emitting Laser (HCSEL), 175

Host material, 133

Hydrogen atom, 8

I

Illuminance, 382

Image converter, 387

Immunofluorescence, 438

Index-guided, 174

Indirect semiconductor. *See* Semiconductor

Inertial confinement fusion, 495

InGaAs, 185, 390, 393

InGaAsP laser, 184

Inhomogeneous saturation. *See* Saturation

Injection seeding, 339

Instantaneous frequency, 325

Insulators, 17

Intensity, 6

Interference, 399

Interference filters, 346

Interferometers, 399

double beam, 399

Fabry-Pérot, 401

Fizeau, 403

Fourier transform, 400

Fox-Smith, 340

Michelson, 376, 400

Interferometry, 475

Iodine laser, 74

J

Jj coupling, 12

Jl coupling, 12

K

KDP, 306, 354, 497

Kepler telescope, 219

Kerr cell, 308

Kerr effect, 308, 363

Kerr lens, 328

Knife edge method, 227

KrF laser. *See* Excimer laser

Krypton ion laser, 83

KTP, 354, 461

L

Larynx, 433

Laser array, 177

Laser-Assisted In-Situ Keratomileusis (LASIK), 425, 431

Laser bar, 177

Laser cladding, 417

Laser classes, 455

Laser Doppler velocimetry, 478

Laser fusion, 495

Laser goggles. *See* Laser safety eyewear

Laser Interferometer

Gravitational-Wave Observatory (LIGO), 494

Laser Mégajoule, 497

Laser pointer, 460

Laser printer, 465

Laser projector, 201, 460, 467

Laser quenching, 417

Laser safety, 445, 457

Laser safety eyewear, 457

Laser safety officer, 457

Laser stack, 177

Laser surgery, 428

Laser types, 51

LBO, 354

Lead-salt diode laser, 199

Lens, 216

Lens equation, 217

Lidar. *See* Light detection and ranging

Lifetime, 31, 147

Light detection and ranging, 149, 185, 470

Linewidth, 35, 60

Liquid crystal laser, 129

Lithium niobate, 306, 352

Lithotripsy, 425, 432

LITT, 428

Littman-Metcalf configuration, 192

Littrow configuration, 191, 343

Lorentzian profile, 35

LS coupling, 11

Lumen, 381

Luminous flux, 381

Luminous intensity, 381

Lux, 382

Lyot filter, 127, 347

M

Macula, 430, 450

Magnesium fluoride, 246

Marking, 418

Master Oscillator Power Amplifier (MOPA),

137, 176

Material processing, 409

Maximum permissible exposure, 455

MBE. *See* Molecular Beam Epitaxy

- Medicine, 423, 426
MERLIN, 359
Metal-organic chemical vapor deposition, 195
Metals, 17, 414
Metal vapor ion laser, 83
Methane fluoride laser. *See* Far-infrared laser
Mica, 293
Microchannel plate, 387
Microchip laser, 321
Micromachining, 412
Mie scattering, 446, 473
Mirrors, 43, 269, 277
 chirped, 333
 dielectric, 275
 metallic, 274
 phase conjugate, 281
Mode-locking, 322
 active, 327
 colliding pulse, 326
 hybrid, 327
 Kerr lens, 328
 passive, 326
Modes, 209
 Hermite-Gaussian, 214, 236
 in glass fibers, 253
 in planar waveguides, 249
 in rectangular waveguides, 253
 Laguerre-Gaussian, 237
 longitudinal, 231, 322
Mode selection, 336
Mode spacing, 232
Modulators, 299, 303
 acousto-optic, 301, 321
 electro-optic, 305, 320
 FTIR, 299, 321
 mechanical, 299
Molecular beam epitaxy, 195
Molecules, 13
MOS capacitor, 391
Moving slit method, 226
- N
National Ignition Facility, 495
Natural linewidth. *See* Linewidth
Nd:Cr:GSGG laser, 143
Nd:glass laser, 32, 36, 139, 146, 498
Nd:YAG laser, 32, 36, 138, 141, 426
Nd:YLF laser, 138, 143, 426
Nd:YVO₄laser, 138, 144
Neodymium laser, 138
Nitrogen laser, 111
Nobel Prize, 174, 200, 393, 404, 438, 469, 495
Noble gas ion laser, 79
Nonlinear optical effects, 350
Non-radiative transitions, 123, 140
Normalized frequency, 253
Numerical aperture, 181, 248
- O
Optical coherence tomography, 441
Optical communication, 201, 467
Optical density, 457
Optical isolator, 308
Optical materials, 245
Optical parametric amplifier, 357
Optical parametric oscillator, 357
Optical phase conjugation, 281
Optical storage, 200, 464
Optical tweezer, 443
Opto-acoustic imaging, 443
Ordinary refractive index, 292, 352
- P
Parity, 12
Penetration depth, 410, 424, 454
Petawatt power, 333, 498
Phase distortion, 282
Phase-matching, 352
Photoablation, 424, 450
Photodiode, 390
Photodiode array, 391
Photodisruption, 450
Photodynamic therapy, 425, 427
Photoelectric effect, 382, 385, 389
Photolithography, 119, 419
Photomultiplier, 386
Photonic crystal fibers. *See* Fibers
Photonics, 469, 501
Photons, 5
Photorefractive keratectomy, 431
Photoresist, 419
Photoresistor, 389
PIN photodiode, 390
Plane wave, 4, 207
p-n diode, 168
p-n junction, 168
Pockels cell, 305, 319
Pockels effect, 305
Polarization, 6, 289
 circular, 290
 elliptical, 290
 linear, 289
Polarization filters, 294
Polarization-maintaining crystals, 144
Polarization multiplexing, 180
Polarizing prisms, 294
Polycrystalline Infrared (PIR) fibers, 248
Polymer laser, 129

Population inversion, 34, 39, 316
 Porro prism, 273
 Power meter, 382
 Prism, 341
 Prism spectrometer, 397
 Propagation constant, 253
 Proustite, 354
 Pulse compression, 332
 Pulsed operation, 315
 Pulse duration, 60
 Pulse peak power, 53
 Pulse repetition frequency, 53
 Pump laser, 155
 Pump mechanisms, 53
 Pyroelectric detector, 384

Q

Q parameter. *See* Complex beam parameter
 Q-switching, 318
 active, 319
 passive, 321
 Quantum cascade laser, 185, 195
 Quantum dot, 23, 184
 Quantum dot laser, 182
 Quantum number, 8, 9
 Quantum well, 23, 26, 183
 Quantum well laser, 182
 Quantum wire, 23, 184
 Quarter-wave plate, 296
 Quartz, 246, 293
 Quasi-phase-matching, 352

R

Racah coupling. *See* j_1 coupling
 Raman fiber laser, 363
 Raman-Nath regime, 301
 Raman scattering, 359, 439
 Raman spectroscopy, 439
 Rapid prototyping, 420
 Rate equations, 45
 Rayleigh length, 212, 218
 Rayleigh scattering, 261, 446, 473
 Recombination excitation, 490
 Reflectance, 43, 233, 270, 346
 Refraction, 270
 Refractive index, 270
 Regenerative amplifier, 331
 Relaxation oscillation, 316
 Resolving power, 344, 346
 Resonators, 231
 losses, 233
 plane-mirror, 231
 spherical-mirror, 234

stability, 240
 unstable, 241
 Retardation plate, 296
 Retina, 430, 450
 Rhodamine 6G, 122
 Ridge waveguide laser, 175
 Roof prism, 273
 Rotational levels, 14
 Round-trip time, 318
 Rubidium laser. *See* Alkali vapor laser
 Ruby laser, 32, 36, 134
 Russell-Saunders coupling. *See* LS coupling

S

Sapphire, 246, 248
 Saturable absorber, 310, 321, 326
 Saturation, 39
 Scattering, 446
 Schawlow-Townes limit, 369
 Second harmonic generation, 351
 Second harmonic imaging microscopy, 438
 Selection rules, 12, 15
 Selective laser melting, 420
 Self-amplified spontaneous emission, 485
 Self-phase modulation, 265, 363, 405
 Semiconductor, 20, 21, 389
 Semiconductor detector, 389
 Semiconductor laser, 165, 426
 fabrication, 196, 418
 frequency tuning, 189
 Semiconductors, 410
 SESAM, 321, 326
 Shot noise, 373
 Silicon, 246, 363, 390, 393, 469
 Single emitter, 178
 Single longitudinal mode, 186, 194, 337
 Singlet state, 121, 436
 Skin damage, 453, 454
 Slow axis, 172
 Solid-state laser, 133, 412
 diode-pumped, 144, 158
 frequency tuning, 151
 lamp-pumped, 144
 Soliton, 266
 Spatial filter, 221
 Spatial hole burning, 337, 363
 Spectral hole burning, 41, 337
 Spectroscopy, 427, 437, 439
 Speed of light, 5
 Spherical wave, 4, 208
 Spiking, 137, 316
 Spontaneous emission, 31
 Squeezed states, 374

- Stability, 367
 frequency, 59, 369
 pointing, 368
 polarization, 368
 power, 367
- Stability diagram, 240
- Stationary laser operation, 44
- Stimulated Brillouin scattering, 265, 284
- Stimulated emission, 32
- Stimulated Raman scattering, 265, 361, 440
- Stokes Raman scattering, 360
- Streak camera, 388
- Supercontinuum, 265, 363
- Superradiance, 42, 483
- Susceptibility, 350
- Synchronous pumping, 328
- Synchrotron radiation, 480
- T**
- Tapered amplifier, 176
- Tattoo removal, 434
- TEA laser, 102
- Telescopes, 219
- TEM00 mode. *See* Fundamental transverse mode
- Terahertz radiation, 330
- Thermal conductivity, 147
- Thermal detector, 382
- Thermal diffusivity, 410
- Thermal expansion coefficient, 147
- Thermocouple, 382
- Thermopile, 382
- Thin-film polarizer, 295
- Three-level laser, 45
- Threshold condition, 43
- Thulium laser, 150, 426
- Time-bandwidth product, 324
- TiSa laser. *See* Titanium-sapphire laser
- Titanium-sapphire laser, 153, 426
- Total internal reflection, 248, 271
- Transitions, 9
- Transmission factor, 43, 233
- Triplet state, 121, 436
- Twisted-mode technique, 338
- Two-photon fluorescence, 438
- U**
- Ultra-short pulses, 128, 329, 388, 394, 417, 500
- Ultrasound, 301, 303
- Uncertainty principle, 36
- Undulator, 481
- Urology, 432
- UV molecular gas laser, 111
- V**
- Vacuum photodetector, 385
- Vacuum tube, 385
- Valence band, 20, 168
- Vaporization, 409, 429, 447
- Velocimetry. *See* Laser Doppler velocimetry
- Verdet constant, 309
- Vertical Cavity Surface Emitting Lasers (VCSEL), 192, 468
- Vibrational levels, 14
- Vibronic solid-state laser, 151
- Volume Bragg grating. *See* Gratings
- W**
- Wave equation, 207
- Waveguide laser, 175
- Wave impedance, 5
- Wavelength, 7
- Wavelength division multiplexing, 329, 468
- Wave vector, 207, 351, 478
- Welding, 411, 415
- Wiggler, 484
- Wollaston prism, 295
- X**
- X-ray laser, 479, 487
- Y**
- Yb:YAG laser, 144
- Ytterbium laser, 156
- Z**
- Zinc selenide, 246
- Zinc selenide laser, 199, 201
- Zinc sulfide, 246